



---

UNIVERSITEIT • STELLENBOSCH • UNIVERSITY

---

**THE GEOLOGY AND PETROLOGY  
OF THE MERELANI TANZANITE  
DEPOSIT, NE TANZANIA**

Bernard Olivier

Dissertation presented for the degree of  
Doctor of Philosophy at the University of  
Stellenbosch, South Africa.

Promoter: Prof R. Scheepers

December 2006

## **Declaration**

I, the undersigned, hereby declare that the work contained in this dissertation is my own original work and that I have not previously in its entirety or in part submitted it at any university for a degree.

Bernard Olivier

Date: 21/04/06

## Abstract

Tanzanite, a blue/violet gemstone variety of zoisite ( $\text{Ca}_2\text{Al}_2\text{O} \cdot \text{AlOH}[\text{Si}_2\text{O}_7][\text{SiO}_4]$ ) is only produced in NE Tanzania. The only known locality is an approximately  $7\text{km}^2$  deposit in the Merelani area. It is one of the most sought after gemstones in the world with an industry sales value of between hundred and fifty and two hundred million dollars per year. At the current production rates and estimated resources the tanzanite deposit has a life expectancy of around 20 years.

Despite the economical and scientific importance as well as the geological uniqueness of the deposit very little research has been conducted on the geology and petrology of the deposit and the characteristics of tanzanite.

The primary aim of the research summarised in this dissertation was to gain an understanding of the geological conditions that led to the formation of this unique variety of zoisite. In order to achieve this, a variety of geological disciplines were addressed including the lithostratigraphic setting, the deformational history, the metamorphic history and conditions, the geochemical and isotopic composition, the mineral chemistry as well as the physical and optical properties of the tanzanite.

Extensive field work was conducted over a seven year period, which included surface and underground mapping, surface trenching, surface and underground core drilling, structural measurements and an intensive sampling programme. Various analytical techniques were used in order to petrologically and mineralogically investigate both the deposit and tanzanite itself, including optical microscopy, XRF analyses, laser-ablation ICP-MS, quantitative chemical analyses by means of the electron microprobe, XRD analyses, back-scattered electron microscopy, isotope analyses, fluid-inclusion studies, Vis/UV/NIR spectroscopy, IR spectroscopy, and EPR studies.

This study revealed an intricate and complex geological history for the formation of tanzanite. The deposition of carbon-rich layers, formed during the development of a sequence of shallow shelf sediments consisting primarily of various organic carbon ( $\delta^{13}\text{C}$  between  $-22,85\text{‰}$  and  $-26,74\text{‰}$ ) -rich mudstone horizons and limestone beds is

seen as the first phase of the mineralisation process. These Archaean sediments were deposited in a back- or fore-arc spreading basin. The organic carbon-rich mudstone layers acted as the first phase of vanadium accumulation in the stratigraphic sequence, and are intercalated with a material with a volcanic origin (metabasites), which most likely contributed to the enrichment of amongst others V.

Early diagenetic processes were followed by an extended metamorphic and deformation (D1) history, reaching upper granulite facies conditions (10 – 12 kbar and 850 °C to 1000 °C) at ca. 1000 Ma. The high-grade metamorphic history was followed by multiphase retrograde deformation events (D2 and D3) that developed as a result of crustal uplift. The D2 event probably occurred between 850 and 600 Ma at P-T conditions estimated at between 8 to 7 kbar and 700 to 650 °C. A third stage of deformation (D3) resulted in the formation of overprinting structures and occurred during the later stages of the Pan-African (550 – 500Ma) event during amphibolite/greenschist facies conditions (7 to 6 kbar and 600 to 520 °C).

The deformational history of the deposit played a critical role in the mineralisation processes. Of the four main deformation events identified, three played a critical role in the mineralisation process. The first event led to the development of early structural features as defined by F1, S1 and L1. This was followed by a multiphase D2 event consisting of three different orders of folding (F2a, F2b and F2c) and the formation of boudinage. The association between tanzanite and boudins as well as the stacking and multiple duplication of the boudinaged ore-zone through isoclinal folding resulted in multiple “ore-shoots”. These ore-shoots follow the plunge of the F2c fold closures and results in mine-able features within the ore-body. The third deformation event led to complex structural overprinting of the earlier fabric as observed in S3 and L3 and resulted in the deformation of the F2 structures through crosscutting F3 folds.

Calc-silicate layers developed in the stratigraphic sequence as a result of metamorphic and metasomatic interaction between calcium enriched (boudinaged calc-silicates) and depleted horizons (graphitic gneisses) during a skarn-forming episode. V-rich green grossular garnet (tsavorite) crystallised in tension zones within and in proximity to the boudins during prograde metamorphism. Tanzanite mineralisation occurred during the

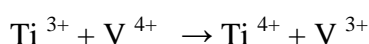


retrograde stages at ca.  $585 \pm 28$  Ma with P-T conditions estimated at ca. 5 to 6 kbar and  $650 \pm 50$  °C.

Two distinctive tanzanite-forming processes are distinguished. The first involves the formation of tanzanite as a result of retrograde reaction of grossular garnet. The second process involves the migration of V and Ca -enriched fluids along brittle shear zones to tension sites where fluids reacted with wall rock during a drop in P-T conditions to precipitate tanzanite.

Fluid inclusion and stable-isotope studies concluded that the ore-forming fluids were derived from the dehydration of the metasedimentary sequence and consisted of a mixture of H<sub>2</sub>O, CH<sub>4</sub>, H<sub>2</sub>S and N<sub>2</sub>.

Mineralogical investigation of tanzanite indicated that trace concentrations of vanadium within its crystals structure causes its blue / violet colour. It was proved that the vanadium originated from the abundant organically derived graphite within the deposit. Spectroscopic and EPR analyses revealed the importance of the Ti<sup>4+</sup> / Ti<sup>3+</sup> ratio within the crystal structure of tanzanite with regard to its colour characteristics. The heating of tanzanite results in a couple valence exchange reaction



which causes an increase the blue / violet colour of tanzanite.

The research conducted led to the development of a successful geological model for the tanzanite mining and treatment activities in the Merelani area of NE Tanzania. As such the research contributed to the establishment of a successful tanzanite mine, based on sound geological principles, which may act as a role model for other gemstone mines worldwide.

## Uittreksel

Tanzaniet is 'n blou edelsteen variëteit van die zoisiet groep van minerale ( $\text{Ca}_2\text{Al}_2\text{O} \cdot \text{AlOH}[\text{Si}_2\text{O}_7][\text{SiO}_4]$ ) en word slegs gemyn in die Merelani gebied in noordoos Tanzanië. Tanzaniet is een van die mees gesogte gekleurde edelstene in die wêreld met 'n industriële verkoopswaarde van tussen honderd en vyftig en twee honderd miljoen Amerikaanse dollar per jaar. Die Merelani myngebied beslaan 'n gebied van ongeveer 7 km<sup>2</sup> en die afsetting het 'n lewensverwagting van ongeveer 20 jaar teen die huidige tempo van ontginning en beraamde reserwes.

Ten spyte van die ekonomiese en wetenskaplike waarde asook die uniekheid van die afsetting is daar baie min navorsing gedoen op die geologie en petrologie van die afsetting en die mineralogiese eienskappe van die mineraal.

Die hoof doel van die navorsing vervat in die proefskrif was om die geologiese toestande wat gelei het tot die vorming van tanzaniet te verstaan. Om die doel te bereik is 'n verskeidenheid van geologiese dissiplines nagevors insluitende die litostratigrafiese opeenvolging, die vervormingsgeskiedenis, die metamorfe toestande en geskiedenis, die geochemie en isotoop samestelling, die mineraalchemie en ook die fisiese en optiese eienskappe van tanzaniet. Laasgenoemde is spesifiek toegepas om die oorsake van kleur en kleur verandering van tanzaniet a.g.v verhitting te bestudeer.

Uitgebreide veldwerk is oor 'n tydperk van sewe jaar onderneem insluitende oppervlak en ondergrondse kartering, oppervlak en ondergrondse kern-boorwerk, sloot-karterings, strukturele data versameling en rotsmonstering. 'n Verskeidenheid analitiese tegnieke is toegepas om beide die afsetting en die tanzaniet petrologies en mineralogies te ondersoek. Die tegnieke het ingesluit; optiese mikroskopie, XSF (X-Straal Fluorisensie) analise, LA IGP-MS (Laser ablasie induktief gekoppelde massa spektrometrie), kwantitatiewe en semi-kwantitatiewe chemiese analyses d.m.v elektron mikrosondes (golflengte dispersie, energie dispersie en teruggekaatste elektron analise), XSD (X-straal diffraksie analises), stabiele isotoop analises, vloeistofinluitsel mikrotermometriese studies, Raman – sonde analise, spektroskopiese analise (sigbare,

ultraviolet en naby-infrarooi golflengtes) en EPR (elektron paramagnetiese resonans) studies.

Die navorsing het 'n ingewikkelde en komplekse geologiese geskiedenis vir die vorming van tanzaniet aan die lig gebring. Koolstofryke moddersteen en kalksteen lae is afgeset tydens die ontwikkeling van 'n opeenvolging van sedimente in 'n vlak see omgewing. Die isotopiese samestelling van die koolstof ( $\delta^{13}\text{C}$  tussen  $-22,85\text{‰}$  and  $-26,74\text{‰}$ ) dui aan dat organiese koolstof dominant was in die opeenvolging. Die Argaiëse sedimente was afgeset tydens die ontwikkeling van agter-eiland kom of 'n kom-omgewing voor 'n subduksiesone. Die organiese koolstofryke moddersteenlae het opgetree as die eerste fase van V verryking in die stratigrafiese opeenvolging. Die stratigrafie is afgewissel met lawa horisonne (nou metabasiet) wat aandui dat die omgewing tydens afsetting in 'n vulkaniese aktiewe sone gelê was en dus moontlik kon bygedrae het tot die V verryking.

Vroeë diagenese is gevolg deur 'n uitgerekte metamorfe en vervormingsepisode (D1) wat hoë granuliet fasies toestande ( $10 - 12\text{ kbar}$  and  $850\text{ °C}$  to  $1000\text{ °C}$ ) bereik het op 'n tydstip ongeveer  $1000\text{ Ma}$  gelede. Die hoëgraadse metamorfe tydperk is gevolg deur ten minste twee retrograad vervormingsepisodes (D2 en D3) wat ontwikkel het as gevolg van korsstyging. Die D2 episode het waarskynlik plaasgevind op 'n tydstip tussen  $850$  en  $600$  miljoen jaar met toestande tussen  $700$  tot  $650\text{ °C}$ . 'n Derde fase van vervorming (D3) het 'n oordruk van strukture tot gevolg gehad en het plaasgevind tydens die latere fases van die Pan-Afrika gebeurtenis ( $550 - 500$  miljoen jaar). Hierdie episode het plaasgevind onder amfiboliet fasies toestande ( $7$  tot  $6\text{ kbar}$  en  $600$  tot  $520\text{ °C}$ ).

Die vervormingsgeskiedenis van die afsetting het 'n kritieke rol gespeel in die ontwikkeling van die tanzaniet mineralisasie. Vier hoof vervormings episodes is herken. Die eerste episode het gelei tot die ontwikkeling van die ouer strukturele verskynsels soos gedefinieer deur F1, S1 en L1. Hierdie episode is gevolg deur 'n multi-fase D2 episode wat saamgestel is uit drie verskillende orde-groottes van verplooiing (F2a, F2b en F2c) asook die ontwikkeling van boudin strukture. Die assosiasie tussen tanzaniet en boudin strukture is duidelik bewys. Die boudin-houdende lae is verder veelvoudig gedupliseer deur isoklinale verplooiing. Ertssones konsentreer rondom die isoklinale plooi-asse in sogenaamde ertsskeute. Die ertsskeute volg die plons van die F2c plooi-asse en definieer hoe konsentrasie tanzaniet sones en dus mynbare gebiede in die

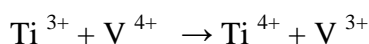
afsetting. Die opeenvolgende vervormingsgeskiedenis kompliseer egter die afsetting verder. 'n Derde vervormingsepisode het gelei tot 'n oordruk van die vroeë maaksels (van F2 en F1) en die uitvolg van die ertsskeute moet ook die ontwikkeling van dwars snydende F3 plooistrukture in ag neem.

Kalk-silikaat lae in die stratigrafiese opeenvolging het ontwikkel deur die metamorfiese en metasomatiese interaksie tussen kalsium ryke (geboudinaseerde kalk-silikate) en kalsium arm horisonne (grafitiese gneisse) gedurende 'n skarn-vormings episode. V-ryke groen grossulariet granaat (tsavoriet) het gekristaliseer in tensiesones binne in en rondom die boudin strukture gedurende pro-graadse metamorfose. Tanzaniet mineralisasie het gevolg na hierdie episode tydens die retrograad stadium van metamorfose, ongeveer  $585 \pm 28$  Ma jaar gelede (5 tot 6 kbar en  $650 \pm 50$  °C).

Twee tanzaniet vormingsprosesse is herkenbaar. Die eerste vind plaas deur die vorming van tanzaniet as 'n retrograad afbreekproduk van grossulariet granaat. Die tweede proses van tanzaniet vorming het plaasgevind deur die migrasie van V en Ca verrykte vloeistowwe langs bros skuifskursones na posisies van rekspanning in boudins waar vloeistowwe gereageer het met die grafitiese wandgesteentes gedurende 'n daling in die druk en temperatuur toestande.

Vloeistofinluitsel mikrotermometrie en stabiele-isotoop studies het bepaal dat die ertsvormende vloeistowwe ontstaan het deur die dehidrasie van die metasedimentêre opeenvolging en saamgestel is uit 'n kombinasie van H<sub>2</sub>O, CH<sub>4</sub>, H<sub>2</sub>S en N<sub>2</sub>.

'n Mineralogiese ondersoek van tanzaniet het aangetoon dat spoorelement konsentrasies van vanadium in die kristal struktuur die blou/ violet kleur veroorsaak. Die studie het ook bewys dat die vanadium afkomstig is van die hoë konsentrasies van organiese grafiet in die afsetting. Spektroskopie en EPR analyses het die belangrikheid van die Ti<sup>4+</sup> / Ti<sup>3+</sup> verhouding binne in die kristalstruktuur met betrekking tot die kleur eienskappe van tanzaniet aan die lig gebring. Die verhitting van tanzaniet veroorsaak 'n gekoppelde valensie uitruilings reaksie:



wat lei tot die blou/ violet kleur van tanzaniet.

Die navorsing vervat in hierdie proefskrif het gelei tot die ontwikkeling van 'n suksesvolle geologiese model vir die ontginning van tanzaniet in die Merelani area in NO Tanzania. Die werk het ook 'n groot bydrae gelewer tot die verstaan van die oorsaak van kleur verandering tydens hittebehandeling. Die navorsing het direk bygedra tot die ontwikkeling van 'n suksesvolle edelsteen myn d.m.v. die toepassing van wetenskaplike geologiese metodiek, wat moontlik as 'n model kan gebruik word vir die bestudering en ontwikkeling van ander edelsteen myne reg oor die wereld.

## **Acknowledgements**

Many thanks to my promoter, Prof Reyno Scheepers with whom I walked a long and fascinating road to try and unravel the deposit. We first visited the tanzanite deposit in January 1999 and never stopped discussing it since.

My sincere thanks to everybody who assisted me on the various aspects of the thesis: Prof A. Kisters and Dr P. Gresse who helped and guided me with the structural aspects of the deposit. Prof den Hartog for all his assistance with the EPR and mineralogical investigations as well as his general assistance during my research period at Gröningen, The Netherlands. Prof I. Buick and Prof A. van den Kerkhof for their assistance with the isotope and fluid inclusion research, respectively. Mr D. Glenister and Mr H. Pienaar for all their help on the gemmological aspects. Loxie Conradie, Stefan Kruger, Johnnie Smit and Esme Spicer for their technical assistance in the Geology Department. Prof G. Stevens for all the help, especially during the last year, with the thesis in general.

I am also grateful for the friendship and assistance of all my fellow students, colleagues and lecturers at the Geology Department, University of Stellenbosch.

To all my friends and colleagues at TanzaniteOne I would like to extend a word of gratitude for their assistance, advice, encouragement and cold beers. I would also like to extend my gratitude to the management of TanzaniteOne Ltd. for their support.

To Mr Tony Hopkins, Mr Ed Nealon and Mr Owen Dix, for all the interesting conversations, not only regarding the tanzanite deposit but also on a variety of other geological topics. In addition, I would also like to thank Mr Ed Nealon, for his support as well as allowing me time off from work to complete the thesis.

Finally, I would like to thank my parents for their love and patience with me during the entire process. I would also like to thank Karen for all her support and attention to detail during the endless proof readings of the thesis. I am also grateful for the understanding of all my friends and loved ones for being pre-occupied with the project.

## Table of Contents

1.	<b>Chapter 1: Introduction</b>	<b>1</b>
1.1	General	1
1.2	Project aims	3
1.3	Thesis structure	4
1.4	Location and access	4
1.5	History of deposit	6
2.	<b>Chapter 2: Regional geology</b>	<b>8</b>
2.1	Introduction	8
2.2	Phanerozoic cover	8
2.3	Mozambique Belt	9
2.4	Tanzanian Craton	14
3.	<b>Chapter 3: Lithostratigraphy of the Merelani tanzanite deposit</b>	<b>15</b>
3.1	Introduction	15
3.2	Data collection	16
3.3	Lithostratigraphy	18
3.4	Metabasite	35
3.5	Neighbouring blocks	36
4.	<b>Chapter 4: Petrography</b>	<b>41</b>
4.1	Introduction	41
4.2	Garnet-sillimanite-biotite gneiss (GNG)	41
4.3	Dolomitic marble	45
4.4	Banded calc-silicate hornfels (BCF)	47
4.5	Graphite - calc-silicate schist (GCS)	51
4.6	Kyanite - graphite gneiss (HW / FW and LK 3, 4, 5, 6)	53
4.7	Graphite - plagioclase gneiss (JW-zone, C- and D-zone)	58
4.8	Pyroxene relict units	60
4.9	Calc-silicate skarn boudins	62
4.10	Low-pressure site pockets and veins	65

4.11	Skarnoid reaction zones	69
4.12	Secondary alteration minerals	71
5.	<b>Chapter 5: Structure and deformation</b>	<b>76</b>
5.1	Introduction	76
5.2	Pre-deformational lithological variation	76
5.3	First phase of structural deformation (D1)	77
5.4	Second phase of structural deformation (D2)	81
5.5	Third phase of structural deformation (D3)	91
5.6	Late stage brittle deformation (D4)	98
5.7	Boudinage	102
5.8	Discussion	116
5.9	Conclusions	122
6.	<b>Chapter 6: Mineral chemistry and classification</b>	<b>124</b>
6.1	Introduction	124
6.2	Garnet - sillimanite - biotite gneiss (GNG)	125
6.3	Banded calc-silicate hornfels (BCF)	134
6.4	Graphite - calc-silicate schist (GCS)	136
6.5	Kyanite - graphite gneiss	140
6.6	Graphite - plagioclase gneiss	141
6.7	Pyroxene relicts and calc-silicate skarn boudins	147
6.8	Low – pressure sites	152
6.9	Possible tanzanite formation reactions	155
7.	<b>Chapter 7: Geochemistry</b>	<b>159</b>
7.1	Introduction	159
7.2	Analytical techniques	159
7.3	Geochemical composition of lithological units	160
7.4	Discriminant analyses	167
7.5	Element behaviour	170
7.6	Conclusions	175
8.	<b>Chapter 8: Stable isotope analyses</b>	<b>176</b>
8.1	Introduction	176



8.2	Analytical technique	176
8.3	Results	177
8.4	Origin of fluids	179
8.5	Conclusions	181
9.	<b>Chapter 9: Conditions of metamorphism in the mining area</b>	<b>183</b>
9.1	Introduction	183
9.2	Thermobarometry of the garnet - sillimanite - biotite gneiss (GNG) units	183
9.3	Isotopic thermometers	186
9.4	General mineral stability fields	187
9.5	P-T Path	190
9.6	Conclusions	192
10.	<b>Chapter 10: Fluid and mineral inclusions associated with tanzanite mineralisation</b>	<b>194</b>
10.1.	Introduction	194
10.2	Microthermometry	194
10.3	Raman analyses	205
10.4	Influence of inclusions on the colour of tanzanite	210
10.5	Mineral inclusions in tanzanite	210
10.6	Conclusions	212
11.	<b>Chapter 11: Protolith</b>	<b>213</b>
11.1	Introduction	213
11.2	Gneisses	213
11.3	Marbles and calc-silicates	219
11.4	Conclusions	224
12.	<b>Chapter 12: Mineralogical properties of coloured zoisite</b>	<b>227</b>
12.1	Introduction	227
12.2	Structural overview of zoisite	227
12.3	Chemical composition of coloured zoisites	230
12.4	UV/Visible/NIR analyses	241

12.5	Fourier Transform Infrared (FTIR) analyses	256
12.6	Electron Paramagnetic Resonance (EPR)	259
12.7	Conclusions	268
<b>13.</b>	<b>Chapter 13: Thermal and radiation treatment of coloured zoisites</b>	<b>270</b>
13.1	Thermal treatment of coloured zoisites	270
13.2	Radiation treatment	284
13.3	Conclusions	285
<b>14.</b>	<b>Chapter 14: Mining implications and deposit overview</b>	<b>288</b>
14.1	Introduction	288
14.2	Mining	288
14.3	Resource estimation	289
14.4	Alluvial tanzanite potential	293
14.5	Other potential economic minerals within the mining area	295
14.6	General implications of this study on the mining of the deposit	296
14.7	Overview of conclusions	298
	<b>References</b>	<b>301</b>
	<b>Addendum A: Drill hole logs and technical specifications</b>	<b>323</b>
	<b>Addendum B: Surface geological map of Block C</b>	<b>324</b>
	<b>Addendum C: Surface map of F3 fold</b>	<b>325</b>
	<b>Addendum D: Microprobe analyses</b>	<b>326</b>
	<b>Addendum E: Norm-calculations</b>	<b>378</b>
	<b>Addendum F: XRF analyses</b>	<b>380</b>
	<b>Addendum G: Correlation matrix</b>	<b>404</b>
	<b>Addendum H: Drill hole plots of (Root1/Root2)*100</b>	<b>407</b>
	<b>Addendum I: Drill hole plots of vanadium concentrations</b>	<b>409</b>
	<b>Addendum J: Fluid inclusion data</b>	<b>411</b>
	<b>Addendum K: Electron microprobe data of coloured zoisite</b>	<b>417</b>
	<b>Addendum L: Laser ablation ICP-MS of coloured zoisite</b>	<b>423</b>

## List of Figures

Figure 1.1	Locality map	2
Figure 1.2	Satellite image of the Lelatema antiform	5
Figure 2.1	Simplified geological map of Tanzania	10
Figure 3.1	Surface geological map of mining area	19
Figure 3.2	Drill hole intersections of the DM2	21
Figure 3.3	Drill hole intersections of the JW-zone	27
Figure 3.4	Drill hole intersections of the BCF	33
Figure 3.5a	Photograph of kyanite crystals from the kyanite-graphite gneiss	37
Figure 3.5b	Photograph of blue zoisite, quartz and calcite in hand sample	37
Figure 3.5c	Photograph of tremolite-actinolite crystals in hand sample	37
Figure 3.5d	Photograph of altered metabasite outcrop	37
Figure 3.6	Photographs of various lithological units in drill core	39
Figure 3.7	Photographs of various lithological units in drill core	40
Figure 4.1	Photomicrographs of the GNG units	44
Figure 4.2	Photomicrographs of the DMD units	46
Figure 4.3	Photomicrographs of the BCF units	50
Figure 4.4	Photomicrographs of the GCS units	54
Figure 4.5	Photomicrographs of the kyanite-graphite gneisses	57
Figure 4.6	Photomicrographs of the graphite-plagioclase gneisses	59
Figure 4.7	Photomicrographs of the banded graphite-plagioclase gneisses	61
Figure 4.8	Photomicrographs of the pyroxene relict units	63
Figure 4.9	Photomicrographs of the skarn boudins and surrounding skarnoid reaction zones	66
Figure 4.10	Photographs of low-pressure pockets within boudins	70
Figure 4.11	XRD pattern of halloysite	74
Figure 4.12	XRD pattern of montmorillonite	75
Figure 5.1	Satellite image of Lelatema Antiform	78
Figure 5.2	Photographs of F1 folds in the metabasite	79
Figure 5.3	Stereoplot of S1 foliations	80
Figure 5.4	Stereoplot of L1 lineations	80
Figure 5.5	NW-SE cross section of mine lithologies	85
Figure 5.6	3-D representation of various folding phases	86
Figure 5.7	Transverse section of isoclinal folding and boudinage	86
Figure 5.8a	Photograph of sheared fold hinges	87
Figure 5.8b	Photograph of parasitic fold on the limbs of the F2c folds	87
Figure 5.9	Photographs of tight isoclinal folding	88
Figure 5.10	Stereoplot of F2c fold axes	89
Figure 5.11	Fold hinge behaviour of F2c folds	89
Figure 5.12	Stereoplot of L2 mineral lineations	90
Figure 5.13	Photograph of F3 associated pegmatite	92
Figure 5.14	Stereoplot of strike and dip of the ore-zone	95
Figure 5.15	Diagrammatic representation of the ore-zone	96
Figure 5.16	Photographs of F3 folding	99
Figure 5.17a	Stereoplot of faults and fractures	101
Figure 5.17b	Rose diagram of fault and fractures	101
Figure 5.18	Chocolate tablet boudinage and boudin axes	102

Figure 5.19	Transverse section of F2c folding within a fold stack	104
Figure 5.20	Photographs of boudins	106
Figure 5.21	Types of boudins and their pressure shadow positions	107
Figure 5.22a	Photograph of a silicified boudin located between fold stacks	108
Figure 5.22b	Photograph of a boudins replaced by pegmatite	108
Figure 5.23	Stereoplot of boudin x-axes orientation	109
Figure 5.24	Photograph of synform fold nose and associated boudinage	113
Figure 5.25	Mapped boudinaged layers	114
Figure 5.26	Photograph of boudinaged layers	114
Figure 5.27	Proposed nomenclature of isoclinal folds within a fold stack	115
Figure 5.28	Stepwise formation of the Lelatema antiform	119
Figure 6.1	Contours of chemical zoning of garnet within the GNG	126
Figure 6.2	Chemical zoning profiles of garnet within the GNG	127
Figure 6.3	Biotite classification diagram for the GNG	129
Figure 6.4	[Ti], [Al] and [Si] correlations for mica from the GNG	130
Figure 6.5	Classification diagram of feldspars within the GNG	132
Figure 6.6	AFM projection of the GNG	133
Figure 6.7	Classification diagram of the feldspar compositions of the BCF and GCS	135
Figure 6.8	Classification diagram of pyroxenes within the GCS and BCF	136
Figure 6.9	Zoning of grossular garnet from the GCS	139
Figure 6.10	Classification diagram of plagioclase within the kyanite-graphite gneiss and graphite-plagioclase gneiss	141
Figure 6.11	Mica classification from the kyanite-graphite gneisses and graphite-plagioclase gneiss	144
Figure 6.12	AFM and AKF projections of graphite-plagioclase gneiss and kyanite-graphite gneiss	145
Figure 6.13	CIPW-norm data plots for graphite-plagioclase gneiss and kyanite-graphite gneiss	146
Figure 6.14	Classification diagram of pyroxene within the boudins and pyroxene relict units	148
Figure 6.15	SiO <sub>2</sub> -Al <sub>2</sub> O <sub>3</sub> -MgO-CaO diagrams of the pyroxene units	151
Figure 6.16	Locality of sample 18	151
Figure 6.17	SiO <sub>2</sub> -Al <sub>2</sub> O <sub>3</sub> -MgO-CaO diagrams of the calc-silicate boudins	153
Figure 6.18	ACF diagram of pyroxene units and calc-silicate boudins	154
Figure 6.19	SEM image of tanzanite bearing rock	157
Figure 6.20	Hand sample indicating tsavorite replacement by tanzanite, quartz and calcite	157
Figure 6.21	Rock specimen showing the replacement of garnet by tanzanite	158
Figure 6.22	Pegmatite associated replacement of zoisite	158
Figure 7.1	Scatterplot of canonical scores from discriminant function	169
Figure 9.1	T-Xco <sub>2</sub> diagram of reaction 18 at P <sub>fluid</sub> = 2 kbar and 7 kbar	191
Figure 9.2	P-T path	191
Figure 10.1	Photomicrograph of tanzanite fluid inclusions	195
Figure 10.2	Frequency histogram of Th values for quartz and tanzanite	197
Figure 10.3	Frequency histogram of Tm values for quartz and tanzanite	197
Figure 10.4	Frequency histogram of Th values for quartz	198
Figure 10.5	Frequency histogram of Tm values for quartz	199

Figure 10.6	Second generation of fluid inclusion within quartz and tsavorite	199
Figure 10.7	Frequency histogram of Th values for tsavorite	200
Figure 10.8	Frequency histogram of Tm values for tsavorite	201
Figure 10.9	Photomicrographs of fluid inclusions within quartz	202
Figure 10.10	Raman spectrum of fluid inclusions in quartz	206
Figure 10.11	Raman spectrum of fluid inclusions in quartz (type 2)	207
Figure 10.12	Raman spectrum of fluid inclusions in tanzanite	208
Figure 10.13	Raman spectrum of the structural bands of tanzanite	208
Figure 10.14	SEM image of mineral inclusions within tanzanite	211
Figure 11.1	Chemical classification of the gneisses	215
Figure 11.2	Normalised spider diagrams of gneisses	217
Figure 11.3	Normalised REE plots for gneisses	218
Figure 11.4	Normalised spider diagram for marble composition	220
Figure 11.5a	Normalised REE patterns of the dolomitic marble	222
Figure 11.5b	Normalised REE pattern of the calc-silicate boudins	222
Figure 11.6	Normalised REE patterns of the calc-silicate boudins, marbles, GCS and BCF units	223
Figure 12.1	Octahedral chains in zoisite	228
Figure 12.2	Structure of zoisite	229
Figure 12.3	Vanadium zonation analyses in zoisite	236
Figure 12.4	Vanadium and chromium zonation patterns within tanzanite	238
Figure 12.5	Photographs of colour zoned zoisites	240
Figure 12.6	Photographs of sample 80	242
Figure 12.7	Electric vector rotational diagram for tanzanite sample	245
Figure 12.8	UV/Vis/NIR spectra of blue zoisite	246
Figure 12.9	UV/Vis/NIR spectra of green zoisite	252
Figure 12.10	UV/Vis/NIR spectra of colourless zoisite	254
Figure 12.11	UV/Vis/NIR spectra of orange zoisite	255
Figure 12.12	FTIR spectra of blue zoisite	257
Figure 12.13	FTIR spectra of colourless zoisite	258
Figure 12.14	EPR spectra of blue zoisite	262
Figure 12.15	EPR spectra of blue zoisite	263
Figure 12.16	High-field EPR of blue zoisite	264
Figure 12.17	Angular rotational EPR diagram of blue zoisite	266
Figure 12.18	EPR spectra of green zoisite	267
Figure 12.19	EPR spectra of blue zoisite	269
Figure 13.1	In situ heating UV/Vis/NIR spectra of blue zoisite	274
Figure 13.2	UV/Vis/NIR spectra of blue zoisite before and after heat treatment	275
Figure 13.3	UV/Vis/NIR spectra of green zoisite before and after heat treatment	276
Figure 13.4	UV/Vis/NIR spectra of colourless zoisite before and after heat treatment	277
Figure 13.5	EPR spectra of blue zoisite before and after heat treatment	280
Figure 13.6	EPR spectra of green zoisite before and after heat treatment	281
Figure 13.7	EPR spectra of colourless zoisite before and after heat treatment	282

Figure 13.8	UV/Vis/NIR spectra of blue zoisite before and after $\gamma$ -radiation	286
Figure 14.1	Longitudinal section of the mining area	290
Figure 14.2	Bravo Shaft decline and drives	291

## List of Tables

Table I	Mineral and general abbreviation list	xviii
Table II	Definition of frequently used terms	xix
Table 3.1	Average strike and dip measurements	20
Table 3.2	Stratigraphy and proposed nomenclature for the lithological units within the deposit	23
Table 3.3	Depth of calc-silicate boudin intersection in drill holes	31
Table 5.1	Plunge and plunge direction of F2c folds	100
Table 5.2	Summary of structural deformation events	122
Table 7.1	Average geochemical composition of the various lithological units within the deposit	166
Table 7.2	Raw coefficients for the canonical variables used in the discrimination functions	168
Table 7.3	Classification matrix obtained from the discrimination functions	169
Table 7.4	Vanadium ICP-MS analyses of graphite	173
Table 7.5	Vanadium ICP-MS analyses of graphite	173
Table 7.6	Vanadium ICP-MS and XRF analyses of graphite	173
Table 8.1	Stable isotope analyses	182
Table 9.1	Thermobarometric calculations from the GNG	186
Table 10.1	Bulk ionic concentrations of fluid inclusions in tsavorite, quartz and tanzanite	204
Table 11.1	REE values of rocks within the deposit	225
Table 12.1	Average and standard error calculations of microprobe data of coloured zoisites	231
Table 12.2	Summary of averages and standard errors of laser-ablation ICP-MS analyses	233
Table 12.3	UV/Vis/NIR spectrophotometer interval and slit size	241
Table 12.4	Colour and orientation of blue zoisite	243
Table 12.5	UV/Vis absorption peaks of blue zoisite	247
Table 12.6	Colour and orientation of green zoisite	250
Table 12.7	UV/Vis absorption peaks of green zoisite	251
Table 12.8	Colour and orientation of colourless zoisite	253
Table 12.9	Colour and orientation of orange zoisite	253
Table 12.10	FTIR peaks zoisite	257
Table 12.11	Angular dependence of Mn <sup>2+</sup> hyperfine splitting resonance	261
Table 14.1	Weight fractions and fraction percentages of soil samples	294

Table I. Mineral and selective general abbreviation list (mineral abbreviations after

Abbreviation	Mineral Name	Abbreviation	Description
Ab	Albite	Afgem	African Gem Resources Limited
Alm	Almandine	Alt	Alteration
An	Anorthite	AIM	Alternative investment market
And	Andradite	BIF	Banded iron formation
Bio*	Biotite	CPR	Competent persons report
Cal	Calcite	cpt	Carat per tonne
Cpx	Clinopyroxene	ct	Carat (5 ct = 1 g)
Czo	Clinozoisite	cts	Carats
Di, Diop*	Diopside	EOH	End-of-Hole (drill hole)
Dol	Dolomite	EPR	Electron paramagnetic resonance
En	Enstatite	FW	Footwall
Fs	Ferrosilite	gpt	Gram per tonne
Grp, Gr*	Graphite	HMS	Heavy media separation
Grs, Gross*	Grossular	HREE	Heavy rare earth element
Grt	Garnet	HW	Hanging wall
Kfs	K-feldspar	IR	Infra red
Ky	Kyanite	LOI	Lost on Ignition
Mc	Microcline	LREE	Light rare earth element
Me*	Meionite	NIR	Near infra red
Opx	Orthopyroxene	REE	Rare earth element
Or	Orthoclase	S.G.	Specific gravity
P	Prehnite	t	Tonnes
Plg*	Plagioclase	UV	Ultra violet
Prp	Pyrope	Vis	Visible
Py	Pyrite	VMS	Volcanic massive sulphide
Qtz	Quartz		
Rt	Rutile		
Scp	Scapolite		
Sil*	Sillimanite		
Spess	Spessartine		
Ttn	Titanite		
Tz*	Tanzanite		
Uvaro	Uvarovite		
Wo	Wollastonite		
Zoi*	Zoisite		
Zrn	Zircon		

Kretz, 1983, except where indicated with an \*).

*Table II. Definition of frequently used terms.*

Term	Definition
Alteration minerals	Secondary minerals that formed in the upper portions of the deposit due to weathering caused by a surface oxidation table.
Calc-silicate hornfels	A group of hornfels that forms from the thermal alteration of impure carbonate units such as limestone. The rock is usually fine-grained with no distinct foliation but is often banded. Unlike a standard hornfels it is not necessary dark in colour and occurs in shades of light grey.
Metasomatism	The process of changing the chemical composition of a rock through interaction with fluids. It can occur through the action of fluids from an igneous or metamorphic origin and creates skarns and greisens. Since metamorphic reactions are fluid driven, metamorphism and metasomatism almost always occur together. When it is associated with shear zone, as is the case with the Merelani deposit, it results in the shear zone being highly metasomatised and hydrated, while the surrounding rock is often only dehydrated with minor chemical exchange.
Relict	The remainder of the competent unit, usually in the core of the boudin, primarily responsible for boudin formation. It formed from the skarn alteration of the original dolomitic marble unit that was intercalated within the graphitic gneisses.
Skarn	Primarily defined by its mineralogy the rock consists predominantly of pyroxenes, garnet and other calc-silicate minerals. Skarns are in their broadest sense formed by mass and chemical transport and reaction between adjacent lithologies through a variety of metasomatic processes. Skarn formation involve fluids from a magmatic, metamorphic, meteoric or marine source and therefore need not be igneous in origin. Two adjacent sedimentary layers such as a black shale and a limestone may react to exchange metals and fluids during metamorphism, creating a skarn.
Skarnoid	A rock intermediate between a purely metamorphic rock and a purely metasomatic skarn. It is normally created by the interaction between metamorphic-sedimentary layers and is also known as chemical skarns.



# Chapter 1

## Introduction

### 1.1. General

Tanzanite is a blue / violet vanadium-bearing gemstone variety of zoisite ( $\text{Ca}_2\text{Al}_3(\text{SiO}_4)_3(\text{OH})$ ) which only occurs in the Merelani area of NE Tanzania (Figure 1.1). The deposit covers an area of approximately 7 km by 1 km and its current estimated life expectancy is less than 20 years. Tanzanite is one of the most sought after gemstones in the world and has an estimated yearly industry sales value of around US\$200 million. Since the discovery of tanzanite in the late sixties very little has been published on the geological setting, structural deformation, genesis and colour related mineralogy of this popular gemstone.

This study was developed over the past seven years together with the start and development of the first commercial tanzanite mine and was sponsored by TanzaniteOne Ltd. in order to resolve the lack of geological information and understanding of the deposit. Very little previous geological work and research has been done on the deposit since the discovery of tanzanite in 1967. The lack of geological information can be attributed mainly to the inaccessibility of the deposit due to control by small-scale artisanal mining, a situation that continued until 1998. The publications that were done on the deposit and surrounding areas by e.g. Saria (1973), Dolenc (1976), Malisa (1987), Davies and Chase (1994), Martineau and Davies (1996) and Muhongo et al. (1999) will be discussed in the relevant chapters. The previous work was also hampered by the lack of outcrop, drill core, underground and surface exposures all brought about by the start of the large-scale tanzanite mining from which this study benefited. This study was subsequently initiated by the Gemstone Research Centre (University of Stellenbosch) and sponsored by the only large-scale commercial tanzanite mining company active in the area at that stage (AFGEM Ltd., now TanzaniteOne Ltd.) to address the lack of geological knowledge and understanding of the deposit through a multi-disciplinary approach.

This project was designed to give a general overview of the deposit, thereby creating a base study for future additional work and research to build and develop from. It will describe, for the first time, the lithological units of the Merelani tanzanite deposit as well as their petrography, chemical composition, mineral compositions and protolith. Importantly, it will also describe the complex structural deformational history of the deposit and its association with tanzanite mineralisation and subsequent mining. New data will be presented on the mineralogy of tanzanite and other coloured zoisites from the Merelani deposit, indicating the source of colour as well as the reasons for the colour change of tanzanite as a result of heat treatment.

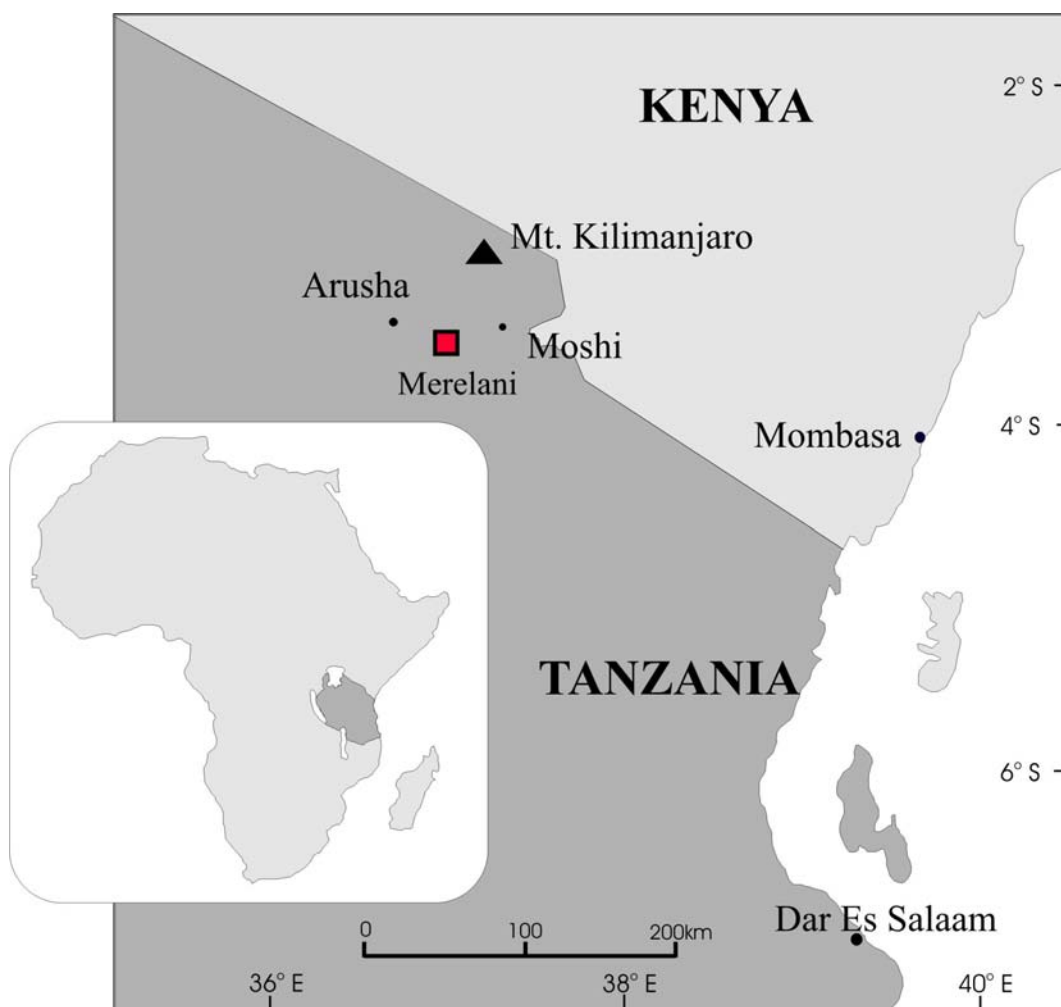


*Figure 1.1. The Merelani tanzanite deposit is situated in north-eastern Tanzania, approximately 70 km southwest of Mt. Kilimanjaro, between the towns of Arusha and Moshi.*

## 1.2. Project aims

The project aims to provide a general overview of the geology of the tanzanite deposit as well as to describe the colour related mineralogy of tanzanite by employing the following methods:

- Investigation of the lithological units within the tanzanite deposit through logging and sampling of over 2 500 m of drill core.
- Mapping of outcrops as well as large areas exposed through trenching.
- Petrographic investigations of over 400 samples was conducted in order to mineralogically and texturally describe and characterise the various lithological units associated with the tanzanite deposit.
- Detailed structural investigation of the deposit in order to describe the deformation of the ore-zone and the controlling factors for tanzanite mineralisation.
- Mineralogical investigation by microprobe analyses of the various minerals within the tanzanite deposit. This was done in order to classify and describe the various minerals present within the deposit, as well as the mineralogical reactions that shaped its evolution.
- Geochemical studies to describe and classify the various lithological units in the deposit. The geochemical database was also used to create a statistical discrimination function of the ore-zone for use in tanzanite exploration.
- Isotopic investigation of the minerals associated with tanzanite in order to investigate the origin of the minerals and hydrothermal fluids.
- Geothermobarometric studies in order to determine the pressure - temperature pathway of the deposit and conditions of tanzanite mineralisation.
- Fluid inclusion studies of tanzanite and associated minerals in order to characterise the fluids involved in tanzanite mineralisation.
- Mineralogical investigation into the origin of colour in tanzanite and other coloured zoisites from the deposit.
- Heat and radiation treatment of tanzanite in order to investigate colour change of tanzanite as a result of heating.

### **1.3. Thesis structure**

The structure of the thesis is governed by the aims of the project as defined by the needs of the mining company (TanzaniteOne Ltd.). The outline of this study as well as the location and history of the deposit is described in Chapter 1. Chapter 2 discusses the regional geological setting of the tanzanite deposit, while Chapter 3 describes and names the various lithological units within the deposit. The petrography of these lithological units is described in Chapter 4. The structural characteristics of the deposit, with specific relevance to the structural controls on tanzanite mineralisation, are described in Chapter 5. In Chapter 6 the geochemical composition of the various units within the deposit are described from an exploration viewpoint. The stable isotope signature of selected minerals associated with tanzanite mineralisation is presented in Chapter 8. Chapter 9 evaluates possible geothermobarometric calculations and estimates the pressure and temperature conditions of the deposit and tanzanite mineralisation. The fluid composition associated with tanzanite mineralisation is investigated by means of fluid inclusion studies in Chapter 10. The protolith of the deposit is described in Chapter 11. Chapter 12 describes the mineralogy of tanzanite with specific detail given to the colour related mineralogy of tanzanite. The reasons for the change in colour of tanzanite as a result of heat treatment will be described in Chapter 13. Chapter 14 discusses the mining and ore resource calculations of TanzaniteOne Ltd. as well as the implications of this study on the mining of tanzanite. It also gives an overview of the main geological features and summarises the most important conclusions derived from this study. Mineral abbreviations follow Kretz (1983), unless otherwise indicated, and are listed in Table I. The definitions of crucial geological terms used in the dissertation are listed in Table II.

### **1.4. Location and access**

Tanzanite is mined in the vicinity of Merelani, a mining village situated on the western flank of the Lelatema mountain range in Tanzania, East Africa (Figure 1.2). The Merelani mining area is located in the north-eastern part of Tanzania (Figure 1.1), situated 16 km southeast of Kilimanjaro International Airport. The deposit is situated between latitude 3°33" and 3°33"5'S and longitude 36°57" and 37°04" E. The nearest towns are Arusha and Moshi, accessible from the mine via a 16 km dirt road to Kilimanjaro airport followed by a 45 km stretch of tar road.

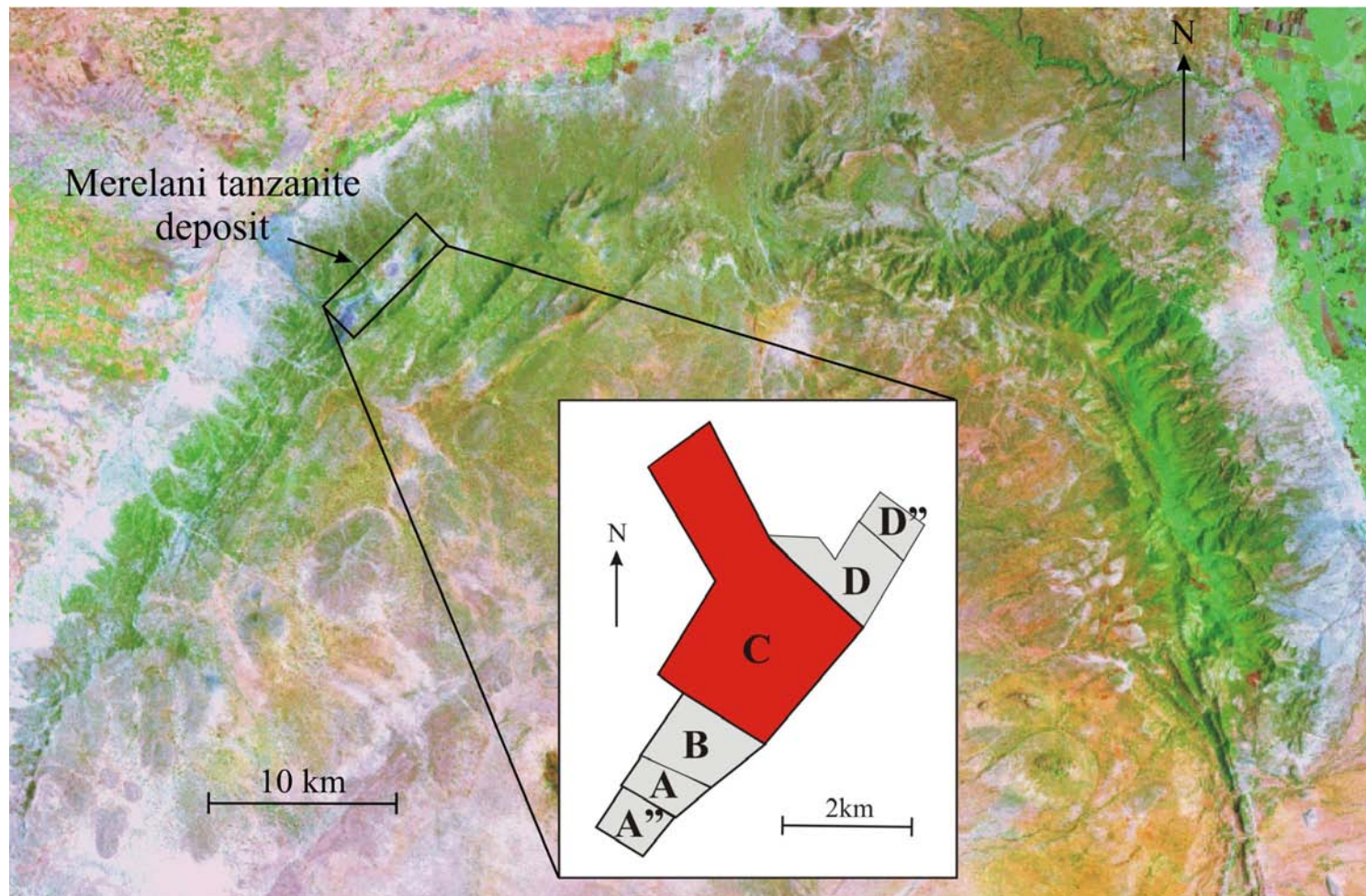


Figure 1.2. False colour satellite image indicating the locality of the Merelani tanzanite deposit on the north-eastern flank of the Lelatema antiform. The inset shows the subdivision of the Merelani tanzanite deposit into five main blocks by the Tanzanian government as well as the newly allocated Block A extension.

## **1.5. History of the deposit**

The discovery of tanzanite reads like a modern day myth with a multitude of variations, including anything from a field fire to lightning resulting in the colouration and subsequent discovery of tanzanite by the local Maasai herdsmen. According to local beliefs, various individuals have been credited with the discovery of tanzanite, including Manuel D'Souza and Ali Jaluawatu. In 1984, the government of Tanzania officially acknowledged Jumanne Ngoma, a local gypsum miner, as the discoverer of tanzanite. He came across the then unknown blue mineral in January 1967, while walking through the field in the Merelani area. Later that year the samples were sent to the Smithsonian Institute and Tiffany's New York for further investigation, which resulted in tanzanite being identified as an unknown gemstone variety of zoisite. Tiffany's subsequently named tanzanite after the country of origin and called it "the gemstone find of the century."

From April 1968 to early 1969, 78 small prospecting/mining claims were allocated by the Tanzanian government. Private prospectors and local miners subsequently worked the deposit until 1971. During this period from 1968 to 1971, Ali Jaluawatu, a Tanzanian farmer, started larger scale mining operations in the area now known as Block C. He apparently produced between 200 and 400 kg of gem-quality tanzanite from approximately 28 000 tons of rock (Davies and Chase, 1994). The main tanzanite-bearing ore-zone is still named after him, namely the JW-zone.

In 1971, the government nationalised all mining activities in Tanzania. The gemstone mines, including the Merelani mines, were subsequently placed under the control of a government owned company called Tanzania Gemstone Industries Ltd. (TGI). In 1972, the State Mining Corporation (STAMICO) was formed and took over control of TGI. During the period between 1972 and 1976 only about 125 kg of tanzanite was recovered (Haule et al., 1978). The Merelani area was under government control until 1983 when the government started its transition period toward privatisation. The deposit subsequently lay abandoned until 1986 when illegal miners started moving into the area. In 1989, SAMAX Ltd. reported approximately 30 000 illegal miners on the deposit, mining in a haphazard and dangerous fashion. In 1990, the Ministry of Home Affairs cleared the area of all illegal miners and subdivided the area into five main areas or

blocks (Figure 1.2). Block C, the largest of the five blocks comprising an area of eight square kilometres was awarded to Graphtan Ltd., a joint venture company managed by the UK-based company SAMAX Ltd.. Graphtan Ltd. predominantly focused on mining graphite and only started a tanzanite evaluation-drilling project in 1996. By the end of 1996, Graphtan Ltd. ceased its operations and was liquidated in mid-1998. At the end of 1998, AFGEM Ltd. conducted a preliminary investigation and subsequently entered a bid for the Block C mining licence. In July 1999, AFGEM Ltd. was awarded the mining licence after submitting the highest tender. AFGEM Ltd. was listed on the Johannesburg Stock Exchange (JSE) in August 2000. In 2003, AFGEM Ltd. was bought by TanzaniteOne Ltd., a UK (AIM) listed company, with a current (April 2005) market capitalisation of £66.5-million.

Mining is currently conducted in a formal as well as informal manner by TanzaniteOne Ltd. and local miners, respectively. The mining area is currently subdivided into six licence areas, namely Blocks A extension, A, B, C, D and D extension (Figure 1.2). Formal mining is conducted in Block C, while Blocks B and D are subdivided into 50 m by 50 m mining plots and are being informally mined by individual local miners or consortiums of local miners. Recently, larger scale locally owned mining commenced in Blocks A and D extension.

## Chapter 2

### Regional Geology

#### 2.1. Introduction

The Merelani tanzanite deposit is situated in the “Ruby belt” as defined by Dirlam et al. (1992) extending from northern Mozambique to central Kenya. The area contains numerous gemstone deposits including ruby, sapphire, emerald, various gemstone varieties of garnet, beryl, alexandrite and tanzanite.

The three main stratigraphic domains in NE Tanzania are the Tanzania Craton, Mozambique Belt and Phanerozoic cover (Figure 2.1). The Merelani area is in close proximity to all three domains (Figure 2.1). The basement of the Mozambique Belt is predominantly Usagaran (Early Proterozoic) with a pervasive Pan-African (Neoproterozoic) overprint (Möller et al., 1998). Tertiary rift volcanic cover rocks occur to the north of the Merelani area, while the Tanzania Craton lies to the west (Figure 2.1). NE Tanzania was affected by different phases of metamorphism (as indeed was much of East Africa) as a result of intercratonic movement and subsequent tightening of basinal structures, creating a complex metamorphic history for the Merelani area.

#### 2.2. Phanerozoic cover

The Phanerozoic cover in NE Tanzania formed partly due to Upper Cenozoic volcanism associated with the East African Rift System and overlies the Usagaran basement (Fairhead, 1976, 1980). The Rift System formed simultaneously with the Cenozoic domal uplift in Kenya and resulted in radial block faulting in northern Tanzania. This caused the formation of a chain of WSW-ENE volcanic centres to which Mt. Kilimanjaro, Mt. Meru and Mt. Lengai belong (Fairhead, 1980) (Figure 2.1). N-S trending rift structures occur between the contact of the Mozambique Belt and the Archaean Tanzania Craton. The main phases of rift faulting in the area are estimated at 2.1 Ma, 1.2 Ma and 0.4 Ma, with the latter two followed by major episodes of magmatism (Dawson, 1992, 1997).



The Cenozoic volcanoes of NE Tanzania formed due to a sequence of volcanic events. The first phase of eruptions consisted of late Miocene alkali diatremes. The next phase involved the extensive extrusion of phonolitic lava from major centres, followed by the first major phase of faulting during the early Pliocene. Basaltic lava, nephelinite-phonolite-trachyte lava and pyroclastic rock were extruded during the Pliocene in rift depressions. The final phase of faulting in the Pleistocene resulted in the formation of numerous small basalt and obsidian cones, large calderas and felsic rocks (Pallister, 1971).

The Central Rift Valley, the Rungwe volcanic rocks and the Meru-Kilimanjaro area in the north, are all associated with the Neogene volcanic event (Harris, 1981). Kilimanjaro consists of alkali gabbro – syenite, - nepheline syenite and phonolite. Mt. Meru consists of nepheline syenite – ijolite ± carbonite and is considered to be an active volcano, last erupting in 1910. Parasitic cones are another prominent feature of the area (Dawson, 2002).

In NE Tanzania, continental facies Karoo sedimentary rocks deposited in the Uppermost Dwyka or Lower Ecca can reach up to 3 000 m in thickness and are continuous with the coastal Karoo of Kenya. The Karoo formations occupy troughs, which were down-warps or faulted precursors of the Tertiary rift depressions (Pallister, 1971).

### **2.3. Mozambique Belt (East African Orogen)**

The Mozambique Belt is a subject of intense controversy, with numerous different opinions on its orogenic setting and age, as well as various viewpoints and estimations regarding the granulite and amphibolite facies metamorphism and associated deformation. It is not the aim of the author to discuss all the different work done on the Mozambique Belt, but rather to give a brief overview of certain aspects of a much debated and poorly understood subject.

The Mozambique Belt (Holmes, 1951) is polycyclic as a cumulative result of multiple collisional orogenies and occurs over a large area of eastern Africa. The Mozambique Belt extends for over 7 000 km from the Arabian Nubian Shield in the north to Antarctica in the south and contains elements of both opening and closure of the

Mozambique Ocean (Cutten, 2002). Burke et al. (1977) first introduced the idea of a plate tectonic origin for the Mozambique Belt, which is now commonly accepted. They indicated that it developed due to the accumulation of new crustal material within a series of sinuous basinal depression, during standard Wilson cycles. Paleomagnetic

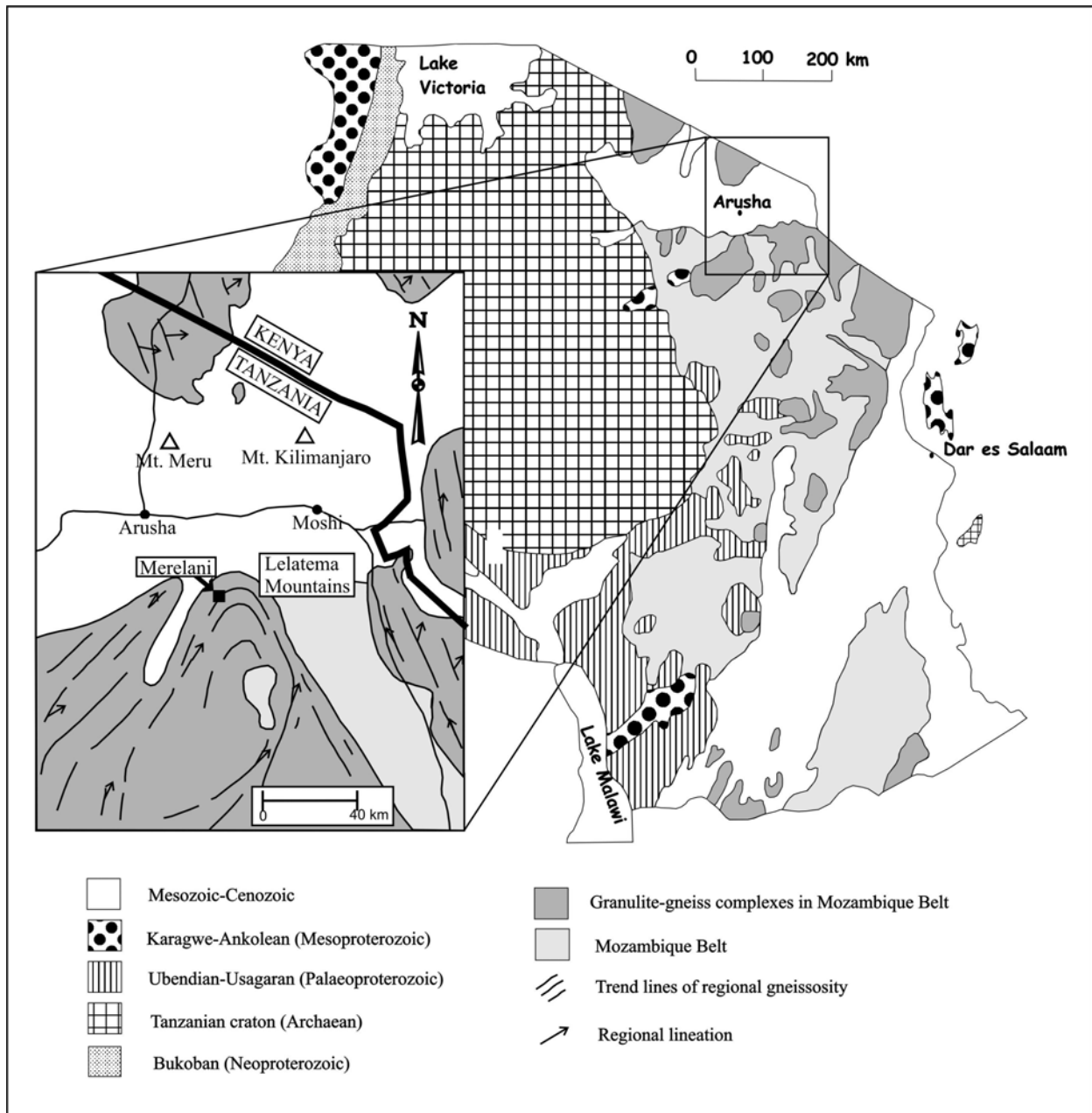


Figure 2.1. Geological map of Tanzania (comprised from various sources including, Shackleton 1993a; 1993b). Inset indicates the Lelatema granulites situated within NE Tanzania.

evidence also suggests that the belt formed as the result of the closure of the “Mozambique Ocean” (Hoffman, 1991; Shackleton, 1993a, 1996; Grunow et al., 1996) and subsequent collision and amalgamation of East and West-Gondwana during the broad Neo-proterozoic “Pan-African” event (Jacobs et al., 1998). Geochronologic and paleomagnetic data point towards an age of ca. 600 Ma for the continent-continent collisions, with final plate coalescence and the end of compressional deformation at ca. 550 Ma (Shackleton et al., 1996). According to Pinna (1995) the continuity of features typical of magmatism and similar metamorphic sequences from northern Mozambique to central Kenya, suggests that the bulk of the crust was emplaced and structured by a similar major event at ca. 1000 Ma. This points to a dual nature for the Mozambique Belt, Meso to Neoproterozoic (ca. 1000 Ma) for the bulk of the crustal growth and Pan-African (ca. 600 Ma) for the intracontinental tectonics influenced by major pre-Pan-African structures. The main result of Pan-African tectonics along East Africa was exhumation through up-thrusting and tilting of ever-deeper sections of the continental crust toward the east. The Mozambique Belt in Tanzania and Kenya experienced even further uplift during the Phanerozoic East African Rift formation (Stern, 1994).

Large complexes of granulite facies rocks occur throughout the Mozambique Belt. In NE Tanzania the granulite complexes represent the best exposures in the Mozambique Belt, forming a north-south trending discontinuous belt of structurally and petrographically similar rocks, some of which have been interpreted as fault-bounded mountain ranges (Bagnall, 1963; Muhongo, 1990; Möller et al., 1998) (Figure 2.1). These granulites give important insights into the tectonic evolution of the Mozambique Belt. The orogeny of the granulites is still a highly disputed subject. Maboko and Nakamura (1995) suggested that granulites, like the Uluguru complex, might form in a collisional orogen, representing exotic slices probably derived from the underthrust plate, whereas most of the Mozambique rocks belong to the western “Usagaran” plate. They suggested that the thermal perturbation responsible for metamorphism was preceded by regional crustal thickening in a collisional orogen. Appel et al. (1998) argued that the Eastern Granulites in Tanzania are not a result of continent-continent collision, but the result of a composite anti-clockwise P-T path for granulite metamorphism consistent with magmatic underplating, residence in the mid-lower crust, subsequent cooling (640 Ma – 620 Ma), and exhumation prior to ca. 500 Ma. Muhongo and Lenoir (1994) also argued that the Pare and Uluguru Mountains show no evidence

of thermal overprinting and that they represent thrust sheets or nappes that developed during the consumption of the “Mozambique Ocean” as the Proto-Gondwana fragments were colliding. Möller et al. (1998) subsequently subdivided the granulites into Mid to Late Proterozoic (e.g. Pare and Usambara Mountains, Uмба Steppe and Eastern Uluguru Mountains), which may constitute Proterozoic arcs or a distal zone of late Proterozoic continental margins with limited mixing, and Late Proterozoic to Early Proterozoic granulites. The latter granulites include the Rayner complex, Vijayan and Wami complex and Western Uluguru Mountains, suggesting extensive mixing of material of different crustal ages, therefore representing older reworked crustal precursors. Granulites of the Usagaran complex (Usambara-, Pare Mountains, and Uмба- and Maasai Steppe) exhibit a range of structures including superimposed folding, tight recumbent folds, isoclinal folds, thrusts, shear zones, boudinage and possible sheath folds (Pallister, 1971; Hepworth, 1972; Shackleton, 1986, 1993a, 1993b, 1996). In general, the Usagaran complex is divided into two granulite divisions, the lower division (Usambara and Para Mountains) and upper division (Uмба and Maasai Steppe), with the Merelani area belonging to the latter. Cross-folding is characteristic of the upper division and indicates two fold trends, early isoclinal folding with shallow or steeply plunging fold-axes to the NE followed by slightly more open folding to the NNW - SSE. These granulites frequently contain repetitions of crystalline limestone, graphitic gneisses and psammitic gneisses (Coolen et al., 1982; Pinna, 1995).

Based on Rb-Sr biotite ages, the Mozambique Belt in Tanzania can be subdivided into a Neoproterozoic (Pan-African) metamorphic domain to the east and the Usagaran/Ubendian (Early Proterozoic) domain to the west (Möller et al., 1998).

### **2.3.1. Early Proterozoic**

The Usagaran and Ubendian Belts were formerly believed to have formed during two separate orogenies, but it has later been established that they formed simultaneously during the Early Proterozoic (ca. 2000 - 1900 Ma) Usagaran-Ubendian orogeny (Quennel et al., 1959; Wendt et al., 1972; Priem et al., 1979). The Usagaran-Ubendian event was an important crust-forming episode and resulted in large amounts of juvenile Usagaran-Ubendian crust being accreted onto the Tanzanian Craton (Maboko and Nakamura, 1996). The Usagaran and Ubendian complexes represent a combination of older altered shelf-facies metasedimentary and younger meta-igneous rocks. This

suggests that the metasedimentary rocks were derived from an older exposed hinterland and that some igneous material is a juvenile addition to the crust (Möller et al., 1998). High-grade metamorphism, intense flattening and shearing, as well as major nappe structures are all characteristics of these pre-Gondwana plate assemblages. The Usagaran becomes progressively imbricated in the Neoproterozoic metamorphic domain to the north- and south-east, resulting in a thorough resetting of the isotopic system during the Pan-African thermo-tectonic episode. This resetting resulted in ages of between 400 and 600 Ma for the eastern zone of the Usagaran supergroup (Coolen et al., 1982; Cahen et al., 1984; Pinna, 1995).

The rocks of the Usagaran are extensively synorogenically migmatized, but their association with granitoid intrusions are not completely clear and appears to be minimal. A granitic event, however, did occur in the Usagaran Belt, especially in the south, approximately 1800 to 1900 Ma ago (Harpum, 1970; Wendt et al., 1972; Muhongo and Lennoir, 1994). Maboko and Nakamura (1996) interpreted these granitoids to be partial melt products of a volcano-sedimentary sequence consisting of new material added to the crust during Ubendian-Usagaran orogenesis, interbedded with sedimentary rocks derived from the Tanzanian Craton. A second major episode of granite intrusion occurred much later at  $766 \pm 40$  Ma (Cahen et al., 1984). Pegmatites are widespread in the Usagaran and several episodes were identified, most of which belong to the Ubendian-Usagaran orogeny.

### **2.3.2. Neoproterozoic**

The Pan-African event is characterised by NNE to NNW trending shear zones that rework both the craton and the Usagaran/Ubendian complexes. Large areas, especially in the east, show intense Pan-African reworking and a complete transposition of the older structures under amphibolite facies and even granulite facies conditions (Pinna, 1995).

Two phases of Pan-African metamorphism are recognised in the Furua and Wami river granulites and Uluguru Mountains to the south of the Merelani area: an older granulite facies metamorphism (M1) followed by partial retrogradation in the amphibolite facies (M2) (Coolen, 1980; Andriessen et al., 1985; Muhongo and Tuisku, 1996). The M1 granulite-facies metamorphism occurred from approximately 715 Ma to 690 Ma ago,

according to zircon U-Pb values for the granulites (Andriessen et al., 1985; Maboko et al., 1985; Maboko and Nakamura, 1995; Muhongo and Lenoir, 1994) and can be related to crustal thickening. M2 amphibolite-facies retrogression and isobaric cooling, as a result of thermal relaxation, followed until termination at approximately 650 Ma as indicated by Rb-Sr data (Muhongo, 1990). Maboko et al. (1985) calculated the metamorphic conditions at 8 – 9 kbar and 700 – 820 °C for M1, and 5 kbar and 600 °C for M2. This was followed by cooling through the closure temperature of hornblende to K-Ar (490 – 550 °C) approximately 630 Ma ago. Slow cooling prevailed to ca. 540 - 500 Ma as indicated by Rb-Sr and K-Ar mica ages (Andriessen et al., 1985; Maboko et al., 1985). Four main Pan-African pegmatic events were identified in Tanzania by Cahen et al. (1984), at  $819 \pm 15$  Ma,  $624 \pm 24$  Ma,  $597 \pm 10$  Ma and  $474 \pm 20$  Ma.

## 2.4. Tanzania Craton

The Tanzania Craton is approximately 1 000 km by 500 km in extent and forms part of a ring of Archaean cratons surrounding the Congo Basin. Limited geochronological dating has been done on the craton. Walraven et al. (1994) established Pb-Pb ages of ca. 2720 Ma for the Tanzanian Craton. Bell and Dodson (1981) determined Rb-Sr isochron ages of ca. 2 550 Ma on post-orogenic granitoids, indicating the lower age limit of the craton. Similar lower limit Rb-Sr ages of  $2578 \pm 82$  Ma were determined from the Dodeman gneiss by Wendt et al. (1972).

The Tanzania Craton is bounded by early Proterozoic and younger mobile belts; the NW-N trending Ubendian Belt to the southwest; the ENE-trending Usagaran Belt to the south, southeast and east; the Mozambique Belt also to the east; the Kibaran to the northwest; and the Ruwenzori Belt to the north (Figure 2.1) (Cahen et al., 1984; Gabert, 1984; Goodwin, 1991). The craton is divided into a lower basement in the central and southern parts and an upper basement to the north. The lower basement contains medium to high-grade gneiss-migmatites and Dodeman schist belts, with the schists widely intruded and metamorphosed by 2.6 Ga old granitoid plutons. The upper basement consists of the older Nyanzian schist belts, comprising mafic-felsic volcanic rocks, BIF, greywacke and slates, all intruded by approximately 2.8 Ga old granitoids (Quennell et al., 1959; Goodwin, 1991, 1996).

## Chapter 3

### Lithostratigraphy of the Merelani tanzanite deposit

#### 3.1. Introduction

The Merelani tanzanite deposit is situated within the Lelatema Mountains, which forms part of a north-south trending discontinuous belt of granulite complexes found in NE Tanzania (described in Chapter 2). The Merelani deposit is situated on the north-western flank of the semi-circular Lelatema Mountains. According to Malisa (1987), the mountains form a large “eye fold”, with a maximum plunge of ca. 60° to the NE. Hepworth (1972) ascribed this fold structure to superimposed folding of NW-SE folds and NE-SW folds of Mozamibiquan age (ca. 1000 Ma).

The Lelatema Mountains are defined by the Lelatema fault system which cuts the Maasai Steppe, generally tilting slightly toward the SSE, but with localised tilting toward the NE occurring in the Merelani area. The Lelatema anticline is bordered to the north by Phanerozoic volcanic rocks, predominantly originating from Mt. Kilimanjaro (70 km to the north) and Mt. Meru (50 km to the west). The dominant foliation direction of rocks in the Lelatema Mountains, including the Merelani area, is to the NE or NNE, dipping toward the NW. The Lelatema Mountains consist predominantly of varying layers of gneisses, schists, calc-silicates and dolomitic marble. The gneisses and schists are probably metamorphosed shelf-type sediments.

The Lelatema Mountains were briefly described by Quennel et al. (1959) as part of the geological summary of Tanganyika. The Lelatema Mountains were subsequently mapped on a 1:125 000 scale by MacFarlane (1975). Preliminary work on the geology of the area, as well as geological mapping of the mountains and the mining area, was done by Saria (1973), Dolenc (1976), Cilek (1980) and Malisa (1987). However, due to the limited outcrops and only small-scale mining exposures, no detailed description of the lithological units within the tanzanite mining area was done. The subsequent work done by Davies and Chase (1994), McRobbie et al. (1995) and Martineau and Davies (1996) focused mainly on the graphite potential of the area, while the tanzanite geology and mineralisation was of secondary importance. The previous work on the deposit

played a crucial role in guiding the subsequent research on the deposit. The aim of this chapter is therefore to describe, for the first time, the various lithological units of the Merelani tanzanite deposit in detail. The structural features of the rocks, including the multiple folding events, boudinage and brittle deformation will be discussed in detail in Chapter 5.

## **3.2. Data Collection**

### **3.2.1. Core Drilling**

Due to restricted outcrop, a large amount of the lithostratigraphic information of the mine area is based on data from surface and underground diamond-drilling programs, including:

- Eight diamond drill holes (termed Lower Horizon drill holes, LHD) drilled in 1996 by Graphtan Ltd., a subsidiary of SAMAX Ltd. All the drill holes, except LHD 1, were drilled vertically on the central garnet-sillimanite gneiss (see Section 3.3. for description) in order to crosscut the 40 - 50° NW dipping Lower Horizon (Figure 3.1). Preliminary logging of the drill holes was done before Graphtan Ltd. was declared insolvent in 1997. These drill cores were subsequently re-investigated, logged in detail and also extensively sampled during the present study.
- A drilling program by AFGEM Ltd. in 2000 was initiated to intersect and locate the ore zone (JW-zone, Figure 3.1) at a greater depth. The core was logged and sampled by the author. An important aim of the exploration drill hole program was to establish if the JW-zone is continuous along strike and down dip, to what degree it undulates down dip and whether or not it still contained the tanzanite-bearing boudinaged calc-silicate layers.

A summary of the drill hole logs, including the technical specifications of all 13 drill holes are shown in Addendum A. In addition to the surface-drilling programme, numerous underground core drill holes were drilled in order to investigate the layers surrounding the JW-zone.

The surface drill hole data revealed a surface related oxidation zone that can clearly be identified in the upper area of the garnet-sillimanite-biotite gneiss with a base occurring



at a depth of between 50 and 75 m in the core. The zone is characterised by an abundance of secondary alteration minerals, such as clays and iron oxides, which cause a yellowish colouration and a more brittle texture (see further discussion in Chapter 4). The presence of the oxidation zone led to a general misinterpretation by previous workers. The clay minerals present in this zone were incorrectly identified as epidote associated with the tanzanite formation.

Twenty-nine drill holes were drilled in the Upper Horizon (see Section 3.3 for description) in 1992 by Graphtan Ltd. in order to establish the graphite potential. Although the Upper Horizon was subsequently mapped in detail for its graphite potential, little was known about its tanzanite-bearing potential. Poor quality tanzanite was recovered during the opencast graphite-mining project.

### **3.2.2. Surface Mapping and Trenching**

The surface geological map of the Block C mining area (Addendum B) was composed by combining data collected during various programs:

- 6 trenches crosscutting the lithological units of the Lower Horizon positioned between Bravo Shaft and Shaft 1 (Figure 3.1). These trenches confirmed the lithological sequence observed in the drill holes.
- A 315 m long trench crosscutting the lithologies of the Upper Horizon, mapped by Gessner (2004).
- A 250 m long trench along the strike of the JW-zone located from CT shaft to Shaft 1 (Figure 3.1).
- A trench located between Bravo Shaft and CT Shaft, exposing the F3 intrafolial fold discussed in Chapter 5 (Addendum C).
- Extrapolation of underground exposures and drill hole information across the Block C mining areas.
- Information gathered by Graphtan Ltd., especially from their Upper Horizon graphite opencast mining activities.
- Underground mapping of Lower Horizon lithologies in the mine as well as in previous artisanal shafts. Some of the artisanal shafts were also mapped by Graphtan Ltd.

### 3.3. Lithostratigraphy

The Merelani mine succession is subdivided into two units, the Upper and the Lower Horizon, separated by a thick unit of garnet-sillimanite-biotite gneiss (see Figure 3.1 and Addendum B) (Saria, 1973; Dolenc, 1976; Cilek, 1980; Davies and Chase, 1994; Martineau and Davies, 1996). The Upper Horizon consists of small units of graphite-mica gneiss, surrounded by units of kyanite-graphite gneiss. A transition zone, consisting primarily of quartz, feldspar and mica, separates the kyanite-graphite gneiss from the thick unit of garnet-sillimanite-biotite gneiss that divides the Upper and Lower Horizon. The Lower Horizon is composed of a repetition of kyanite-graphite gneiss, graphite-plagioclase gneiss, graphite-calc-silicate schist and banded calc-silicate hornfels around a central unit of dolomitic marble.

Generally, strike direction of the rocks is between 35 and 55° NE and the rocks dip between 30 and 60° to the NW (Table 3.1). Figure 5.5 shows a NW to SE cross-section along the trench crosscutting the lithologies indicated in Figure 3.1. The general stratigraphy of the Merelani deposit is summarised in Table 3.2. It should be taken into account that the strike and dip values can be locally influenced by the presence of boudins and folds and will be further discussed in Chapter 5. The average strike and dip taken from 305 measurements over the whole Block C mining area is 047/45 NW. The average dip of the rocks is used to determine the corrected thickness of the stratigraphic layers intersected in the drill holes.

This study focuses mainly on the Lower Horizon, since this is currently the main producer of gemstone quality tanzanite. The Upper Horizon will only be discussed briefly, however, it should be noted that this horizon could be an important source of tanzanite in the future and warrants further research.

#### 3.3.1. Nomenclature

The proposed nomenclature for the lithostratigraphic units identified by means of the trenching, drilling and underground exposures are listed in Table 3.2. The nomenclature of the layers is based on the petrographic and geochemical data of the units that will be described later in the thesis (Chapters 4, 6 and 7).

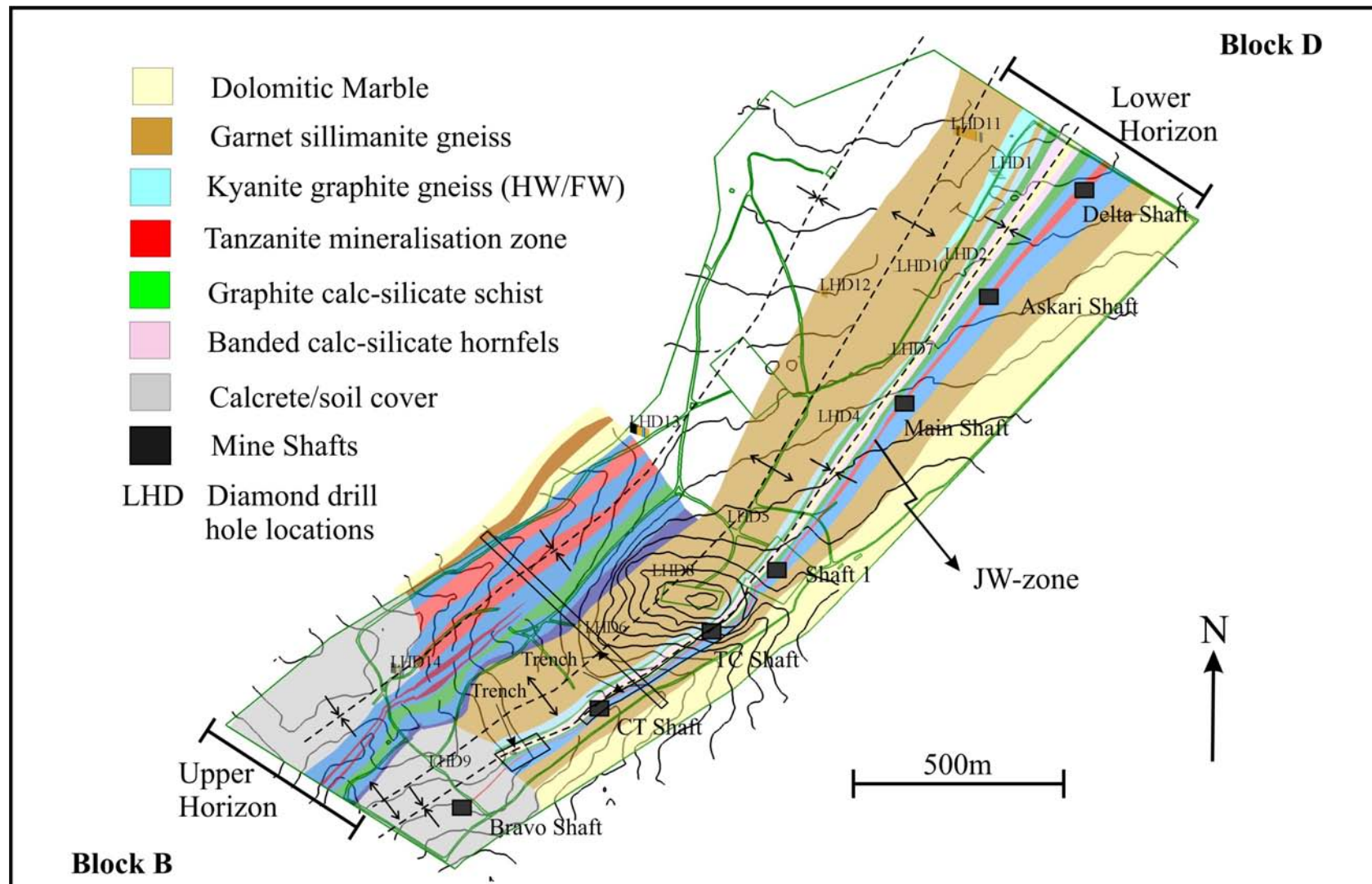


Figure 3.1. General surface geological map of the Block C mining area. The map also indicates the positions of the mineshafts, surface drill holes and trenches. Addendum A shows the positions and logs of the drill holes. Addendum B shows a detail surface geological map of the mine area as developed from the present study.

Table 3.1. Average strike and dip measurements for each shaft and average strike and dip over the whole Block C mining area (n indicates the number of measurements).

Shaft	Strike	Dip	n
<b>Bravo Shaft</b>	041	47 NW	21
<b>CT Shaft</b>	051	40 NW	41
<b>CT Trench</b>	052	45 NW	180
<b>Main Shaft</b>	048	44 NW	21
<b>Askari Shaft</b>	051	51 NW	17
<b>Delta Shaft</b>	039	43 NW	25
<b>Average</b>	047	45 NW	

### 3.3.2. General stratigraphic units

#### *Dolomitic Marble (DM)*

Dolomitic marble (DM1 and DM3) ridges flank the Merelani deposit on the south-eastern and north-western side (Figure 3.1 and Addendum B), creating a NE-SW trending depression in which the deposit is situated. A comparatively small dolomitic marble unit (DM2) is located within the Lower Horizon (Table 3.2). The dolomitic marble is very coarse-grained and white in colour (Figure 3.6.b). The dolomitic marble units extend for tens of kilometres and represent the main rock type within the Lelatema Mountains.

The DM1 and DM3 are generally several hundred metres thick. The central dolomitic marble (DM2) has been intersected in twelve of the drill holes and varies in thickness from between 10.8 and 0.4 m. Drill hole LHD 13 does not intercept the DM2 unit (Addendum A). The DM2 unit forms the centre of the Lower Horizon stratigraphic duplication as indicated in Addendum B and Table 3.2. The DM2 unit may therefore represent the core of a syn- or antiformal structure and will be further discussed in Chapter 5. The absence of the DM2 unit in the deepest drill hole (LHD 13) thus suggests the existence of a synform. There is also a prominent decrease in the thickness of the DM2 unit from the NE to the SW (Figure 3.2). The thinning of the DM2 toward the SW is associated with a thickening of the banded calc-silicate hornfels and will be further discussed in Section 3.3.3.

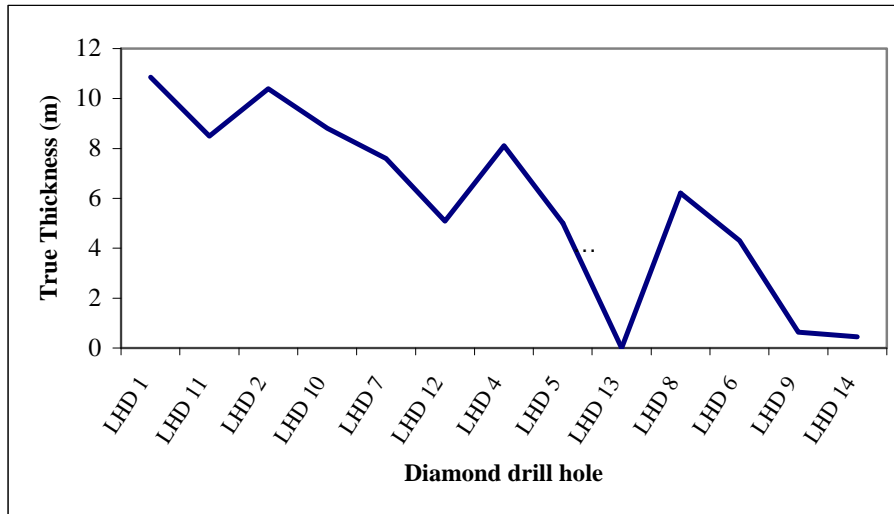


Figure 3.2. Corrected thickness of the central dolomitic marble unit (DM2). The drill holes are positioned from left to right according to their position on the mine area from NE to SW.

Accessory minerals such as graphite, biotite and chlorite often result in a greyish colour for the dolomitic marble. Additional accessory minerals include pyrite, native sulphur, plagioclase, olivine and diopside. The dolomitic marbles often contain zones and layers of impure marble with a generally higher silica content and varying in size from mm scale to several metres. The impurities are often good shear sense and fold sense indicators. Malisa (1987) also observed isoclinal folding within the marble of the Lelatema Mountains. Dolomitic marble outcrop exposures are often coloured black as a result of algae growths and in some cases field fires.

#### ***Garnet-sillimanite-biotite gneiss (GNG)***

The garnet-sillimanite-biotite gneiss occurs as a thick central unit (GNG2) between the Upper and Lower Horizons, as well as on both sides (GNG1 and GNG3) of the mine succession and in contact with the dolomitic marble (Figure 3.1 and Addendum B). The central unit reaches its maximum width in the centre of Block C where it forms a NE-SW trending topographic ridge with a thickness of 90 m. The gneiss thins out from the centre toward the NE and SW from where it extends into Blocks D and B respectively (Figure 3.1). The gneiss is medium- to coarse grained, with a spotted appearance due to the presence of large purple garnet porphyroblasts surrounded by yellow-white to blue-white

elongated crystals of sillimanite, feldspar and quartz (Figure 3.6.a). The gneissosity is defined by sillimanite and biotite.

In surface outcrop, garnet has a reddish-brown colour and the matrix is yellowish, due to weathering and oxidation. The gneiss consists predominantly of garnet, sillimanite, quartz, K-feldspar, biotite and plagioclase; with pyrite, rutile, titanite, kyanite, graphite, muscovite, zircon, haematite, ilmenite and apatite as accessory minerals. Though the gneiss is relatively uniform, it is evident that some degree of migmatitisation did occur. Possible anatexis of the gneiss resulted in pegmatitic zones, varying from millimetres to metres in thickness, which contain high amounts of quartz and K-feldspar. Kyanite becomes progressively more abundant towards the contact with the kyanite-graphite gneiss (LK1 and LK4). The GNG units also contain numerous breccia zones of up to several metres thick. The breccia zones are characterised by a high Fe content (defined predominantly by oxidised pyrite crystals), as well as the partial or complete disappearance of almandine-rich garnet.

Table 3.2. Generalised stratigraphy and proposed names for the various lithological units listed from north west to south east within the Merelani tanzanite deposit.

PROPOSED MINERALOGICAL NAME
Dolomitic marble (DM3)
Garnet-sillimanite-biotite gneiss (GNG3)
UPPER HORIZON
Kyanite-graphite gneiss (UK4)
Biotite-graphite gneiss (FL2)
Kyanite-graphite gneiss (UK3)
Biotite-graphite gneiss (FL1)
Kyanite-graphite gneiss (UK2)
Graphite calc-silicate schist (UH-GCS)
Kyanite-graphite gneiss (UK1)
Transition zone
Garnet-sillimanite-biotite gneiss (GNG2)
LOWER HORIZON
Kyanite-graphite gneiss (LK4)
Graphite-plagioclase gneiss (C-zone)
Kyanite-graphite gneiss (LK3)
Graphite calc-silicate schist (GCS2)
Banded calc-silicate hornfels (BCF2)
Dolomitic Marble (DM2)
Banded calc-silicate hornfels (BCF1)
Graphite calc-silicate schist (GCS1)
Kyanite-graphite gneiss (LK2)
Graphite-plagioclase gneiss (JW zone)
Kyanite-graphite gneiss (LK1)
Garnet-sillimanite-biotite gneiss (GNG1)
Dolomitic marble (DM1)

***Superficial deposits***

Neogene and Recent superficial deposits cover the majority of the Merelani tanzanite deposit. Malisa (1987) described the calcrete and soil cover present within the Lelatema Mountains. A thin layer of calcareous soil, gravel and laterite overlies the south-western part of Block C and part of Block B. A silicified calcrete layer covers most of the north-eastern part of Block C and generally increases in thickness toward the NE, where it can reach well over 20 m. The cover extends into the neighbouring Block D where it reaches even greater vertical dimensions. Thus, most of the tanzanite-bearing Lower Horizon is covered by and therefore in contact with the calcrete layer. Eluvial material from the gneisses and calc-silicates were cemented during the calcrete formation, causing the bottom of the calcrete layer to contain various minerals including tanzanite, tsavorite, diopside, garnet, kyanite and quartz. The tanzanite-bearing potential of the soil cover is discussed Chapter 12. The calcrete has been a significant source of eluvial tanzanite in the past but is currently close to being mined out due its high accessibility.

**3.3.3. Lower Horizon*****Kyanite–graphite gneiss (LK)***

Six kyanite-graphite gneiss units are present in the Lower Horizon. The LK units listed from east to west on the mine are as follows:

- Kyanite – graphite gneiss unit 1 (LK1), forming the structural footwall (FW) of the boudinaged graphite – plagioclase gneiss locally termed the JW-zone, which hosts the tanzanite-bearing calc-silicate horizon.
- Kyanite – graphite gneiss unit 2 (LK2) forming the structural hanging wall (HW) unit of the boudinaged tanzanite ore zone.
- Kyanite – graphite gneiss unit 3 (LK 3) forming the FW unit of the C –zone.
- Kyanite – graphite gneiss unit 4 (LK 4) forming the HW unit of the C –zone
- Kyanite – graphite gneiss unit 5 (LK5) forming the FW unit of the D –zone.
- Kyanite – graphite gneiss unit 6 (LK6) forming the HW unit of the D-zone.

Both the LK1 and LK2 units contain pegmatites, although it is more pronounced in the HW where it sometimes forms a characteristic HW pegmatite layer. This pegmatitic layer is



normally between 10 and 35 cm thick and is often close to the contact with the mineralised graphite-plagioclase gneiss, therefore serving as a HW indicator. The HW, including the pegmatite layer, and to a lesser extent the FW, exhibit a wave-like undulatory pattern as a result of deformation caused by the boudinaged tanzanite-bearing graphite-plagioclase gneiss. Thus, the HW and the FW represent more competent layers, surrounding the more sheared graphite-biotite gneiss that hosts the calc-silicate layers and subsequently the tanzanite mineralisation. The LK1 and LK2 units as intersected in the drill core have an average thickness of 8.5 m and 4.3 m, respectively. The various thicknesses of the HW and FW units intersected in the drill holes are indicated in Addendum A. LK1 is underlain by GNG1 and contains progressively more sillimanite towards GNG1. Sillimanite post-dates the kyanite in the crystallisation history and can be seen to overgrow kyanite porphyroblasts. The LK1 unit sometimes contains tremolite- actinolite crystals on the contact with the JW-zone (Figure 3.5.c). These crystals may be up to several centimetres in size.

LK3 and LK4 are usually separated by a graphite-plagioclase gneiss termed the C-zone. Where the C-zone is absent, LK3 and LK4 are indistinguishable. Similarly to LK1, LK4 is also adjacent to a garnet-sillimanite-biotite gneiss unit, and it also shows a gradual increase in sillimanite content toward the gneiss.

LK5 and LK6 occur within the GNG2 and therefore technically belong to neither the Upper Horizon nor Lower Horizon (see Table 3.2). Only limited data is available from these units since they are exclusively observed in drill holes LHD 1 and LHD 11 (Addendum A) and are covered by a thick calcrete layer. Correlation between these units and known units from the Upper Horizon is therefore difficult. It is probable that these units pinch out toward the SW while extending into Block D following the general fan-like widening of the layers (Figure 3.1 and Addendum B). Drill hole LHD 1 intersects units LK6 and LK5 at shallow depths of 32 to 34 m and 53 to 62.5 m, respectively (Addendum A). Since these intersections are within, or close to the oxidation level, oxidation presented an obstacle in characterising the geochemical compositions of LK5 and 6. This will be further discussed in Chapter 11.

The kyanite gneisses are medium-grained and consist of quartz, feldspar, kyanite and graphite with sillimanite, mica, and pyrite present in variable amounts. The LK1 and LK2 units are indicated in Figures 3.7.a and 3.7.b. Light to dark blue kyanite crystals that are often several centimetres in diameter are characteristic of these gneisses (Figure 3.5.a). The units are weakly foliated and exhibit a noticeable gneissosity due to preferred orientation of graphite, mica and the presence of elongated grains of quartz, feldspar and kyanite. The gneiss is dark-grey to bluish-grey in colour and is occasionally banded on a mm to cm scale. The banding is due to the presence of alternating elongated quartz- and feldspar-rich layers. It also contains mica-rich zones of varying size that are devoid of kyanite.

#### ***Graphite – plagioclase gneiss (ore zone)***

The graphite-plagioclase gneiss occurs as four units, the Ali Juuyawatu zone (JW-zone), footwall alteration unit (FW-alt) located within LK1, C-zone and D-zone. From a mining viewpoint, the JW-zone is of primary importance since it hosts the calc-silicate layer, which in turn hosts the tanzanite mineralisation. As a result of shearing, the calc-silicate layer was subjected to intense boudinage and folding while the JW-zone underwent plastic deformation. This resulted in the JW-zone wrapping around the boudinaged calc-silicates. The structural aspects of the unit are discussed in detail in Chapter 5.

The JW-zone intersected in the drill holes varies in thickness (calculated at 45°) from 0.6 m to 6.2 m. The average thickness of the JW-zone is 2.91 m, with a dip of 45°. There is a general thickening of the JW-zone toward the NE and SW borders, as evident in Addendum B. It also appears as if there is a slight increase in the thickness of the JW-zone with increasing depth. The average true thickness of the JW-zone intersected above 150 m is 2.0 m, while the average thickness of the JW-zone intersected below 150 m is 3.7 m. See Addendum A for the various thickness and depth intersections of the JW-zone in the drill holes.

The JW-zone contains lenses of kyanite-graphite gneiss resembling the LK1 and LK2 units. From a mining aspect, these lenses may be misleading since they are often confused with

the true hanging wall or footwall units. The occurrence of the lenses of kyanite-graphite gneiss within the JW-zone is the result of:

- Duplication of the JW-zone through isoclinal folding and associated shearing. This can lead to the entrapment and dragging of the kyanite gneiss from either the HW or FW into the JW-zone.
- The skarn-related origin of the JW-zone. Since the JW-zone appears to form from the isochemical metamorphism and associated mass transfer between the kyanite gneisses and the calc-silicates, it stands to reason that in areas where the metasomatic transfer of components and dehydration were not as pervasive, kyanite-graphite gneiss pockets or lenses can still remain within the JW-zone.

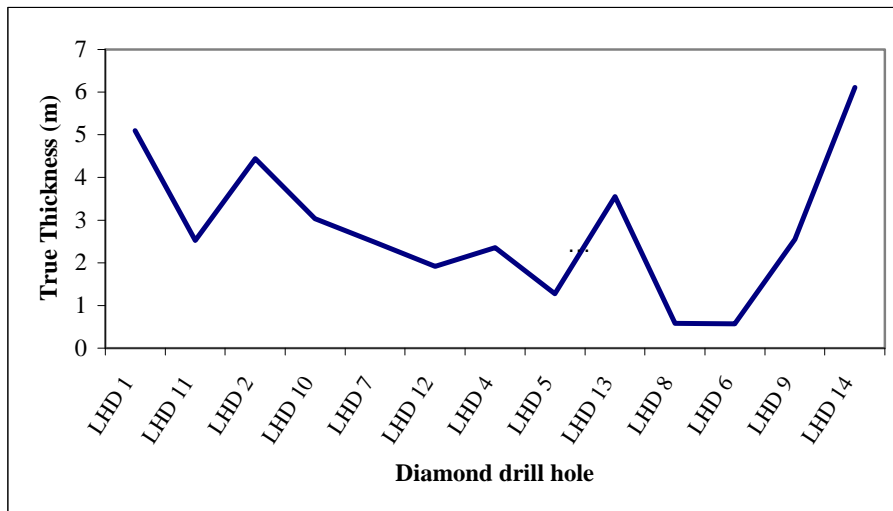


*Figure 3.3. The thickness of the JW-zone as intersected in the diamond drill holes. The drill holes are positioned from left to right according to their position on the mine area from NE to SW.*

Dehydration zones within the FW of the JW-zone have been identified both in the drill holes and through underground development. The zones identified through the core drilling vary in thickness from 0.65 to 2.3 m. Large FW dehydration zones have been identified through underground development, where they may occur only a few cm below the JW-zone. This could lead to a total ore-zone unit of up to 35 m thick. The dehydration zones within the FW of the JW-zone are also referred to as FW-alteration zones (FW-alt). Tanzanite mineralisation from a FW-alteration zone has been recovered in Block D. The

FW-alteration commonly contains higher mica content than the normal JW-zone. The FW-alteration units are also formed through skarn interaction along shear zone hosted calc-silicate units, similar to that of the main skarn alteration zone (JW-zone), see Chapter 5.

The C-zone is a narrow horizon of relatively similar composition to the JW-zone and is situated between LK4 and LK3. The C-zone is usually highly weathered in most of the drill-core because it was intersected in the oxidation zone. The thickness of the C-zone intersected in the drill-core is usually less than 1 m in thickness except for LHD 12, where the true thickness of the C-zone is 3.0 m. The total calculated thickness of the C-zone and its surrounding HW and FW units varies between 3.5 and 7.2 m.

The D-zone is situated between LK6 and LK5, and follows the same pinching structure proposed for the kyanite gneisses. The D-zone and the surrounding kyanite-graphite gneiss were only intersected in LHD 1 and LHD 11. It is therefore believed to pinch out towards the SW past LHD 11, as indicated in Addendum B. The D-zone extends toward Block D, where it widens in a similar fashion to the other units. The D-zone, in Block D, constitutes a source of tanzanite, hosted in a similar boudinage calc-silicate layer as the case with the JW-zone. The total true thickness of the D-zone and its surrounding kyanite-graphite gneiss units is approximately 20 m.

All four units consist of quartz, feldspar, graphite and mica; with pyrite and titanite as the predominant accessory minerals (Figure 3.7.c). The units are similar to the surrounding kyanite-graphite gneisses, with the most important differences being:

- the absence of  $\text{Al}_2\text{SiO}_5$ .
- an increase in plagioclase content with the anorthite content of the plagioclase also increasing toward the calc-silicate zones (see Chapter 6). This minor chemical exchange is associated with the more pronounced skarn-forming reactions observed in the calc-silicate shear-zone.
- an increase in the amount of dehydration, as a result of the coupled metasomatic effect between the highly metasomatised and hydrated cal-silicate bearing shear zone.

- a decrease in the mica content as a result of the increased dehydration.
- higher amounts of secondary alteration minerals, including gypsum and clay minerals.
- the presence of small amounts of diopside close to the calc-silicate contact.
- a finer grain-size compared to the kyanite-graphite gneisses.

All the above-mentioned characteristics of the graphite-plagioclase gneiss are due to the mass transfer balancing of the skarn forming reactions within the calc-silicate units. This resulted in the dehydration of the gneiss surrounding the shear zone associated calc-silicates, while the calc-silicates themselves are highly hydrated. The graphite-plagioclase gneiss therefore forms through the skarn associated dehydration of the kyanite-graphite gneisses surrounding the shear zone hosted calc-silicates.

#### *Calc-silicates*

The calc-silicate units are present as intensely boudinaged and isoclinally duplicated layers associated with shearing within the JW-zone and to a lesser extent the C- and D-zones. The calc-silicate boudins and associated structures will be discussed and illustrated in detail in Chapter 5.

The boudinaged calc-silicate layers within the JW-zone are the main tanzanite producer in the Merelani area, and therefore also in the world. The down-dip extent of the calc-silicate unit is not certain, since mining in Block C currently only extends to vertical depths of about 250 m. However, petrographic and geochemical studies of the drill-core indicate that the calc-silicate layer is present in the JW-zone at depths of up to 230 m (Table 3.3), while the JW-zone itself has been intersected at a vertical depth of 280 m. Figure 3.7.d illustrates the calc-silicate boudin intersected in LHD 14 at a depth of 230 m. The continuation of the calc-silicate unit along strike was established by the trenches, artisanal mining shafts and the fact that the same horizon is being mined in Blocks D and B.

Small amounts of calc-silicates are also present in the C-zone. It is not presently known to what extent the calc-silicates are boudinaged and consequently its tanzanite-bearing

potential remains unclear. It is however unlikely that the C-zone could prove to be a major tanzanite producing layer since it is generally only one to two metres thick.

The calc-silicates can be divided into three types:

- 1) *Skarnoid reaction zones*: The reaction layers or zones envelope and connect the shear zone related calc-silicate boudin structures that will be described in Chapter 5 and are generally light grey in colour. The skarnoid reaction layers form the boundary between the graphitic gneisses and the sheared and boudinaged calc-silicates. The reaction layers are usually around 20 cm in diameter, but widen and become more pronounced in the vicinity of a boudin. In the presence of a boudin, the skarnoid layer splits and wraps around it. A stringer of clear quartz is often present within the layer, interconnecting the boudins. The skarnoid reaction layers represent the stretched, sheared, metasomatic and metamorphic reaction zone between the two rock types. The reaction zones or layers have been identified in the Block C mineshafts and in the drill core from the block but probably also exist in the neighbouring areas where their identification is obscured by limited face exposures. The rock is highly banded and foliated and fine- to medium-grained. The foliation is defined by the preferred crystallographic orientation of graphite and the presence of elongated, parallel-oriented quartz and zoisite grains. Banding occurs on a mm to cm scale and consists of alternating bands of quartz, calc-silicates, graphite and later alteration minerals, all of which will be discussed in Chapter 4. The structural deformation of the reaction zones will be discussed in Chapter 5.
- 2) *Boudins*: The boudins occur within the various skarnoid reaction zones. The majority of boudins consist of two distinct rock types:
  - *Pyroxene relicts*. Diopside is the main rock-forming mineral in the relict units, with grossular, quartz, pyrite and graphite occurring in minor amounts. The relict units represent the original competent unaltered boudinaged layer that formed through the metamorphism of an impure limestone.

- *Calc-silicate skarn boudins.* The skarn boudins primarily consist of diopside, quartz, graphite, pyrite, haematite, zoisite (occasionally tanzanite), grossular garnet and its gem variant tsavolite (the US spelling of tsavorite instead of tsavolite is commonly used in the industry and will be used throughout this study) as well as several secondary alteration minerals like halloysite, goethite, illite etc. Figure 3.5.b shows blue zoisite crystals (tanzanite) occasionally present in the boudins surrounded by quartz and minor calcite. Chemical skarn processes caused by metasomatic fluids of metamorphic origin (see Chapters 7 and 8) resulted in the alteration of the diopside-rich rock (pyroxene relicts) and the formation of the calc-silicate skarn boudin material.

Table 3.3. Depth of calc-silicate boudin intersections in the drill holes.

Drill hole no.	Host rock	Depth of boudin intersection
LHD 6	JW-zone	121.80 m
LHD 7	JW-zone	98.75 m
LHD 9	C-zone	35.95 m
	JW-zone	100.5 m
LHD 10	JW-zone	178 m
		181.5 m
LHD 11	D-zone	64.25 m
LHD 14	JW-zone	224 m
		227 m
		231 m

- 3) *Low – pressure pockets within the skarn boudins:* The boudins contain pockets of coarse-grained quartz, grossular garnet, zoisite (predominantly tanzanite), pyrite, calcite, graphite and diopside. The pockets are situated in various types of low-pressure sites within and adjacent to the boudins and are discussed in detail in Chapter 5, together with boudinage, folding and deformation of the calc-silicate

units. These pockets are the main source of gemstone quality tanzanite and tsavorite.

***Banded calc-silicate hornfels (BCF)***

The hornfels is banded on a mm to cm scale, consisting of alternating layers of calc-silicates (calc-silicate hornfels) and zones with a higher quartz and feldspar content (quartzo-feldspathic hornfels) (Figure 3.6.c). The hornfels is fine- to medium-grained and light grey in colour, with no distinct foliation. The banding is further defined by thin layers of sulphides, especially abundant in the transition zones between the calc-silicate and quartzo-feldspathic zones. The transition zones are often darker in colour, while the calc-silicate zones are lighter grey. The BCF tends to become coarser grained from the quartzo-feldspathic zone through the transition zone to the calc-silicate zone. The quartzo-feldspathic zone consists primarily of microcline and quartz with minor amounts of plagioclase, muscovite, pyrrhotite and pyrite, and accessory amounts of graphite, diopside and titanite. The transition zone varies in mineral content but primarily consists of plagioclase, microcline, quartz, muscovite, pyrrhotite, pyrite, titanite, diopside, scapolite and graphite. The calc-silicate zone consists mainly of diopside, calcite, scapolite and subordinate amounts of quartz, plagioclase, microcline with accessory pyrrhotite, pyrite, muscovite, graphite and titanite.

The hornfels occur as two units (BCF1 and BCF2) surrounding the dolomitic marble (DM2) and has the same strike and dip as the other units. The calc-silicate hornfels formed through the thermal metamorphic alteration of the impure outer part of the original limestone bed, while the purer inner limestones recrystallised as dolomitic marbles. The same rock type has also been identified in other areas within the Lelatema Mountains where impure limestones formed the contact between the dolomitic marble and the surrounding gneiss and schist.

The hornfels therefore represents the pre-metamorphic impure limestone in contact with the surrounding graphitic gneiss and schists, while the dolomitic marbles (e.g. DM2) formed from the purer limestones. The drill hole data indicates that the thickness of the hornfels



often has an inverse relationship with the thickness of the dolomitic marble. This is illustrated in Figure 3.4, which shows an increase in the thickness of the BCF2 unit toward the south-eastern border compared to the decrease in the thickness of the marble as discussed in Section 3.3.2.

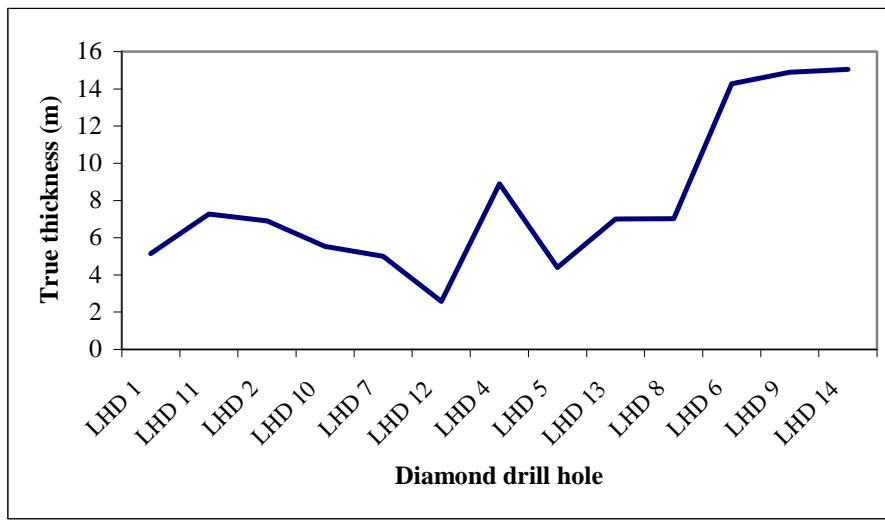


Figure 3.4. The thickness of the BCF-zone as intersected in the diamond drill holes. The drill holes are positioned from left to right according to their position on the mine area from NE to SW.

#### ***Graphite-calc-silicate schist (GCS)***

The graphite-calc-silicate schist units 1 and 2 (GCS1 and GCS2) occur next to the two banded calc-silicate hornfels units (BCF1 and BCF2) in the Lower Horizon. A similar unit, called the UH-GCS is present in the Upper Horizon. The schist consists of quartz, feldspar, graphite, grossular and diopside; with pyrite, haematite, titanite, serpentine and clay minerals as accessory minerals. Units GCS1 and GCS2 intersected by the core have an average calculated thickness of 2.6 m and 4.3 m, respectively. The schistosity is defined by abundant amounts of sub-parallel aligned graphite flakes. The conspicuous nature of the graphite results in the schist exhibiting a greyish to “silver” colour. The schist further has a distinct green spotted appearance due to the presence of disseminated green grossular. It also contains zones that are enriched in calc-silicate minerals, similar to that described for

the BCF, only smaller and less frequent. The calc-silicate-rich areas consist mainly of diopside, scapolite and grossular garnet with variable amounts of quartz, graphite and plagioclase. The schist can therefore be subdivided in calc-silicate-rich and -poor zones, with the calc-silicate-rich zones comprising approximately 20 % of the rock. Figure 3.6.d indicates the GCS layer intersected in the drill hole.

#### **3.3.4. Upper Horizon**

The Upper Horizon has previously only been mapped and studied from a graphite-bearing viewpoint. Very little is currently known about the tanzanite potential of the Upper Horizon, but preliminary investigations carried out during the present study indicate distinctive similarities between the Upper and Lower Horizons. As indicated in Addendum B and Table 3.2, the Upper Horizon predominantly consists of small units of graphite-mica gneisses, surrounded by units of kyanite-graphite gneiss. A transition zone that consists primarily of quartz and feldspars separates the kyanite-graphite gneiss from the thick unit of garnet-sillimanite-biotite gneiss that separates the Upper and Lower Horizons. The strata of the Upper Horizon have similar strike and dip to the layers in the Lower Horizon.

The general structural stratigraphy of the area is given in Table 3.2. The previously termed Main Alteration Zone (MAZ) located in the Upper Horizon resembles the graphite calc-silicate gneisses (now termed UH-GCS) and not the JW-zone as suggested by Davies and Chase (1994). During the graphite mining activities, the MAZ was the main producer of graphite containing up to 24 wt % graphite with 96% carbon purity (Davies and Chase, 1994). However, it is unlikely that this unit has any significant tanzanite-bearing potential and it is more possible that the tanzanite recovered from the graphite open pit operations originates from the graphite-mica gneisses that resemble the JW-zone in the Lower Horizon.

In general, the Upper Horizon appears to be more sheared than the Lower Horizon. The Upper Horizon is also characterised by the abundance of pegmatite. Centimetre-scale drag folds and metre scale chevron folds have been identified in the Upper Horizon, but to date no isoclinal folding structures similar to that of the Lower Horizon have been identified.

The importance of the isoclinal folding will be discussed in Chapter 5. The possibility that the Upper and Lower Horizons could be linked through a large isoclinal fold is discussed in Chapter 5. Although McRobbie et al. (1995) suggested that the Upper and Lower Horizon could have been detached through local duplexing to form two adjacent horizons; little supporting evidence has been observed. The Upper Horizon strata are crosscut by numerous small faults ( $330/80^{\circ}$ ) with no or little displacement. These features are further discussed in see Chapter 5. In general, the rocks of the Upper Horizon can be distinguished from those of the Lower Horizon by the higher amount of mica in the rocks, especially green mica, termed fuchsite when coloured by chromium.

### **3.4. Metabasite**

The Lelatema anticline contains several outcrops of metabasite mapped by Malisa (1987) and Cunningham (2001). Of specific importance to the tanzanite lithologies is a metabasite outcrop identified in the field approximately 2 km north east of the Block C mining area (Point A (UTM): 282992; 9607964). The metabasite is located on the eastern flank of the dolomitic marble that forms the eastern ridge (DM1) of the tanzanite deposit. The metabasite also strikes in a NE-SW direction and dips between  $10$  and  $65^{\circ}$  NW and is therefore sub-parallel to the mine lithologies. The outcrop varies between 1 m to 10 m in thickness and was traced out over a distance of approximately 3.5 km to the SW of point A (Gessner, 2004).

The metabasite has a spotted appearance due to the presence of dark pyroxenes surrounded by light coloured fine-grained quartz crystals. Pinkish to reddish garnet of up to 3 cm in diameter is also a distinctive feature of the metabasite. The garnet is more prominent close to the contact with the surrounding dolomitic marble suggesting a skarn-like reaction. The metabasite also contains numerous leucosomes consisting predominantly of feldspar. The leucosomes are often boudinaged and folded, both along strike and along dip and are therefore an important indicator of the structural deformation history of the area. The metabasite is of additional importance to the structural evolution of the Merelani area since the structural features (S1, L1 and F1) associated with the first deformational event area are still preserved within the rock. The metabasite can thus be used as an indicator of the

original fabric that was obliterated during the subsequent deformation. These structural features will be discussed in Chapter 5.

### **3.5. Neighbouring Blocks**

The artisanal and small scale mining blocks surrounding the commercially mined Block C area have also been investigated. The majority of the information is beyond the scope of this work and therefore only the main stratigraphic features will be dealt with. The various blocks are indicated in Figure 1.2.

#### **3.5.1. Block A extension**

Lithological units resembling the Upper Horizon have been identified through trenching in the Block A extension area. The lithological units consist of alternating units of kyanite-graphite gneiss and graphite gneiss. A stratigraphic unit resembling an altered metabasite occurs within two kyanite-graphite gneiss units (Figure 3.5.d).

The gneisses are sandwiched by extensive units of dolomitic marbles. A small garnet-sillimanite-biotite gneiss unit has been observed in contact with the westerly dolomitic marble unit. The general strike and dip of the area resembles those observed in Block C. Lithologies resembling the Lower Horizon have not been observed.

#### **3.5.2. Block A**

Both the Upper and Lower Horizon appear to be present in the Block A area. The block is flanked on the eastern and western side by dolomitic marble ridges. The rocks have a general strike of 40 to 60° NE-SW and dip between 20 and 45° NW. The garnet-sillimanite-biotite gneiss (GNG1) unit has a thickness of approximately 5 m, while the central garnet-sillimanite-biotite gneiss (GNG2) is around 30 m thick. The Lower Horizon dolomitic marble unit (DM2) has also been observed, with a thickness of approximately 15 m. The JW-zone and surrounding HW and FW kyanite-graphite gneiss are identifiable within the block. The LK1 FW unit is exceptionally wide, with a thickness of approximately 300 m. The FW unit also contains a small FW- alteration unit close to the contact with the GNG1 unit.

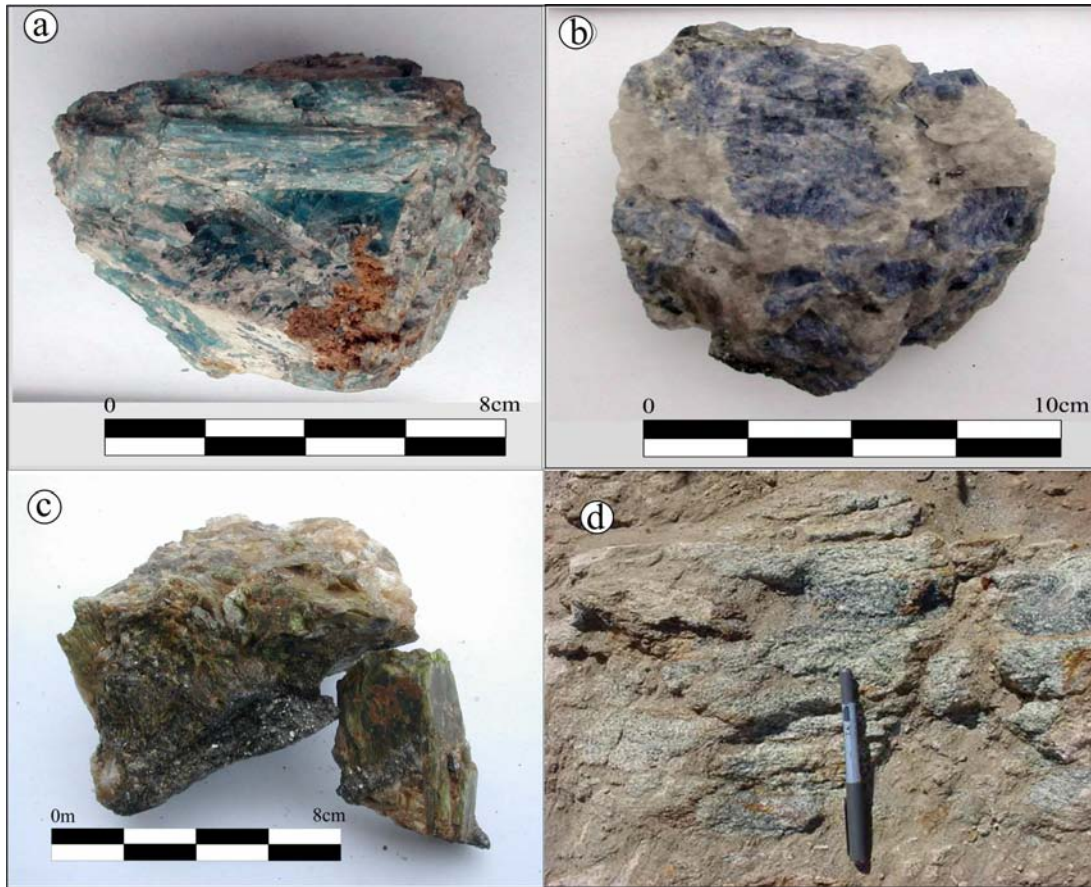


Figure 3.5. a) Cluster of large kyanite crystals from kyanite-graphite gneiss unit 2 (LK2). b) Blue zoisite crystals surrounded by quartz and minor amounts of calcite, from a boudinage calc-silicate situated within the JW-zone. c) Tremolite-actinolite crystals located in the kyanite-graphite gneiss unit 1 (LK1) close to the contact with the JW-zone. d) Altered metabasite outcropping in Block A extension.

### 3.5.3. Block B

Due to the extensive small-scale mining activities in the Block B area, no visible outcrops could be observed. The small-scale underground development reveals, however, that both the Lower and Upper Horizon are present in the block and both are being extensively and haphazardly mined.

### 3.5.4. Block D

The Block D area is mined in a similar fashion to the Block B area. A thick calcrete layer of up to 100 m thick covers the Block D area. Underground visits indicate that the JW-zone, D-zone, Footwall alteration unit and Upper Horizon are being extensively mined.

#### **3.5.4. Block D extension**

The Block D extension area consists of very similar stratigraphic units as observed throughout the rest of the deposit. However, a clear distinction between the Upper and Lower Horizons is difficult. It is possible that certain stratigraphic units were pinched or sheared out. Underground development indicates the possibility of eluvial and alluvial tanzanite. The Block D extension area is situated in a low-lying area and it is possible that weathered tanzanite could have accumulated in the approximately 40 m thick overburden.

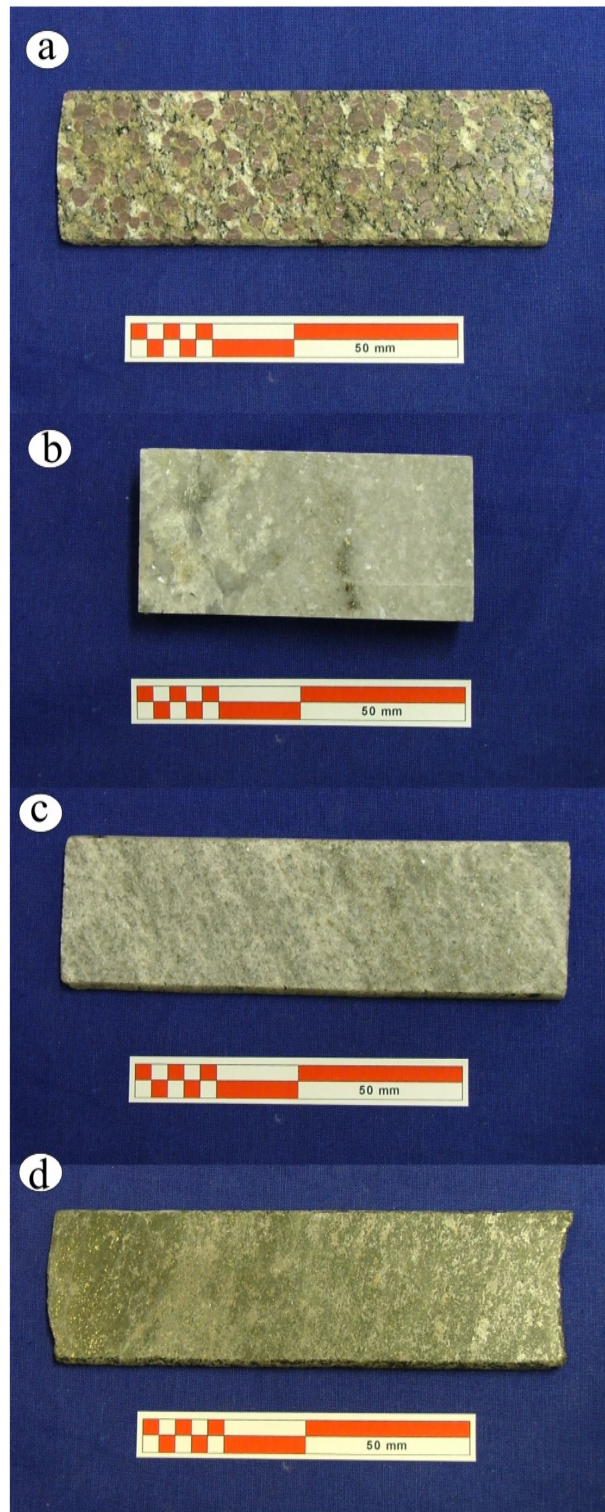
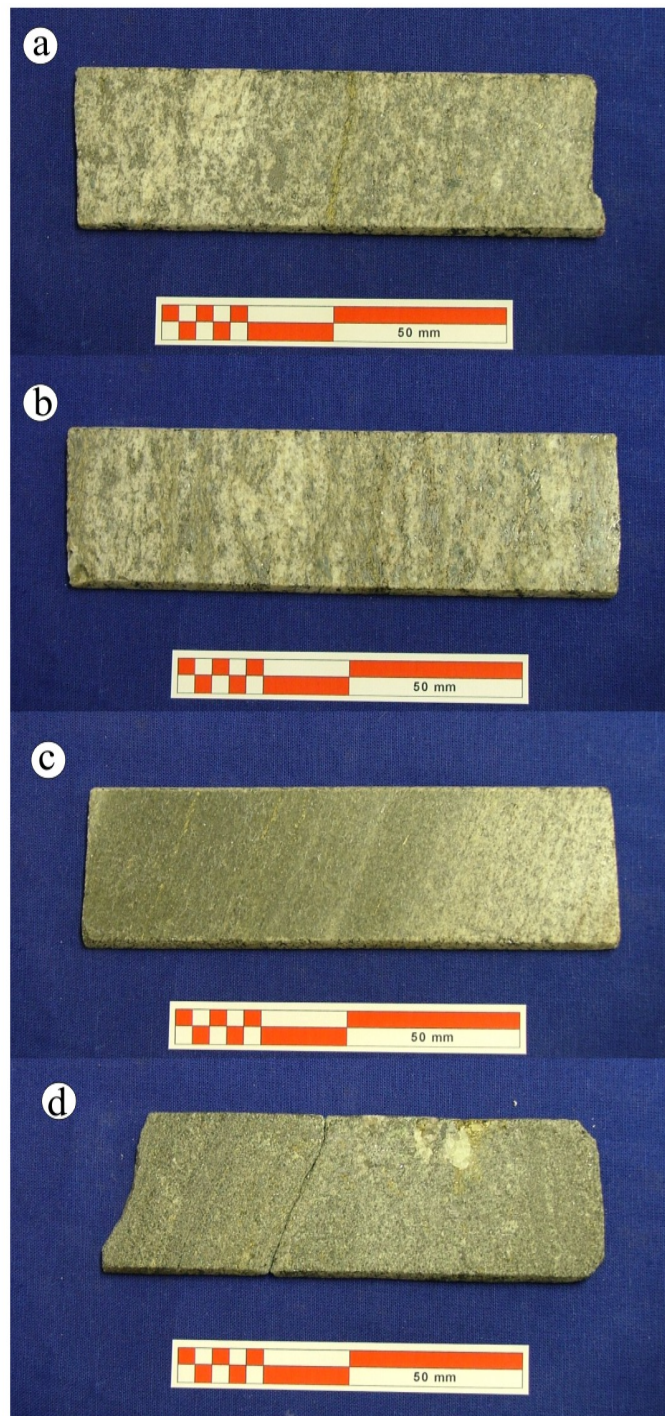


Figure 3.6. Diamond drill core of a) Garnet-sillimanite-biotite gneiss. b) Dolomitic marble. c) Banded calc-silicate hornfels. d) Graphite-calc-silicate schist.





*Figure 3.7. Diamond drill core of a) Kyanite-graphite gneiss unit 2 (LK2) which represents the hanging wall of the JW-zone. b) Kyanite-graphite gneiss unit 1 (LK1), representing the footwall unit of the JW-zone. c) Graphite-plagioclase gneiss (JW-zone). d) Calc-silicates from a boudin structure located within the JW-zone.*



## Chapter 4

### Petrography

#### 4.1. Introduction

A detailed petrographic description of the various lithological units identified within the tanzanite-bearing Lower Horizon is of utmost importance in describing and understanding the deposit. For this study, more than 400 polished thin sections were petrographically and mineralogically investigated by the author. The selection of specimens for petrographic and geochemical analyses is of vital importance in any geological study. In the Merelani deposit it is of even greater importance, since the surface outcrop is usually highly altered.

As discussed in Chapter 3, an oxidation zone which occurs from the surface to a depth of 55 to 75 m, had a weathering effect on the rocks within the zone. This investigation benefited largely from the drill holes and large-scale mine development predominantly in Block C, but also in Block D extension.

#### 4.2. Garnet-sillimanite-biotite gneiss (GNG)

Quartz (ca. 35 vol%) occurs as large granular crystals, aggregates of small recrystallised crystals and as numerous small inclusions predominantly present in garnet and K-feldspar. The large granular quartz porphyroblasts exhibit undulatory extinction and the edges are frequently resorbed. The porphyroblasts are commonly divided into smaller crystals by paragenetically-formed later minerals. A second generation of quartz consists mostly of large crystals and is probably formed due to unification recrystallisation of granular quartz. The large recrystallised quartz is commonly elongated (parallel orientated) contributing to the foliation. Aggregates of smaller recrystallised quartz grains form interlocking mosaic textures and are predominantly found between closely spaced quartz porphyroblasts.

Garnet (ca. 20 vol%) occurs as porphyroblasts up to 9 mm in diameter, enveloped by sillimanite and biotite, which define the foliation. The garnet porphyroblasts vary from euhedral to anhedral, but are predominantly subhedral in form. The porphyroblasts

commonly have a cloudy core, due to an abundance of fine inclusions resulting in a poikiloblastic texture (Figure 4.1.c). Large inclusions of quartz, sillimanite, biotite, pyrite, rutile, graphite and to a lesser degree K-feldspar and kyanite, occur mostly near the rim of the porphyroblasts, resulting in a poikiloblastic texture. The garnet poikiloblasts are commonly fractured with quartz, sillimanite, biotite and rutile filling the fractures.

Two generations of sillimanite (15 to 20 vol%) have been identified. The first generation consists of mats of sub-parallel fibrolitic needles. The fibrolitic sillimanite is often parallel to the cleavage of biotite. The fibrolitic needles also occur as inclusions in K-feldspar, quartz and garnet (Figure 4.1). Island relicts of quartz are present within swarms of fibrolite, which is also associated with K-feldspar, indicating possible formation through the “second sillimanite isograd” reaction as defined by Carmichael (1978). This is confirmed by the presence of K-feldspar and fibrolitic sillimanite as inclusions in garnet. The fibrolite is often overgrown by a second generation of sillimanite consisting of idioblasts of elongated prismatic crystals up to 5 mm long. The second generation of sillimanite occurs in an aggregate of biotite and quartz crystals. The sillimanite idioblasts commonly exhibit pleochroic haloes around zircon inclusions.

Biotite (5 to 10 vol%) predominantly occurs as aggregates around garnet porphyroblasts (Figure 4.1.a). Biotite crystalloblasts can range in size up to 2.5 mm long. Two “types” of biotite have been optically identified. Since no age relationship distinction could be made between the different biotites, the term A and B biotite will be used rather than first and second type. Type A biotite is strongly pleochroic ranging from light brown to red-brown. Type B biotite exhibits only weak pleochroism and appears darker brown in colour. The mineral chemistry of the biotite will be discussed further in Chapter 6. Both types of biotite contain inclusions of zircon, resulting in characteristic pleochroic haloes.

K-feldspar (ca. 10 vol%) occurs predominantly as large porphyroblasts and well-developed microcline-string-perthite. The crystalloblasts can be up to 2 cm in diameter, but are normally around 5 mm. The best-developed string perthites are usually associated with intense undulatory extinction. The microcline-microperthite frequently contains large rounded quartz inclusions, sometimes exhibiting corona textures. In general,

alteration of the K-feldspar is only minor and mostly restricted to slight alteration to clay and sericite in intercrystal cracks.

Plagioclase (ca. 5 to 10 vol%) usually only occurs as a subordinate mineral, although amounts vary substantially. Plagioclase crystals are generally smaller than 2 mm in diameter and commonly exhibit Carlsbad twinning.

### **Accessory minerals**

Pyrite and rutile are the two most common accessory minerals. Pyrite is often associated with biotite and graphite. Rutile is sometimes weakly pleochroic with a reddish-brown to golden brown colour. The grains are typically idiomorphic to hypidiomorphic and up to 1 mm in diameter. Rutile crystals can be locally abundant and sometimes exhibit two distinct cleavages planes intersecting at ca. 60°. Rutile is commonly associated with biotite while garnet and rutile crystals are often situated on the rim and sometimes inside the garnet granoblasts. Rutile is possibly associated with hydrothermal fluids and may be related to the abundant amounts of titanite present in the skarnoid associated graphite-plagioclase gneiss.

Relicts of kyanite occasionally occur within garnet porphyroblasts, where it was probably sheltered from retrograde replacement. Kyanite was probably replaced by sillimanite according to Carmichael's reaction, described in Chapter 6, but its time of formation is not entirely clear. Small amounts of isolated graphite needles are scattered throughout the gneiss. Other accessory minerals include zircon, apatite, ilmenite and titanite. No haematite or muscovite were observed in any of the thin sections, but were described by Malisa (1987) in similar garnet-sillimanite-biotite gneisses within the Le-latema Mountains.

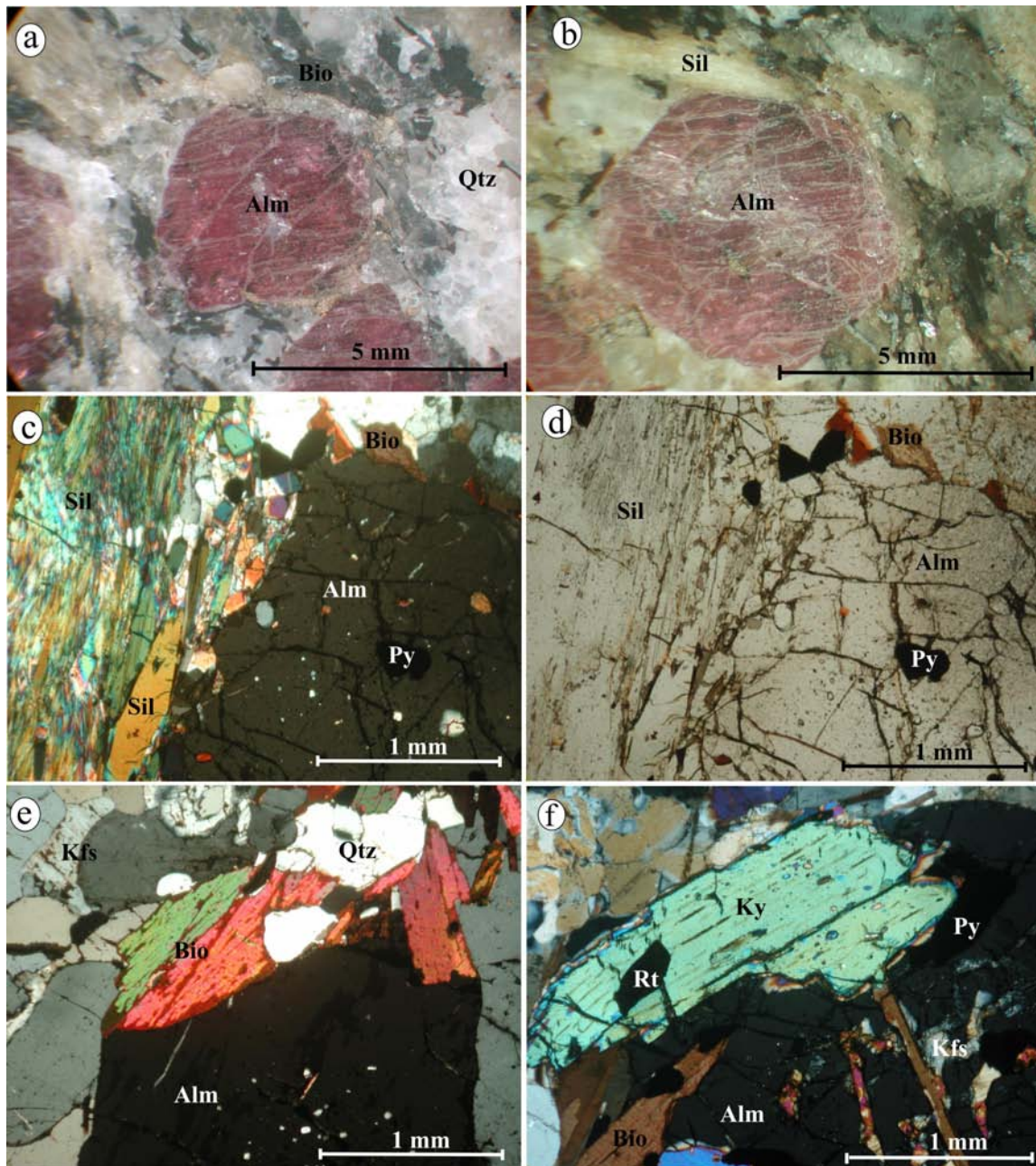


Figure 4.1. Photomicrographs of garnet-sillimanite-biotite gneiss. *a* and *b*) Stereoscopic microscope reflective light photographs of the gneiss showing the large garnet crystals surrounded by quartz, sillimanite and biotite. *c* and *d*) Crossed (left) and uncrossed (right) polars images of the GNG unit showing the fibrolitic sillimanite overgrown by later sillimanite idioblasts. *e*) Crossed polar image displaying the association of biotite with the garnet porphyroblasts. *f*) Kyanite relict situated partly within a garnet porphyroblast. The porphyroblast also contains inclusions of K-feldspar, biotite, pyrite and quartz. A rutile inclusion is located within the kyanite relict.

### 4.3. Dolomitic marble

Dolomite (up to 75 vol%) is the main rock-forming mineral in the dolomitic marble units. Dolomite is predominantly subhedral and coarse-grained, with grains ranging up to 8 mm in diameter. Dolomite displays an equigranular mosaic texture, with parallel and inclined twin lamellae. The lamellae show high interference colours. Dolomite was distinguished from calcite by means of staining, using Alizarin red S (Figure 4.2).

Calcite (15 - 25 vol%) occurs as medium- to coarse-grained, subhedral to anhedral crystals. Calcite forms intergrowths with dolomite and is relatively evenly scattered throughout the marble.

Quartz (ca. 5 vol%) occurs as medium- to coarse-grained crystals. Quartz often has an irregular to lobate texture with resorbed edges.

Pyrite, graphite and native sulphur occur as accessory minerals throughout the marble. Pyrite occurs as large euhedral grains of up to several centimetres in diameter. Pyrite crystals with nodular shapes resembling small droplets have also been observed in the marble. Graphite occurs both as localised clusters and as small isolated grains throughout the marble. Native sulphur crystals may be locally abundant and occur as large (several centimetres in diameter) grains with a light yellow to green-yellow colour.

The dolomitic marble contains isolated areas where various other minerals are present in locally abundant amounts, including:

- Plagioclase, as large poikiloblastic crystals of up to 6 mm in diameter. Plagioclase contains numerous inclusions of micas and chlorites and is often highly sericitised.
- Titanite crystals, as irregular to lobate crystals of up to 1 mm in diameter.
- Diopside, as medium-grained subhedral crystals, usually in an advanced state of alteration to microscopic-grained mass probably consisting of a mixture of chlorite, serpentine and carbonates.
- Chlorite and colourless phlogopite, as large (centimetre size) aggregates of randomly orientated medium to coarse-grained flakes.



- Pyrite, as euhedral to subhedral grains that vary from 0.1 mm up to several centimetres in diameter.
- Pyrrhotite, as isolated, subhedral, medium-grained crystals.

The presence of accessory serpentinised olivine and muscovite was described by Malisa (1987) in similar dolomitic marbles within the Lelatema Mountains.

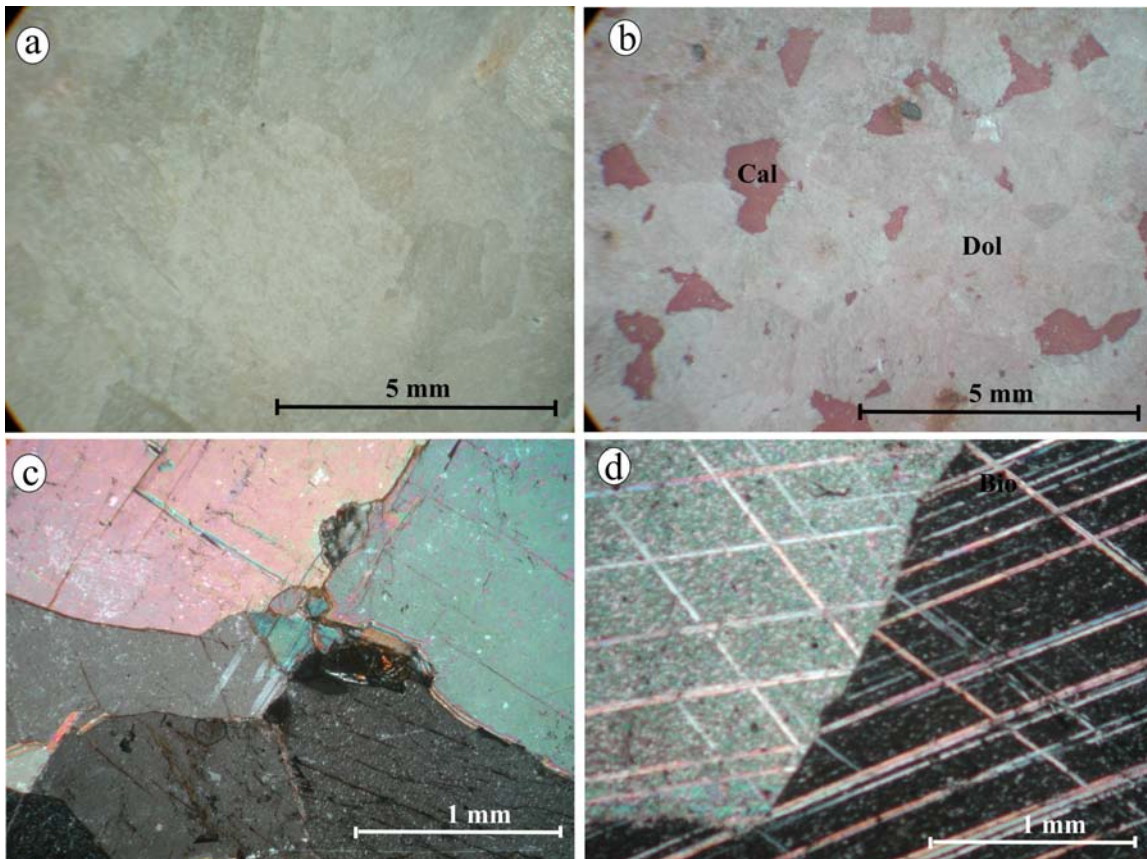


Figure 4.2. Photomicrographs of the dolomitic marble units, DM1, DM2 and DM3. a and b) Stereoscopic microscope reflective light photographs of the dolomitic marble units. The marble in photograph b is treated with Alizarin red S, resulting in the calcite being coloured red, while the dolomite remains uncoloured. c and d) Crossed polar images of the dolomitic marbles indicating its coarse-grained nature.

#### 4.4. Banded calc-silicate hornfels (BCF)

The rock can be divided in three zones due to the presence of alternating seams or layers of calc-silicates and silicates, as described in Chapter 3, namely the quartzo-feldspathic zone, the transition zone and the calc-silicate zone (Figure 4.3). The calc-silicate constituent is however predominant, resulting in the inclusion of the term “calc-silicate” in the general name of the hornfels.

**Quartzo-feldspathic zone:** Constituent minerals are microcline, quartz, sulphides, muscovite, plagioclase and graphite.

K-feldspar commonly displays crosshatched twinning characteristic of microcline. K-feldspar predominantly occurs as granoblastic-polygonal textures comprising of aggregates of subhedral grains. The grains are normally around 0.4 mm in diameter with polygonal grain boundaries. Quartz and K-feldspar represent the main-rock forming minerals in the quartzo-feldspathic zone. Quartz is clear and often shows undulose extinction. It is also present as aggregates of similar grain size and shape to the K-feldspar. Plagioclase appears as isolated fine-grained crystals, sometimes displaying polysynthetic twinning. Muscovite consists of sub-parallel aligned crystals usually neighbouring graphite, and small-elongated aggregates up to 0.5 mm. Graphite is present as isolated flakes of sub-parallel alignment and around 0.5 mm in length. The main sulphides in the quartzo-feldspathic zone are pyrite, usually present as subhedral grains of around 0.5 mm but up to 1.5 mm in diameter. Minor amounts of small pyrrhotite grains are also found in the quartzo-feldspathic zone. Titanite is present as small amounts of isolated rounded grains of around 0.2 mm in diameter.

**Transition zone:** Constituent minerals are plagioclase, quartz, K-feldspar, sulphides, muscovite, diopside, graphite and titanite.

Plagioclase is present throughout the transition zone, but is locally abundant, forming large crystals of up to 5 mm in diameter. The plagioclase appears to be of earlier origin, since it is overgrown by scapolite. Inclusions of diopside and graphite have been observed in the plagioclase. The plagioclase has an anorthite content of 80 to 90%, therefore classifying as bytownite. A second generation of plagioclase, possibly similar

to that of the quartzo-feldspathic zone, appears to have been altered to K-feldspar, suggesting a period of potassium metasomatism. Quartz is present as a) large crystals with irregular to lobate grain boundaries of up to 2 mm in diameter; b) smaller quartz grains similar to that in the quartzo-feldspathic zone and c) as myrmekitic intergrowths in plagioclase, K-feldspar and diopside. Type 'a' quartz is often fractured and commonly displays undulose extinction.

The appearance of K-feldspar is similar to that of the quartzo-feldspathic zone, but the amount present decreases towards the calc-silicate zone. The K-feldspar is present as microcline. Titanite, muscovite and sulphides are most abundant in the transition zone. Titanite is light - to red brown pleochroic and usually occurs as small rounded crystals of around 0.3 mm in diameter. Muscovite not only increases in quantity, but also reaches its largest grain size in the transition zone. Muscovite is present as individual crystals, but also as aggregates that can reach up to 1 mm in diameter. Sulphides form microscopic and macroscopic stringers that enhance the banding of the hornfels. The transition zone consists of both pyrrhotite and pyrite in roughly equal amounts. The pyrrhotite is commonly anhedral and sometimes contains euhedral cubic or pentagonal dodecahedrons pyrite overgrowths. Graphite is as abundant as in the quartzo-feldspathic zone and also exhibits the same shape.

**Calc-silicate zone:** Constituent minerals are diopside, scapolite, carbonates, quartz, K-feldspar and sulphides.

Diopside is the main rock-forming mineral in the calc-silicate zone. It forms large (up to 3 mm in diameter) anhedral to subhedral crystals, but is present predominantly as crystals smaller than 1mm. Diopside is colourless to pale green in colour and often contains clouded cores. Scapolite and carbonates are present in only slightly lesser amounts than diopside. Scapolite is present as large anhedral crystals of up to 2 mm in diameter. Straight grain boundaries are sometimes observed between scapolite and calcite. Scapolite formed as an alteration product of plagioclase. Scapolite is colourless with interference colours varying from low first order grey to high first order. Carbonates are slightly cloudy with high interference colours. The carbonates contain both inclined and straight twin lamellae. The carbonates are usually anhedral, although aggregates sometimes show straight grain boundaries. Both calcite and dolomite are



present and can range up to 2 mm in diameter. The carbonate minerals tend to increase in grain size towards the middle of the calc-silicate zone.

Quartz occurs as an accessory mineral in the calc-silicate zone and is restricted to isolated crystals of around 0.4 mm in diameter. Quartz is clear and contains no fractures, but exhibit limited undulatory extinction. Small rounded quartz inclusions are present in diopside. K-feldspar is predominantly anhedral, colourless and closely resembles quartz. Orthoclase is the main K-feldspar present and no twinning is observed.

Plagioclase is restricted to relict crystals as a result of partial replacement by scapolite. Plagioclase ranges from <0.1 mm to over 0.6 mm in width and is characterised by polysynthetic twinning and low interference colours. Optical investigation suggests an anorthite content of around 80%, which correlates well with the anorthite composition of the plagioclase in the transition zone. Since no plagioclase was observed without the association with scapolite it suggests that the replacement is incomplete.

Titanite, of similar colour and pleochroism to that observed in the transition zone, is present in the calc-silicate zones, but the crystals are generally more oval shaped. Titanite decreases in content, but usually increases in size from the transition zone, ranging up to 1 mm along the elongated axis. Muscovite is also less abundant with respect to the transition zone. Muscovite is mostly confined to the vicinity of graphite flakes where it occurs as isolated elongated but poorly developed grains. Sulphides predominantly consist out large (up to 1 mm in diameter) anhedral pyrrhotite grains, with minor amounts of euhedral pyrite. Graphite is present as isolated randomly orientated flakes of up to 1 mm in diameter.

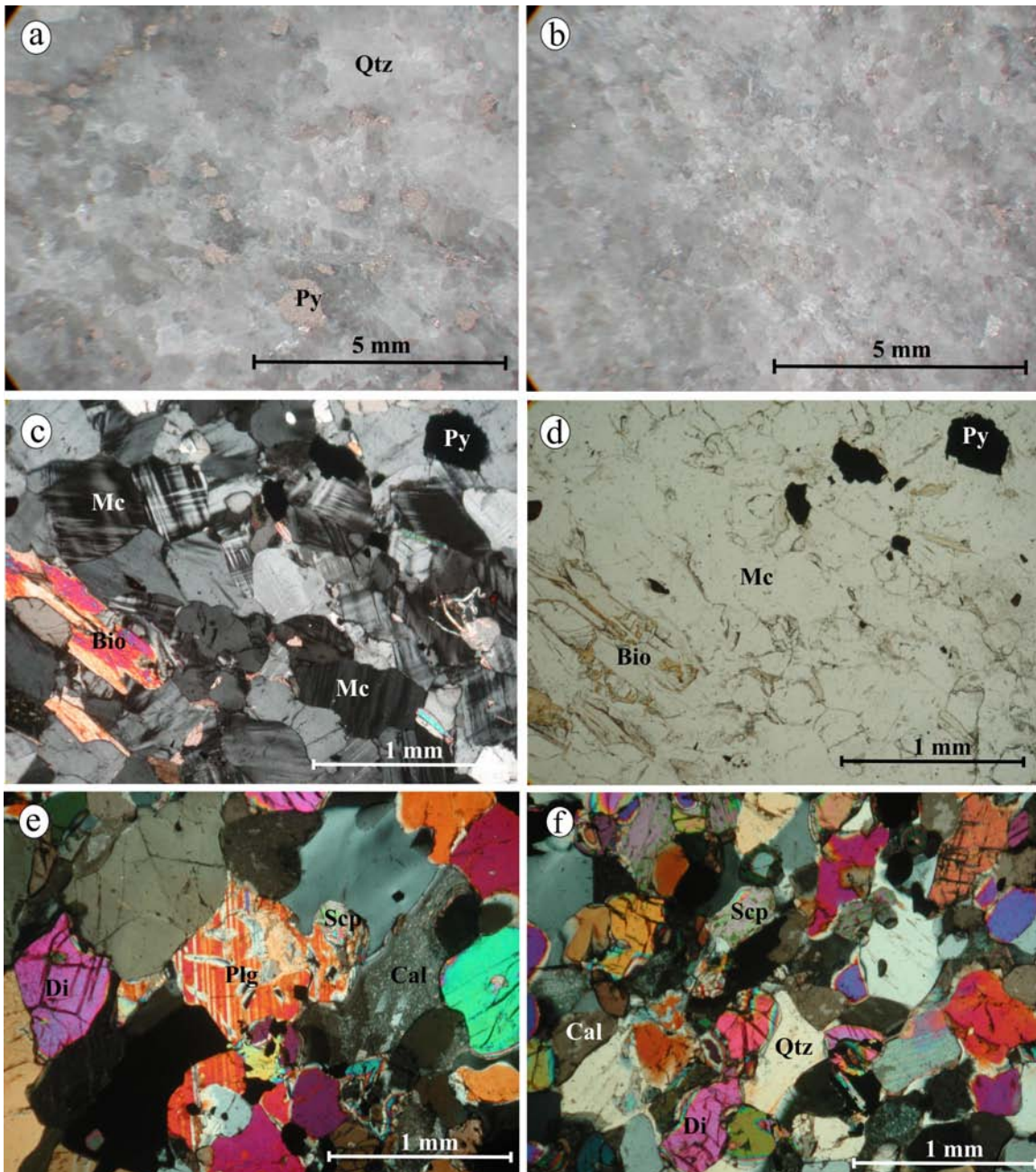


Figure 4.3. Photomicrographs of the banded calc-silicate hornfels. *a* and *b*) Stereoscopic microscope reflective light photographs of the hornfels indicating the presence of pyrrhotite, quartz and other light minerals, including calc-silicates. *c* and *d*) Photomicrographs of the BCF with crossed (*c*) and uncrossed (*d*) polars. The photographs are of the quartzo-feldspathic-rich zone of the BCF and contain numerous microcline crystals and minor amounts of muscovite. *e* and *f*) Cross polar photomicrographs of the calc-silicate zone of the BCF comprising of diopside, scapolite, calcite, plagioclase and quartz.

#### 4.5. Graphite-grossular-calc-silicate schist (GCS)

Quartz (15 to 50 vol%) is the main rock-forming mineral throughout most of the schist, except in and adjacent to the calc-silicate-rich zones. Quartz occurs as medium- to coarse-grained crystals and as smaller recrystallised grains. The large (up to 3 mm long) crystals are sometimes elongated parallel to the schistosity. The quartz grains are usually slightly strained, exhibiting limited undulose extinction. They are often highly fractured with the fractures filled with serpentine, clay and calcite. The recrystallised quartz (ca. 0.2 mm in diameter) occurs throughout the schist, but is the only quartz present in the calc-silicate zone.

Graphite is a very conspicuous constituent of the schists. The graphite content can be up to over 20 wt% but is normally around 10 to 12 wt% (Davies and Chase, 1994). Graphite forms large isolated veinlets and plates consisting of flaky graphite aggregates (Figure 4.4). The graphite flakes can range up to 2 mm in length. The graphite flakes and clusters exhibit a preferred orientation due to the sub-parallel alignment of the individual flakes. Pyrite and small grossular crystals are commonly associated with the graphite. The graphite content decreased dramatically in the calc-silicate zones, where it normally occurs as less than 5 wt%.

Grossular (ca. 10 vol%) occurs predominantly as anhedral skeletal porphyroblasts of over 5 mm in diameter (Figure 4.4). The grossular porphyroblasts are usually intensely fractured. The fractures often radiate from titanite crystals commonly associated with the garnet. The grossular is clear to light green in colour under the microscope and generally near isotropic. The grossular is possibly of a rare distinctively green hydrogrossular type and will be further discussed in Chapter 6. Small grossular crystals occur in the calc-silicate-rich zones within the schist. All the grossular crystals are light green in colour and of a slightly darker shade than the skeletal porphyroblasts. The grossular grains are almost exclusively restricted to graphite and pyrite grain boundaries and are usually smaller than 0.2 mm in diameter. No evidence of the grossular porphyroblasts was observed in the calc-silicate zones.

Diopside (5 to 30 vol%) is relatively common throughout the schist and is one of the main constituents of the calc-silicate-rich areas. Diopside occurs as anhedral to

subhedral crystals, usually smaller than 0.4 mm outside of the calc-silicate-rich zones, but can be as big as 0.8 mm within these zones. The diopside frequently contains inclusions of titanite and in the calc-silicate-rich zones inclusions of grossular are also sometimes present. Pleochroism can range from greenish, yellowish, bluish to pinkish in colour. The diopside is sometimes altered to a microscopic-grained yellow-green mass, especially along cleavage planes. The presence of alteration-rich patches possibly suggests the complete alteration of some diopside grains.

Scapolite (0 to 20 vol%) is restricted to the calc-silicate layers. It is present as irregular-shaped, medium-grained crystals that form veins of around 3 mm in width. The veins are all parallel to each other and to the schistosity. Scapolite is often cloudy due to the presence of numerous small inclusions, the most prominent of which is titanite. The partial replacement of plagioclase by scapolite is sometimes still observable.

Plagioclase (5 to 20 vol%) is present as two types in the schist. The majority of plagioclase is situated in the calc-silicate-rich areas, where it occurs as large crystals of over 2 mm in diameter. The plagioclase in these areas is of an almost pure anorthite composition. Scapolite forms as a replacement mineral of plagioclase. It only occurs as relicts in scapolite veins and commonly contains large inclusions of diopside, quartz and graphite, which often divides the plagioclase into segments. The second type of plagioclase occurs as isolated medium-grained crystals outside of the calc-silicate zones. Plagioclase is close to the albite end-member and is often fractured and cloudy.

Minor amounts of K-feldspar are scattered throughout the schist, normally occurring as isolated crystals of up to 1 mm in diameter.

Titanite is a very common accessory mineral throughout the schist. It is strongly pleochroic from light to dark brown. Titanite occurs as inclusions in quartz, diopside, feldspar and especially grossular, often resulting in radiating fractures.

An alteration mass is present as very fine-grained, yellow-green intergrowths probably of uralite, chlorite and carbonates, sometimes overgrown by serpentine fibres, possibly chrysotile. The matted alteration mass commonly exhibit undulatory extinction and normally occurs as an accessory mineral, but is much more abundant in localised areas.

The presence of diopside relicts in the alteration masses suggests that the formation of the mass is at least partly related to the alteration of diopside. The alteration minerals will be further discussed in Section 4.12.

Pyrite (ca. 5 vol%) is almost exclusively associated with graphite, often occurring as fillings between graphite crystals. The pyrite is sometimes rimmed by carbonates, especially calcite and siderite. Calcite occurs as an accessory mineral throughout the schist and sometimes appears as fillings in fractures. Calcite is locally abundant, especially in fractures and appears to be related to the formation of serpentine.

#### **4.6. Kyanite - graphite gneiss (HW / FW and LK 3, 4, 5, 6)**

Quartz (ca. 50 vol%) is the main rock-forming mineral in the gneiss. Quartz within the kyanite-graphite gneisses occurs in four main forms:

- 1) Large relict grains of over 1 cm in length. The relict grains are frequently elongated and sub-parallel aligned. The grains exhibit undulose extinction almost without exception. The formation of sub-grains is very common with the sub-grains frequently aligned parallel relative to the elongation of the super individual. The relict grains can sometimes contain deformation lamellae diagonal to the elongation of the grains. The relict quartz has irregular to lobate grain boundaries, characteristic of grain boundary migration recrystallisation (Passchier, 1996). Quartz is commonly fractured, with the fractures often stained reddish-brown, probably due to the presence of iron oxides.
- 2) Small recrystallised grains often surround and divide the large relict grains. The grains probably formed due to the dynamic recrystallisation of the superindividuals. The grains are around 0.02 mm in diameter and occur as both elongated and well-rounded crystals.



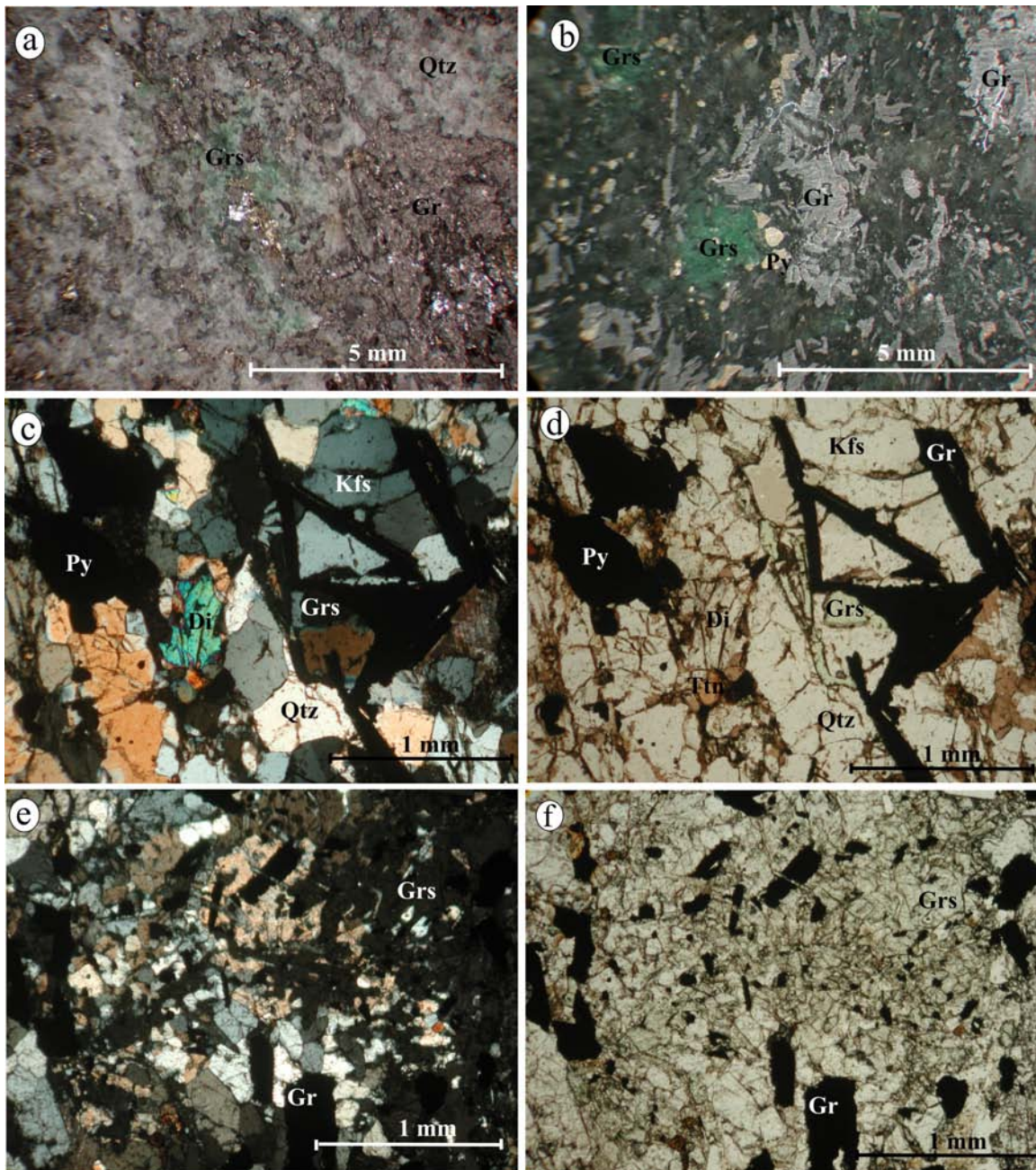


Figure 4.4. Photomicrographs of the graphite-calc-silicate schist. *a* and *b*) Stereoscopic microscope reflective light photographs of the schist, clearly indicating the presence of the distinctive green grossular porphyroblasts and the high graphite content. Photograph *a* is unpolished, while photograph *b* is polished resulting in a darker texture. *c* and *d*) Photomicrographs of the GCS with crossed (*c*) and uncrossed (*d*) polars. The presence of grossular garnet, quartz, K-feldspar, graphite, titanite and pyrite is visible. The uncrossed polar image shows the light green colouration of the grossular garnet. *e* and *f*) Crossed (*e*) and uncrossed (*f*) photographs of the GCS, indicating the presence of large disseminated grossular garnets within the schist.

- 3) Intermediate size grains of between 0.2 mm and 1 mm in diameter. The quartz has similar characteristics as the relict quartz grains, except that they show little or no elongation. The grains probably formed as a result of complete sub-grain formation and division of the relict grains.
- 4) Myrmekitic quartz that is commonly present in the plagioclase.

Biotite (ca. 2 to 10 vol%) can vary considerably in content through the gneiss. It does, however, have a tendency to concentrate in graphite-rich areas. Biotite is present as aggregates and individual flakes of around 0.3 mm in length, although it can be substantially larger, especially when associated with graphite. Biotite is colourless to light brown in colour and often resembles muscovite.

Kyanite (ca. 5 to 10 vol%) is a very conspicuous and characteristic mineral of the gneiss. It occurs as large porphyroblasts, poikiloblasts and skeletal crystals usually with an elongated bladed form (Figure 4.5). Kyanite can range up to centimetres in diameter, but is mostly smaller than 0.4 mm in diameter. Kyanite is colourless with a well-developed [100] cleavage and is occasionally twinned parallel to the length of the crystals. It occurs randomly orientated with no preferred orientation of the [100] cleavage plane. Poikiloblastic kyanite contains large amounts of quartz blebs as inclusions (Figure 4.5.c and d). When the quartz is well developed it can result in a skeletal structure often with lobate grain boundaries for the kyanite. Kyanite crystals are sometimes altered, especially along the cleavage planes, causing a cloudy appearance. Sillimanite fibres occasionally corrode kyanite marginally, sometimes forming limited to well-developed parallel growth replacements.

Feldspar frequently occurs as separate aggregates combining to produce feldspar-rich layers. The layers vary in thickness from <1 mm to ca. 1 cm in diameter and is predominantly parallel to the schistosity. K-feldspar is the main feldspar phase, occurring as clear to cloudy grains. The presence of alternating layers rich in feldspar and quartz give the rock a banded texture visible on a macro and micro-scale. The size of the K-feldspar grains in the layers appears to correlate with the thickness of the layers varying in size from 0.2 mm to 5 mm in diameter. K-feldspar and plagioclase are present within the bands, although both also occur as isolated grains. Plagioclase, classified as oligoclase, occurs primarily as single grains within the feldspar-rich zone,

and isolated grains throughout the rock. Plagioclase is usually smaller than the K-feldspar. Polysynthetic twinning is well developed in certain grains. Both K-feldspar and plagioclase exhibit varying degrees of localised alteration, although sericitisation was never observed.

Graphite is fairly uniformly distributed throughout the gneiss and is normally around 1 mm in diameter. Larger graphite flakes of up to 6 mm have been observed associated with the pegmatitic layers within the gneisses. The graphite content in the gneisses varies between ca. 8 to 10 vol%.

Sillimanite is present as accessory mineral in the hanging wall (LK2), but is locally abundant in the footwall where it can constitute almost half of the aluminium silicate content. Sillimanite occurs as fibrolite and as large acicular crystals, but the age relationship is difficult to establish. Fibrolite inclusions are present in plagioclase, K-feldspar as well as quartz, and appear to be replacing muscovite. Columnar sillimanite commonly replaces kyanite.

Muscovite is present as an accessory mineral and is predominantly present as aggregates that rim kyanite porphyroblasts, although isolated flakes are also present. Green mica (fuchsite) porphyroblasts, with a  $V_2O_3$  content of up to 2.69% (Malisa, 1987) occur mainly in the Upper Horizon, but is also present in minor amounts in LK3 and LK4. Pyrrhotite and pyrite are the main sulphides present in the gneiss, with pyrrhotite usually predominant. Both minerals exhibit anhedral to subhedral grains of up to 3 mm in diameter. They are commonly associated with graphite, forming in interstitial cavities between graphite grains. Chalcopyrite is sometimes present as small inclusions within pyrrhotite. Sphalerite, zircon, apatite, titanite and rutile are present as accessory minerals throughout the gneiss.



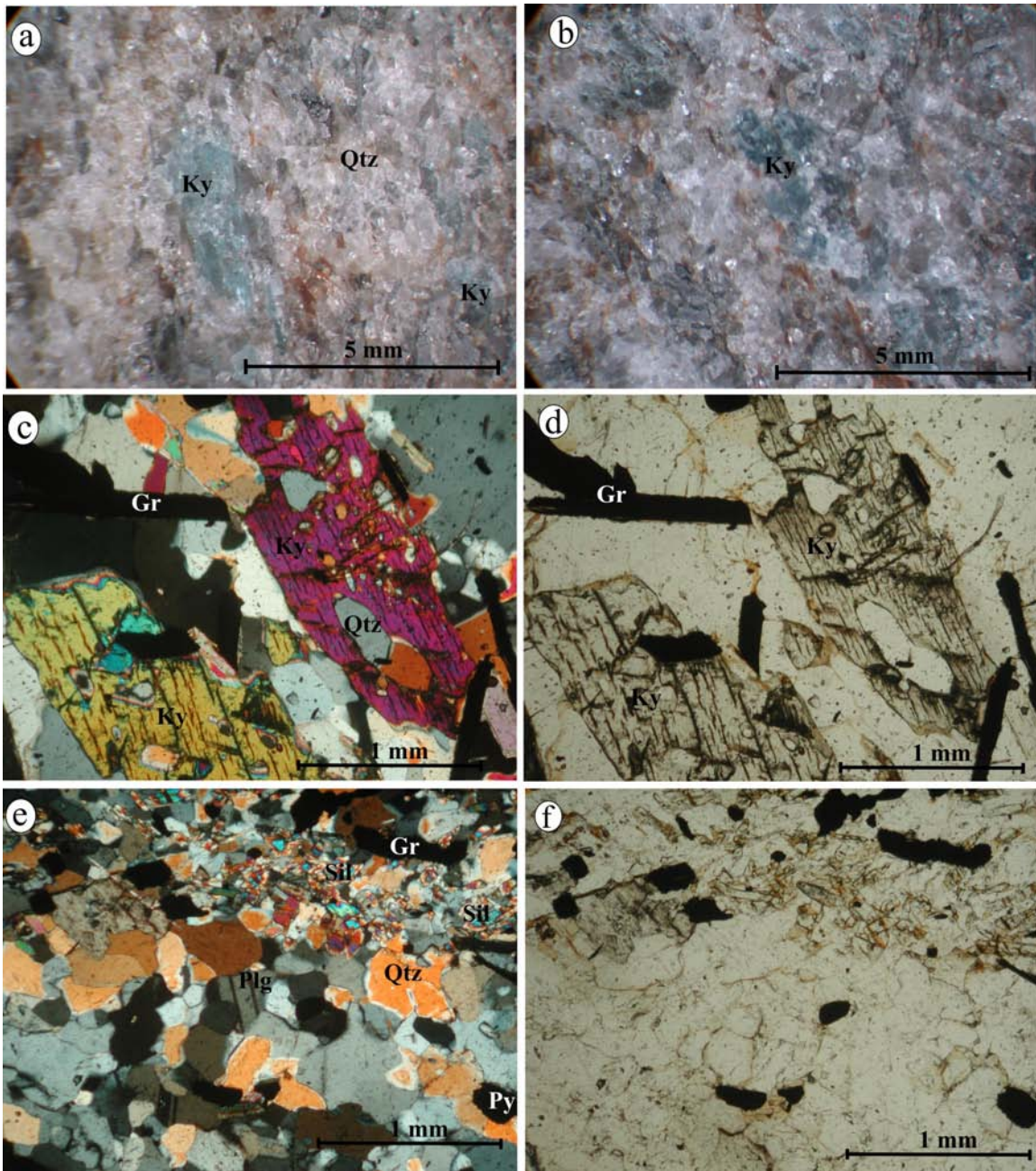


Figure 4.5. Photomicrographs of the kyanite-graphite gneisses. *a* and *b*) Stereoscopic microscope reflective light photographs of the LK2 (HW) and LK1 (FW) units. Both the units contain high amounts of characteristic light blue kyanite crystals. *c* and *d*) Photographs with crossed (*c*) and uncrossed (*d*) polars, illustrating the large kyanite porphyroblasts present in both units. The specific photographs are of the LK2 unit. *e* and *f*) Crossed (*e*) and uncrossed (*f*) polar images of the LK1 unit in close proximity to the neighbouring sillimanite bearing GNG unit. This resulted in sillimanite occurring within the normally predominantly kyanite-bearing gneiss.

#### **4.7. Graphite - plagioclase gneiss (JW-zone, C- and D-zone)**

As described in Chapter 3, the graphite-plagioclase gneiss appears to be a skarn associated metasomatic alteration and dehydration product of the kyanite-graphite gneiss and is therefore relatively similar to the latter (Figures 4.5, 4.6 and 4.7). This section aims to only highlight the differences between the two gneisses.

Quartz (ca. 45 vol%) is relatively similar to that described for the kyanite-graphite gneisses. The average grain size does however tend to be smaller in the graphite-plagioclase gneiss compared to the kyanite-graphite gneiss. The decrease in grain size is most pronounced in certain areas, especially close to the calc-silicate contact, where evidence of dehydration is observed.

Feldspar still occurs as aggregates that form layers, but plagioclase supersedes K-feldspar as the dominant feldspar present. Plagioclase (ca. 20 vol%) therefore increased in content compared to the kyanite-graphite gneisses. The plagioclase content tends to first increase followed by a slight decrease towards the calc-silicate zones, although local deviation does occur. Plagioclase aggregates can be up to centimetres in diameter and consist of interlocked plagioclase grains. Plagioclase grains vary from 0.1 mm to over 3 mm in diameter and are usually subhedral in shape. The mineral is clear to cloudy in colour and most of the plagioclase has well developed polysynthetic twins. Rare kink-banding can be observed in the plagioclase grains. Optical investigation of the plagioclase reveals an increase in the anorthite content towards the calc-silicate zones ranging from oligoclase to anorthite. This change in composition is confirmed by microprobe analysis and will be discussed in Chapter 6 and provides evidence for a typical calc-silicate skarn zonation pattern.

Biotite occurs as an accessory mineral but still has the same composition as the biotite present in the kyanite-graphite gneisses. Biotite tends to decrease in quantity with an increase in plagioclase.



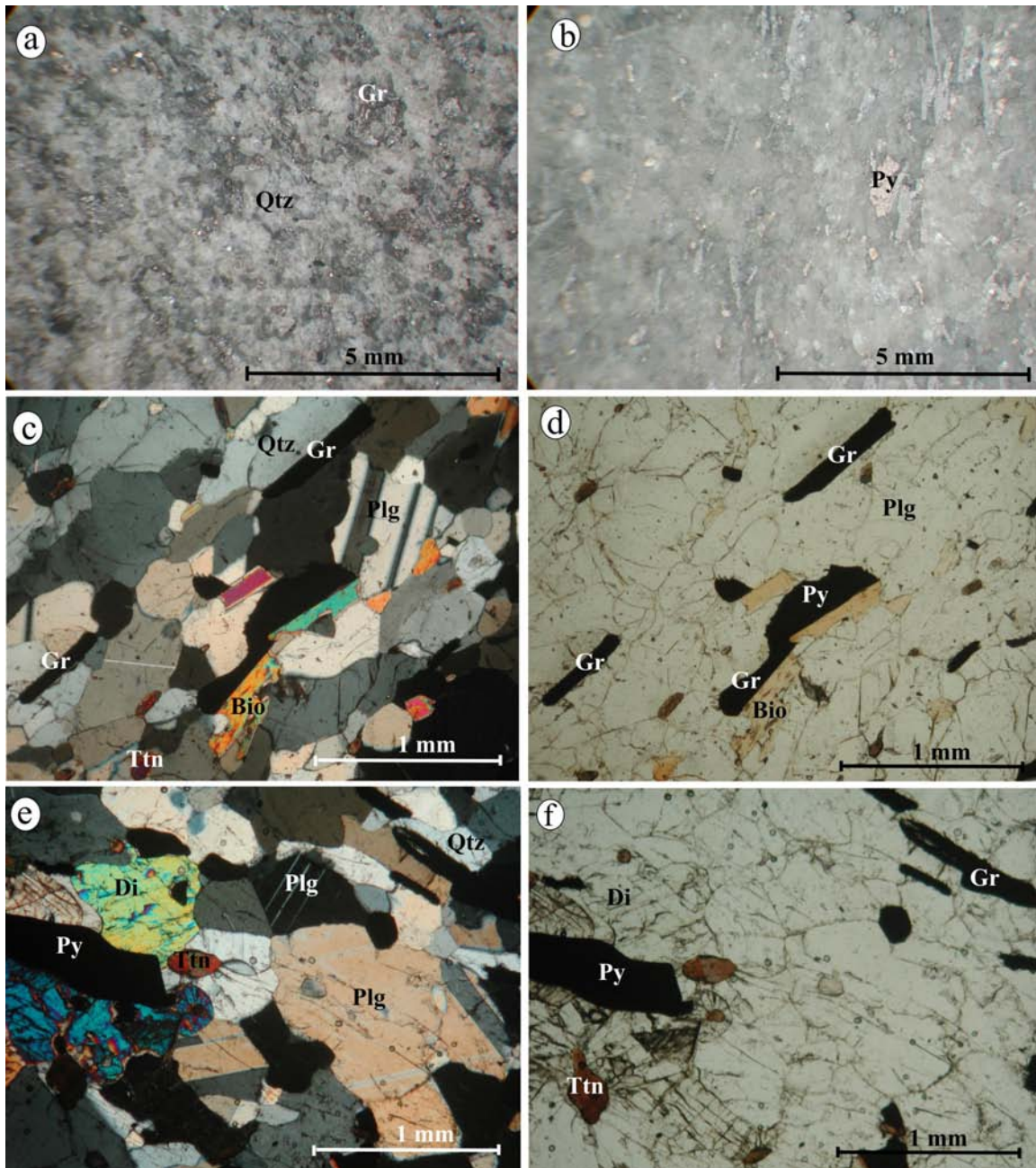


Figure 4.6. Photomicrographs of the graphite-plagioclase gneiss (JW-zone). *a* and *b*) Stereoscopic microscope reflective light photographs of JW-zone, with photograph *a* of an unpolished sample and *b* of a polished sample. *c* and *d*) Crossed (*c*) and uncrossed (*d*) polar photomicrographs of a typical JW-zone comprising of quartz, plagioclase, graphite, biotite, K-feldspar and pyrite. *e* and *f*) Crossed (*e*) and uncrossed (*f*) polar images of the contact between the JW-zone and the reaction zone surrounding the calc-silicate boudins. Notice the high amounts of plagioclase within the JW-zone.

Titanite increases in quantity and grain size towards the contact with the calc-silicate units. Titanite occurs as subhedral crystal and tends towards a diamond shape usually smaller than 0.5 mm (Figures 4.6 and 4.7).

Small amounts of diopside, tremolite, chlorite, calcite, serpentine and clay minerals are present in localised areas in the vicinity of the calc-silicate units. The minerals tend to concentrate in vein-like zones, along which fluid migration appears to have occurred. The channel ways are characterised by the abundance of graphite and follow the preferred orientation of the graphite flakes.

Diopside is present in slightly higher amounts than the other “vein” minerals and also occurs outside the vein-like structures. It is usually present as anhedral grains smaller than 0.2 mm in diameter. Tremolite forms radiating crystals and is an alteration product of diopside.

#### **4.8. Pyroxene relicts**

Diopside (ca. 70 to 80 vol%) is the main rock-forming mineral of the pyroxene relicts within the boudins (Figure 4.8). Diopside occurs as relatively equigranular interlocking polygonal grains of between 0.2 mm and 0.8 mm in diameter. Diopside is usually clear to light greyish in colour and forms euhedral to subhedral crystals. Diopside interference colours vary from upper to lower second-order colours. The grain boundaries are usually straight and 120 ° triple junctions are commonly observed. Diopside is sometimes cloudy along the cleavage planes, indicating the initiation of alteration. Diopside grains can occasionally contain numerous small rounded inclusions of pyrite.

Grossular (ca. 5 to 20 vol%) is sometimes present as clusters of euhedral to subhedral grains that form irregular-shaped veins that crosscut and replace the diopside matrix (Figure 4.8.a). The grossular grains present in the veins consist of dodecahedral and trapezohedral crystals, and also slightly more rounded variants of the two. The individual grossular grains in the veins are sometimes difficult to distinguish and are usually smaller than 0.5 mm in diameter. The grossular veins can however be over 1 cm in width, and several centimetres



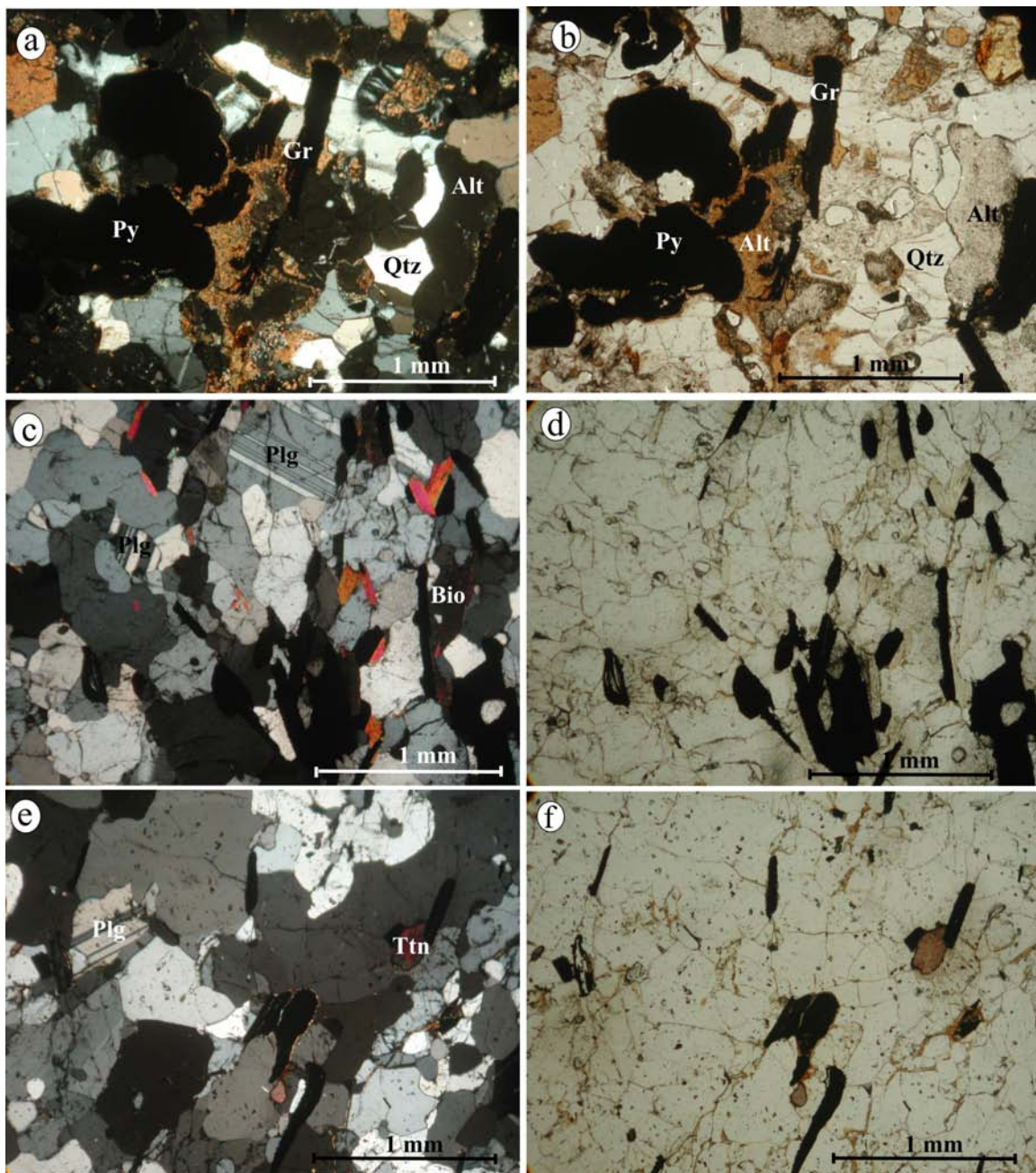


Figure 4.7. Photomicrographs of the graphite-plagioclase gneisses. *a* and *b*) Highly weathered D-zone with crossed (*a*) and uncrossed (*b*) polars. *c* and *d*) C-zone with crossed (*c*) and uncrossed (*d*) polars comprising of quartz, plagioclase, graphite and biotite. *e* and *f*) JW-zone with crossed (*e*) and uncrossed (*f*) polars with similar composition to the C-zone except for a higher amount of titanite present.

long. Grossular also occurs as aggregates of smaller than 0.5 mm in diameter and less commonly isolated grains replacing the diopside matrix. Partly developed grossular veins completely surround diopside grains that have not been replaced. The grossular is sometimes poikiloblastic, containing inclusions of diopside and graphite, especially in the partially developed veins.

Quartz (ca. 5 to 10 vol%) is present in minor amounts throughout the relict units. It occurs in higher amounts when associated with the grossular veins. All the quartz grains are clear and exhibit no undulose extinction. Quartz associated with grossular often forms in interstitial positions and can sometimes assume the grain boundary form of grossular. The quartz present in the matrix is usually smaller and has irregular grain boundaries.

Graphite (ca. 5 vol%) is a common accessory mineral. It usually occurs as isolated decussate flakes of around 0.5 mm in length. Pyrite (ca. 5 vol%) occurs as solitary euhedral to subhedral crystals of around 0.1 mm to 0.8 mm in diameter. Oxidation rims are sometimes present around pyrite. Plagioclase is also present in accessory amounts and occurs as medium-grained subhedral crystals, occasionally forming small clusters. Titanite occurs as rounded fine-grained crystals, with limited pleochroism. Titanite is often partly altered to leucoxene. Other accessory minerals include apatite, ilmenite, rutile and zircon.

#### **4.9. Calc-silicate skarn boudins**

Quartz (ca. 10 – 65 vol%) is a major constituent of the calc-silicate skarn boudins and is usually one of the main rock-forming minerals together with locally abundant grossular, diopside and zoisite (Figure 4.9). It occurs as equidimensional grains, as well as elongated crystals. The elongated quartz grains range to over 3 mm in length, are often undulose and exhibit sub-grain development. They are frequently fractured perpendicular to the elongation and less commonly occur parallel to it. The equidimensional quartz is medium-grained, possibly as a result of complete sub-grain development of the elongated grains. Both frequently occur as sub-parallel veins along the preferred orientation of the graphite grains.



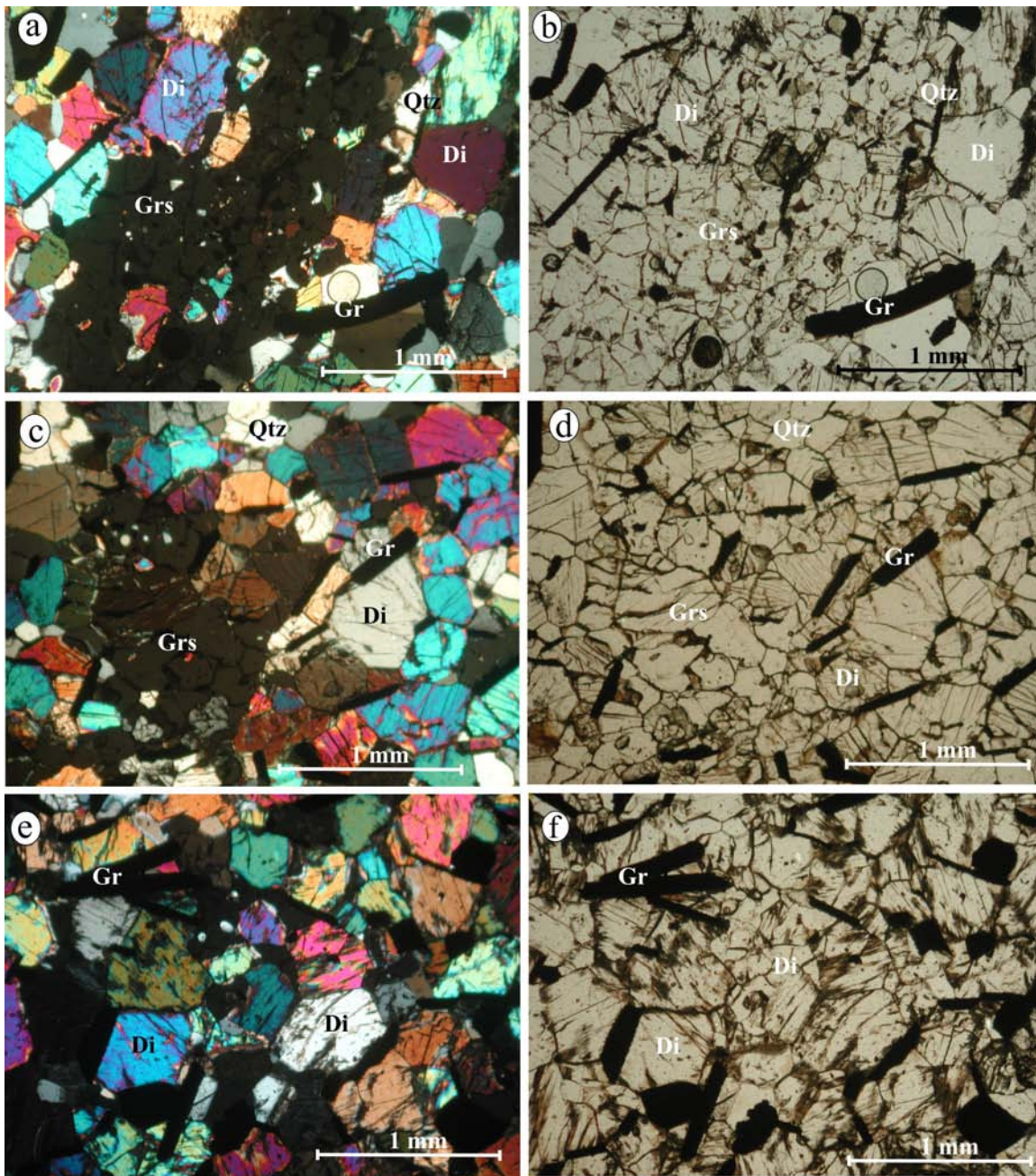


*Figure 4.8. Photomicrographs of the pyroxene relict units, with the crossed polars on the left and uncrossed polars on the right. a to d) Diopside grains, the main mineral constituent of the pyroxene units, partly replaced by grossular garnet. e and f) Slightly weathered diopside within the pyroxene relicts.*

Grossular is locally abundant and constitutes one of the main rock-forming minerals in certain areas. It forms aggregates of medium-grained subhedral to anhedral crystals (Figure 4.9). The aggregates form veins usually several centimetres thick and tens of millimetres long. The grossular veins have a sub-parallel alignment similar to the preferred orientation direction of the graphite and quartz veins. The aggregates contain isolated grains and clusters of quartz and diopside.

Zoisite is locally abundant and occurs as elongated euhedral to subhedral grains. It is often rectangular in shape, with a well-developed cleavage parallel to the elongation (Figure 4.9c, d, e, f). The zoisite grains usually vary from 0.1 mm to 2.5 mm in length. It is often fractured and cloudy in colour, with varying degrees of alteration to serpentine, halloysite and clay minerals. Zoisite also appears as vein-like aggregates that are of smaller dimensions than the grossular veins. The elongation direction and the direction of the sub-parallel veins are similar to that of the grossular and quartz veins.

Diopside is present in a similar fashion to that described for the mantle boudins. The diopside is sometimes completely replaced by grossular, quartz, and zoisite. Large areas of the boudins do however still consist of relict mantle-boudin diopside. Most of the diopside occurs near the centre of the boudin and surrounds, or is close to, the low-pressure site pockets, as described below. Diopside is sometimes altered to clay minerals.

Graphite content varies considerably throughout the boudins. There are large areas, especially near the centre of the boudins that have the same comparatively low graphite content as that of the mantle boudin graphite. Other areas, however, contain abundant amounts of graphite. The graphite commonly occurs as large clusters of up to several centimetres in diameter that consist of flakes of between 0.2 mm and 3 mm in length. The aggregates are sometimes elongated parallel to the preferred orientation of the graphite flakes. The graphite aggregates frequently contain large pyrite crystals situated between individual flakes.

Pyrite (ca. 5 vol% ) is usually associated with graphite. It is present as subhedral to anhedral grains of more than 0.5 mm in diameter. The pyrite grain shape is frequently controlled by the shape of the graphite flakes and aggregates. Feldspar (ca. 5 vol%) is



present as plagioclase and to a lesser degree, K-feldspar. Both are found as isolated crystals that resemble the grain size and shape of the equidimensional quartz.

Carbonates (< 5 vol%) are present as veins and elongated aggregates of up to several centimetres in diameter. Magnesite usually occurs as extremely fine-grained intergrowths. Dolomite and calcite appears in a similar fashion as the magnesite, but is coarser-grained. Titanite is similar to that describe for the mantle boudin, except that it is frequently altered to leucoxene.

Other accessory minerals include apatite, allanite, mica, rutile, ilmenite, magnetite, zircon, beryl and tremolite. Tourmaline was observed by McRobbie et al. (1995) within boudin structures of the Upper Horizon, but was not observed in this study within the calc-silicate skarn boudin matrix. Green tourmaline was observed by the author in the low-pressure pockets within the boudins (see Section 4.10) and as inclusions in quartz within the boudins (see Chapter 10).

#### **4.10. Low-pressure site pockets and veins**

Since the minerals present in the low-pressure sites within the calc-silicate skarn boudins are extremely coarse-grained, they are not described here microscopically, but as they occur in hand specimen (Figure 4.10).

Quartz is by far the main rock-forming mineral in the low-pressure pockets and veins. It occurs as extremely coarse-grained aggregates of up to 0.5 m in diameter. Quartz ranges from translucent to exceptionally clear and transparent in colour. It is sometimes stained by Fe-oxides and hydroxides, especially when associated with pyrite. Quartz crystals vary from euhedral to anhedral as a function of spatial limitations during growth. Grossular, zoisite, pyrite, calcite and to a lesser extent graphite are all situated in between the quartz aggregates in the pockets.

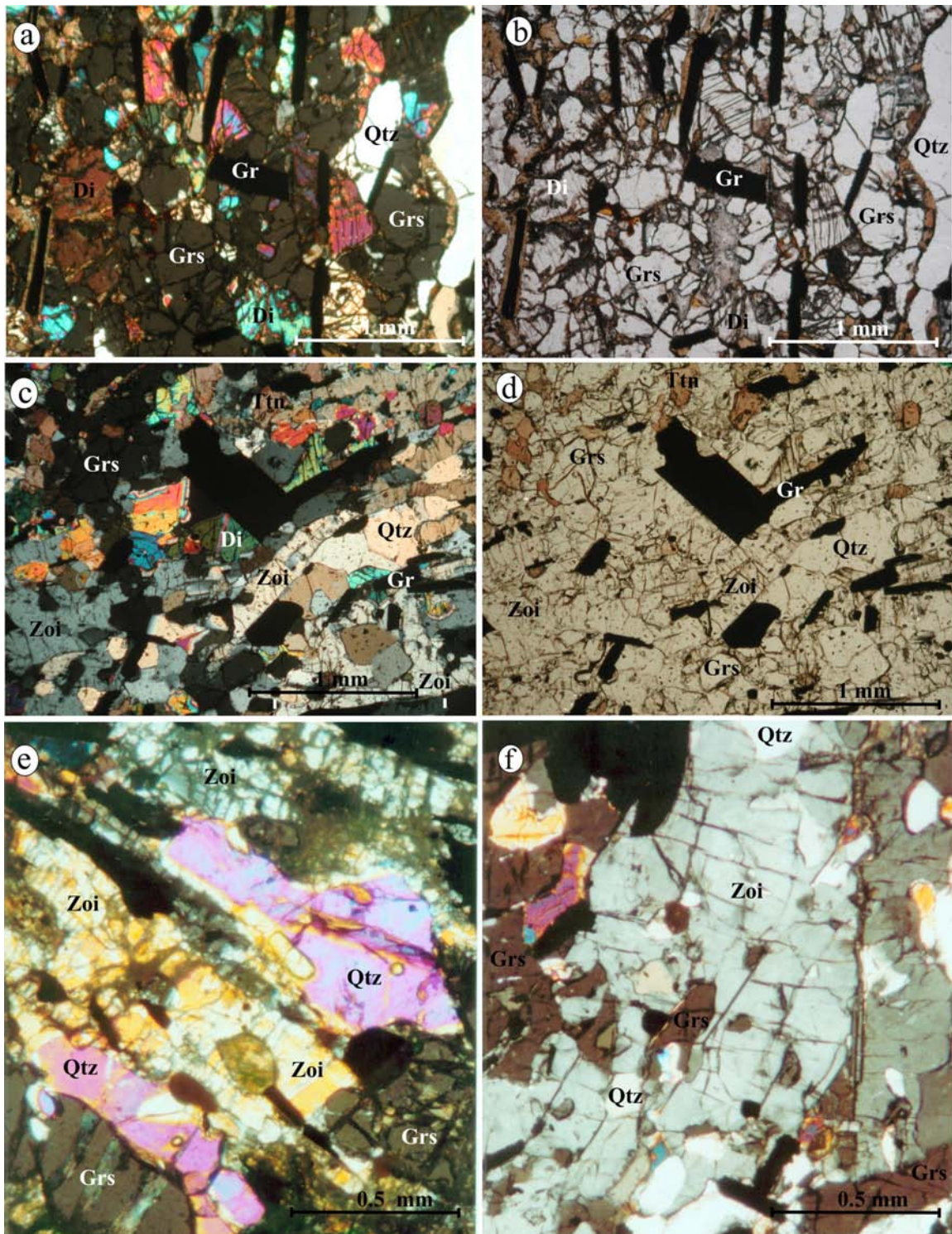


Figure 4.9. Photomicrographs of the calc-silicate skarn boudins and surrounding skarnoid reaction zones. a to d) Crossed (a and c) and uncrossed (b and d) polar images of the calc-silicate skarn boudins with locally abundant grossular garnet and zoisite. e) Crossed polar photomicrograph of a skarnoid reaction zone around a boudin structure. f) Crossed polar image of zoisite from a boudin matrix containing inclusions of grossular garnet and quartz.

Carbonates are locally abundant in the pockets and veins, but are usually restricted to cavities in the low-pressure pockets. Calcite is by far the main carbonate mineral present, although magnesite and dolomite are sometimes observed. Quartz and calcite represent the majority of the minerals present in the low-pressure pockets and veins. Other minerals present in the pockets and veins, like tanzanite, tsavorite and pyrite, are often situated within the matrix of quartz and calcite. Two generations of calcite are present; a) clear, almost transparent euhedral to subhedral crystals closely associated with zoisite and grossular. This calcite is related to the formation of zoisite and will be discussed under Chapter 6; b) a white to creamy cryptocrystalline cementation mineral which occasionally forms the main matrix mineral in selected pockets. This calcite is a product of far later fluid migration, possibly related to the formation of the clay minerals.

Grossular garnet occurs as large grains of up to 10 cm in diameter. Grossular, for similar reasons as the quartz, also occurs as euhedral to anhedral grains. The grossular garnet ranges in colour from a light green to an exquisite dark green. The grossular is commonly fractured, but unfractured, transparent, darker green crystals frequently classify as gem-quality garnet (tsavorite).

Zoisite occurs predominantly as its gemstone variant tanzanite, except when it is too highly fractured to be of any value. Tanzanite crystals can range up to several centimetres in diameter (Figure 4.10) and can weigh hundreds of carats. The large tanzanite crystals are usually fractured, making the large unfractured tanzanite crystals highly sought after. The mineral is usually surrounded by quartz  $\pm$  calcite. Tanzanite crystals are characterised by their intense blue/violet colour and strong trichroism. The trichroism is mainly violet, greyish dark blue, red-brownish or green/yellow and will be discussed in detail in Chapter 13. The shape varies from euhedral to anhedral crystals, depending on its growth capabilities. The well-developed crystals always tend towards an orthorhombic crystal structure. Small quantities of gemstone quality zoisite are also found in other colours. This includes green, greenish blue, pink, yellow, violet to reddish purple, colourless and bicoloured (Barot and Boehm, 1992; Dirlam et al., 1992). Halloysite is sometimes present in fractures and on the surface of zoisite (tanzanite). Poor quality tanzanite is also associated with grossular garnet (tsavorite), where it occurs as fine intergrowths with quartz  $\pm$  calcite in fractures and on the surface of the

garnet. Zoisite nodules of up to 5 cm in diameter, frequently surrounded by graphite, have been observed in the low-pressure pockets. Well-rounded zoisite crystals with radiating growth patterns have also been observed within the low-pressure pockets.

Pyrite occurs as large, massive pods and stringers, within the low-pressure sites. The pods and stringers can be several centimetres in diameter and consist of subhedral to euhedral coarse-grained individual crystals. Large octahedral crystals of up to 30 cm in diameter, which are often twinned, have been recovered (Figure 4.10). The pyrite is occasionally altered to Fe-oxides and hydroxides, including goethite and haematite. The Fe-oxides commonly stain the surrounding minerals in the pockets and also the minerals in the skarnoid calc-silicate boudins.

Graphite occurs as aggregates forming irregular pods of several centimetres in diameter and as isolated medium to coarse-grained flakes with a random orientation. The graphite content in the low-pressure pockets of the boudins is often far higher than in the surrounding boudin. Graphite is also present as inclusions in quartz, zoisite/tanzanite and garnet (Gübelin and Wiebel, 1975). Tanzanite located within the graphite-rich pockets is often well preserved from structural deformation and are therefore of a high quality.

Prehnite crystals are sometimes present within the carbonates situated within the low-pressure pockets. The prehnite crystals can be several centimetres in diameter and can be locally abundant comprising up to 20% of low-pressure pockets. Prehnite appears to replace various minerals within the low-pressure sites, including tanzanite and quartz.

Tourmaline crystals are sometimes present within the low-pressure pockets, where it occurs as elongated, light green minerals of several centimetres long. The tourmaline crystals are usually located within the pockets with high carbonate content.

Sphalerite and tremolite-actinolite may occur within the low-pressure pockets, but are usually not present in high amounts. Small pale green beryl crystals have been identified within the low-pressure site pockets but are rare. The sphalerite has a dark red-brown colour and is sometime slightly transparent, while the tremolite-actinolite crystals are usually green in colour.

#### 4.11. Skarnoid reaction zones

Quartz (50 to 70 vol%) is the main rock-forming mineral of the reaction zones. The quartz content of the reaction zones is highest where the reaction zone is poorly developed and essentially consists of a quartz stringer connecting the boudins. The strong foliation of the rock is partially caused by the preferred orientation of elongated quartz grains. Not all the quartz grains are elongated, but together they still form distinct bands. The pronounced banding is a result of complete sub-grain development of previous elongated quartz grains. Elongated grains can range up to 3.5 mm in length, while sub-grains are usually around 0.5 mm in diameter.

Zoisite (5 to 30 vol%) occurs predominantly as elongated columnar crystals, which are locally abundant. Zoisite is strongly poikiloblastic and can be up to 5 mm in length. It contains numerous inclusions of (in decreasing order) quartz, garnet (grossular-rich), diopside, titanite, graphite and sulphides. Zoisite is clear to greyish in colour and displays middle first-order grey interference colours. It has a well-developed cleavage direction perpendicular to its elongation. Zoisite is elongated parallel to the foliation and often forms sub-parallel veins or bands that are divided by quartz veins.

Graphite (ca. 5 vol%) is present as isolated flakes and more commonly as aggregates. The graphite flakes vary in length from 0.1 mm to 2 mm. Graphite clusters and individual flakes have a preferred orientation that defines the foliation of the rock together with the same preferred orientation of other minerals. Graphite present in the alteration zones often contains a small rim of clay/pyrophyllite minerals. Graphite in these areas often has irregular and dusty grain boundaries under high magnification.

Pyrite (ca. 5 vol%) occurs as large subhedral cubic crystals and as elongated anhedral crystals. The subhedral crystals are usually large and can be up to 3 mm in diameter. The elongated grains are smaller in size (up to 1 mm in length) and are aligned parallel to the foliation. The pyrite grains are sometimes highly oxidised, especially in the clay/pyrophyllite zones, and probably caused the brown staining of the pyrophyllite.



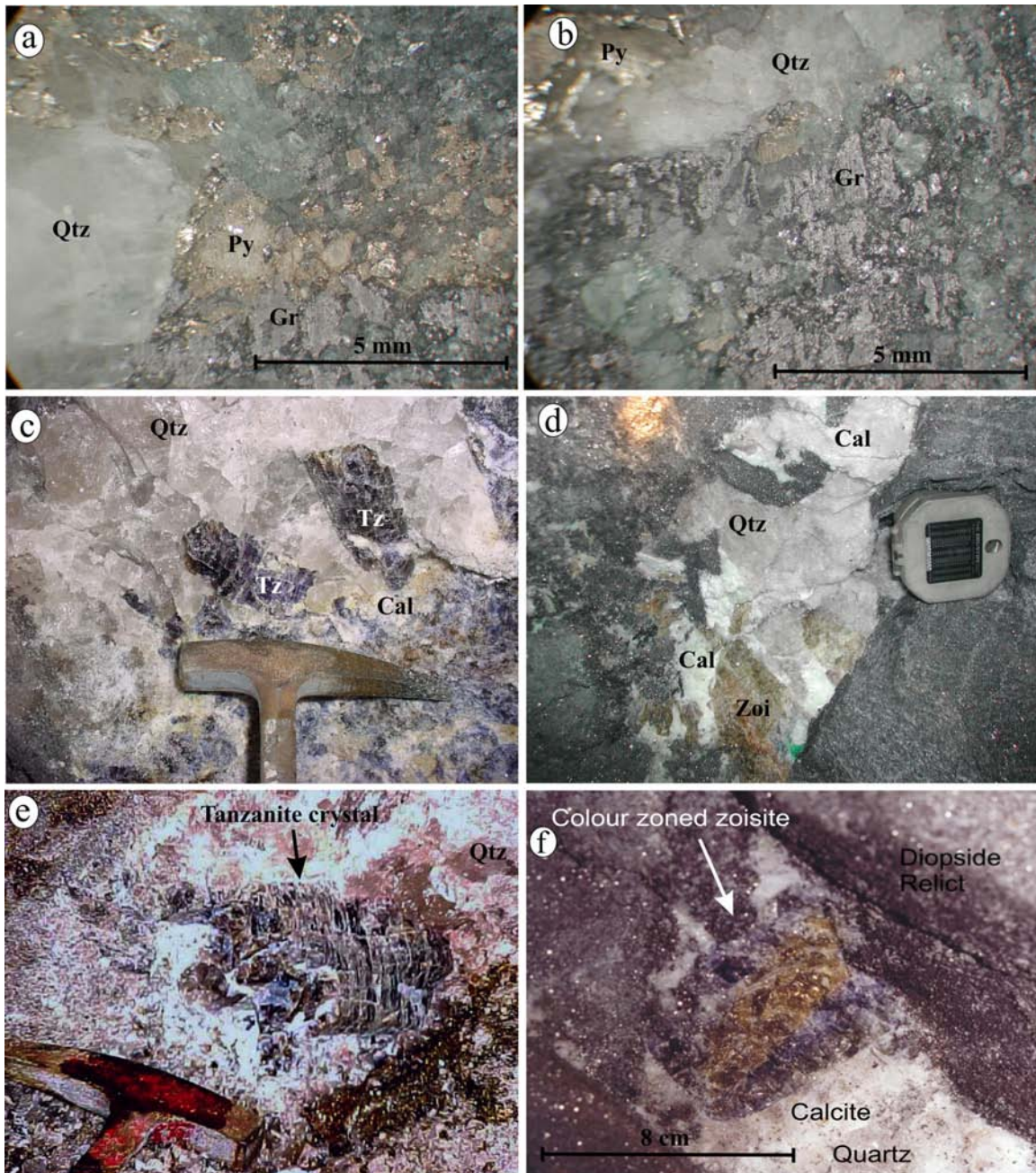


Figure 4.10. Photographs of the low-pressure pockets within the calc-silicate skarn boudin structures. a and b) Stereoscopic microscope reflective light photographs of predominantly quartz and pyrite within a low-pressure pocket. c to f) Various underground photographs of zoisite and tanzanite-bearing low-pressure pockets located within the boudin structures.

Titanite is present as an accessory mineral and occurs as subhedral to rounded grains. Titanite is small and usually approximately 0.4 mm in diameter. Titanite is slightly pleochroic, from light to darker brown. It is commonly altered to leucoxene in the clay / pyrophyllite-rich areas.

Grossular (5 to 20 vol%) occurs as medium-grained aggregates and as large porphyroblasts of up to 5 mm in diameter. The aggregates are subhedral to anhedral and are usually associated with zoisite. The porphyroblasts do not necessarily occur with any other calc-silicate minerals and tend to be elongated in the direction of foliation. The porphyroblasts are fractured with absorbed and altered grain boundaries. Grossular porphyroblasts, similar to most of the other minerals, also occur in bands within the grey-layer rock.

Diopside (5 to 10 vol%) occurs as fine- to medium-grained anhedral crystals. Diopside is sometimes elongated, parallel to the foliation, and commonly occurs as inclusions in zoisite. It is restricted to areas with low clay / pyrophyllite content and even in the relatively unaltered zones, different stages of alteration to clay minerals / pyrophyllite can be observed.

Muscovite occurs as an accessory mineral and is only present in small veins adjacent to the surrounding pelites.

Secondary alteration minerals constitute a significant part of the studied reaction zones and will be further discussed in Section 4.12.

#### **4.12. Secondary Alteration minerals**

As noted in Chapter 3, the existence of a near-surface oxidation zone was established through the study of 13 diamond drill holes drilled in the Block C area, as well as the far deeper levels of mine development, especially in the commercially mined Block C area. The weathering zone is probably the result of downward water circulation from the recent shallow lake that covered the majority of the area.

The presence of the oxidation zone throughout the upper parts of the deposit caused the formation of various secondary minerals. This resulted in confusion in identifying the minerals, mineral assemblages and metamorphic conditions by earlier workers (e.g. Dolenc, 1976; Malisa, 1987; Davies and Chase, 1994) who only had access to shallow developments and surface outcrop. Clay minerals misidentified as epidote and chlorite, resulted in the formation of tanzanite being contributed to the infiltration of hydrothermal fluids under lower-greenschist facies conditions.

The minerals that formed as a result of the oxidation are difficult and sometimes even impossible to identify through normal petrography and was further investigated and identified through X-Ray diffraction (XRD), see Section 4.12.1. Only the weathered minerals observed within the calc-silicate boudins and surrounding gneisses will be briefly discussed here.

Halloysite is present as irregular clots and as fracture fillings in zoisite/tanzanite located within the low-pressure site pockets and veins within the boudin structures (see Section 4.10). The halloysite clots vary considerably in size and can be up to tens of centimetres in diameter. Halloysite is usually white in colour, although it sometimes has a bluish tint or is stained brown by iron oxides. It often contains inclusions of graphite flakes and small tanzanite crystals.

A mixture of clay minerals from the smectite group and pyrophyllite can constitute between 5 and 40 vol% of the skarnoid reaction zone mineral assemblage, see Section 4.11. The alteration is especially prominent in the shallower areas of the mines where the influence of weathering was greater. The clay minerals are yellowish to light brown in colour, with a patchy appearance. Pyrophyllite is clear to light brown in colour, and is probably stained by the presence of Fe-hydroxides and Fe-oxides. XRD patterns for the clay minerals indicate that both halloysite and illite are present. The clay minerals and pyrophyllite often occur as bands, alternating with the quartz bands. Both the clay mixture and pyrophyllite is near isotropic, although the pyrophyllite-rich areas occasionally show second-order interference colours. Pyrophyllite sometimes exhibits a sieve texture, similar to the texture commonly displayed by serpentine. The development of clay and pyrophyllite-rich zones within the layered rock appears to be a



result of the alteration of calc-silicates within the rock. In areas where the alteration is less pronounced, the partial alteration of diopside, grossular and zoisite is observed.

#### 4.12.1 X-Ray Diffraction

X-Ray Diffraction (XRD) analyses were performed using a Phillips 1410 with Cu K $\alpha$  radiation. The clay minerals were orientated in an aqueous suspension in order to enhance yield from the basal d-spacing. The smectite group clay minerals were identified by also treating the samples with glycol, resulting in a characteristic shift in the peak positions, enabling positive identification.

The following alteration minerals were identified within the calc-silicate boudins and surrounding gneisses by means of XRD analysis:

- Limonite is a common constituent of the boudins and low-pressure pockets within the upper portions of the deposit. The hydrated Fe-oxides predominantly comprise of goethite and haematite that formed through the leaching of sulphur from the pyrite and other iron sulphides. Both the haematite and goethite occur as deep red to brown crystals and masses.
- Halloysite is by far the main kaolinite group clay mineral, although minor amounts of kaolinite have also been identified through XRD analysis. Halloysite is a very important alteration mineral commonly present in the calc-silicate skarn boudin structures. Through the combination of petrography and XRD studies, halloysite is proved to be an alteration product of zoisite and more importantly tanzanite. Samples in varying stages of alteration were petrographically examined and a clear relationship between halloysite and zoisite alteration were identified. Halloysite is not a known alteration product of tanzanite and this reaction warrants further investigation. Two types of halloysite were identified through XRD analyses (Figure 4.11). The 10 Å halloysite is a hydrate, while the 7 Å halloysite is not hydrated and therefore only an aluminium silicate hydroxide. XRD analysis of several halloysite samples reveals an approximate 60:40 distribution relationship between the 10 Å and 7 Å halloysite minerals.

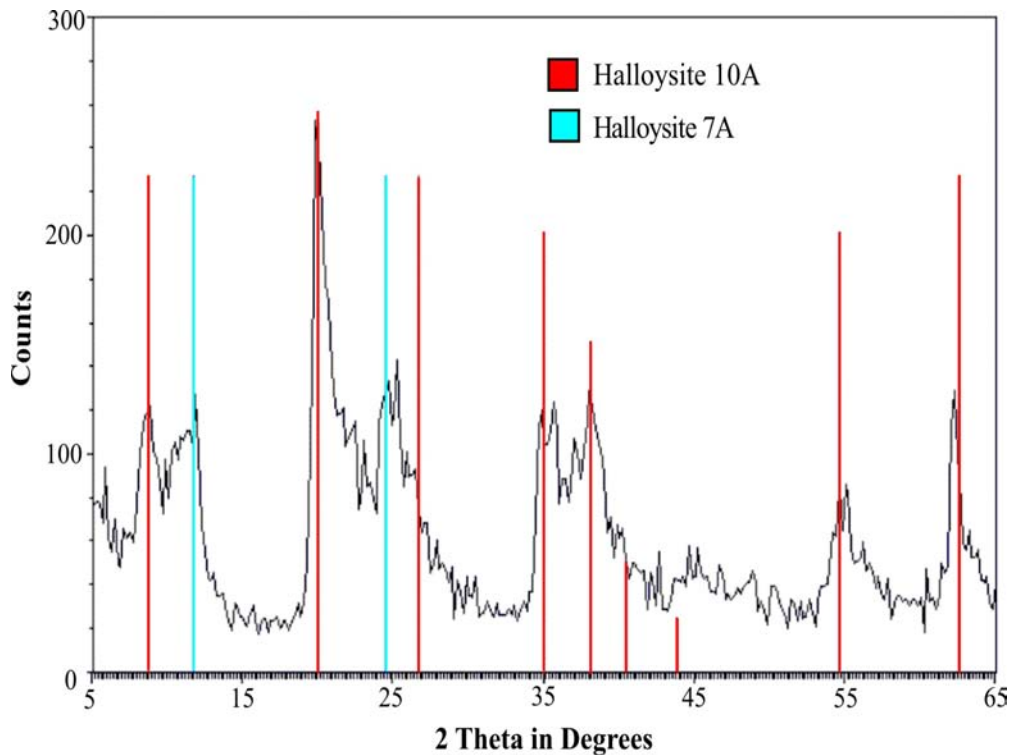


Figure 4.11. XRD pattern of halloysite indicating the typical relationship between the 10 Å halloysite and 7 Å halloysite minerals commonly present within the skarn boudin structures.

- Montmorillonite is the main smectite group clay mineral present and constitutes one of the most abundant weathering minerals present in the skarn boudin structures. Montmorillonite was most likely the main clay mineral misidentified as epidote by previous workers. The montmorillonite in the boudins has been identified through XRD as the 15 Å montmorillonite mineral (Figure 4.12). Glycol treatment of the montmorillonite resulted in a shift of positions of the main peak from  $5.88^\circ$  to  $5.0^\circ$  (Figure 4.12).
- Serpentine is found within the weathered skarn boudin structures. The serpentine probably formed through the alteration of various calc-silicates within the boudins. The formation of serpentine from the alteration of the pyroxenes could also be contributed to the formation of magnetite through the liberation of Fe.
- Illite and sericite are common alteration products within the gneisses. Sericite formed predominantly by the alteration / weathering of the feldspars within the gneisses.
- Pyrophyllite has been identified as a minor alteration product of presumably feldspar and muscovite within the gneisses.

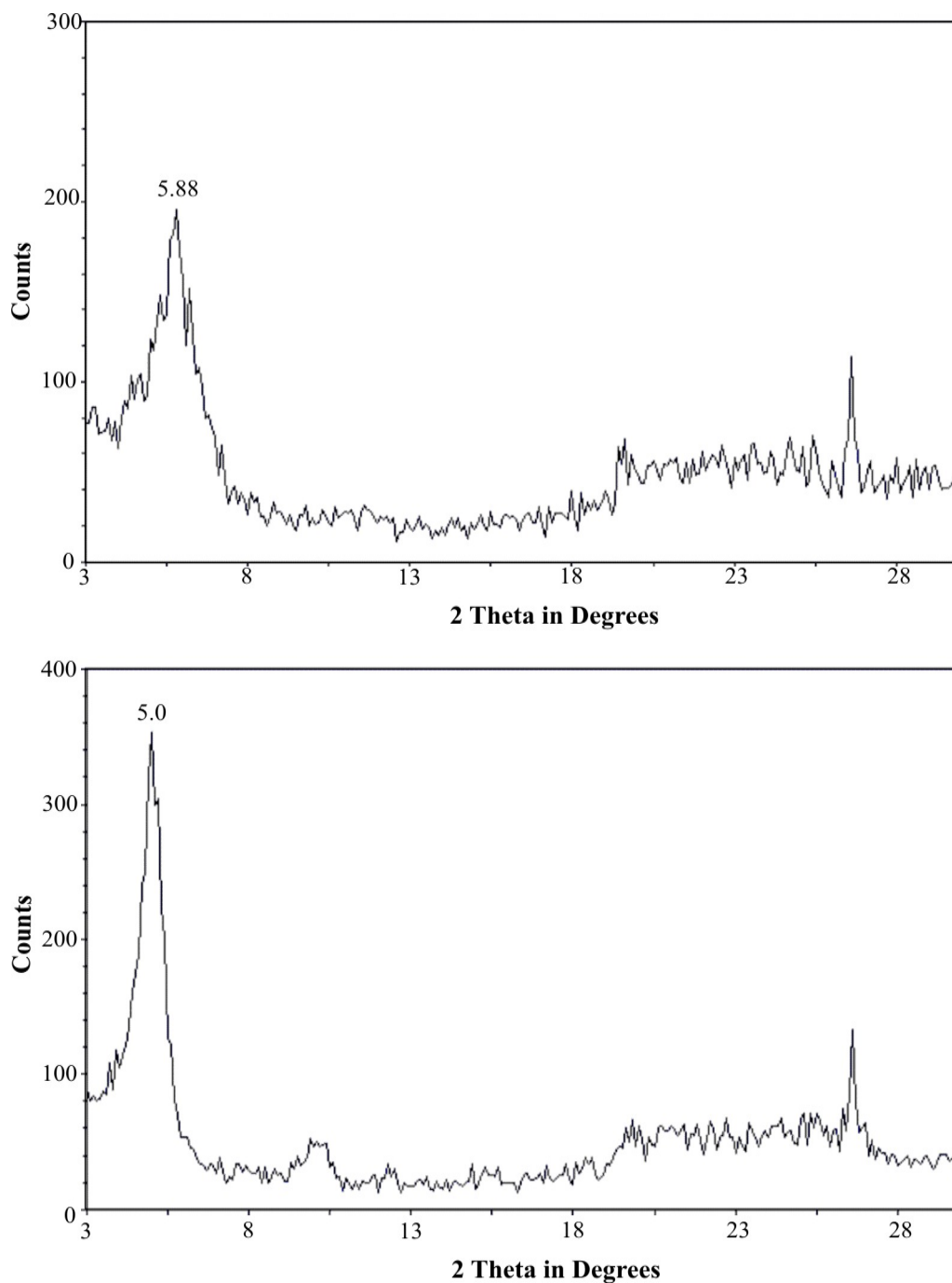


Figure 4.12. XRD pattern of montmorillonite from weathered skarn boudins within the JW-zone. Top: Untreated montmorillonite pattern with its main 2 Theta peak situated at  $5.88^\circ$ . Bottom: Glycol treated montmorillonite sample indicating the shift in the main peak towards  $5.0^\circ$ .

## Chapter 5

### Structure and deformation

#### 5.1. Introduction

The structural deformation history of the Merelani tanzanite deposit consists of a complex sequence of deformation events that generated the conditions and structural setting conducive for tanzanite mineralisation. Almost all the structural features described in this chapter have only been identified within the last few years since commercial mining activities have created large surface and underground exposures. The structural and deformational features of the deposit will be discussed in chronological order. Boudinage and its associated ore-zone morphology will be described and discussed after the deformational features.

#### 5.2. Pre-deformational lithological variation

The original depositional sedimentary thickness appears to have influenced the later deformational patterns within the deposit. The deposition of the shelf-type sediments is associated with a back arc environment and will be discussed in Chapter 11. The sedimentary units were essentially planar, but local variation in thickness on a metre to hundred metre scale has been identified on the mine area and surrounding Lelatema Mountains. Variation in the volcano-sedimentary depositional duration and sequence resulted in:

- Lithologically similar units with different relative thickness and dimensions.
- Lithological units with varying thickness along strike and dip.

The irregular original sedimentary thickness resulted in a degree of inhomogeneity in the morphology and distribution of subsequent deformation events. It is also possible that non-translation deformation could have occurred under low temperature and pressure conditions, probably close to the boundary between diagenesis and metamorphism. This non-translation deformation could have developed high and low strain zones as a result of thickness variations in the original sedimentary succession. This could have contributed to the occurrence of high strain zones and folding during

prograde metamorphism. These thickness variations could also have formed due to deformation and therefore may not be of primary origin. Any evidence of depositional and post depositional non-translation deformation would have been obliterated by subsequent metamorphism and deformation. Since little evidence currently exists for the presence of the non-translation low-pressure deformation event, it will not be classified as the D1 deformation event.

### **5.2.1. SS Foliation**

The original foliation (S0) or bedding is completely obliterated and transposed by later planar surfaces (S1, S2 and S3).

## **5.3. First phase of structural deformation (D1) (layer transposition)**

The first phase of structural ductile deformation (D1) resulted in the development of F1 folds, which foliated the schists and gneisses, developing a high-grade ductile planar S1 foliation.

### **5.3.1. F1 folding event (intrafolial folds)**

Evidence of the F1 folding event in the mine area is completely transposed by the superimposed F2 folding event. From the S1 foliation direction it can be inferred that the F1 fold axes must strike N-S. The F1 folding event is however still observable ca. 50 km SW of the mine area. The km-scale F1 fold is clearly visible on the satellite image of the Lelatema antiform (Figure 5.1). The F1 fold hinge is situated on the southwestern limb of the antiform. The evolution of the Lelatema antiform through the refolding of the F1 fold by the F2 folding event will be discussed in Section 5.4.6.

A F1 folding event is also preserved in the metabasite (described in Chapter 3) and riverbed outcrop ENE of the mine site within the Lelatema antiform. Small-scale intrafolial folds observed in the metabasite and riverbed outcrop is believed to be representative of the large F1 folding event (Figures 5.2.a and b). The S1 foliations in the metabasite is axial-planar with the F1 intrafolial folds, which have a NNW to NNE plunge direction. The pegmatic veinlets observed in the riverbed by Gresse (2002) and metabasite developed small intrafolial folds by means of partial anatexis of the more competent quartz-feldspar bands within the less competent host rocks. Both S and Z

shaped intrafolial folds were observed in the metabasite (Figures 5.2.a and b). However, it should be pointed out that the S and Z-type folds were not observed within connecting layers therefore not implying sheath folding.

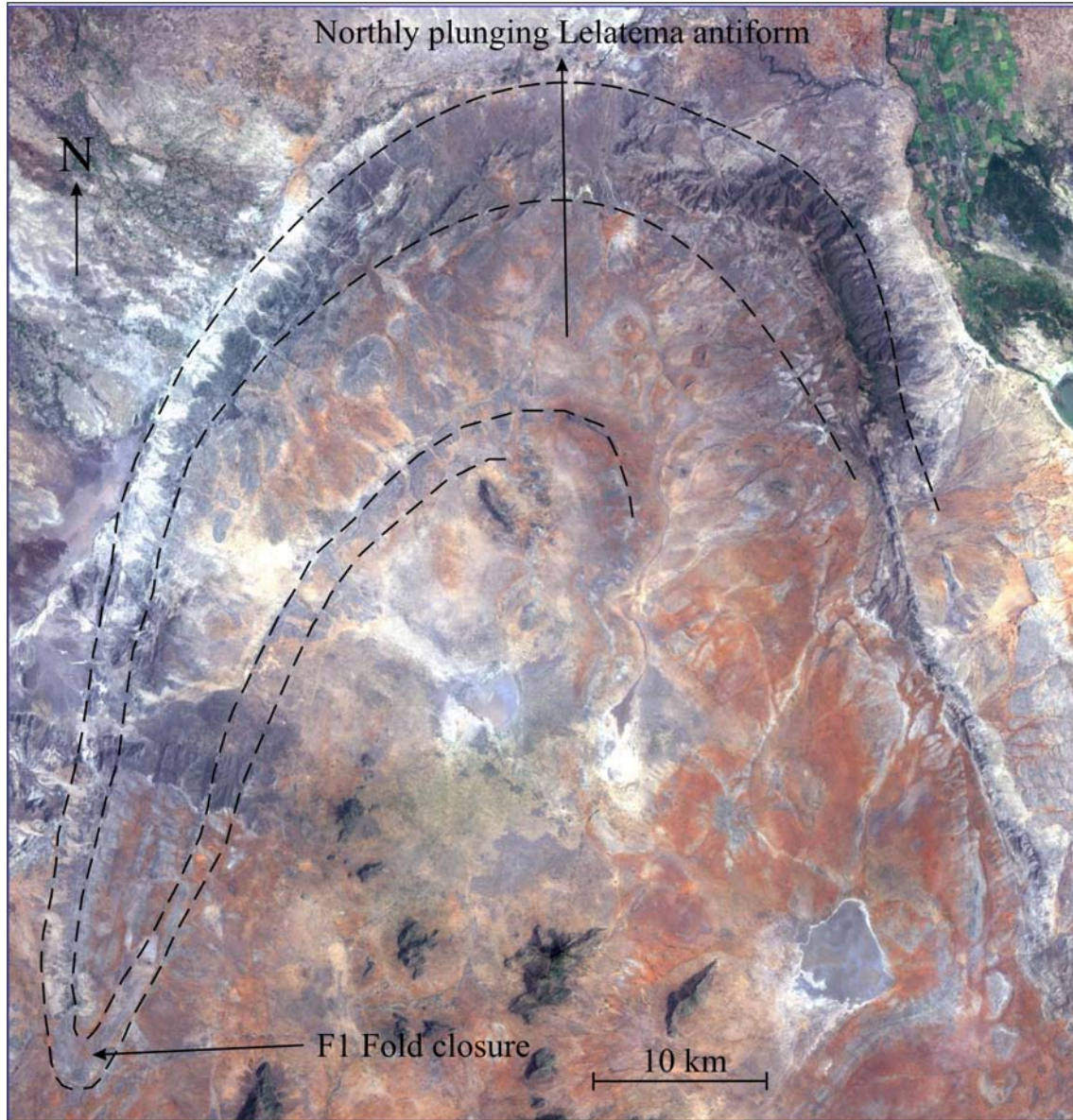


Figure 5.1. True colour (TM bands 1, 2, 3) satellite image of the Lelatema antiform. The image clearly shows the F1 fold closure on the south western limb of the antiform.

### 5.3.2. S1 foliation

The S1 foliation is axial-planar to the F1 folds and is predominantly overprinted by the later S2 foliation. The S1 foliation is only preserved within the mine area as relicts in certain units, where the S1 foliation was sheltered from the S2 foliation overprint. The S1 foliation observed in the Block C mine area strikes in a north-easterly direction and



dips between 28 to 65° NW, with an average dip of around 50° (Figure 5.3). The S1 foliation in the mine area is predominantly defined by graphite and mica within the gneisses. The S1 foliation measured in the mine region is comparable to the S1 foliations measured in the metabasite and the S1 foliations measured by Gresse (2002) in the riverbed outcrop ENE of the mine site. The S1 foliation in the metabasite dips at approximately 40° WNW and the S1 foliation of the riverbed outcrop has an average dip of 52° NW (Figure 5.3).

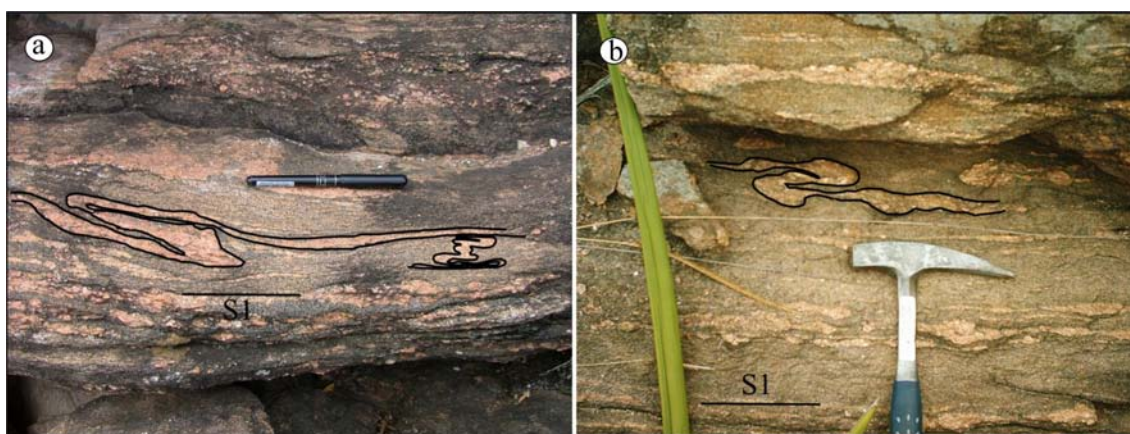


*Figure 5.2. F1 folded veins in metabasite showing relict intrafolial F1 fold hinges and fold-limb attenuation. Both S and Z type intrafolial folds are observed.*

### 5.3.3. L1 lineation

The L1 lineation was not observed on the deposit and appears to have been completely transposed by the L2 lineation, see Section 5.4.5. An L1 lineation was however identified by the author in the metabasite situated NE of the tanzanite deposit (see Chapter 3 for description of the metabasite). The lineation within the metabasite is defined by elongated pyroxene crystals. The L1 lineation obtained from this study and by Gessner (2004) for the metabasite plunges on average 20 to 30° to the WSW. The L1 lineational plunge measurements of the metabasite, obtained from this study and that of Gessner (2004), are indicated in Figure 5.4.

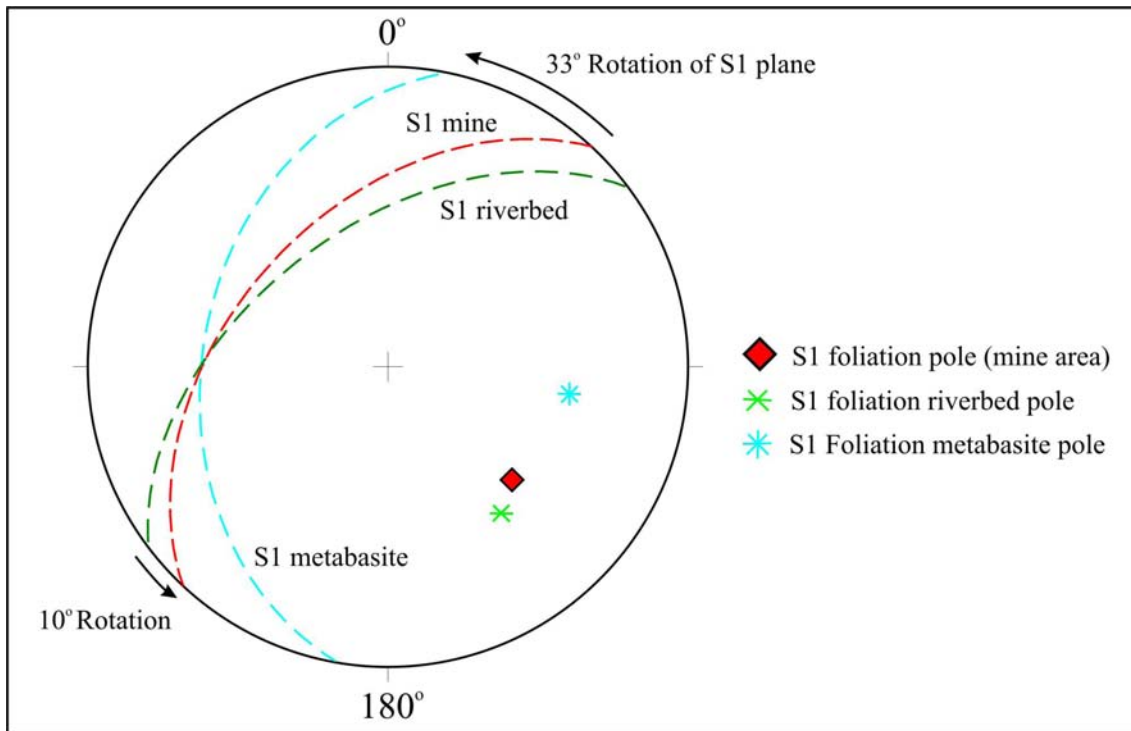


Figure 5.3. A stereonet plot of the S1 foliation on the mine, the S1 foliation obtained by Grasse (2002) from the Riverbed outcrop and the S1 foliation obtained from the metabasite. The metabasite has a 33° westerly rotation of the S1 plane, while the riverbed values have a 10° easterly rotation relative to the S1 foliation measured on the mine.

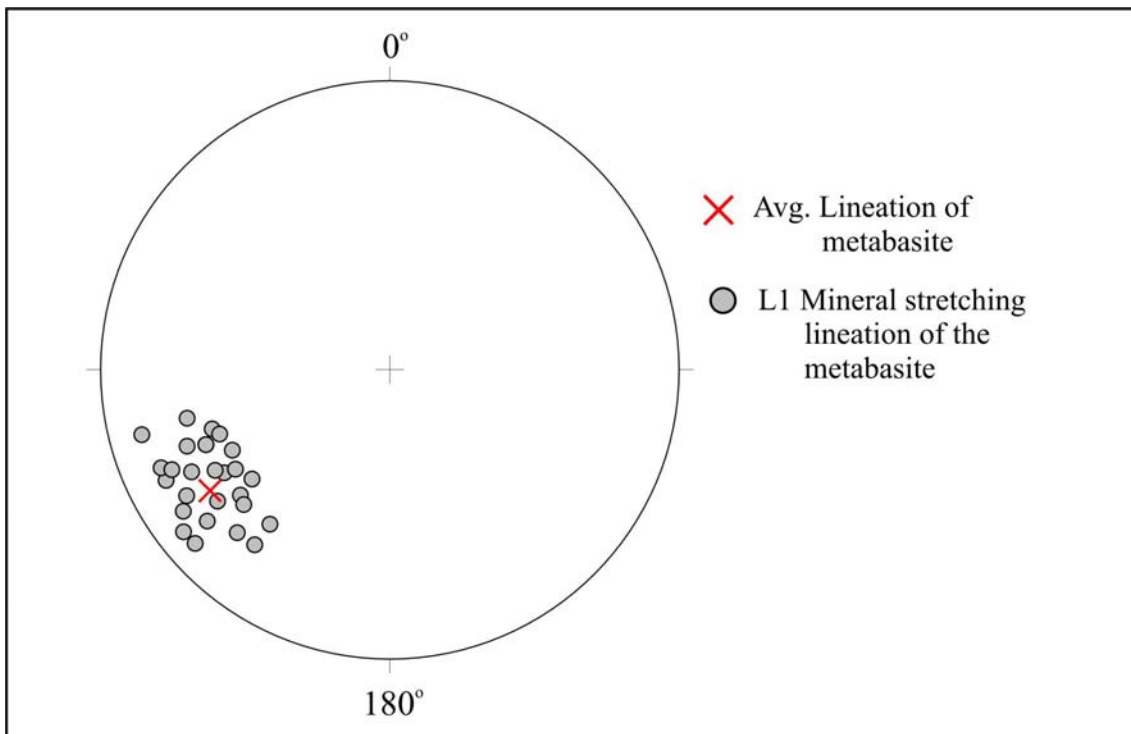


Figure 5.4. The L1 mineral stretching lineations from the metabasite outcrop. The lineations have a shallow SW plunge.



## **5.4. Second phase of structural deformation (D2)**

Ductile folding (F2) associated with the second phase of structural deformation (D2) refolded and overprinted the earlier structures, fabrics and rocks. The D2 event caused both the competent calc-silicate layer in the succession to develop boudinage and the multiple-order second folding (F2) event. The F2 event resulted in the formation of second and third order parasitic folds, as will be indicated below. Boudins are the most important structural feature associated with tanzanite mineralisation and also developed during the second phase of structural deformation and will be discussed in detail in Section 5.7.

### **5.4.1. Lelatema antiform (F2a)**

The Lelatema fold is a northerly plunging antiform with a maximum plunge of 60° N as measured by Malisa (1987). The fold has a half-wavelength of 32 km and amplitude of 11 km (Figure 5.1). The plunge of the antiform is parallel to the regional northerly plunging stretching lineation as indicated by Hepworth (1972), Malisa and Muhongo (1990) and Shackleton (1993a). Satellite imaging of the Lelatema antiform suggest that the antiform is the result of flattening and layer-parallel extension as a result of compression, followed by refolding of the original F1 fold (Figure 5.1). The tanzanite deposit is situated on the north-westerly limb of the antiform (Figure 1.2). Second order drag folds (F2b) are developed on the limbs of the antiform, with the deposit possibly located on Z-shaped antiformal / synformal drag folds with a magnitude of hundreds of metres (see Figure 5.28, Section 5.8). The proposed formation of the antiform will be discussed in Section 5.8. The formation of the Lelatema antiform tilted all the rock units on the north-western limb, including the rocks of the Merelani tanzanite area. This resulted in a general dip of 45° NW for all the rocks within the deposit, as discussed in Chapter 3.

### **5.4.2. Second order parasitic folds (F2b)**

The repetition of layers observed within the Lower Horizon and Upper Horizon, as well as the positioning of the deposit on the westerly limb of the Lelatema Antiform, suggests the existence of second order parasitic folds within the mining area. Gresse (2002) observed a second generation foliation (S2) within the Riverbed outcrop NE of the tanzanite deposit. The S2 foliation traverses banding and S1 foliation and resulted in

fold-hinge transposition with S2 shear cleavages causing layer duplication in fold hinges. Similar S2 shear cleavage and layer intersections were observed in the mine area. This suggests that shearing occurred along the S2 plane and could have resulted in the formation of local duplication within the Lower and Upper Horizon (Figures 5.5 and 5.6). Similar duplication due to folding within and between the Lower and Upper Horizon has been proposed by Davies and Chase (1994), Martineau and Davies (1996) and Rutahindurwa et al. (1997). There is, however, currently not sufficient evidence for a Lower and Upper Horizon linkage and field observations from a trench across both horizons did not produce enough support for the theory. There is however significant indications that second order drag folds resulted in the duplication of layers within the Lower Horizon and possibly the Upper Horizon. This would explain the existence of the geochemically similar JW-zone, C-zone and D-zone and their surrounding hanging and footwall kyanite-graphite gneiss layers (LK1, LK2, LK3, LK4, LK5 and LK6) as well as the duplication of the GSC and BCF (Figure 5.5 and Chapter 7).

The second order parasitic folds have half wavelengths and amplitudes of between 150 and 250 m (Figure 5.5). The down-plunge extent of the second order parasitic folds can be traced out over several kilometres, stretching the majority of the strike-length of the tanzanite deposit, with possible fold closures identified in Blocks A and D. It has not been conclusively established whether the Lower Horizon second order fold is a synform or antiform. Current evidence suggests that the fold in the Lower Horizon could be a synform (Figures 5.5 and 5.6) owing to:

- The overall shape of the third order drag folds in the JW-zone (see Section 5.4.3) is Z – folds. The JW-zone is on the eastern limb of the second order drag fold and would therefore indicate a synformal structure.
- The disappearance of the DM3 in depth, which forms the core of the second order F2b fold. The deepest drill hole in the mine area (LHD 13, Addendum A) was drilled to a total depth of 370 m and did not intercept the DM2, but it did intercept all the other lithological units. This could be caused by a synformal fold closure situated between 205 m (dolomitic marble unit 2, intercepted in LHD 14) and 270 m depth (no intercept in LHD 13).

The similarities between the layers in the Upper Horizon and Lower Horizon could also be explained by a primary depositional feature and subsequent similar reaction skarn-type alteration and identical deformational and metamorphic histories.

### **5.4.3. Third order drag folds (F2c)**

Third order drag folds are present on the limbs of the second order drag folds described in Section 5.4.2 (Figures 5.5 and 5.6). The third order drag folds are in the order of tens of metres and were influenced by axial-planar shearing resulting in complex isoclinal fold structures. The isoclinal folding combined with shear resulted in the duplication and “stacking” of the mineralised boudin zones within third order fold zones located on the limbs of the second order drag folds. The isoclinal folding therefore caused multiple duplication of the boudinage ore zone along dip formed through shear duplexing that will be further described in Section 5.7. The isoclinal folding resulted in up to seven boudinage layers being present in the fold stacks. The F2c isoclinal folds are important structural features since they delineate the boudinage tanzanite ore-shoots. The association between the F2c folds and boudinage will be discussed in Section 5.7.

The graphite-plagioclase gneisses that host the boudinaged and isoclinally folded calc-silicates are effectively shear zones. Shearing is the driving mechanism behind the isoclinal duplication and is enhanced by the abundance of graphite within the gneisses and on the contact with the calc-silicates.

#### *Isoclinal “fold-stack” description and distribution pattern*

The F2c isoclinal folds occur in fold stacks comprised of either four (Askari Shaft, Main Shaft and Shaft 1) or six (Bravo Shaft) individual tight isoclinal folds (Figure 5.7). The fold stacks in the Bravo shaft area have a separation distance of around 60 to 80 m, while the majority of folds stacks observed in the rest of the mine area have 80 to 120 m spacing between successive fold stacks. Unfolding of the isoclinal folds within a fold stack also indicates an original unfolded layer-length of 80 to 120 m long.

The fold stacks are characterised by a change in dip and strike of the surrounding altered graphitic gneiss host rock. In general, the dip of the host rock shallows out (dip decreases) as a fold stack is approached in the down dip direction, with the foliation wrapping around the fold-thickened lens (Figure 5.7). The opposite is true for the Bravo

Shaft area, where the dip increases as the fold-stacks are approached. The general shape of the fold stacks in Bravo shaft is that of an S – fold, while the general shape of the fold stacks in the rest of the mining area is that of a Z – fold. The isoclinal folding within a fold stack for a) the general model and b) the Bravo shaft model is indicated in Figure 5.7. The reason for this variance is not yet clear. In general, the dip variation associated with the fold stacks are caused by large shear duplexes developing as a result of the isoclinal fold hinges.

#### *Individual isoclinal fold description and distribution*

The F2c isoclinal folds vary in size from mm-scale folds to several metres in size. The size of the isoclinal folds is influenced by the thickness of the pre-boudinage competent calc-silicate layer, as well as the amount of boudin concentration through isoclinal folding and associated shearing. In areas with large-scale boudinage, the outer-limbs of the fold may be separated by over 5 m of boudinaged material. The inner-limb distances of the folds are normally separated by a less than 0.5 m “fold-nose layer” of brown altered graphitic gneiss. This layer is used in the mine as an indicator for the location of the associated isoclinal fold. In areas with poorly developed boudinage, the isoclinal folds could occur on a cm-scale (Figure 5.9).

The amplitude between the antiformal fold closure (locally termed “up-dip”) and synformal fold closure (termed “down-dip”) within an individual fold stack can vary from over 50 m to only a few centimetres (Figure 5.9). The isoclinal folds frequently contain internal disharmonic parasitic folds in the tight fold closures. The antiform shaped isoclinal folds contain far more pronounced disharmonic folding in the fold nose area than the synformal folds. Millimetre scale pyrite stringers are also present as parasitic drag folds on the limbs and especially in the fold nose of isoclinal folds where they occur as overturned M-folds. These folds are valuable local shear sense indicators. They can be classified as fourth order drag folds on the limbs of the third order drag folds (Figure 5.8.b). As previously indicated, the folded calc-silicate boudinage layers are enveloped by dehydrated graphitic gneisses (see Chapters 3 and 7). The enveloping gneiss was subsequently dragged under semi-ductile conditions away from the isoclinal fold noses during axial-planar shearing (Figure 5.8.a). This is locally termed the termination structures and consists of small-scale sheared fold hinges textures within the graphitic gneiss.

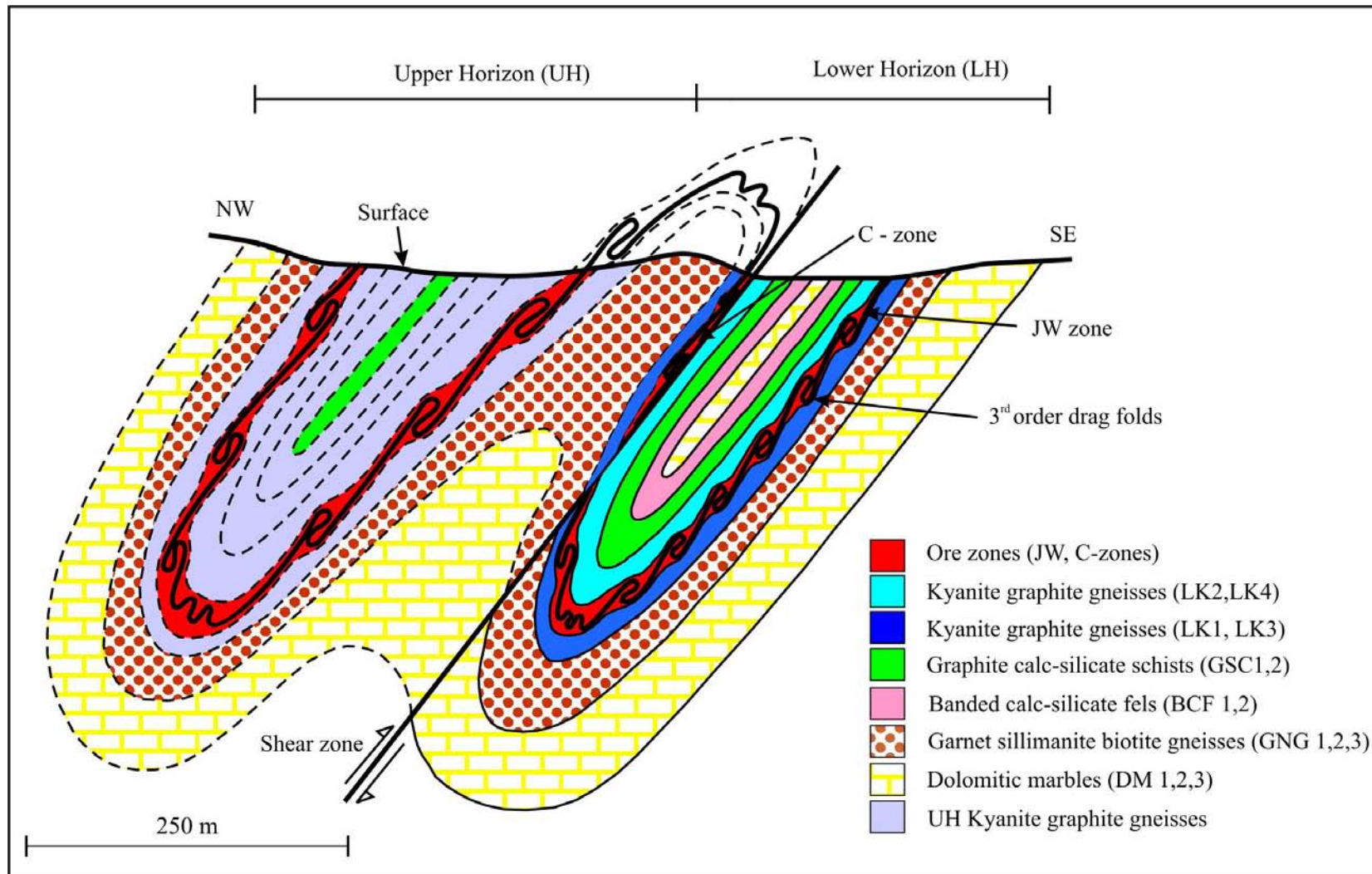


Figure 5.5. A NW to SE cross section of the Block C lithologies. The figure also shows the proposed second order parasitic folding with third order drag folding on its limbs. The second order folding resulted in a duplication of the JW- ore zone. The possible linkage through second order folding of the Upper and Lower Horizon is also indicated.

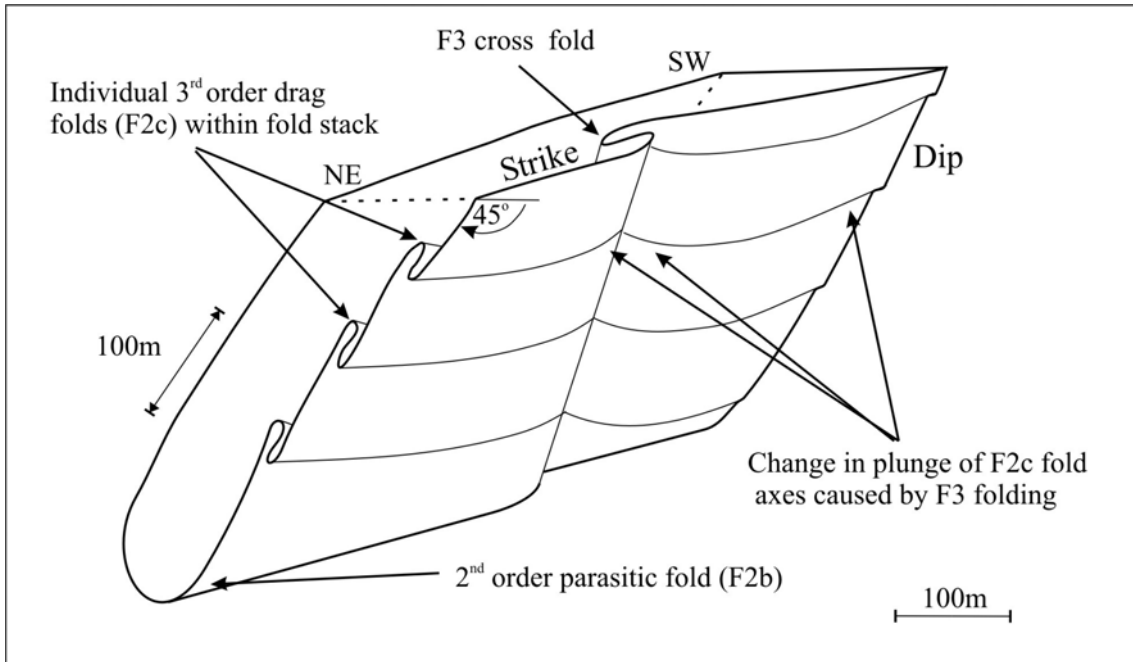


Figure 5.6. Three-dimensional representation of F3 cross folding, F2b second order parasitic folding and F2c third order isoclinal drag folding.

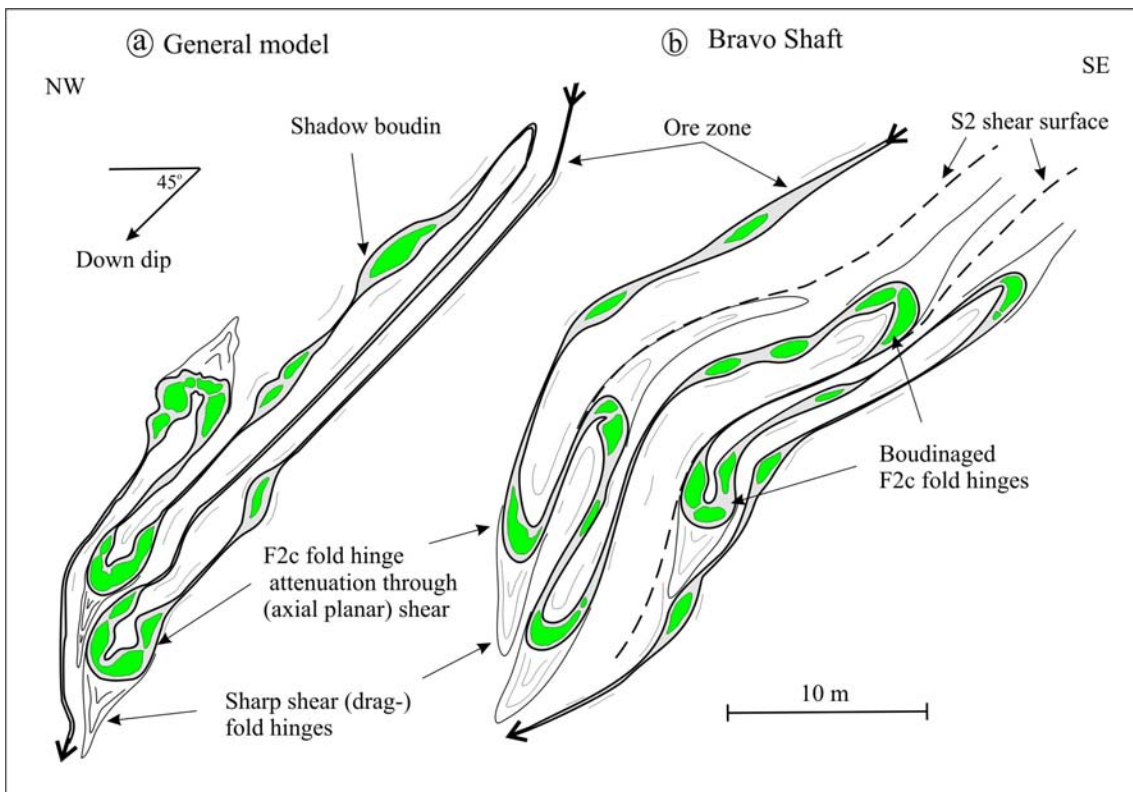


Figure 5.7. Transverse section of third order isoclinal drag folding and boudinage within a fold stack looking towards the NE. Generally the folding is in the shape of a Z (a), but in the case of Bravo Shaft (b) the folding is in the shape of an S.



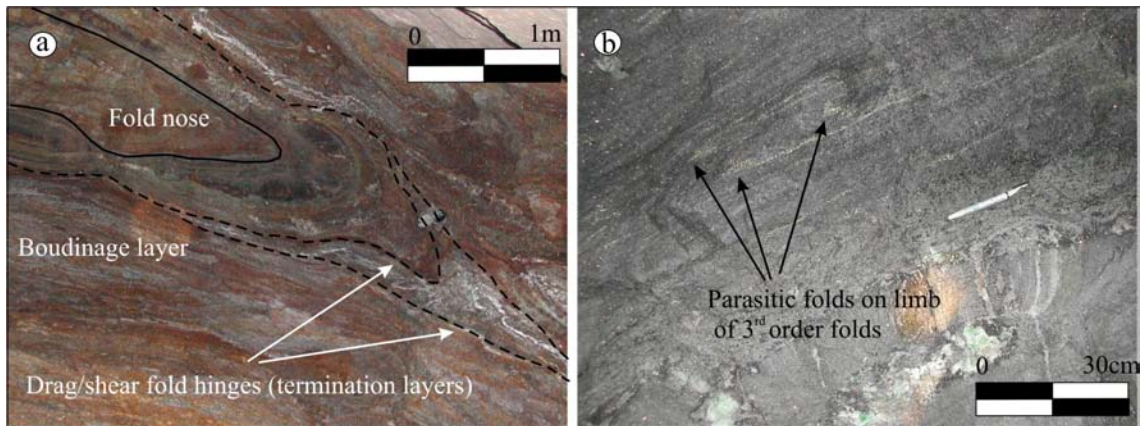


Figure 5.8. a) Sheared fold hinges, locally called the termination layers. b) Parasitic folds defined by pyrite stringers on the limb of the third order isoclinal folds.

### *F2c Fold axis morphology*

The down-plunge behaviour of the various fold axes within a fold stack down plunge could only be properly investigated once sufficient fold-nose related “ore-shoots” had been mined along plunge. The F2c folds have an average plunge of  $10^{\circ}$  NE. The fold-axes of the various synformal and antiformal isoclinal folds within a fold stack are normally sub-parallel. In general, the fold axes of the isoclinal folds within the fold stacks are sub-parallel to the L2 lineation direction that varies between  $10$  and  $35^{\circ}$  NNE.

The plunge of the individual F2c folds within a fold stack may vary locally, resulting in non-cylindrical double plunging folds that vary between  $36^{\circ}$  NE to  $5^{\circ}$  SW (Figure 5.10). This results in a variation in the relative positioning of the F2c folds within a fold stack (Figure 5.11). The variation in the plunge of the F2c is caused by the presence of the F3 cross folds. Detailed investigation of the plunge, orientation and behaviour of the various fold axes reveal a distinct interference pattern created by the later F3 cross folds (see Section 5.5.1). The influence of the F3 cross folds on the F2c isoclinal folds will be discussed in Section 5.5.1. The down-plunge continuation of isoclinal folds are only preserved between adjoining F3 cross folds, which are normally separated by around 550 to 700 m. The down-plunge continuation of the isoclinal folds is therefore not yet known and the possibility exists that the folds could pinch out due to layer parallel and axial plane shearing.

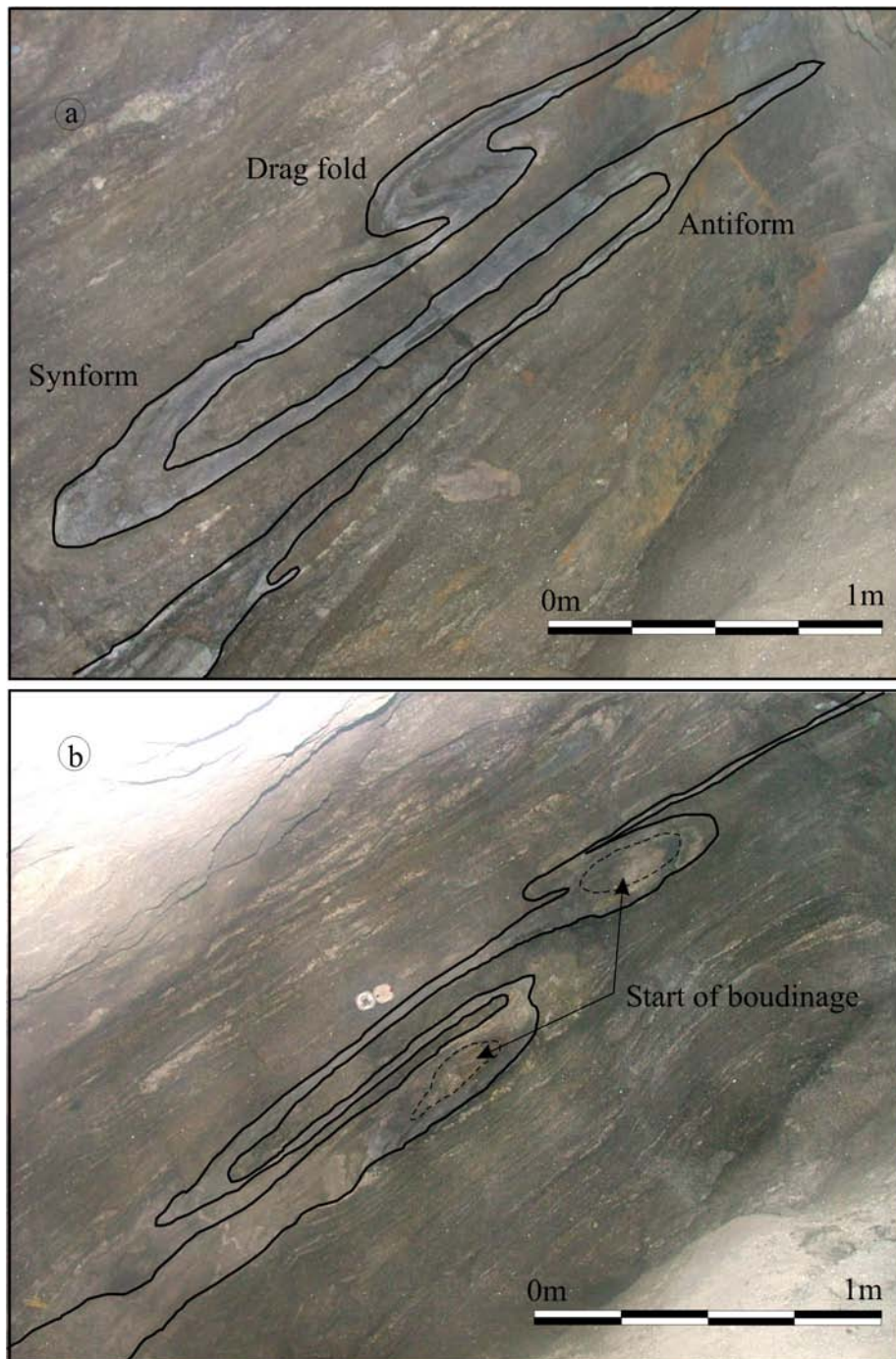


Figure 5.9. Tight isoclinal folding on a metre scale photographed in Askari shaft level 8, NE drive. Photograph (b) was taken 5 m further NE along plunge from photograph (a) and shows the start of boudins associated with the isoclinal folds.



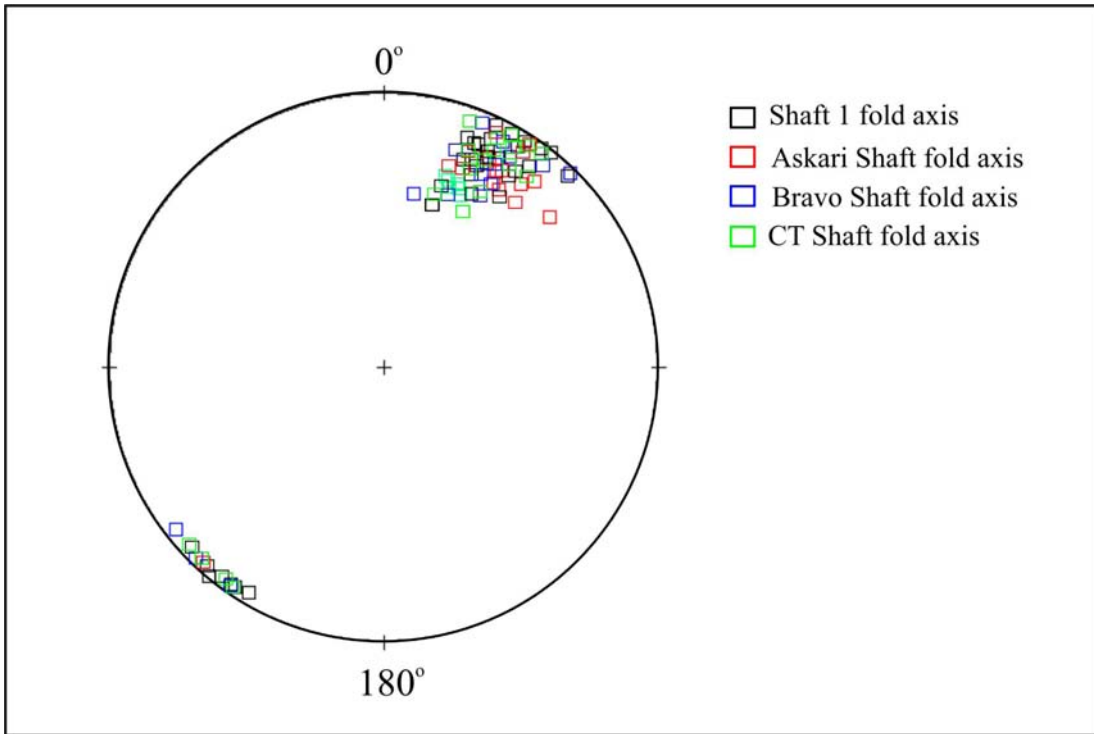


Figure 5.10. Stereoplots of F2c fold axes measured in four shafts located within the Block C mining area. The variation in the plunge of the F2c fold axes is caused by the influence of the F3 cross folds, see Section 5.5.

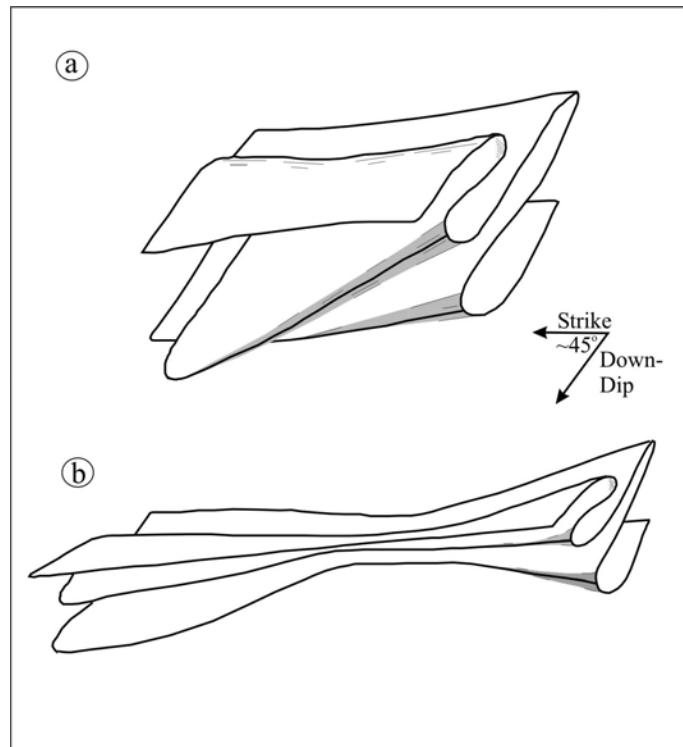


Figure 5.11. Enlarged view of selected areas indicated in Figure 5.15. a) Non-cylindrical, double plunging third order drag folds within a fold stack. b) Widening and thinning of the fold stack along plunge.

#### 5.4.4. S2 Foliation

The D2 deformation event and associated refolding resulted in the formation of the S2 foliation. The S2 foliation dips towards the NW and is usually parallel to S1. The major distinguishing factor between the S1 and S2 foliation is that the S2 is axial-planar to the F2 folds and intersects banding in the F2 fold hinges and older F1 intrafolial fold hinges (Gresse, 2003). This resulted in fold hinge transposition of the F2 folds and possible layer duplication through S2 shear cleavage and layer intersection (see Section 5.4.3).

#### 5.4.5. L2 Lincation

The L2 stretching lineation plunges on averages 10 to 35° to the NNE (Figure 5.12). This north-easterly plunge conforms to the regional lineation trends observed within the Lelatema granulites, by Hepworth (1972), Malisa (1987), Malisa and Muhongo (1990) and Shackleton (1993a). Slickenside lineations are often associated with the L2 lineations at large angles with it (Figure 5.12), these will be further discussed in Section 5.7.

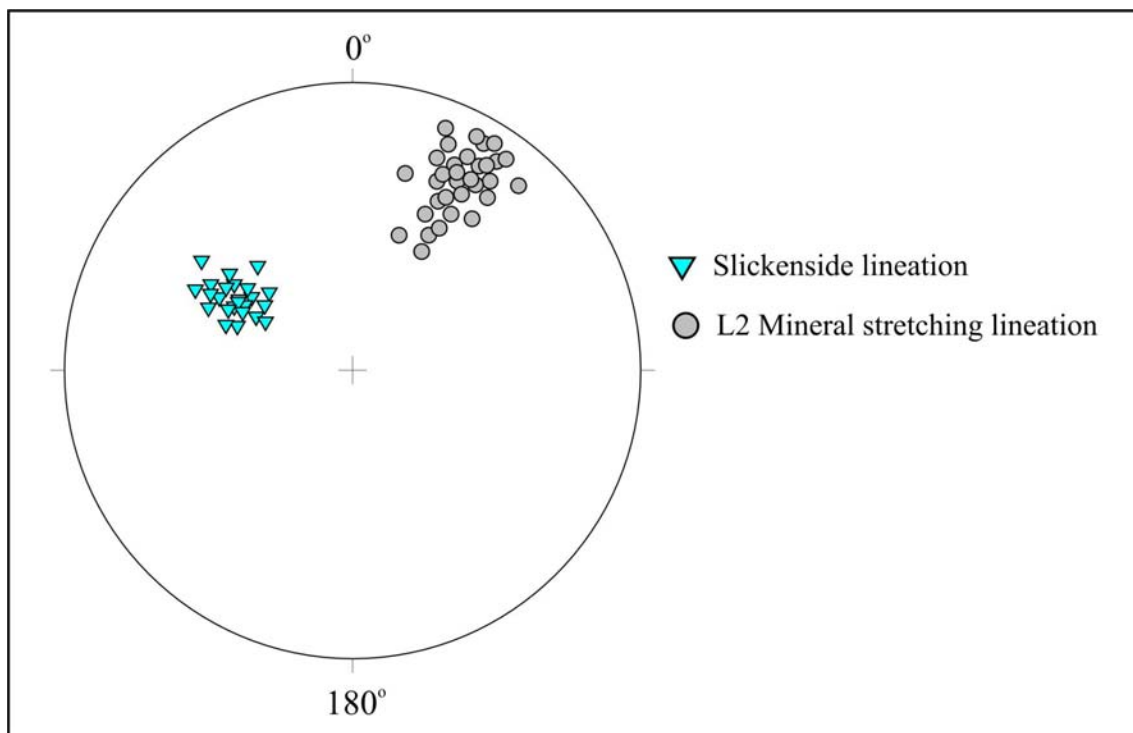


Figure 5.12. The L2 mineral stretching lineations on the mine have a NE orientation with the slickenside lineation at great angles to it.

## 5.5. Third phase of structural deformation (D3)

### 5.5.1. Late-stage cross folding (F3)

#### *Geometry, distribution and shape of the F3 folds*

The F3 folds are tight cross folds with an amplitude and wavelength of tens of metres scale, probably throughout the 7 km strike length of the deposit. Four F3 folds have been identified to date; while indications of another two cross folds have been observed. The cross folds appear to have a separation distance of between 500 and 750 m. Addendum B indicates the positions of three F3 folds located within the Block C area. The cross folds vary in strike-parallel dimensions (half wavelength) from less than 10 m to over 100 m in width. The down-plunge extent of the fold axes has been traced for up to a 180 m. Precise information on the fold geometry, orientation and frequency of the cross folds along strike and dip is currently still restricted, but increasing mine development will improve the understanding thereof.

The study of the cross folds is further complicated by the presence of large pegmatic bodies within the F3 fold hinges. The pegmatite bodies are mostly concentrated in, but not restricted to, the core of the isoclinal folds. The pegmatites are attributed to water-rich melt infiltration during the formation and later ductile/ brittle stage of the formation of the F3 folds. Figure 5.13 indicates the start of an approximately 100 m long pegmatic zone located in the core of a large cross fold situated at level 17 in Main Shaft. The pegmatites associated with the F3 folds crosscut and obliterate all the structural features of the gneisses, including the S1/S2 gneissosity and F2c isoclinal folding. Figure 5.13 shows the pegmatite replacement associated with the F3 cross folds. The pegmatite is normally very coarse grained and contains high amounts of feldspar.

The cross folds have so far only been identified within the Lower Horizon, but given the similarity between the two horizons (possibly as a result of duplication through the F2b) it is very likely that the same structures will be present in the Upper Horizon (see Section 5.4). The cross folds are often located in the pinching areas of “mega-boudins” present in the GNG units (Addendum B).

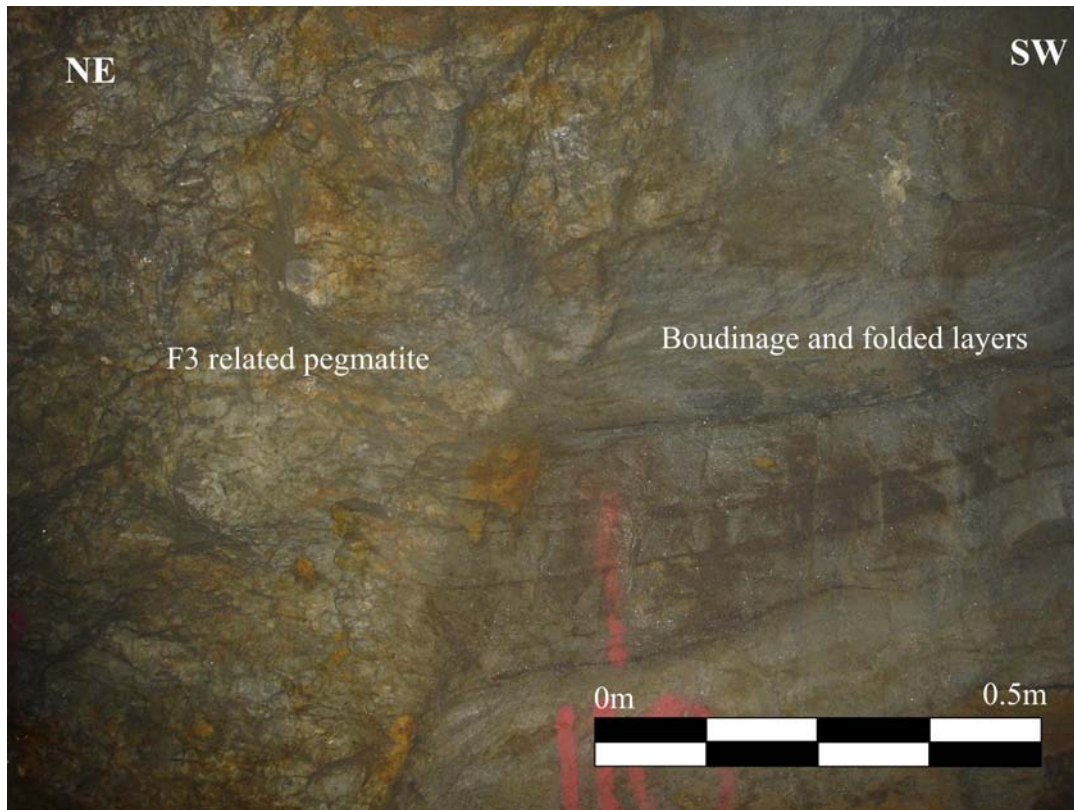


*Figure 5.13. A large pegmatite body crosscuts the boudinage layers and surrounding rocks. The pegmatite is associated with a large F3 intrafolial fold. The photograph is taken at level 17 in Main Shaft at the beginning of a 100 m long F3 fold. The majority of the F3 fold is replaced by pegmatite.*

The cross folds deform the majority of layers within the Lower Horizon, but are concentrated and centred around the JW-zone. The folding is most pronounced within this zone due to the difference in competence between the boudinaged calc-silicate bearing JW-zone and the surrounding gneisses and associated axial-planar and layer parallel shearing of the JW-zone. The F3 cross folds formed under semi-ductile conditions, resulting in unpredictable deformation of especially the core units (JW zone). Cross folds generally display S-type morphology (Addendum C).

Localised sinistral layer-parallel shear, which is opposite to the observed mine-scale dextral shear direction, has been observed within the cross folds. The major shear component associated with the cross folds, however, conforms to the dextral layer-parallel shearing sense.

*Fold axes description*

The F3 cross folds appear to have sub-parallel fold axes, with a general plunge of 30 to 40° in the direction 290 to 330° (Figure 5.15). Due to the sub-parallel nature of the fold axes and because of the limited number of cross folds exposed, only a small data set has been recorded (Figure 5.15). The fold axes appear fairly constant along plunge, but the inter-limb angle, amplitude and wavelength of the folds change drastically along plunge. This complicates underground down-plunge projection of the fold axes making a projection of ore-zone deformation difficult to predict. The half wavelength of a F3 cross fold located at Main Shaft changes from less than 10 m (level 7, Figure 5.16a and b) to over 100 m (level 17) over a 150 m down plunge extent.

*Influence of F3 folds on F2c isoclinal folds*

Isoclinal fold axes plunge steeply (ca. 30–35° NE) on the NE limbs of the F3 cross folds. The plunge of the fold axes gradually decreases towards the NE away from the F3 cross fold closures. As the successive F3 fold is approached, the plunge of the fold axes very gradually rotates to the NE and eventually changes to a low angle SW plunge. Thus on the SW side of the F3 fold the interference with the isoclinal folds results in a low-angle south westerly plunge. Thus, in general, F2c fold axes show variation in orientation from SW to NE as they are deflected by the steep plunging F3 folds and also exhibit differences in angle of plunge for the same reason (Figure 5.15).

The plunge and plunge-direction of a “DF1” synform (nomenclature of the F2c ore-shoots will be discussed in Section 5.7.7) present in Shaft 1 and Main Shaft, were measured over a distance of 696 m, from one F3 cross fold to next. The plunge and plunge-direction of the fold axes changed from 027 / 30° NNE on the SW limb of the first F3 fold to 031 / 05° SW on the NE limb of the succeeding F3 fold. Since the measurements were not taken at set intervals, the weighted averaged of 030 / 12° ENE of the fold axis was calculated over the distance (Table 5.1), for a total of 26 measurements. The same pattern of fold axis deflection was observed in all the other fold axes within different fold-stacks once the locality of the plunge measurements could be related relative to the F3 cross fold closures. Table 5.1 also shows measurements recorded for three different F2c isoclinal fold axes:

- The Askari Shaft synform fold axis was measured on the SW limb of a F3 cross fold and changed from 031 / 23° NNE to 031/18 NNE over a 90 m distance in a NE direction from the F3 fold closure.
- The Bravo Shaft level 8 antiform changed from 028 / 8° NNE to 044 / 2° NE over a 217 m distance towards the NE approaching a F3 cross fold.
- The Bravo Shaft level 17 synform changed from 031 / 12° NE (ca. 140 m SW of F3 fold) to 052 / 5° SW (ca. 10 m SW of F3 fold) to 010 / 36° NNE (ca. 10 m NE of F3 fold) over a distance of 240 m.

The F3 cross folds therefore causes the F2c isoclinal folds to become double-plunging folds (Figure 5.15).

#### *Influence of F3 on strike and dip of ore-zone*

The F3 cross folds influence almost all the pre-existing structural features present in the rocks of the mine area. The F3 folds affected L2 lineation, rotated the boudin structures, influenced the plunge of the F2c isoclinal folds and resulted in a change in strike and to a lesser degree the dip of the layering, not only within the folded area but up to a 100 m away from the F3 folds.

Figure 5.14 indicates the change in strike direction of the JW-zone over a 120 m distance from the F3 fold at Main Shaft to the F3 fold itself. The strike of the JW-layer rotated approximately 40° westward over the 120 m distance towards the F3 fold (Figure 5.14). There is little or no change in the dip over the 120 m distance leading up to the fold, but the dip and dip direction both change drastically within the F3 fold itself (Figure 5.14).

The influence of the F3 cross fold on the strike and dip is evident from the geological map of the Bravo F3 fold trench (Addendum C). The influence of the F3 cross folds can also be seen in the average strike data of each shaft as discussed in Chapter 3, Table 3.1. The shafts on the SW side of known F3 folds, e.g. Bravo Shaft and Main Shaft have more north-north-easterly strike directions (avg. of 044.5°). The shafts on the NE side of the F3 folds, e.g. CT Shaft and Askari Shaft have more north-easterly strike directions (avg. 051°). From this trend it could be implied that Delta Shaft, with an average strike direction of 039°, could be located on the south-westerly side of a cross fold. This

would imply that a fifth cross fold might be situated within the neighbouring Block D area.

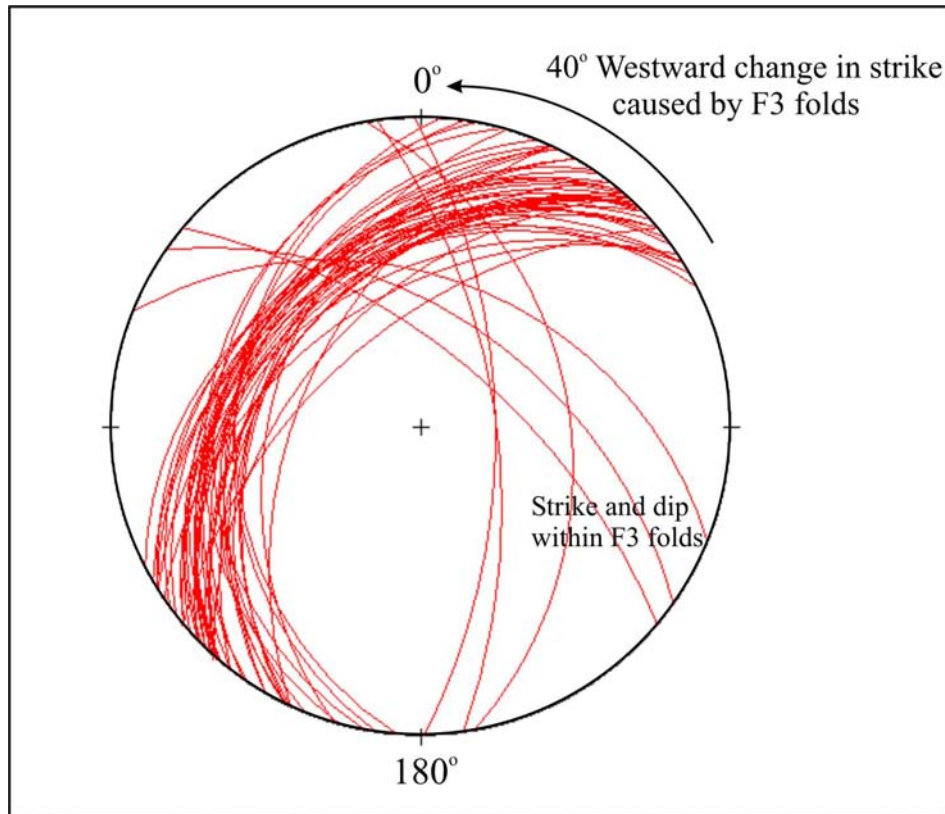


Figure 5.14. The great circles to the current bedding plane of the JW-zone over a 120 m distance. The measurements started 120 m SW of the Main shaft F3 fold and ended within the F3 fold.

#### *F3 influence on tanzanite mining*

The kinematics of the F2 cross folds suggest that an apparent displacement of linear structures like the F2c isoclinal folds could exist when they crosscut the F3 fold axes. It is not yet known whether or not any displacement, either up or down, occurs along the F3 fold axes. Initial indications do not suggest any displacement of the F2c isoclinal fold axes across the F3 fold axes. This has important implications for the mining of tanzanite since highly mineralised ore-shoots associated with the F2c folds could be situated up to several tens of metres up or down the F3 cross fold axes on the opposite side of the F3 folds (Figure 5.15).

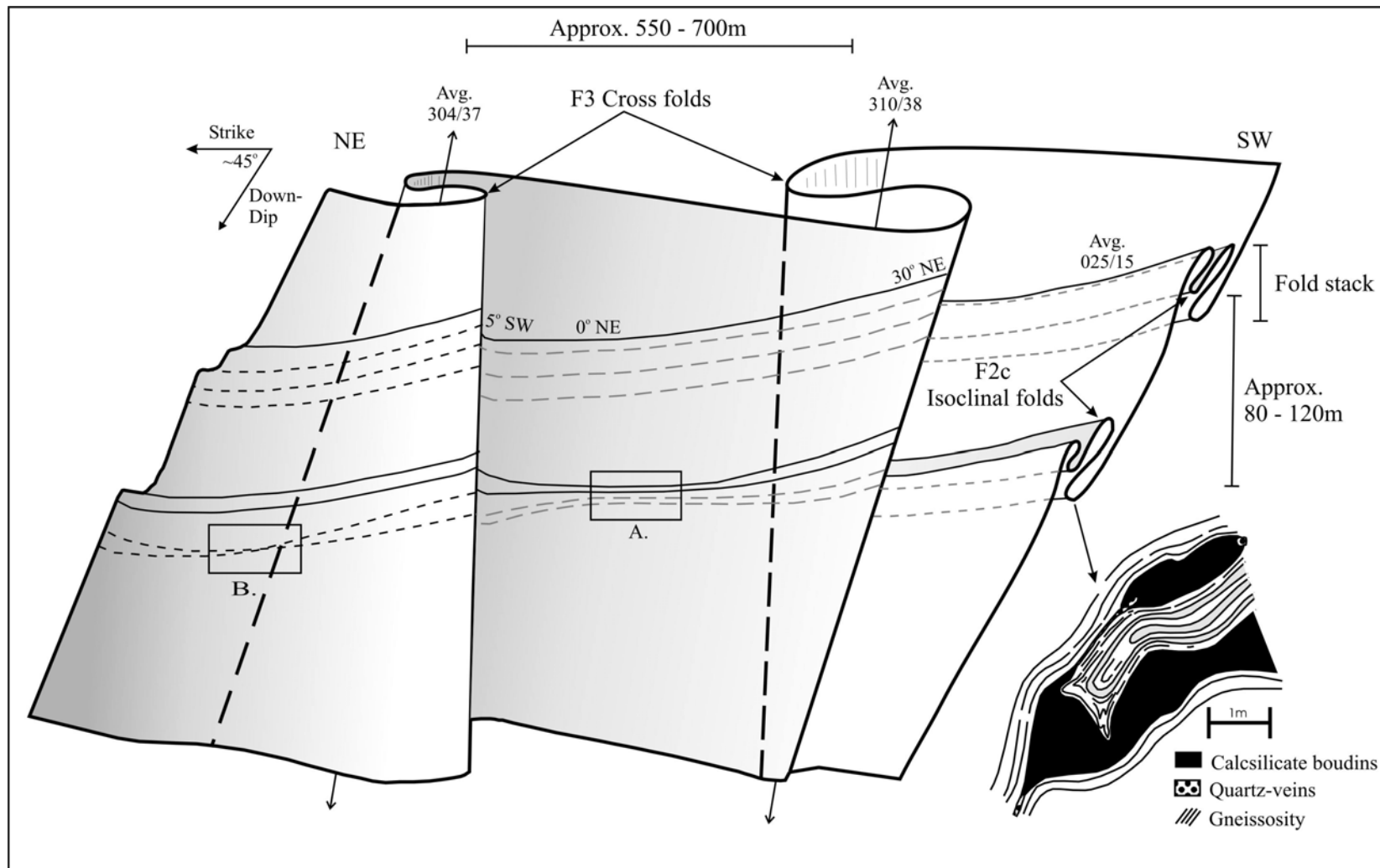


Figure 5.15. Diagrammatic representation of JW-zone. The diagram indicates the presence of the F2c isoclinal folds that form the boudinaged ore-shoots of the deposit situated within the fold stacks. F3 cross folds occur along the strike of the ore zone and influence the plunge of the F2c isoclinal folds.



*Example of F3 folding*

Addendum C shows a plan view of a cross fold located 80 m NE along strike of Bravo Shaft in Block C (Addendum B). The cross fold stretches over a 80 m distance and caused semi-ductile deformation of the units, especially the JW-zone. The diagram illustrates the drastic change in strike and dip along the cross fold. The overall shape of the Bravo Shaft strike fold (Addendum C) is an S-fold, but the more incompetent layers in the core of the fold are more plastically deformed. Multiple third order F2c isoclinal folds with associated skarn boudins (Figure 5.16.c and d) are exposed on surface, inside the F3 cross fold (Addendum C).

**5.5.2 L3 lineation**

North-westerly trending L3 stretching lineations with an average plunge of 25° SW occurs on the south-westerly limbs of F3 cross folds. The general NNE L2 lineation plunge is however present throughout the rest of the cross folds. The development of F3-associated L3 lineation did therefore not completely alter the pre-existing L2 lineation. The L3 lineation, similar to the L2 lineation, is defined by graphite, mica and elongated crystals of kyanite.

Lineation trends measured in NE Tanzania and southern Kenya by Weiss (1959) and Hepworth (1972) also identified isolated WNW-ESE lineation directions of an unknown origin. They suggested that it might pre-date the general NE lineation trends. It is however possible that the lineation trends that they measured may have been L3 lineation associated with similar F3 cross folds as observed in the Merelani tanzanite deposit.

## 5.6. Late stage brittle deformation (D4)

The deposit was subjected to late stage brittle deformation that resulted in the formation of faults, fractures and shearing during the retrograde metamorphic isobaric cooling path.

### 5.6.1. Faults and fractures

The majority of the faults and fractures dip steeply to either the NE or SW and strike NW – SE. Faults and fractures measured in different areas in Block C are indicated in Figure 5.17. These faults and fractures trend perpendicular to the gneissosity of the gneisses and schists, but have little or no displacement on them. Strike-slip faults display sinistral displacement of normally less than 20 cm. Layer parallel shearing and fracturing, dipping at lower angles (50 to 70°) to the north-west and south-east are subordinate and display very little displacement. Faulting and fracturing are influenced by the presence of boudin-rich areas and even individual boudins. Boudin-rich areas are often bounded by cm-scale high angle NW-SE strike fractures. Similar fractures are sometimes located in pinching areas of individual boudins.

Only one example of significant dip-slip fault movement was observed in the mining area. A ca. 5 m wide high-angle fault (110 / 76° SW) intersected Main Shaft at level 180 (ca. 103 m vertical depth). The fault had normal displacement of between 1 and 2 m.

Fracturing is also caused by brittle deformation of the F3 cross folds as described in Section 5.5.1. Fractures run sub-parallel to the F3 fold axes and are located adjacent to or within F3 cross folds. The fractures are often associated with pegmatic zones within the cross folds. The pegmatic areas contain high proportions of easily weatherable feldspar that channel meteoric fluid movement along the fractures.

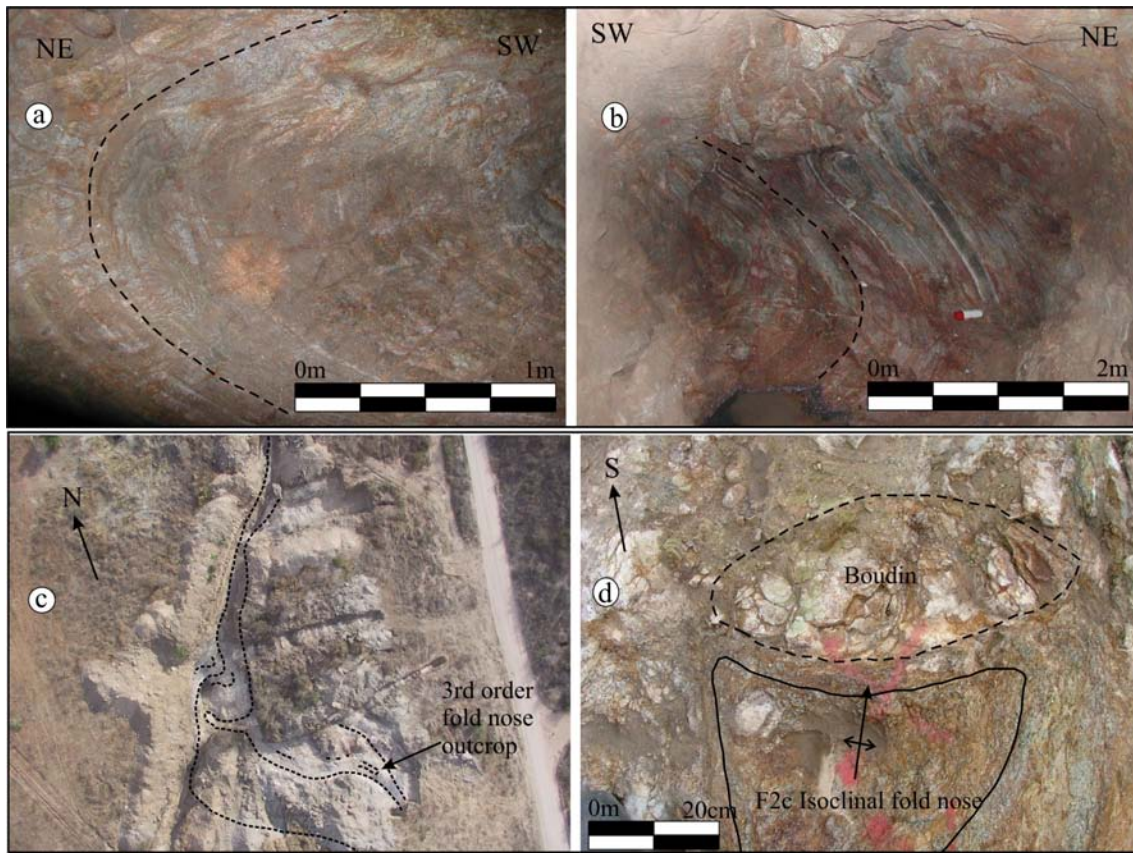


Figure 5.16. a and b) F3 intrafolial folds observed in Main Shaft, Level 7. c) Large intrafolial fold exposed through trenching 80 m NE of Bravo Shaft. d) SSW plunging third order isoclinal antiformal fold nose on the southern limb of the intrafolial fold. Note the boudinage associated with the folding.

Table 5.1. Plunge and plunge direction of F2c folds influenced by F3 folds.

Plunge and direction of Shaft 1 synform, DF1				Plunge and direction of Askari Shaft level 9 fold axis			
Distance (m)	Direction	Plunge		Distance (m)	Direction	Plunge	
20	027	30	NE	14	031	23	NE
56	030	19	NE	18	048	20	NE
131	030	19	NE	31	033	24	NE
145	021	20	NE	39	027	16	NE
164	023	19	NE	56	039	14	NE
171	026	14	NE	62	030	19	NE
198	022	13	NE	71	037	18	NE
217	026	14	NE	90	031	18	NE
224	020	12	NE	Average	34.4	19	NE
235	026	14	NE	Weighted Avg.	33.5	18.9	NE
245	027	18	NE				
263	026	16	NE				
300	025	9	NE				
306	023	13	NE				
511	029	14	NE				
540	036	11	NE				
552	044	4	NE				
575	038	1	NE				
587	211	5	SW				
622	036	2	NE				
645	038	1	NE				
657	211	5	SW				
671	214	4	SW				
680	215	4	SW				
690	220	1	SW				
696	025	3	NE				
Average	29.6	9.5	NE				
Weighted Avg.	29.9	11.9	NE				
				Plunge and direction of Bravo Shaft level 8 fold axis			
				Distance (m)	Direction	Plunge	
				0m (shaft)	028	8	NE
				217m	044	2	NE
				Plunge and direction of Bravo Shaft level 17 fold axis			
				Distance (m)	Direction	Plunge	
				141 from shaft	031	12	NE
				165m	052	5	SW
				240m	010	36	NE

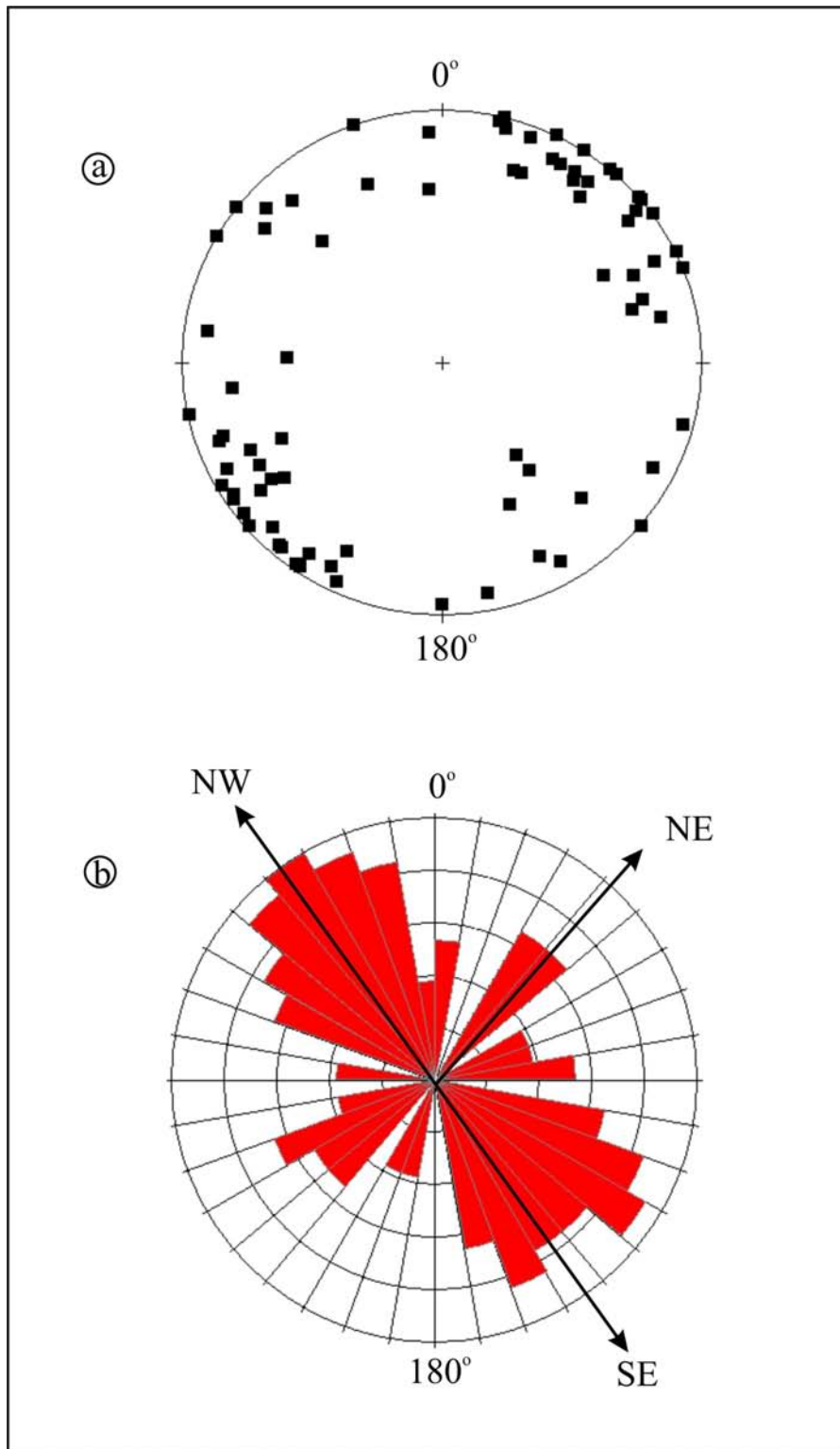


Figure 5.17. Lower hemisphere equal area projections of a) stereoplot of the pole to the fault planes of 85 fault and fracture measurements. b) rose diagram of the great circles obtained from the stereoplot 5.17.a, indicating the dip and strike of the faults and fractures. The rose diagram shows that the majority of the faults and fractures are striking perpendicular to the gneissosity of the rocks, in a NW – SE direction. A second smaller set of layer parallel fractures and faults are striking in a NE – SW direction.

## 5.7. Boudinage

Boudins are the most important structural feature associated with tanzanite occurrence since tanzanite mineralisation is exclusively restricted to it.

### 5.7.1. Boudin geometry

All the boudins observed in the mine area have a disk-like or lenticular three-dimensional shape, described as chocolate-tablet boudin structures (Wegmann, 1932; Ghosh, 1988). The boudins therefore have a roundish, lensoid geometry (Figure 5.18.a). The short axis of the boudins ( $z$ ; with  $x \geq y \geq z$ ) lies perpendicular to the gneissosity ( $S1/S2$ ) of the enveloping gneisses. The boudin axes in the plane of the  $S1/S2$  gneissosity are usually of equidimensional shape ( $x \approx y$ ) (Kisters et al., 2000). The boudin axes and their geometry are indicated in Figure 5.18.b.

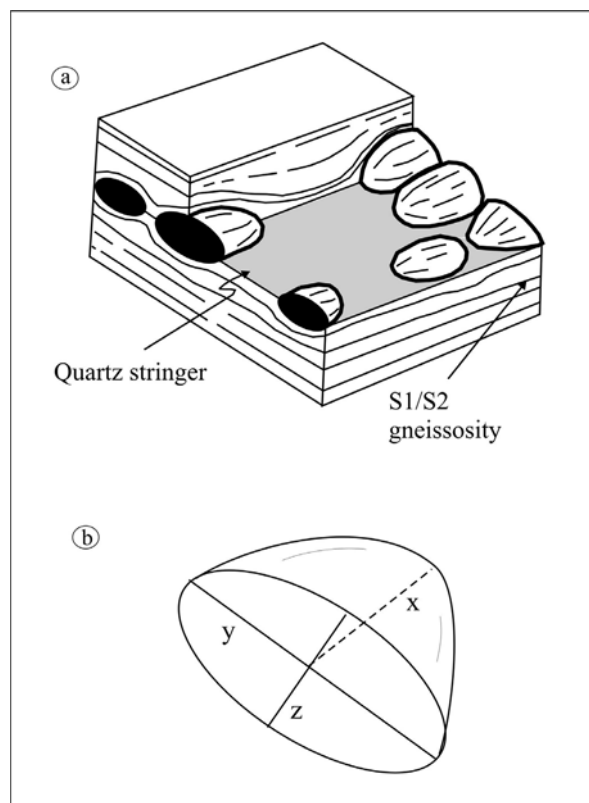


Figure 5.18. a) Chocolate-tablet boudinage adapted from Park (1997). b) Boudin axes geometry.

### 5.7.2. Boudin distribution

Boudinage is a fairly common structural feature within the Lelatema Mountains and occurs in the dolomitic marble layers, the metabasite located east of the mine area and also as isolated boudins in the Lelatema gneisses and schists. Boudinage has also been observed by the author within the other granulites situated in NE Tanzania, such as the Para and Usambara mountains. Boudin development in NE Tanzania was furthermore identified by various authors including Pallister (1971), Hepworth (1972) and Shackleton (1986, 1993b, 1996) within the Usagaran complex consisting of the Usambara-, Pare Mountains, and Umba - and Maasai Steppe.

Within the mine area, boudinage is confined to the calc-silicate layers present within the graphite-plagioclase gneisses (JW-zone, C-zone, D-zone and Upper Horizon alteration zones). These enveloping host rock gneiss units are again less competent than the surrounding kyanite-graphite gneisses (HW and FW units), leading to the formation of high strain zones characterised by shearing that accompanied regional metamorphism. This resulted in boudinage and folding concentrated within the competent units. Of these units, the JW-zone is by far the most important containing not only the best-developed boudinage and most intense folding, but also the bulk of tanzanite mineralisation. These units are indicated on the surface geology map of the mine (Addendum B). Small, poorly developed boudins have, however, also been observed within the banded-calc-silicate units (BCF units).

Based on the dimensions and distribution of chocolate-tablet boudins within the ore zone (JW-zone), they can be classified into two groups:

1) *Boudins within and associated with third order isoclinal folds (F2c).*

The vast majority of boudins are associated with isoclinal folding. Isoclinal folding caused concentration of boudins, multiple duplication and shear-stacking of the original boudinaged layer. Boudins are concentrated in fold closures or in strain shadow positions associated with isoclinal folding. The latter is locally referred to as “pressure shadow boudins” (Figure 5.7 and 5.19). The figures show the relative positions of boudinage and folding as observed in Shaft 1 and in Bravo Shaft. Boudinage and associated isoclinal folding created “ore-shoots” within the ore-body. The ore-shoots follow the plunge of the third order (F2c) folds and will be



discussed in Section 5.7.7. The lateral extent of these boudins normally varies from 1 to 3 m with a maximum diameter of over 6 m. The thickness of the boudins ranges from ca. 0.5 to 2.5 m with maximum thickness of over 4 m being recorded.

2) *Boudins situated on the limbs of the 3<sup>rd</sup> order isoclinal folds (F2c).*

They normally occur as isolated boudins on the fold limbs of the 3<sup>rd</sup> order (F2c) folds and are often separated by tens of metres. There is a drastic decrease in the size and frequency of boudinage away from the isoclinal fold hinges. The limb-boudins are normally substantially smaller with average lateral dimensions ranging from less than 5 cm to 1 m and average thickness of between 2 cm and 0.5 m

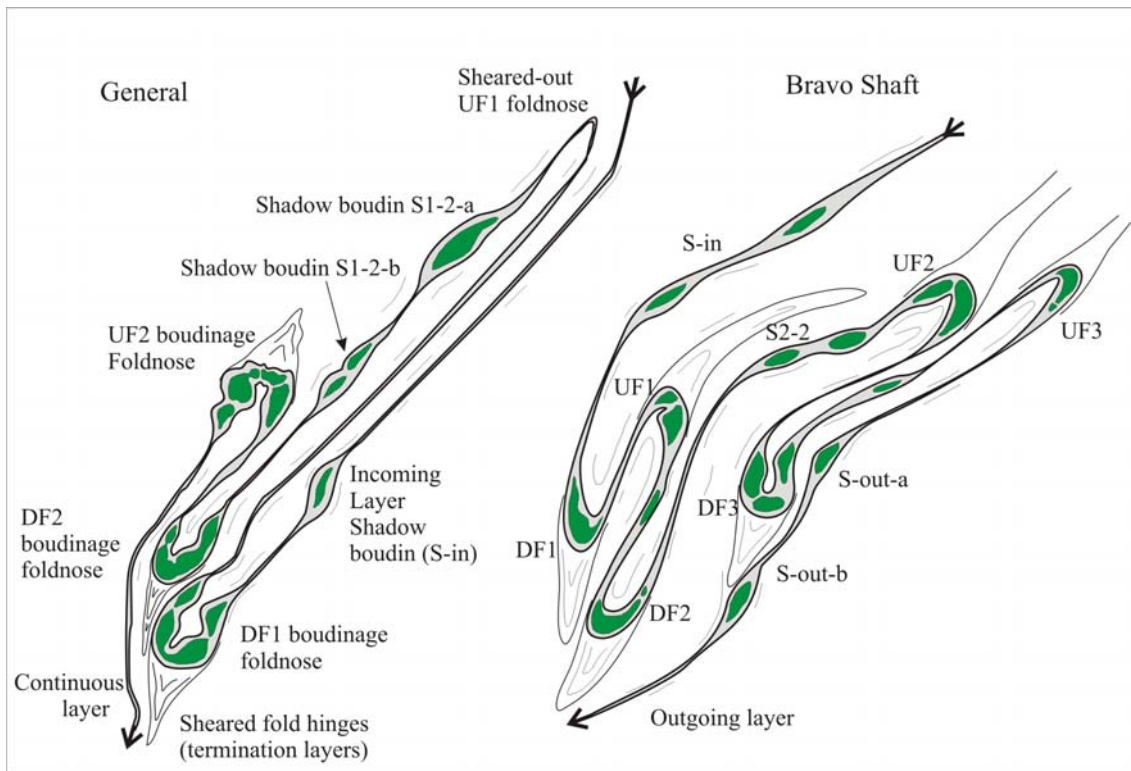


Figure 5.19. Transverse section of shear related isoclinal folding and boudinage within a fold stack looking towards the NE. The figure indicates the proposed nomenclature for the ore-shoots.

### 5.7.3. Boudin Types

After the boudin formation, further deformation, chemical skarn metasomatism, metamorphism in fluid infiltration followed. This resulted in the current occurrence of boudins in various stages of “preservation”. The skarn reactions associated with the

boudins and surrounding layers and its influence on the boudins will be discussed in Chapters 7 and 11.

- *Relict boudins.* These boudins consist of a core of competent diopside-rich calc-silicate rock termed the “relict” (Figure 5.20.b and c). The relict units contain mm-scale banding parallel to the S1/S2 gneissosity, but little or no banding in the dip direction (perpendicular to S1/S2). The relict is often slightly rotated around an axis perpendicular to the S1/S2, with joints in the surrounding less competent hydrothermally altered garnetiferous calc-silicates acting as slip planes (Figure 5.20). The rotation of the relict units may be attributed to later layer parallel shearing associated with F2. This resulted in the relict boudins frequently exhibiting a rhomboidal shape (Figures 5.20 and 5.21). The relict boudins are mostly situated within third order fold closures or are associated with third order isoclinal folds. Boudins with well-defined relicts normally display the highest tanzanite grades.
- *Silicified boudins.* These boudins are normally isolated structures situated on the fold limbs of third order isoclinal folds and are therefore located outside boudinaged and isoclinally folded ore-shoots. These boudins often consist of completely silicified calc-silicate relict material (Figure 5.22.a). It appears as if the metasomatic exchange reactions involved with the isolated boudin structures resulted in extensive silica alteration. The boudins normally contain poorly developed pressure shadow pockets, resulting in few pressure shadow associated minerals like quartz, calcite, zoisite and garnet. The pressure shadow pockets within the boudin structures will be described in detail under the Section 5.7.5.
- *Pegmatic boudins.* Pegmatite replacement occurs in both the relict boudins and silicified boudins. Pegmatite replacement is often confined to the boudin structures while the surrounding gneisses remain unaltered. Small remnants of the relict units are sometimes still present within the pegmatite boudins. The pegmatite replacement is especially pronounced in the areas close to or within the F3 cross folds. Figure 5.22.b shows a boudinaged layer that is replaced by pegmatite.

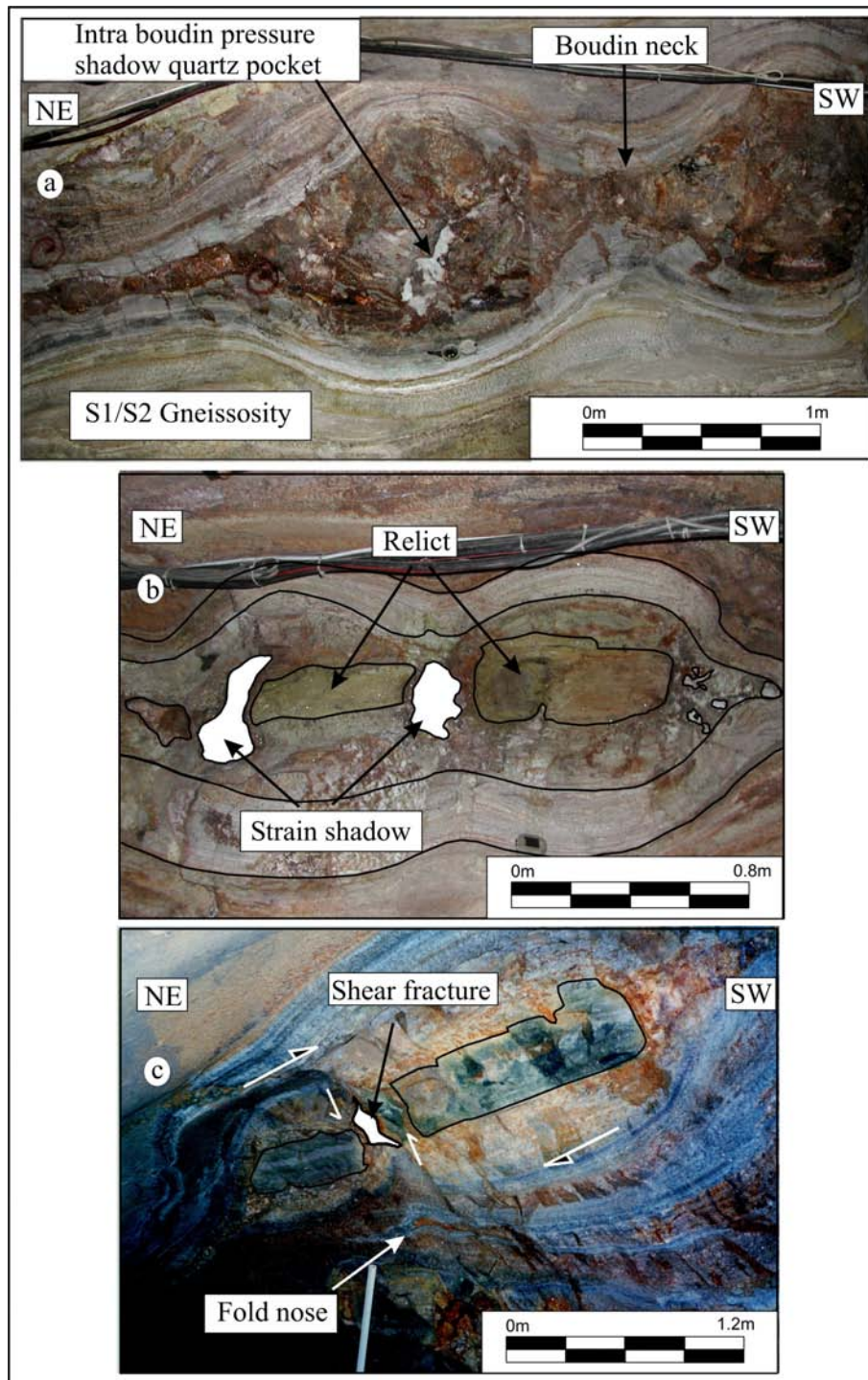


Figure 5.20. Photographs of boudin structures in the Block C area. Tanzanite mineralisation occurs in various pressure shadow positions within the boudins.

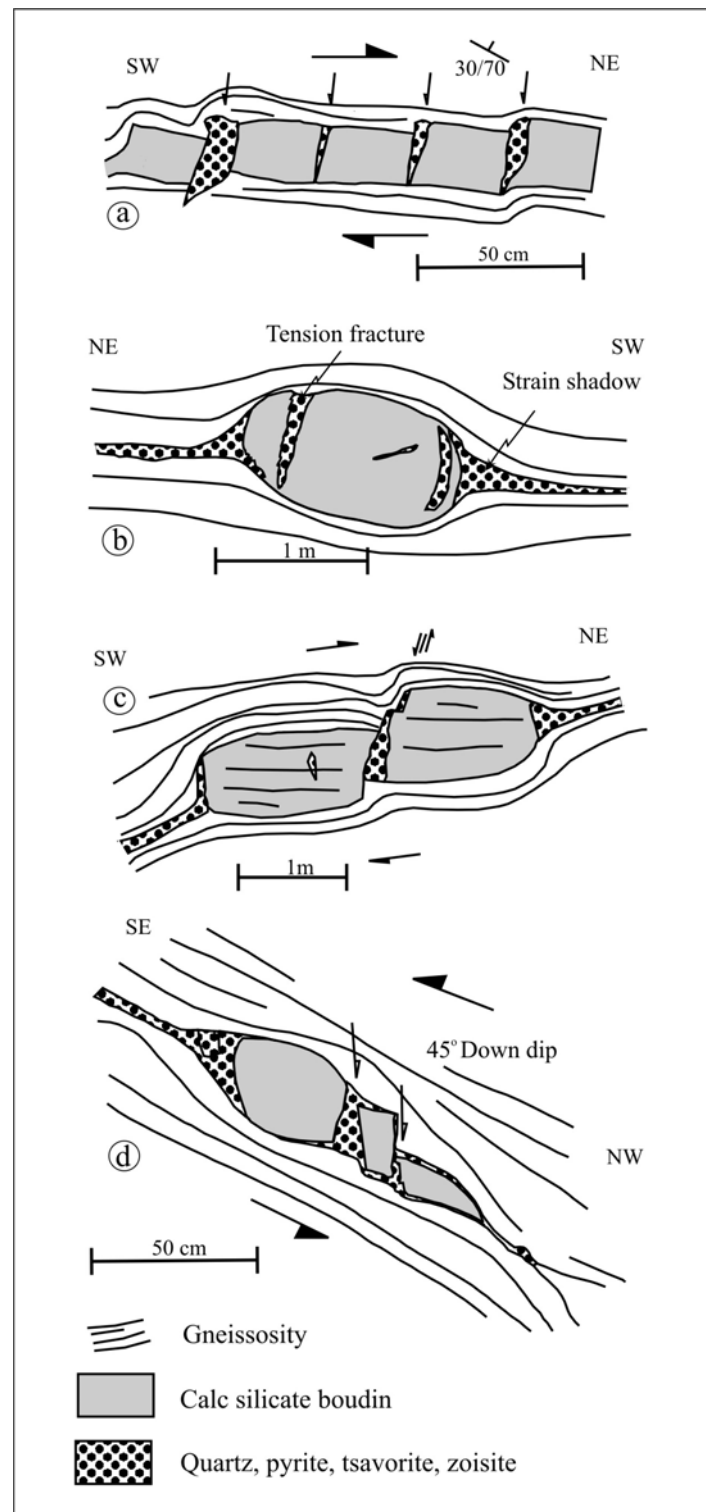


Figure 5.21. Various types of boudins and associated pressure shadow mineralisation observed in the Merelani deposit, adapted from Kisters et al. (2000).

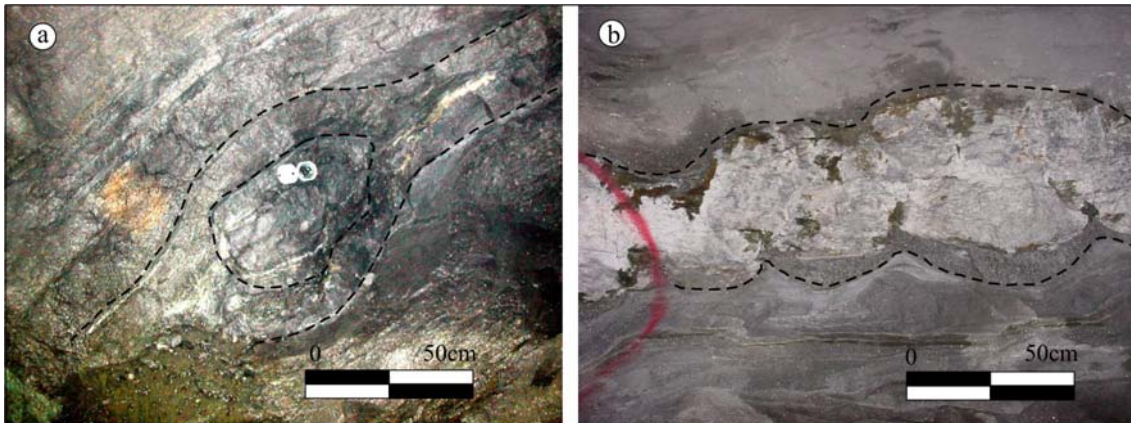


Figure 5.22. a) Silicified boudin located between folds stacks. b) Boudins replaced by pegmatite. The scar folds that developed near the separation zones between the boudins are still visible.

#### 5.7.4. Boudin orientations

Boudin x-axis measured over a 2 km strike distance in Block C exhibit plunge directions varying from north to west to south-west. The varying boudin x-axis orientation is indicated in Figure 5.23. The change in plunge direction of the boudins can possibly be explained by rotation of the boudin axes by the F3 cross folds. The reorientation of the boudins caused by the F3 folds will be discussed further in Section 5.7.6.

Sigmoidal shaped boudins are sometimes observed in the boudinaged ore-zone and were interpreted by Gresse (2003) as the result of dextral strike-parallel shear. The SW plunging boudins associated with the F3 cross folds have sinistral sigmoidal shapes as a result of the layer parallel shear associated with the cross fold. The variation in boudin orientation can also be attributed to stretching (flattening) and shear in the foliation plane (Figure 5.23). It can therefore be concluded that the shear orientation and boudin rotation is likely to vary continuously depending on local structural setting.



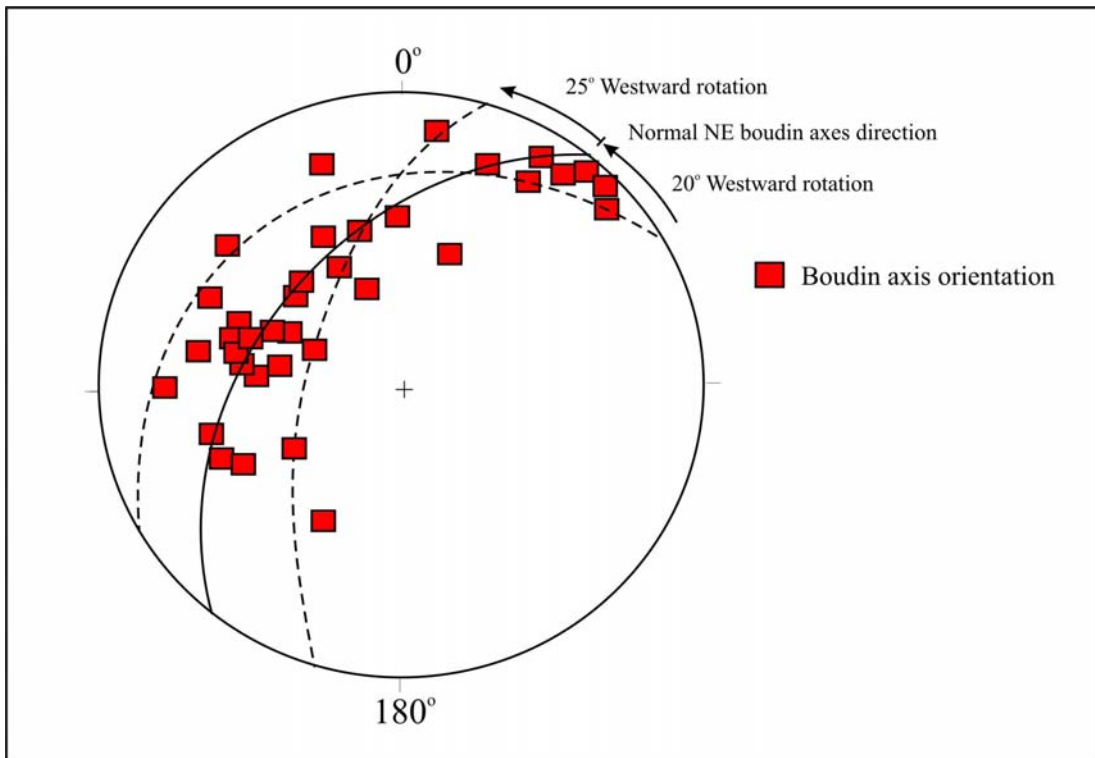


Figure 5.23. Boudin x-axis orientations compiled from the author's measurements, Gresse (2003) and Kisters et al. (2000). The rotation of the boudin axis trends may be explained by the influence of the later F3 cross folds on the boudins.

#### 5.7.5. Boudin low-pressure sites

Pressure shadows within a boudin create sites for new stable minerals to grow, mainly through local stress-induced chemical solutions, diffusion of mobile components and migration towards these sites from the crystalline phase. It is possible that these solutions could have been supplemented by fluids from an external fluid source migrating through the rock successions and accumulating in these zones of lower pressure. Quartz, calcite, pyrite, gypsum, zoisite and garnet are the main minerals in these pressure shadow areas. It is important to note that tanzanite mineralisation is almost exclusively confined to the pressure shadow areas within the boudins.

Three types of pressure shadow regions are observed in the boudins:

1) *In or in close proximity to boudin neck area*

Boudin necking occurs due to pre-fracture plastic deformation. The vast majority of boudins in the Merelani area show some degree of pressure shadow pocket formation in the boudin termination area (Figures 5.20 and 5.21). Ghosh (1988) indicated that for some types of boudins the ductility of rock was greater in a direction parallel to the stretching lineation than perpendicular to it. This

seems to be applicable to the majority of the chocolate-tablet boudins in the Merelani area. The best-developed strain shadow mineralisation of quartz, calcite and tanzanite occur in up- and down-dip boudin terminations compared to the strike direction. Thus, the most favourable locality for tanzanite mineralisation is at boudin terminations along the slickenside lineation direction where more brittle fracturing caused the formation of larger pressure shadows and tension fractures (Figure 5.24). Quartz pockets at the boudin terminations are often wedge-shaped, grading into quartz stringers that connect adjacent boudins, and can be used to trace the strike and down-dip extent of associated mineralised boudins.

2) *Internal pressure shadows*

These occur mainly due to competency difference within a boudin. Internal pressure shadows are often observed where the hard relict layer is preserved within the less competent boudin matrix. Kisters et al. (2000) noted that the occurrence of these isolated pockets within boudins could be an indication of incipient necking of larger boudins as a result of combined ductile necking and later brittle fracturing. The pockets vary in size, from microscopic to 1 m in diameter (Figures 5.20 and 5.21).

3) *Tension and shear fractures*

Brittle fracturing and shearing associated with boudins often resemble Riedel-type shears. Kisters et al. (2000) indicated that wedged-shaped tension fractures close to the necking areas of boudins are commonly developed in barrel-shaped boudins, but occur less commonly in lenticular boudins. They recorded two perpendicular sets of fractures commonly found within the boudins, dipping at ca.  $210 / 75^\circ$  and ca.  $105 / 45^\circ$ . Riedel shear-like fractures are more pronounced outside the intensely boudinaged area and crosscut the gneissosity.

Smaller scale, localised faults and fractures are caused by the boudinage itself and are predominantly situated in the high-tension zones between adjacent boudins. Where the tension and shear fractures are located far from the boudin terminations, they often subdivide the boudin into separate segments. This is observed where elongated segments of the calc-silicate layer have been preserved, without ductile boudinage.



Strömgård (1973) calculated that the length of boudins formed by tension cracking would be in the range of 2 to 4 times the thickness of the competent layer. Kisters et al. (2000) showed that two main shear directions exist within the boudins at almost right angles to each other dipping at ca. 75° NE and ca. 60 – 70° NW, respectively.

#### **5.7.6. Influence of F3 folds on boudin orientation**

As indicated in Section 5.7.4, the change in plunge direction of the boudins can possibly be explained by rotation of the boudin axes by F3 cross folds. This is evident for boudins with a south-westerly plunge direction, which were measured on the eastern limb of a F3 cross fold. The SW plunge direction of the boudins also coincides with the SW plunge direction of both the mineral stretching lineation and 3<sup>rd</sup> folds also present on the easterly side the same F3 cross fold.

The re-orientated boudins fall within the range of strike changes caused by the interference of F3 folds. The westward rotation of the boudin axes on the NNE side of the normal NE direction is therefore contributed to the decreasing distance towards a F3 fold into a north-easterly direction. The westward rotation of the boudin x-axis on the ENE side of the normal direction could be the result of an increasing distance from a F3 fold into a north-easterly direction.

#### **5.7.7. Ore-zone morphology**

Boudins tend to be concentrated in the fold hinges of isoclinal folds, resulting in “ore-shoots” that follow the plunge of the isoclinal fold stacks. The “ore-shoots” created by the isoclinal folds and boudins are of great importance to tanzanite mining since it represents a mineable structure that can be followed down plunge (Figure 5.24). Secondary ore-shoots are sometimes also developed on the limbs of the isoclinal folds. The ore-shoots are referred to as “shadow boudins” (Figures 5.7 and 5.19). Figure 5.24 indicates a typical “face” of an ore-shoot, which would be drilled, blasted and processed for tanzanite. The figure shows the position of the F2c fold hinge in the centre of the ore-shoot, with boudin development surround it. The direction of drilling and subsequent ore-shoot development through blasting is governed by the plunge and orientation of the each individual F2c fold hinge. Since the ore-shoots are usually situated within the F2c fold hinge the sidewall of the ore-shoot drives often contain the boudinage limbs of the F2c folds (Figures 5.25 and 5.26).

The plunge, orientation and behaviour of F2c isoclinal fold-axes are of crucial importance to tanzanite mining (as discussed in Section 5.4.3), since it impacts on the mining method and mine plan. The mining and ore resource calculations of TanzaniteOne Ltd., as well as the importance of this study to tanzanite mining, will be discussed in Chapter 14.

This study established a uniform nomenclature for the various ore-shoots associated with the F2c folds within a fold stack. Figures 5.19 and 5.27 indicate the proposed nomenclature for the isoclinal fold closures and associated pressure shadow boudin structures.

The isoclinal folds and boudins are named from the layer that connects to the adjacent up-dip fold stack, called the incoming layer. If a pressure shadow boudin is present on this layer before the first synformal folds this boudin is referred to as the “shadow boudin on the incoming layer” (S-in). The first synformal isoclinal fold is termed the DF1 (down-dip fold 1), while the first antiformal isoclinal fold is termed the UF1 (up-dip fold 1). Any pressure shadow boudins situated between the synformal and antiformal folds are termed S1-1. If there is more than one pressure shadow boudin present on the limbs these are then subdivided into a and b (Figure 5.27). The same system is used for all the other folds and shadow boudins up to the layer that will connect with the down-dip fold stack, called the outgoing layer. Any boudins associated with the fold stack and boudins on the outgoing layer are termed the shadow boudin outgoing (S-out).



*Figure 5.24. Synformal fold nose with associated boudinage. The boudin contains a well-defined diopside relict and quartz filled pressure shadow area. A mullion structure is visible opposite the fold nose within the boudin.*

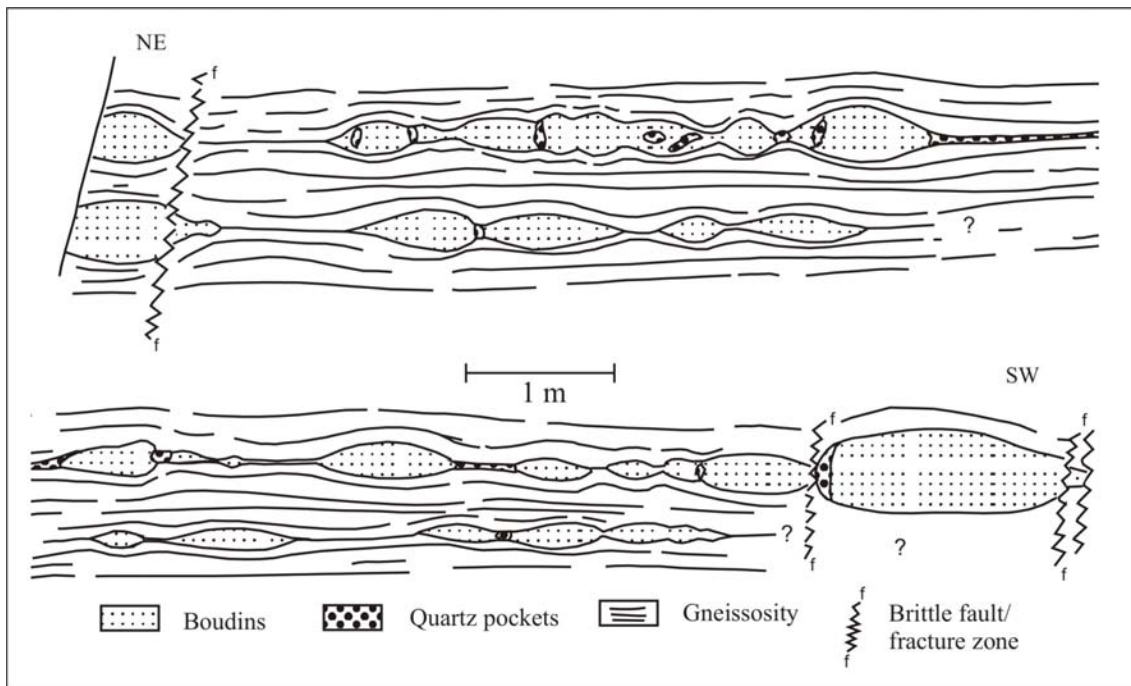


Figure 5.25. Mapped boudinaged layers on the limbs of a synform in Shaft 1, looking up-dip (SE). The two boudinage layers are formed through shear duplexing of the F2c isoclinal folds.



Figure 5.26. Photograph of two boudinaged layers on the limbs of a synform. The photograph was taken 450 m down the plunge of the same fold nose as mapped and indicated in Figure 5.26. The photograph was taken in an up-dip direction toward the SE with the photographer standing in the mined-out F2c fold hinge that linked the two limbs.

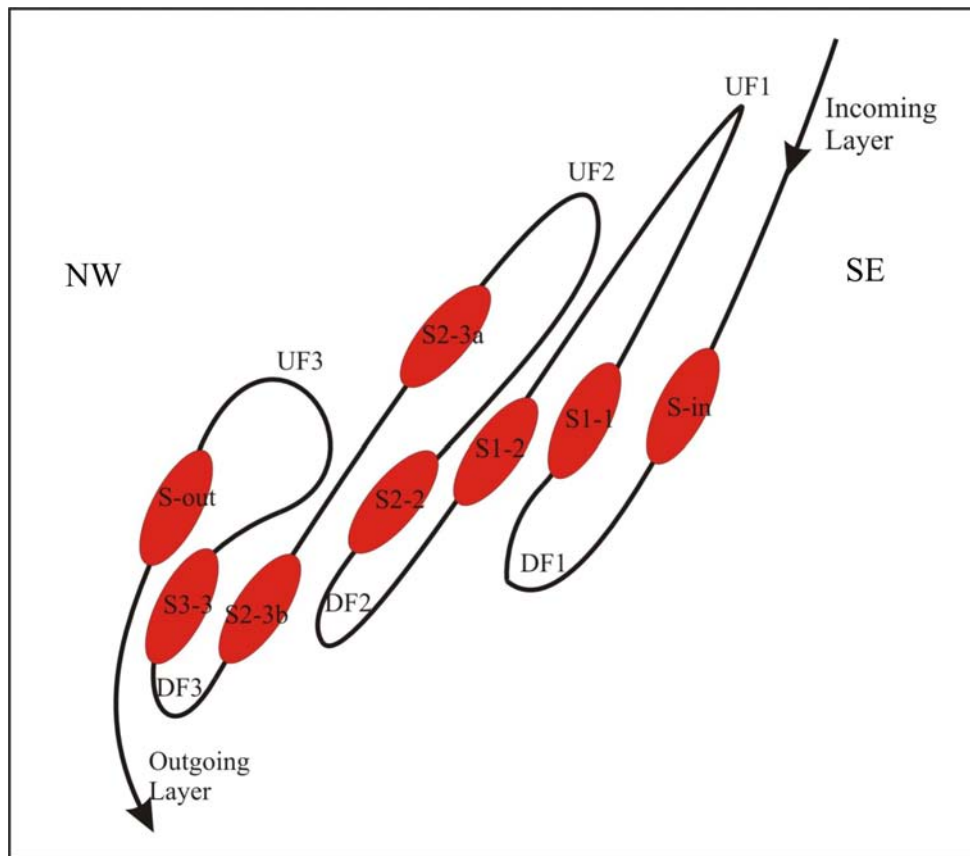


Figure 5.27. Transverse section of isoclinal fold noses and associated pressure shadow boudin positions within a fold stack, looking toward the NE. The proposed nomenclature for the various folds and pressure shadow boudins within the mineable ore-shoots is described in the text.

## 5.8. Discussion

Progressive increase in the metamorphic temperature and pressure conditions, probably due to deep burial and tectonic loading, led to the onset of high-grade ductile deformation. The first phase of structural deformation (D1) is either associated with the prograde metamorphic path towards granulite facies, peak metamorphic condition (M1) or with the M1 event itself. Peak metamorphism (M1) reached granulite facies conditions of ca 9 to 12 kbar and 800 °C to 900 °C (see Chapter 9).

From the great circles obtained from the poles of the S1 foliations measured on the mine, metabasite and riverbed outcrop the relative “rotation” can be measured on a stereoplot (Figure 5.3). This indicates that the S1 foliation in the metabasite displays an approximate 33° westward strike rotation relative to the S1 foliations measured on the mine area, whilst the S1 foliation measured in the riverbed outcrop displays an approximate 10° eastward strike rotation relative to the mine area. The more westerly foliation directions of the metabasite compared to the S1 foliations observed in the mine area may be attributed to the more southerly position of the metabasite outcrop on the western limb of the Lelatema fold, while the riverbed outcrop is located more northerly on the same limb of the Lelatema antiform.

A decrease in the metamorphic temperatures and pressures occurred after peak metamorphic (M1) conditions. This was accompanied by a second phase of structural deformation (D2) as well as crustal uplift resulting in the M2 metamorphic event. The M2 event is characterised by a decrease in temperature from granulite facies to amphibolite facies conditions. The P-T conditions of the M2 event are estimated at 8 to 6 kbar and 700 to 600 °C. Ductile folding (F2) associated with the second phase of structural deformation (D2) refolding and overprinting of the earlier structures, fabrics and rocks. The F1 folding was subsequently entirely transposed by the D2 associated folding phases.

The L2 mineral and regional stretching lineation was created by virtual co-axial shortening associated with early Mozambiquan collisional tectonics during crustal compression. Gresse (2002) contributed both the regional foliation and stretching lineation to underplating and collision between the Mozambique Belt and the Tanzanian



Craton. This was accompanied by westward (transverse) recumbent folding and thrusting similar to that described by Shackleton (1993a) for NE Tanzania.

The S2 foliation and axial plane cleavage is parallel to S1, except in F2c fold closures and is axial-planar to the F2c drag folds. S-C structures are present in areas where the original S1 foliation is orientated at an angle to S2 (e.g. in the F2c fold closures). In general, the S1 and S2 foliations are parallel and often indistinguishable.

The F2 event probably denotes a process of continuous deformation and uplift into the ductile to semi-ductile crustal regimes. The F2 event can be subdivided into three folding phases, with the F2a event being the formation of the Lelatema antiform and the F2b and F2c folding phases being secondary parasitic folding events associated with the formation of the antiform. The three fold phases are related to one event, but are of different orders. The F2b resulted in the formation of second order drag folds on the limbs of the Lelatema anticline while the F2c resulted in third order drag folds on the limbs of the second order drag folds.

The proposed evolution of the antiform is illustrated in Figure 5.28. The development of the Lelatema antiform probably occurs at various stages during the multiphase Pan-African event. Comparison with the structural deformational history of the other granulites within NE Tanzania (Chapter 2) suggests that the D1 event probably occurred at around 720 to 690 Ma ago. This resulted in Step 1 as indicated in Figure 5.28 and led to the formation of the F1 fold with NNE fold axes. Step 2 probably formed shortly after (ca. 690 to 650 Ma) through ductile attenuation of the F1 folds, resulting in ductile flattening, elongation and layer-parallel extension. Step 3, probably occurred between 650 and 550 Ma under more ductile conditions. During step 3, the original F1 folds were refolded and transposed by the F2 folding event. The refolding resulted in the formation of a new large north-easterly plunging antiform. The Lelatema antiform therefore currently plunges towards the NNE and a maximum plunge of 60° was recorded by Malisa (1987). The F2a fold axis of the Lelatema antiform is sub-parallel to the regional NNE plunging stretching lineation L1 created by the F1 folding event. The formation of the F2a Lelatema antiform led to the development of the second and third order parasitic folds on the limbs of the F2a antiform.



The third phase of structural deformation (D3) is probably related to the later stages of the Pan-African event occurring at around 550 to 500 Ma, similar to that observed by Muhongo (1990) and Möller et al. (1998) for the granulites within NE Tanzania. During the D3 event the schists and gneisses was retrograded to amphibolite / greenschist facies (M3; 4 to 5.5 kbar and 600 to 520 °C). During the D3, M3 event, semi-ductile/brittle deformation led to the development of on-strike folding due to compression, followed by a period of intense extension. This resulted in the development of cross folds (F3) and the associated L3 lineation.

The close relationship between the various deformation events is also evident from the similarity between the minerals defining the foliations. All three foliations (S1, S2 and S3) observed in the mine area are defined by graphite, mica and elongated kyanite crystals. The foliations are however preserved in different structural positions within the rocks of the Merelani deposit, as previously indicated.

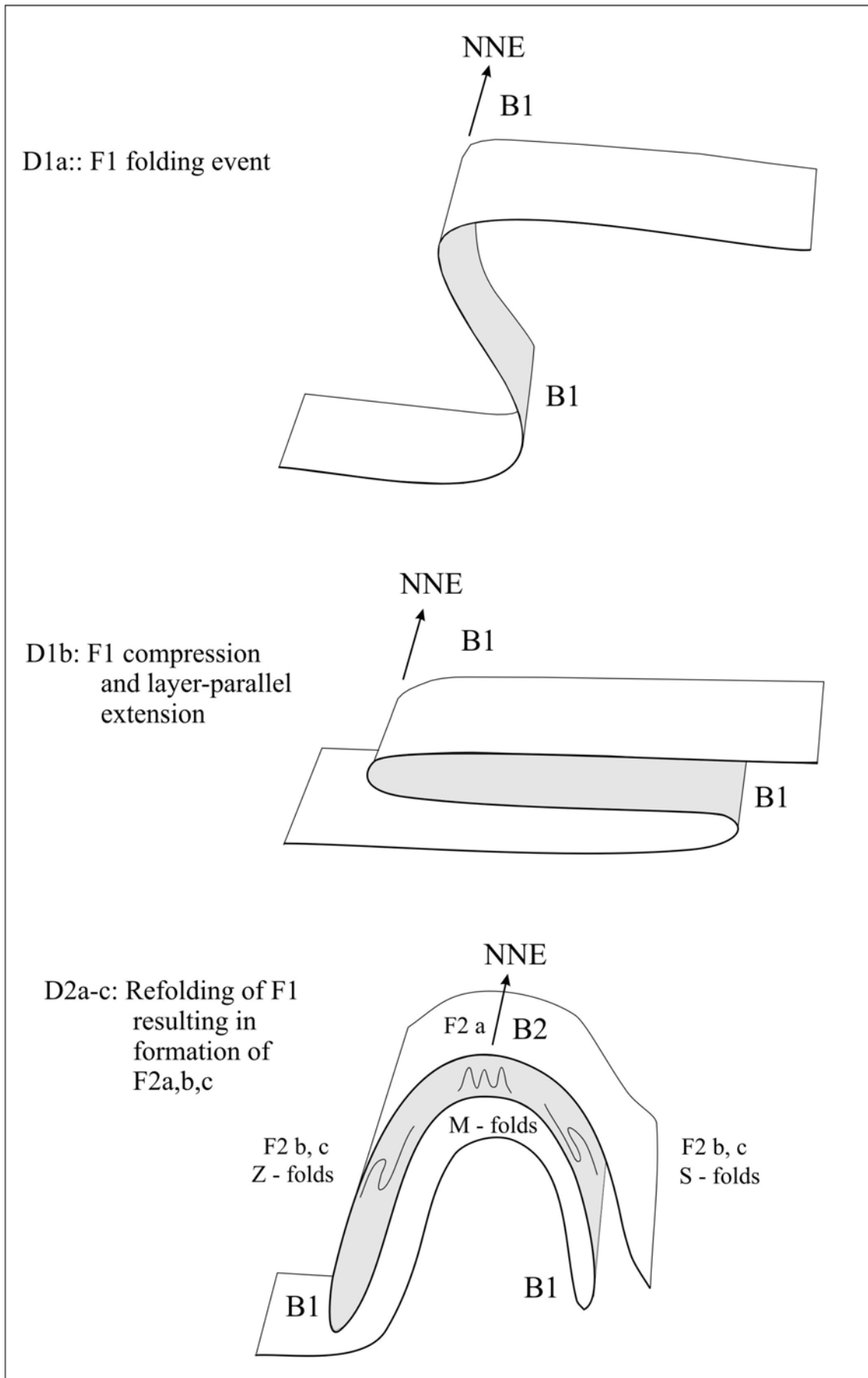


Figure 5.28. Proposed step-wise formation of the Lelatema Antiform.

The boudinage within the tanzanite deposit is characterised by equidimensional translational extensional deformation in two directions within the field of flattening resulting in chocolate-tablet type boudinage (equidimensional boudinage). Boudinage in general was first observed by Ramsay (1866) and Harker (1889) while chocolate-tablet boudinage was defined and described by Wegmann in 1932. It was subsequently described by various authors including Ramberg (1955), Ramsay (1967) and Ghosh (1988). Chocolate-tablet boudins are characterised by “pure-flattening” resulting in  $K$ -values close to zero on the Flinn-diagram (Ghosh, 1993).

The chocolate-tablet boudins present in the Merelani area are similar to those described by Naha and Halyburton (1977) in the Udaipur district, Rajasthan, India, with boudin structures containing two necklines or boudin axes at near perpendicular angles. The two boudin axes are parallel to the regional stretching lineation  $L1$  and perpendicular to the slickenside lineation direction, respectively.

According to Ramsay (1967), Sanderson (1974) and Ghosh (1988, 1993), two sets of boudin axes at high angles to each other cannot result simultaneously from a bulk flattening deformation. Theoretical and experimental work by Ghosh (1988) revealed that the two sets of axes in chocolate-tablet boudins are not absolutely simultaneous. The stress distribution in the competent layer is therefore changed by the first set of boudins that form, although the bulk stress field in the incompetent layer remains the same.

From the geometric principles involved in chocolate-tablet boudinage and the interaction between boudinage and folding as described by Ghosh et al. (1999), it is possible to deduct a model for the timing and forces involved in the formation of the tanzanite deposit boudins. In the case of the Merelani deposit, the first set of boudins axes have developed as a result of stretching along the  $F2a$  fold axes. Through subsequent tightening of these folds and the formation of the  $F2c$  isoclinal folds, the second set of boudins axes could have developed through stretching perpendicular to the fold hinges.

Both boudinage sets therefore formed synchronously with the  $F2$  folding event, but during different phases of it. The deformational features described by Ghosh (1993) and

Ghosh and Sengupta (1999) as an indication of the relationship between boudinage and folding, further supports this argument:

- Extensive pre-folding boudinage is characterised by the occurrence of boudin separation zones at the hinges of folds, which is not observed in the tanzanite deposit.
- Intensive post-boudin plastic deformation results in various deformational structures (e.g. fish-head boudins) not observed in the Merelani boudins.
- Post folding boudin formation results in distortion of the axial surfaces of the earlier folds by the scar folds which developed near the separation zones between the boudins. This feature is also not observed in the Merelani area.
- Small-scale boudinage and isoclinally folded veinlets was also observed within the metabasite outcrop (Figure 5.2). This also suggests that boudinage was chronologically related to folding.

The competent calc-silicate layers that are present within less competent gneisses in the mine area were plastically deformed under high-grade ductile conditions associated with D1 and D2. This caused ductile flow of the gneisses around the more competent diopside-rich calc-silicate layers, followed by tensional separation of blocks within the competent layers. The boudinaged layers were subsequently duplicated by isoclinal folding caused by shearing within the ore zone. This led to the formation of boudin accumulations in F2c fold hinges. The ore zone of the deposit therefore consists of various fold stacks that in turn comprises of up to 7 ore shoots created by the concentration of boudin structures in F2c fold hinges as a result of folding and shear duplication.

The graphite-plagioclase gneiss ore-zones (JW-zone, C-zone, D-zone and Upper Horizons alteration zone) are essentially all shear-zones. Shearing is concentrated around the calc-silicates intercalated with the graphite-gneiss. Shearing along the contact between the gneiss and the calc-silicates created path-ways for fluid migration which is the driving-force behind the skarn reactions that occurred within both the calc-silicates and surrounding gneisses. The contact between the two rock types is defined by the skarnoid reaction zones, described in Chapter 3 and 4.

## 5.9. Conclusions

The variation in sedimentary thickness and cycle times of deposition is considered the first possible influence on the later structural features observed on the mine and surrounding areas. The presence of non-translation deformation is purely hypothetical and possibly resulted in a wave-like deformation of the original sedimentary units under low pressure and temperature conditions. This event, together with the variation in sedimentary thickness, could have contributed to the set intervals observed between deformational features.

*Table 5.2. Summary of main structural features.*

<b>Deformational Event</b>	<b>Structural Feature</b>	<b>Description</b>
D1	F1	Originally NNE plunge refolded through F2 event to SW plunge
	S1	NE strike; dip between 28 to 65° NW (avg. 50° NW)
	L1	WSW trending, plunge at 20 to 30°
D2	F2a	Formation of Lelatema Antiform; N plunge at maximum of 60°
	F2b	2 order parasitic folds on F2a, NE plunge
	F2c	3 order parasitic folds on F2a, NE plunge 5° SW to 30° NE
	S2	Dip NW sub-parallel to S1 but axial-planar to F2
	L2	NNE trending, plunge at 10 to 35°
	Boudinage	N to W to SW trending, low-angle plunge associated with F2c
D3	F3	WNW to NNW plunge at 30 to 40°
	L3	NW trending, plunge at 25°
D4	Faults/Fractures	High angle faults predominantly strike NE –SW

The first deformational event (D1) resulted in the formation of a gentle fold (F1) that subsequently refolded to form the Lelatema Antiform. The folding (F1) and deformation (D1) created the first lineation direction (S1) and has a similar direction and plunge as that of the F1 folding, both heading NW with a plunge of approximately 45°.

The D1 event was followed by the D2 event, which started with the formation of the Lelatema antiform (F2a). Associated with the F2a folding event was the formation of the second foliation direction (S2). The F2a antiformal formation also contained two sets of parasitic folding. The first (F2b) duplicated the limbs of the anticline, while the second (F2c) created metre scale drag folds on the limbs of the larger F2b parasitic folds.

The exact timing of the formation of boudins within the deposit is difficult to determine, but probably occurred in two phases, slightly pre-dating the F2c isoclinal drag folds formation as well as forming synchronically with it. This is evident from the positioning of boudins within the hinge areas of the isoclinal folds as well as the absence of classic post-boudinage plastic deformational structures such as the “fish-head” boudin structures defined by Ghosh (1993). The stacking and multiple duplication of the boudinaged ore-zone by isoclinal folding resulted in multiple ore-shoots situated within individual fold stacks.

The boudins and isoclinal folds were subsequently modified by the third phase of deformation (F3). The SW plunging mineral stretching lineation observed within the F3 cross folds represents the youngest lineation direction and only developed within the F3 cross folds.

The Lelatema Antiform, including the Merelani tanzanite deposit, exhibits late brittle deformation that developed at shallow crustal levels. In the mine area, this deformation resulted in primarily NW-SE trending faults and fractures with little or no displacement on them.

## Chapter 6

### Mineral Chemistry and Classification

#### 6.1. Introduction

In order to further investigate the lithological units identified and described in Chapters 3 and 4, a detailed mineral chemical description and classification of the most important minerals within these units is necessary. This chapter will therefore describe the chemical compositions and formation reactions of the dominant minerals situated within the Merelani tanzanite deposit for the first time.

The major element compositions of the mineral phases were determined by the author on a JEOL 733 electron probe at the Council for Geoscience, Pretoria, RSA. The analyses were performed using an accelerating voltage of 15 kV, a beam current of 40 nA and an analysing spot size of 2 to 3 microns. The counting time at the element peak position was 10 seconds and 5 seconds at two symmetrical background positions. The standardisation procedures and standards as described by de Bruin (2001) were used. Selected minerals were also analysed on a JEOL Superprobe 733 at Rhodes University, Grahamstown, RSA. Analyses were carried out with an acceleration voltage of 20 kV and a beam current of 30 nA.

Imaging and mineral identification was done, by the author, on a Leo® 1430VP Scanning Electron Microscope at the Stellenbosch University. The samples were sputter-coated with carbon. Samples were identified with backscattered electron (BSE) and/or secondary electron images, and phase compositions quantified by EDS analysis using an Oxford Instruments® 133KeV detector and Oxford INCA software. Beam conditions during the quantitative analyses were 20 KV and approximately 1.5 nA, with a working distance of 13 mm and a specimen beam current of -3.92 nA. Despite the relatively low energy of the beam, X-ray counts with the set-up used were typically ~ 5000 cps. The counting time was 50 seconds. Natural mineral standards were used for standardisation and verification of the analyses. Pure Co, as well as Ti and Fe in ilmenite were used periodically to correct for detector drift.



## 6.2. Garnet – sillimanite – biotite gneiss (GNG)

### 6.2.1. Garnet

The electron microprobe data and stoichiometric calculations of 143 garnet analyses are shown in Table 1, Addendum D. Stoichiometric calculations of garnet were done on the basis of 12 oxygens, with the end members calculated after Deer et al. (1992).  $\text{Fe}_2\text{O}_3$  was calculated according to the method of Knowles (1987).

The mean garnet consists of 65.3% mole almandine, 29.4% mole pyrope, 4.8% mole grossular and 0.3% mole spessartine. The values vary from 62.4 to 75.7% almandine, 19.7% to 32.7% pyrope, 3.7% to 6.9% grossular and 0.3% to 1% spessartine (Table 1, Appendix D). Garnet is interpreted as part of the peak metamorphic assemblage. Traverses from rim to rim for a single garnet grain analysed in detail are shown in Figures 6.1.a and 6.2, whilst Figures 6.1.b. and c show the chemical zoning contours of pyrope and almandine. The pyrope component decreases from core to rim, whereas the almandine component increases from core to rim. The garnet is relatively homogeneous in the core, but is progressively more zoned toward the rim. The mineral shows a decrease in Mg and Ca, and an increase in  $\text{Fe}/(\text{Fe}+\text{Mg})$ , Mn and Fe toward the rim (Figure 6.2.a and b). The chemical zoning in the garnet is interpreted as being unrelated to garnet growth, but probably resulted from diffusion processes that occurred during retrogression. This type of zoning is characteristic of retrogression of garnets from high-grade metamorphic terrains and granulites (Grant and Weiblen, 1971; Spear and Peacock, 1989; Spear, 1993).

The retrograde overprint of the garnet is confirmed by retrograde textures and thermobarometric calculations that will be discussed in Chapter 9. The reabsorbed rims of individual garnet grains represent retrograde textures with biotite and fibrolitic sillimanite in reaction zones.

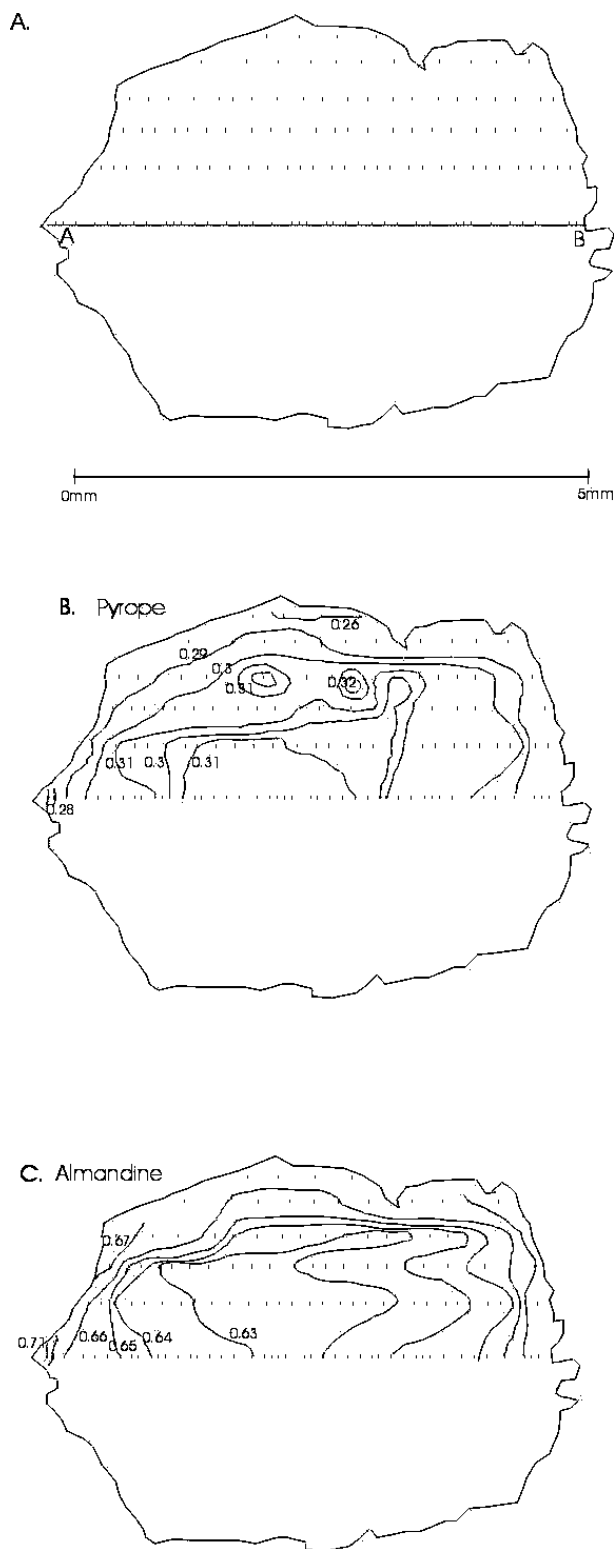


Figure 6.1. Contours of chemical zoning in a garnet from the garnet-sillimanite-biotite gneiss. (a) Each microprobe analysis point is represented by a dot. (b) Pyrope zoning profile. (c) Almandine zoning profile.

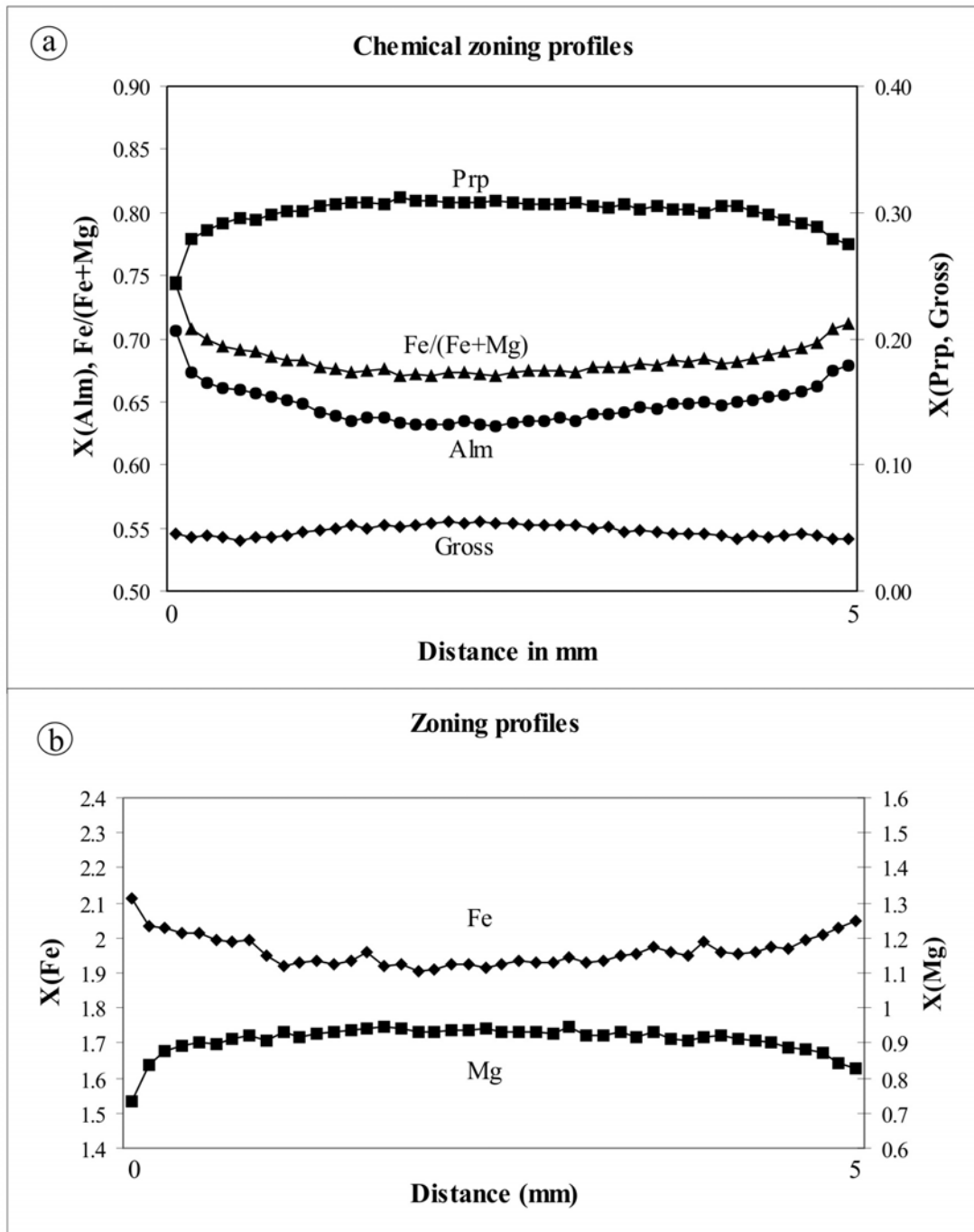
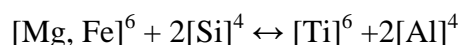


Figure 6.2. a) and b) Chemical zoning profiles along traverse AB as indicated in Figure 6.1.a.

### 6.2.2. Biotite

The major element concentrations and stoichiometric calculations for 33 biotite analyses of the GNG unit are listed in Table 2, Addendum D. The stoichiometric calculations were based on 22 oxygen atoms and Fe was measured as  $\text{Fe}^{2+}_{\text{total}}$  according to the method of Deer et al. (1992). In general, the biotite of the GNG unit plots close to the

eastonite / siderophyllite part of the classification diagram (Figure 6.3), indicating a high amount of  $\text{Al}^{4+}$  present in the biotite. The biotite also plots closer to the Mg end member (previously known as eastonite, see Deer et al., 1992) indicating higher amounts of Mg compared to Fe. As described in Chapter 4, biotite occurs as a light red-brown to red-brown pleochroic variety as well as a non-pleochroic dark red-brown variety. Table 2 in Addendum D shows the chemical analyses of both types of biotite found in garnet-sillimanite-biotite gneiss. The exceptionally high Ti content of both “types” of biotite suggests that they both either originated or were influenced by partial melt. It is evident from the data that type A biotite contains slightly higher amounts of Fe, but lower amounts of Mg compared to type B biotite. This may explain the absence of strong pleochroism in type B biotite, since pleochroism increases with Fe content (Deer et al., 1992). The Ti content is high for both types of biotite, with a tendency for Fe-rich biotite varieties to have higher Ti values. The Ti content ranges from 4.1 wt% (0.43 pfu) to 4.9 wt% (0.53 pfu), with a mean value of 4.5 wt% (0.47 pfu). The Ti content has a positive correlation with  $[\text{Al}]^4$  and a negative correlation with Si (Figures 6.4.a and 6.4.b), suggesting that substitution occurred according to the reaction of Hörmann et al. (1980) and Schreurs (1985):



Schreurs (1985) correlated high Ti presence ( $\text{Ti} > 0.45$  pfu) to low – to intermediate granulite facies metamorphic conditions and the occurrence of partial melt, by using data from the Furua granulite belt in Tanzania of Coolen (1980) as an example. The lack of correlation between  $[\text{Al}]^6$  and  $[\text{Ti}]^6$  further substantiates possible partial melting of the biotite. The formation of biotite within garnet-sillimanite-biotite gneiss possibly occurred along reaction 3, described in Section 6.2.4.

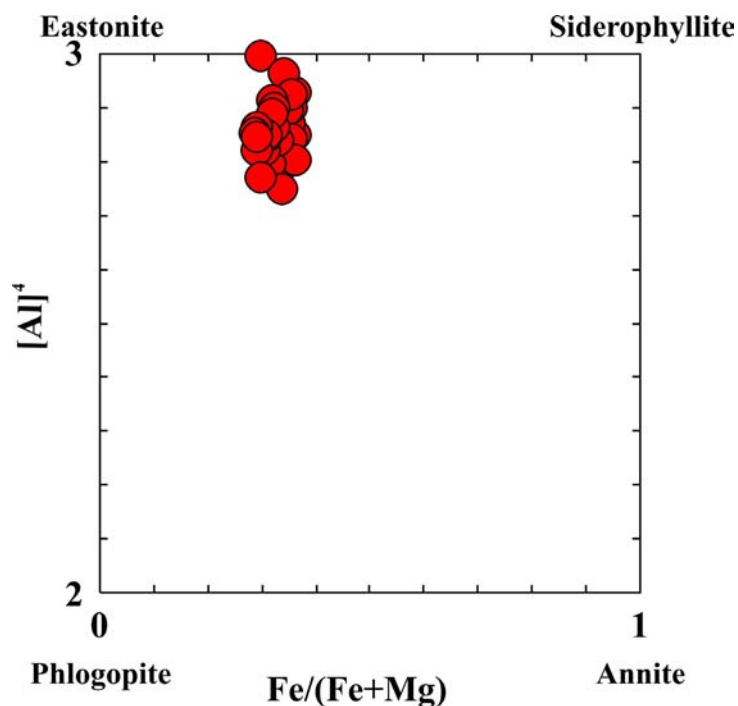


Figure 6.3. Biotite classification diagram for the garnet-sillimanite-biotite gneiss. The plot illustrates high amounts of  $Al^{4+}$  present in the biotite.

### 6.2.3. Feldspar

The major element composition and stoichiometric calculations of plagioclase and K-feldspar within the GNG are listed in Tables 3 and 4, Addendum D. The stoichiometric calculations were based on 32 oxygen ions. Plagioclase classifies as oligoclase and has an average composition of albite 78.0%, anorthite 20.4% and orthoclase 1.6%, (Figure 6.5). The plagioclase displays no compositional linear zoning trend from core to rim. The minimum, maximum and mean values of each element as well as that of the stoichiometric values of plagioclase are shown in Table 3, Addendum D. The plagioclase is used for the geobarometric calculations that will be discussed in Chapter 9. K-feldspar has an average composition of 82.2% orthoclase, 17.3% albite and 0.4% anorthite (Table 4, Addendum D). The K-feldspar has a compositional range of 77.0% to 85.7% orthoclase. The K-feldspar classifies as perthite, according to the nomenclature of Deer et al. (1992) for feldspar with phase separation. The lamellae in the perthite are of similar composition (Ab80; An19; Or1) to the freestanding

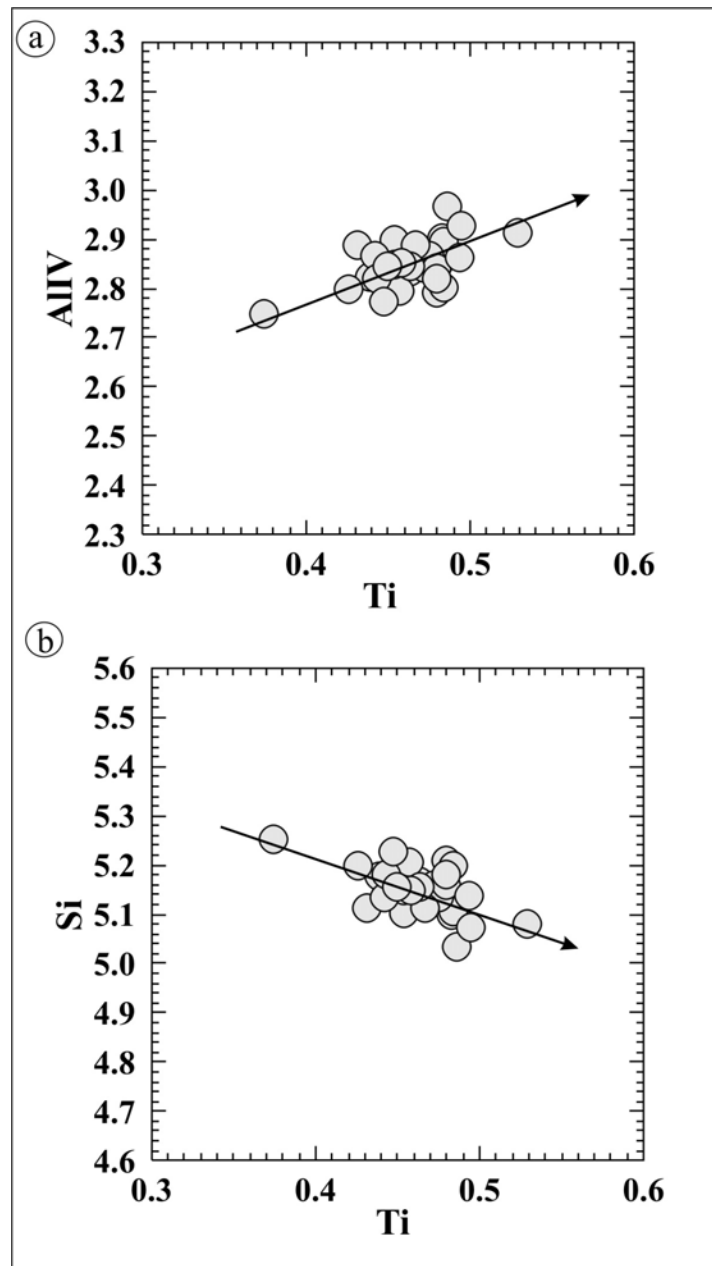


Figure 6.4. There is a moderate correlation between  $[Ti]^6$  and  $[Al]^4$ ,  $[Si]^4$ . (a)  $[Al]^4$  has a positive correlation, while (b)  $[Si]^4$  has a negative correlation with  $[Ti]^6$ . Both diagrams contain regression lines calculated by using the methods applied in the Minpet 2.02 software package.

plagioclase crystals (Figure 6.5). An exsolution origin of the albite component of the microcline is therefore highly unlikely. The string-perthite is therefore more likely to have formed from the retrograde replacement of K-feldspar by oligoclase, probably controlled by the degree of deformation of the K-feldspar grains (Barker, 1998).

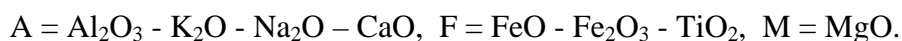
Spear and Parrish (1996) described the presence of primary K-feldspar inclusions in garnet as indicative that the garnet growth occurred at high temperatures. However, the feldspar inclusions may also be related to migmatization, in which case garnet and K-feldspar growth might have been the result of partial melting. This could occur according to the reaction:



This would agree with a partial melting process as suggested by the biotite chemical composition. It could further explain the formation of perthitic K-feldspar from plagioclase as described in Chapter 4. Additional K-feldspar also probably formed through reaction 4, described in Section 6.2.4.

#### 6.2.4 General mineral composition of the GNG

AFM projections indicate that the gneiss falls within the sillimanite zone (Figure 6.6). Due to the presence of K-feldspar and the lack of muscovite, a modified AFM projection of Reinhardt (1968) was used, as indicated in Figure 6.1.4. It is based on the elimination of the common phases, namely K-feldspar, plagioclase, magnetite, ilmenite, and the projection of the remaining components:



The projection indicates a three phase system, sillimanite + biotite + garnet, that is in agreement with the petrographic observations. The presence of kyanite relicts and the absence of staurolite and primary muscovite in the rocks suggest the transition from the kyanite zone to the sillimanite zone, as defined by Yardley (1989). This transition involves the discontinuous reaction:





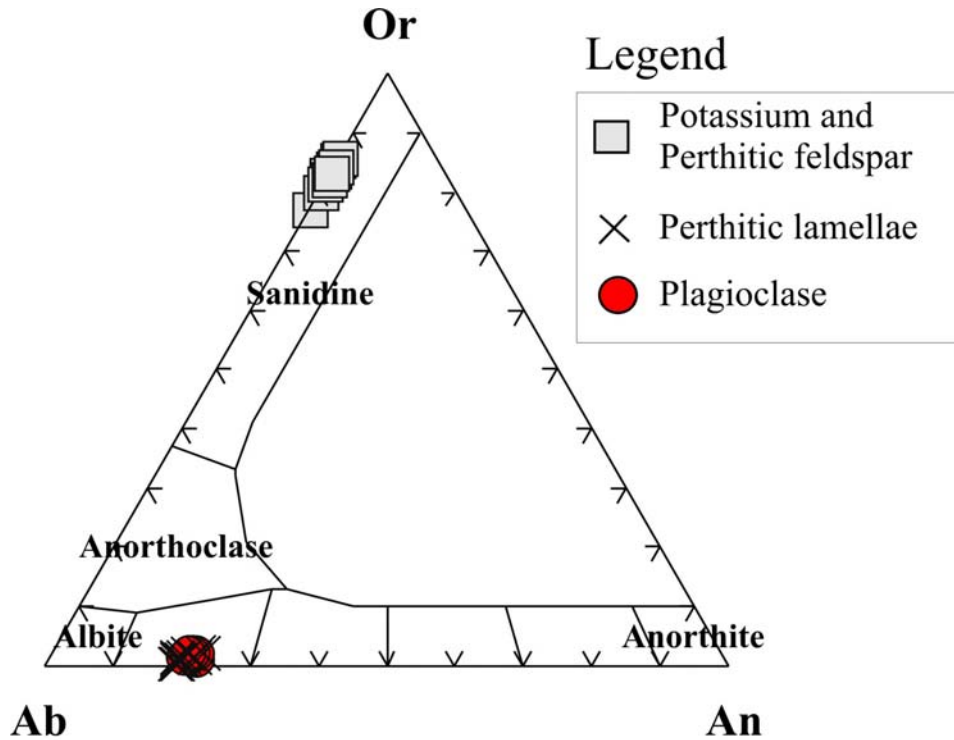


Figure 6.5. Classification diagram of the feldspars present in the garnet-sillimanite-biotite gneiss after Deer et al. (1992).

When the kyanite – biotite assemblage has been stabilised and the sillimanite zone is reached, sillimanite can form through the discontinuous reaction:



This reaction can explain the correlation between fibrolitic sillimanite and biotite as well as the abundance of both minerals as inclusions in garnet. With increasing temperature, the co-existence of K-feldspar and sillimanite could possibly be explained by the growth of additional sillimanite along the “second sillimanite isograd” reaction:



Reaction 3 produces fine-grained sillimanite needles called fibrolite, whereas reaction 4 would favour the development of coarse, prismatic sillimanite grains (Yardley, 1989). Thus, the petrographic observation of fibrolite overgrown by large prismatic sillimanite,

and the presence of fibrolitic inclusions in garnet, suggest the formation of sillimanite through reaction 3, followed by reaction 4 with decreasing temperature.

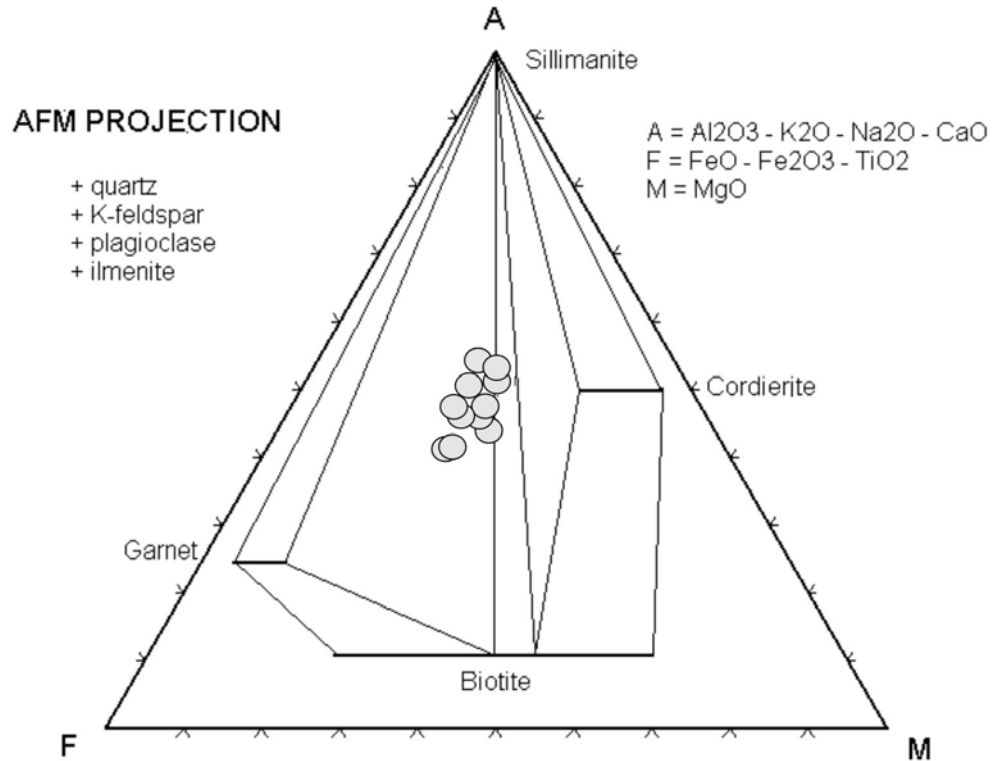


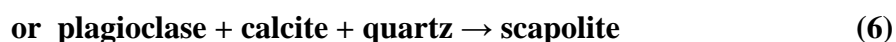
Figure 6.6. Whole rock composition of the garnet – sillimanite – biotite gneiss plotted on the modified AFM projection plane of Reinhardt (1968). The samples all plot within the sillimanite-biotite-garnet tie line triangle.

### 6.3. Banded calc-silicate hornfels (BCF)

#### 6.3.1. Scapolite

The major composition and stoichiometric calculations of scapolite from the calc-silicate hornfels is indicated in Table 5, Addendum D. The meionite (Me) composition of the scapolites was calculated as  $100 \times ((\text{Ca}+\text{Mg}+\text{Fe}+\text{Mn}+\text{Ti}) / (\text{Na}+\text{K}+\text{Ca}+\text{Mg}+\text{Fe}+\text{Mn}+\text{Ti}))$ . The scapolite in the calc-silicate hornfels is calcic-rich with a meionite (Me) content of 82.30% (Table 5, Addendum D). Scapolite is therefore close to the meionite end-member composition of  $3\text{CaAl}_2\text{Si}_2\text{O}_8 \cdot \text{CaO}_3$ . The relatively low total values of the scapolite indicated in Addendum D are due to the absence of  $\text{H}_2\text{O}$ ,  $\text{CO}_2$ ,  $\text{SO}_3$  and Cl in the element analyses.

The scapolite present in the BCF units formed through the replacement of plagioclase (see Chapter 4), probably along the retrograde reactions:



This is confirmed by the presence of calcite in the vicinity of scapolite and plagioclase, and the composition of scapolite and plagioclase, since the meionite content tends to correlate with anorthite content of plagioclase.

#### 6.3.2. Plagioclase

The plagioclase composition and stoichiometric calculations are shown in Table 6, Addendum D. The plagioclase classifies as bytownite with a mean anorthite content of 84.40% (Figure 6.7). The anorthite content of the BCF plagioclases varies from 81.6 to 86.1 wt%.

#### 6.3.3. Potassium Feldspar

The composition and stoichiometric calculation of the analysed K-feldspar within the BCF are indicated in Table 6, Addendum D. The K-feldspar consists on average of 90.3% orthoclase, 9.4% albite and 0.2% anorthite (Figure 6.7).

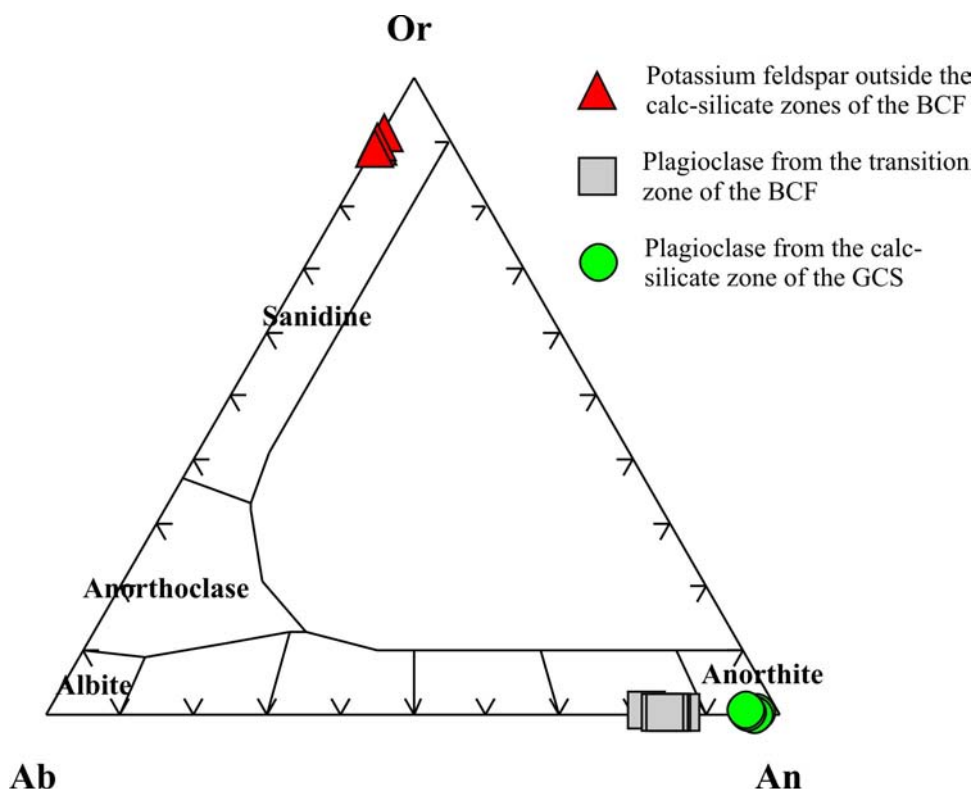


Figure 6.7. Feldspar compositions of the graphite-calc-silicate schist and the banded calc-silicate hornfels.

#### 6.3.4. Clinopyroxene

The major element composition and stoichiometric calculations of the pyroxene within the BCF is listed in Table 7, Addendum D. The clinopyroxene present in the hornfels is situated on the diopside – hedenbergite solid solution series (Figure 6.8). The clinopyroxene has a narrow composition range, with average  $X_{Ca}$ ,  $X_{Mg}$  and  $X_{Fe}$  concentrations of 49.6, 36 and 14.4 mole %, respectively. This results in an average diopside end-member concentration of 60.1% and hedenbergite end-member concentration of 39.9%. The diopside has a higher iron content than that of the graphite-calc-silicate schist, plotting closer to the Hedenbergite composition (Figure 6.8). The clinopyroxene in the calc-silicate hornfels is the only clinopyroxene that does not have an almost pure diopside composition in the whole Merelani succession.

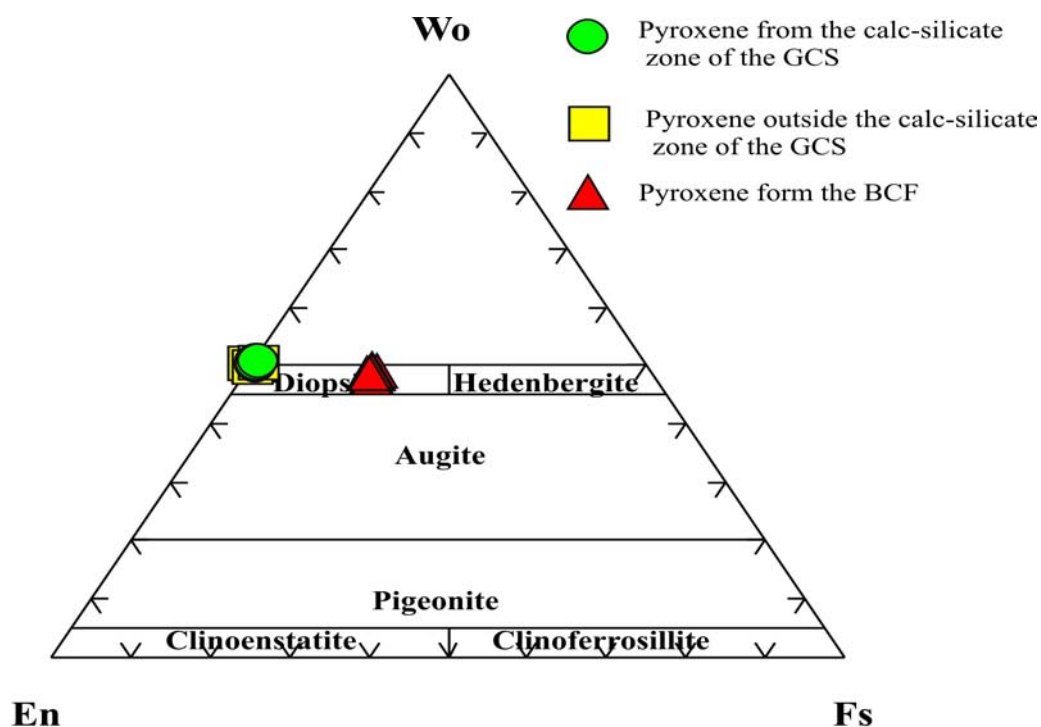


Figure 6.8. Classification diagram after Deer et al. (1992) of pyroxene in the graphite-calc-silicate schist and in the calc-silicate hornfels. The pyroxene within the GCS plot as “pure” diopside, while the pyroxene within the BCF contains higher amounts of iron, therefore plotting closer to the Hedenbergite zone.

### 6.3.5. Mica

The mica within the BCF optically resembles muscovite but microprobe analyses indicate that the mica is phlogopite (Table 8, Addendum D). The stoichiometric calculations shown in Addendum D were calculated on the basis of 22 oxygen ions. The mica composition is close to the theoretical composition of phlogopite, with  $[Al]^4$  concentration of ca. 2.1 pfu and  $Fe/(Fe+Mg)$  values of less than 0.05 pfu.

## 6.4. Graphite - calc-silicate schists (GCS)

### 6.4.1. Garnet

Petrographic investigation revealed garnet porphyroblasts outside the calc-silicate units, and small garnets in the calc-silicate layers, as described in Chapter 4. The element composition and stoichiometric calculations of both types of garnet are shown in Table 9, Addendum D. Garnet porphyroblasts are indicated by data points GCS-G-1 to GCS-G-28, while garnets in the calc-silicate zones are indicated by data points GSC-G-29 to

GCS-G-48. Garnet porphyroblasts have mean garnet values of 94.1% mole grossular, 1.9% mole pyrope, 1.1% mole spessartine and 2.7% mole uvarovite. The values range from 92.2 to 95.6% mole grossular, 1.7 to 2.1% mole pyrope, 0.3 to 1.8% mole spessartine and 1.6 to 4.4% mole uvarovite. Garnet porphyroblasts are slightly zoned, with a decrease in grossular content and increase in spessartine content from the rim to core. Garnet in the calc-silicate zone has mean values of 90.0% mole grossular, 1.3% mole pyrope, 1.2% mole spessartine and 7.3% mole uvarovite. The values range from 88 to 91.7% mole grossular, 1.1 to 1.7% mole pyrope, 1.0 to 1.6% mole spessartine and 5.7 to 9.3% mole uvarovite (Figure 6.9).

Individual garnet grains from the calc-silicate zone show some compositional zoning, with an increase in grossular content with decreasing uvarovite content (Figure 6.9). The total electron microprobe values of the garnet analyses from the calc-silicate zone are very low, with an average for the 20 data points of 89.5%. The average total of the garnet porphyroblasts is slightly higher at 95.6%, but still significantly lower than expected of grossular garnet analysis. In order to investigate the low garnet total, additional microprobe analyses were done on the garnet porphyroblasts to include  $V_2O_3$  and Ni (Table 9.a, Addendum D). From the data it is evident that the grossular porphyroblasts can contain up to 5.6%  $V_2O_3$ . It is also possible that the grossular garnet, especially the garnets within the calc-silicate zones, could contain appreciable concentrations of  $H_2O$  in its structure. This would suggest that the garnets within the calc-silicate zones are probably hydrogrossular garnets.

#### **6.4.2. Clinopyroxene**

Clinopyroxene in the calc-silicate zones and outside of the zones, have the same chemical composition, as shown in Figure 6.8. Clinopyroxene in both zones plot very close to the diopside end member composition. The clinopyroxene has average mole concentrations of 50.5%, 49% and 0.4% for Ca, Mg and Fe, respectively. The pyroxene consists of 99.1% diopside and 0.9% hendenbergite. Stoichiometric calculations of the clinopyroxene give similar values to those obtained from the clinopyroxene in the pyroxene units and will be further discussed in Section 6.6. The diopside probably also originated from the metamorphism of dolomitic units within the schist. The diopside analysis and stoichiometric calculations are listed in Table 10, Addendum D.

### **6.4.3. Plagioclase**

The plagioclase composition and stoichiometric calculations from the calc-silicate-rich zones of the GSC are indicated in Table 11, Addendum D. The plagioclase has a high average anorthite composition of 95.9 %. The plagioclase values are plotted in Figure 6.7.

### **6.4.4 Titanite**

Microprobe analysis of the titanite located within the GCS is shown in Table 12, Addendum D. The titanite stoichiometry was calculated on the basis of 20 oxygens ions. The titanite analysis will be further discussed in Section 6.5.3.

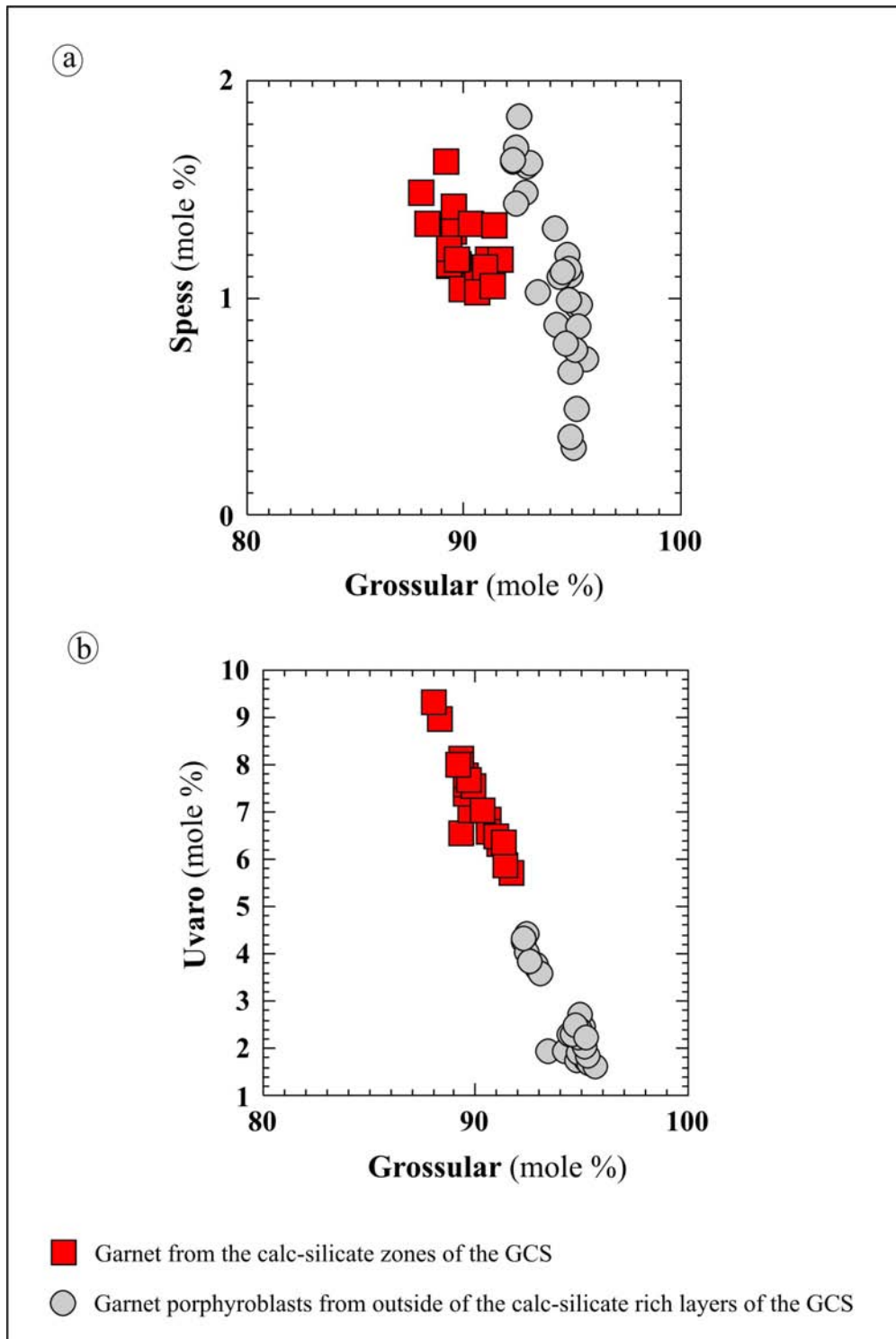


Figure 6.9. Zoning and variation of the a) Spessartine and b) Uvarovite content of the grossular garnet located within and outside of the calc-silicate-rich layers of the GCS.



## 6.5. Kyanite - graphite gneiss

### 6.5.1. Plagioclase

The electron microprobe and stoichiometric calculations of plagioclase from the kyanite-graphite gneiss is listed in Table 13, Addendum D. The analysed plagioclase classify as oligoclase (Figure 6.10). Plagioclase has mean values of 70.5% albite, 28.2% anorthite and 1.3% orthoclase.

### 6.5.2. Mica

The mica from the gneisses was calculated on the basis of 22 oxygen ions (Table 14, Addendum D). As described in Chapter 4, two types of mica are present in the kyanite – graphite gneisses. Microprobe analyses of the two types of mica confirm the petrographic classification of the micas as phlogopite and muscovite. The majority of the mica within the kyanite-graphite gneiss is phlogopite, with average  $X_{Mg}$ ,  $X_{Ti}$  and  $X_{[Al]}^6$  values of 4.4, 0.2 and 0.4 pfu, respectively. Muscovite has average  $X_{Mg}$ ,  $X_{Ti}$  and  $X_{[Al]}^6$  values of 0.2, 0.01 and 2.7 pfu, respectively (Table 14, Addendum D). Figure 6.11 indicates the classification and variation in composition between the micas.

The reason for the existence of two types of mica in the kyanite-graphite gneiss units is not clear. Muscovite appears to be remnants of the prograde breakdown of kyanite related to the upper amphibolite facies transformation of kyanite to sillimanite. The biotite is possibly a retrograde feature associated with the dehydration of the pelites. along the reaction:



Reaction 7 therefore implies that the metapelites passed through the muscovite dehydration-meting curve, but that it did not cross the biotite dehydration-meting curve. The possible P-T constrains defined by the muscovite breakdown and biotite stability will be further discussed in Chapter 9.

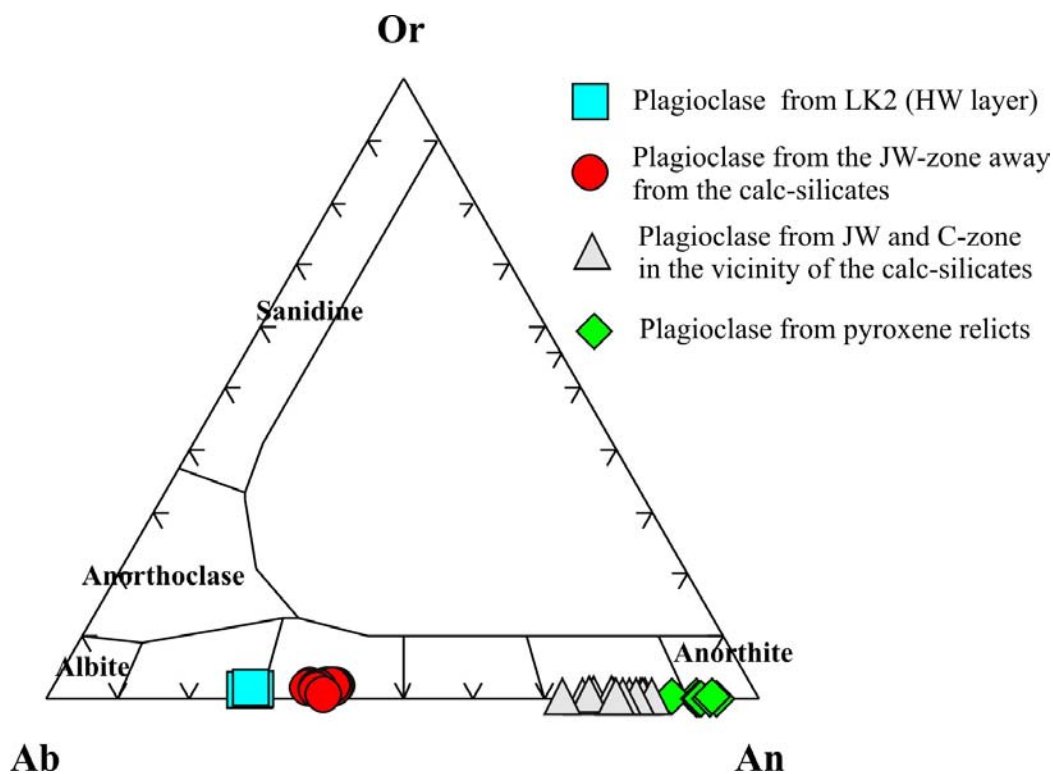


Figure 6.10. Classification diagram of the plagioclase minerals present in the kyanite-graphite gneiss and graphite-plagioclase gneisses. The anorthite content of the plagioclase increases towards the proximity of the calc-silicate skarn boudins within the graphite plagioclase gneisses. The plagioclase situated within the pyroxene relict classify as anorthite.

## 6.6. Graphite - plagioclase gneiss

### 6.6.1. Plagioclase

The range in plagioclase composition within the graphite-plagioclase gneiss is indicative of the skarn interaction and chemical element transfer between the graphite-plagioclase gneisses (especially in the JW-zone) and its intercalated calc-silicate layers. The plagioclase composition is directly related to the distance from the calc-silicate units:

- The plagioclase adjacent to the kyanite – graphite gneiss classify as andesine. It has mean compositional values of 59.9% albite, 38.3% anorthite and 1.7% orthoclase (Figure 6.10). The plagioclase has a small compositional range of between 58.1% and 62.5% anorthite.
- In general, the plagioclase neighbouring the calc-silicate units classify as bytownite. It has an average composition of 80.2% anorthite; 19.4% albite and

0.3% orthoclase (Table 15, Addendum D). The plagioclase has a fairly large compositional range of between 72.2 and 84.7% anorthite. This is due to a centimetre to millimetre scale compositional zoning in the vicinity of the calc-silicates, with the low anorthite values furthest away from the calc-silicates and the highest values closest to it.

Plagioclase classifications are shown in Figure 6.10 with the analyses and calculations listed in Table 15, Addendum D.

### 6.6.2. Mica

The mica in the graphite-plagioclase gneiss is very similar in composition to the phlogopite in the kyanite-graphite gneiss (Figure 6.11). The microprobe analyses and stoichiometric calculations of phlogopite within the graphite-plagioclase gneisses are indicated in Table 16, Addendum D. No muscovite was observed in the rock. This confirms the proposed dehydration origin of the phlogopite, since the graphite-plagioclase gneiss underwent more intense dehydration, metasomatism and recrystallisation, as a result of the chemical skarn interaction with the calc-silicates, compared to the neighbouring kyanite-graphite gneisses (see Chapter 5).

### 6.6.3 Titanite

Microprobe analyses of the titanite located within the graphite-plagioclase gneiss are indicated in Table 17, Addendum D. The titanite analyses were recalculated on the basis of 20 oxygen ions. The titanite crystals from the graphite-plagioclase gneiss are very similar to those of the GCS (Tables 12 and 17, Addendum D). The calculated cation values for Al, Fe<sup>3+</sup> and Ti (SumA, Table 12 and 17) and Mg, Fe<sup>2+</sup>, Mn, Na, Ca, K, Cr and V (SumB, Table 12 and 17) are both close to four. This therefore indicates that the low total values are not due to analytical errors or due to the presence of other elements, such as REE. The low total values for the titanite can therefore be attributed to the presence of unanalysed F and H<sub>2</sub>O. The large theoretical amounts of H<sub>2</sub>O within the titanite can be the result of alteration of the titanite minerals. The only significant difference between the titanite found in the two rock units is the possible substitution of Al and Fe<sup>3+</sup> for Ti for the titanite present in the GCS units.

#### 6.6.4. Whole rock

The whole rock data of the kyanite-graphite gneiss and the plagioclase-graphite gneiss will be discussed and compared together due to their close compositional relationship.

Figures 6.12.a and 6.12.b, are AFM and AKF plots of the kyanite – graphite gneiss and plagioclase – graphite gneiss. Both diagrams indicate that the gneisses have a large “A” component, and are therefore Al rich. The gneisses fall just outside of the composition of normal Al-rich pelites as plotted by Ferry (1992). It is however difficult to detect any element exchange through the AFM and AKF plots, since mass transfer occurs.

Plots of CIPW-norm calculations (Addendum E) are however more useful in examining the compositional changes in the two rock units. Figure 6.13.a and b, indicates the CIPW-norm data plot of quartz – anorthite – albite and corundum – albite – anorthite – orthoclase, respectively. Figure 6.13.a shows a distinct decrease in quartz content and increase in anorthite and to a lesser degree albite content from the kyanite – graphite gneiss towards the plagioclase – graphite gneiss. Figure 6.13.b also indicates the clear trend towards the anorthite component, especially for the plagioclase – graphite gneiss. The increase in the anorthite component is evidence for the skarn interaction between the gneisses and the calc-silicate units. This led to influx of calcium into the gneiss, while aluminium and silica migrated into the calc-silicate units. The slight decrease in Al and Si content and increase in Ca led to the formation of anorthite-rich plagioclase, rather than aluminium silicates, as can be seen in Figure 6.12. The chemical skarn processes and associated metamorphism and metasomatism of the gneisses and calc-silicates will be further discussed in Chapters 7 and 11.

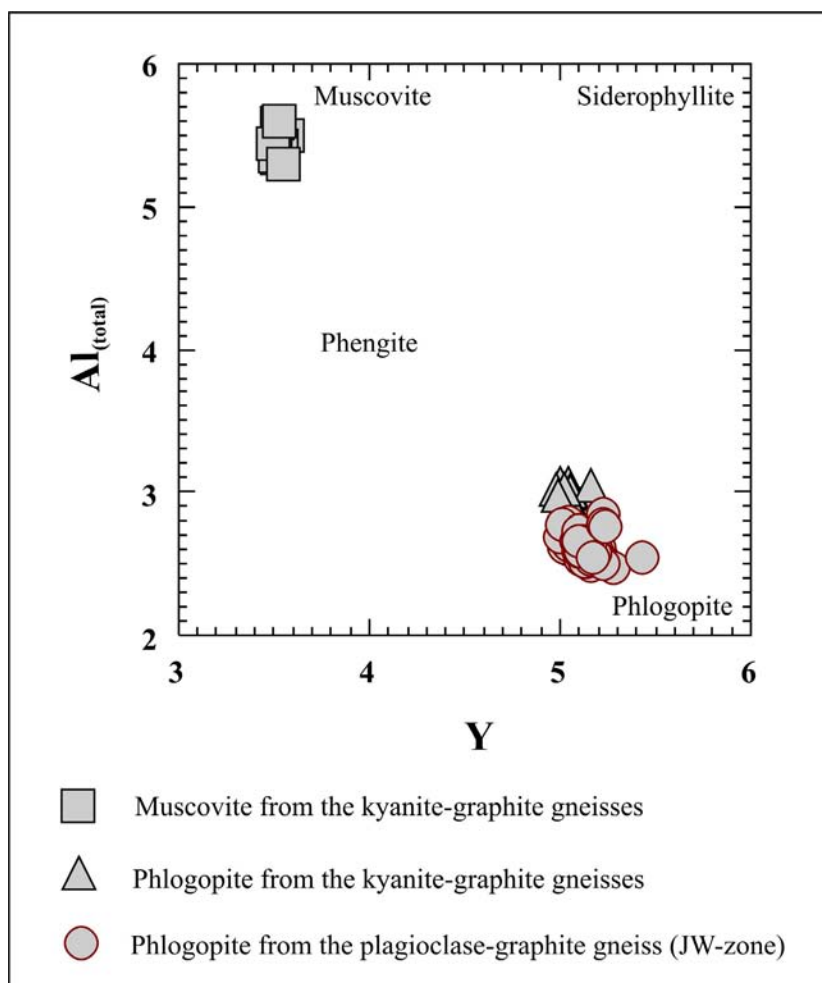


Figure 6.11. Classification diagram for the principle variations in mica composition, after Deer et al. (1992) within the kyanite-graphite gneisses and the graphite-plagioclase gneiss (JW-zone). Y represents Al, Mg, Fe, Mn, Cr and Ti present in the general formula  $X_2Y_{4-6}Z_8O_{20}(OH,F)_4$ .

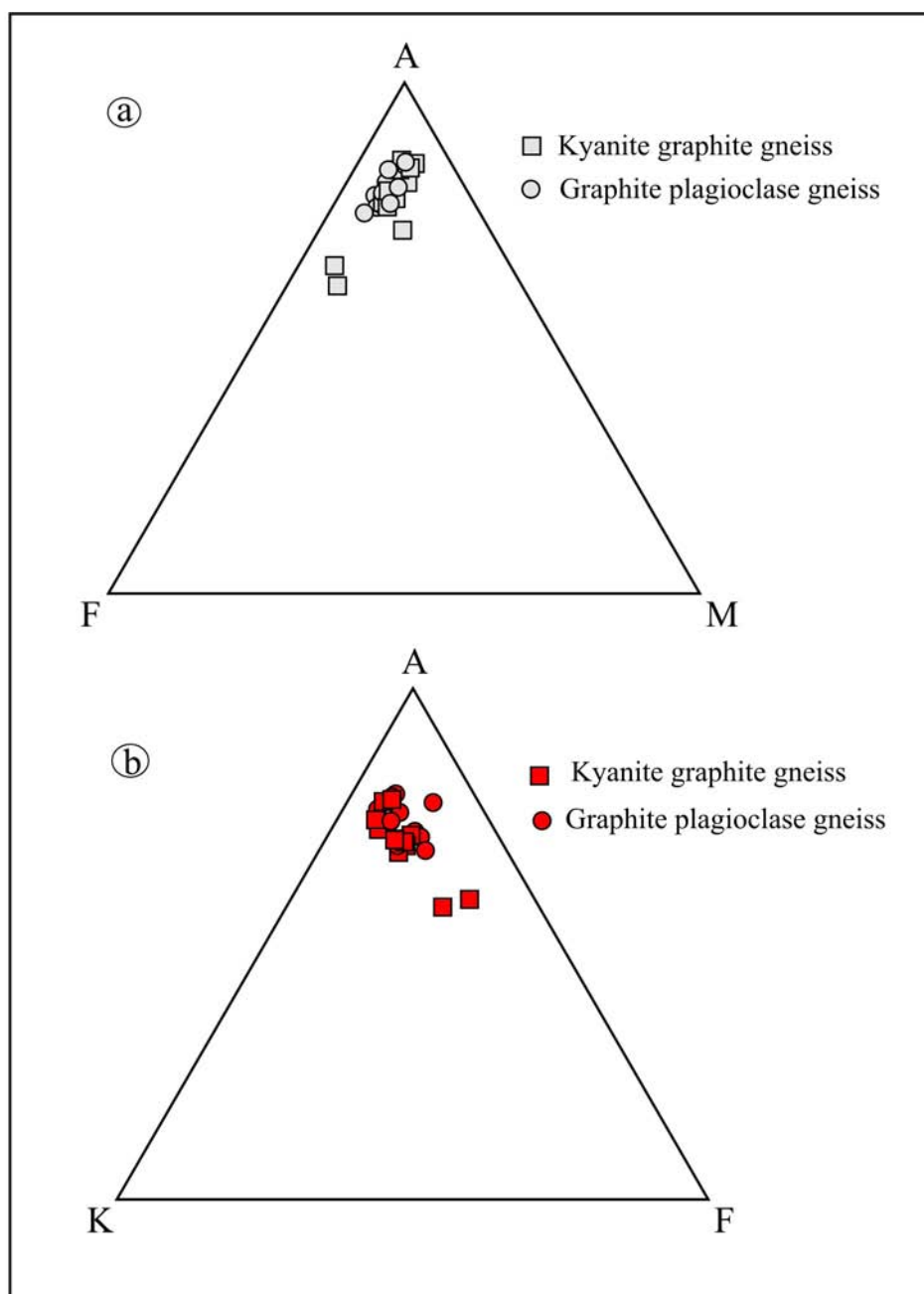


Figure 6.12. (a) AFM and (b) AKF projection of the graphite – plagioclase gneiss and kyanite – graphite gneiss.

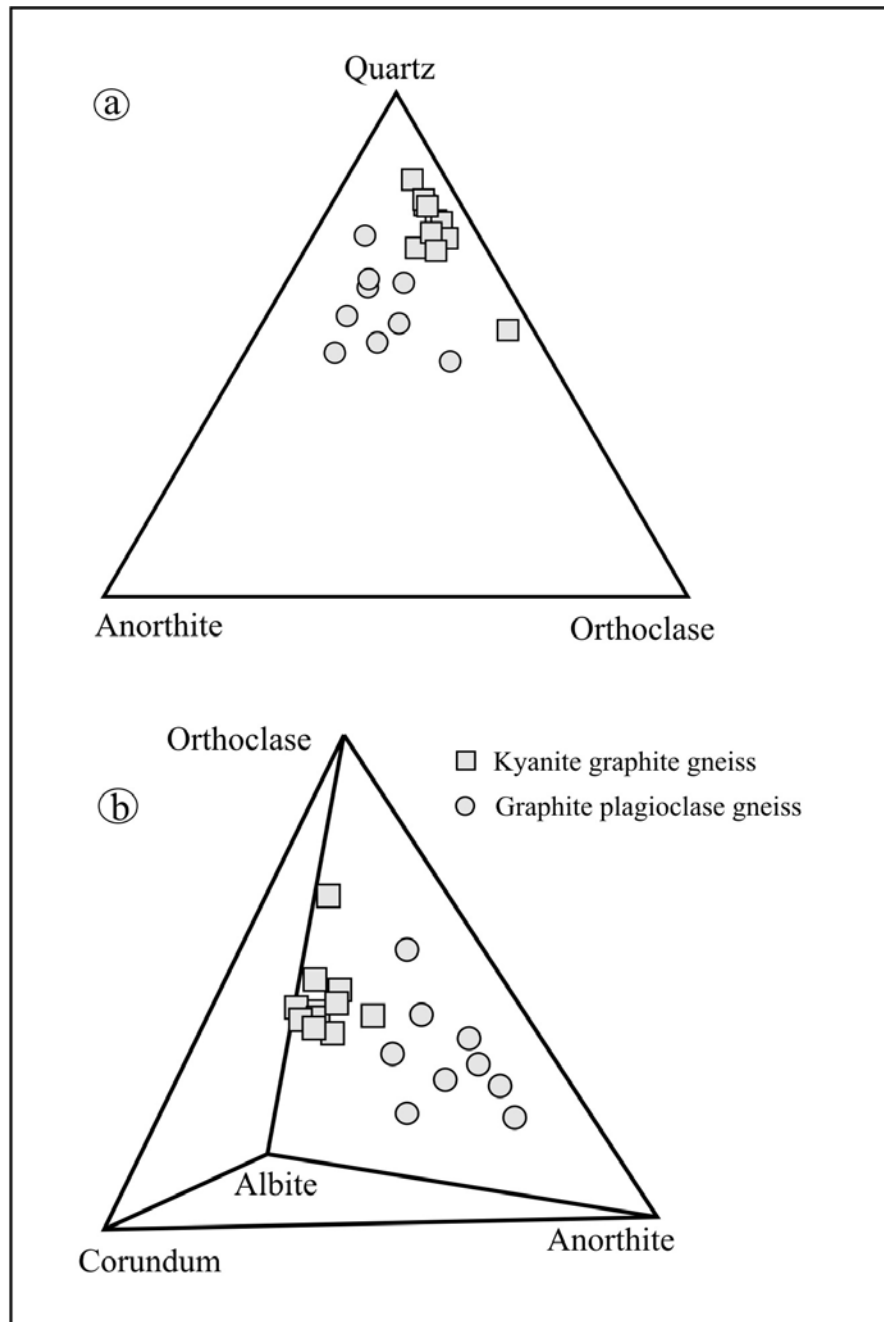


Figure 6.13. CIPW-norm data plots for the graphite – plagioclase gneiss and kyanite – graphite gneiss, with a) quartz-anorthite-orthoclase and b) orthoclase- corundum- albite- anorthite.

## 6.7. Pyroxene relicts and calc-silicate skarn boudins

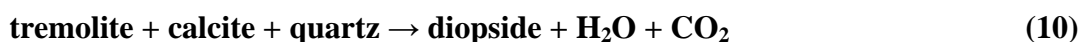
### 6.7.1. Diopside

The pyroxenes present in the pyroxene units, the calc-silicate skarnoid boudins, and skarnoid reaction zones surrounding the boudins, have identical major element chemical composition. However, trace and REE element concentrations between the various pyroxenes could vary as a result of the metasomatism associated with chemical skarn transfer reactions. There is also no variation in the major element composition of the pyroxenes from various “types” of boudins as described in Chapter 5. Table 18, Addendum D indicates the electron microprobe and stoichiometric calculations of 98 pyroxene analyses. All the pyroxenes present in the rock plot close to the diopside end-member (98.7% diopside, 1.3% hedenbergite), with no significant variation in chemical composition (Figure 6.14). Individual pyroxene grains generally show less than 1.5 % variations in composition.  $X_{Ca}$  range from 0.95 to 1.02 with a mean of 0.99 and  $X_{Mg}$  range from 0.89 to 0.99 with a mean of 0.96.  $X_{Mn}$  and  $X_{Na}$  are present in almost insignificantly small concentrations, with pfu values of  $<0.05$ . The pyroxene grains also show no compositional zoning from core to rim. The fact that the diopside present in the calc-silicate skarn boudins is of exactly the same composition as that of clinopyroxene boudins (Figure 6.14), confirms the petrographic deduction that the diopside units present in the calc-silicate skarn boudins are small relict pieces of the older clinopyroxene units. The formation of the diopside probably occurred through:

- the metamorphism of originally impure limestone layers according to the reaction:



- through the step wise prograde reactions:





with reaction (10) occurring in the upper kyanite zone, approaching the sillimanite isograd. The formation of diopside through reactions (8) to (10) could account for the presence of quartz within the pyroxene relict units as well as the occurrence of tremolite inclusions in tanzanite.

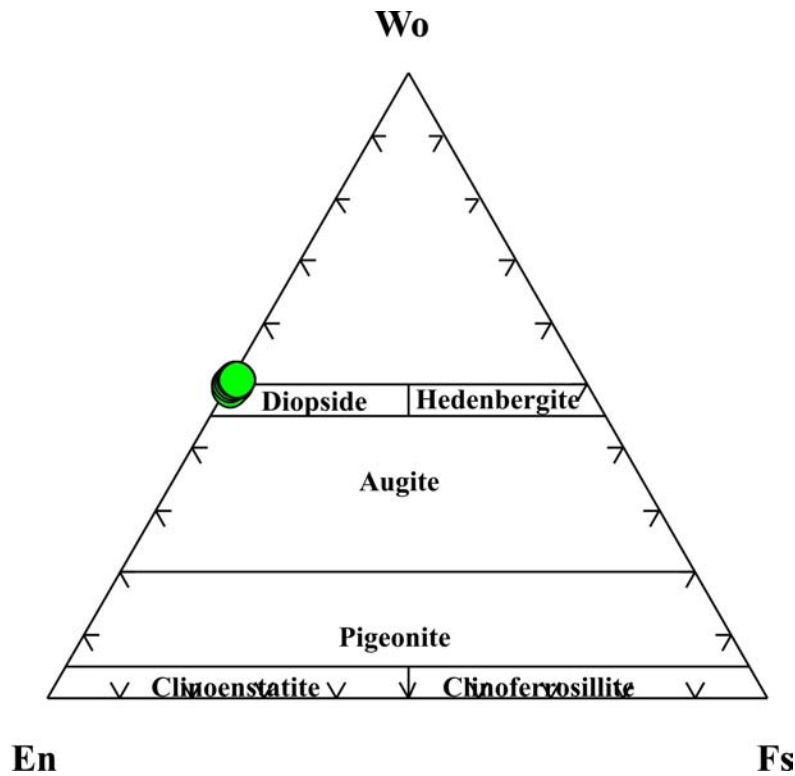


Figure 6.14. The identical classification of all the pyroxene, from the calc-silicate skarn boudin, pyroxene relict unit and from the low-pressure sites.

### 6.7.2. Garnet

The composition of the garnets within the pyroxene relict units and the calc-silicate skarn boudins are identical. Stoichiometric calculations indicate mean garnet values of 96.3% mole grossular, 1.9% mole pyrope, 1.6% mole spessartine, 0.1% mole almandine and 0.1% uvarovite (Table 19, Addendum D). The values range from 94.7 to 97.6% mole grossular, 1.4 to 2.4% mole pyrope, 0.5 to 2.9% mole spessartine, 0 to 0.3% mole almandine and 0 to 0.4% mole uvarovite. The garnet shows no significant compositional zoning from core to rim. The lower than expected microprobe garnet totals (average of 98.5%) is probably as a result of un-analysed  $V_2O_3$ , as indicated in Section 6.2.2.

Petrographic evidence suggests that garnet is related to a later metasomatic fluid infiltration reaction:



This reaction is comparable to similar skarn replacement reactions of clinopyroxene by garnet as described by various authors, e.g. Kato (1991); Newberry, (1991); Gamble, (1982); Burton et al., (1982). The reaction is however highly simplified and probably involved other phases such as  $\text{FeO}_{(\text{aq})}$ ,  $\text{SiO}_{2(\text{aq})}$  and  $\text{H}_2\text{O}$ .

### 6.7.3. Zoisite

The electron microprobe major element composition and stoichiometric calculations of various zoisite crystals, excluding tanzanite, within the calc-silicate skarn boudins are shown in Table 20, Addendum D. The number of ions is calculated on the basis of 13 oxygens. The results indicate a remarkably small variation in composition.  $X_{\text{Fe}}$ ,  $X_{\text{Mg}}$ ,  $X_{\text{Ti}}$  and  $X_{\text{Mn}}$  are typically all less than 0.01 pfu.  $X_{\text{Ca}}$  ranges from 1.86 to 2.05 with a mean value of 2.01 pfu. This mean value of ca. 2 pfu indicates that Ca almost exclusively represents the divalent cations in the A1 and A2 sites. Unfortunately, the microprobe was unable to analyse for SrO,  $\text{V}_2\text{O}_3$  and  $\text{H}_2\text{O}$ , and a subsequent  $\text{H}_2\text{O}$  value of 2.78 wt% was taken from the literature (Deer et al., 1986). When the theoretical  $\text{H}_2\text{O}$  component is added to the relatively low totals (mean of 95.89 wt%), most of the totals fall within the acceptable limits assumed for microprobe analysis.

### 6.7.4. Plagioclase

The small amounts of plagioclase present within the pyroxene relict units have a high anorthite content (Table 21, Addendum D). The plagioclase consists of between 87.9 and 94% anorthite (Figure 6.9 and Table 21, Addendum D).

### 6.7.5. Whole rock

The whole-rock composition of the pyroxene relict units is plotted on a  $\text{SiO}_2 - \text{CaO} - \text{MgO} - \text{Al}_2\text{O}_3$  quaternary plot (Figure 6.15). These parameters were chosen because they represent the bulk of the whole-rock composition of the units. The rock plots within the diopside – grossular – quartz -triangle, with the unaltered rock plotting close

to the composition of diopside and moving towards the  $\text{SiO}_2 - \text{Al}_2\text{O}_3$  tie-line with increasing metasomatism and subsequent grossular + quartz formation (Figure 6.15).

Samples from a calc-silicate skarn boudin are plotted in the system  $\text{SiO}_2\text{-Al}_2\text{O}_3\text{-CaO} \pm \text{MgO}$  as shown in Figure 6.17. a and b. The samples were all taken from one large boudin (boudin 18) that produced high amounts of tanzanite. Sampling was done from top (sample no. 1) to bottom (no. 8) (Figure 6.16). The chemical compositions of the boudin samples are indicated in Table 1, Addendum F. Sample no. 5 is from the tanzanite bearing unaltered centre of the boudin, while samples 2, 3, 4 and 7 contain variable amounts of zoisite and grossular and underwent some skarn alteration. Sample no.6 consists predominantly of quartz and halloysite, with minor amounts of other clay minerals. The influence of weathering and subsequent clay formation caused the depletion of the mobile elements such as Ca and Mg and resulted in the increase in silica and aluminium content.

The pyroxene units and calc-silicate skarn boudins are plotted together in an ACF diagram (Figure 6.18). The pyroxene units plot predominantly within the diopside-grossular-zoisite tie line triangle. Although some of the samples plot close to the composition of anorthite, no anorthite was observed in any of the samples. There is an almost complete transition from the unaltered pyroxene units to the calc-silicate skarn boudins in the direction of the A-parameter, as indicated by the arrowed trend line.

The trend fits in with the theory that selected mineralisation within the calc-silicate skarn boudins formed through metamorphism of the pyroxene units, as discussed above and in Section 3. The metamorphism, metasomatism and fluid movement as well as the temperature and pressure constraints will be further discussed in Chapters 7, 8 and 9.

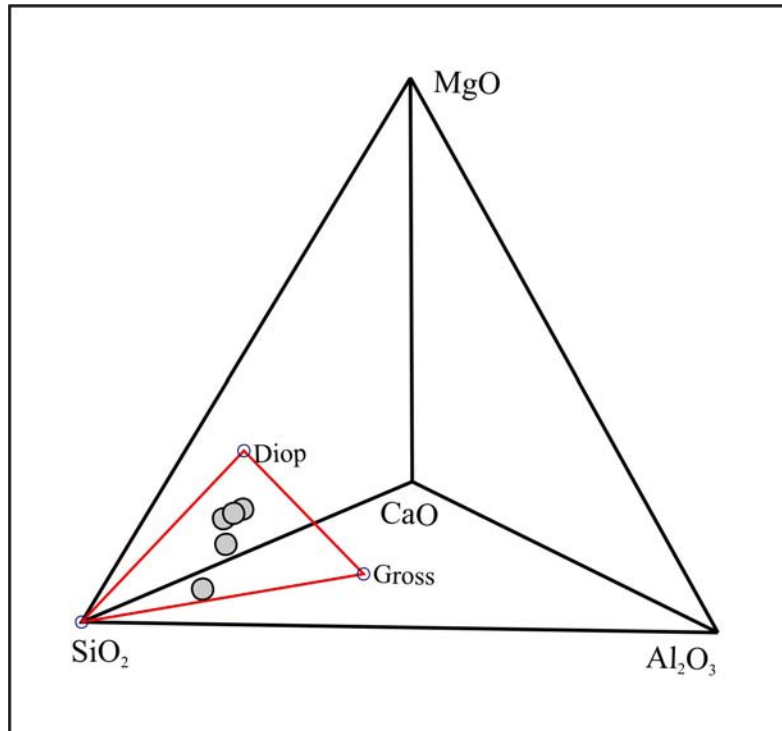


Figure 6.15.  $\text{SiO}_2\text{-Al}_2\text{O}_3\text{-MgO-CaO}$  tetrahedral diagram showing the whole-rock composition of the pyroxene units.

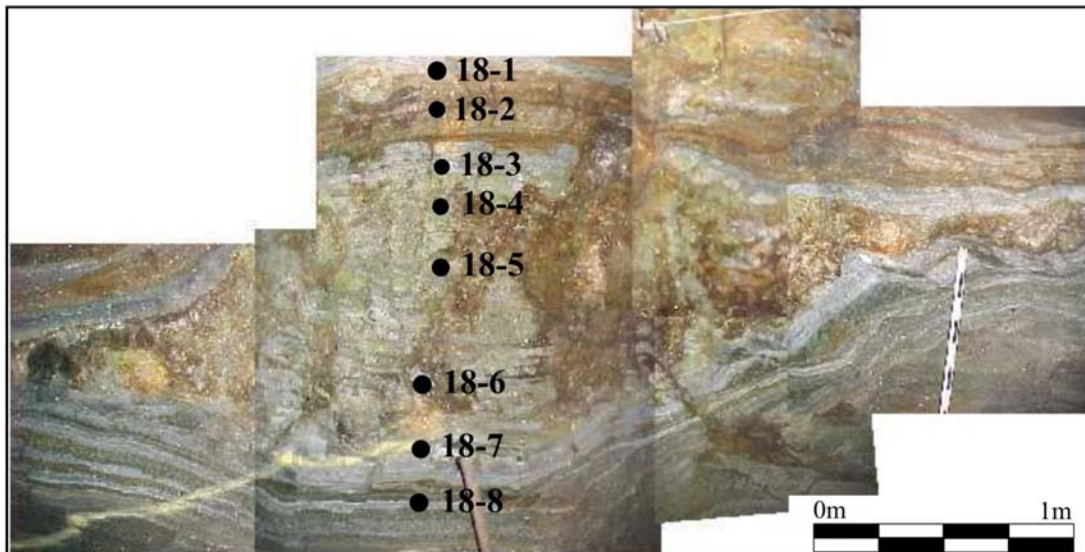


Figure 6.16. Boudin no. 18 sampled from top to bottom, sample no. 18-1 to 18-8. The geochemical composition of the boudin is indicated in Table 1, Addendum F.

## 6.8. Low-pressure sites

### 6.8.1. Tsavorite

The major element composition, including  $V_2O_3$  and  $Cr_2O_3$ , of gemstone quality green grossular garnet, called tsavorite, from the Merelani tanzanite deposit is indicated in Table 22 and 23, Addendum D. The stoichiometric calculations were based on 12 oxygen ions.

The microprobe analyses of the tsavorite crystals from the deposit were divided into two groups. Table 22, Addendum D indicates tsavorite from boudin structures with little or no tanzanite mineralisation. Table 23, Addendum D indicates tsavorite from boudin structures with high gemstone quality tanzanite mineralisation. A comparison of the 90 analyses in Table 22, with the 34 analyses of Table 23, reveals no significant difference in the composition of the tsavorite associated and not associated with tanzanite mineralisation. The tsavorite not associated with tanzanite has an average composition of 96.95% Grossular, 1.9% Pyrope, 0.9% Spessartine and 0.1% Almandine (Table 22, Addendum D). The tsavorite associated with tanzanite has an average composition of 97.04% Grossular, 1.9% Pyrope, 0.8% Spessartine and 0.1% Almandine (Table 23, Addendum D). Both tsavorite groups have average vanadium ( $V_2O_3$ ) values of 0.23% (2300 ppm) and average chromium ( $Cr_2O_3$ ) values of 0.04% (400 ppm).

The green colouration of the grossular found in the Merelani area has previously been attributed to the presence of chromium (Gübelin and Weibel, 1975). Schmetzer et al. (1978) suggested that vanadium is also an attributing factor in the colouration of the green garnet in the Merelani area. It is however evident from the generally low  $Cr_2O_3$  values obtained from the microprobe analysis, that most, if not all, of the tsavorite in the Block C Merelani area is primarily coloured by vanadium. This study therefore clearly indicates that vanadium rather than chromium is the main colouring agent of the Merelani tsavorites. Gübelin and Weibel (1975) as well as Webster and Anderson (1983) described similar vanadium coloured tsavorite from the Lualenyi deposit in Kenya. They concluded from absorption band studies and garnet formula calculations that vanadium is present in its trivalent ( $V^{3+}$ ) state similar to that of chromium ( $Cr^{3+}$ ) in tsavorite. The general formula for garnet is  $R_3^{2+} R_2^{3+} Si_3 O_{12}$ , with  $Ca^{2+}$  and  $Al^{3+}$  in the  $R^{2+}$  and  $R^{3+}$  sites, respectively, in the case of pure grossular. Thus,  $V^{3+}$ , as is the case

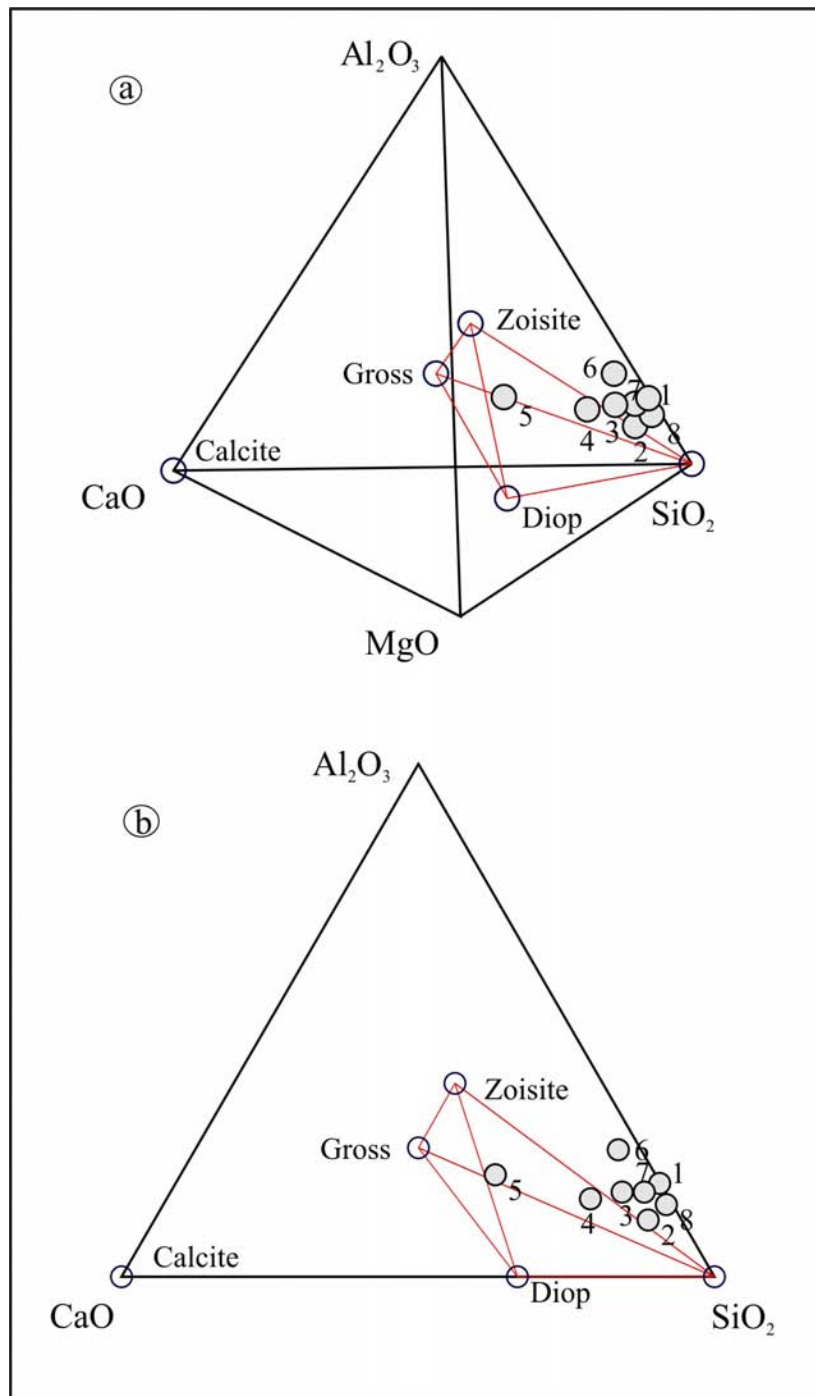


Figure 6.17. (a)  $SiO_2$ - $Al_2O_3$ - $MgO$ - $CaO$  tetrahedral diagram showing the whole-rock plotting positions of a calc-silicate skarn boudin. The sample on the grossular-quartz tie line is a tanzanite bearing pocket in the center of the boudin. (b) The same dataset plotted in a  $SiO_2$ - $Al_2O_3$ - $CaO$  ternary diagram.

with  $Cr^{3+}$ ,  $Fe^{3+}$ , etc., would substitute for  $Al^{3+}$  in the crystal structure of grossular. A insignificant amount of  $V^{3+}$  can however also be present in the  $R^{2+}$  due to similar

reasons as the substitution of small amounts of  $\text{Al}^{3+}$  for  $\text{Si}^{2+}$ . Gübelin and Weibel (1975) found up to 3.3 wt%  $\text{V}_2\text{O}_3$  in tsavorite from the Lualenyi deposit. The accuracy of the analysis is however questionable as it was done by means of colourimetry.

### 6.8.2. Tanzanite

The major, trace and REE composition of tanzanite and other coloured zoisites from the Merelani deposit will be discussed in detail in Chapter 12. The mineralogical investigation discussed in Chapter 12 proves that tanzanite is coloured by  $\text{V}^{3+}$ , which is an important factor in the discussion of the tanzanite formation reactions in Section 6.9.

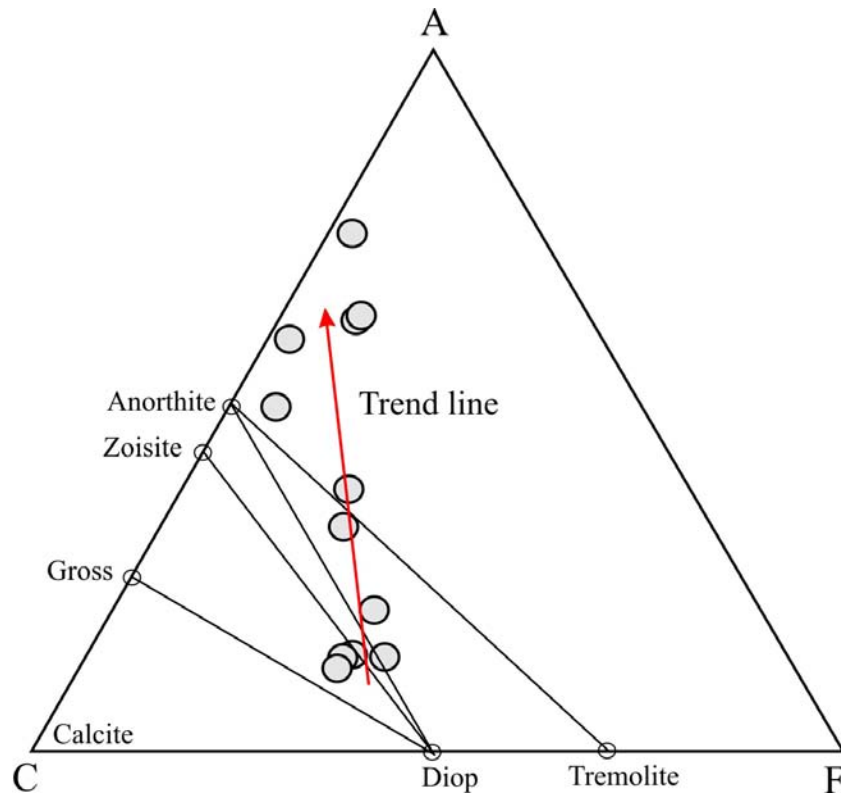


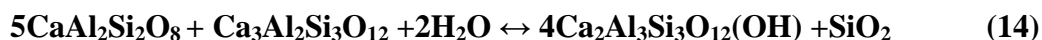
Figure 6.18. ACF diagram showing the plotting positions and trend of a combination of the pyroxene units and the calc-silicate skarn boudins.

## 6.9 Possible tanzanite formation reactions

The majority of zoisite formation within calc-silicates necessitates the presence of anorthite within the equation, the most common being:



as defined by Boettcher (1970);



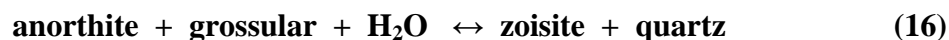
as defined by Newton (1965);



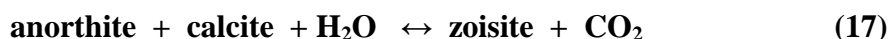
as defined by Storre and Nitsch (1972);

McRobbie et al. (1995) and Davies and Chase (1994) proposed that tanzanite formed through two reactions:

- 1) amphibolite to lower greenschist facies retrograde reaction:



- 2) saussuritic plagioclase breakdown reaction:



However, these equations have serious shortcomings, suggesting that they may not be valid:

- There is a lack of evidence for lower greenschist facies conditions. All the petrographic evidence and thermobarometric calculations of this study points towards a lower P-T limit indicative of lower-amphibolite facies conditions. The intense later-stage alteration that is present in the upper-areas of the mine and the lack of drill hole data made previous identification of the metamorphic facies very difficult.
- Anorthite is absent in the calc-silicate skarn boudins, low-pressure sites and pyroxene units. Assuming that all the anorthite was consumed during the reactions, anorthite should still be present in large amounts in the relict pyroxene



units, from which the skarn boudins formed. As indicated in Chapter 4, accessory amounts of plagioclase are present within the relict pyroxene units but in too small amounts to explain the high amounts of zoisite formation. Anorthite is present in the pelites surrounding the calc-silicate units (see Chapter 4) and therefore tanzanite can occur almost adjacent to anorthite. This is especially true when the calc-silicate unit or boudin is quite thin or stretched out. It could therefore be argued that tanzanite could have formed through the interaction of the anorthite in the pelites and the grossular in the calc-silicates with migrating fluids to form tanzanite along reaction 1 (p. 135). However, this would not explain the formation of tanzanite not adjacent to the pelites.

- The presence of clear calcite intergrown with the tanzanite and quartz cannot be explained by the reactions, with the reverse situation being implied by reaction 3 (p. 136).

This study indicated the association between zoisite, quartz and calcite within the calc-silicate skarn boudins (Chapters 3 and 4). Optical, petrographical, SEM and fluid inclusion studies of both zoisite (tanzanite) and grossular garnet (tsavorite) on the deposit also revealed an alteration reaction between the two minerals (Figures 6.19, 6.20 and 6.21). Zoisite forms through the alteration of the grossular garnet within the calc-silicate skarn boudins. It is therefore suggested here that tanzanite and zoisite formed through the reaction:



since vanadium is already present in the green grossular garnet (tsavorite) the equation can be written as:



This reaction is therefore dependant on the influx of fluids into the system. The possible source of the fluids will be discussed in Chapter 11. The alteration of zoisite and tanzanite by feldspar associated with pegmatite formation has been observed (Figure 6.22). As indicated in Chapter 5, the pegmatite formation post-dates tanzanite formation and sometimes causes the “destruction” of gemstone quality tanzanite within the deposit.

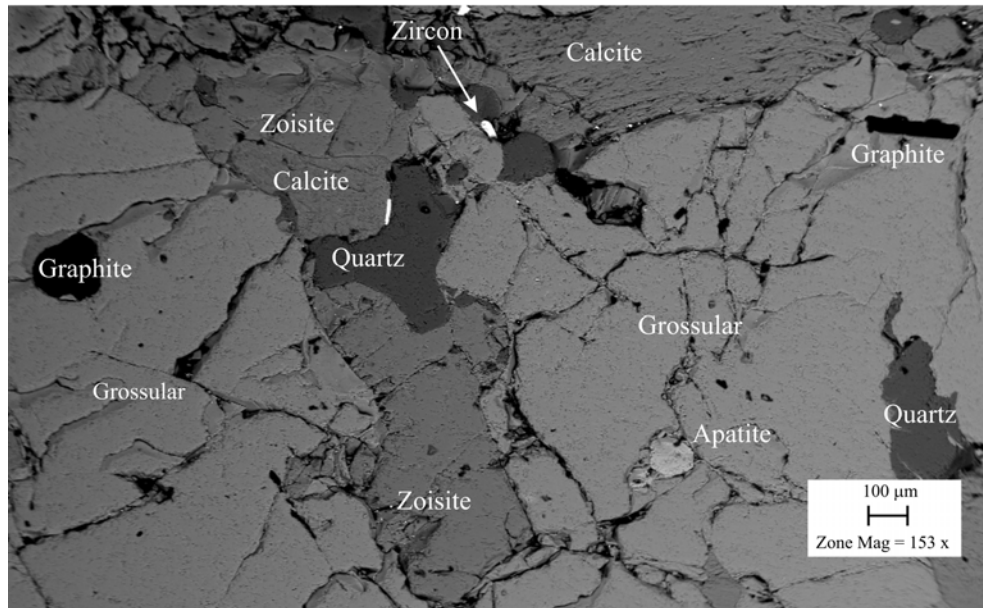


Figure 6.19. SEM image indicating the association between grossular garnet, zoisite, calcite and quartz. Graphite, apatite and zircon are also present.



Figure 6.20. Tsavorite replaced by tanzanite, quartz and calcite in hand sample. Tanzanite, quartz and calcite are replacing the euhedral tsavorite crystal from the side and from the top and are not situated within the tsavorite crystals, which would imply the reverse of reaction 18.

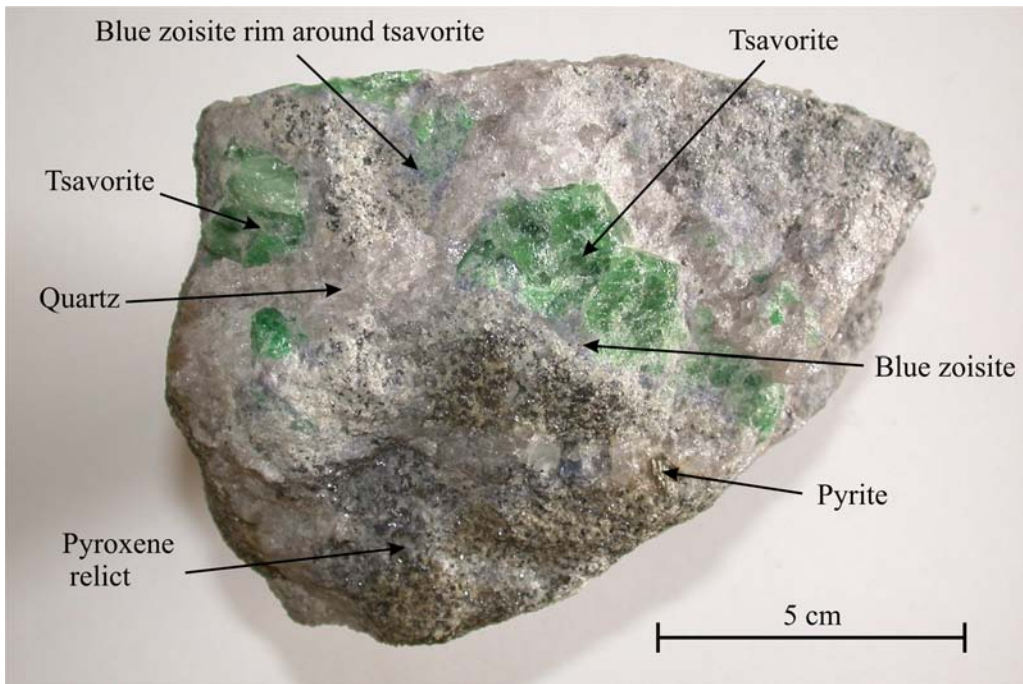


Figure 6.21. Rock specimen indicating the replacement of green grossular garnet by blue zoisite (tanzanite). The specimen also contains relict pyroxene and pyrite.

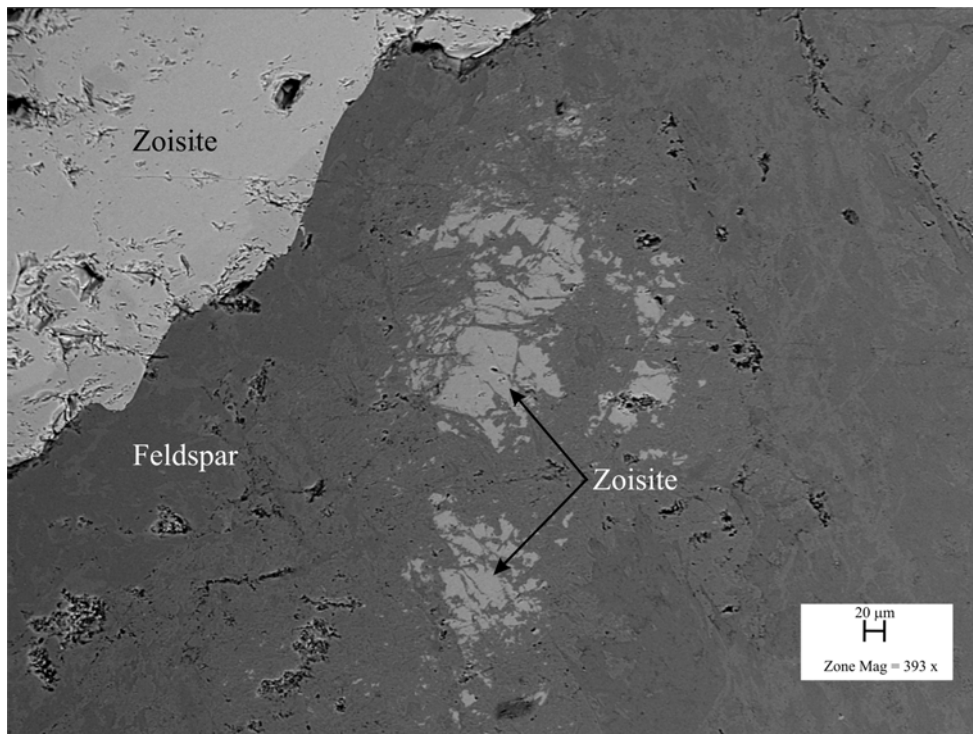


Figure 6.22. Pegmatite-associated replacement of zoisite and tanzanite by feldspar.

## **Chapter 7**

### **Geochemistry**

#### **7.1. Introduction**

The geochemistry of the various lithological units, defined in Chapter 3, plays an important role in classifying and distinguishing these units. Understanding the geochemical composition and variation of the different units, but especially the main ore zone (JW-zone), is of utmost importance in understanding the tanzanite deposit. The geochemical database on the various horizons will serve as the base for a future exploration programme and aims to characterise the ore-zone (JW-zone) and its surrounding lithological units in other areas. The geochemical quantification of the ore-zone and its surrounding units is an important exploration tool for identifying other similar units that could be potential tanzanite-bearing ore zones.

#### **7.2. Analytical techniques**

Whole rock chemical analyses were conducted by X-Ray fluorescence spectrometry (XRFS) on a Philips 1404 Wavelength Dispersive spectrometer, at the University of Stellenbosch. The spectrometer is fitted with a Rh tube, six analysing crystals (LIF200, LIF220, LIF420, PE, TLAP and PX1) and the detectors are a gas-flow proportional counter, scintillation detector or a combination of the two. Major elements were analysed on fused glass beads at 50 kV and 50 mA tube operating conditions and trace elements were analysed on powder briquettes at 60 kV and 40 mA tube operating conditions. A lost-on-ignition (LOI) determination was performed at 950 °C. Matrix effects in the samples were corrected for by applying theoretical alpha factors and measured line overlap factors to the raw intensities measured with the SuperQ Philips software. Standards that were used in the calibration procedures for both major and trace element analyses are as follows: AGV-1 (Andesite from USGS), BHVO-1 (Basalt from USGS), JG-1 (Granodiorite), JB-1 (Granodiorite), GSP-1 (Granodiorite from USGS), SY-2 (Syenite), SY-3 (Syenite), STM-1 (Syenite), NIM-G (Granite), NIM-S (Syenite), NIM-N (Norite), NIM-P (Pyroxenite), NIM-D (Dunite), BCR (Basalt), GA (Granite), GH (Granite), DRN (Diorite), and BR (Basalt).

The hot acid method normalised by  $K_2Cr_2O_7$  was used to calculate the Fe concentrations from the total Fe concentrations.

### **7.3. Geochemical composition of lithological units**

#### **7.3.1. Garnet-sillimanite gneiss (GNG)**

The garnet-sillimanite gneiss occur as three units, GNG1, GNG2 and GNG3 (Table 3.2 and Chapter 3). The geochemical average, minimum, maximum, standard deviation and standard error of all three units are indicated in Table 2, Addendum F. The average cumulative GNG values for the three units are shown in Table 7.1. The three garnet-sillimanite gneiss units have very similar chemical compositions. The only minor differences between the units are the slightly lower  $SiO_2$  and slightly higher  $Al_2O_3$  and  $Fe_2O_3$ (total) content of the GNG3 unit compared to the other two units, as evident from Table 1, Addendum F. The AFM whole-rock projection of the gneiss was discussed in Section 6.1.

#### **7.3.2. Banded calc-silicate hornfels (BCF)**

The average, minimum, maximum, standard deviation and standard error of chemical composition of the BCF units (BCF1 and BCF2) are provided in Table 3, Addendum F. The chemical composition of the two BCF units, as described in Chapter 3, is almost identical. The average cumulative geochemical composition for the two BCF units is indicated in Table 7.1.

Both the banded calc-silicate hornfels (BCF) and graphite-calc-silicate schist (GCS) have petrographically been identified as consisting of intercalated calc-silicates and quartzo-feldspathic zones (see Chapter 4). This is confirmed when the element concentrations of the layers are compared (Table 1, Addendum F). There are however significant geochemical differences between the two units, the most significant being the graphite content, as discussed petrographically (Chapter 4) and represented by the lost-on-ignition (LOI) content. The average LOI content of BCF is 5.01 wt%, while the LOI of the GCS is 21.25 wt%. Since the amount of carbonates is only slightly larger in the GCS than in the BCF, due to the presence of scapolite, these values suggest a large (10 to 15 wt%) difference in graphite content. Rb has an average concentration of 97 ppm in the BCF, which is significantly higher than that of the GCS (15 ppm). The

reason for the higher Rb values is probably due to larger amounts of K-feldspar in the BCF, as indicated by the average  $K_2O$  value of 2.67 wt%. The BCF has lower concentrations of Zn and Ni compared to the GCS. The small amounts of graphite in the BCF compared to the GCS and calc-silicate boudins, resulted in far lower concentrations of organically associated elements, with V, Cr and Mo present only in 63 ppm, 129 ppm and 4 ppm, respectively.

### 7.3.3. Graphite calc-silicate schist (GCS)

The average, minimum, maximum, standard deviation and standard error of chemical composition of the GCS units (GCS1 and GCS2) are summarised in Table 4, Addendum F. The two GCS units (GCS1 and GCS2) present in the Lower Horizon (see Chapter 3) are almost identical in composition. The average composition of the Lower Horizon GCS units is indicated in Table 7.1. The composition of the GCS unit located within the Upper Horizon (UH-GCS) also compares well with that of the Lower Horizon (Table 4, Addendum F). The UH-GCS has high  $Fe_2O_3/FeO$  values (average of 7.3) compared to that of the Lower Horizon (average of 2), even though the  $Fe_2O_3$ (total) content of both is ca. 3.9 wt%. This indicates a higher amount of oxidation present within the Upper Horizon. The UH-GCS has lower Ba concentrations and slightly higher V, Cr, Zn and Ni concentrations (Table 4, Addendum F).

The GCS has the highest concentration of graphite of all the different lithological units within the Merelani tanzanite succession. The opencast mining operations of SAMAX Ltd. within the UH-GCS resulted in an average extracted graphite concentration of 11 wt% Cg, with a quality of ca. 96% Cg. Graphite concentrations of over 25 wt% Cg were recorded from this unit. The graphite quality is further enhanced by the extraordinary coarse flake size of ca. 300 microns (Davies and Chase, 1994; McRobbie et al., 1995). The LOI values obtained from the geochemical analyses represent the graphite content of the GCS, although it also includes the presence of small amounts of carbonates present within the GCS. The average LOI content of the GCS is 21.25 wt%. A correlation matrix (Table 1, Addendum G) of all the GCS units reveals a moderate positive correlation between LOI and Ni (correlation coefficient,  $r = 0.73$ ), V ( $r = 0.63$ ) and Mo ( $r = 0.59$ ). The majority of other elements within the GCS have no correlation with the LOI content (Table 1, Addendum G). The correlation between the graphite

content and the Ni, V and Mo content of the GCS results in high concentrations of these elements compared to those of the other units (Table 1, Addendum F).

#### 7.3.4. Kyanite-graphite gneisses

The geochemical analyses of the kyanite-graphite gneisses were divided into five groups, namely: Upper Horizon kyanite gneisses (UK), LK4, LK3, LK2 and LK1, in accordance with the lithological division, as indicated in Chapter 3. The mean, minimum, maximum, standard deviation and standard error of the analysed elements for all five kyanite-graphite gneisses are indicated in Table 5, Addendum F.

The SiO<sub>2</sub> content of the kyanite-graphite gneiss vary from 56.97 to 72.2 wt% with an average of 65.96 wt% (Table 7.1). The mean SiO<sub>2</sub> content for UK, LK4, LK3, LK2 and LK1 are 68.19, 66.43, 63.93, 64.64 and 67.6 wt%, respectively. The mean Al<sub>2</sub>O<sub>3</sub> content for the UK, LK4, LK3, LK2 and LK1 are 11.39, 10.51, 11.08, 11.47, 12.41 wt%, respectively. The variation of some of the major elements can be attributed to presence of small pockets of calc-silicates, especially within the FW units of the C-zone and JW-zone (LK3 and LK1, respectively). This is also evident from the variation of CaO (0.01 to 14.7 wt%), MgO (0.15 to 2.6 wt%) and Fe<sub>2</sub>O<sub>3</sub>(total) (4.72 to 7.36 %), with average values of 1.76 %, 1.10 % and 4.98 wt%, respectively. The highest CaO values are present within the JW-zone FW (LK1) unit, as indicated in Table 5, Addendum F and coincide with the lowest values for SiO<sub>2</sub> and Al<sub>2</sub>O<sub>3</sub>, as expected for calc-silicate-rich zones within the gneisses. Na<sub>2</sub>O, K<sub>2</sub>O and TiO<sub>2</sub> show a far more restricted distribution range throughout the various kyanite-graphite gneisses, with average values of 1.00, 2.25 and 0.66 wt%, respectively. The graphite content of the gneisses is indicated by the LOI values, with a mean of 9.78 wt% for all the kyanite gneisses. There is a slight negative correlation between SiO<sub>2</sub> and Al<sub>2</sub>O<sub>3</sub> (correlation coefficient,  $r = -0.38$ ) as well as for SiO<sub>2</sub> and TiO<sub>2</sub> (correlation coefficient,  $r = -0.48$ ), as usual for shale-like sediments (see Table 2, Addendum G). The gneisses are generally acidic in composition.

The large-ion-lithophile (LIL) element ratios are also fairly restricted, with K/Rb values ranging from 0.76 to 1.0 (Table 1, Addendum F). The HW unit (LK2) of the JW-zone is slightly enriched in most minor and trace elements compared to the other kyanite gneisses, containing the highest values for Ba, V, Zn, Ni, Sr, Cu, Nd, La, Mo and Nb in

decreasing content (Table 5, Addendum F). No enrichment trends were observed for the other kyanite gneisses. The most important minor elements within the kyanite gneisses are Ba, V, Zn, Cr and Ni with average values of 1780, 871, 420, 354 and 260 ppm, respectively. In general, the transition metals are often closely associated with each other, having similar behavioural patterns (Feng and Kerrich, 1990). This is also true for the kyanite-graphite gneisses, with most of the transition elements having a strong correlation, as indicated in Table 2, Addendum G. In the case of vanadium there is a strong correlation with Mo ( $r = 0.79$ ), Ni ( $r = 0.76$ ), Rb ( $r = 0.76$ ), Cr ( $r = 0.74$ ), Zn ( $r = 0.68$ ), Ba ( $r = 0.65$ ) and Cu ( $r = 0.65$ ). Vanadium also shows a strong correlation with LOI ( $r = 0.66$ ) indicating a possible association with graphite that will be further discussed in Chapter 11.

### 7.3.5. Graphite - plagioclase gneisses

The graphite-plagioclase gneisses are geochemically subdivided into four main groups, Upper Horizon alteration zone, C-zone, JW-zone and FW-alteration zone. The mean, minimum, maximum, standard deviation and standard error of all four groups are shown in Table 6, Addendum F.

The chemical composition of the graphite-plagioclase gneisses are very similar, with all four zones having average  $\text{SiO}_2$  values of between 65.4 and 66 wt% and average  $\text{Al}_2\text{O}_3$  values of between 10.2 and 11.8 wt%. The average  $\text{Fe}_2\text{O}_3(\text{total})$  content of the gneiss vary from 4.1 to 6.4 wt%, while the average CaO content varies between 3.0 to 4.0 wt%, see Table 6, Addendum F. The average values for CaO, MgO,  $\text{Na}_2\text{O}$ ,  $\text{K}_2\text{O}$  and  $\text{TiO}_2$  for all the graphite-plagioclase gneisses are 3.47 wt%, 1.1 wt%, 1.2 wt%, 1.70 wt% 0.6 wt%, respectively. The JW-zone has the highest Ba, V, Zn, Ni, Sr and Rb content. The average Ba, V, Zn, Cr and Ni content for all the graphitic gneisses are 1411, 763, 403, 316 and 244 ppm, respectively. The Sr and Zr content of the gneisses are 231 and 207 ppm, respectively, while all the other analysed minor elements are present in concentrations of less than 100 ppm.

In general, the graphite-plagioclase gneiss is chemically very similar to the kyanite-graphite gneiss (Table 1, Addendum F). The only significant difference is the higher CaO content of the graphite gneiss compared to the kyanite gneiss. The kyanite gneiss also has slightly higher concentrations of  $\text{SiO}_2$ ,  $\text{Al}_2\text{O}_3$ ,  $\text{K}_2\text{O}$ , Ba and V (Table 1,



Addendum F). Despite the geochemical similarity, it is still possible to accurately distinguish chemically between the kyanite gneisses and the graphite-plagioclase gneiss, as will be discussed in Section 7.4.

### 7.3.6. Pyroxene relict units

The average, minimum, maximum, standard deviation and standard error of the pyroxene relict units are indicated in Table 7, Addendum F. The pyroxene relict units have a fairly large compositional range depending of the amount of skarn-related hydrothermal alteration. The SiO<sub>2</sub> content vary from 35.26 to 55.87 wt%, while the Al<sub>2</sub>O<sub>3</sub> content vary from 3.63 to 13.36 wt%. The CaO and MgO content varies from 16.34 to 27.27 wt% and 2.47 to 17.18 wt%, respectively. The average Fe<sub>2</sub>O<sub>3</sub>(total) content of the pyroxene relicts is 3.14 wt%, with an average Fe<sub>2</sub>O<sub>3</sub>/FeO ratio of less than 1.3. The sample W2B (Table 1, Addendum F) that was taken within the oxidation zone close to the surface, however, have a Fe<sub>2</sub>O<sub>3</sub>/FeO ratio of 4.0, indicating a high degree of oxidation. The pyroxene relicts have very low concentrations of minor and trace elements. Vanadium, Zn and Zr are the only additional elements present in appreciable amounts, with average values of 469 ppm, 193 ppm and 157 ppm, respectively.

### 7.3.7. Calc-silicate skarn boudins

The average, minimum, maximum, standard deviation and standard error of the calc-silicate skarn boudins are shown in Table 8, Addendum F. Petrographic, optical and mine mapping of the calc-silicate skarn boudins revealed that the boudins formed through the skarn associated metasomatic, metamorphic and hydrothermal alteration of the pyroxene units and associated interaction with the surrounding graphitic gneiss. This observation is further confirmed by the geochemical analyses of the calc-silicate skarn boudins. The skarn boudins have an exceptionally large chemical compositional range as a result of varying skarn interaction. The SiO<sub>2</sub> content ranges from 47 to 64 wt%, with an average value of 56.89 wt%. The Al<sub>2</sub>O<sub>3</sub>, CaO, Fe<sub>2</sub>O<sub>3</sub>(total) and MgO content of the boudins vary with more than 10 wt% between the minimum and maximum values, with average values of 11.09, 10.59, 5.91 and 3.5 wt%, respectively (Table 8, Addendum F). The minor element composition of the boudins also varies considerably with Zn (229 to 4508 ppm), Ba (2.5 to 2360 ppm), Ni (83 to 2298 ppm), V (333 to 1746 ppm), Sr (75 to 1009 ppm) and Cr (70 to 564 ppm). A comparison with the pyroxene

relict units therefore indicates that the hydrothermal skarn-related fluids were enriched in Zn, Ba, Ni, V, Sr and Cr, but did not cause a significant change in the Zr, Cu, Pb, Co and Th content of the original units. The chemical composition of the boudins within the graphite-plagioclase gneisses situated within the Upper Horizon is similar to that of the Lower Horizon (Table 8, Addendum F).

### **7.3.8. Skarnoid reaction zones**

The chemical composition of the skarnoid reaction zones or layers varies considerably, similar to that of the skarn boudins, but the composition is closer to that of the graphite-plagioclase gneisses. The average, minimum, maximum, standard deviation and standard error of the skarnoid reaction zones are indicated in Table 9, Addendum F. The SiO<sub>2</sub> content have a high maximum value of 75.33 wt% as a result of the presence of quartz stringers within the reactions zones as described in Chapters 3 and 5. The average Al<sub>2</sub>O<sub>3</sub> (12.78 wt%) content of the zones are higher than that of the gneisses and boudins. This could possibly be as a result of the metasomatic interaction between the graphitic gneisses and the calc-silicate boudins. Aluminium possibly migrated from the gneisses toward the calc-silicates and resulted in accumulation of Al within the shear zone contact. The average Fe<sub>2</sub>O<sub>3</sub>(total), Fe<sub>2</sub>O<sub>3</sub>, FeO, CaO, Na<sub>2</sub>O and K<sub>2</sub>O content of the skarnoid reaction zone are located between the respective element concentrations of the graphite-plagioclase gneisses and the skarn boudins (Table 7.1). Similarly, the Ba, Cu, Ga, Ni and Zn contents of the skarnoid reaction zones are also located between the respective values obtained from the graphite-plagioclase gneiss and skarn boudins. A noticeable exception to this is the V content of the skarnoid reaction zone (average of 1402 ppm), which is considerably higher than both the graphitic gneiss and the boudins. The high V content is probably related to the higher concentration of graphite within the skarnoid zones as indicated by the high LOI values (average of 13.1 wt%). Graphite is concentrated in the zones due to intensive shearing since, as described in Chapter 5, the skarnoid reaction zones envelope the boudins and represent the core of the shear zone situated between the graphitic gneiss and calc-silicate boudins.

### **7.3.9. Dolomitic Marbles**

The chemical composition of the three dolomitic marble layers (DM1-3), including the mean, maximum, minimum, standard deviation and standard error is indicated in Table 9, Addendum F. The composition of the marble varies slightly depending on the amount

Table 7.1. Average composition of the various lithological units within the Merelani tanzanite deposit (n indicates the number of samples).

	GNG	BCF	GCS	Kyanite Gneiss	Plagioclase Gneiss	Reaction zone	Relict	Boudin	Marble	
n	12	21	22	70	53	12	11	15	8	
SiO <sub>2</sub>	58.07	60.94	53.52	65.96	65.70	66.05	46.54	56.89	6.76	wt%
TiO <sub>2</sub>	1.45	0.50	0.41	0.66	0.59	0.65	0.37	0.46	0.12	wt%
Al <sub>2</sub> O <sub>3</sub>	20.08	9.46	7.66	11.37	11.08	12.78	8.35	11.09	2.27	wt%
Fe <sub>2</sub> O <sub>3</sub> T	11.61	4.89	3.90	4.98	4.85	5.74	3.14	5.91	1.15	wt%
FeO	7.63	2.74	1.24	2.01	1.90	0.81	1.31	0.71	0.61	wt%
Fe <sub>2</sub> O <sub>3</sub>	1.71	1.93	2.48	2.98	3.06	4.05	1.65	5.87	0.25	wt%
MnO	0.08	0.08	0.06	0.04	0.05	0.06	0.39	0.14	0.02	wt%
MgO	3.28	2.29	1.01	1.10	1.08	0.85	10.81	3.51	11.97	wt%
CaO	0.84	11.50	9.69	1.76	3.47	4.66	23.56	10.59	37.32	wt%
Na <sub>2</sub> O	0.51	0.25	0.16	1.00	1.16	0.52	0.39	0.23	0.08	wt%
K <sub>2</sub> O	1.82	2.67	0.50	2.25	1.69	1.19	0.04	0.67	0.42	wt%
P <sub>2</sub> O <sub>5</sub>	0.12	0.09	0.28	0.29	0.14	0.09	0.10	0.13	0.03	wt%
Cr <sub>2</sub> O <sub>3</sub>	0.04	0.02	0.04	0.03	0.03	0.01	0.01	0.02	0.01	wt%
LOI	1.86	5.01	21.25	9.78	9.10	13.10	6.06	12.01	38.22	wt%
NiO	0.01	0.01	0.07	0.04	0.04	0.06	0.02	0.04	0.00	wt%
TOTAL	99.89	97.76	98.84	99.34	99.15	99.28	99.76	98.52	98.37	wt%
H <sub>2</sub> O	0.30	0.18	0.75	0.23	0.44	1.64	0.25	1.89	0.12	wt%
As	8.33	10	10.00	10	10	10	12	0	10	ppm
Ba	457	863	1184	1780	1412	1231	48	610	578	ppm
Ce	57	24	29	34	36	125	55	64	1	ppm
Co	18	9	5	11	26	9	5	2	5	ppm
Cr	392	129	382	354	316	327	78	339	28	ppm
Cu	60	68	61	100	77	74	18	41	4	ppm
Ga	25	14	15	14	15	22	32	34	5	ppm
Hf	6	5	5	7	7		5		5	ppm
Mo	6	4	96	54	52	57	13	41	2	ppm
Nb	15	15	8	13	12	12	13	7	4	ppm
Ni	72	37	534	260	244	405	84	612	7	ppm
Pb	9	14	9	13	10	4	7	3	5	ppm
Rb	68	97	15	56	44	53	4	17	18	ppm
Nd	29	22	28	28	25	35	43	37	16	ppm
Sc	16	15	10	14	13	16	10	9	7	ppm
Sr	143	274	321	202	231	309	187	283	91	ppm
Ta	5	6	5	5	5	6	5	0	5	ppm
Th	7	10	7	8	8	12	12	11	4	ppm
U	2	0	36	10	17	26	12	22	1	ppm
V	264	63	1548	871	763	1402	469	884	26	ppm
W	3	5	3	4	3	2	3	2	3	ppm
Y	43	37	65	40	41	62	39	56	11	ppm
Zn	148	132	1161	420	403	861	183	1195	44	ppm
Zr	220	117	126	200	207	244	157	216	25	ppm
La	17	19	24	23	25	42	26	45	1	ppm

of impurities present. This is evident from the minimum and maximum concentrations of SiO<sub>2</sub> (1.4; 17.7 wt%), Al<sub>2</sub>O<sub>3</sub> (0.31; 7.25 wt%) and Fe<sub>2</sub>O<sub>3</sub>(total) (0.15; 3.21 wt%). Except for Ba (average of 578 ppm) and Sr (average of 91 ppm), all the other minor elements are present in concentrations of less than 50 ppm (Table 1, Addendum F). The marble contains ca. 12 wt% MgO, 37 wt% CaO and 38 wt% LOI which represents the (CO<sub>3</sub>)<sup>2-</sup> concentration, thus equating to approximately 59% Ca(CO<sub>3</sub>)<sub>2</sub> and 28% Mg(CO<sub>3</sub>)<sub>2</sub>.

#### 7.4. Discriminant analyses

The geochemical signature of the JW-zone and surrounding rock was calculated using the complete geochemical database of the Merelani mining area in a discriminant analyses. Discriminant analysis is a statistical technique used for classifying samples into predefined groups. A large number of variables (in this case major and minor elements) are examined in order to isolate the ones that most effectively classify the samples. The raw coefficients for the canonical variables were calculated with Statistica 7.0 and are listed in Table 7.2, in decreasing order of importance for discrimination. The values obtained for Root 1 and Root 2 in Table 7.2, represent the raw coefficients for elements used to classify the different layers and are substituted into the function:

$$F_i = a_i x_1 + b_i x_2 + c_i x_3 \dots p_i x_p - \text{constant for each root}$$

where  $x_1, x_2 \dots x_p$  are the discriminating variables (Root 1 and Root 2 as listed in Table 7.2),  $a_i, b_i \dots p_i$  are the discriminating function (the concentration of SiO<sub>2</sub>, Al<sub>2</sub>O<sub>3</sub>, etc. in wt% for each sample) and  $F_i$  is the discriminant score.

The  $F_i$  values are plotted in Figure 7.1, and show a clear discrimination between the JWZ, LK2 (HW) and LK1 (FW). The discrimination function was subsequently used to classify “unknown” rock compositions into the predefined categories. Table 7.3 indicates the classification of the “unknown” samples into either boudin, C-zone, JW-zone, GCS, LK1, LK2, LK3, LK4 or BCF. The discrimination matrix shows a remarkable discrimination factor of 98.92% between the different layers, with only one sample of LK3 falling into the predefined group of LK2.

From this it can be deduced that each of these layers has a unique geochemical signature that can be used to distinguish the layers from each other. The discrimination function can further be used to classify unknown units. This is of the utmost importance in the exploration of tanzanite through the identification of its host rock and surrounding layers. This information therefore enables one to predict whether an unknown layer is suitable as a possible ore zone.

*Table 7.2. Raw coefficients for the canonical variables used to calculate the Root 1 and Root 2 discrimination functions.*

	Root 1	Root 2
Ni	0.003961	-0.00014
U	0.213366	-0.15973
Th	0.32734	0.219691
Na <sub>2</sub> O	2.207977	-1.78371
Pb	-0.20455	0.046783
Ga	0.191613	0.12471
Sr	-0.00124	0.002895
MnO	1.354818	-45.4958
Zr	0.028661	-0.00928
W	-0.6243	0.446989
Cr <sub>2</sub> O <sub>3</sub>	104.5445	110.4151
Cr	-0.01196	0.000678
MgO	-0.91567	0.59222
Al <sub>2</sub> O <sub>3</sub>	-0.8588	-0.01532
Nb	0.355182	0.387311
Mo	0.070949	-0.00178
Co	0.108456	-0.09558
Cu	-0.02017	0.014273
Ba	0.0017	-0.00091
Fe <sub>2</sub> O <sub>3</sub> T	0.580862	-0.82778
Constant	-16.778	-2.9372
Eigenval	16.38859	7.680432
Cum.Prop	0.6809	1

In order to obtain a “down-the-hole” geochemical signature of the JW-zone, a single discrimination function was achieved by dividing the canonical score of Root 1 by those of Root 2 and multiplying it by 100. This provided consistent numerical values of between 0 and 40 for the JW-zone, enabling the characterisation of this lithological unit with a more than 95% confidence level. The results of these calculations are plotted in Addendum H for the selected drill holes. The value calculated for the JW-zone in each of the drill holes varies between 0 and 40 and is used as an indication of the intersection

of the zone. In all the drill holes, the geochemistry confirms the classification through logging, petrography and mineral chemistry.

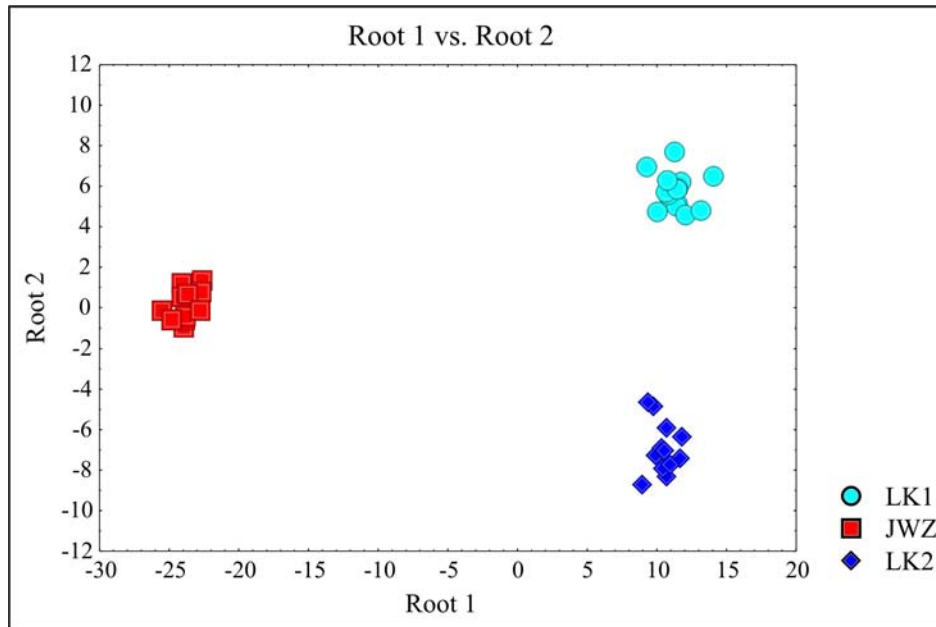


Figure 7.1. Scatter plot of canonical scores of the Root 1 and Root 2 discrimination function of the LK1, LK2 and JW-zone.

Table 7.3. Classification matrix obtained from the Root 1 and Root 2 canonical discrimination functions. Rows represent the observed classifications and the columns the predicted classifications.

	Percent	Boudin	C-zone	JWZ	GCS	LK1	LK2	LK3	LK4	BCF
Boudin	100	5	0	0	0	0	0	0	0	0
C-zone	100	0	9	0	0	0	0	0	0	0
JWZ	100	0	0	12	0	0	0	0	0	0
GCS	100	0	0	0	12	0	0	0	0	0
LK1	100	0	0	0	0	14	0	0	0	0
LK2	100	0	0	0	0	0	12	0	0	0
LK3	88.888	0	0	0	0	0	1	8	0	0
LK4	100	0	0	0	0	0	0	0	9	0
BCF	100	0	0	0	0	0	0	0	0	11
Total	98.924	5	9	12	12	14	13	8	9	11

## 7.5. Element behaviour

### 7.5.1. Vanadium

#### *Introduction*

Despite the important role of V in the tanzanite formation process in the Merelani deposit, little is known about its origin. The situation is further complicated by the general lack of knowledge regarding the migration of V under high metamorphic conditions. In order to attempt to solve some of the questions regarding the role of V during several processes including the formation of tanzanite, a more detailed investigation into the behaviour of the element was conducted.

Compared to upper crustal rocks, the rocks of the Upper and Lower Horizons are particularly enriched in Ba, V, Zn, Cu and Cr. Enrichment in these elements are mostly contributed to an oceanic environment and / or the contribution of seafloor volcanism. Of these elements, V is the most important, since it is the main colouring agent of tanzanite and tsavorite (see Chapters 6 and 12). Vanadium is also present in fuchsite that is abundant in the Upper Horizon. Malisa (1987) also reported moderate amounts (average 310 ppm) of V present in pegmatites in the area. Vanadium was most likely incorporated into the pegmatite due to the anatectic origin of the pegmatites from the gneisses.

ICP-MS and XRF analyses were carried out on graphite samples and whole rock samples in order to shed more light on the question of the origin of V in the deposit (Table 7.4, 7.5 and 7.6). The ICP-MS analyses were conducted at the University of Cape Town and the analytical technique will be discussed in Chapter 12.

#### *Vanadium “Down-the-hole” variation*

Addendum I indicates the “down-the-hole” V concentration plots of selected drill holes within the mining area. From the plots, it is evident that the highest V values are found in the GCS units. There is a characteristic decrease in V values from the GCS to the JW-zone in all the drill holes. This decline in V values may be used as a diagnostic aid in distinguishing the lithostratigraphic units and can be of use to identify the true HW and FW units intersected in underground drilling.

The “down-the-hole” V, Ba, Zn, Cu, Mo and Cr values indicate a distinct repetitive distribution pattern centered around the central dolomitic marble (DM2) unit (Addendum I). This is also strong supporting evidence of a repetition of lithologies around the central dolomitic marble and may confirm the existence of the second order F2 fold as indicated in Chapter 5.

#### *Contents of V in graphite*

1 gram of graphite was separated from each sample in order to conduct ICP-MS analysis aimed at determining the V content of the sample. The graphite was concentrated from crushed samples by means of a gravity-shaker from where it was hand picked. Two methods were attempted in order to try to determine the V content of the graphite. In the first method the samples were brought to solution in 65% nitric acid and 40% hydrofluoric acid. The solution and residue were subsequently washed and filtered with distilled H<sub>2</sub>O. The samples were then analysed using an ICP-MS calibrated with a V standard in order to determine the amount of V present on the surface of the graphite. In the second method the same amount of graphite (1g) was taken from the same samples and slowly heated to 1000 °C. The residue was then brought to solution using the same method as described above and analysed in order to determine the V content present in the crystal structure of the graphite. Results from the ICP-MS are listed in Table 7.4.

It is clear from the results that the graphite contains exceptionally high amounts of V. However, V values obtained from ICP-MS analyses of the graphite do not correlate well with the whole-rock V content obtained from the XRF analyses conducted on the corresponding sample (see Table 7.4 and Table 7.6). According to this data, less than 28% of the vanadium in the rock is situated in the graphite. This is however not the case, since the sample “G-Boudin” consists of ca. 51% graphite, 36% quartz and minor amounts of feldspar. Thus, all the V concentrations determined for the whole-rock analysis must be situated in the graphite. This suggests that either the V concentrations obtained from the XRF analysis are inaccurate, or the methods used, as described above, for removing the V from the graphite is ineffective.



It is clear from Table 7.4 and 7.5 that there is a decline in the V content present on the surface of the graphite towards the calc-silicate unit (LK1 – JWZ – Boudin). The reason for this could be three-fold:

- 1) the vanadium adjacent to and present in the calc-silicates could have been leached from the units and incorporated into other minerals.
- 2) graphite could have formed due to decarbonation reactions related to the formation of the calc-silicate unit, therefore “diluting” the V content of the analysed graphite.
- 3) different types of organic matter could have existed within different parts of deposit. Varying organic matter could have had different V absorption abilities, therefore causing the variation in V content.

The isotopic values of the graphite indicate that all the graphite sampled were of similar biogenetic origin (Chapter 8). This would suggest that some amount of V mobilisation must have occurred from the graphite. It is therefore highly likely that the graphite was the source of the V that is present in tanzanite and tsavorite. This is not an uncommon phenomenon, since V is a common constituent of organic matter. Vanadium concentrations of up to 3000 ppm and 5000 ppm have been recorded in bituminous limestones and bituminous shales, respectively (Wedepohl, 1974). Wedepohl (1974) also suggested that V accumulation in bituminous sediments is not only controlled by the primary V content of organic matter but also by the reducing character of the environment.

The question regarding the mobility of V still remains. In general, V is not a highly mobile element and usually only migrates when it is oxidised to its pentavalent state (Wedepohl, 1974). This would imply that, either oxidizing fluids caused the migration of V, or that oxidizing conditions prevailed during the migration of the V. However, the highly reducing nature of the sediments suggests that this was not the case. Vanadium has been noted by various authors (e.g. Jamieson and Strong, 1981) to migrate during metasomatism. V can migrate as a complex, or in its soluble quinquevalent state.

Table 7.4. Vanadium ICP-MS analysis of graphite from various layers.

Sample	Location	Vanadium (ppm) on surface of graphite	Number of analysis
G-UK1	Upper Horizon	1849.19	3
G-LK1	FW of JW-zone	750.368	3
G-JW	JW-zone	551.006	6
G-Boudin	Graphite pocket	228.75	4

Table 7.5. Vanadium ICP-MS analysis

Sample	Location	Vanadium situated in graphite crystal structure (ppm)	Number of analysis
G-UK1	Upper Horizon	2666.7	2
G-LK1	LK1	1702	2
G-JW	JWZ	1933.4	2
G-Boudin	Graphite pocket	153.4	2

Table 7.6. Vanadium ICP-MS and XRF analysis

Sample	Whole-rock vanadium content	Whole-rock graphite vol %	% Vanadium situated in graphite
Upper Horizon	-	10%*	-
LK1	774.62	7.7%	17%
JWZ	1156.68	7%	12%
Graphite pocket	459.93	51.2%	17%

\* The graphite samples from the Upper Horizon were taken from the processing plant.

### 7.5.2. Skarn reactions

Metasomatism and chemical diffusion as mechanisms for mass transfer during metamorphism is a complex topic that requires in-depth investigation in order to accurately define it. It is not the aim of this study to precisely quantify the possible skarn reactions between the gneisses and calc-silicate rocks within the Merelani deposit. It is however evident from the petrography, mineral chemistry and rock geochemistry that skarn associated metamorphism and metasomatism strongly affected the rock units surrounding the shear zones, with the most important being the JW-zone. The shear zone provided path-ways for the metamorphic fluids that interacted with both the calc-silicates and the gneisses. This resulted in the recrystallisation of the gneisses surrounding the calc-silicates and the creation of the calc-silicate skarn boudins and surrounding skarnoid reaction zones.

Metasomatic interaction between calc-silicates and pelitic schists is a well-documented occurrence (Vidale, 1969; Brady, 1977; Buick et al., 1993; Stowell et al., 1996; Dunkley et al., 1999). Chemical diffusion can result in Ca diffusion and to a lesser extent Mg diffusion into the pelites, balanced by Al and Si diffusion into the calc-silicates or marbles. Vidale (1968) indicated that a steep chemical gradient exists between gneisses and calc-silicates resulting in amongst others, Al and Si migration toward the calc-silicates from the gneisses. It is possible that V could also have migrated from the gneisses toward the calc-silicates in Chapter 11. Vidale (1969) also indicated that the outward flow of H<sub>2</sub>O and CO<sub>2</sub> from the calc-silicates carries other chemical constituents, such as Ca and Mg toward the gneisses.

Skarn metasomatism associated with a shear zone is often also driven by redox-oxidation difference between the wall rocks and calc-silicate. Both chemical diffusion and fluid-driven metasomatism can result in an increase in anorthite content of the plagioclase toward the calc-silicate boudins as described in Chapter 6. It also results in the formation of the skarnoid reactions zones, with a composition close to that of the gneisses, but with increased concentrations of, amongst others, Ca (Table 1, Addendum F). The calc-silicate skarn boudin composition is closer to that of the pyroxene relict, but contains higher amounts of Si, Al, Fe, V, Ba, Zn, Ni, Sr and Cr and lower amounts of Ca and Mg. It is possible that all these elements could have been mobilised through the skarn reactions resulting in the change in mineral assemblage from pyroxene-rich

calc-silicates to skarn boudins comprising of amongst others, garnet, pyroxene, zoisite and quartz.

## **7.6. Conclusions**

The geochemical investigation of the JW-zone and surrounding lithologies indicates that the chemical compositions of the lithologies are unique and therefore suitable for geochemical exploration. A geochemical discriminant based on this geochemical database can be used in the exploration of potential tanzanite-bearing layers. The association between graphite and V is important in the exploration for tanzanite deposits.

The geochemical data proved that the Lower Horizon lithologies on the HW and FW side of the central dolomitic marble (DM2) have corresponding signatures. This is further support for the possible folding of the Lower Horizon around the central dolomitic marble (proposed in Chapter 5). The C-zone most likely represents a duplication of the JW-zone by folding and thus a potential tanzanite mineralised zone.

There is also a corresponding geochemical similarity between specific lithological units of the Lower and Upper Horizons. This supports the theory that the two horizons may also be linked through a second order parasitic fold structure, with the folding centred around GNG2 unit (Chapter 5).

The geochemical similarity between the JW-zone of the Lower Horizon and the graphite-plagioclase gneisses (alteration zones) of the Upper Horizon may indicate the existence of unexplored tanzanite-bearing zones within the Upper Horizon. The Upper Horizon alteration zones could therefore represent a potential source of tanzanite mineralisation.

## Chapter 8

### Stable Isotope Analyses

#### 8.1. Introduction

The aim of the stable isotope investigation of the Merelani deposit was to determine the origin of a) the graphite and b) the hydrothermal fluids associated with tanzanite mineralisation. The carbon isotope values of the graphite from the deposit were used to determine whether or not the graphite is of organic origin, which is of crucial importance in understanding the depositional setting. The oxygen and hydrogen stable isotope signatures of quartz, calcite and tanzanite were used to evaluate the origin of the fluids related to the mineralisation of tanzanite.

#### 8.2. Analytical Techniques

The oxygen, hydrogen and carbon isotopes were analysed at the Department of Archaeology at the University of Cape Town on a Finnigan MAT 252 mass spectrometer. The oxygen isotope ratios were determined by conventional fluorination methods (Clayton and Mayeda, 1963) using  $\text{ClF}_3$  as the oxidising reagent (Borthwick and Harmon, 1982). Data is reported in  $\delta$  notation where  $\delta^{18}\text{O}$  is  $(R_{\text{sample}}/R_{\text{standard}} - 1) \times 10^3 \text{ ‰}$  and R is the ratio of  $^{18}\text{O}/^{16}\text{O}$ .

Carbon and oxygen isotopes were analysed following conventional phosphoric acid techniques (McCrea, 1950). The standard  $\delta$  notation was used, where  $\delta^{18}\text{O}$  is  $(R_{\text{sample}}/R_{\text{standard}} - 1) \times 10^3$  and R is the ratio of  $^{18}\text{O}/^{16}\text{O}$  and similarly for  $\delta^{13}\text{C}$ . Raw data was converted relative to the SMOW and PDB scales using the accepted calibration values of the NBS-19 standard with  $\delta^{18}\text{O}$  SMOW = 28.64 ‰ and  $\delta^{13}\text{C}$  (PDB) = 1.95 ‰.  $\delta^{18}\text{O}$  values are given relative to SMOW where  $\delta^{18}\text{O}$  SMOW =  $(\delta^{18}\text{O}$  PDB) + 30.91 (Coplen et al., 1983 and Coplen, 1993).

### 8.3. Results

Graphite is a major component in all the pelites, occurs as an accessory mineral in the calc-silicate layer and is present in subordinate amounts in the dolomitic marble units. Despite the importance of graphite in the Merelani area, its nature and origin has not yet been determined. In this study six graphite samples from different lithological units were analysed for its  $\delta^{13}\text{C}$  values. The  $\delta^{13}\text{C}$  values obtained for the graphite ranged from  $-22.85\text{‰}$  to  $-26.74\text{‰}$  (Table 8.1).

In general, the  $\delta^{13}\text{C}$  values for graphite occupy a large possible range from  $> -1\text{‰}$  to  $< -50\text{‰}$  depending on various factors such as grade of metamorphism and composition of original organic matter (Bowen, 1988). The  $\delta^{13}\text{C}$  values ( $-22.85\text{‰}$  to  $-26.74\text{‰}$ ) for the Merelani tanzanite deposit are typical of graphite from an organic origin and are very similar to  $\delta^{13}\text{C}$  values obtained from organic Archaean carbon by Vry et al. (1988). The abundant graphite within the deposit therefore appears to originate from the metamorphism of original Archaean organic material. It is however also possible that some of the graphite could have formed from the decarbonation of the marble units. Decarbonation of this nature would occur near or at peak metamorphic conditions (ca. 9 – 12 kbar and 800 – 900 °C). The  $\text{CO}_2$  expelled from the marble may have produced graphite that would then isotopically fractionate, under the high temperature and pressure with the organic graphite. Due to the abundance of organic graphite, fractionation would cause only slightly higher  $\delta^{13}\text{C}$  values for the marble graphite than those of the organic graphite (Bowen, 1988). This may account for some of the high graphite concentrations observed in certain calc-silicate skarn boudins within the deposit.

Eleven quartz samples from different localities in the Merelani deposit were analysed for  $\delta^{18}\text{O}$ . The  $\delta^{18}\text{O}$  values range from  $19.62\text{‰}$  to  $21.77\text{‰}$ , for the different units (Table 8.1). All the  $\delta^{18}\text{O}$  values of the quartz minerals correlate well with values for quartz from metamorphosed shales (Hoefs, 1997). There is however, a tendency for quartz in the calc-silicate units to have higher  $\delta^{18}\text{O}$  values (e.g.  $21.95\text{‰}$  and  $21.77\text{‰}$ ) compared to that of the pelites (e.g.  $19.62\text{‰}$ , Table 8.1).

Chamberlain et al. (1990) and Stern et al. (1992) suggested that in closed system reactions, small  $\delta^{18}\text{O}$  (1–2‰) isotopic resetting can occur, opposed to the large isotopic resetting observed (e.g. Cartwright and Valley, 1992; Cartwright et al., 1995) as a result of copious amounts of external fluid infiltration. This would imply that the abundant quartz found in the calc-silicates, especially in the low-pressure sites, was not isotopically overprinted by externally derived fluids. Thus, the majority of fluids involved in the mineralisation of tanzanite and associated minerals were derived from the dehydration of the pelites.

According to Valley (1986) and Buick (1998) the fluids produced as a result of decarbonation of marbles are enriched in both  $^{13}\text{C}$  and  $^{18}\text{O}$  and therefore a lowering in both the  $\delta^{13}\text{C}$  and  $\delta^{18}\text{O}$  values is expected for calcite in the marble. It is however not possible to lower the  $\delta^{18}\text{O}$  for carbonates by more than ca. 2 to 3‰ through devolatilisation alone. Thus, where decarbonation is the primary isotopic fractionation process, large scale lowering of  $\delta^{13}\text{C}$  values and small scale lowering of  $\delta^{18}\text{O}$  values of the calcite is to be expected. A slight increase in  $\delta^{18}\text{O}$  is therefore typical for quartz forming from the fluids released through the decarbonation reaction.

The decarbonation of the marble unit may have been followed by an influx of fluids from some external source. Most of the fluids originate from the dehydration of the pelitic units neighbouring the calc-silicate unit, but additional externally derived hydrothermal fluids may also have circulated. These fluids could lower the  $\delta^{18}\text{O}$  values of the quartz in the pelites, but were probably buffered by the calc-silicate unit, contributing to the variation in the  $\delta^{18}\text{O}$  values for the quartz.

The isotopic signature of the marbles all contains very high  $\delta^{18}\text{O}$  values (ca. 25 – 28 ‰) and relatively high  $\delta^{13}\text{C}$  values (2 – 4 ‰). These values compare very well with that of unaltered marbles (25  $\delta^{18}\text{O}$  and 0  $\delta^{13}\text{C}$ ) as defined by Buick (1998) and Hoefs (1997), indicating a lack of isotopic excursion. The values are consistent with a dolomitic protolith that has not been infiltrated by any externally derived fluids (I Buick, La Trobe University, pers. comm.).

The isotopic signature of the calcite sample ( $24.2 \delta^{18}\text{O}$  and  $-8.5 \delta^{13}\text{C}$ ) in the boudinaged calc-silicate layer indicates a large decrease in  $\delta^{13}\text{C}$  and very little decrease in  $\delta^{18}\text{O}$  values compared to the unaltered marble signature. This is in agreement with expected  $\delta^{18}\text{O}$  and  $\delta^{13}\text{C}$  values as a result of decarbonation. The values indicate only a slight possible influence from externally derived hydrothermal fluids, since these would cause significant depletion in the  $\delta^{18}\text{O}$  values for calcite, quartz and zoisite. It can therefore be assumed that devolatilisation followed by dehydration and internal fluid circulation was the major driving force in the crystallisation of most of the minerals in the calc-silicate units.

It is possible that the carbonates interacted with the abundant organic graphite present in the surrounding pelites. A complete equilibration reaction between calcite and organic graphite is however unlikely, as this would result in  $\delta^{13}\text{C}$  values of around  $-20\text{‰}$  and even lower. Limited diffusional exchange between calcite and graphite could possibly explain the slightly higher  $\delta^{13}\text{C}$  values of ca.  $-23\text{‰}$  for graphite in the calc-silicate zone, compared to the  $-25.5\text{‰}$  in the pelites.

#### 8.4. Origin of the fluids

The timing and origin of the fluid-flow during metamorphism, especially of granulites is a highly controversial topic. This is further complicated by the complex nature of the fluids in the Merelani tanzanite deposit (see Chapter 10). As indicated, the isotope signature of the skarns indicates that the hydrothermal fluids originated from an internal source, instead of being derived from an external source. Thus, four possible models can be postulated to explain the origin of the hydrothermal fluids resulting in the formation of tanzanite and associated minerals:

- 1) The internal origin of the hydrothermal fluids suggests that the fluids were expelled through the dehydration of the pelites during increased metamorphism. The pelites would subsequently be completely dehydrated when it reached granulite facies. This therefore implies that the formation of tanzanite and its associated minerals occurred during the prograde metamorphic P-T path. It is generally accepted that the progression from amphibolite to granulite facies is accompanied by a decrease in  $\text{H}_2\text{O}$ -activity and that many granulite facies terrains are characterised by low water fugacities ( $f \text{H}_2\text{O}$ ). The mechanisms



resulting in the low H<sub>2</sub>O-activity for granulites at peak metamorphism are described by Lamb et al. (1987) and Valley et al. (1990). Fission track dating performed by Naesser and Saul (1974) of tanzanite indicates an approximate age of  $585 \pm 28$  Ma for the formation of tanzanite. This age would however post-date granulite facies conditions within the Mozambique belt of north-eastern Tanzania. It is however possible that the 585 Ma age does not represent the age of tanzanite formation, but only a later Mozambique overprint, suggesting that tanzanite formation could be older than  $585 \pm 28$  Ma. However, a prograde metamorphic origin for tanzanite does not agree with the petrographic and structural observations, as described in Chapters 4 and 5.

- 2) The hydrothermal fluids resulting in the formation of tanzanite could be derived from an external source, such as the presence of an igneous intrusion. Since the isotopic study is relatively limited, more detailed isotope analyses of the deposit could result in a better understanding of the fluid source and possibly indicate an external fluid origin. It is also possible that the standard external isotope signature could have been masked or overprinted, due to various factors, resulting in the dehydration-type signature.
- 3) The fluids expelled from the dehydration of the pelites during prograde metamorphism could have been trapped within the system and only liberated at a later stage. The fluids could have accumulated within structural traps formed by the impermeable dolomitic marbles. These fluids could subsequently be released during the F2 folding event as described in Chapter 5 and would migrate and interact along the shear zones, especially the JW-zone. This type of scenario could explain the  $585 \pm 28$  Ma age of tanzanite as well as the petrographic and structural observations.
- 4) Studies by various authors such as Valley et al. (1990), Lamb et al. (1987), Watson and Brenan (1987), Todd and Evans (1993) and Newton (1986), led to new insight on of the subject of fluid behaviour during retrograde metamorphism. The retrograde path of granulites may involve an increase in H<sub>2</sub>O-activity under selected P-T conditions. The H<sub>2</sub>O-activity is especially sensitive to the P conditions, with a decrease in P resulting in an increase in H<sub>2</sub>O-activity. Harlov et al. (1998) indicated that in the case of supercritical salt solutions, pressures of  $\leq 5$  kbar are needed for the H<sub>2</sub>O-activity to be proportional to the mole fraction. Therefore, if we assume a period of near

isobaric cooling as proposed by Muhongo et al. (2000) for the Merelani area and also proposed in Chapter 9, then there may have been a substantial drop in T before P dropped enough for an increase in the H<sub>2</sub>O-activity to occur. The drop in pressure was probably related to the exhumation of the granulites due to crustal underplating during the waning stage of metamorphism (Appel et al., 1998). The post-metamorphic fluids may therefore interact with the rock upon uplift. These fluids would subsequently have an “internal” isotope signature and fit in well with the petrographic and structural observations.

The isotopic evidence therefore suggests that the fluids involved in tanzanite mineralisation originated through above-mentioned scenario 3 or 4. Regardless of the origin of the fluids, all fluids would migrate and concentrate along the shear zones such as the JW-zone.

## **8.5. Conclusions**

The carbon isotope signature of the graphite from the Merelani deposit indicates that the graphite is of organic origin and possibly Archaean in age. Small amounts of graphite, probably located within the calc-silicate boudin, could have formed from the carbonate decarbonation. The oxygen isotope signatures of quartz and tanzanite indicate that the majority of fluids within the graphitic gneisses and calc-silicates originated from the dehydration of the pelites. The isotopic signature of the marbles also indicates no infiltration of externally derived fluids. The migration of fluids was concentrated along the shear zones and resulted in the crystallisation of tanzanite within low-pressure pockets situated within the boudin structures hosted by, for instance, the JW-shear zone. Tanzanite mineralisation is therefore primarily the result of fluid recycling within the metasedimentary package.

Table 8.1. Oxygen and carbon stable isotope values from the Merelani tanzanite deposit.

Carbon - Stable Isotope (Graphite)			
Sample code	Description	Value(‰)	
ITZ 2	Tanzanite-bearing rock	-26.01	
ITZ 5	Calc-Silicate	-23.48	
ITZ 10	JWZ LHD 2	-24.35	
ITZ 12	Upper Horizon Gneiss	-25.57	
ITZ 15	HW	-26.74	
ITZ 19	Block D	-22.85	
Oxygen Isotope (Quartz)			
Sample	Description	Value (‰)	
ITZ 3	Tanzanite-bearing rock	21.1	
ITZ 6	Sample 3x	21.26	
ITZ 7	Boudins 8A	21.95	
ITZ 8	Sample 2x	20.64	
ITZ 11	JWZ LHD 2	20.94	
ITZ 13	Pelite Upper Horizon	19.62	
ITZ 14	LHD 2 (133 m)	19.62	
ITZ 16	HW	20.27	
ITZ 18	Block D	20.78	
ITZ 20	Block D (2)	21.77	
ITZ 21	Block C pegmatite	21.04	
Oxygen Isotope (Zoisite)			
Sample	Description	Value (‰)	
ITZ 4	Tanzanite-bearing rock	17.3	
ITZ 9	Boudin 8A	17.39	
ITZ 17	Block D	18.49	
Oxygen / Carbon isotopes (Marbles)			
Sample	Description	Carbon (‰)	Oxygen (‰)
B-14	Marble 1	2.7	25.8
B-15	Marble 2	3.2	25.7
B-43	Marble 3	2.2	25.6
B-59	Marble 4	2.6	26.2
M-1	Marble 5	3.7	26.1
M-2	Marble 6	3.7	26.1
M-3	Marble 7	3.7	28.3
M-4	Marble 8	3.7	28.2
Oxygen / Carbon isotopes (Calcite)			
Sample	Description	Carbon (‰)	Oxygen (‰)
ITZ 1	Calcite 1	-8.5	24.2

## Chapter 9

### Conditions of Metamorphism in the Mining Area

#### 9.1. Introduction

The metamorphic evolution of the Lelatema Mountains has been described by Muhongo et al. (1999) and Tuisku and Muhongo (1999). These studies established that the first metamorphic event took place under granulite facies conditions (ca. 7 kbar and 800 °C). This was followed by a period of isobaric cooling during which the area underwent retrogression to 6.5 kbar and 610 °C. These studies mainly utilised the garnet-biotite geothermometer and garnet-plagioclase- $\text{Al}_2\text{SiO}_5$ -quartz geobarometer to establish the metamorphic P-T conditions. The peak metamorphic conditions (7 kbar and 800 °C) calculated for the Lelatema Mountains are however significantly lower than those obtained from similar granulites within NE Tanzania (9.5 to 11 kbar and 750 to 900 °C), with P-T conditions of up to 17 kbar and 1150 °C reported by Muhongo and Tuisku (1996).

The main aim of this chapter is to indicate that the commonly used garnet-biotite geothermometer and garnet-plagioclase- $\text{Al}_2\text{SiO}_5$ -quartz geobarometer is not suitable for calculating the peak P-T conditions of the Merelani area. Additional P-T estimates of the mine area will be investigated with the aim of establishing a possible P-T path for the deposit and tanzanite formation itself.

#### 9.2. Thermobarometry of the garnet-sillimanite gneiss (GNG) units

The garnet-sillimanite gneiss is the only rock unit within the mine succession on which thermobarometric calculations can be done. The petrography and mineral chemistry of the minerals within the GNG units were described in Chapters 3 and 6, respectively. The mineral assemblage of the GNG units only allows the use of the garnet-biotite thermometry for temperature calculations and garnet-plagioclase- $\text{Al}_2\text{SiO}_5$ -quartz (GASP) barometry for pressure calculations. Mineral analyses were obtained using an electron probe at the Council for Geoscience, Pretoria, RSA (as described in Chapter 6) and are listed in Addendum D.

Thermocalc (version 3.2, 2002; HP98 dataset of Holland and Powell, 1998), as well as various other geothermometric and geobarometric calculations, were used in order to establish if the GNG unit can be used for P-T calculations of the Merelani deposit. The AX program of Holland and Powell (1998) was used to calculate activities for phases in Thermocalc.

In granulite-facies rock, peak temperature conditions are usually calculated by using garnet cores and matrix biotite isolated from garnet, since these minerals are assumed to preserve their high-grade compositions. However, this is only applicable if the chemical composition of the garnets were not altered through chemical zoning. The almandine garnets from the GNG units (Chapter 6) exhibit typical granulite-facies zoning patterns (Frost and Chacko, 1989). This zoning pattern of the garnets is characterised by retrograde rims that show an increase in Fe and Mn and a decrease in Mg and  $Mg/(Mg+Fe)$  toward the rim, similar to that indicated in Figures 6.1 and 6.2 for the garnet of the GNG units. The zoning in the garnet is not related to garnet growth, but to chemical zoning as a result of diffusional processes that occurred during retrogression (Grant and Weiblen, 1971; Spear and Peacock, 1989). The increase in almandine and decrease in pyrope content at garnet rims are retrograde features and indicative of diffusional zoning (Grant and Weiblen, 1971; Spear and Peacock, 1989). Diffusional zoning is typically caused by a change in the P-T conditions without growth of the crystal (Ferry, 1992). Furthermore, it is likely that the Fe-Mg exchange reaction between garnet rim and biotite continued even after the barometric (garnet-plagioclase-aluminosilicate-quartz) reaction closed (Frost and Chacko, 1989). This is confirmed by the lack of zoning observed in the biotite. The biotite is therefore believed to be in equilibrium with the rim of the garnet and thus, the core of the garnet and the matrix biotite of the GNG units are in disequilibrium and not suitable for determination of peak temperatures through garnet-biotite thermometry.

Cooling temperatures are usually obtained from the compositions of the garnet rims and adjacent biotite. The rims of the almandine garnet from the GNG show distinct retrograde zoning patterns (Figures 6.1 and 6.2). The zoning profiles of the almandine garnets suggest that the rims of the garnet porphyroblasts were in equilibrium with the neighbouring biotite and therefore can be used to calculate the closure temperature of the rock. The closure temperatures obtained for the gneiss, as calculated by means of

various geothermometric calibrations, are indicated in Table 9.1 and vary from 489 to 670 °C.

Metamorphic pressures were estimated for garnet samples with neighbouring plagioclase minerals. The pressure was calculated in conjunction with the temperatures obtained from the geothermometry. Even though plagioclase in the garnet gneiss is virtually unzoned, the most sodic rim compositions of the plagioclase were used for the barometric calculations. The average pressures obtained from the GASP barometer, calculated according the calibrations of Ghent (1976) resulted in pressures of around 7 kbar (Table 9.1). The pressures obtained from the garnet – plagioclase barometer may be far lower than the peak metamorphic pressures of the area due to retrograde resetting and recrystallisation of the plagioclase in the matrix. The plagioclase is therefore out of equilibrium with the garnet core and therefore not suited for precise geobarometric calculations. The barometric calculations of the GNG unit is further complicated by the small amounts and grain size (< 2mm) of the plagioclase minerals in the gneiss. Ideally, plagioclase inclusions within the garnet should be used for geobarometric calculations, unfortunately no plagioclase inclusions were observed in the garnet from the GNG units.

The GASP geobarometer, as indeed most common geobarometers, are net-transfer reactions and therefore frequently have closure temperatures significantly higher than that of the exchanged reactions involved in the geothermometers. This often results in the thermobarometry indicating a near isobaric cooling path whether or not this was indeed followed by the terrain (Frost and Chacko, 1989). The isobaric cooling path indicated by Muhongo et al. (1999) and Tuisku and Muhongo (1999) for the Merelani area may well be the result of such ion-exchange re-equilibration and therefore not necessarily true.

The pressures obtained by the rocks can also be deduced from the presence of kyanite relicts within the garnet of the GNG zones, as indicated in Chapter 4. The presence of relict kyanite indicates pressures of around 5.5 kbar for the average closure temperatures listed in Table 9.1. Pressures of over 7.5 kbar are inferred from the highest recorded closure temperature (670 °C). Since closure temperatures were used, far higher pressures can be assumed for peak metamorphic conditions.

Thermocalc was unable to calculate P-T conditions from various analyses of garnet, biotite and plagioclase from the GNG unit due to the lack of intersection between the barometric and thermometric calibration curves.

*Table 9.1. Garnet-biotite geothermometric and GASP barometric calculations from the garnet-sillimanite-biotite gneiss (GNG) units.*

Avg. Temperature Calculation (°C)	Sample 082		Sample 108	
	Core	Rim	Core	Rim
Ferry and Spear (1978)	717	538	627	586
Hodges and Spear (1982)	709	531	620	588
Indares and Martignole (1985)	549	535	530	489
Dasgupta et al. (1991)	682	670	667	627
Bhathacharya et al. (1992)	607	600	589	568
Avg. Pressure Calculation (bars)	Sample 082			
Ghent (1976)	7033			

### 9.3. Isotopic thermometers

Isotope values for co-existing minerals can also be used as possible geothermometers. Assuming that quartz and zoisite formed together under retrograde metamorphic conditions, as discussed earlier, oxygen isotope partitioning can be used to determine the temperature of formation. In order to use this technique, it is assumed that the minerals equilibrated with oxygen from the same reservoir at the same temperature, with no subsequent alteration in isotopic composition. If this is the case, then the different  $\delta^{18}\text{O}$  values of two co-existing minerals, as indicated in Table 8.1, can be used to determine the temperature of final equilibration (Bowen, 1988). The equation

$$\delta^{18}\text{O}_{\text{quartz}} - \delta^{18}\text{O}_{\text{zoisite}} = 1.56(10^6\text{T}^{-2}) \quad (20)$$

is used to determine the fractionation of oxygen in the quartz-water and zoisite-water system. Similar equations, with empirical values determined by Friedman and O'Neil (1977) were used for quartz-calcite and calcite-zoisite fractionation calculations.

Substituting  $\delta^{18}\text{O}$  values given in Table 8.1 for co-existing minerals in their relevant positions in equation **20** yields quartz and zoisite (tanzanite) equilibration values of

649.3 °C and 698.6 °C. Similarly, if  $\delta^{18}\text{O}$  values for calcite and zoisite with their fractionation factor of 1.06 (Friedman and O'Neil, 1977) are substituted into equation 20, temperatures of ca. 400 °C are obtained. The  $\delta^{18}\text{O}$  values of calcite in the calc-silicate boudins, as discussed in Chapter 8, are not significantly altered by decarbonation and subsequent metasomatism. It is therefore expected that calcite is not in equilibrium with zoisite. Therefore, although calcite and zoisite are currently co-existing minerals, they did not undergo oxygen fractionation and are thus not suitable for  $\Delta$  oxygen fractionation thermometry.

The disequilibria of calcite and zoisite are confirmed by the fact that quartz and calcite are also not in equilibrium (negative values were obtained from equation 20). It can therefore be concluded that the specific calcite is not in equilibrium with quartz or zoisite, but that quartz and zoisite formed simultaneously, as indicated petrographically, after peak metamorphic conditions.

## 9.4. General mineral stability fields

### 9.4.1. Garnet-sillimanite-biotite gneiss

The mineral assemblages of the garnet-sillimanite gneisses (GNG1, 2, 3) also indicate upper amphibolite to lower granulite-facies metamorphic conditions, consistent with the high-grade regional M1 metamorphic conditions of the rocks of the Mozambique Belt in north-eastern Tanzania (Kisters et al., 2000). Whitney and Dilek (1998) described similar mineral assemblages and reaction textures, in the Gümüsler gneiss in Turkey, to those observed in the garnet-sillimanite-biotite gneiss in the Merelani deposit.

These include:

- The co-existence of K-feldspar and sillimanite together with an absence of primary muscovite in the gneiss are indicative of relatively high temperature conditions in the range of ca. 640 to 800 °C. The co-existence of K-feldspar and sillimanite occur along the “second sillimanite isograd” reaction:



The reaction is valid for pressures ranging from 2 to 6 kbar (Helgeson et al., 1978 and Spear, 1993).



- The absence of growth zoning in garnet and the presence of diffusional zoning imply the partial homogenisation of growth zoning. This in turn also only occurs at relatively high temperatures. The homogenisation of the core of the garnet might imply limited consumption during the growth history of the garnet.
- The partial melting, as described in Chapter 6 for the garnet-sillimanite gneiss, occurs above 650 °C. Spear and Parrish (1996) described the presence of primary K-feldspar inclusions in garnet as indicative of garnet growth continuing at high temperatures. This suggests temperatures similar to those obtained from the geothermometric calculations (ca. 700 °C).
- The presence of kyanite relicts in the garnet suggests that the garnet was in the kyanite zone during some stage of its growth. This implies either a drop in pressure at ca. 700 °C or an increase in temperature during the growth of the garnet from the kyanite zone into the sillimanite zone. As indicated in Chapter 6, the petrographic evidence favours an increase in temperature.

#### 9.4.2. Banded Calc-silicate hornfels (BCF)

Certain pressure and temperature deductions can be made from the presence of meionite and its formation reactions (see Chapter 6). This is enhanced by the fact that meionite has the most restricted  $T - X_{CO_2}$  stability of all carbonates. Scapolite with a meionite content of 83% (see Chapter 6) is usually more stable at temperatures above ca. 650 °C and up to 1000 °C at high  $X_{CO_2}$  (Newton and Goldsmith, 1976). At temperatures <650 °C,  $X_{CO_2} \geq 0.12$  and 5 kbar, scapolite will generally break down to plagioclase and calcite. In the presence of H<sub>2</sub>O-rich fluids the scapolite would be replaced by plagioclase + grossular + cancrinite + CO<sub>2</sub>. Zoisite, plagioclase, grossular and cancrinite will form from scapolite at temperatures below 580 °C and  $X_{CO_2} < 0.12$  at 5 kbar (Aitken, 1983).

Since the plagioclase and calcite is only partially replaced by scapolite, it can be deduced that the reaction was incomplete. This implies that there was a change in metamorphic conditions between ca. 650 °C and ca. 550 °C, either in the form of a change in  $X_{CO_2}$  and  $X_{H_2O}$  or a dramatic change in temperature and/or pressure conditions.

The presence of grossular garnet with plagioclase and scapolite possibly suggests an increase in  $X_{H_2O}$ . The lack of zoisite development implies that during the increase of water activity the temperature did not drop below 580 °C or that  $X_{CO_2}$  was not sufficiently low (see Figure 2 in Aitken, 1983).

Pyrrhotite is the main sulphide mineral in the BCF and is sometimes overgrown by small euhedral pyrite crystals (see Chapter 4). This growth of pyrite at the expense of pyrrhotite implies a drop in the activity of sulphur and therefore a decrease in sulphur content during retrograde cooling. This retrograde re-equilibration of pyrrhotite and pyrite usually takes place between ca. 600 °C and 300 °C (Craig and Vokes, 1993). It is very difficult, however, to make any clear deductions from the pyrrhotite / pyrite ratio since it is influenced by a number of factors. These include whether or not the pyrrhotite is primary, sulphur activity, Fe availability and the prograde history.

#### 9.4.3. Tanzanite formation

The following reaction for zoisite formation was defined by Kerrick in 1974:



As described in Chapter 6, this reaction is proposed for tanzanite formation. Kerrick (1974) quantified the reaction experimentally at  $P_{fluid} = 2$  and  $P_{fluid} = 7$ , enabling the calculation of the temperature and  $X_{CO_2}$  conditions at the given pressures. At a constant  $P_f$  of 2 kbar, the equation is valid at temperatures of 400 to 500 °C and  $X_{CO_2}$  of 0.02 to 0.06. The temperature and  $X_{CO_2}$  conditions of the equation are almost directly proportional, resulting in an increase in  $X_{CO_2}$  with an increase in T. At a constant  $P_{fluid}$  of 7 kbar, temperature and  $X_{CO_2}$  conditions of ca. 650 to ca. 720 °C and 0.05 to 0.18, respectively, exist. The equation is therefore valid for a wide range of temperatures (400 to 720 °C) and fluid pressures (2 to 7 kbar) with only a moderate range of  $X_{CO_2}$  conditions (0.02 to 0.18) (Figure 9.1). If we assume that tanzanite formation occurred at temperatures between 550 and 650 °C, then fluid pressures of around 5 to 6 kbar and  $X_{CO_2}$  of between 0.1 and 0.2 can be deduced from the equation presented by

Kerrick (1974). Isolated prehnite replacement textures (described in Chapter 3) within the low-pressure pockets of boudins indicate that temperatures dropped below 400 °C after the crystallisation of zoisite (tanzanite) since:



at 400 °C and 2 kbar, as defined by Kerrick (1974).

### 9.5. Pressure Temperature Path

This study provided significant petrographic evidence for a clockwise P-T path for the metamorphic evolution of the Merelani area, opposed to the anti-clockwise P-T path proposed by Muhongo (1999). This would therefore imply a deviation from the standard anti-clockwise P-T path proposed by Möller et al. (2000) and Appel et al. (1998) for the other granulites in NE Tanzania.

Little information was obtained of the prograde P-T path due to the pervasive retrograde overprint. Thus, three possible prograde P-T paths can be argued, as indicated in Figure 9.2:

- 1) A high-pressure prograde path with a large isothermal decompression path is indicated by the mineral composition and initial microprobe data of the metabasites east of the deposit. This would imply pressure conditions above 12 kbar and comparatively low temperatures.
- 2) An isobaric prograde P-T path.
- 3) Adiabatic compression path with increasing pressure resulting in an increase in temperatures up to ca. 850 °C.

The maximum temperature conditions of the rocks were defined as  $880 \pm 10$  °C through the graphite lattice parameter calculations of Malisa (1988). The onset of the retrograde P-T path is characterised by isothermal decompression, which intersected the muscovite dehydration-melting curve, but not the biotite dehydration-melting curve. Muscovite is absent from the GNG units, but biotite is present and stable, inferring that the metamorphic conditions allowed for the breakdown of muscovite but not of biotite. The garnet-biotite thermometry and garnet-plagioclase- $\text{Al}_2\text{SiO}_5$ -quartz (GASP) barometry

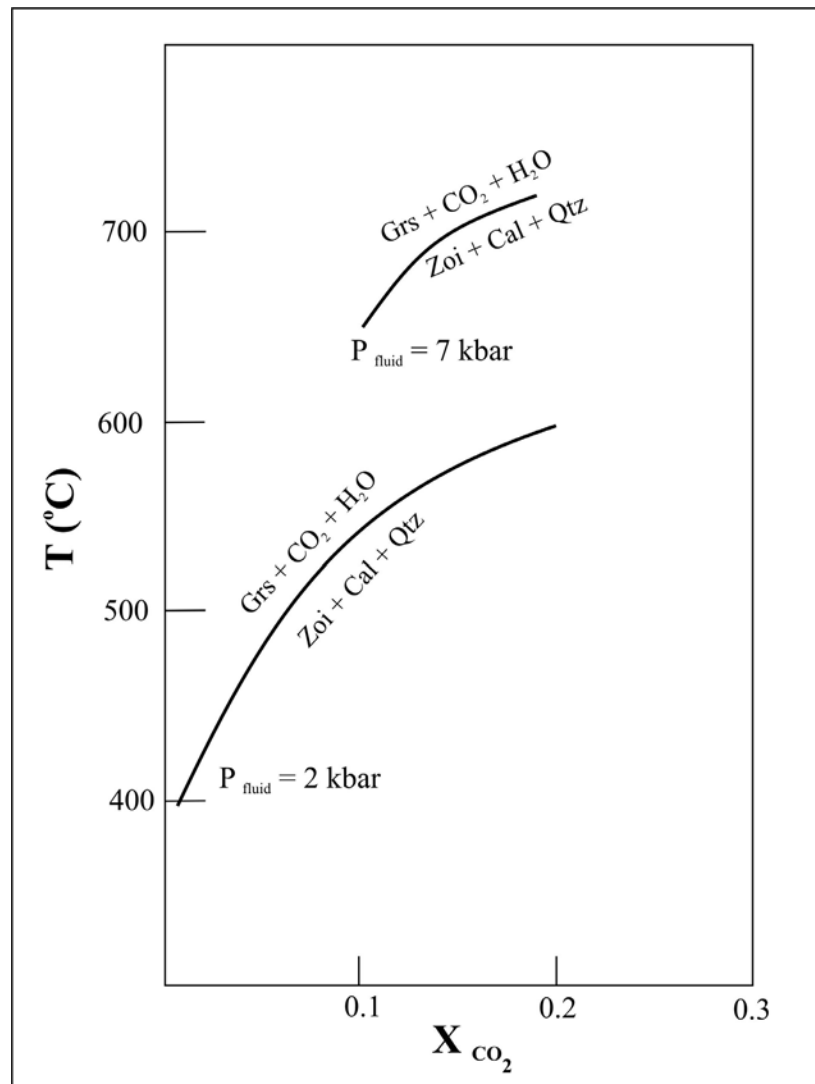


Figure 9.1.  $T$ - $X_{\text{CO}_2}$  diagram at  $P_{\text{fluid}} = 2 \text{ kbar}$  and  $P_{\text{fluid}} = 7 \text{ kbar}$  for reaction 18, proposed for the formation of tanzanite.

calculations of the GNG units indicated retrograde pressures and temperatures of 7 kbar and 720 °C. An adiabatic decompression path followed, resulting in tanzanite formation at around 6 to 5 kbar and  $650 \pm 50$  °C. The retrograde path continued, resulting in temperatures below 500 °C and ca. 4.5 kbar.

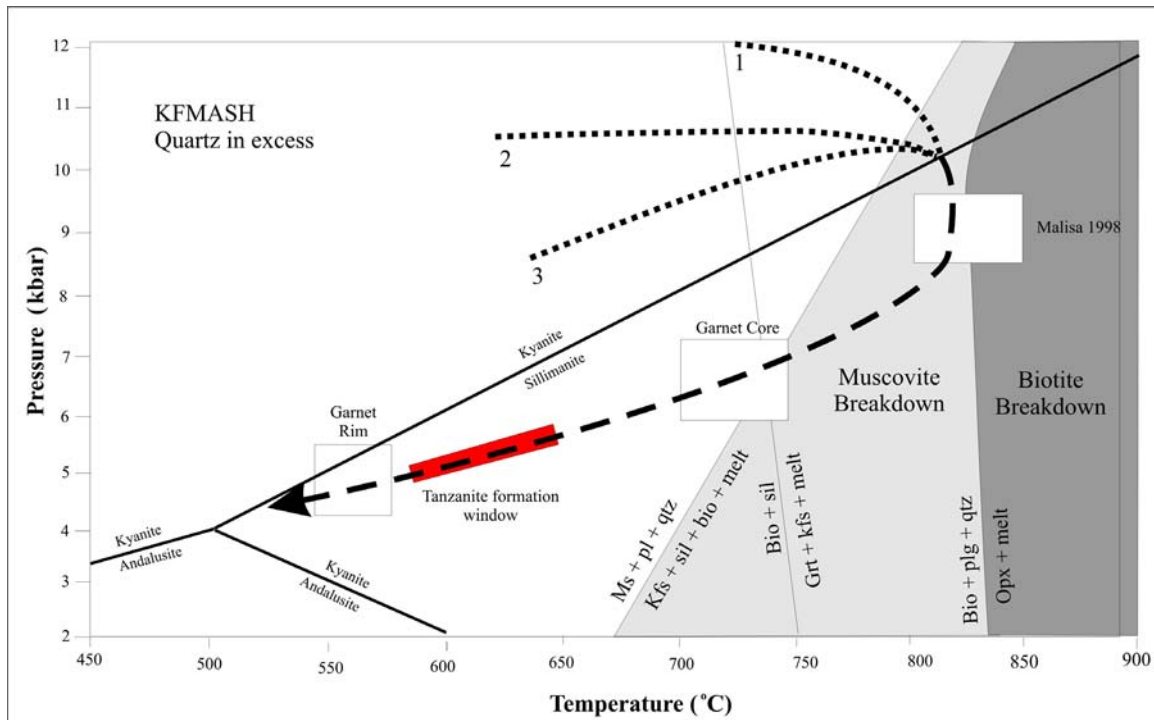


Figure 9.2. *P-T* path for the rocks of the Merelani tanzanite deposit.

## 9.6. Conclusions

Muhongo et al. (1999) and Tuisku and Muhongo (1999) calculated that the M1 event of the Merelani area occurred at lower temperature and pressure conditions (ca. 800 °C and 7 kbar) compared to the other granulite-facies rocks in the Mozambique Belt of Tanzania. Malisa (1987) calculated slightly higher pressures ranging from 7.7 to 9.1 kbar for the garnet-sillimanite-biotite gneisses within the Lelatema Mountains through the method of Newton and Haselton (1981). The Usambara granulites display temperature and pressure conditions of ca. 900 °C and 9.5 to 12 kbar, which equates to 33 – 38 km in depth. The Uluguru granulites display pressure and temperature conditions of 13 to 17 kbar and 950 °C to 1100 °C (Coolen, 1980; Muhongo and Lenoir, 1994; Muhongo and Tuisku, 1996). Muhongo et al. (1999) indicated that the M1 event within the Lelatema Mountains was followed by near-isobaric amphibolite-facies retrogression (M2) to 6 – 6.5 kbar and 670-610 °C. Möller et al. (2000) and Appel et al. (1998) indicated that the majority of the granulites in Tanzania have an anti-clockwise *P-T* evolution path. A similar anti-clockwise *P-T* path was proposed by Muhongo (1999) for the Merelani area. However, this study provided evidence for a clockwise *P-T* path and also indicated the presence of a substantial retrogressive overprint, as indicated by amongst others, kyanite replacement by sillimanite (Chapters 4 and 6) and

the garnet zonation patterns (Chapter 6). The retrogressive overprint may result in a lowering of the temperatures and especially the pressures obtained from the thermobarometric calculations of the garnet-sillimanite-biotite gneisses. It is therefore possible that the P-T conditions of the Lelatema Mountains, including the mine area, could be similar to that of the other granulite complexes of NE Tanzania. The pressure and temperatures obtained from the garnet-sillimanite-biotite gneisses are therefore influenced by retrograde metamorphic resetting.

Not enough data exists to accurately determine the pressure and temperature conditions of tanzanite formation. The isotopic temperature calculations for tanzanite indicate formation temperatures of ca. 650 to 700 °C. From the zoisite formation reaction of Kerrick (1974), as well as the structural observations and mineral chemistry (see Chapters 5 and 6) temperatures of ca. 600 – 650 °C and pressures of ca. 5 - 6 kbar can be inferred. Thus an average estimation for the P-T conditions for tanzanite formation would be ca. 5 - 6 kbar and  $650 \pm 50$  °C.

## **Chapter 10**

### **Fluid and Mineral Inclusions associated with Tanzanite**

#### **Mineralisation**

##### **10.1. Introduction**

The study of the different fluids involved in the crystallisation process of tanzanite and its associated minerals, is of the utmost importance in understanding its conditions of formation. The different fluid inclusions associated with quartz, tsavorite and tanzanite can also be used as a potential tool for the exploration of tanzanite. Fluid inclusions are abundant in tanzanite and associated quartz and tsavorite. The presence of sulphur-rich inclusions in tanzanite and associated quartz and tsavorite is evident from the distinct sulphur odour omitted when the crystals are crushed. In order to investigate the fluids associated with tanzanite mineralisation, microthermometry was conducted, by the author, on fluid inclusions in quartz, tanzanite and tsavorite. The microthermometric investigation was complimented by Raman analyses. The various mineral inclusions found in tanzanite were identified through microscopic and SEM EDAX investigations.

##### **10.2. Microthermometry**

Various subhedral to euhedral mineral specimens were selected with emphasis on the quartz and tanzanite being in equilibrium. Most of the samples were taken from isolated low-pressure pockets in boudins where shearing would be less severe in order to obtain possible primary inclusion populations.

Double polished thick sections of between 80 and 120  $\mu\text{m}$  were used for the microthermometry and subsequent Raman studies. The wafers were petrographically studied and meticulously mapped prior to microthermometric experiments (Figure 10.1). Heating experiments were done with the aim of determining the minimum temperature of entrapment, while cooling experiments give an indication of the fluid composition. All samples were analysed at least twice in order to identify “leaking” inclusions and these inclusions were subsequently omitted. The samples were analysed at the University of Stellenbosch on a Linkam TMS 92 Heating and Cooling apparatus

with a Linkam LNP 2 controller in conjunction with an Olympus BH-2 optical microscope. The instrument was calibrated by means of synthetic inclusions.

Capillary Electrophoresis analyses were conducted to determine the bulk ionic concentration of fluid inclusions. 1 gram of each sample was crushed to  $\pm 50 \mu\text{m}$  in 5 ml of deionised water and analyses on a Water Quanta 4000 Capillary Electrophoresis instrument with chromate electrolyte and a pH of 8.0 at the University of Stellenbosch.

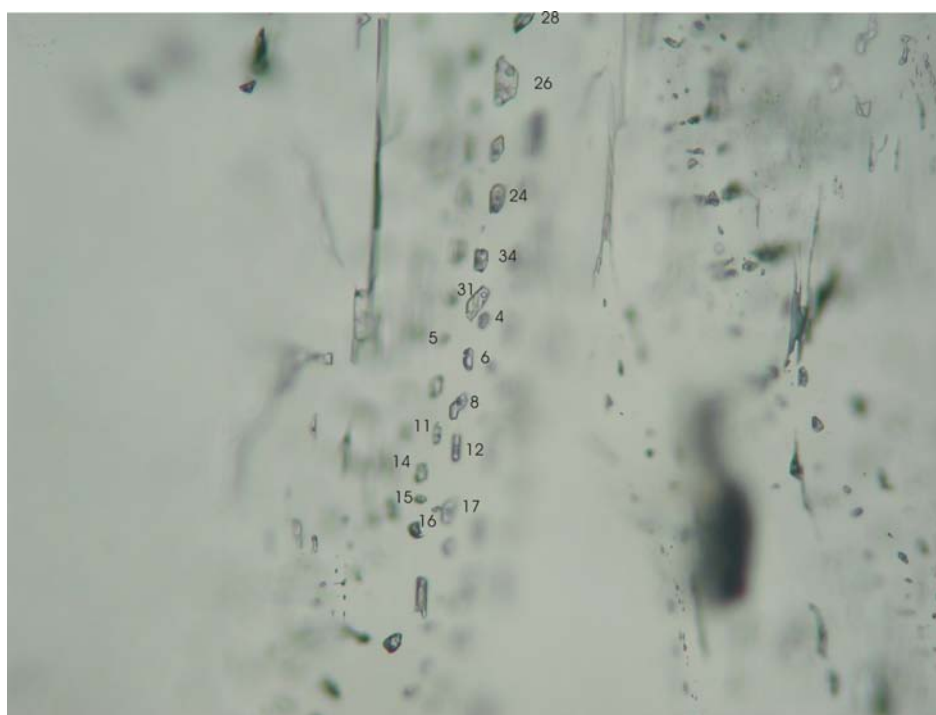


*Figure 10.1. Photomicrograph of primary fluid inclusions located within tanzanite (numbers correspond to data in Table 1, Addendum J).*

### **10.2.1. Tanzanite and Quartz**

Two quartz samples (Qtz 1 and Qtz 2) and one tanzanite sample (Tanz 1) were examined in detail. Preliminary investigations of numerous tanzanite and quartz samples were done before representative samples were selected for a more detailed microthermometric investigation. All the preliminary investigated tanzanite and quartz samples that were analysed had approximately similar homogenisation (Th) and melting (Tm) temperature values to the selected samples. All the samples were taken from high tanzanite mineralised boudins systems situated within a synformal fold. The fold is classified as DF1 according to the system proposed in Chapter 5 and is located in Shaft 1, Block C (Figure 3.1).



Three types of fluid inclusions were petrographically identified in the quartz samples, whereas only one of the three populations was found in the tanzanite sample.

### ***Type 1 inclusions***

This population is one of the dominant populations of fluid inclusions present in quartz and the only population identified in the tanzanite samples. Type 1 inclusions observed within the quartz are normally rounded with what appears to be a double liquid phase (or double meniscus) inclusion surrounding a large vapour inclusion (Figures 10.6 and 10.9). The inclusions have an average degree of fill of between 0.85 and 0.65, with the degree of fill ( $f$ ) defined as equal to  $\text{Vol}_{(\text{liquid})} / \text{Vol}_{(\text{total})}$ . The vapour phase normally vibrates under room temperature conditions. The inclusions are relatively small, with the majority being smaller than 2  $\mu\text{m}$  although inclusions of around 3  $\mu\text{m}$  have been observed. The fluid inclusions observed in the tanzanite sample are more angular and elongated than the type 1 inclusions within the quartz samples. The inclusions are normally larger than those observed in the quartz, and range up to 10  $\mu\text{m}$  in size. The degree of fill is higher in the tanzanite and is normally between 0.95 and 0.75. Vibrating vapour phases within the inclusions are also commonly observed. The population predominantly homogenises ( $T_h$ ) between 31 °C and 38 °C in the quartz sample (Qtz 1) and has its main homogenising peaks between 37.5 °C and 45 °C in the tanzanite sample (Tanz 1) (Figure 10.2). The melting temperatures ( $T_m$ ) for the population vary from –88.5 to –85.5 °C for quartz (Qtz 1) and –85.5 to –83.5 °C for tanzanite (Tanz 1) (Figure 10.3).

### ***Type 2 inclusions***

Type 2 inclusions consist of monophasic vapour inclusions. The inclusions are relatively small with the majority of inclusions <2  $\mu\text{m}$ . They are sometimes elongated and are more angular than the rounded type 1 inclusions and they are often dark brown in colour. No phase transition took place upon heating to 300 °C. Decreasing temperatures resulted in the formation of a possible liquid phase, and the temperature of the critical point was established at below –87 °C. The triple point could not be reached upon further cooling with the liquid nitrogen cooling system.

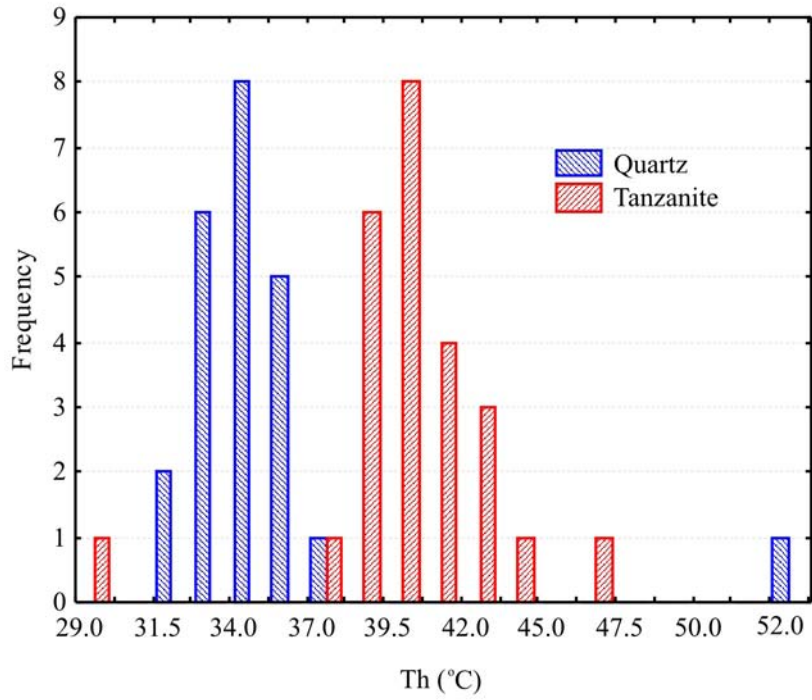


Figure 10.2. Frequency histogram of the homogenising temperatures ( $T_h$ ) of samples Qtz 1 and Tanz 1.

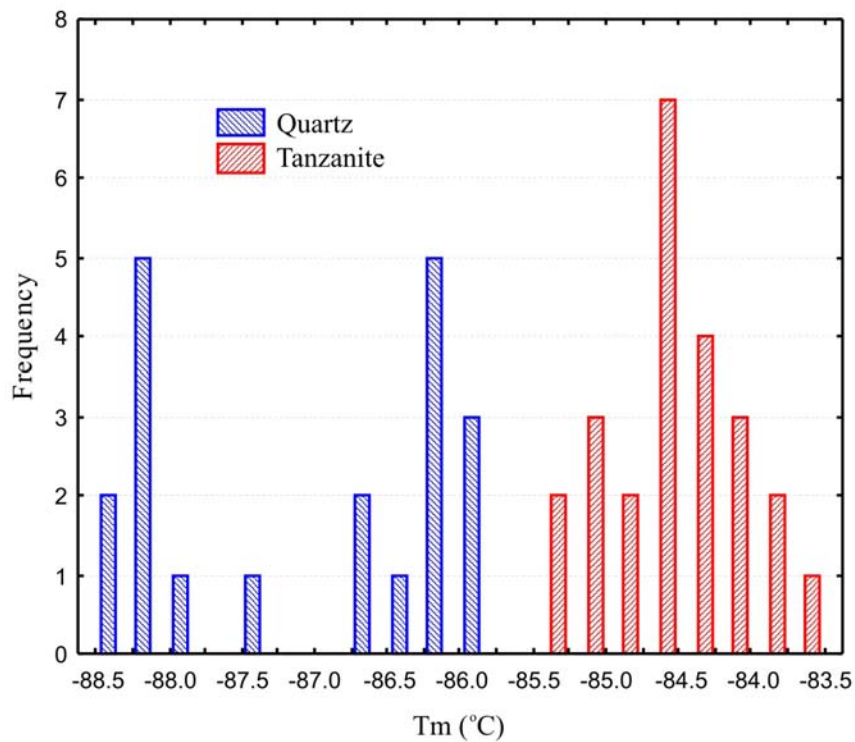


Figure 10.3. Frequency histograms of the melting temperatures ( $T_m$ ) of samples Qtz 1 and Tanz 1.

Since the inclusions could not be accurately studied with the liquid nitrogen cooling system, laser Raman spectroscopy was used in order to investigate and characterise these inclusions (Section 10.3.2).

### *Type 3 inclusions*

The shape and size of type 3 inclusions are very similar to those of the type 2 inclusions, except for the presence of a vapour phase. The vapour phase is normally quite small at room temperature resulting in a high degree of fill ( $f$ ) of between 0.90 and 0.80. The third population of fluid inclusions identified in the quartz sample (Qtz 2) has its main  $T_h$  between 140 °C and 180 °C, with only one inclusion having a higher  $T_h$  value of 210.7 °C (Table 1, Addendum J and Figure 10.4). The  $T_m$  for this population is between -5 °C and -2 °C (Table 1, Addendum J and Figure 10.5).

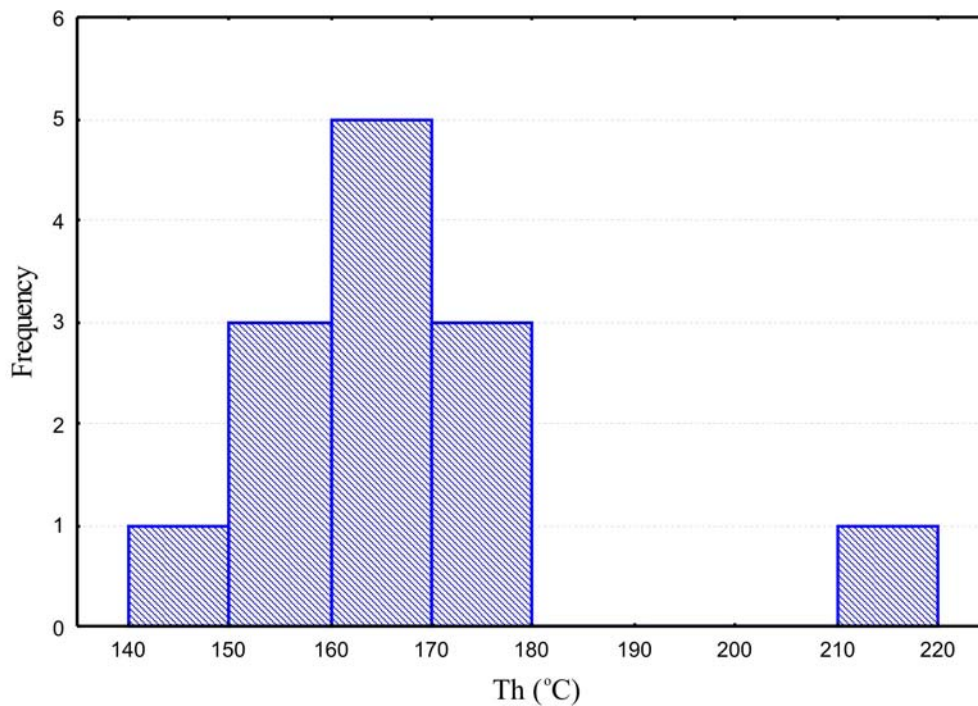


Figure 10.4. Frequency histograms of the homogenising temperatures ( $T_h$ ) of sample Qtz 2.

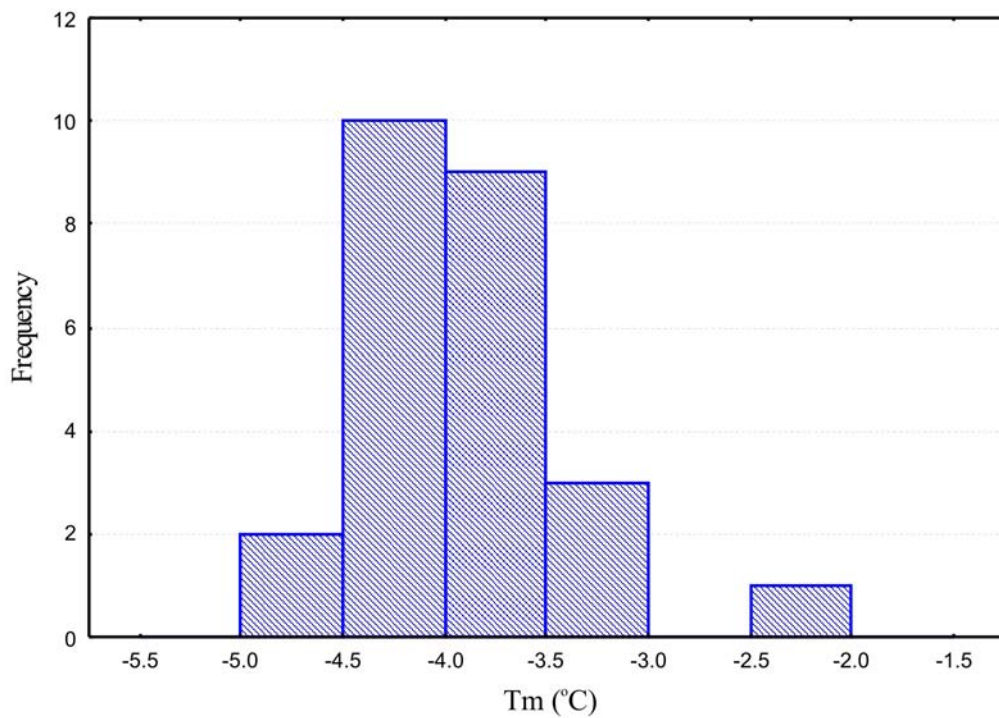


Figure 10.5. Frequency histograms of the melting temperatures ( $T_m$ ) of samples *Qtz 2*.

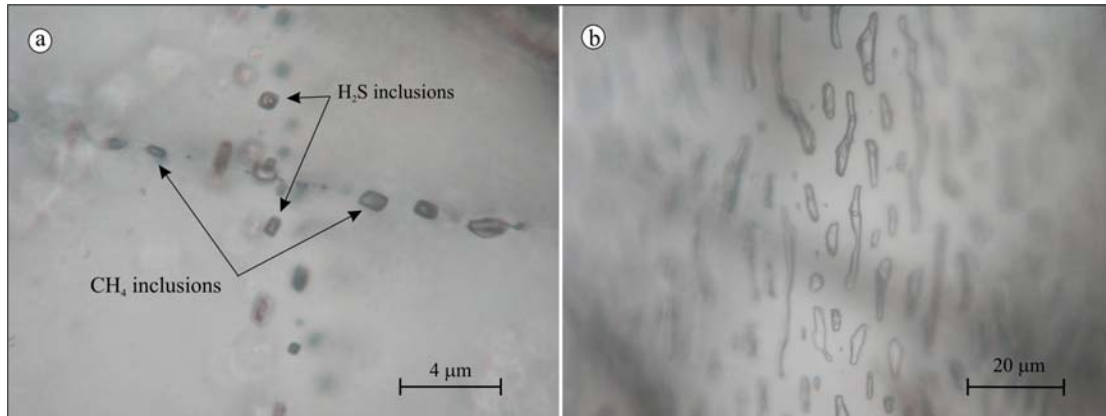


Figure 10.6.a) Type 1 ( $H_2S$ ) and type 2 ( $CH_4$ ) secondary fluid inclusions observed within the quartz samples. b) Numerous large fluid inclusions present within the tsavorite samples.

### 10.2.2. Tsavorite

Tsavorite contains more abundant and larger fluid inclusions than those present within the quartz and tanzanite samples. Inclusions of over 0.05 mm in diameter have been observed within the tsavorite samples, but the majority of the inclusions vary between 0.01 mm and 2  $\mu\text{m}$  (Figure 10.6.b).

Three tsavorite samples (Tsavo 1, 3 and 6) were examined in detail. The samples are from the same locality as the tanzanite and quartz samples described above. The homogenisation and melting temperatures of the tsavorite samples exhibit a very wide range in values. The  $T_h$  for samples Tsavo 3 and Tsavo 6 are very similar and range from  $-45.5\text{ }^{\circ}\text{C}$  to a maximum of  $30\text{ }^{\circ}\text{C}$  (Figure 10.7).  $T_h$  for sample Tsavo 1 is approximately  $45\text{ }^{\circ}\text{C}$  lower than for samples Tsavo 3 and 6 and range between  $-80\text{ }^{\circ}\text{C}$  and  $5\text{ }^{\circ}\text{C}$  (Figure 10.7). The overall size of the distribution range for the samples is very similar. The main  $T_h$  peaks for Tsavo 1 occur at around  $-25\text{ }^{\circ}\text{C}$ , while the main  $T_h$  peaks for Tsavo 3 and 6 are found between  $10\text{ }^{\circ}\text{C}$  and  $20\text{ }^{\circ}\text{C}$  (Figure 10.7).

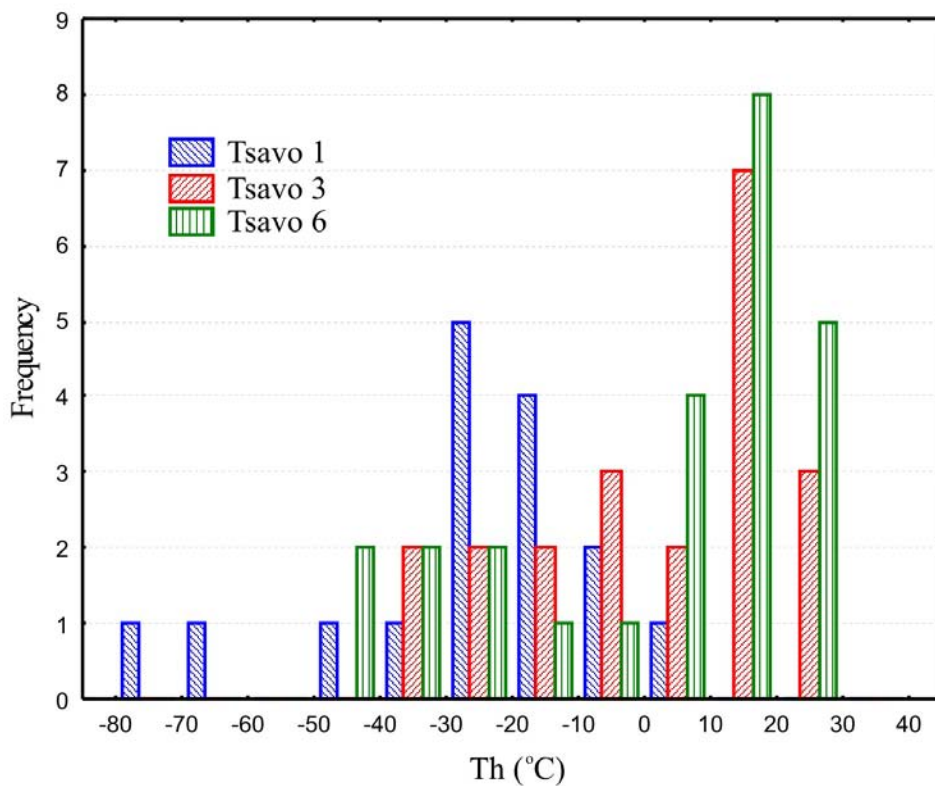


Figure 10.7. Frequency histogram of the homogenising temperatures ( $T_h$ ) of samples Tsavo 1, Tsavo 3 and Tsavo 6.

The  $T_m$  for all three tsavorite samples show very similar distribution patterns.  $T_m$  ranges from  $-120\text{ }^{\circ}\text{C}$  to around  $40\text{ }^{\circ}\text{C}$ .  $T_m$  shows two main frequency distribution peaks, a major peak located between  $10\text{ }^{\circ}\text{C}$  and  $30\text{ }^{\circ}\text{C}$  and a smaller peak between  $-100\text{ }^{\circ}\text{C}$  and  $-80\text{ }^{\circ}\text{C}$  (Figure 10.8).

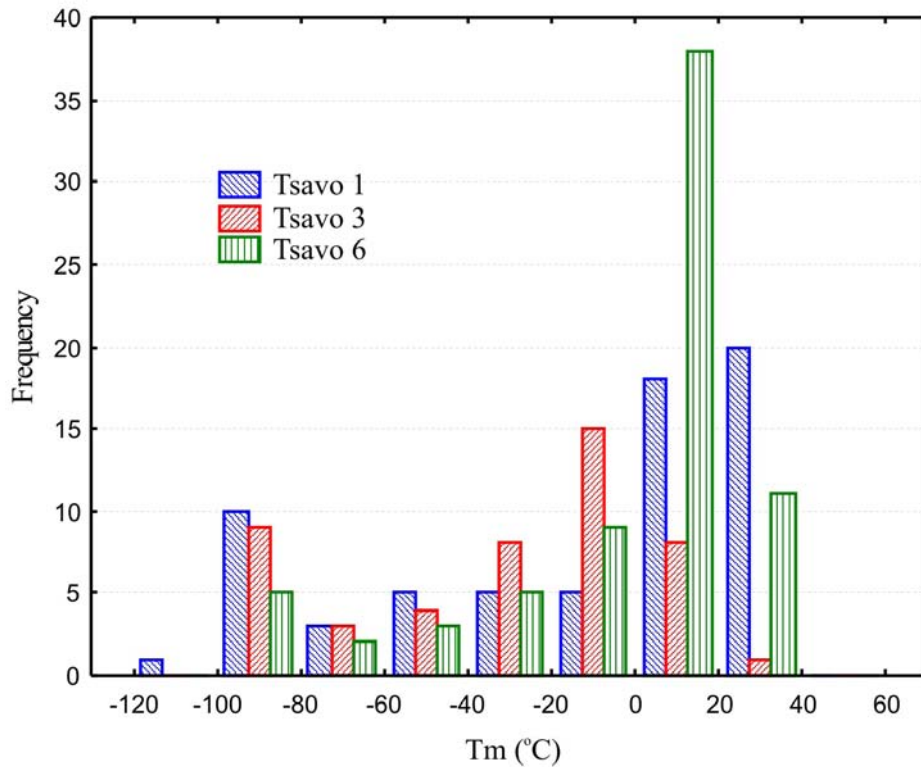


Figure 10.8. Frequency histogram of the melt temperatures of samples Tsavo 1, Tsavo 3 and Tsavo 6.

### 10.2.3. Discussion

All the fluid inclusions observed in the quartz samples normally occur along zones or lines within the quartz. It is however very difficult to determine whether the fluid inclusions occur along growth zones (therefore primary inclusions) or along annealed microcracks and deformation features (secondary inclusions).

Type 3 fluid inclusions are older than type 1 and type 2 fluid inclusions and only comprise about 5 to 10 % of total fluid inclusions present in the quartz. A petrographic investigation of the type 3 fluid inclusions suggests that the inclusions could be primary inclusions. These inclusions were only observed in samples with limited deformational features, which also support the older origin of the fluid inclusion population.

The type 1 and 2 fluid inclusions appear to be secondary fluid inclusions that formed along annealed microcracks. The two types of fluid inclusion tracks crosscut each other, but it is virtually impossible to determine the relative ages (Figure 10.9). The two types



of fluid inclusions occur in approximately equal amounts and together make up more than 90% of the fluid inclusion populations observed in the quartz samples.

As stated earlier, the type 1 fluid inclusions present in both quartz and tanzanite are quite similar and are therefore believed to be related to the same fluid / deformation event. However, while the type 1 fluid inclusions appear to be of secondary origin within the quartz samples, the inclusions might be of primary origin in terms of tanzanite crystallisation.

The type 1 fluid inclusions observed in the quartz is the only population of fluid inclusions identified in the tanzanite samples. The fluid inclusions in the tanzanite sometimes occur along cleavage planes, especially the perfect [100] cleavage plane and the [010] plane that might represent growth zones (Figure 10.1).

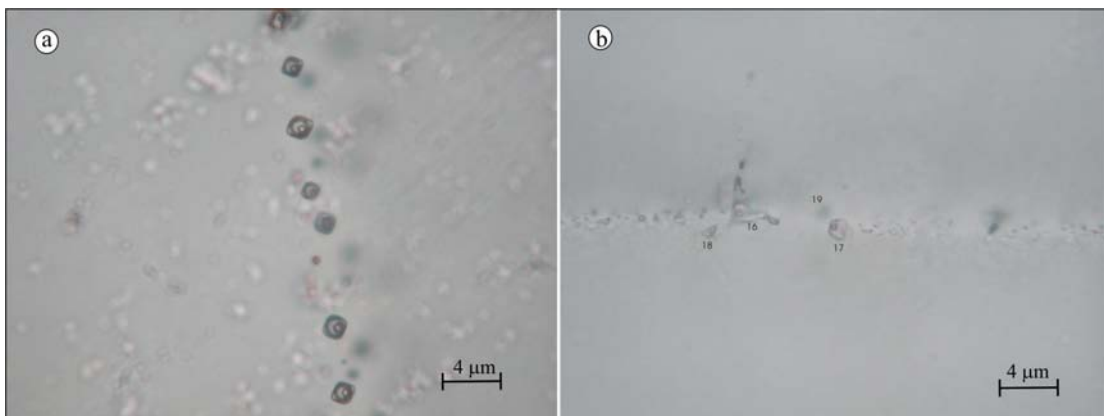


*Figure 10.9. a) Type 1 H<sub>2</sub>S-rich inclusions observed within the quartz samples with their characteristic double meniscus fluid phase and vibrating vapour phase. b) Type 3 H<sub>2</sub>O-rich fluid inclusions within the quartz samples, believed to be of primary origin.*

The only work found in the literature on fluid inclusions in tanzanite and its associated minerals was done by Malisa et al. (1986). They studied only the homogenising temperatures of 27 inclusions within tanzanite, which were found to be between 37 °C and 51 °C. These values correlate well with the data obtained in this study for the tanzanite inclusions, although their upper limit is slightly higher. They also concluded that the fluid population within the tanzanite was of primary origin.

T<sub>m</sub> of type 1 fluid inclusions (−88.5 to −85.5 °C for quartz and −85.5 to −83.5 °C for tanzanite) are close to the triple point of H<sub>2</sub>S at −85.5°C, as defined by Lemmon et al.

(2001). The slight melting point depression for the quartz sample may indicate trace amounts of other components such as CH<sub>4</sub> and N<sub>2</sub>. The amounts cannot be very high, as other phase transitions besides melting and homogenisation, are not observed. Raman spectroscopy of the quartz samples indicated that trace amounts of CH<sub>4</sub> are present in the H<sub>2</sub>S inclusions (further discussed in Section 10.3.2). If the approximated homogenisation averages of 35 °C and 40 °C for quartz and tanzanite, respectively are calculated by means of the equations of Bakker (2003), it would correspond to a molar volume of 45.79 cm<sup>3</sup>/mole (d = 0.744 g/cm<sup>3</sup>) and 46.65 cm<sup>3</sup>/mole (d = 0.73 g/cm<sup>3</sup>), respectively.

No thermodynamic modelling curves have yet been developed for the H<sub>2</sub>S ± CH<sub>4</sub> ± N<sub>2</sub> system, making P-T conditions calculation impossible (A van den Kerkhof, Universität Göttingen, pers. comm.). Roedder (1963) also reported that the determinations of the sulphur species in fluid inclusions is some of the most difficult and least accurate of all inclusion analysis.

Type 3 fluid inclusions appear to be primary fluid inclusions preserved from the quartz recrystallisation process and have an average T<sub>m</sub> of -4 °C. This would correlate with H<sub>2</sub>O inclusions with approximately 11% salt content. In order to investigate the salt composition, Capillary Electrophoresis was used. The results from these Capillary Electrophoresis analyses are listed in Table 10.1. From the table it is evident that the majority of salts present in the quartz are NaCl and KCl in a 2:1 ratio.

The fluid inclusions in 12 crystallographically orientated tanzanite samples were also optically investigated. The majority of samples appear to have a random distribution of fluid inclusions without a preferred direction of elongation. However, some samples did have fluid inclusions parallel to the [100] and [010] plane with a preferred elongation along the gamma direction (see Chapter 12).

The microthermometry results obtained from the tsavorite inclusions are complex and difficult to interpret. The wide range of T<sub>h</sub> and T<sub>m</sub> attained from the tsavorite inclusions suggests a complex mixture of inclusions (Figures 10.7 and 10.8). It is therefore possible that the ratio of compositions within the inclusions vary from inclusion to inclusion resulting in the wide data range within a sample. The three



different samples analysed show the same range of Th and Tm, which would support the argument (see Figures 10.7 and 10.8). It is also possible that the different generations and subsequent different fluid compositions are petrographically difficult to distinguish and therefore were classified as the same type of inclusion. Raman spectroscopy would have been the ideal method to investigate the fluid inclusions within tsavorite, however, the mineral unfortunately fluoresces under Raman wavelength (see Section 10.3.4).

*Table 10.1. Bulk ionic concentration (ppb) of fluid inclusions in tsavorite, quartz and tanzanite.*

	Tsavorite Sample 2	Tsavorite 991968 A	Tsavorite 991968 B	Quartz 991868 A	Quartz 99187 A	Quartz 99187 B	Tanzanite Sample 1	Tanzanite 99187
<b>Anions</b>								
<b>HS<sup>-</sup></b>	5.64			2.24				
<b>Cl<sup>-</sup></b>	10.88	4.59	2.54	3.94	12.41	19.46	41.97	33.31
<b>SO<sub>4</sub><sup>2-</sup></b>	7.26	3.19	0.05	0.55	0.48	0.75	0.31	5.87
<b>NO<sup>3-</sup></b>				0.02	0.08	0.12	0.19	3.07
<b>Ox<sup>-</sup></b>		0.1	0.05	0.04	0.08	0.13	0.33	0.14
<b>F<sup>-</sup></b>					0.15	0.24		50.73
<b>Form.<sup>-</sup></b>				0.14	0.08	1.25	0.59	
<b>HCO<sup>3-</sup></b>	38.51	26.02	10.35	1.61	0.3	0.47	20.11	13.74
<b>Ac.<sup>-</sup></b>		0.18		0.26	0.46	0.73		
<b>Prop.<sup>-</sup></b>	9.05	7.57	0.26	2.03	12.54	19.66	53.8	14.65
<b>Cations</b>								
<b>NH<sup>4+</sup></b>	2.85	2.1	0.48	0.54	12.59	19.73	10.76	15.56
<b>K<sup>+</sup></b>	3.48	2.39	1.06	1.34	8.26	12.95	10.71	6.51
<b>Na<sup>+</sup></b>	2.4	2.64	1.13	2.39	15.38	24.11	35.41	9.76
<b>Ca<sup>2+</sup></b>	156.05	95.14	45	0.8	1.06	1.66	41.4	108.15
<b>Sr<sup>2+</sup></b>							0.3	0.14
<b>Mg<sup>2+</sup></b>	2.2	0.89	0.35	0.09	2.38	3.73	3.47	4.92
<b>Mn<sup>2+</sup></b>				0.03				
<b>Li<sup>+</sup></b>				0.06	0.6	0.94	1.37	0.15
<b>Zn<sup>2+</sup></b>			0.03		1.13	1.77		13.07

### 10.3. Raman analyses

Laser Raman spectroscopy was done on the fluid inclusions studied by means of microthermometry, in order to further investigate the molecular species present in the inclusions.

#### 10.3.1 Technical specifications

Laser Raman analyses were done on a Micro-Raman system with a CCD detector at the Department of Physics, University of Witwatersrand. A laser spot size of approx. 1 $\mu$ m, 514.5 nm excitation and a single spectrograph mode with 600 grooves / mm grating was used. The samples were calibrated on the 546.074 nm Hg line.

#### 10.3.2 Quartz

The type 1 and type 2 fluid inclusions identified in the quartz samples and described in Section 10.2.1 were both analysed by means of Raman spectroscopy.

Raman analysis of type 1 inclusions within the quartz samples revealed a primary peak at 2582  $\text{cm}^{-1}$  and a smaller peak at 2915  $\text{cm}^{-1}$ . This is clearly illustrated in a typical Raman spectrum obtained from population type 1 inclusions within quartz (Figure 10.10). Raman absorption spectra for the quartz crystal structure results in the peaks at 1081  $\text{cm}^{-1}$  and 1160  $\text{cm}^{-1}$ . The primary peak located at 2582  $\text{cm}^{-1}$  correlates with the Raman peaks for H<sub>2</sub>S liquid as defined by Dubessy et al. (1992). The smaller peak observed at 2915  $\text{cm}^{-1}$  coincides with the signatures obtained for CH<sub>4</sub> by van den Kerkhof (1987) and Larsen et al. (1992).

The type 2 fluid inclusions present in the quartz samples only have one distinctive Raman peak located at around 2912  $\text{cm}^{-1}$ . This peak therefore also represents the presence of CH<sub>4</sub> as described above. A small peak is also sometimes observed around 2330  $\text{cm}^{-1}$  which would indicate the presence of small quantities of N<sub>2</sub> as defined by Andersen et al. (1989, 1993) and Darimont et al. (1988). No evidence of the H<sub>2</sub>S was observed in the population 2 fluid inclusions. Figure 10.11 shows a typical Raman spectrum obtained for the type 2 fluid inclusions present in the quartz.

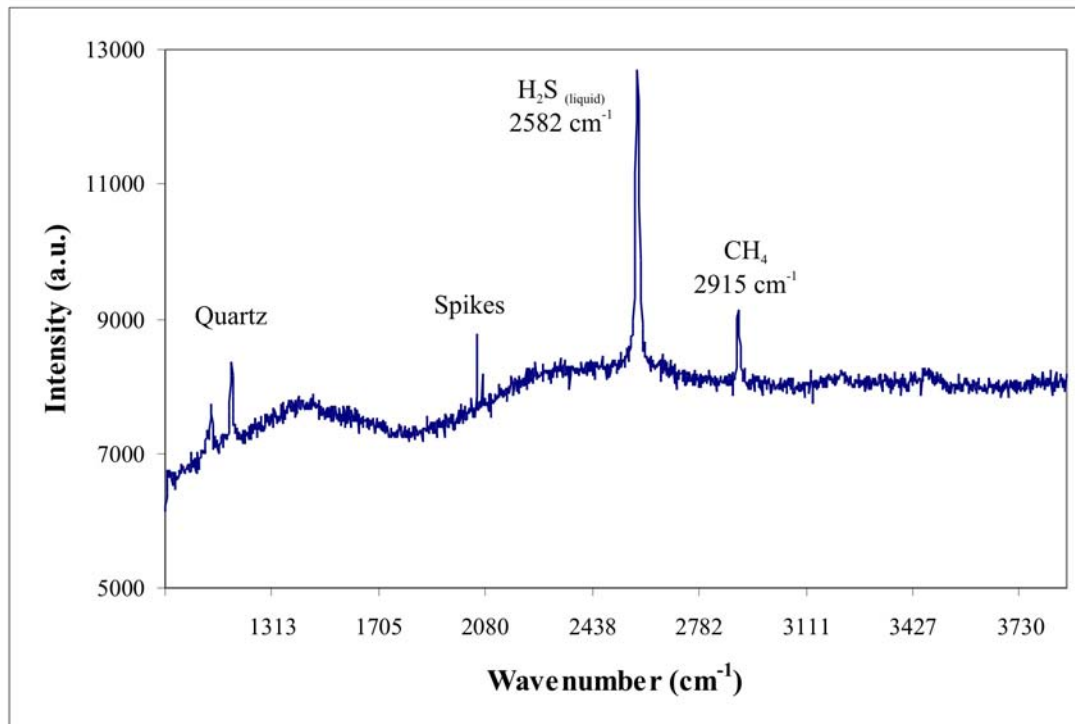


Figure 10.10. Raman spectrum of typical type 1 fluid inclusions observed in the quartz samples. The inclusions primarily consist of  $\text{H}_2\text{S}$  with minor amounts of  $\text{CH}_4$  also present. The bands of the quartz host mineral is located below  $1300\text{cm}^{-1}$  while the spikes at around  $2100\text{cm}^{-1}$  are a result of cosmic rays.

### 10.3.3. Tanzanite

Raman analyses of inclusions present in tanzanite indicate three types of fluid compositions.

- 1) The majority of fluid inclusions present in the tanzanite samples only consist of  $\text{H}_2\text{S}_{\text{liquid}}$  with its peak at approximately  $2580\text{cm}^{-1}$ .
- 2) Larger inclusions of up to  $10\ \mu\text{m}$  primarily consist of  $\text{H}_2\text{S}_{\text{(liquid)}}$  but also have two smaller peaks at  $2330\text{cm}^{-1}$  ( $\text{N}_2$ ) and  $2910\text{cm}^{-1}$  ( $\text{CH}_4$ ) (Figure 10.12).
- 3) Isolated inclusions within tanzanite produced broad Raman absorption peaks at  $2573\text{cm}^{-1}$ . Rosasco and Roedder (1979), as well as van den Kerkhof (1988), identified the Raman peaks at around  $2574\text{cm}^{-1}$  as indicative of  $\text{HS}^-$ .

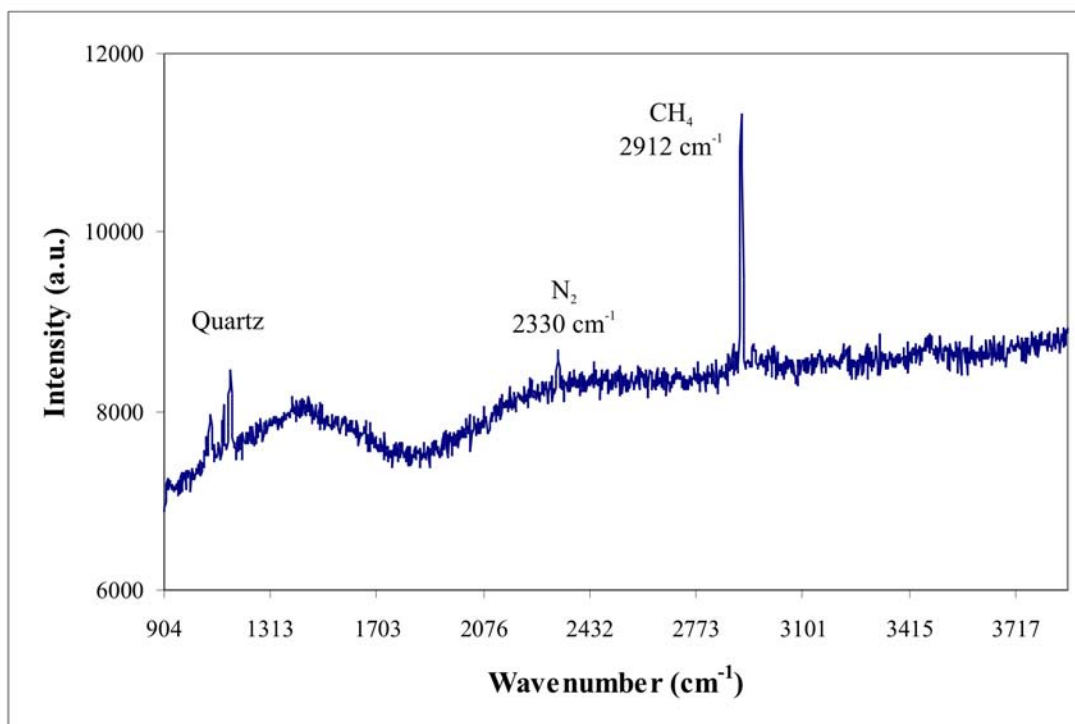


Figure 10.11. Raman spectrum of a typical type 2 inclusion observed in the quartz samples. The inclusion is primarily comprised out of  $\text{CH}_4$  ( $2912\text{ cm}^{-1}$ ), with minor amounts of  $\text{N}_2$  observed at  $2330\text{ cm}^{-1}$ .

Over 15 Tanzanite structural peaks were observed by Raman spectroscopy and are located between  $336\text{ cm}^{-1}$  and  $1100\text{ cm}^{-1}$  (Figure 10.13). An additional broad peak located at  $3153\text{ cm}^{-1}$  is probably the result of the OH groups situated within the crystal structure of tanzanite. Since laser Raman spectroscopy results in such a distinctive and clear pattern for tanzanite, the method could prove useful in the study of tanzanite structural changes during heating.

Localised areas of fluorescence within the tanzanite samples were observed. The fluid inclusions located within the fluorescent areas could not be studied by means Raman spectroscopy.

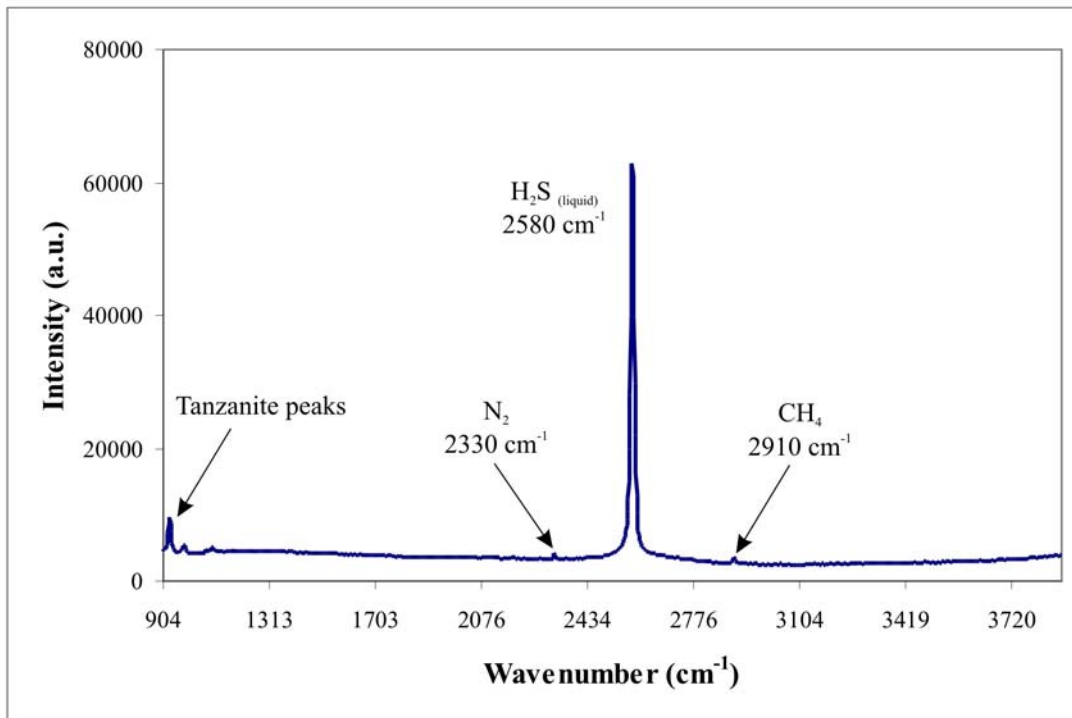


Figure 10.12. Raman spectrum of an H<sub>2</sub>S-rich fluid inclusion within tanzanite. The spectrum is dominated by the strong H<sub>2</sub>S peak located at 2580 cm<sup>-1</sup>. This inclusion also contains trace amounts of N<sub>2</sub> (2330 cm<sup>-1</sup>) and CH<sub>4</sub> (2910 cm<sup>-1</sup>) that is not always present together with the H<sub>2</sub>S-rich fluid inclusions within tanzanite.

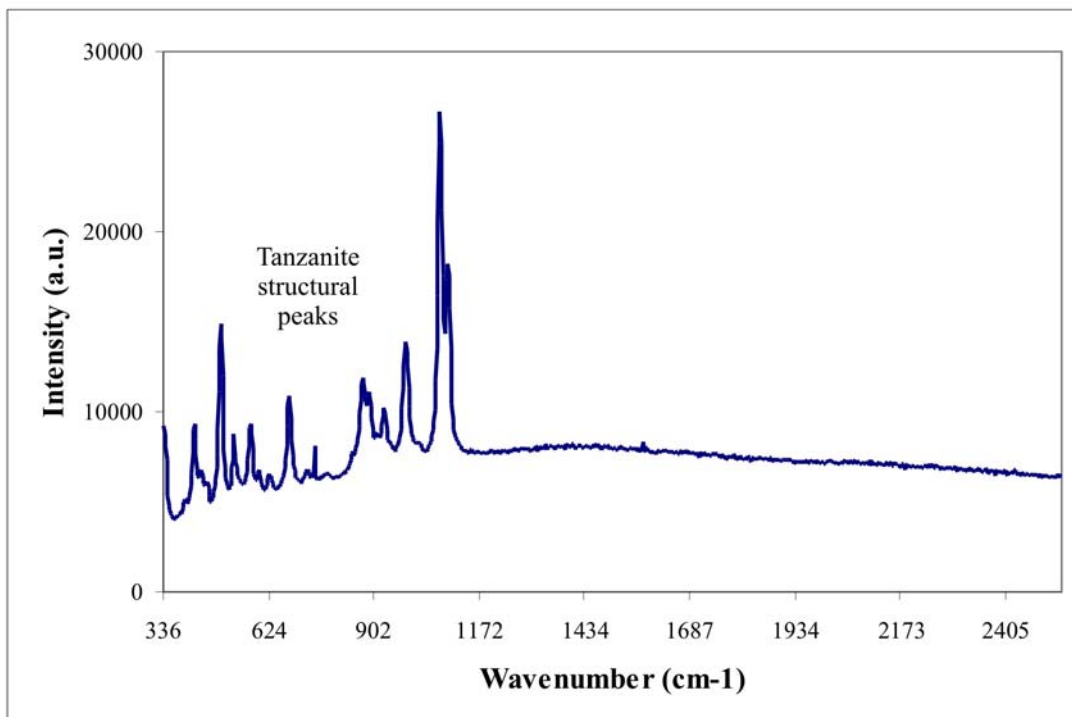


Figure 10.13. Raman spectrum of the structural bands of tanzanite.

#### 10.3.4. Tsavorite

Laser Raman spectroscopy of tsavorite proved to be unsuccessful since tsavorite is highly fluorescent. Various Raman instrumental settings including a Krypton laser beam which has a longer wavelength and therefore excites less fluorescence, were experimented with, with little success. The only peaks observed over the fluorescent background, were two small peaks situated at  $2581\text{ cm}^{-1}$ ,  $2816\text{ cm}^{-1}$  and a broader peak located at around  $3361\text{ cm}^{-1}$ . The peak at  $2581\text{ cm}^{-1}$  belongs to  $\text{H}_2\text{S}$  and is similar to the peaks observed in the quartz and tanzanite specimens and described in Sections 10.3.2 and 10.3.3. The peak at  $2816\text{ cm}^{-1}$  could not be identified through comparison with known peaks and is located between the known peaks of methanol and formaldehyde. The broad peak located at  $3361\text{ cm}^{-1}$  could be the result of a salt and OH molecular mixture as defined by Chou et al. (1990).

#### 10.3.5. Discussion

The data obtained from Raman spectroscopy correlate well with the data from the microthermometry. Type 1 fluid inclusions analysed in the quartz predominantly consists of  $\text{H}_2\text{S}_{\text{liquid}}$  and minor amounts of  $\text{CH}_4$ . As discussed, the melting point of  $\text{H}_2\text{S}$  is around  $-85.5\text{ }^\circ\text{C}$  while that of  $\text{CH}_4$  is around  $-182.5\text{ }^\circ\text{C}$ . This would explain the slightly lower  $T_m$  values of up to  $-88.5\text{ }^\circ\text{C}$  obtained for the quartz samples. The majority of Raman spectroscopy for the tanzanite inclusions indicates almost pure  $\text{H}_2\text{S}$  samples. This also agrees with the microthermometric  $T_m$  values obtained from the tanzanite inclusions, which is close to the  $T_{\text{triple}}$  values of  $\text{H}_2\text{S}$ . Raman spectroscopy of larger tanzanite inclusions did however show signs of trace amounts of  $\text{CH}_4$  and  $\text{N}_2$  together with the  $\text{H}_2\text{S}$ .

Type 2 fluid inclusions observed in the quartz samples comprises predominantly of  $\text{CH}_4$  with minor amounts of  $\text{N}_2$  and can therefore not be studied accurately with liquid nitrogen cooling stage microthermometry system.

#### **10.4. Influence of inclusions on the colour of tanzanite**

Malisa et al. (1986) described possible gas- or fluid-filled gas inclusion in microcracks that resemble natural decrepitation cracks in natural blue tanzanite. They suggested that these cracks seem to be absent from tan-coloured tanzanite. It was therefore concluded that the blue tanzanite is, in effect, tan-coloured tanzanite that was subjected to higher temperatures.

In order to investigate their hypothesis, the fluid inclusions from 20 tan-coloured and 20 natural blue tanzanite crystals were compared. A further five zoisite crystals of green colour, five pinkish crystals as well as five colourless zoisite crystals from the same locality were also preliminarily investigated in order to test the hypothesis. No apparent difference could be observed between the different coloured zoisites. The sample range was however quite small and therefore not conclusive. The theory nevertheless merits further investigation. It is however the opinion of the author that the colour of the zoisite is rather a function of the amount, valence state and site occupation of certain minor and trace elements, as will be discussed in Chapters 12 and 13.

#### **10.5. Mineral inclusions in tanzanite**

Various mineral inclusions of varying quality and colour have been optically identified within tanzanite. By far the most common mineral inclusion in tanzanite and its associated mineral assemblage (quartz and calcite) are graphite needles. Dunn (1975) also identified graphite inclusions within tanzanite and suggested that there might be an epitaxial relationship with the {0001} elongation of graphite parallel to the {010} of tanzanite. This was also observed in some of the graphite inclusions in tanzanite samples studied during the present investigation, although the majority of the inclusions appear to have a random distribution. This coincides with the preferred orientation of certain fluid inclusions within tanzanite described in Section 10.2.3. Other mineral inclusions identified through optical microscopy include actinolite needles, diopside, quartz and titanite. This agrees well with the inclusions identified by Malisa et al. (1986), who also petrographically identified xenotime and rutile inclusions while Gubelin and Weibel (1975) identified the occurrence of tremolite-actinolite needles in tanzanite. Although no xenotime was observed during the present study, SEM EDAX

studies did identify zircon inclusions in tanzanite. The SEM EDAX analysis also identified the existence of apatite and calcite inclusions within tanzanite.

SEM analysis revealed Ni-Cu metal inclusions present within tanzanite, especially along a reaction zone associated with V zoning (Figure 10.14). Initial SEM EDAX analysis of the metal inclusions indicate approximate percentages of 60% Ni, 30% Cu, 2% Fe, 1% Mn and 0.5% S.

Similar mineral inclusions appear to be present in quartz associated with tanzanite mineralisation. Quartz with large (up to several centimetres long) elongated green mineral inclusions has been observed together with tanzanite. Petrographic investigation indicated that the mineral is part of the tourmaline group. This was confirmed by means of SEM EDAX analyses, which indicated that the elongated green mineral is the Mg-rich tourmaline, dravite. It is therefore also possible that dravite can occur as inclusions within tanzanite.

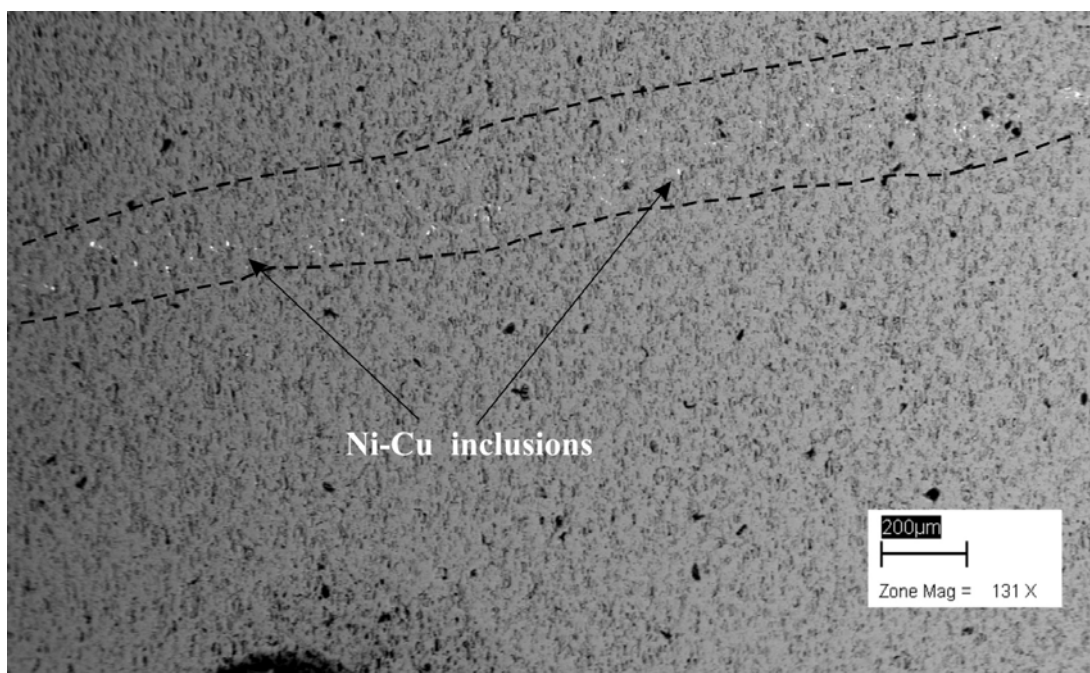


*Figure 10.14. SEM backscattered electron image of Ni-Cu metal inclusions observed within a zoned tanzanite crystal.*



## 10.6. Conclusions

The similarities between type 1 inclusions within quartz and tanzanite suggest that they formed during the same event, with tanzanite crystallisation occurring simultaneously to quartz recrystallisation. Type 1 inclusions are therefore primary in tanzanite, but secondary in quartz. The type 3 (H<sub>2</sub>O-rich) fluid inclusions are considered primary quartz inclusions, while the type 2 (CH<sub>4</sub>) inclusions are secondary, but predating the type 1 (H<sub>2</sub>S) event that coincided with tanzanite crystallisation.

In general, fluid inclusions could prove a useful tool in the exploration of tanzanite. It appears that the type 1 fluid inclusions observed in the quartz and tanzanite could be used as an important indicator of the ore-forming fluids involved with tanzanite mineralisation. A more detailed fluid inclusion study may therefore reveal further changes in the fluid compositions of type 1 inclusions within barren and tanzanite mineralised areas. The quartz samples in this study were all associated with tanzanite mineralisation and it is therefore quite possible that quartz further away from tanzanite-mineralised areas could have a different fluid inclusion population event, without type 1 inclusions. This could prove invaluable since quartz is a far more common mineral, not only within the surrounding host rock but also within the skarn boudins, compared to tanzanite. Ideally, if a continuous range of fluid inclusion compositions can be identified within quartz, which can be correlated with its associated distance from tanzanite mineralisation, it could prove to be extremely valuable in terms of tanzanite exploration. For instance, if an exploration drill hole intersects quartz then the fluid inclusions within the quartz may possibly be used as an indicator of the proximity to, or potential of, tanzanite mineralisation.

The results obtained from this fluid inclusion investigation led to further research into the use of fluid inclusions as an indicator of tanzanite mineralisation and exploration by TanzaniteOne Ltd. The initial results obtained from the follow-up fluid inclusion study indicate that the fluid inclusion populations within quartz can be used as an indicator to the proximity of tanzanite mineralisation.

## Chapter 11

### Protolith

#### 11.1. Introduction

The main aim of the protolith study of the Merelani tanzanite deposit is to investigate the nature of the sediments, the depositional environment and possible origin of the calc-silicate skarn boudins. This information is of considerable importance in understanding the deposit and also for future exploration for tanzanite deposits.

In the protolith study of the Merelani area, as is the case with most metamorphic terrains, rare-earth elements (REE's), Th, U, Zr, Hf, Y, Ti, Nb, Ta, and Sc are predominantly used since they have a low solubility during weathering, metamorphism and the diagenetic processes.

The REE and trace elements were analysed with a Perkin-Elmer Sciex ELAN 6000 ICP-MS instrument at the University of Cape Town. The sample preparation and detection limits were similar to those described by le Roux et al. (2001) and Grégoire et al. (2000).

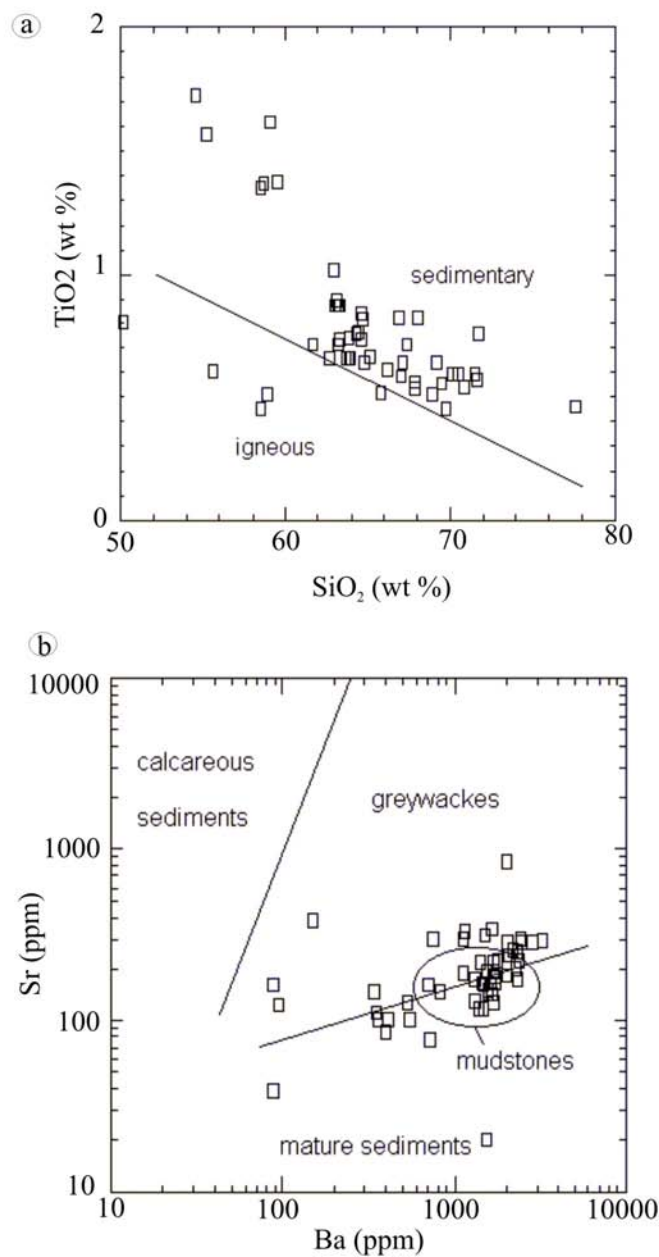
#### 11.2. Gneisses

##### 11.2.1 Major and trace elements as protolith indicators

Major and trace element data of the gneisses are indicated in Table 1, Addendum F, with REE data of selected samples listed in Table 11.1.

The first step in investigating the protolith of the gneisses is to determine whether they are of magmatic or sedimentary origin. Both Figure 11.1.a and Figure 11.1.c clearly indicate that the gneisses are of sedimentary origin, with over 90% of the samples plotting in the sedimentary field. Muhongo (1990) extensively employed the same classification diagrams in order to classify other granulite complexes and gneisses in eastern Tanzania. He concluded that the majority of the granulites are of sedimentary origin, while most of the garnet gneisses appear to be of igneous origin. He further

stated that some metasedimentary granulites and gneisses of eastern Tanzania consist of a mixture of lithic sandstones, mudstones and calcareous sediments, all of which are derived from continental upper crustal material. This also appears to be the case for the gneisses from the Merelani area, as suggested from Figure 11.1.b and Figure 11.1.c. The gneisses plot both in the greywacke and mudstone field (Figure 11.1.b) and primarily in the sandstone field (Figure 11.1.c). The trace element plots (Figure 11.1.b) further suggest that the sediments are relatively mature.



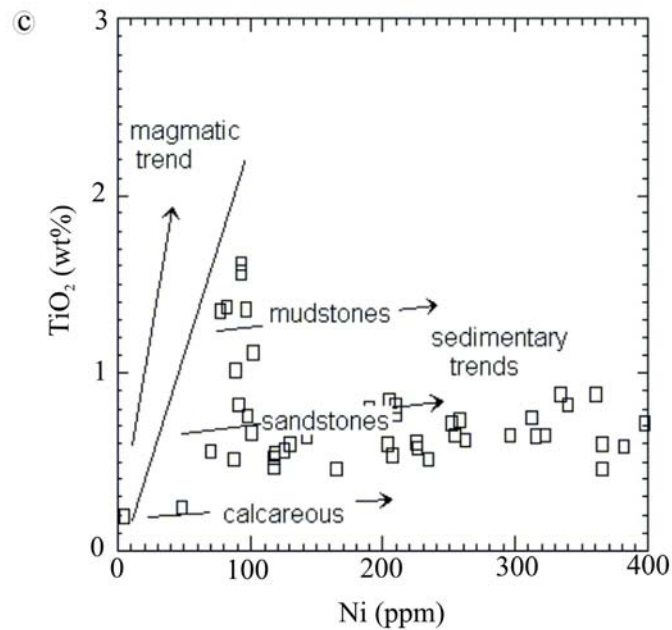


Figure 11.1. Chemical classifications of the Merelani gneisses. a)  $\text{SiO}_2 - \text{TiO}_2$  (after Tarney 1977). b)  $\text{Sr} - \text{Ba}$  plot (after Floyd et al., 1989) and c)  $\text{TiO}_2 - \text{Ni}$  (after Floyd et al., 1989).

Another possible method to investigate the geochemical characteristics of the gneisses is to compare it, through an enrichment factor, to NASC (North American Shale Composition). The enrichment factor ( $E_x^*$ ), as used by Hassan et al. (1999) and Taylor and McLennan (1985) for any element (x) is given by:

$$E_x^* = (C_x \text{ sample} / C_{\text{Al}} \text{ sample}) / (C_x \text{ standard} / C_{\text{Al}} \text{ standard})$$

where  $C_x$  is the concentration of the element,  $C_{\text{Al}}$  is the concentration of Al and NASC is used as standard.

In general, the major elements of the gneisses compare reasonably well with the NASC values, with  $\text{SiO}_2$ ,  $\text{TiO}_2$ ,  $\text{Fe}_2\text{O}_{3(\text{total})}$  and  $\text{Na}_2\text{O}$  having enrichment values ( $E_x^*$ ) relatively close to 1.  $\text{K}_2\text{O}$ ,  $\text{CaO}$  and  $\text{MnO}$  are however strongly depleted relative to NASC. The average total Fe content of the graphitic gneisses is around 6 wt%, while the GNG units have higher Fe content (ca. 12 wt%), indicating some comparison with banded iron formation (BIF). The oxidation state of the gneisses varies considerably, as indicated by

the  $\text{Fe}_2\text{O}_3/\text{FeO}$  ratios in Table 1, Addendum F. The average  $\text{Fe}_2\text{O}_3/\text{FeO}$  ratio for the gneisses is 1.47. The  $\text{Fe}_2\text{O}_3/\text{FeO}$  ratios of samples from the upper portion of the core are generally  $>2$ , while deeper samples have values of  $<1.3$ . This confirms the presence of an oxidation zone in the upper portions of the Merelani succession.

Sr and especially Rb and Ba are enriched relative to MORB (Figure 11.2.a), but compared to NASC, Sr and Ba are enriched, while Rb is depleted (Figure 11.2.b). Ba and Sr have average enrichment factors ( $E_x^*$ ) of 2.09 and 1.19, respectively, while Rb has an average ( $E_x^*$ ) value of 0.36. The enrichment in large-ion lithophile elements are sometimes contributed to seafloor alteration or to a subduction component (Cornell et al., 1996).

The Th / U ratios of metamorphic rocks are frequently used to determine the maturity of the rocks. Since most of the gneisses in this area have high graphite content, little of the uranium has been oxidised from  $\text{U}^{4+}$  to  $\text{U}^{6+}$ , resulting in higher than usual  $\text{U}^{4+}$  values and subsequently lower Th / U ratios. The Th / U values obtained for the gneisses vary considerably, from ca. 0.1 to ca. 2 (Table 1, Addendum F), depending on a few factors, most notably the graphite content of the gneiss. Despite the high variability of the Th / U content, the values are all considered very low, with ca. 4.5 typical of sedimentary rocks (Bhatia and Taylor, 1981). These values therefore also suggest a limited amount of recycling of the gneisses, implying relative immaturity. If the high graphite content is taken into account these values would suggest either an island arc volcanic or inter-arc basin environment (Bhatia and Taylor, 1981). The high La / Th values of ca. 5 (Table 7.1) also imply some degree of felsic volcanic input into the gneisses. Condie and Wronkiewicz (1990) showed that the Cr / Th ratio may also be an excellent indicator of protolith. The Cr / Th ratios for the gneisses vary between 10 and 80 with an average ratio of ca. 28. This value is very close to the Cr / Th ratio for average Archaean upper crust of 31. Cr and Sc content range from 40 to 478 ppm (avg. 193 ppm) and 6 to 26 ppm (avg. 14), respectively. The low Sc values are also indicative of a sedimentary origin for the gneisses, since Sc is enriched through magmatic processes. Both Ni and Zn are highly enriched relative to NASC, while Zr shows a slight depletion from NASC. The high concentrations of Ni (300 ppm) and especially Zn (0.45 wt%) in the graphitic gneiss and schist further support a volcanic arc protolith environment for

deposition of the deposit with a signature resembling that of a volcanic massive sulphide (VMS).

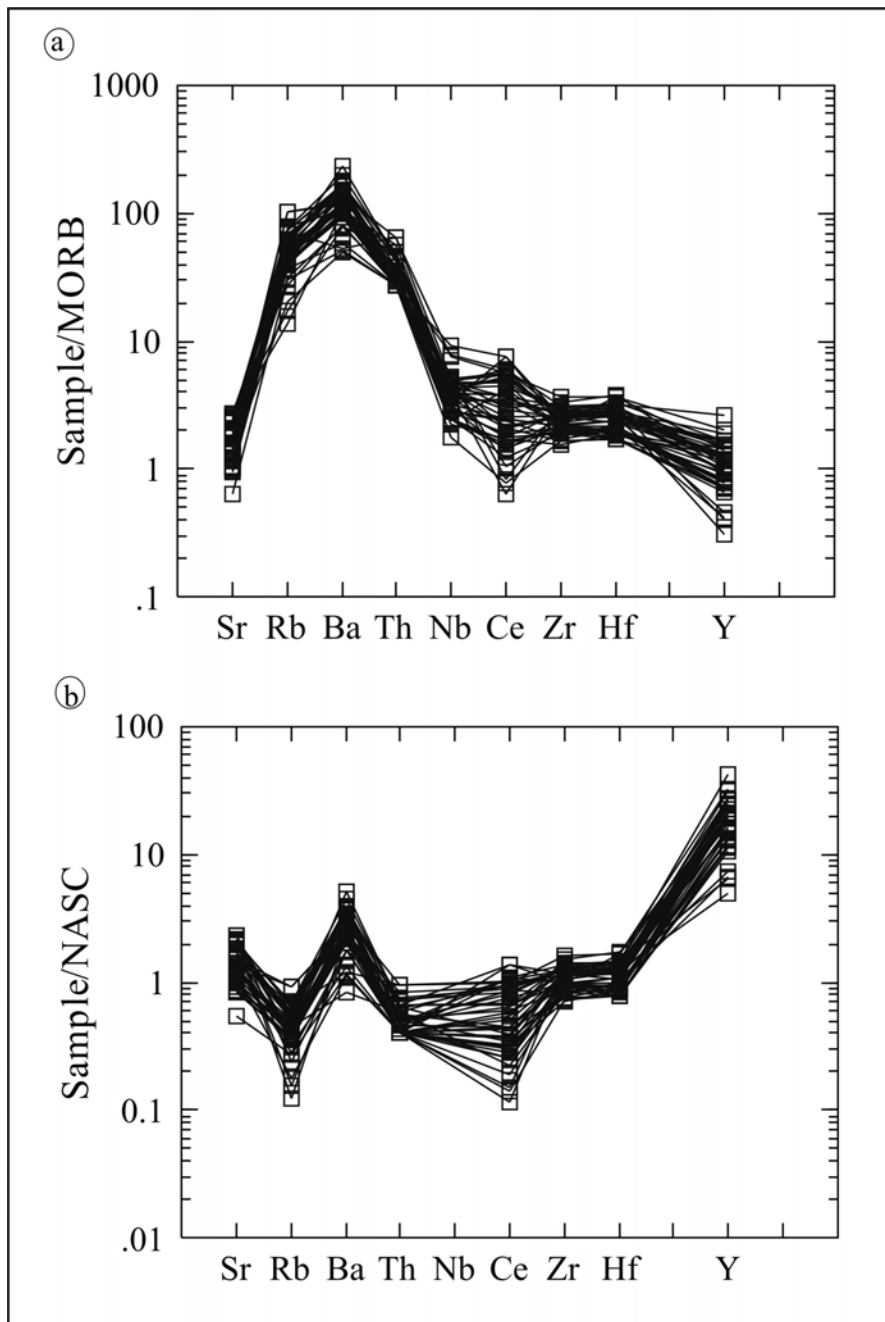


Figure 11.2. a) MORB – normalised spider diagram and b) NASC – normalised spider diagram for 43 gneiss samples.

### 11.2.2. Rare Earth Elements (REEs) as protolith indicators

The REE distribution patterns of the gneisses and schists are not significantly influenced by metamorphism and are thus useful in the protolith study of metamorphic rocks. It should however be noted that REE patterns are modified by melting and melt extraction

(Weaver, 1980). Nine gneiss samples were selected for REE analysis (Table 11.1). The chondrite - normalised patterns for the samples are shown in Figure 11.3.a, b and c. The total REE ( $\Sigma$  REE) content varies from 94.16 to 220.94 ppm with an average of 151.64 ppm.

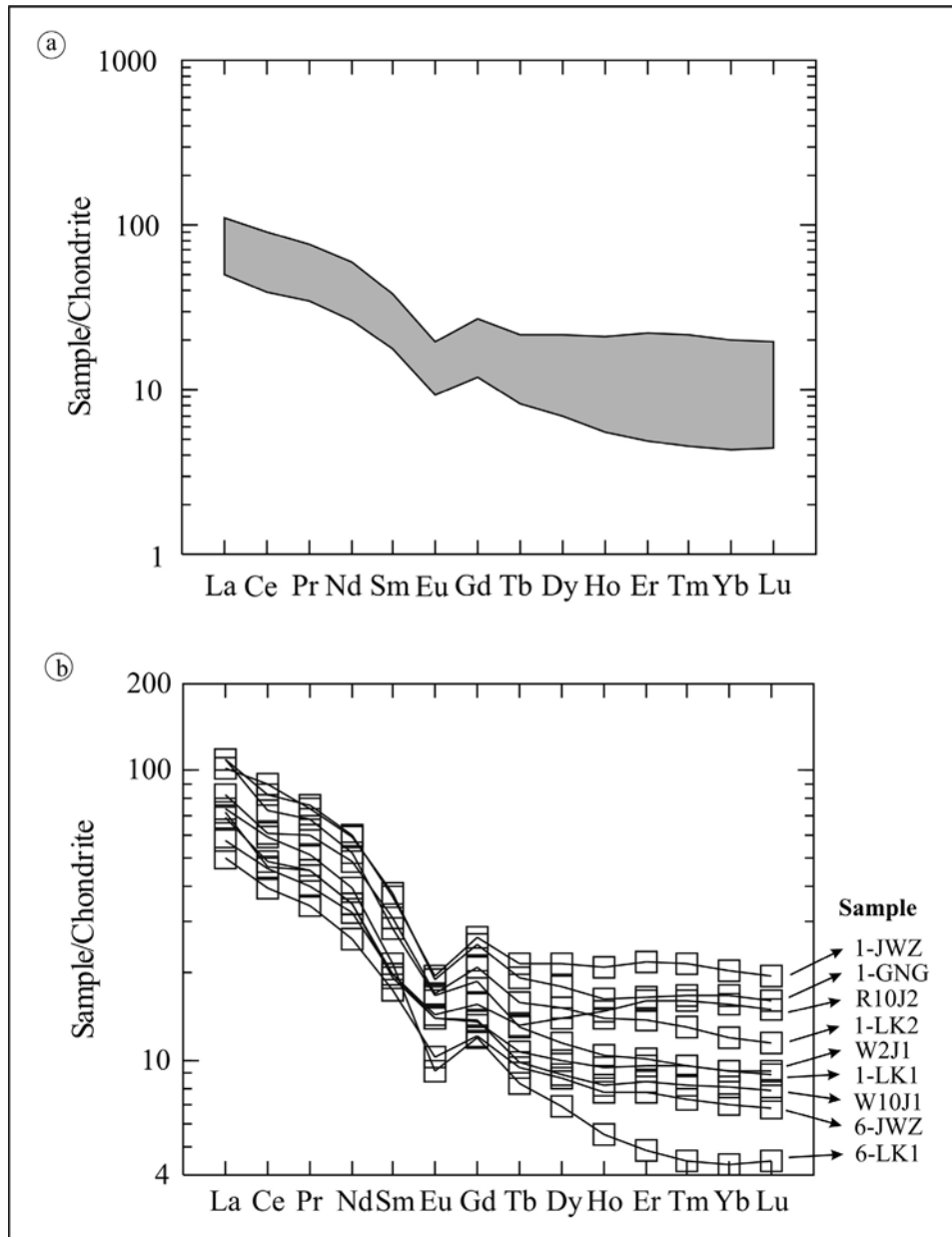


Figure 11.3. Chondrite normalised REE plots for 9 gneiss samples with a) general REE trend of gneisses and b) closer view of the gneiss REE distribution, indicating the sample names.

Even though the REE values show a considerable range, all the samples display a similar general trend and negative Eu anomaly. The average  $\Sigma$  REE content for the gneisses is quite close to the  $\Sigma$  REE for NASC of 188.68 ppm (Taylor and McLennan,

1985). The gneisses are enriched in LREE and MREE and have a moderate fractionation profile, with an average  $[\text{La}/\text{Yb}]_n$  ratio of 7.1 (Table 11.1). The LREE's display some fractionation with an average  $[\text{Ce}/\text{Sm}]_n$  of 2.35, while the HREE's are only slightly fractionated from each other, with an average  $[\text{Gd}/\text{Yb}]_n$  of 1.55. The gneisses have a relatively strong negative Eu anomaly as depicted by the average  $\text{Eu}/\text{Eu}^*$  of 0.70.

In general, the gneisses exhibit REE compositions that are comparable to NASC values as listed by Haskin et al. (1968). The REE patterns imply derivation from a typical fractionated upper continental crust and therefore support a possible volcanic arc associated black shale protolith for the gneisses (Hassan et al., 1999).

### **11.3. Marble and calc-silicates**

The protolith classification of marbles and calc-silicates will be discussed together due to the similar nature of the rocks. The graphite calc-silicate schist (GCS) is included in this discussion because it contains a high calc-silicate component and is therefore both calc-silicic and gneissic in nature.

#### **11.3.1. Major and trace elements as protolith indicators**

The calc-silicate skarn boudins formed from the skarn alteration of the pyroxene units which in turn form via the prograde metamorphism of an originally impure limestone layer or layers, probably of roughly similar composition to the impure marbles. From the comparison between the impure marbles and calc-silicates (Table 7.1), it is clear that the only major difference is the presence of  $\text{SiO}_2$  and some  $\text{Al}_2\text{O}_3$  in the calc-silicates balanced by the presence of  $\text{CaCO}_3$  and to a lesser extent  $\text{MgCO}_3$  in the impure marbles. This could be explained by the skarn interaction between the pelites and the impure marbles, with Si and Al introduced into the marbles, coupled with the liberation of  $\text{CO}_3^{2-}$  while Ca and Mg migrated towards the pelites.

The Ce concentration in marbles is sometimes used as a protolith indicator and will be discussed in conjunction with the REE's. Selected average trace element concentrations of the marbles, normalised to Phanerozoic limestone compositions, are plotted in Figure 11.4. It is evident that Ni, Cr and especially Sr are depleted relative to the limestone



composition even though Sr is one of the most abundant trace minerals. Ba, Nb and Y are enriched relative to limestone composition. In general, all the elements are present in values close to 1, indicating a similar composition to that of the Phanerozoic limestone.

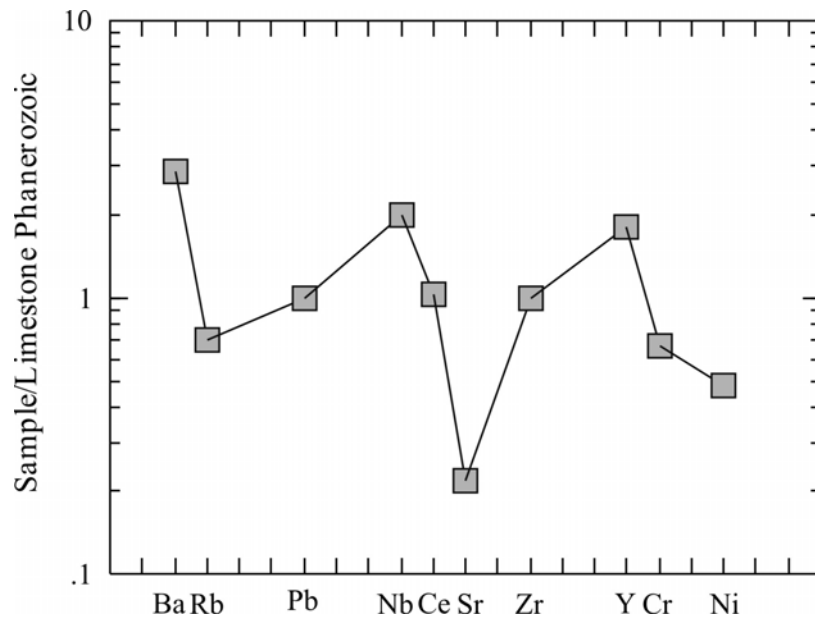


Figure 11.4. Phanerozoic limestone normalised spider diagram of the average dolomitic marble composition.

### 11.3.2. Rare earth elements (REEs) as protolith indicator

The marbles have total REE ( $\Sigma$ REE) values of between 6.93 ppm and 140.98 ppm, depending on the purity of the marble, see Table 11.1. These values compare well with the average  $\Sigma$ REE concentrations of 88 ppm for impure limestones (Bellanca et al., 1997). The chondrite-normalised REE patterns for the pure and impure marbles are plotted in Figure 11.5.a. The marbles are moderately fractionated with an average  $[\text{La}/\text{Yb}]_n$  ratio of 7.1. The LREE / HREE fractionation is represented by the Er / Nd values of marine sediments (de Baar et al., 1988). Limestone usually has Er / Nd values of around 0.12, which is very close to the average Er / Nd value of 0.13 obtained for the Merelani marbles (Table 11.1). The LREE is strongly fractionated with average  $[\text{Ce}/\text{Sm}]_n$  values of 2.83, while the HREE is relatively poorly fractionated with an average  $[\text{Gd}/\text{Yb}]_n$  ratio of 1.2. The pure marble has a strong negative Eu anomaly, as indicated by the average Eu / Eu\* ratio of 0.61, while the impure marble has a smaller Eu anomaly, with an average Eu / Eu\* ratio of 0.81 (Table 11.1). Cerium has been identified as a sensitive indicator of the redox conditions prevailing during formation of

marine sediments (Wright et al., 1987; Liu et al., 1988; Schijf et al., 1995). Ce can oxidise from its soluble  $Ce^{3+}$  state to the highly insoluble  $Ce^{4+}$  state in a seawater environment. It is therefore possible to deduce the redox conditions of the water present during the sedimentation process by examining the Ce anomaly of the sediments. This is expressed by the parameter  $Ce / Ce^*$ , defined as being equal to  $3Ce_n / (2La_n + Nd_n)$  (de Baar et al., 1985). Limestone sediments that formed under normal oxidising conditions usually have  $Ce / Ce^*$  values of  $<0.45$ , therefore displaying a strong negative anomaly. The Merelani marbles, however, show no significant Ce anomaly (Figure 11.5.a) with an average  $Ce / Ce^*$  ratio of 0.80 (Table 11.1), indicating deposition in an anoxic, reducing environment.

The calc-silicate boudins range substantially in  $\sum REE$ , depending on, amongst others, the degree of skarn related fluid interaction and weathering. The samples that underwent little skarn related alteration (samples no. R5B2, W2BR, R7NB1) have  $\sum REE$  concentrations of 55.31 ppm, 88.03 ppm and 183.36 ppm, respectively. The calc-silicate skarns have  $\sum REE$  values of between 158.5 and 241.04 ppm. Despite the range in  $\sum REE$ , the REE patterns are very similar, as can be seen in Figure 11.5.b. The REE of the calc-silicate skarn boudins also have an almost identical REE pattern to that of the marbles. The impure marble has a very similar pattern to one of the calc-silicate skarn boudin REE patterns. The pure marbles have a very similar pattern to that of the calc-silicates, except for the lower REE concentrations (Figure 11.5.b).

The calc-silicate skarn boudins and the marbles were both normalised to the chondrite composition (Figure 11.6.a) as well as NASC (Figure 11.6.b) in order to show the remarkable similarity between the two patterns. The REE pattern of the calc-silicate skarn boudins therefore confirms the development of the calc-silicate boudins from an original limestone unit enveloped within the black shales.

The REE patterns of GCS and BCF normalised to the chondrite and NASC compositions, are shown in Figure 11.6.a and b, respectively. The REE patterns of the units fall within the range of the REE patterns of the calc-silicate skarn boudins.

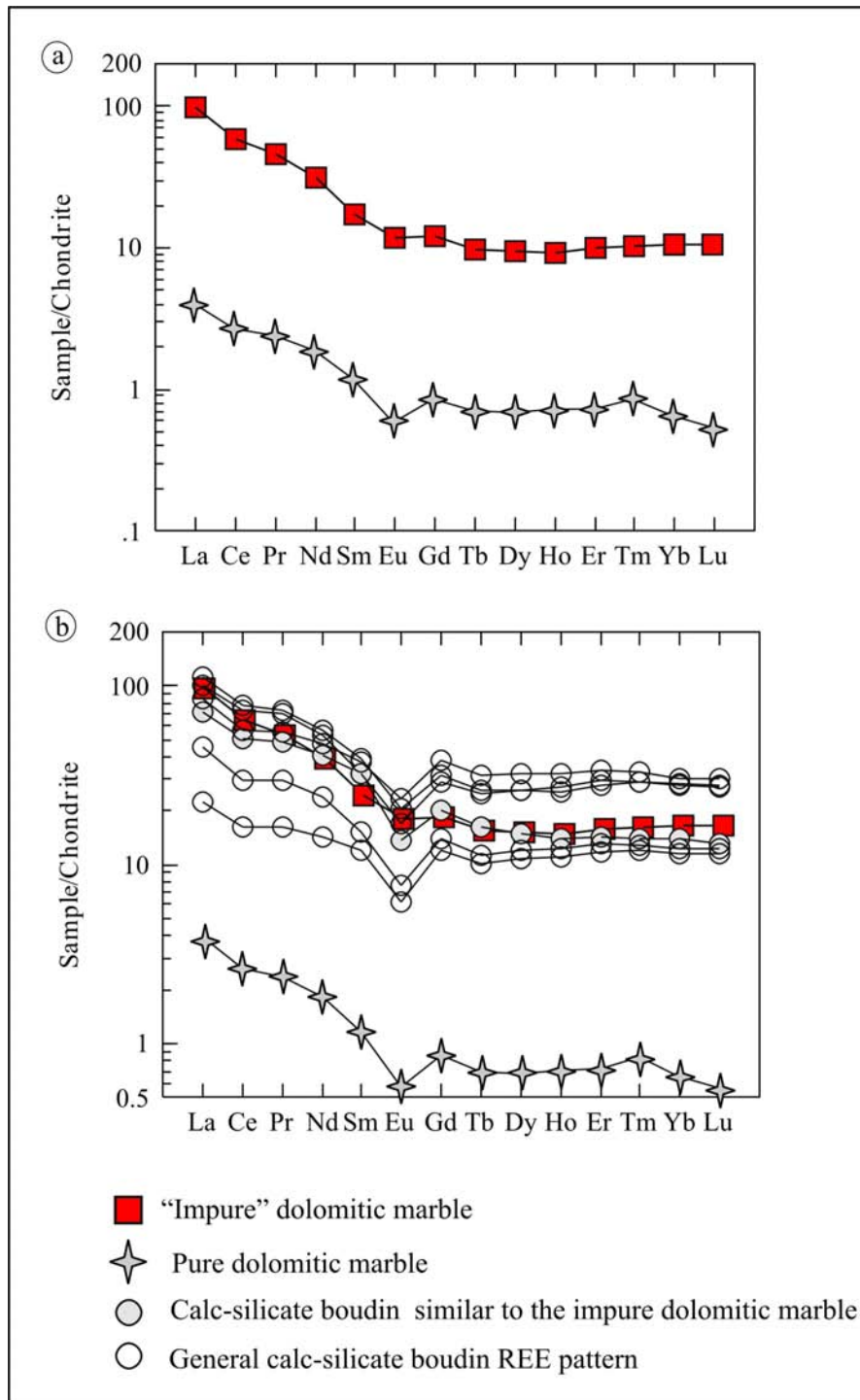


Figure 11.5. Chondrite normalised REE patterns for a) the "impure" and "pure" dolomitic marbles and b) calc-silicate skarn boudins, with the superimposed REE patterns of the "impure" and "pure" dolomitic marbles.

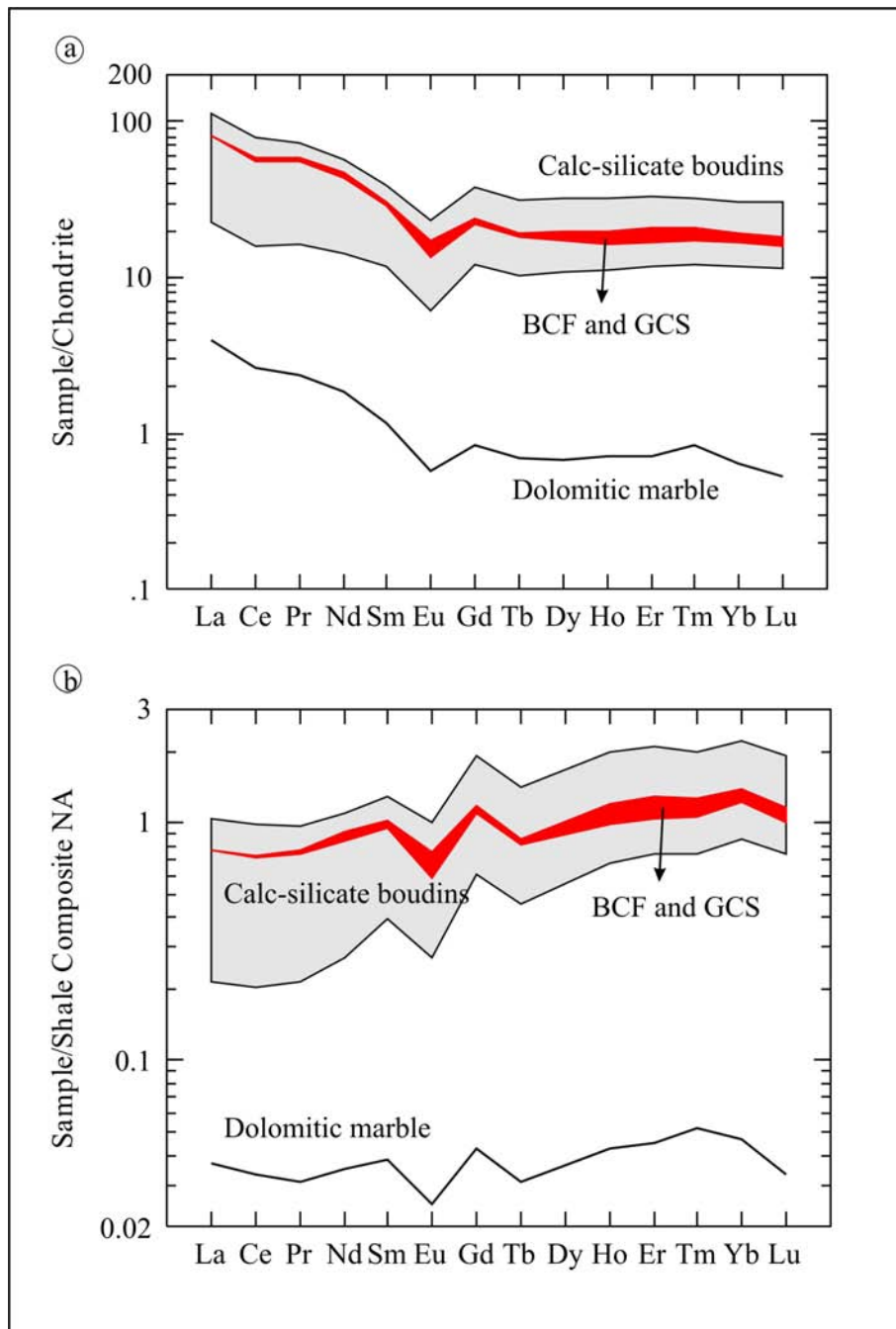


Figure 11.6. a) Chondrite and b) NASC normalised REE patterns of the calc-silicate skarn boudins, marbles, GCS and BCF units.

## 11.4. Conclusions

The organic origin of the graphite as indicated by the isotope values (see Chapter 8) as well as the sedimentary classification diagrams point towards an organic-rich mudstone origin of the gneisses. The gneisses therefore have a black shale-like protolith as indicated by the similarity with NASC. The tanzanite-bearing calc-silicate skarn boudins intercalated within the gneisses originate from syndepositional impure limestones. This is confirmed by the organic origin of the graphite situated within the calc-silicates, as opposed to a possible decarbonation origin (see Chapter 8). The trace element and REE distribution patterns of the gneisses and calc-silicates indicate a volcanic arc environment associated with a back- or fore-arc spreading basin. The limestone may therefore be coral-algal carbonates either associated with the back- or fore-arc shelf breaks and gravitational flow or indicative of a shallow depositional environment for mudstones within the coral-algal growth zone. The volcanic influence in the depositional setting resulted in the enrichment of Zn, Ni and Ba in the shales.

Table 11.1. REE values (ppb) of various rock types present in the Merelani tanzanite deposit.

Sample	La	Ce	Pr	Nd	Sm	Eu	Gd	Tb	Dy	Ho	Er	Tm
18-2	59.64	96.16	12.35	47.56	8.08	1.18	6.42	0.78	4.36	0.83	2.24	0.29
18-3	40.87	74.65	9.91	40.43	9.03	1.80	9.64	1.52	9.90	2.18	6.92	1.03
18-4	37.24	69.91	9.48	37.88	7.45	1.20	6.11	0.95	5.72	1.18	3.53	0.50
18-5	26.14	48.83	6.64	29.02	7.41	1.47	8.87	1.43	9.98	2.33	7.38	1.04
18-7	35.06	64.50	8.85	37.70	8.61	1.60	9.45	1.51	10.07	2.25	6.92	0.97
18-8	32.93	61.52	8.60	36.17	6.69	1.54	5.49	0.79	4.98	1.01	3.03	0.44
1DOLST	1.44	2.53	0.32	1.30	0.27	0.05	0.26	0.04	0.26	0.06	0.18	0.03
9DOLS	36.43	56.11	6.25	22.58	3.99	1.02	3.71	0.57	3.65	0.79	2.50	0.37
R7N B-1	30.73	53.52	7.49	34.07	8.62	2.02	11.76	1.84	12.40	2.76	8.34	1.16
W2 B-R	16.69	28.35	4.01	17.08	3.53	0.67	4.24	0.66	4.55	1.04	3.26	0.46
R5 B2	8.30	15.37	2.21	10.10	2.75	0.54	3.69	0.59	4.11	0.94	2.95	0.43
1-GCS1	29.72	53.72	7.93	33.96	7.10	1.50	7.24	1.11	7.43	1.69	5.18	0.74
1-BCF1	29.85	55.56	7.58	30.91	6.64	1.18	6.65	1.06	6.56	1.37	4.15	0.61
1-LK1	20.97	43.62	5.47	22.89	4.56	1.22	4.14	0.62	3.82	0.80	2.39	0.34
1-LK2	30.33	58.50	8.20	34.63	7.12	1.47	6.39	0.92	5.75	1.18	3.44	0.46
6-LK1	27.17	56.21	7.01	27.97	4.97	0.80	3.68	0.48	2.64	0.47	1.21	0.16
1-JWZ	40.21	79.25	10.44	42.43	8.50	1.70	8.16	1.25	8.23	1.79	5.45	0.77
6-JWZ	18.29	37.68	4.70	18.76	4.04	0.89	3.71	0.55	3.29	0.66	1.92	0.26
W2 J1	40.06	69.82	9.26	37.03	6.61	1.45	5.75	0.75	4.37	0.88	2.50	0.34
R10 J2	25.31	46.41	6.22	24.79	4.58	1.25	4.77	0.76	5.33	1.25	3.97	0.57
W10 J1	26.33	44.70	6.20	24.74	4.46	1.21	4.19	0.57	3.40	0.70	2.11	0.29
W10 G1	30.92	60.40	8.43	34.02	6.41	1.05	5.45	0.80	4.89	0.97	2.79	0.40
R7W G1	59.30	109.39	15.57	67.28	16.08	3.02	17.98	2.97	20.44	4.53	13.91	1.98
W10 G2	39.85	68.78	8.89	36.42	7.54	1.46	8.23	1.29	8.65	1.96	6.10	0.84
1-GARNET	37.62	86.04	10.08	41.86	8.71	1.65	7.67	1.11	6.87	1.39	4.13	0.60
Avg. gneiss	29.59	58.03	7.51	30.57	5.95	1.29	5.38	0.78	4.86	1.01	3.01	0.42
Chondrite	0.37	0.96	0.14	0.71	0.23	0.09	0.31	0.06	0.38	0.09	0.25	0.04
NASC	31.1	66.7	*	27.4	5.59	1.18	*	0.85	*	*	*	*

Table 11.1. Continued.

Sample	Yb	Lu	[La/Sm] <sub>n</sub>	[La/Yb] <sub>n</sub>	Eu/Eu*	Er/Nd	[Ce/Sm] <sub>n</sub>	[Gd/Yb] <sub>n</sub>	ΣREE	Ce/Ce*	[La/Sm] <sub>n</sub> *
<b>18-2</b>	1.85	0.28	4.64	21.73	0.50	0.05	2.87	2.81	242.04	0.78	1.33
<b>18-3</b>	7.03	1.05	2.85	3.93	0.59	0.17	2.00	1.11	215.95	0.82	0.81
<b>18-4</b>	3.45	0.50	3.15	7.29	0.55	0.09	2.27	1.44	185.09	0.83	0.90
<b>18-5</b>	6.92	1.04	2.22	2.55	0.55	0.25	1.59	1.04	158.50	0.80	0.63
<b>18-7</b>	6.38	0.95	2.56	3.72	0.54	0.18	1.81	1.20	194.80	0.80	0.73
<b>18-8</b>	2.98	0.45	3.10	7.46	0.78	0.08	2.22	1.49	166.63	0.80	0.89
<b>1DOLST</b>	0.16	0.02	3.36	5.98	0.61	0.14	2.27	1.31	6.93	0.81	0.96
<b>9DOLS</b>	2.60	0.40	5.74	9.45	0.81	0.11	3.39	1.16	140.98	0.80	1.64
<b>R7N B-1</b>	7.50	1.15	2.24	2.77	0.61	0.24	1.50	1.27	183.36	0.75	0.64
<b>W2 B-R</b>	3.02	0.47	2.98	3.73	0.53	0.19	1.94	1.14	88.03	0.75	0.85
<b>R5 B2</b>	2.88	0.44	1.90	1.95	0.52	0.29	1.35	1.04	55.31	0.77	0.54
<b>1-GCS</b>	4.73	0.70	2.63	4.25	0.64	0.15	1.83	1.24	162.77	0.77	0.75
<b>1-BCF1</b>	4.16	0.60	2.83	4.85	0.54	0.13	2.02	1.30	156.88	0.82	0.81
<b>1-LK1</b>	2.28	0.35	2.89	6.20	0.86	0.10	2.31	1.47	113.48	0.90	0.83
<b>1-LK2</b>	2.95	0.44	2.68	6.95	0.66	0.10	1.98	1.76	161.76	0.82	0.77
<b>6-LK1</b>	1.08	0.17	3.44	17.03	0.57	0.04	2.73	2.77	134.03	0.91	0.98
<b>1-JWZ</b>	5.02	0.74	2.98	5.42	0.62	0.13	2.25	1.32	213.94	0.86	0.85
<b>6-JWZ</b>	1.74	0.26	2.85	7.10	0.70	0.10	2.25	1.73	96.75	0.91	0.81
<b>W2 J1</b>	2.26	0.34	3.81	12.00	0.72	0.07	2.55	2.06	181.42	0.80	1.09
<b>R10 J2</b>	3.87	0.57	3.48	4.42	0.82	0.16	2.45	1.00	129.63	0.82	0.99
<b>W10 J1</b>	2.00	0.30	3.72	8.89	0.86	0.09	2.42	1.70	121.21	0.77	1.06
<b>W10 G1</b>	2.59	0.36	3.03	8.08	0.54	0.08	2.27	1.71	159.48	0.84	0.87
<b>R7W G1</b>	13.02	1.97	2.32	3.08	0.54	0.21	1.64	1.12	347.44	0.78	0.66
<b>W10 G2</b>	5.54	0.82	3.33	4.86	0.57	0.17	2.20	1.20	196.36	0.79	0.95
<b>1-GARNET</b>	4.14	0.61	2.72	6.14	0.62	0.10	2.38	1.50	212.46	0.98	0.78
<b>Avg. gneiss</b>	2.82	0.42	3.13	7.09	0.70	0.10	2.35	1.55	151.64	0.86	0.89
<b>Chondrite</b>	0.25	0.04	*	*	*	*	*	*	*	*	*
<b>NASC</b>	3.06	0.456	*	*	*	*	*	*	*	*	*

## Chapter 12

### Mineralogical properties of coloured zoisites

#### 12.1. Introduction

Despite the fact that tanzanite is one of the most popular gemstones in the world, little is known about its mineralogy, especially with relation to its colour and colour change due to heating. Most of the mineralogical research conducted on tanzanite was done soon after its discovery in 1967 by various authors, including Meen (1968), Hurlbut (1969), Faye and Nickel (1971), Tsang and Ghose (1971), Dunn (1975), Gübelin and Weibel (1975) and Nassau (1983). This study however, presents new data made possible by considerable advances in the analytical methods, as well as the wide range of gemstone quality coloured zoisites from the Merelani deposit made available to the author. This led to new insight into the chemical composition, causes of colour as well as colour-change upon heating of tanzanite and other coloured zoisites. A combination of laser-ablation ICP-MS, electron microprobe analyses, UV/Vis/NIR spectroscopy, FTIR, Electron Paramagnetic Resonance (EPR), heating experiments, as well as radiation experiments were used.

The general gemmological characteristics (including colour, pleochroism and R.I.) of blue and green coloured zoisite have been described by various authors (e.g. Meen, 1968; Faye and Nickel, 1971; Webster and Anderson, 1983; Dirlam et al., 1992) and will therefore not be described again in this study.

#### 12.2. Structural overview of zoisite

The epidote group is the most common of the Sorosilicates and consists of a wide variety of chemically complex minerals with the general formula  $X_2Y_3O(Si_2O_7)(SiO_4)(OH)$ , as defined by Nesse (1991). Zoisite is the orthorhombic member of the epidote group, with the formula  $Ca_2Al_2O.AiOH[Si_2O_7][SiO_4]$  while clinozoisite is the monoclinic member (Deer et al., 1986). Tanzanite is the blue to violet variant of zoisite. Dollase (1968) redefined and described the structure of zoisite and clinozoisite after initial work by Ito et al. (1954) and Fesenko et al. (1955). The cell parameters of zoisite (space group Pnma) are:



$$a = 16.212 \pm 0.008 \text{ \AA}, b = 5.559 \pm 0.006 \text{ \AA}, \text{ and } c = 10.036 \pm 0.004 \text{ \AA}.$$

Dollase (1968) describes the structure of zoisite as edge sharing endless octahedra chains parallel to the short b axis. Zoisite has two types of Al-O octahedral, as proposed by the modified notation of Brinkmann et al. (1969), effectively dividing the Al sites into two crystallographic positions, as illustrated in Figure 12.1. Al(i) consists of 3 shared edges per octahedron, while Al(ii) consists of 2 shared edges. Thus, the Al(i) position is an eightfold general co-ordinate with point group symmetry 1, while Al(ii) is a four-fold special co-ordinate with point group symmetry  $m$  (Figures 12.1 and 12.2).

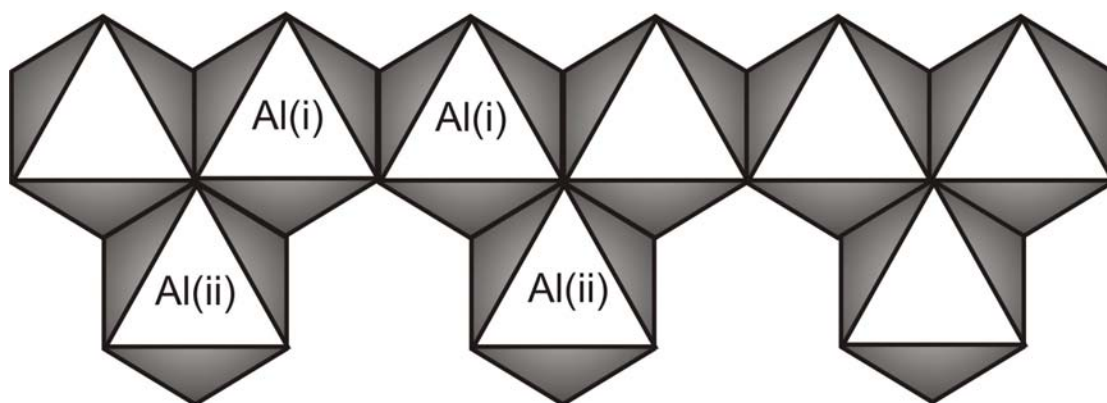


Figure 12.1. Idealised octahedral chains in zoisite (modified from Dollase, 1968, using the notation proposed by Brinkmann et al., 1969).

The Al-O octahedral chains are cross-linked by the remaining cations, which consist of  $\text{Si}_2\text{O}_7$  double tetrahedron, isolated  $\text{SiO}_4$  tetrahedron and calcium-polyhedra. Dollase (1968) described the presence of two calcium sites within irregular shaped cavities between the Al-O chains. The calcium sites are referred to as the Ca(i) and Ca(ii) sites and are both seven-coordinated. The structure of zoisite, viewed nearly along the b-axis, is illustrated in Figure 12.2.

Deer et al. (1986) referred to the different descriptions sometimes used for the axes of zoisite, with some authors using the X-ray indices and other the morphological system. It should therefore be noted that:

$$a \text{ (X-ray)} = b \text{ (Morphological)}$$

b (X-ray) = c (Morphological)

c (X-ray) = a (Morphological)

Perfect cleavage: (100) (X-ray) = (010) (Morphological)

In this study the X-ray axial classification system was used.

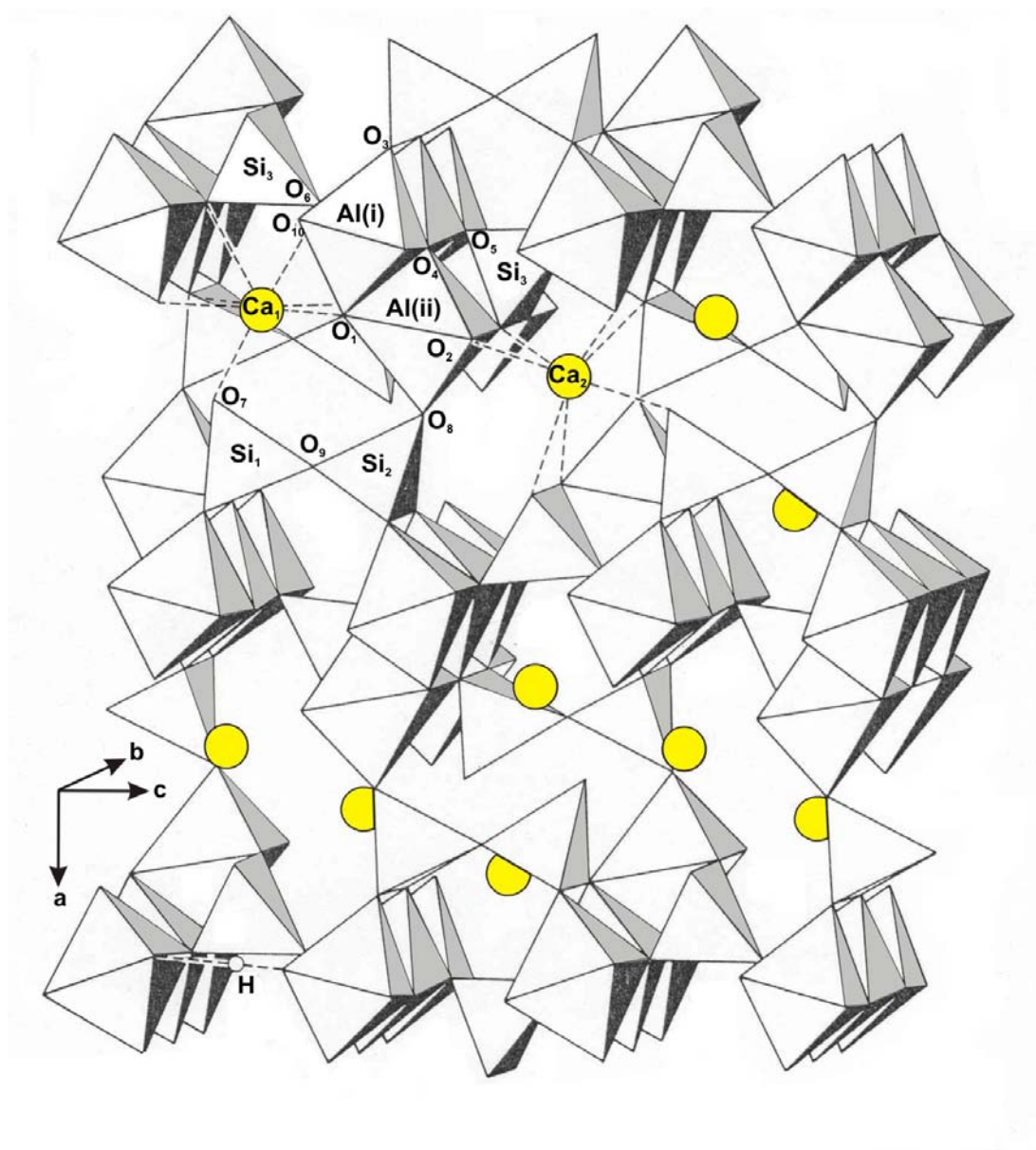


Figure 12.2. The structure of zoisite modified after Dollase (1968); with notations as proposed by Brinkmann et al. (1969).

### **12.3. Chemical composition of coloured zoisites**

#### **12.3.1. Technique specifications**

An electron microprobe was used to establish the major element concentrations of the various coloured zoisites and a laser ablation ICP-MS system for the trace and REE concentrations.

The ICP-MS analyses were done, by the author, on a LSX-200 laser ablation system at the Department of Geoscience, University of Cape Town, RSA. The system has a relative energy of 20, pulse rate of 2 p/s, burst count of 500, spot size of 3 $\mu$ m and laser energy of 5 mJ. The standards SRM 1612 and 610m, prepared by the National Institute of Standards and Technology in the USA, were used.

#### **12.3.2. Major elements**

The major element compositions of the coloured zoisite vary very little between specimens with different colours. Table 12.1 summarises the major element composition and stoichiometric values of the four main groups of coloured zoisite found within the Merelani tanzanite deposit. All the analyses were conducted on gemstone quality material namely, blue zoisite (tanzanite), green zoisite (sometimes erroneously called green tanzanite) as well as orange and yellow / colourless zoisites (no gemmological variety name).

The major element concentrations of the coloured zoisite, summarised in Table 12.1, compare well with the microprobe data of other zoisite, as analysed by Deer et al. (1986) and Kepezhinskas and Khlestov (1971). The complete list of major element compositions and stoichiometric calculations obtained from the microprobe analyses of the various zoisite samples are indicated in Tables 1 to 4, Addendum K.

The high quality of the microprobe analyses are indicated by the sum of the ions obtained from the stoichiometric calculations, see Table 12.1. Thus, the low total values of the analyses can be attributed to the presence of H<sub>2</sub>O and other trace and REE present in the zoisites. The calculation of the water content of the various coloured zoisite samples also included the presence of trace and REE concentrations. The estimated H<sub>2</sub>O

content of the zoisites also compare well with the analytical H<sub>2</sub>O concentrations obtained by Deer et al. (1986).

*Table 12.1. Average and standard error calculations of the microprobe data of coloured zoisites from the Merelani deposit. The stoichiometric calculations were based on 13 oxygen and OH ions. The number of cases used for the calculation of the average values are indicated by n. \* Estimated average H<sub>2</sub>O content.*

	Blue		Green		Orange		Yellow	
	Avg	±St. error	Avg	±St. error	Avg	±St. error	Avg	±St. error
SiO <sub>2</sub>	39.11	±0.045	39.53	±0.086	39.00	±0.057	39.56	±0.082
Al <sub>2</sub> O <sub>3</sub>	33.00	±0.063	33.22	±0.077	32.70	±0.061	32.98	±0.070
CaO	24.75	±0.025	25.07	±0.043	24.56	±0.028	24.74	±0.039
TiO <sub>2</sub>	0.03	±0.006	0.06	±0.007	0.02	±0.002	0.03	±0.000
V <sub>2</sub> O <sub>3</sub>	0.06	±0.008	0.02	±0.005	0.06	±0.004	0.05	±0.012
Cr <sub>2</sub> O <sub>3</sub>	0.04	±0.003	0.04	±0.008	0.04	±0.008	0.02	±0.006
FeO	0.02	±0.003	0.01	±0.004	0.03	±0.005	0.01	±0.003
MgO	0.03	±0.003	0.01	±0.002	0.09	±0.012	0.03	±0.004
MnO	0.19	±0.019	0.11	±0.019	0.34	±0.020	0.05	±0.005
Na <sub>2</sub> O	0.02	±0.003	0.02	±0.003	0.03	±0.005	0.02	±0.004
K <sub>2</sub> O	0.01	±0.002	0.01	±0.003	0.01	±0.002	0.01	±0.001
Total	97.14	±0.101	98.05	±0.190	96.74	±0.113	97.50	±0.153
H <sub>2</sub> O*	2.62		1.73		2.16		2.30	
Si	2.993	±0.002	2.996	±0.002	2.998	±0.002	3.014	±0.002
Al IV	0.011	±0.002	0.006	±0.002	0.005	±0.001	0.000	±0.000
Sum_T	3.004	±0.001	3.002	±0.001	3.003	±0.001	3.014	±0.002
Al VI	2.962	±0.002	2.959	±0.002	2.955	±0.002	2.959	±0.003
Ti	0.000	±0.000	0.004	±0.000	0.000	±0.000	0.000	±0.000
Cr	0.002	±0.000	0.001	±0.000	0.002	±0.000	0.001	±0.000
Fe <sup>2+</sup>	0.001	±0.000	0.000	±0.000	0.001	±0.000	0.000	±0.000
Mn	0.010	±0.001	0.007	±0.001	0.022	±0.001	0.003	±0.000
Mg	0.003	±0.000	0.000	±0.000	0.009	±0.001	0.002	±0.000
Ca	2.029	±0.002	2.036	±0.003	2.023	±0.003	2.019	±0.003
Na	0.001	±0.000	0.003	±0.000	0.002	±0.001	0.001	±0.000
K	0.001	±0.000	0.001	±0.000	0.000	±0.000	0.000	±0.000
V	0.002	±0.001	0.000	±0.000	0.000	±0.000	0.001	±0.001
Sum_B	2.044	±0.003	2.046	±0.003	2.056	±0.003	2.026	±0.003
N	55		21		27		21	

The SiO<sub>2</sub> content of the green and colourless / yellow samples is approximately 0.5 wt% higher than those of the blue and orange samples. The Al<sub>2</sub>O<sub>3</sub> content of the green samples is slightly higher than that of the other colours. This could indicate a lesser amount of substitution of minor elements like V and Sr. As will be illustrated; the V content of the green samples is slightly lower, while the Ti content is slightly higher than the other colours.

Deer et al. (1986) indicated that minor replacement of Si by Al occurs within zoisites. This is also evident from Table 12.1 and Table 1 to 4, Addendum K, presenting the microprobe data and stoichiometric values of the zoisites. The samples shown in Tables 1 to 4, Addendum K, were stoichiometrically calculated based on 13 O and OH.

The data obtained from the microprobe analyses suggest that significant amounts of MnO are present in especially the orange and blue samples. Mn may thus be a possible colour-producing element within the zoisites. However, the probe data listed in Table 1, Addendum K, indicates that almost half of the blue samples analysed contain between 0.05 wt% and no detectable MnO. Contrary to the above, this would therefore suggest that Mn is not a significant colouring agent for the blue zoisites (tanzanite). All the orange samples analysed however contains MnO, with values ranging from 0.08 to 0.51 wt%. It is therefore possible that Mn may be a chromophore for the orange zoisites. A non-transparent pink zoisite (thulite) has been analysed by Deer et al. (1986) and the colouring agent was found to be Mn. Thulite, however, also contains up to 4.3 wt% total Fe and up to 0.56 wt% MgO, unlike the Merelani zoisites which contain very little Fe and Mg, see Table 12.1.

All the other elements analysed by means of the microprobe, including TiO<sub>2</sub>, V<sub>2</sub>O<sub>3</sub>, Cr<sub>2</sub>O<sub>3</sub>, FeO, MgO, Na<sub>2</sub>O and K<sub>2</sub>O are all present in less than 0.1 wt%, with standard errors of less than 0.02 wt%, within the Merelani zoisites (Table 12.1).

In general, therefore, microprobe data alone is inadequate to investigate the small concentrations and deviation in concentrations of elements acting as chromophores for the zoisites. The trace and REE present within the zoisites were subsequently investigated by means of laser ablation ICP-MS.

### 12.3.3. Trace Elements

The coloured zoisites from the Merelani deposit were divided into 5 groups, blue, green, orange, “golden” and colourless for investigation by laser ablation ICP-MS. The average and standard error of the most important trace element and REE concentrations of the various coloured zoisite are presented in Table 12.2.

*Table 12.2. Summary of the averages and standard errors of the most significant trace and REE concentrations within the coloured zoisites as obtained by laser-ablation ICP-MS in ppm). n indicates the number of analyses used for the calculation of the average and standard error values.*

	Blue	Green	Orange	“Golden”	Colourless
	Avg $\pm$ Std error	Avg $\pm$ Std error	Avg $\pm$ Std error	Avg $\pm$ Std error	Avg $\pm$ Std error
Ti	606 $\pm$ 14	707 $\pm$ 39	582 $\pm$ 6	585 $\pm$ 5	523 $\pm$ 3
V	1872 $\pm$ 85	1698 $\pm$ 91	931 $\pm$ 37	1592 $\pm$ 22	393 $\pm$ 35
Cr	131 $\pm$ 6	120 $\pm$ 11	53 $\pm$ 3	143 $\pm$ 6	19 $\pm$ 2
Fe	28 $\pm$ 4	9 $\pm$ 4	111 $\pm$ 17	44 $\pm$ 6	1 $\pm$ 4
Zn	0 $\pm$ 0	1 $\pm$ 1	7 $\pm$ 2	1 $\pm$ 0	5 $\pm$ 5
Ga	139 $\pm$ 5	134 $\pm$ 7	280 $\pm$ 7	199 $\pm$ 13	88 $\pm$ 2
Sr	1862 $\pm$ 116	1805 $\pm$ 210	3726 $\pm$ 90	2740 $\pm$ 87	2017 $\pm$ 75
Y	110 $\pm$ 10	62 $\pm$ 10	32 $\pm$ 3	138 $\pm$ 12	19 $\pm$ 4
Zr	20 $\pm$ 2	43 $\pm$ 8	19 $\pm$ 1	16 $\pm$ 1	3 $\pm$ 0
La	53 $\pm$ 14	25 $\pm$ 14	2631 $\pm$ 357	291 $\pm$ 49	11 $\pm$ 2
Ce	92 $\pm$ 22	40 $\pm$ 21	2881 $\pm$ 257	517 $\pm$ 83	16 $\pm$ 3
Pr	11 $\pm$ 2	5 $\pm$ 2	333 $\pm$ 42	66 $\pm$ 10	2 $\pm$ 0
Nd	49 $\pm$ 8	19 $\pm$ 8	965 $\pm$ 106	271 $\pm$ 42	7 $\pm$ 1
TREE	278 $\pm$ 48	127 $\pm$ 48	6951 $\pm$ 741	1316 $\pm$ 200	55 $\pm$ 8
n	42	24	28	17	21

Table 12.2 excludes elements such as Co, Ni, Cu and Pb, normally considered important chromophores. These elements as well as Sc, Rb, Th, U, Sm, Eu, Gd, Dy, Er, Yb, Lu, Hf and Ta concentrations are all listed in Table 1, 2, 3, 4 and 5, Addendum L, for blue, green, orange, “golden” and colourless zoisite, respectively. In general, these elements occur in such low quantities within all the various coloured zoisites that they are often present in concentrations below the detection limit of the laser ablation ICP-MS.

Less than 10 ppm Co, Ni and Rb are present in all of the samples from the various colours, as indicated in Tables 1, 2, 3, 4 and 5, Addendum L. Both Th and U are present in less than 40 ppm in all the samples, with no apparent colour related distribution

pattern. The colourless samples contain less than 40 ppm Mn, while the other colour varieties of zoisite all contain less than 100 ppm Mn. This is significantly lower than the values obtained from the microprobe analyses in Table 12.1. This could imply calibration and therefore accuracy problems associated with the Mn values obtained through microprobe analyses of the zoisites, but are probably related to the relatively low detection limit for this element.

### ***Titanium***

Titanium is considered a partial chromophore depending on its valence state and normally results in a green colouration of the mineral (Rossman, 1988). The average Ti values vary slightly between the different coloured zoisites and are indicated in Table 12.2. Green zoisite has the highest average Ti content ( $707 \pm 39$  ppm), while the colourless zoisite has the lowest content ( $523 \pm 3$  ppm). The blue, orange and “golden” coloured zoisites all have average Ti values of approximately 600 ppm. The relatively small differences in Ti concentrations, however, appear to contribute to the colour of the zoisite and will be further discussed in Section 12.4 and Chapter 13.

### ***Vanadium***

Vanadium is a very dominant, yet fairly rare chromophore and results in either a green, blue or red colouration for minerals depending on their crystal structure. The distinct violet-blue colouration of gemstone quality tanzanite is due to the substitution of trivalent vanadium ( $V^{3+}$ ) for  $Al^{3+}$  in a similar fashion as described for tsavorite (Hurlbutt, 1969; Schmetzer and Bank, 1979; Webster and Anderson, 1983; Deer et al., 1986). The exact amount of V present in the structure of tanzanite was previously unknown, with values being inferred from imprecise methods, such as colourimetry. Laser ablation ICP-MS analyses of tanzanite crystals, however, revealed that there are between 972 ppm and 6196 ppm V present in the crystal structure of tanzanite (Table 1, Addendum L). Blue zoisite (tanzanite) has the highest V content ( $1872 \pm 85$  ppm), while the colourless zoisite has the lowest ( $393 \pm 35$  ppm) content. The association between the V content and colour of the zoisite is illustrated in Figure 12.3. It is evident from the figure that there is a strong correlation between the colour of the zoisite and V content. In general, the blue part of colour-zoned zoisite has a V content of at least 1200 ppm higher than the colourless section. Tables 1, 2, 3, 4 and 5, Addendum L, indicate the difference in V content for several colour-zoned zoisite samples. The bottom

diagram in Figure 12.3 shows two distinct V peaks, with V concentrations ranging to over 6 000 ppm. These high values are located on the blue / colourless contact and could represent a vanadium-rich front. This would therefore suggest that during zoisite crystallisation or recrystallisation, V was present in high concentration and migrated in a mobile state through some of the crystals. Subsequent changes in the crystallisation conditions probably prohibited the complete movement of V through certain minerals. It may also indicate that vanadium-bearing fluid changed its oxidation potential and therefore its ability to keep V in solution. A sudden change in oxidation conditions could remove V from solution creating colourless zoisite.

The average V content of the green zoisite is only ca. 175 ppm lower than the blue zoisite, suggesting that the difference in colour is probably not exclusively due to the presence of V (Figure 12.5.c and Table 12.2). Laser ablation ICP-MS analyses of several green to blue zoned zoisite crystals are indicated in Table 2, Addendum L. For samples 68 and 91 the difference in V content between the blue and green parts of the crystal is fairly large (918 and 746 ppm, respectively). For sample 58, the difference in V content is 559 ppm while for sample 89 the difference is only 375 ppm. In sample 61 the green part of the zoisite only has a 31 ppm higher V concentration compared to that of the blue part of the crystal. These results therefore indicate that the difference in colour between the green and blue zoisites is controlled by more than only a difference in V content.

The orange zoisites have average V contents of  $931 \pm 37$  ppm (Table 12.2). Even though these values are relatively high, they are overshadowed by extremely high REE concentrations, which are more likely to contribute to the colour of the orange zoisite. No colour-zoned orange zoisite was observed.

The “golden” coloured zoisites have average V values of  $1592 \pm 22$  ppm. The V values of the “golden” and blue-zoned zoisite (Sample 59) are indicated in Table 4, Addendum L. The V values of the “golden” section of the crystal are on average 310 ppm lower than the blue part of the crystal. The “golden” coloured zoisites have almost equal percentages of V and REE present, suggesting that the colouration could be due to a combination of these elements (Table 4, Addendum L).



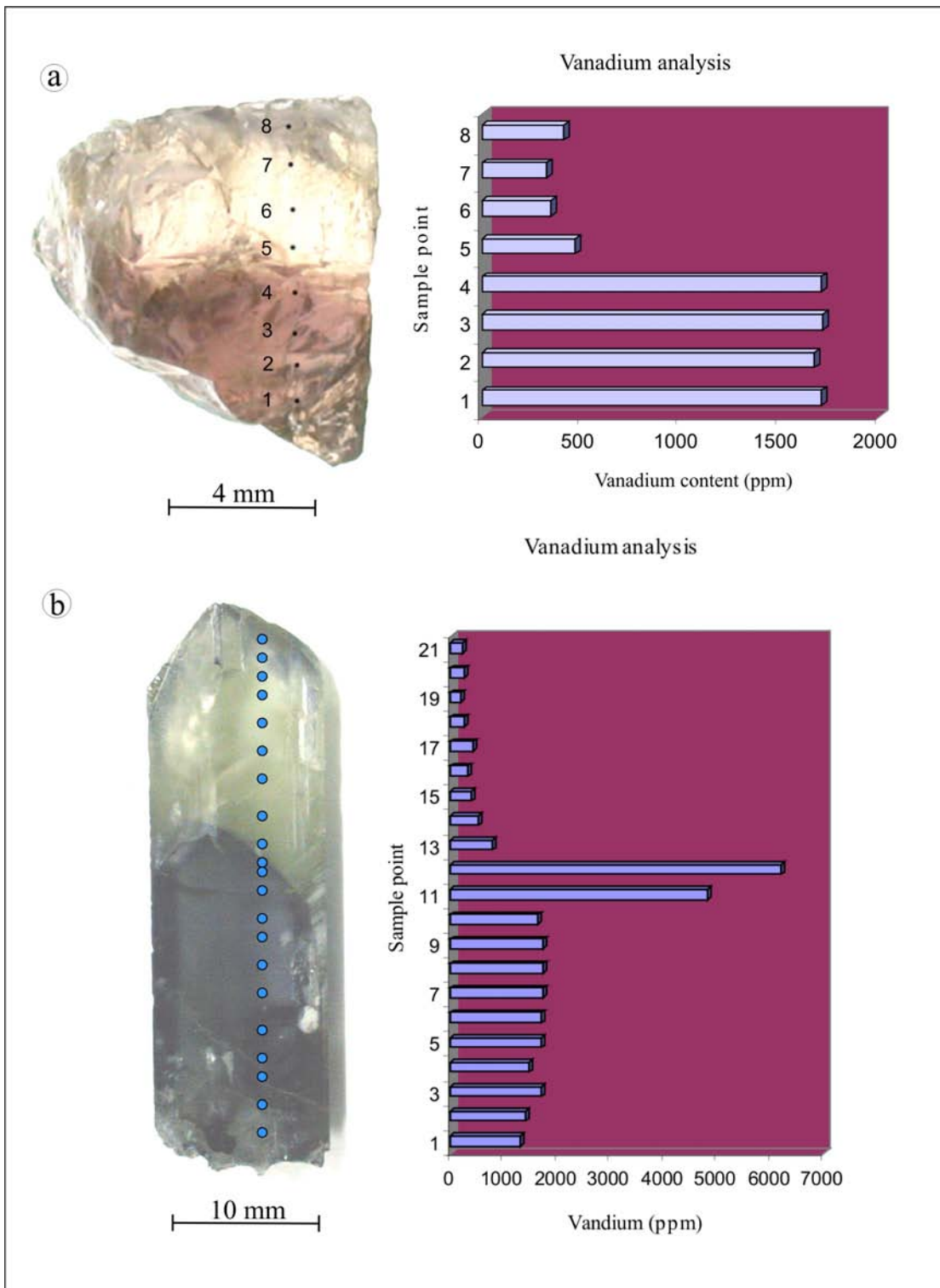


Figure 12.3. Vanadium analyses of two blue and colourless zoned zoisites referred to as sample G39 and sample 50 (Table 1, Addendum L) and indicated in Figure 12.3.a and b, respectively. The ICP-MS laser ablation values (in ppm) of the zoned crystals are indicated in the graphs. The localities of the sample points are indicated on the photographs. Figure 12.3.b indicates the presence of high V peaks located on the blue / colourless boundary of the crystal.

### ***Chromium***

Chromium is one of the most common and important chromophores in minerals used as gemstones. Chromium normally causes a green colour in gemstones (such as in emeralds), although it can also produce a red colour in certain minerals for example in corundum. Schmetzer and Bank (1979) as well as Barot and Boehm (1992) suggested that the green colouration of certain zoisites could be caused by higher concentrations of Cr compared to that of blue zoisite (tanzanite). However, as evident from Table 12.2, the green zoisite from the Merelani deposit has, on average, slightly lower Cr concentrations than tanzanite. The Cr distribution throughout the coloured zoisites mimics that of V but at a concentration of approximately 15 times lower, see Figure 12.4. The average concentrations of the Cr within the coloured zoisites are indicated in Table 12.2. The individual concentrations of the Cr within the various coloured and colour-zoned zoisites are indicated in Addendum L. Since the concentration of the Cr within the coloured zoisites is low, it is unlikely that the presence of Cr has any significant influence on the colour of zoisite.

### ***Iron***

Iron is also a well-known chromophore and produces green, blue, yellow and brown colours in minerals. The average Fe content for the orange coloured zoisites is  $111 \pm 17$  ppm while that of all the other coloured zoisites is below 50 ppm (see Table 12.2). In general, all the zoisites from the Merelani area have lower Fe concentrations than is normally reported for zoisite minerals (See Table 1 in Deer et al., 1986 for comparative zoisite analysis).

### ***Zinc***

The Zn values for the coloured zoisites from the Merelani area are all below 10 ppm (see Table 12.2).

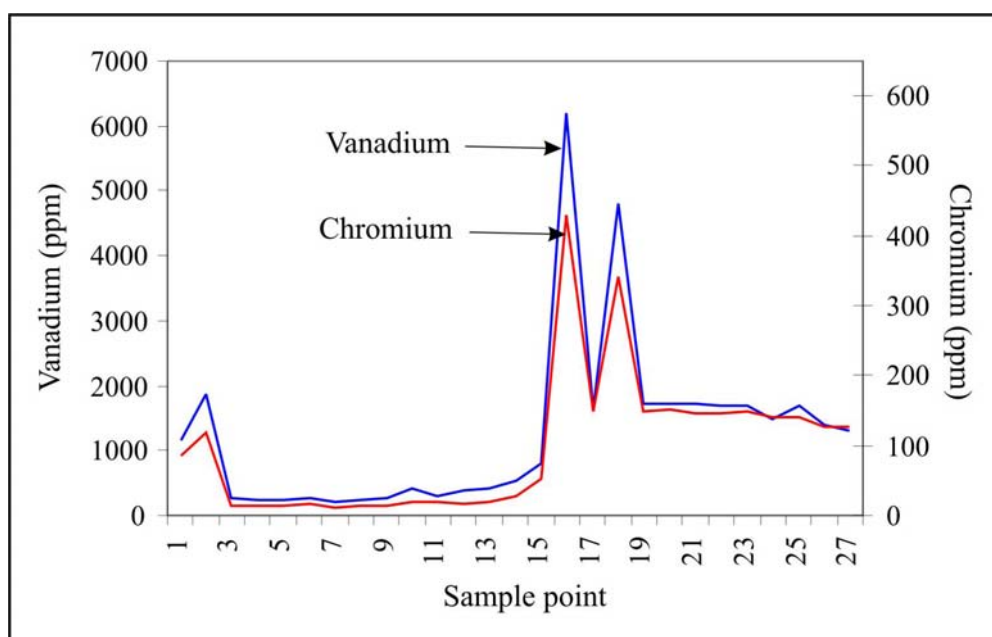


Figure 12.4. V and Cr distribution patterns within a zoned tanzanite sample (sample 50) indicating the similar distribution pattern for V and Cr despite the significant difference in concentrations.

### Gallium

Gallium is not a chromophore element and therefore does not influence the colour of the zoisites. There is however a small difference in the Ga concentrations within the different coloured zoisites. Gallium values obtained for the coloured zoisites are indicated in Table 12.2. The Ga concentrations range from less than 90 ppm for the colourless zoisites to about 280 ppm for the orange zoisites. The average Ga concentrations for both the blue and green zoisites are around 140 ppm, while the “golden” zoisites have average concentrations of around 200 ppm.

### Strontium

The Strontium concentrations are the highest of all the minor elements present within the Merelani zoisites. Sr probably replaces Ca within the crystal structure of the zoisites. This would explain the reverse correlation between the values for Ca and Sr within the coloured zoisites. The orange coloured zoisites have the lowest concentrations of Ca (Table 12.1) but the highest concentrations of Sr. Strontium is not a chromophore element and therefore, despite its high quantities, will not influence the colour of zoisite. Unlike all the other minor elements present on the Merelani zoisites the concentrations of Sr is not lower in the colourless samples opposed to the coloured samples (Table 12.2). The highest concentrations of Sr are present in the orange and

“golden” coloured samples with average values of  $3726 \pm 90$  and  $2740 \pm 87$  ppm, respectively. The colourless samples have average Sr concentrations of  $2017 \pm 75$  ppm while the blue and green samples have the lowest concentrations of  $1862 \pm 116$  and  $1805 \pm 210$  ppm, respectively.

### ***Yttrium***

Yttrium is considered separately from the other REE, since it does not fit in with the general pattern observed for the REE located within the Merelani zoisites. As expected, the colourless samples have the lowest Y concentrations of  $19 \pm 4$  ppm. The unexpectedly low concentrations of Y in the orange samples ( $32 \pm 3$  ppm) could be the result of site occupation by other REE such as neodymium and praseodymium, which both have very similar atomic radius to that of Y. The blue, green and “golden” zoisites have Y concentrations of  $110 \pm 10$ ,  $62 \pm 10$  and  $138 \pm 12$  ppm, respectively.

### ***Zirconium***

The average Zr concentrations in the coloured zoisites are all below 45 ppm (Table 12.2). Figure 12.5.a, b and c shows the typical colour zonation observed in the coloured zoisite samples. Figure 12.5.d shows an example of a yellow / colourless sample.

#### **12.3.4. Rare Earth Elements (REE)**

The orange zoisite variety has exceptionally high REE concentrations, with an average total rare earth element concentration (TREE) of  $6951 \pm 741$  ppm (excluding Y and Sc). The “golden” zoisite also has significant concentrations of REE, with TREE values of  $1316 \pm 200$  ppm. The blue, green and colourless zoisite variants have comparatively low total REE concentrations of  $278 \pm 48$ ,  $127 \pm 48$  and  $55 \pm 8$  ppm, respectively (see Table 12.2). Almost all the REE present are light REE (LREE), with the heavy REE (HREE) (excluding Y) constituting less than 0.005% of the TREE present within any given sample. In general, Ce is present in the highest concentrations followed by La, Nd and Pr (see Table 12.2).

The various colours caused by the presence of the trivalent 4f Lanthanides (LREE) were defined and described by Nassau (1983). The presence of Ce normally results in a colourless to yellow colouration of a mineral. Lanthanum is not a chromophore, while Nd is associated with an orange to lilac colour and Pr with a green colour, but is present

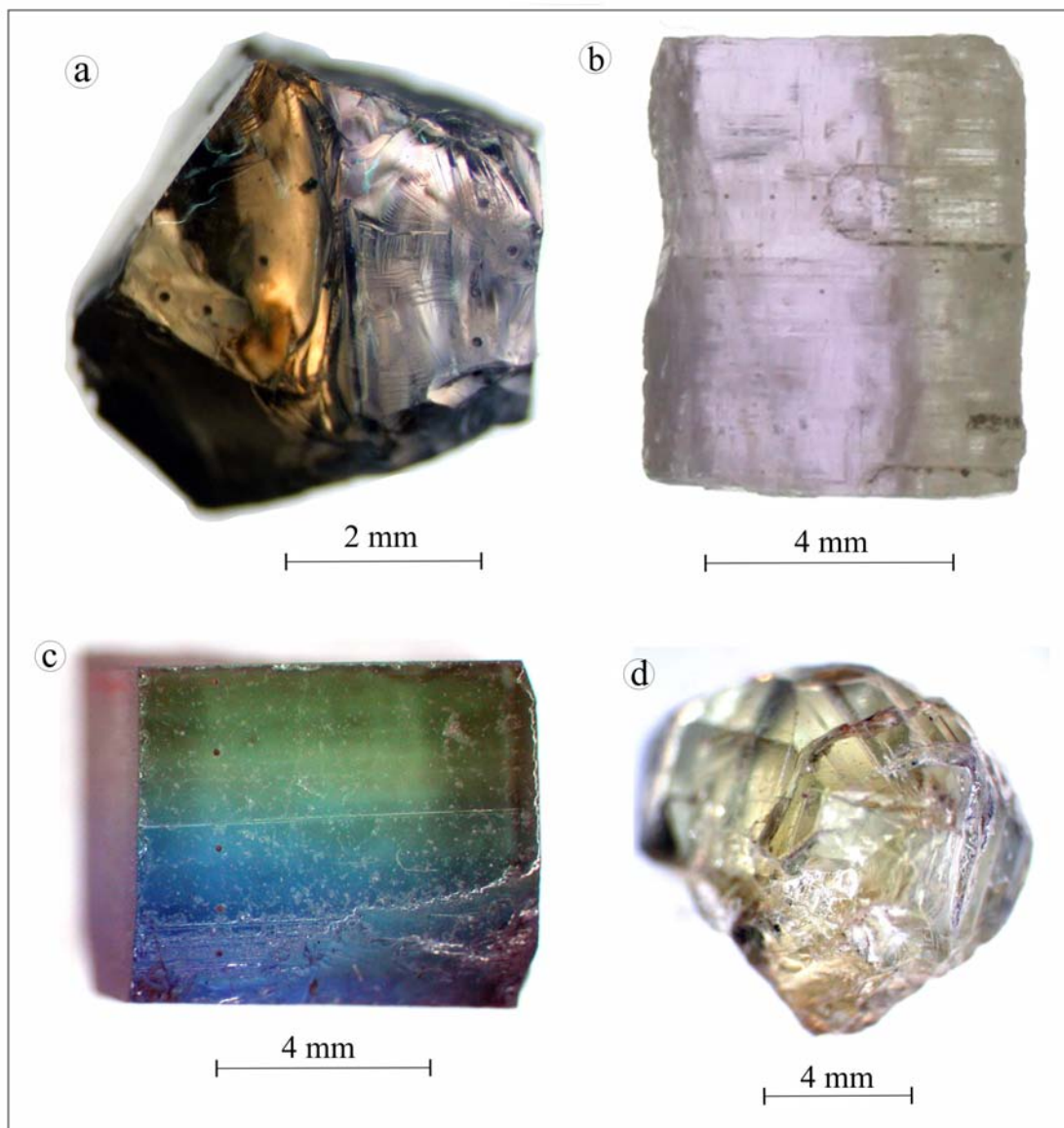


Figure 12.5. a) Sample 59, showing distinct zoning between a “golden” and blue colouration. b) Sample 60, showing blue / violet and colourless zonation. c) Sample 89 exhibiting blue and green zonation. d) Unzoned colourless zoisite (sample 99). The trace and REE concentrations of the samples are presented in Tables 1, 2, 3, 4 and 5, Addendum L.

in far lower concentrations than Nd and Ce (Table 3, Addendum L). Neodymium and Ce are therefore the main REE chromophores within the orange zoisites. Myer (1966) did not detect any significant concentrations of REE within any of the zoisite samples analyses by him through semi-quantitative spectrography.

These REE-rich zoisites have not been described anywhere in the literature and may represent a new gemstone variety of zoisite and will be further described in Section 12.4. Figure 12.6 shows the trichroism of an orange REE coloured zoisite (sample 80) and its REE concentrations.

## 12.4. UV/Visible/NIR analyses

### 12.4.1 Methods and Materials

Over 220 polarised UV/Visible/NIR spectra were obtained, by the author, from 22 orientated tanzanite samples. Windows were polished on the orientated specimens perpendicular to all three the crystallographic axes in order to improve the purity of the spectra. The spectra were restricted to a wavelength (nm) interval of 250 nm to 2200 nm since total absorbance normally occurs below about 300 nm and a high noise signal was apparent for wavelength values over 2200 nm. The samples were analysed on a Perkin-Elmer Lambda 9 UV/Visible/NIR spectrophotometer. The spectrophotometer consists of an ultraviolet (UV), visible light (Vis) and near infrared (NIR) light source and detectors. The spectra were collected at a speed of 204 nm / min with a peak threshold of 0.02 Å and a 0.5 second response time.

*Table 12.3. Light source interval and slit size for the Perkin-Elmer Lambda 9 UV/Vis/NIR Spectrophotometer.*

Light Source	Bottom limit	Peak	Slit size
Ultra Violet	200 nm	319.2 nm	2.0 nm
Visible	319.2 nm	860.8 nm	2.0 nm
Near Infrared	860.8 nm	2500 nm	20.32 nm

Suitable single crystals over a wide range of colours were selected for polarised absorption spectroscopy. The crystals were all orientated by optical investigation and in some cases by means of the spindle-stage method. Windows were polished on both

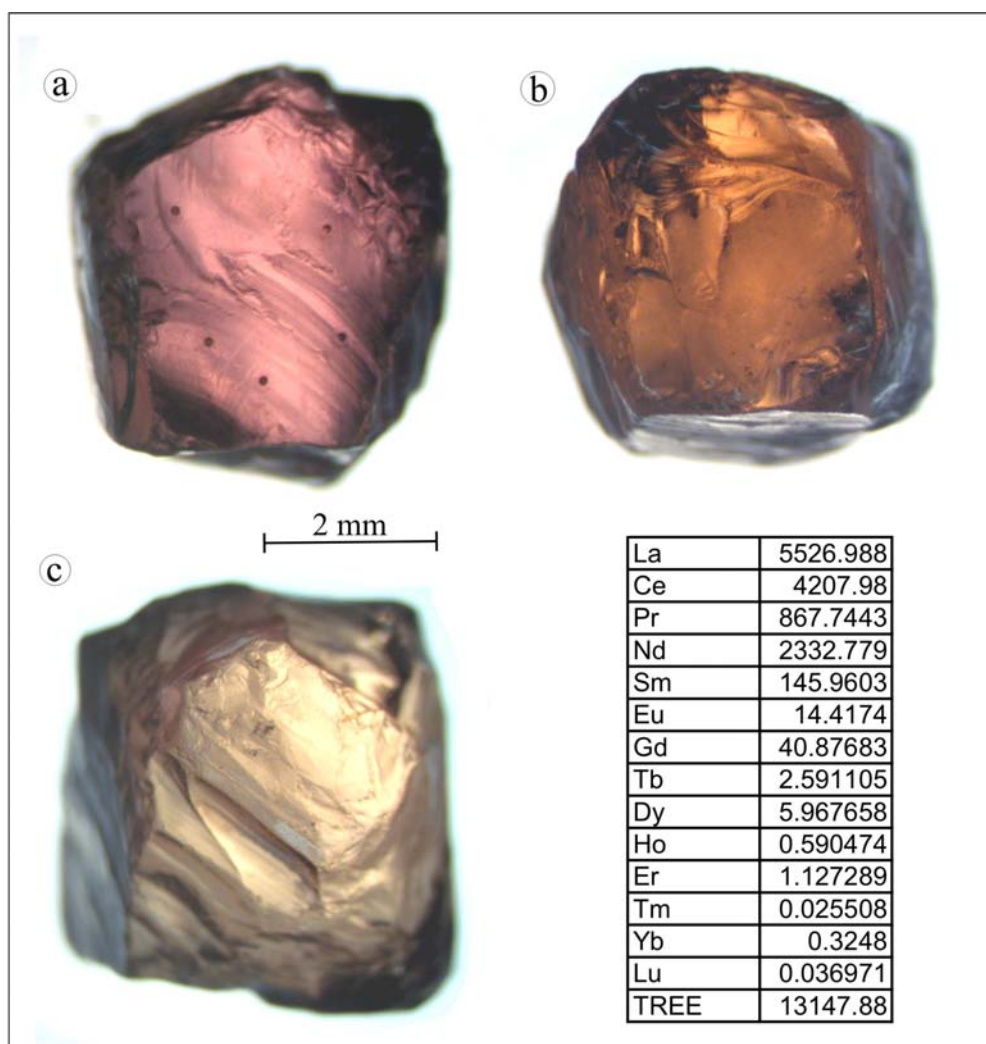


Figure 12.6. Sample 80, representing the trichroic orange variety of zoisite coloured by REE. The REE concentrations are indicated in the accompanying table with TREE concentrations of over 1.3 wt%. The zoisite is weakly trichroic with a) light purple b) yellowish-orange and c) orange-yellow.

sides of all three crystallographic axes. The optical axes were calculated for selected crystals and two windows were polished on one of the optical axis. Unless otherwise indicated, all spectroscopic patterns were normalised to a 1 mm sample thickness.

The aim of the spectroscopic analyses was to obtain the polarised single crystal electronic absorption spectra of a variety of zoisite specimens, representing the typical pleochroism and colour ranges. This was done in order to investigate the difference in the various colours, the crystallographic orientations, pleochroism and the elements contributing to the colours.

#### 12.4.2. Blue zoisite (tanzanite)

Optical and spectroscopic investigation of orientated blue zoisite (tanzanite) samples revealed a strong trichroism with:

- A violet colour present when the electric vector (E) is parallel to alpha, while a blue colour is present when the electric vector is perpendicular to gamma.
- A Blue colour observed when the electric vector (E) is parallel to beta. A red / yellow or green colour is visible when the electric vector (E) is perpendicular to alpha.
- Red / yellow / green colours present when the electric vector (E) is parallel to gamma and a violet colour is observed when the electric vector is perpendicular to beta.

The colour and orientation of the blue coloured zoisites are summarised in Table 12.4.

*Table 12.4. The colour and orientation of the blue zoisites.*

Colour	//Electric Vector	⊥Electric Vector	Section	Index	Axis
Violet	alpha	beta	ac	(210)	B
Blue	beta	gamma	bc	(100)	A
Red / yellow / green	gamma	alpha	ab	(001)	C

In order to investigate whether the colour optima for the various crystallographic axes coincide with the electric vector directions, rotated polarised spectroscopic analyses were done. Sample RB1 was selected and polished, as described above, for rotational



spectroscopic investigation. Each crystallographic axes was investigated spectroscopically by rotating the polarisation filter stepwise while repeating the analyses. Care was taken not to change the conditions of analysis in order to enable comparison of the rotated spectroscopic data. For each spectroscopic analysis, the polarisation filter was rotated by  $10^\circ$  from the direction parallel to the electric vector through  $90^\circ$  ending perpendicular to the electric vector (Figure 12.7). This resulted in a composite spectrum indicating the colour change associated with the change in orientation of the electric vector (see Figure 12.7).

The various colour maxima are close to the parallel and perpendicular orientations of the electric vector. There is however a slight discrepancy of approximately  $10^\circ$ , as evident from Figure 12.7, for the E// $\beta$  direction. This could imply a  $10^\circ$  offset between the principal axis and the crystallographic a-axis and needs to be investigated further. The rotation of the electric vector does not influence the peaks located at wavelengths greater than 900 nm, with no distinct pattern for the H<sub>2</sub>O peaks located at between 1500 nm and 2200 nm. Table 12.5 indicates the peak locations for the three crystallographic axes as determined by spectroscopic investigations of the blue zoisite (tanzanite).

### ***Discussion***

The optical spectrum absorption values of a mineral are used to investigate the colour of a mineral. The location of the largest absorption peaks represent the predominant colour absorbed by the mineral and therefore indicate the colour that is subtracted out of its colour spectrum. The maximum absorption is more importantly also used to determine the colour-causing elements (also called chromophores or ligands) present within the mineral. The maximum and minimum absorptions for the different crystallographic axes are indicated in Table 12.5. It should be noted that for some of the blue zoisites analysed certain peaks are more pronounced than is commonly the case. These stronger than usual absorption peaks are sometimes observed as small signals along crystallographic axes where they are normally not present.

The absorption peaks of other V-bearing minerals and gemstones have been studied and identified by various authors, including McClure (1962), McFarlane (1964), White et al.

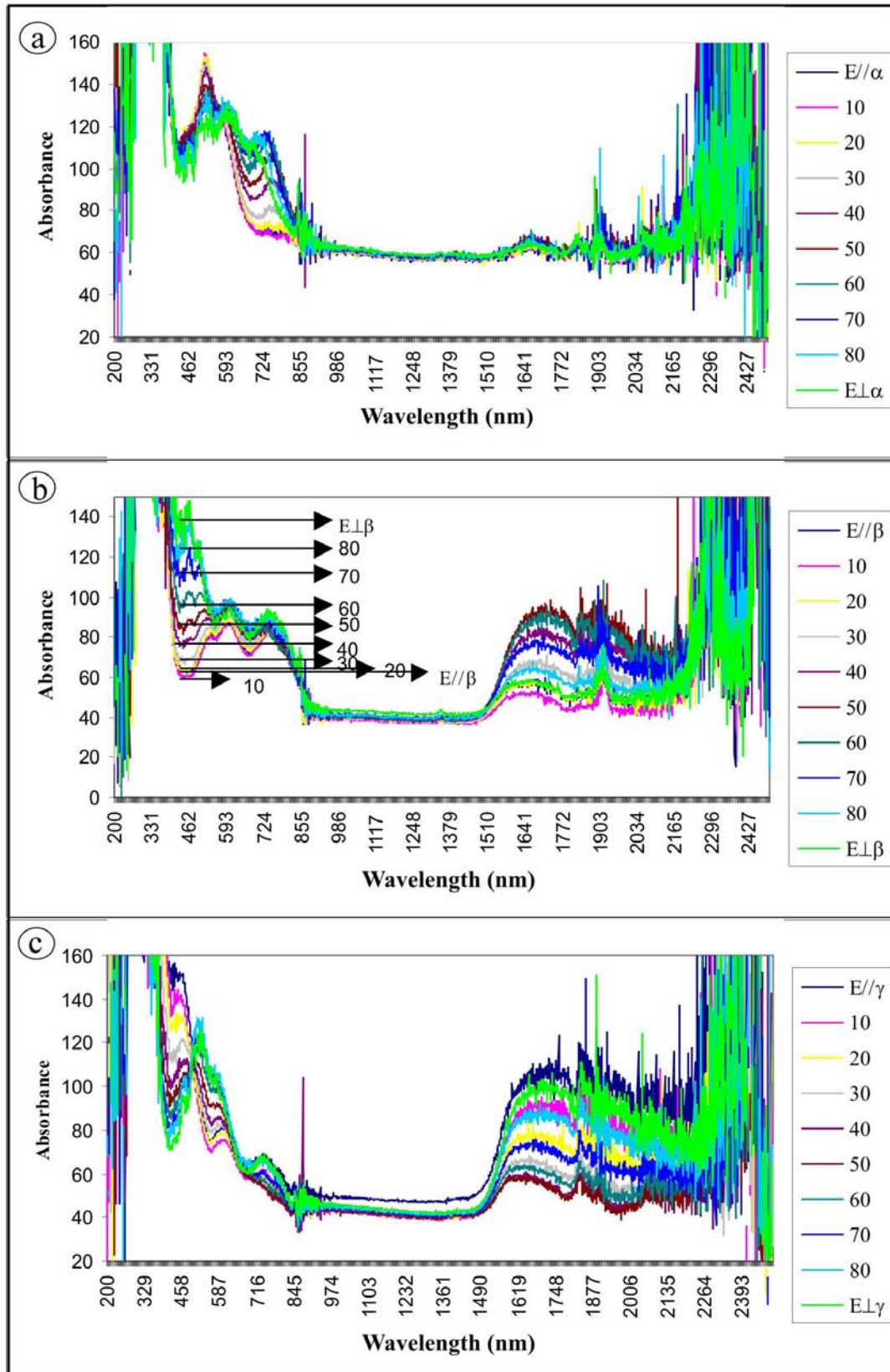


Figure 12.7. Electric vector rotational diagram indicating the change in UV/Vis/NIR absorbance with change in orientation of the electric vector for a)  $E//\alpha$  rotated to  $E\perp\alpha$ . b)  $E//\beta$  rotated to  $E\perp\beta$ . c)  $E//\gamma$  rotated to  $E\perp\gamma$ .

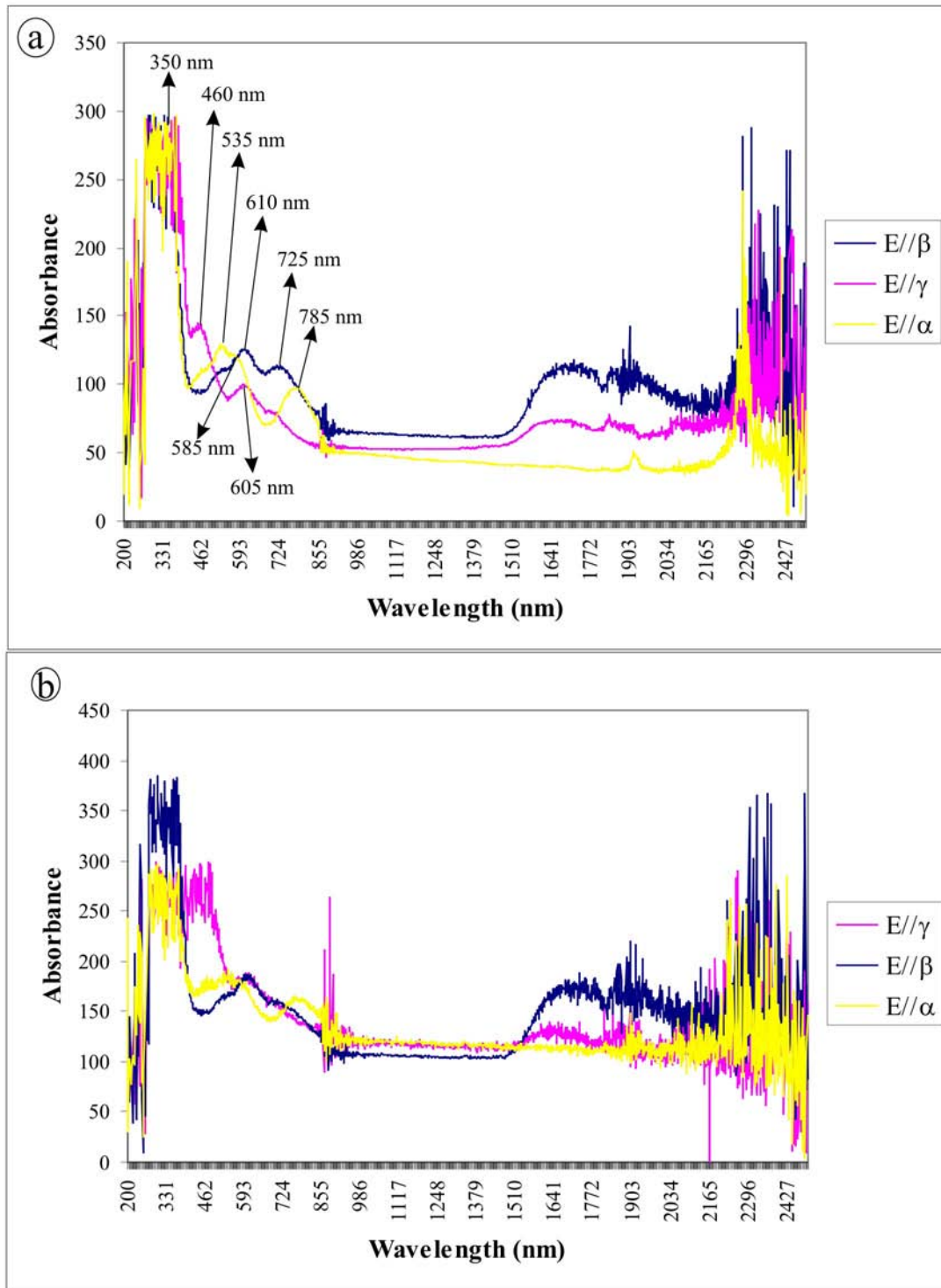


Figure 12.8. UV/Vis/NIR spectra of two blue zoisite samples, with a) sample RB8 and b) sample Rb10. The UV/Vis/NIR spectra of both samples clearly illustrates the difference in absorbance along the three crystallographic axes. The dominant visible spectrum peaks of the blue zoisites are indicated in Figure 12.8.a.

(1967), Rossman (1974), Gübelin and Weibel (1975), Schmetzer and Otteman (1979), Schmetzer (1982). The spectroscopy of V-bearing zoisites was studied by Faye and Nickel in 1971. From the previous work it is evident that the majority of peaks, as

indicated in Table 12.5, can be attributed to the presence of V within the zoisite crystals. This is supported by the low trace element concentrations of other possible ligands such as Cr, Mn and Fe<sup>3+</sup> as discussed in Section 12.3. The majority of optical absorptions can therefore be ascribed to the electronic transitions between the d orbitals of primarily V<sup>3+</sup>, but possibly also V<sup>4+</sup>.

*Table 12.5. Colour and UV/Vis absorption peaks along the three crystallographic axes of blue zoisites.*

Axis	Colour	Absorptions depressions	Absorption peaks
E // $\alpha$ (E $\perp\gamma$ )	Violet	400 – 440 nm; 650 – 720 nm	Broad peak between 290 and 380 nm. Large absorption peak at 520 nm with a superimposed peak at 580 nm. Absorption peak of varying intensity centred at 780 nm.
E // $\beta$ (E $\perp\alpha$ )	Blue / Tan	410 – 490 nm; 650 – 700 nm	Broad peak between 290 and 380 nm. Two broad absorption peaks from 585 to 625 (600 nm) and 700 to 770 nm (730 nm), with a shoulder peak at around 535 nm.
E // $\gamma$ (E $\perp\beta$ )	Red / yellow / green	525 – 575 nm; 790 – 850 nm	Broad absorption peak located between 290 and 380 nm. Absorption peak located between 420 and 480 nm and centred at approx. 450 nm. Absorption peak between 585 to 615 nm, normally centred at ca. 600 nm.

McClure (1962) and McFarlane (1964) showed that V<sup>3+</sup>-bearing corundum have broad absorption peaks at between 295 and 320 nm and sharper peaks at around 400 nm and 570 nm. From Table 12.5 it is evident that the absorption peaks for the blue zoisite correlate very well with these values. Faye and Nickel (1971) also indicated that the blue colouration of zoisites could be related to the presence of V ions. They argued that the spectra must be due to either V<sup>2+</sup>, V<sup>3+</sup> or V<sup>4+</sup> since V<sup>5+</sup> cannot give rise to intra-cation transition. Furthermore they showed that V<sup>2+</sup> has a complex absorption spectrum and has a relatively large size (0.88 Å) and low stability and is therefore an unlikely ion in the structure of zoisite. They concluded that it is possible that minor amounts of V<sup>4+</sup>

could be present within the zoisite structure, but that the majority of V present within the zoisites is probably  $V^{3+}$ .

The absorption peak located at about 450 nm observed when  $E//\gamma$  could possibly be related to the presence of  $V^{4+}$  within the crystal structure of the blue zoisite. The 450 nm absorption peak is the only peak significantly influenced by heating and will be discussed in detail in Chapter 13. This however implies that the peak is not caused by  $V^{3+}$ , since it behaves differently from the  $V^{3+}$  peaks, which is not influenced by heating. This peak has been contributed to the presence of  $V^{4+}$  within other minerals such as apophyllite, as described by Rossman (1974).  $V^{4+}$  however also has a characteristic absorption peak located at approximately 830 nm, which was not observed in any of the natural zoisite samples. It is therefore unlikely that  $V^{4+}$  is present in substantial amounts within blue zoisite in its natural form. It is also possible that the absorption peak could be related to the presence of Ti within the zoisite structure. Even though the presence of Ti as a chromophore is not common, it has been identified as a colouring agent in various minerals as described by Faye and Harris (1969), Lehmann (1969), Manning (1969), Faye and Nickel (1971), Ihinger and Stolper (1978), Burns (1981), Cohen and Makar (1984, 1985) and Schmetzer (1987).  $Ti^{4+}$  contains no valence d-electrons and is therefore not a chromophore and has no visible light absorption spectrum.  $Ti^{3+}$  has one valence electron that can be excited into a higher energy state by visible light and therefore will have absorption in the optical range (Rossman, 1988).  $Ti^{3+}$  is only found in highly reducing environments. As described earlier, the Merelani tanzanite deposit occurred under highly reducing conditions, due to the presence of large amounts of graphite. It is therefore possible that  $Ti^{3+}$  could occur within the crystal structure of tanzanite and other zoisites from the Merelani deposit and the 450 nm peak could be explained by its presence. The presence of  $Ti^{3+}$  instead of  $V^{4+}$  is further supported by its more suitable charge opposed to that of  $V^{4+}$  for substitution into the Al positions (Faye and Nickel, 1971).

McClure (1962) as well as Tsang and Ghose (1971) studied the crystal field parameters and the site occupations for various elements within zoisite. They indicated that the average metal-oxygen distances for the Al(i) and Al(ii) sites are 1.89 Å and 1.97 Å, respectively. From the crystal field parameters they were able to conclude that the absorption band near 750 nm can be assigned to  $V^{3+}$  within the Al(ii) sites. They further

indicated that the mirror plane of zoisite is perpendicular to the a axis and that the absorption peak at 750 nm for E// $\beta$  would result in a stronger peak than for E// $\alpha$  and E// $\gamma$ . This coincides well with the data obtained from this study as indicated in Figure 12.8 and Table 12.5.

From the work done by McClure (1962) it is also possible to deduct that the absorption peak for E// $\alpha$  located at approx. 450 nm can also possibly be enhanced as a result of distortion of the oxygen octahedra due to compression along the B-axis.  $Ti^{3+}$  is normally a weak chromophore and is therefore often overprinted by the presence of other ligands. If the 450 nm peak is caused by the presence of  $Ti^{3+}$  then this enhancement as a result of the oxygen octahedron distortion could explain why it is the only observable peak associated with  $Ti^{3+}$ , see Figure 12.8.

Tsang and Ghose (1971) calculated that the absorption intensities for the Al(i) and Al(ii) sites are fairly similar. This would therefore suggest a possible random distribution for elements such as  $V^{3+}$  and  $Ti^{3+}$  between the two types of sites. Tsang and Ghose (1971) also indicated that due to the absence of any point group symmetry in the Al(i) site, the anisotropy in absorption intensities is expected to be less pronounced.

### ***Near infrared (NIR) spectroscopy***

The near infrared (NIR) spectrum of the blue zoisite is also indicated in Figures 12.7 and 12.8. The peaks located at between 860 and 900 nm are caused by the transition from a visible light source to the near infrared light source. No absorption peaks are located between 900 nm and 1480 nm for any of the crystallographic axes.

The standard 1<sup>st</sup> OH stretching band overtone for hydrous minerals is normally located at 1.4  $\mu$  (1400 nm), but the OH feature of zoisite occurs at 1.68  $\mu$  (1680 nm). Zoisite also has an unusually weak band located at 1.85  $\mu$  (1850 nm). The very low OH energy band for zoisite was discussed by Langer and Lattard (1980). The H<sub>2</sub>O bend and stretching mode for zoisite is located at 1.9  $\mu$  (1900 nm). Lattice or bending modes of Al-OH in combination with OH group features occur at 2.3  $\mu$ , 2.35  $\mu$  and 2.48  $\mu$  (USGS Zoisite description HS347).

The OH group and H<sub>2</sub>O-related features are identical for all the different coloured zoisite including the orange zoisites, see Figures 12.8, 12.9, 12.10 and 12.11. The OH and H<sub>2</sub>O features can be used to identify the crystallographic axis for zoisite, especially along the B-axis (E// $\alpha$ ), which contains low OH and H<sub>2</sub>O peaks. The A-axis usually contains the largest amounts of OH and H<sub>2</sub>O absorption, while the absorption along the C-axis is normally slightly lower.

### 12.4.3 Green zoisite spectrum

The colours and crystallographic orientation of the green zoisite is listed in Table 12.6. From this table it is evident that the alpha, beta and gamma colours all differ from those of the blue tanzanite.

*Table 12.6. Colour and crystallographic orientation of the green zoisite.*

Colour	// Electric Vector	$\perp$ Electric Vector	Section	Index	Axis
Purple	Alpha	beta	ac	(210)	B
Grey Blue	Beta	gamma	bc	(100)	A
Green to yellow-green	Gamma	alpha	ab	(001)	C

If the electric vector (E) is parallel to alpha (E// $\alpha$ ) a purple colour is observed, opposed to the violet colour observed for E// $\alpha$  of the blue zoisite. The purple colour can be described as a mixture of violet and red. When E// $\beta$ , a far less intense blue colour, best described as grey blue, is observed compared to that of the blue zoisite. When the electric vector is parallel to gamma (E// $\gamma$ ) it results in a green to yellow green colour.

In general, the peaks observed for the blue zoisite agree with those of the green zoisite, however, certain distinct differences do occur. The first difference is that the peak located at 360 nm to 380 nm is sharper and narrower than that observed in the blue zoisite. The most significant difference however, is the presence of a peak at ca. 750 nm present in the green zoisites for both E// $\alpha$  and E// $\beta$  that is not present in the blue zoisites (see Table 12.7 and Figures 12.8 and 12.9).

Rossmann (1988) indicated that the presence of an absorption peak at 750 nm in synthetic rutile is indicative of an intervalence charge-transfer between  $Ti^{4+}$  and  $Ti^{3+}$ . This type of intervalence charge transfers has been shown to produce strong absorption within the visible range (Burns, 1981). It is therefore possible that the main difference in colour between the blue zoisites and the green zoisites is due to the presence of an intervalence charge-transfer between  $Ti^{4+}$  and  $Ti^{3+}$  within the green zoisites. This theory is further supported by the presence of slightly higher concentrations of Ti within the green zoisites, as indicated in Table 12.1.

*Table 12.7. Colour and UV/Vis absorption peaks along the three crystallographic axes of green zoisites.*

Axis	Colour	Absorption peaks
E // $\alpha$ (E $\perp$ $\gamma$ )	Purple	Sharp peak located between 280 and 310 nm. Large absorption peaks between 510 nm and 620 (560 nm) and 730 to 810 nm (centre at 765 nm).
E // $\beta$ (E $\perp$ $\alpha$ )	Grey Blue	Broad absorption peak located between 280 and 380 nm. Broad absorption peak located between 540 and 680 nm, with two shoulder peaks at 500 and 720 nm, creating a large superimposed peak from 480 to 760 nm.
E // $\gamma$ (E $\perp$ $\beta$ )	Green to yellow - green	Broad peak between 270 and 380 nm Sharp absorption peak located between 430 and 465 nm, centred at around 445 nm. Absorption peak from 585 to 625 (600 nm) and a broad peak between 700 to 790 nm (740 nm).

#### 12.4.4. Yellow to colourless zoisite

The absorption spectrum of the light yellow to colourless zoisites is indicated in Figure 12.10. The yellow to colourless zoisites has little absorption of visible light, resulting in low absorption peaks. The lack of absorption peaks, similar to that of the green and blue zoisite, is due to the low concentrations of V within the yellow to colourless zoisites, as discussed in Section 12.3. The only significant peak present in the yellow to colourless zoisites is located between 425 and 480 nm, with a centre at 450 nm. As discussed for



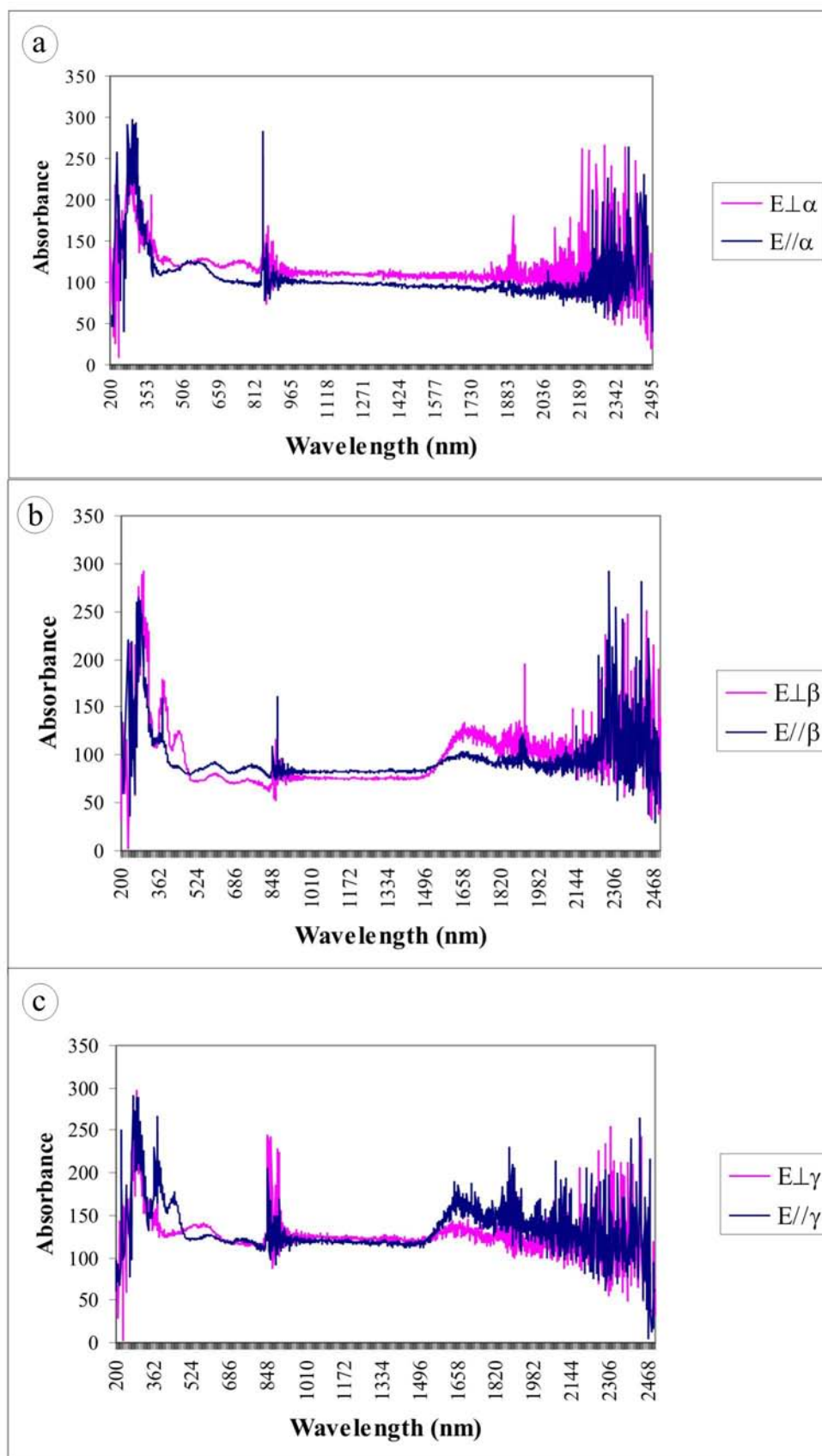


Figure 12.9. UV/Vis/NIR absorbance spectra of the three crystallographic axes of the green zoisite sample G89, with a) E//α; b) E//β and c) E//γ.

the blue zoisites, this peak is due to the presence of  $Ti^{3+}$ . This is confirmed by the trace element concentrations of the various coloured zoisites, since the colourless zoisites contain significantly less V, but almost similar Ti concentrations to that of the blue and green zoisite, see Table 12.2.

*Table 12.8. Colour and crystallographic orientation of the yellow/colourless zoisite.*

Colour	//Electric Vector	⊥Electric Vector	Section	Index	Axis
Light grey green	alpha	beta	ac	(210)	B
Light purple	beta	gamma	bc	(100)	A
Light greenish yellow	gamma	alpha	ab	(001)	C

In general, the presence of an average of 523 ppm Ti within the yellow to colourless zoisites is the only significant chromophore and results in the 450 nm absorption peak.

#### 12.4.5 Orange zoisite

The orange zoisite is weakly trichroic with the colours and crystallographic orientation listed in Table 12.9. The orange zoisites have a completely different visible absorption spectrum relative to that of the other coloured zoisites. In general, all three crystallographic axes have the same sharp, narrow peaks located at:

- 520 to 535 nm
- 575 to 585 nm
- 745 to 750 nm
- 795 to 805 nm

*Table 12.9. Colour and crystallographic orientation of the orange zoisite.*

Colour	// Electric Vector	⊥ Electric Vector	Section	Index	Axis
Orange yellow	alpha	beta	ac	(210)	B
Light purple	beta	gamma	bc	(100)	A
Reddish orange	gamma	alpha	ab	(001)	C

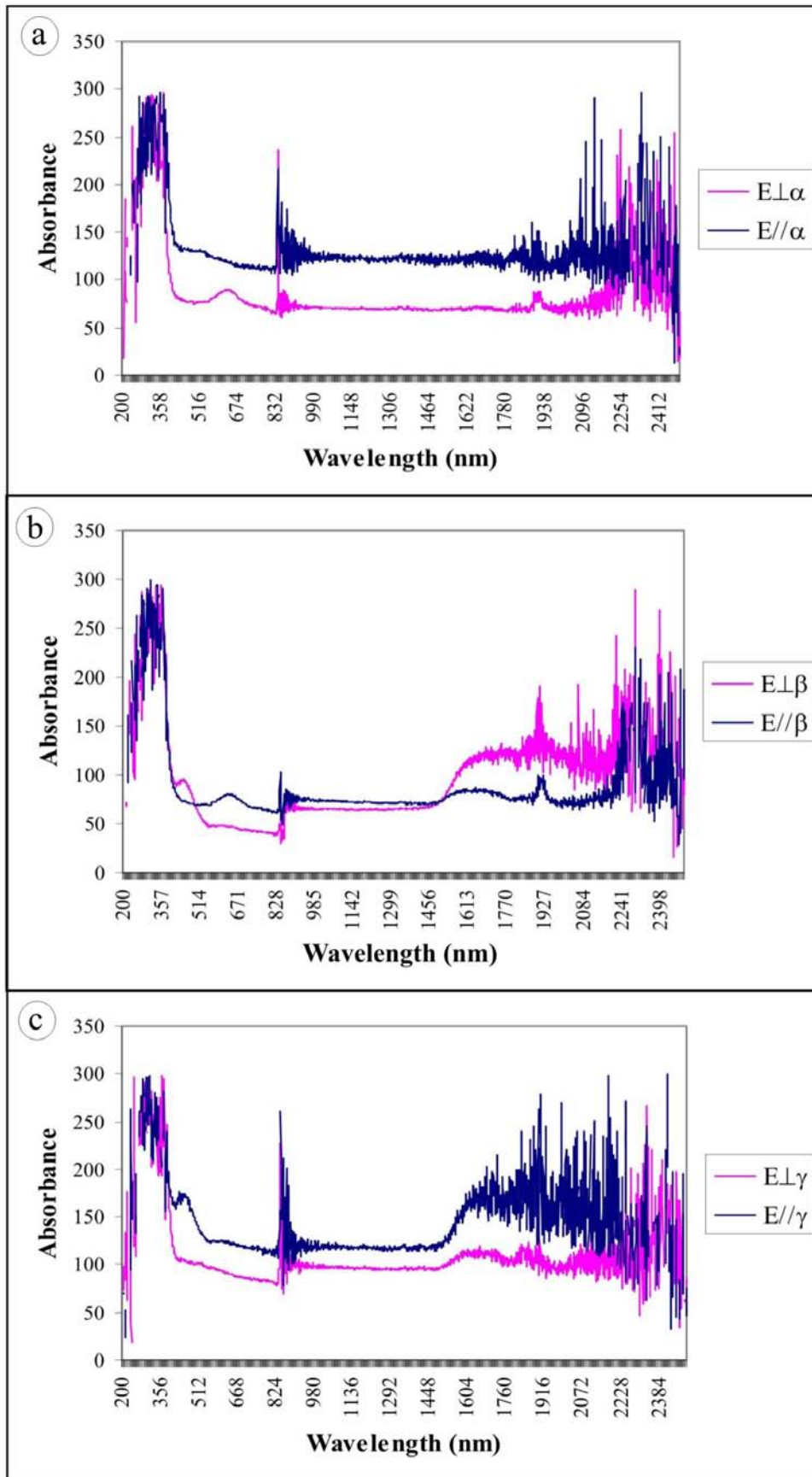


Figure 12.10. UV/Vis/NIR spectrum of a yellow to colourless zoisite (sample Ry) containing very few trace element concentrations.

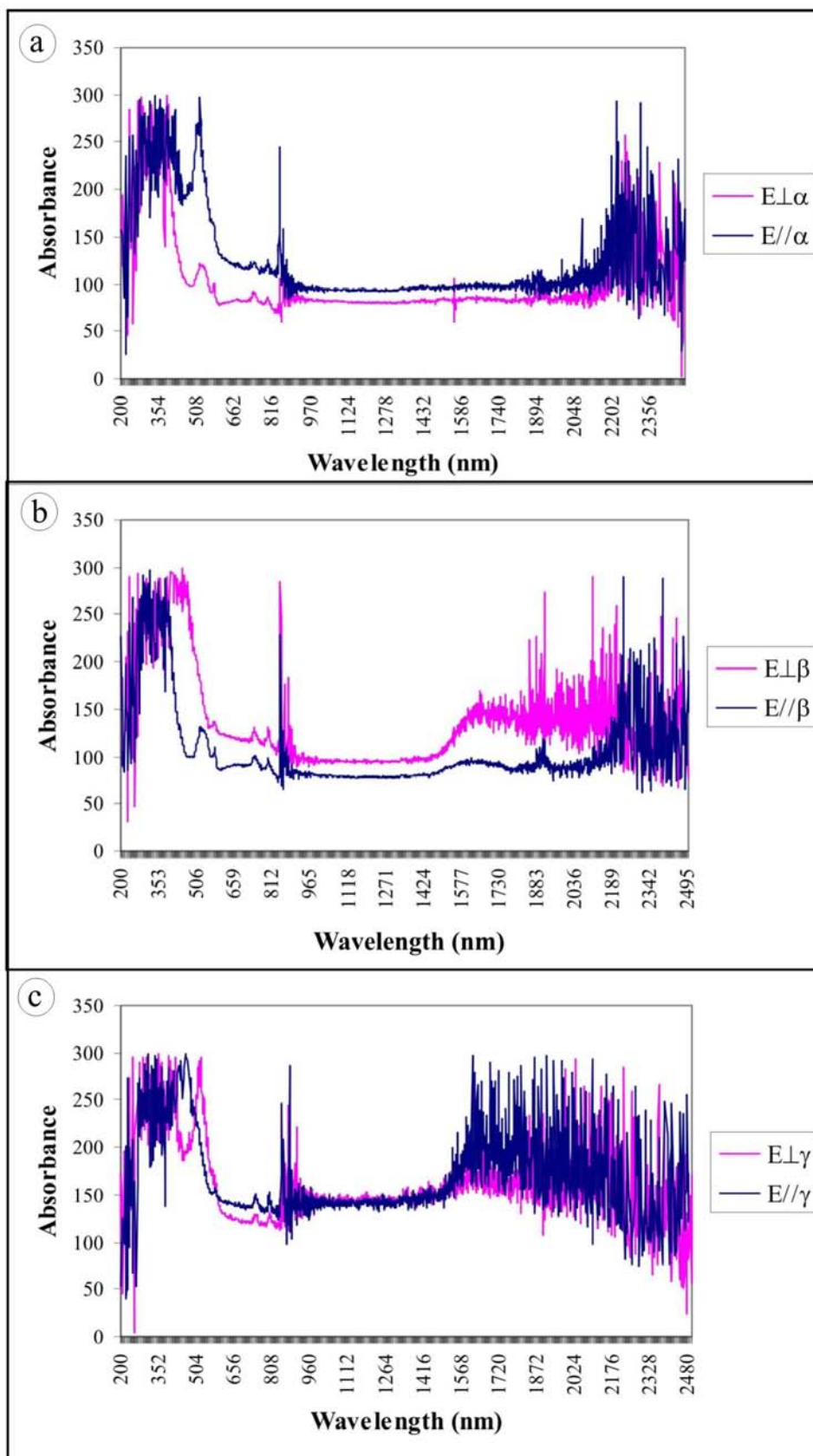


Figure 12.11. UV/Vis/NIR spectrum of an orange zoisite coloured by the presence of REE. The absorption spectrum is from sample 80 and has a thickness of ca. 4.5 mm.

Comparison of the absorption peaks observed for the orange zoisite with absorption peaks of known elements in the literature reveal a positive correlation with the peaks produced by  $\text{Nd}^{3+}$ , see Figure 12.8. The only significant deviation from  $\text{Nd}^{3+}$  absorption peak localities is the occurrence of an additional peak for  $E//\alpha$  located at 465 nm and the absence of the 520 to 535 nm peak also for  $E//\alpha$ . The same absence of the peak located between 520 and 535 nm is also observed for the  $E\perp\gamma$ , however the peak at 465 nm is not present. The peak located at 465 nm can once again be attributed to the presence of  $\text{Ti}^{3+}$ , similar to that of the blue, green and yellow to colourless zoisites.

The author believes that spectroscopic data, in conjunction with the crystal chemistry of the orange zoisite, is conclusive proof for the classification of a new gemstone variety of zoisite, predominantly coloured by Nd.

### **12.5. Fourier Transform Infrared (FTIR) analyses**

FTIR analyses were conducted, by the author, on a Nicolet Magan-IR 560 spectrometer at the University of Cape Town, South Africa. The system was configured to cover the Mid-IR range from 650 to 4000  $\text{cm}^{-1}$  using a nitrogen cooling system, XT-KBr beam splitter and DTGS detector. The analyses followed standard procedures and settings as described by Mendelsohn and Milledge (1995). A minimum of six scans was performed per analysis at a spectral resolution of 23.142  $\text{cm}^{-1}$ .

The selected single crystal zoisite samples were crystallographically orientated and flat windows were polished on both sides of all three crystallographic axes and one of the optic axis. The crystals were cut with a diamond saw along the three axes and the optical axis into thin wafers of approximately 0.5 mm. The wafers were subsequently polished and cleaned.

FTIR analyses were conducted on both the blue zoisite (tanzanite) samples and yellow to colourless zoisite samples. As expected, the FTIR spectrum for the two colour varieties of zoisite are virtually identical since the trace element concentrations does not influence the symmetry, stretching and molecular vibrations. Figure 12.12 and 12.13 indicate the FTIR spectrum for the blue and yellow/colourless zoisites, respectively.

Table 12.10 indicates the main absorption peaks identified through FTIR for the various crystallographic axes and the optical axis. The peaks located between 3150 and 3250  $\text{cm}^{-1}$  are probably still related to OH-stretching vibrations similar to those described for the NIR spectra. The OH-stretching peaks are more prominent for the optical axis compared to the other crystallographic axes. The broad peak located between 1600 and 1700  $\text{cm}^{-1}$  can probably be attributed to  $\text{H}_2\text{O}$  bending vibrations within the zoisite structures.

Table 12.10. Predominant FTIR peaks in  $\text{cm}^{-1}$  for the different crystallographic axis and optical axis of zoisite.

Axis	Main FTIR peaks ( $\text{cm}^{-1}$ )
A-axis	700; 1300; 1695; 1790; 2190; 3170
B-axis	700; 1300; 1695; 1790; 2190; 3170
C-axis	1300; 1790, 1900; 3185
Optical axis	1300; 1695; 1790; 2130; 3125; 3240

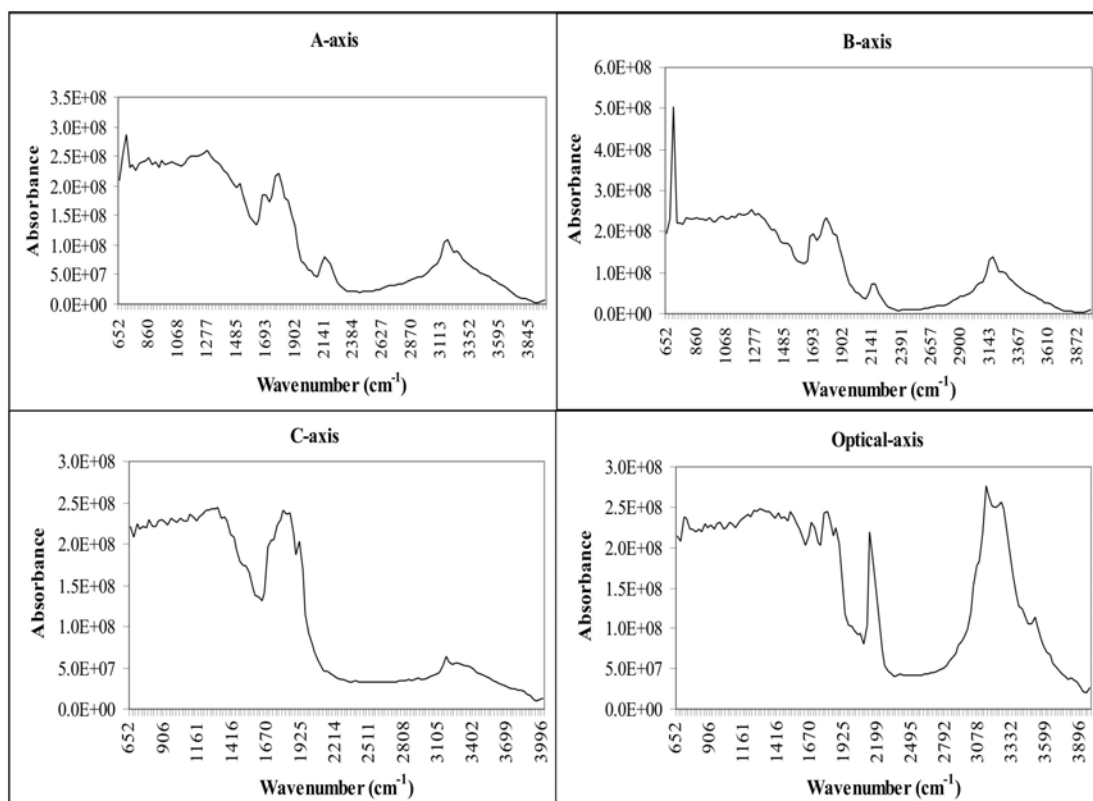


Figure 12.12. FTIR absorption spectrum of blue zoisite (Sample 4) along the three crystallographic axes and the optical axis.

The remaining peaks are caused by the creation of a dipole moment of an infrared wavelength, by interaction of polyatomic molecules within the zoisite structure (Langer and Lattard, 1980). It is likely that the FTIR absorption of the zoisites might increase as a result of heating. This is caused by a change in the molecular vibrations (e.g. between Si and O) within the crystal structure, possibly associated with the liberation of a bonding electron.

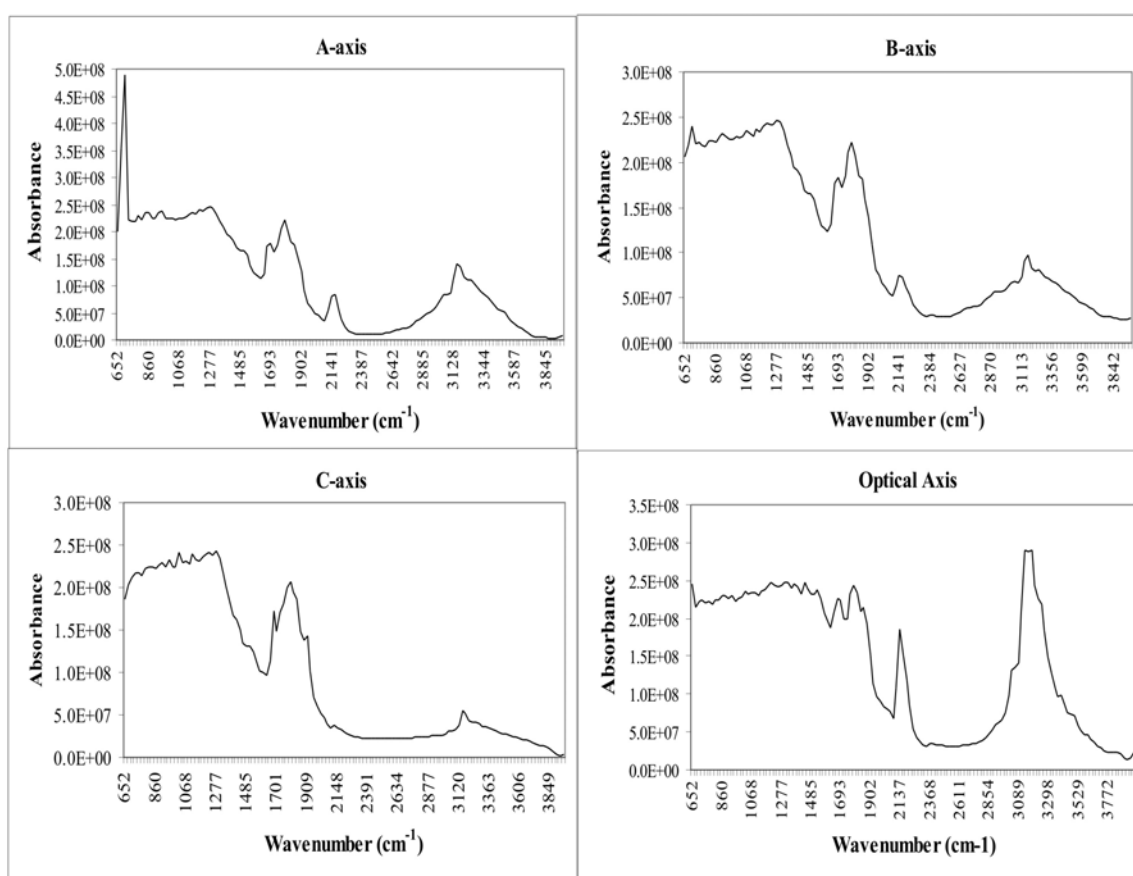


Figure 12.13. FTIR absorption spectrum of colourless zoisite (Sample 3) along the three crystallographic axes and the optical axis.

## 12.6. Electron Paramagnetic Resonance (EPR)

### 12.6.1. Introduction

EPR studies are powerful and complex tools used in many fields of physics, chemistry, biology and mineralogy. The theory and application of the technique in mineralogy has been described in detail by various authors including, Altshuler and Kozyrev (1964), Burns (1970), Pake and Estle (1973) and Calas (1988). The standard notations, as defined by these authors, were used in this study. The spin Hamiltonian ( $\hat{H}$ ) is therefore defined as:

$$\hat{H} = \beta(g_z H_z S_z + g_x H_x S_x + g_y H_y S_y) + D[S_z^2 - \frac{1}{3}S(S+1)] + E(S_x^2 + S_y^2) + A_z S_z I_z + A_x S_x I_x + A_y S_y I_y$$

for the principle coordinate system (x, y, z)

The g factor is defined as:  $gBH = \hbar\omega$  where

B - Bohr value

H - magnetic field

$\hbar$  - Planck's constant

$\omega$  - wave frequency x  $2\pi$

The spin Hamiltonian delineates the three major types of interactions which can affect the electronic energy ground state of a paramagnetic centre:

- Zeeman splitting
- Fine-structure or zero-field splitting (ZFS)
- Hyperfine structure (HFS)

Together these interactions describe the structural and chemical environment of the paramagnetic centre and can be correlated with the presence of transition metal ions. Only S-state and effective S-state ions have an EPR detectable signal at room temperature. This therefore limits the technique predominantly to the following ions at room temperature,  $V^{4+}$ ,  $V^{2+}$ ,  $Cr^{3+}$ ,  $Mn^{2+}$ ,  $Fe^{3+}$ ,  $Cu^{2+}$ ,  $Gd^{3+}$ ,  $Eu^{2+}$  and  $Mo^{5+}$  (Calas, 1988).



### 12.6.2. Instrument specifications

The EPR spectra were obtained, by the author, on a Varian Centuries Series ESR (EPR) spectrometer at the Solid State Physics Laboratory, Rijks University, Groningen, the Netherlands. The samples were analysed at 300K on X-band. The ESR analyses were done in conjunction an Oxford Instruments flow cryostat. A maximum scan range of 10 000 Gauss was used.

### 12.6.3. Sample preparation

Six coloured zoisite single crystals were analysed by means of electron paramagnetic resonance. Only samples that had no inclusions, no internal fractures and were of a high optical clarity were selected. The specific samples were further optically and chemically scrutinised in order to select samples with a spread in colour and trace element chemistry. The samples were all crystallographically orientated by means of optical methods. Windows were subsequently polished perpendicular to all three crystallographic axes, in a similar fashion, as described for the optical spectroscopic analysis (see Section 12.5).

### 12.6.4. Blue zoisite (tanzanite)

The EPR spectra of tanzanite along the three crystallographic axes are indicated in Figure 12.14. The peak located at 760 Gauss for H//a and at 670 Gauss for H//c is most likely due to the presence of Fe<sup>3+</sup>. Rotational EPR analysis of the blue zoisite samples indicates the angular dependence of the Fe<sup>3+</sup> peak. The Fe<sup>3+</sup> peak is not absent for H//b but located below 550 Gauss and subsequently not detectable. The Fe<sup>3+</sup> peak therefore has a highly anisotropic g factor. In general, the effective g-values of Fe<sup>3+</sup> are located at 2 and 6 with the isotropic transition at  $g_{\text{eff}} = 4.3$ . The g-values obtained from this study for the blue zoisite however indicate that the signal at  $g_{\text{eff}} = 4.3$  is almost negligible, while the signal at  $g_{\text{eff}} = 2$  is the predominant signal. The isotropic transition signal indicates a strong rhombic distortion, while the  $g = 2$  signal is attributed to isolated, slightly distorted and coupled Fe<sup>3+</sup> ions. This rhombic distortion is well documented for Fe<sup>3+</sup> in other minerals as indicated by Castner et al. (1960), while Tsang and Chose (1971) also found  $g_z$  values of  $1.96 \pm 0.01$  for their zoisite samples. They concluded that the Fe<sup>3+</sup> ions are located in the Al(ii) sites of zoisite and has a point group symmetry  $m$  with the (010) plane as the mirror plane.

Rotation of the EPR spectrum to ca.  $45^\circ$  between the A- and B-axes show a slight distortion in the symmetry, with the  $\text{Fe}^{3+}$  peak located at 700 gauss (Figure 12.15.a). The EPR spectrum at ca.  $45^\circ$  between the A-axis and C-axis shows a far stronger symmetry distortion with the  $\text{Fe}^{3+}$  peak located at ca. 1760 gauss (Figure 12.15.b). In general, no hyperfine splitting associated with  $\text{Fe}^{3+}$  was observed for any of the blue zoisite samples. However, the four peaks located at 591, 737, 896 and 1080 gauss for the sample rotated  $45^\circ$  between the A-axis and B-axis could possibly be the hyperfine splitting peaks of  $\text{Fe}^{3+}$ , only observable when it is close to the isotropic transition. The two additional peaks needed for a nuclear spin ( $I$ ) of  $5/2$  for  $\text{Fe}^{3+}$  are expected to be located below 550 gauss and therefore not detectable.

The EPR spectra of all the blue zoisites analysed indicate a characteristic six line hyperfine splitting (HFS) signal, see Figure 12.14 and 12.16. This signal is most likely caused by the presence of trace concentrations of  $\text{Mn}^{2+}$  within the zoisite structure. De Biasi and Fernandes (1984) indicated that the sharp six line HFS signal of  $\text{Mn}^{2+}$  is caused by concentrations of less than 0.1 wt% Mn, while higher concentrations caused a significant broadening of the signal due to spin-spin interactions. The peak positions for the three crystallographic axes, as well as the spectrum measured  $45^\circ$  between the A-axis and B-axis, are indicated in Table 12.11 and Figure 12.15.

*Table 12.11. Limited angular dependence of the hyperfine splitting (gauss) of the  $\text{Mn}^{2+}$  resonance as measured for sample 4.  $M_I$  indicates the various hyperfine splitting due to nuclear spin of  $\text{Mn}^{2+}$ .*

Axes	Peak 1 $M_I = (+5/2)$	Peak 2 $M_I = (+3/2)$	Peak 3 $M_I = (+1/2)$	Peak 4 $M_I = (-1/2)$	Peak 5 $M_I = (-3/2)$	Peak 6 $M_I = (+5/2)$
A-axis	1753	1844	1936	2029	2126	2225
B-axis	1752	1842	1931	2027	2122	2221
C-axis	1741	1833	1924	2022	2119	2220
$45^\circ$ AB-axis	1750	1841	1936	2030	2129	2230

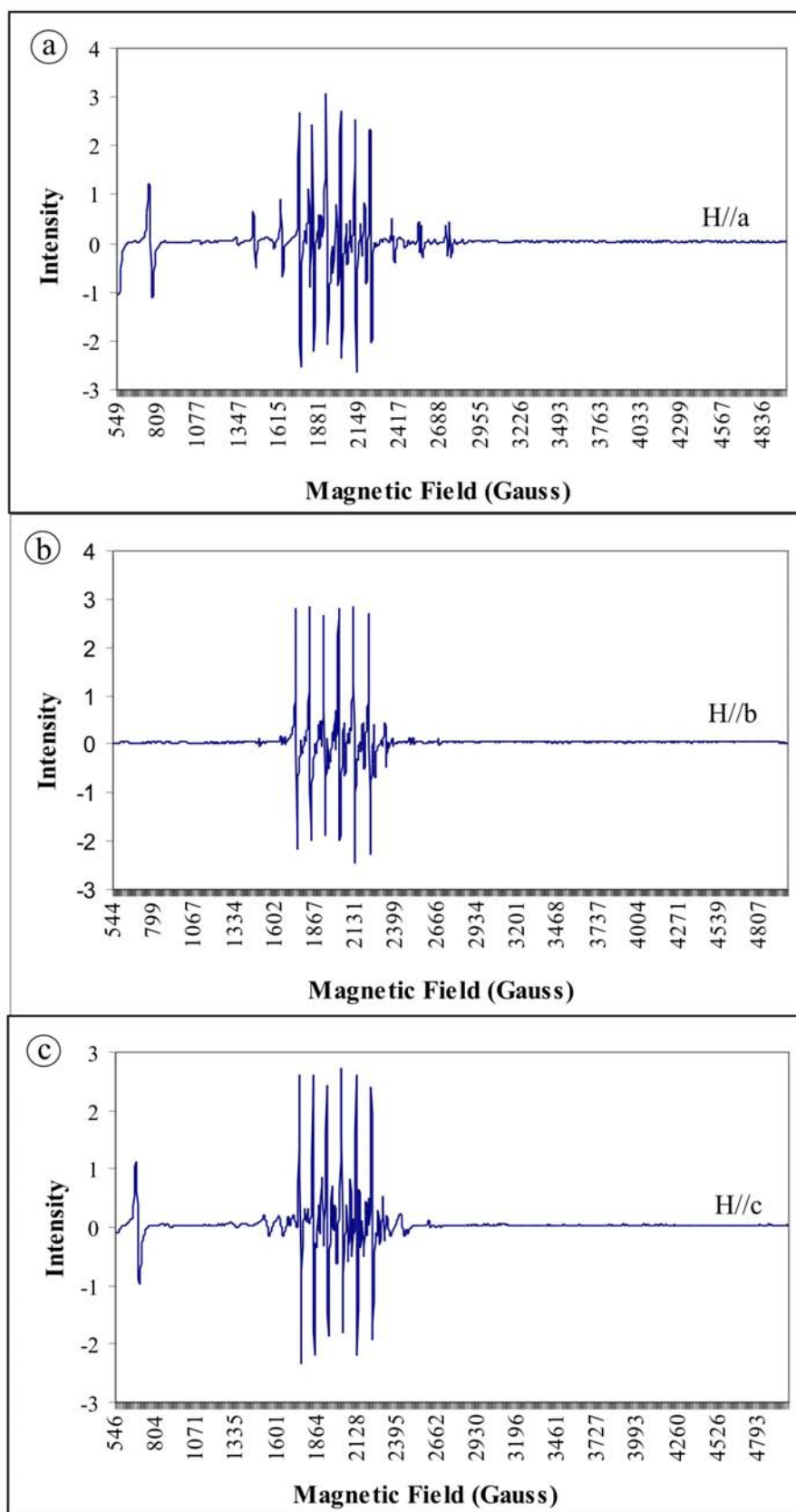


Figure 12.14. EPR spectrum of blue zoisite along its crystallographic axes at 9.375 GHz with a magnetic field scan range of 550 to 5000 Gauss, with a) magnetic field ( $H$ ) parallel to A-axis; b)  $H//b$  and c)  $H//c$ .

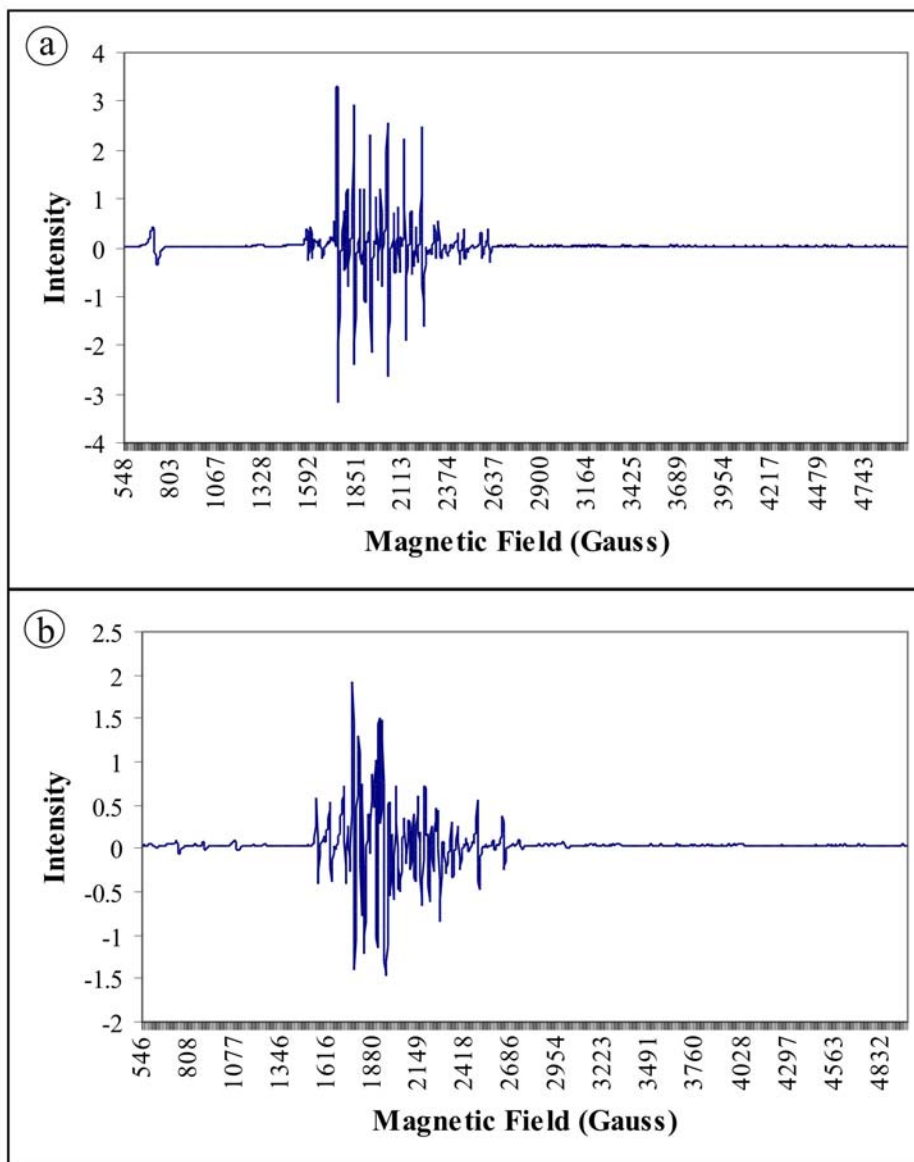


Figure 12.15. EPR spectrum of blue zoisite measured between its crystallographic axes at 9.375 GHz with a magnetic field scan range of 550 to 5000 Gauss, with a) measured at a 45 degree angle between the *a*-axis and *b*-axis and b) 45 degree angle between the *A*-axis and *C*-axis.

From Table 12.11 it is evident that the  $\text{Mn}^{2+}$  HFS signal has virtually no angular dependence, thus indicating limited distortion from octahedral symmetry. Figure 12.16.a indicates the high field (2210 to 4200 Gauss) signal for  $\text{Mn}^{2+}$  with its six-fold HFS pattern indicated by  $X_1$ . “Spin forbidden” transitions results in some identifiable fine structure lines within the HFS pattern of  $\text{Mn}^{2+}$  and is indicated by  $X_2$  in Figure 12.16.b.

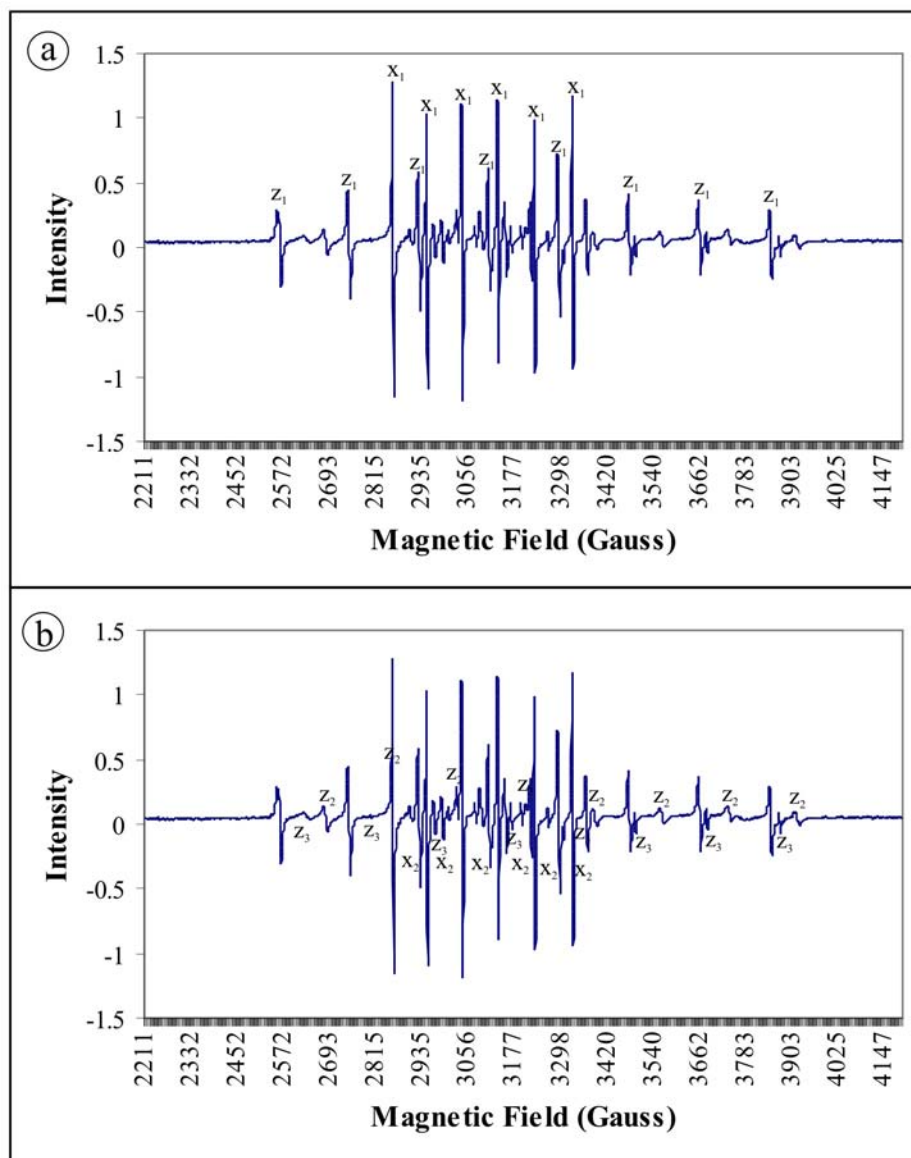


Figure 12.16. High field EPR spectrum of blue zoisite (sample 2) for  $H//a$ . a) Hyper fine splitting pattern of the six-fold  $Mn^{2+}$  ( $X_1$ ) and eight-fold  $V^{4+}$  or  $Ti^{3+}$  ( $Z_1$ ) signal. b) Identifiable "spin forbidden" transitions of  $Mn^{2+}$  ( $X_2$ ) and  $V^{4+}$  or  $Ti^{3+}$  ( $Z_2$  and  $Z_3$ ).

The g-value obtained from this study for the blue zoisite of  $g = 2.0$  falls within the error range obtained by Tsang and Chose (1971), for  $Mn^{2+}$  within zoisite. They calculated the g-value of the central  $Mn^{2+}$  transitions as  $2.003 \pm 0.005$  and that the  $Mn^{2+}$  ions in zoisite replace  $Ca^{2+}$  in the Ca(i) site.

The eight-fold EPR signal observed for the blue zoisite can be attributed to the presence of either  $V^{4+}$  or  $Ti^{3+}$  (including the  $Ti^{3+}/Ti^{4+}$  redox reaction) within the crystal structure (see Figures 12.14 and 12.16). Both ions have a nuclear spin of  $7/2$ , thus resulting in an

eight-fold signal. The g-value obtained for the central transitions of the eight-fold pattern in this study varies between 1.92 and 1.96. The standard g-factor for  $V^{4+}$  and  $Ti^{3+}$  is approximately 1.94 and 1.95, respectively and can therefore not be used to distinguish between the two ions (Calas, 1988).  $Ti^{3+}$  however, generally does not have an EPR signal at room temperature. The  $Ti^{3+}$  EPR signal increases as the measurement temperature decreases. Thus, a temperature-dependant EPR study on the coloured zoisites could be useful in conclusively determining which ion is causing the eight-fold signature.

For this study, it can therefore be inferred that the eight-fold HFS signal can be attributed to the presence of trace amounts of  $V^{4+}$  ions. The percentage of  $V^{4+}$  ions compared to the  $V^{3+}$  ions present within the blue zoisite is probably very small, resulting in the lack of  $V^{4+}$  peaks detected through UV/Vis spectroscopy.

The central transition field strength of the eight-fold structure is dependent on the orientation of the crystal, with H//a resulting in the strongest signal (Figure 12.16). The eight-fold HFS caused by  $V^{4+}$  is clearly visible in Figure 12.16. Figure 12.16.b indicates some fine structure line of  $V^{4+}$  caused by “spin forbidden” transitions. Two sets of fine structure line were identified in Figure 12.16.b and are indicated by  $Z_2$  and  $Z_3$ . The signal is also angle dependent and thus anisotropic. The anisotropic nature of the signal is indicated in the angular EPR diagram (Figure 12.17). The gauss interval between the two outer peaks of the HFS varies from 1313 gauss to 412 gauss for H//a and H//b respectively. Figure 12.17 also indicates the splitting of each of the eight-fold HFS signals with rotation away from the crystallographic axes. The six-fold HFS pattern shows a negligible small angular dependence and no observable splitting of the HFS signals upon rotation, see Figure 12.17.

#### 12.6.5. Green zoisite

The EPR spectroscopic signal of the green zoisite contains the same basic features as that of the blue zoisite. The HFS signal of  $Fe^{3+}$  is easily identifiable in Figure 12.18.a and is of similar intensity to that observed for the blue zoisites. Both the six-fold  $Mn^{2+}$  HFS signal and the eight-fold  $V^{4+}$  signal obtained for the green zoisite is far weaker than that of the blue zoisite. The scale of Figure 12.18.b was adjusted in order to observe both the six-fold and eight-fold signal present in the green zoisite. It is also

evident from Figure 12.18.b that the signal contains little or no observable “spin forbidden” transitions, making the signal of the green zoisite less complex. The reason for the weaker signal is not clear, but it could suggest slightly different site occupancy and possibly changes in the valence states of Mn and more importantly V within the green zoisite compared to that of the blue zoisite. If this is the case, then detailed EPR analysis of the green zoisite could give valuable insight into the causes of the colour within the green and blue zoisites.

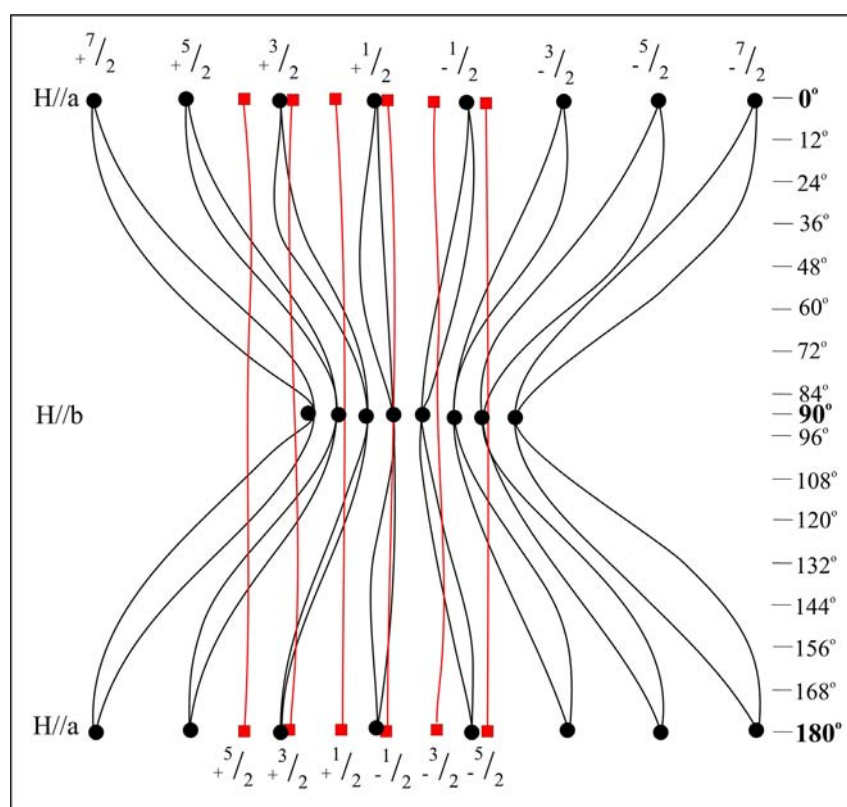


Figure 12.17. Angular rotational EPR diagram of blue zoisite (tanzanite) over 180 degrees. The signal was measured in 6-degree intervals. The eight-fold  $V^{4+}$  signal is indicated in black and the six-fold  $Mn^{2+}$  signal is indicated in red.

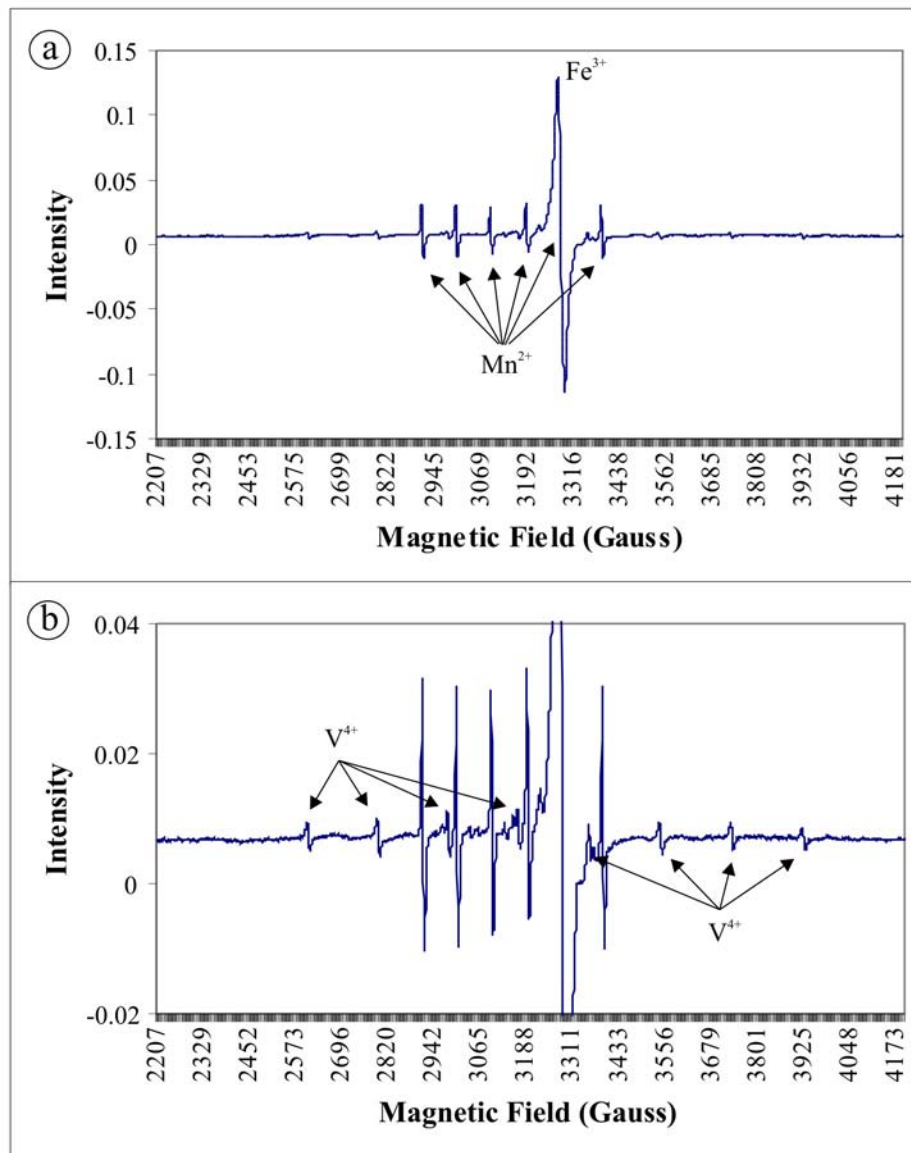


Figure 12.18. EPR spectrum of green zoisite with  $H//C$ -axis at 9.375 GHz with a magnetic field scan range of 2207 to 4200 Gauss. a) EPR signal indicating the presence of  $\text{Fe}^{3+}$  and  $\text{Mn}^{2+}$ . b) Magnification of Figure 12.18.a in order to observe the eight-fold signal caused by either  $\text{V}^{4+}$  or  $\text{Ti}^{3+}$  within the green zoisites.

### 12.6.6. Colourless to yellow zoisite

The high field EPR spectra of the colourless zoisite along the three crystallographic axes are indicated in Figure 12.19. The EPR signal of the colourless to light yellow zoisite samples have some significant differences to that of the blue and green zoisites:

- The eight-fold EPR pattern attributed to  $\text{V}^{4+}$  is significantly stronger within the colourless zoisite compared to the green or blue zoisites.



- The eight-fold EPR pattern is the dominant signal within the colourless zoisites, while the six-fold  $\text{Mn}^{2+}$  EPR pattern is the dominant signal of both the blue and green zoisites.

The higher intensity of the eight-fold HFS pattern within the colourless zoisite compared to that of the blue and green zoisite indicates that the signal is not caused by a chromophore ion. Thus, since little or no colour is observed within these zoisites it can be assumed that the ions causing both the six- ( $\text{Mn}^{2+}$ ) and eight-fold EPR ( $\text{V}^{4+}$ ) pattern for the blue and green zoisite do not contribute significantly to the colour of the zoisite.

### 12.7. Conclusions

Laser ablation ICP-MS analyses of tanzanite indicate that V is the main chromophore present, followed by Ti. The UV/Vis/NiR spectroscopic investigation of tanzanite reveals that the colour prior to heating is caused by the presence of  $\text{V}^{3+}$  and  $\text{Ti}^{3+}$ . The presence of  $\text{Ti}^{3+}$  within the zoisites results in a red, yellow or green colour along the E// $\gamma$  axis. The EPR analyses of tanzanite further indicate that  $\text{Fe}^{3+}$  and  $\text{Mn}^{2+}$ , as well as small quantities of  $\text{V}^{4+}$  are also present. The UV/Vis/NiR spectroscopic study of tanzanite however, indicates that neither  $\text{Fe}^{3+}$ ,  $\text{Mn}^{2+}$  nor  $\text{V}^{4+}$  contributes to the colour of tanzanite.

The chemical composition of green coloured zoisites is almost identical to that of tanzanite. The difference in colour is probably related to the presence of an intervalence charge-transfer between  $\text{Ti}^{4+}$  and  $\text{Ti}^{3+}$ , not observed in tanzanite. The absence in colour of the yellow/colourless samples is caused by the lack of chromophores in the crystal structure of the zoisites. This study identified a possible new gemstone variety of zoisite with an orange colour caused by the presence of rare earth elements and more specifically  $\text{Nd}^{3+}$ .

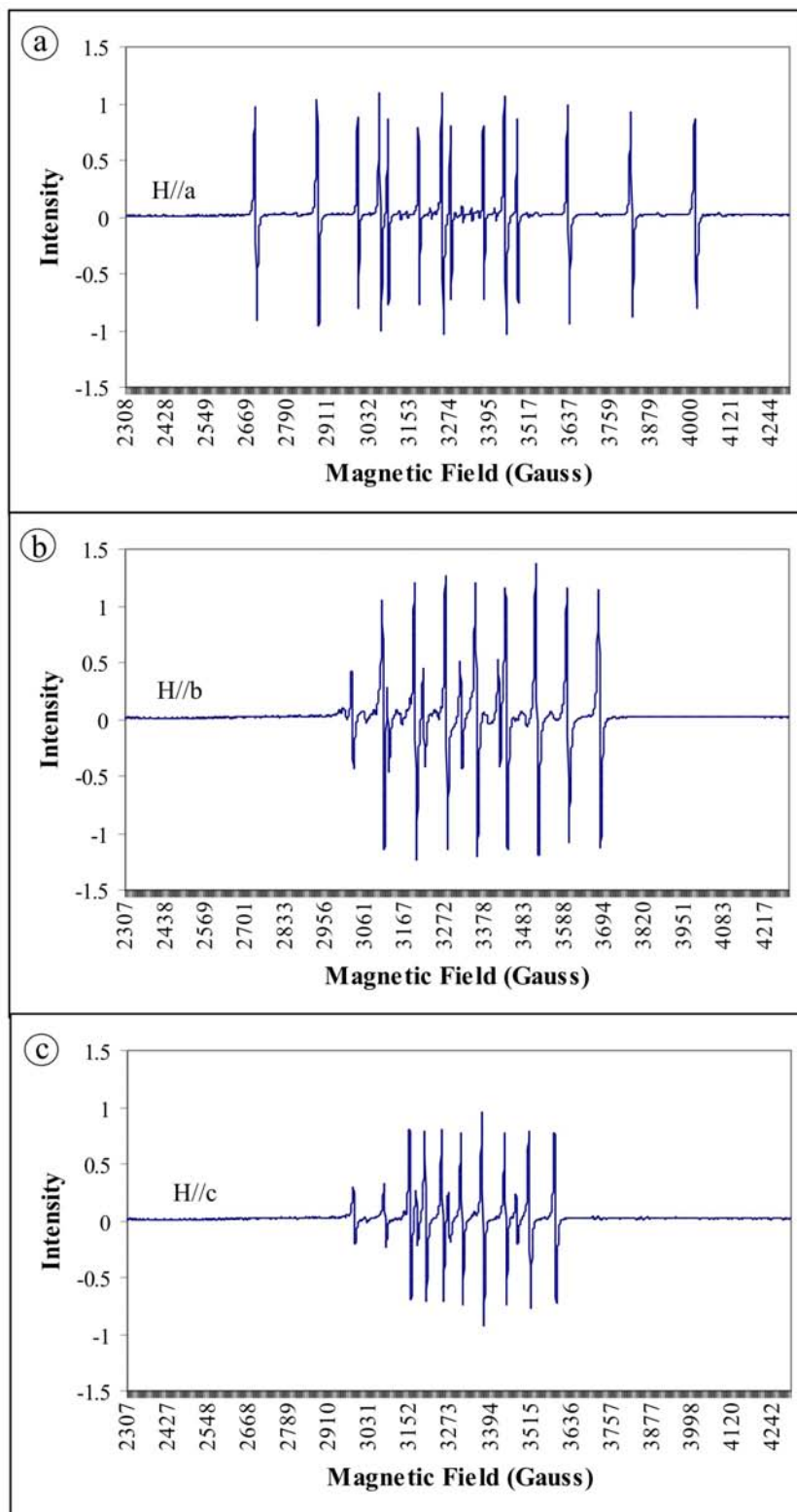


Figure 12.19. EPR spectrum of colourless zoisite along its crystallographic axes at 9.375 GHz with a magnetic field scan range of 2305 to 4300 Gauss, with a) magnetic field ( $H$ ) parallel to  $A$ -axis; b)  $H//b$  and c)  $H//c$ .

## Chapter 13

### Thermal and radiation treatment of coloured zoisites

#### 13.1. Thermal treatment of coloured zoisites

##### 13.1.1. Introduction

All commercial tanzanite has been heated in order to enhance its colour. This includes tanzanite that is naturally intensely blue. Only tanzanite specimens earmarked for exhibition and the collectors market are usually not heated in order to exhibit the strong trichroism of untreated tanzanite. Heat treatment of tanzanite causes a change from a trichroic mineral (blue, violet and red / yellow / green) to dichroic mineral (blue and two violet directions). Heating causes a more intense blue and violet colour in all tanzanites, including tanzanite crystals that have a transparent brownish colour. Various authors including, Webster and Anderson (1983) as well as Zancanella (2004) have suggested that this colour change in blue zoisite (tanzanite) is probably due to the change in the valence state of vanadium within the zoisite structure. They suggested that the colour change is a result of  $V^{3+}$  changing to  $V^{4+}$  brought about by the addition of energy through the heating process. This has been accepted by the industry and has virtually gone unchallenged for the last few decades. It will subsequently be proven in this chapter that the change in colour of tanzanite through heating is not caused by a change in the valence state of V.

##### 13.1.2. Spectroscopy

Two heating procedures were used by the author in collaboration with the UV/Vis spectroscopy in order to investigate the change in spectrum of various coloured zoisites during and after heat treatment. The ten coloured zoisite samples were spectroscopically analysed before heating, then heated within a furnace to a predetermined temperature and subsequently spectroscopically reanalysed. The second method employed involved the in-situ spectroscopic analysis of four coloured zoisite samples while heated in a specially developed heating oven. The oven consists of a temperature resistant ceramic capsule containing a rheostatically controlled heating element covered with an Al-plate. The capsule has a removable lid for sample access as well as two windows to allow the

transmission of spectroscopic light from the source through the sample and to the spectroscopic detector. An adjustable temperature detector is placed on the sample in order to measure the temperature of the sample. For the in-situ spectroscopic investigation, large homogeneous tanzanite samples, prepared as described in Chapter 12, were cut into three crystallographic orientated cubes of equal sizes. The sample pieces were polished and individually heated while spectroscopically analysing each along a different crystallographic axis. Unless otherwise indicated, all the samples were heated to 550 °C using step-wise increments over a time period of approximately 6 hours.

### ***Blue zoisite***

UV/Visible/NIR Spectroscopic analyses of the heated and in-situ heated blue zoisites revealed several changes in its spectra, compared to that of the untreated blue zoisites described in Chapter 12. The most significant change in the crystallographically orientated spectra of the blue zoisite occur along E// $\gamma$ . Upon heating to over 360°, all the blue zoisite samples analysed exhibit a sharp disappearance of the prominent peak located at ca. 450 nm. As discussed in Chapter 12, this peak is due to the presence of Ti<sup>3+</sup> within the structure of blue zoisite. The addition of energy through heating of the blue zoisite therefore causes a change in the valence state of Ti<sup>3+</sup> to Ti<sup>4+</sup> through oxidation. As previously discussed, Ti<sup>3+</sup> is a chromophore with a 3d<sup>1</sup> configuration, while Ti<sup>4+</sup> has a 3d<sup>0</sup> configuration and is therefore non-chromophoric. This valence state change would therefore explain the disappearance of the Ti<sup>3+</sup> absorption spectrum and the lack of any additional peaks occurring as a result of heating since Ti<sup>4+</sup> has no d-orbital absorption spectrum. Thus, the change in valence state from Ti<sup>3+</sup> to Ti<sup>4+</sup> results in a decrease in the absorbance centred around 450 nm, thereby causing an increase in the violet colour along E// $\gamma$ .

Heating of tanzanite also causes a general increase in the absorbance between 500 and 880 nm for all three crystallographic axes. Figure 13.1 illustrates the stronger absorbance observed for all three crystallographic axes, between 500 nm and 880 nm after heating. All the peaks attributed to the presence of V<sup>3+</sup> in Chapter 12, are still present along the three crystallographic axes after heating, but their absorbance has been enhanced by the heating process. The only additional peak observed after heating is

centred at 550 nm for E// $\gamma$ . This peak is however present for both E// $\alpha$  and E// $\beta$  before and after heating and has also been attributed to the presence of V<sup>3+</sup>. It is possible that this peak was present for E// $\gamma$  prior to heating, but that it was overshadowed by the presence of the strong absorption peak located at ca. 450 nm. The higher absorbance of the peaks located at 550 nm and 600 nm as well as the general increase in the absorbance between 500 nm and 860 nm will result in an increase in the violet and blue colour observed for the samples.

In-situ heating spectroscopy analyses of the blue zoisites revealed that the amount of absorbance of the peaks located between 500 and 860 nm is strongly temperature dependent. Figure 13.1 illustrates the difference in absorbance along the three crystallographic axes measured at 25 °C, 400 °C, 550 °C and 700 °C. For E// $\alpha$  the amount of visible absorption in the 500 to 860 nm range is the highest at 700 °C, although almost identical amounts of absorption occurs at 550 °C. For E// $\beta$  the absorption of the 500 to 860 nm area is approximately identical at temperatures of 400 and 550 °C. For E// $\gamma$  the highest absorption of the area between 500 and 860 nm is observed at 550 °C. For this sample, the optimum heating temperature would therefore be 550 °C, since it results in the highest accumulative 500 to 860 nm absorption along all three axes. The general colour change in blue zoisite upon heating is therefore primarily the result of the disappearance of the 450 to 460 nm peak for E// $\gamma$ . This causes the spectrum of E// $\gamma$  to approach that of E// $\alpha$ , resulting in a similar violet colour along both axes. The colour change of blue zoisite upon heating is therefore caused by the disappearance of the red/yellow/green colour caused by the 450-460 nm Ti<sup>3+</sup> peak, resulting in a violet colour for the axis.

This simplified example illustrates the possibility of utilising spectroscopic analysis to determine the optimum heating temperature of tanzanite in order to achieve the most intense blue/violet colours. If tanzanite is heated to either a too low or a too high temperature, the blue/violet colour is significantly lighter than the optimum colour for the specific crystal. This may result in a substantial decrease in the value of the heated tanzanite crystal. The optimum temperature required for each tanzanite crystal to achieve the best colour also varies significantly. This is probably because of the varying concentrations of V within the different tanzanite crystals, as indicated in Chapter 12. It

is therefore advisable that a spectroscopic database be developed linking the trace element concentration of V and possibly Ti within tanzanite to the optimum heating temperature required. Thus, when the value of the tanzanite to be heated justifies the costs involved, the crystal can be analysed, for example, by means of laser ablation ICP-MS in order to determine the optimum heating temperature as indicated by the database.

The absorption spectrum of samples not heated in-situ but spectroscopically measured before and after heat treatment do not always show the same increase in absorbance of the 500 to 860 nm area, see Figure 13.2. The NIR spectrum of none of the coloured zoisite shows any change during heating (see Figures 13.2, 13.3, and 13.4).

### ***Green zoisite***

The spectrum of a typical green zoisite crystal before and after heat treatment to 550 °C is indicated in Figure 13.3. The UV/VIS/NIR spectrum of the green zoisites remains virtually unchanged after heating. The lack of any significant colour change of the green zoisite as a result of heating is also evident from a visual and optical comparison of the samples before and after heat treatment. In Figure 13.3 a small increase in the absorbance for both E// $\alpha$  and E// $\gamma$  is observable between 400 nm and 860 nm. The absorbance centred around 330 nm for E// $\beta$  however decreases slightly as a result of heat treatment. Unlike the blue zoisite samples, no peaks disappear or appear as a result of heating of the green zoisite. This includes the peak located at 450 to 460 nm for E// $\gamma$ , which is considered the crucial factor in the colour change of blue zoisite. Since the chemical composition of the green zoisite is very similar to that of blue zoisite, the different thermal behaviour is probably related to variation in the site occupancies of especially V and Ti within the zoisite structure. The thermal inertness of the green zoisite warrants further investigation and could lead to a better understanding of the causes of colour in tanzanite.

### ***Yellow / colourless zoisite***

Figure 13.4 indicates a typical spectroscopic spectrum of yellow/colourless zoisites before and after heat treatment. As discussed in Chapter 12, the colourless zoisites usually have only one prominent peak that is located at about 450 nm, attributed to the presence of Ti<sup>3+</sup>. Figure 13.4 clearly illustrates the disappearance of the 450 nm peak for

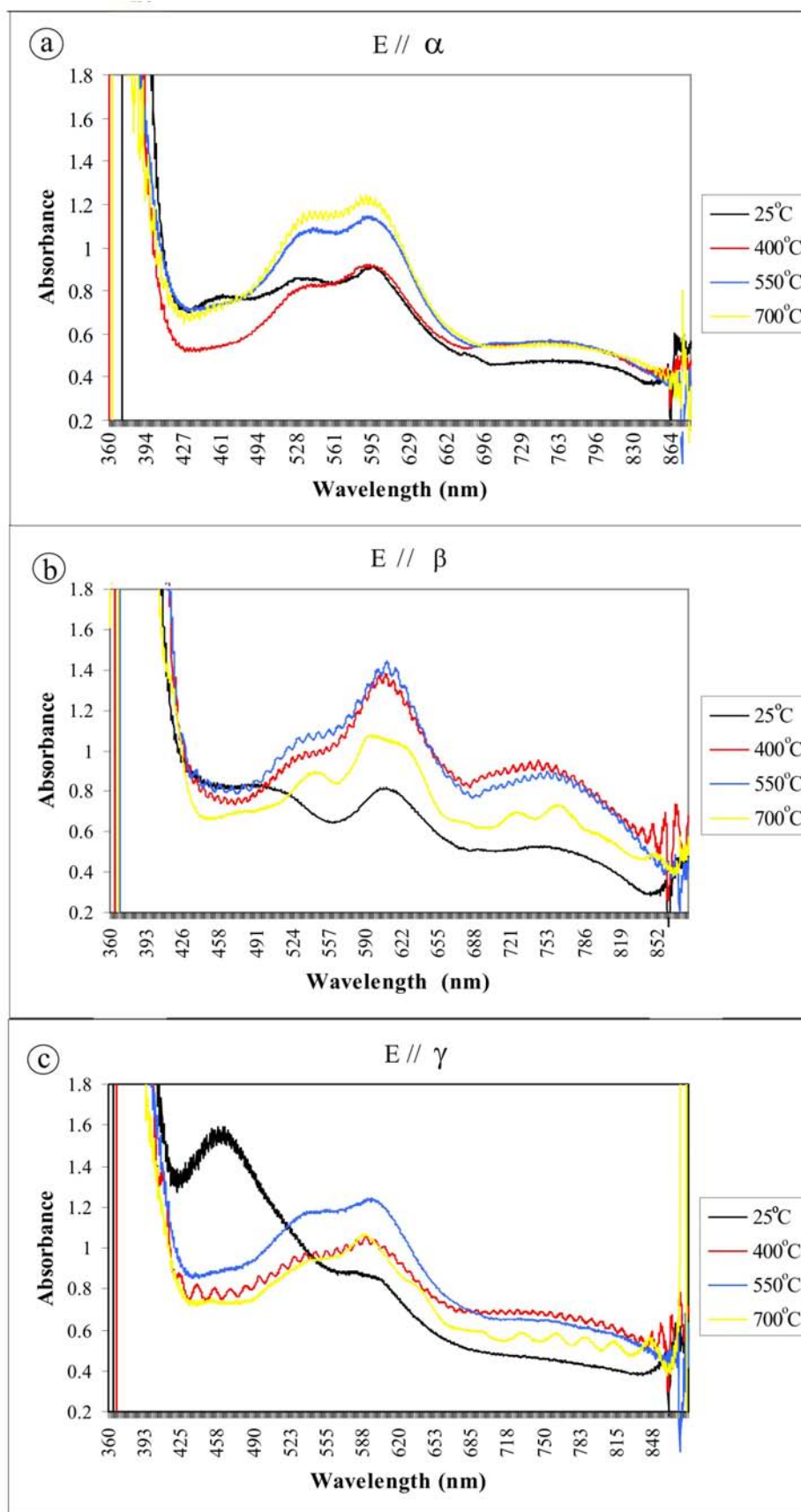


Figure 13.1. In-situ heating of UV/Vis spectroscopically analysed blue zoisite sample (sample 8). All three crystallographic axes were separately analysed from three different cut and polished pieces of the same sample.

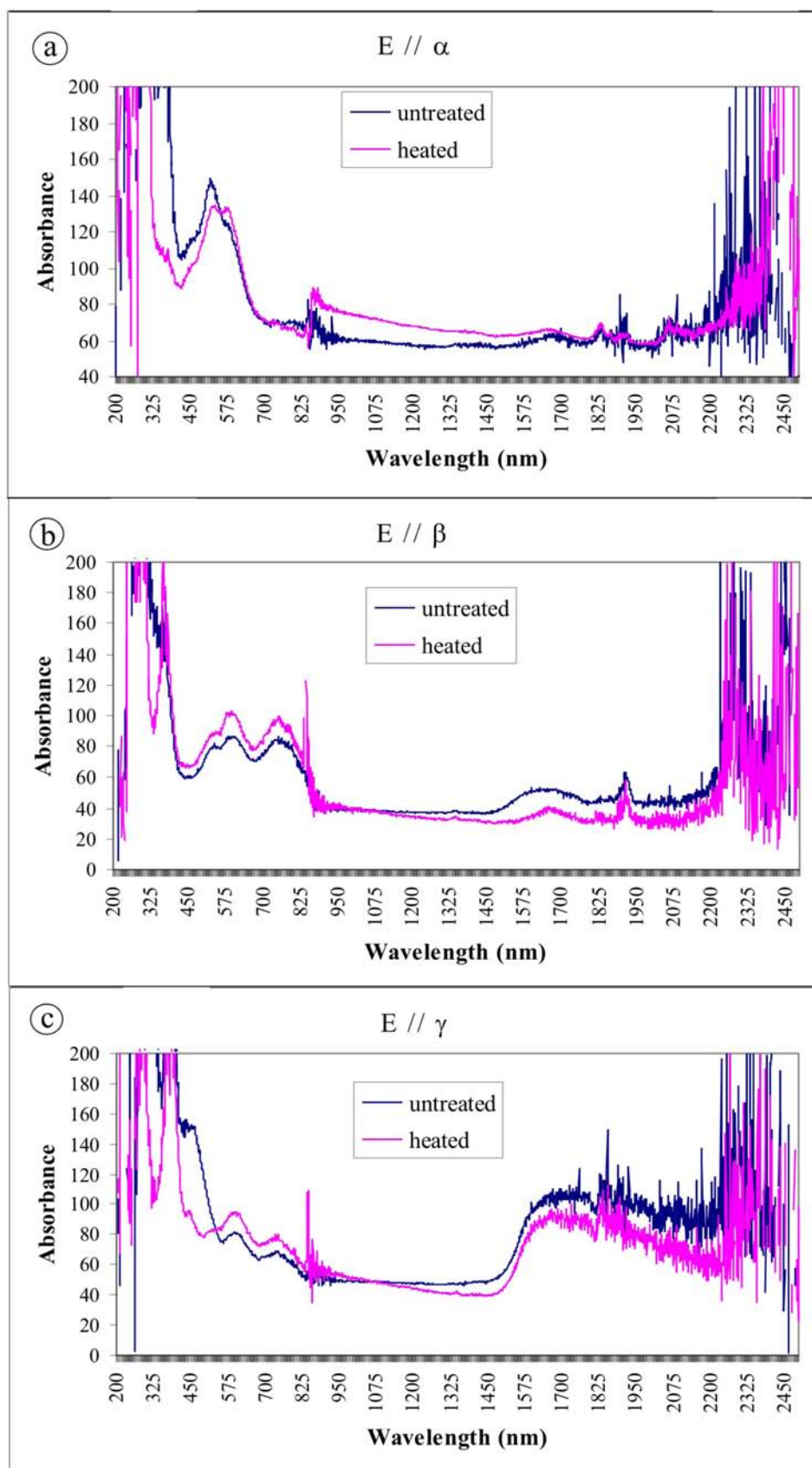


Figure 13.2. UV/Vis/NIR spectroscopic analysis of blue zoisite (sample Rb1) before and after heat treatment, with a) E// $\alpha$  b) E// $\beta$  and c) E// $\gamma$ .



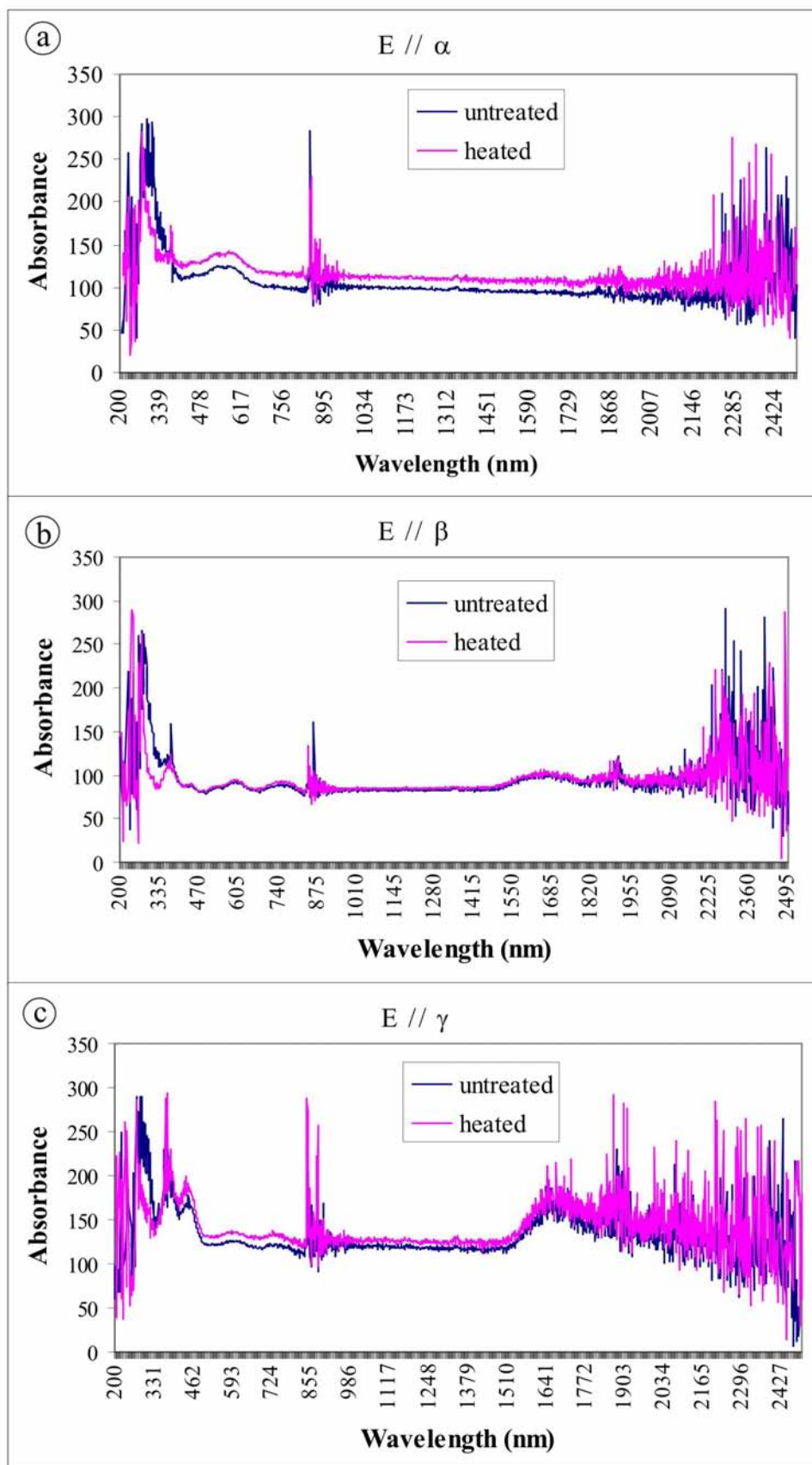


Figure 13.3. UV/Vis/NIR spectroscopic analysis of green zoisite (sample G89), before and after heat treatment, with a)  $E//\alpha$  b)  $E//\beta$  and c)  $E//\gamma$ .

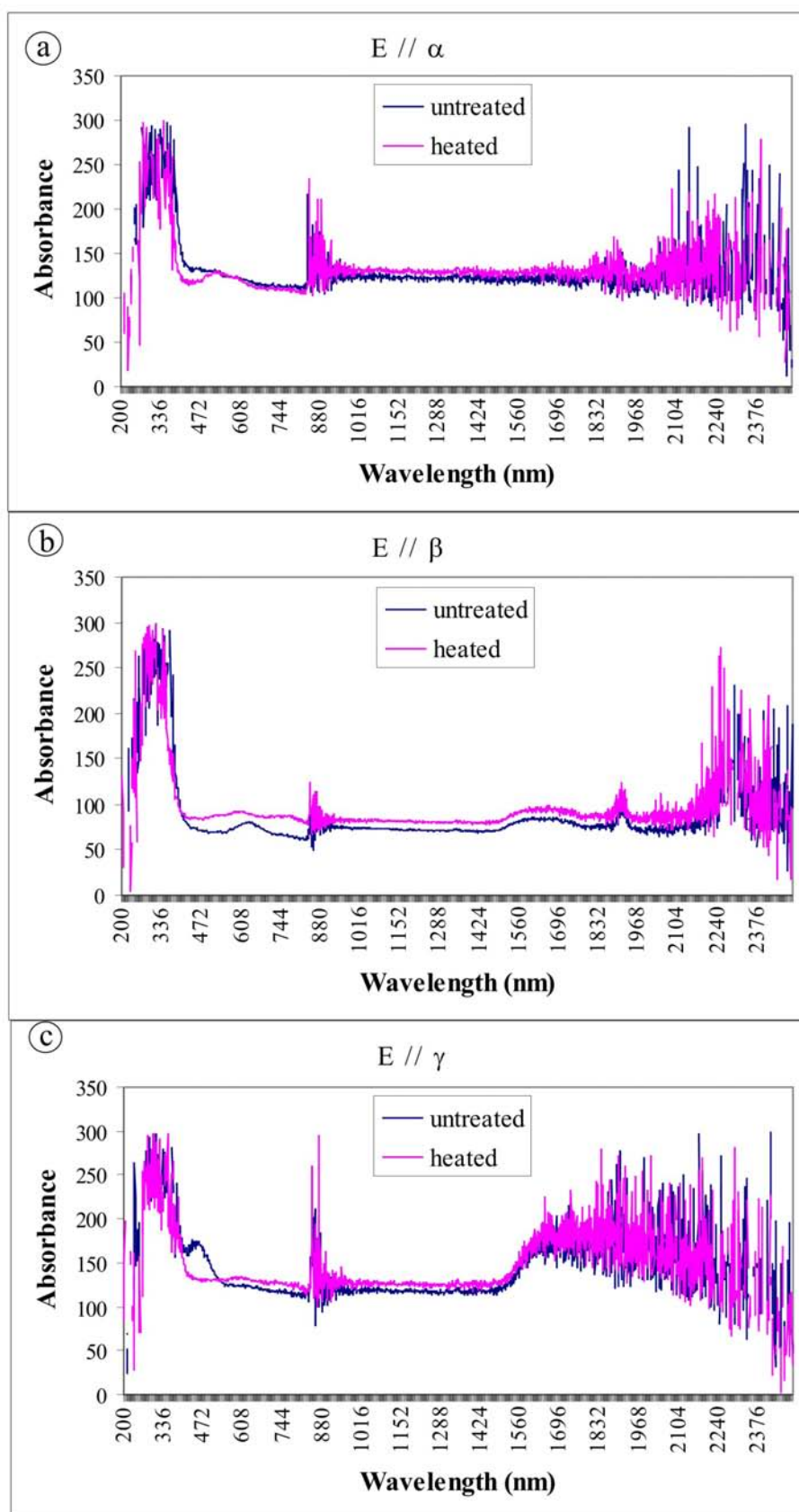


Figure 13.4. UV/Vis/NIR spectroscopic analysis of yellow/colourless zoisite (sample Ry1) before and after heat treatment, with a)  $E // \alpha$  b)  $E // \beta$  and c)  $E // \gamma$ .

E// $\gamma$ , after heating to 550 °C. Despite the disappearance of the 450 nm peak, the yellow / colourless zoisites undergo no significant colour change upon heating.

### 13.1.3. Electron Paramagnetic Resonance (EPR) of coloured zoisites

The influence of heating on the EPR spectrum of coloured zoisite was investigated by comparing the EPR signal of blue, green and colourless / yellow zoisites before and after heat treatment. The EPR patterns of the unheated zoisite samples were discussed in Chapter 12. The samples were subsequently heated to 550 °C, as described in Section 13.1.2 and re-analysed by means of EPR.

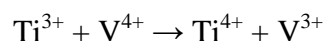
Figures 13.5, 13.6 and 13.7 present the EPR spectra of blue, green and colourless zoisite samples before and after heat treatment. The EPR spectra of all three colour variants of zoisite exhibit similar changes due to heat treatment:

- A decrease in the amount of “spin forbidden” transitions, resulting in less complex HFS patterns.
- An approximately 10-fold increase in the size of the EPR HFS peaks. The increase in peak size was compensated by increasing the gain size of the EPR spectrometer. This could be due to a change in the valence state of ions unobservable by EPR at room temperature as a result of heat treatment.
- A decrease in the eight-fold HFS pattern compared to the other HFS signals. The eight-fold HFS signal has been discussed in Chapter 12 and is attributed to the presence of  $V^{4+}$  within zoisite. The decrease in the  $V^{4+}$  EPR signal is especially prevalent in the colourless and to a lesser extent the green samples, see Figure 13.6 and 13.7. The  $V^{4+}$  eight-fold HFS EPR signal of the colourless zoisite changed from being the strongest pattern before heating to a very weak signal after heating. The weak eight-fold signal of the green zoisite virtually disappeared after heating.

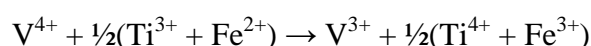
### *Discussion*

The decrease in the  $V^{4+}$  EPR signal therefore suggests a change in valence state of the ion as a result of heating to a valence state without an EPR signal at room temperature. Either the  $V^{4+}$  ion can be oxidised to  $V^{5+}$  or it could participate in a coupled intervalence charge transfer reaction with  $Ti^{3+}$  during heating. The UV/Vis spectroscopic analysis

discussed in Section 13.1.2 indicated the possibility of the transition of  $\text{Ti}^{3+}$  to  $\text{Ti}^{4+}$  as a result of heat treatment. It is therefore likely that a  $\text{V}^{4+}$  conversion to  $\text{V}^{3+}$  is a coupled reaction with the  $\text{Ti}^{3+}$  to  $\text{Ti}^{4+}$  valence change upon heating, e.g. along the following reaction:



The presence of V, Ti and Fe in zoisite / tanzanite may also suggest a coupled net-transfer reaction, accounting for the colour change with heating:



The amount of Ti and Fe involved would depend on its availability in the crystal structure of zoisite/tanzanite. The intervalence charge transfer proposed in both reactions, would result in an addition of  $\text{V}^{3+}$  ions, possibly explaining the increase in the  $\text{V}^{3+}$  visible spectrum absorbance peaks of the coloured zoisite after heating, as indicated in Chapter 12. It should be remembered that  $\text{V}^{3+}$  is the main V ion present in the coloured zoisites and that  $\text{V}^{4+}$  present before heating is only a small fraction of the total V content of the zoisites (see Chapter 12).

#### 13.1.4. Additional heating experiments

##### *Pressurised heating experiments*

Two tanzanite crystals were selected for the experiment. Both crystals had a good ratio between cracks and clear area in order to sufficiently monitor any annealing of the cracks. The samples were subsequently optically studied and photographed.

The samples were sealed in a specially made gold-capsule, with 100  $\mu\text{m}$  distilled water and 0.10997 g tanzanite powder. The container was placed into the pressure valve and heated to 620  $^{\circ}\text{C}$  and 2 kbar at 60  $^{\circ}\text{C}/\text{minute}$ . The temperature and pressure were kept constant for 144 hours and then reduced to room temperature and pressure conditions at a rate of 120  $^{\circ}\text{C}$  and 400 kbar per minute.

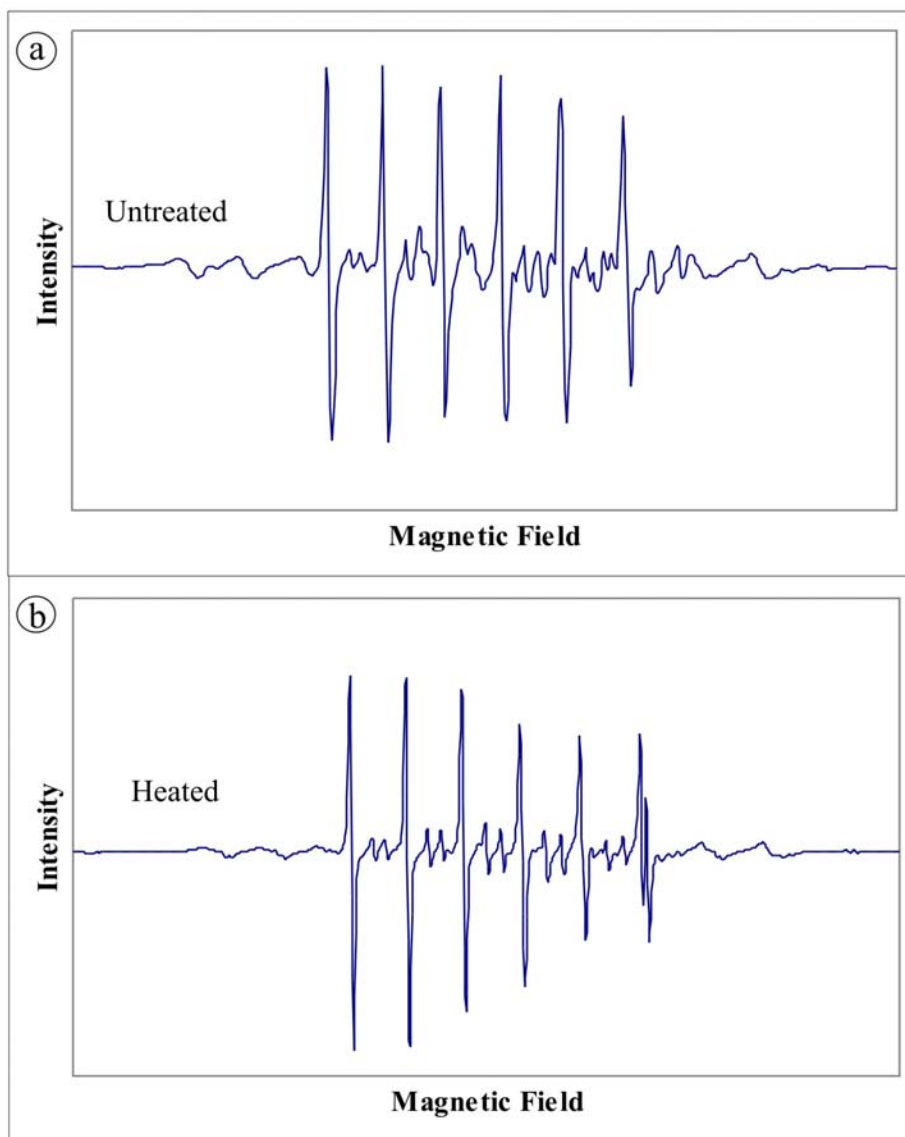


Figure 13.5. The untreated and heated EPR spectrum of blue zoisite (EPR 4).

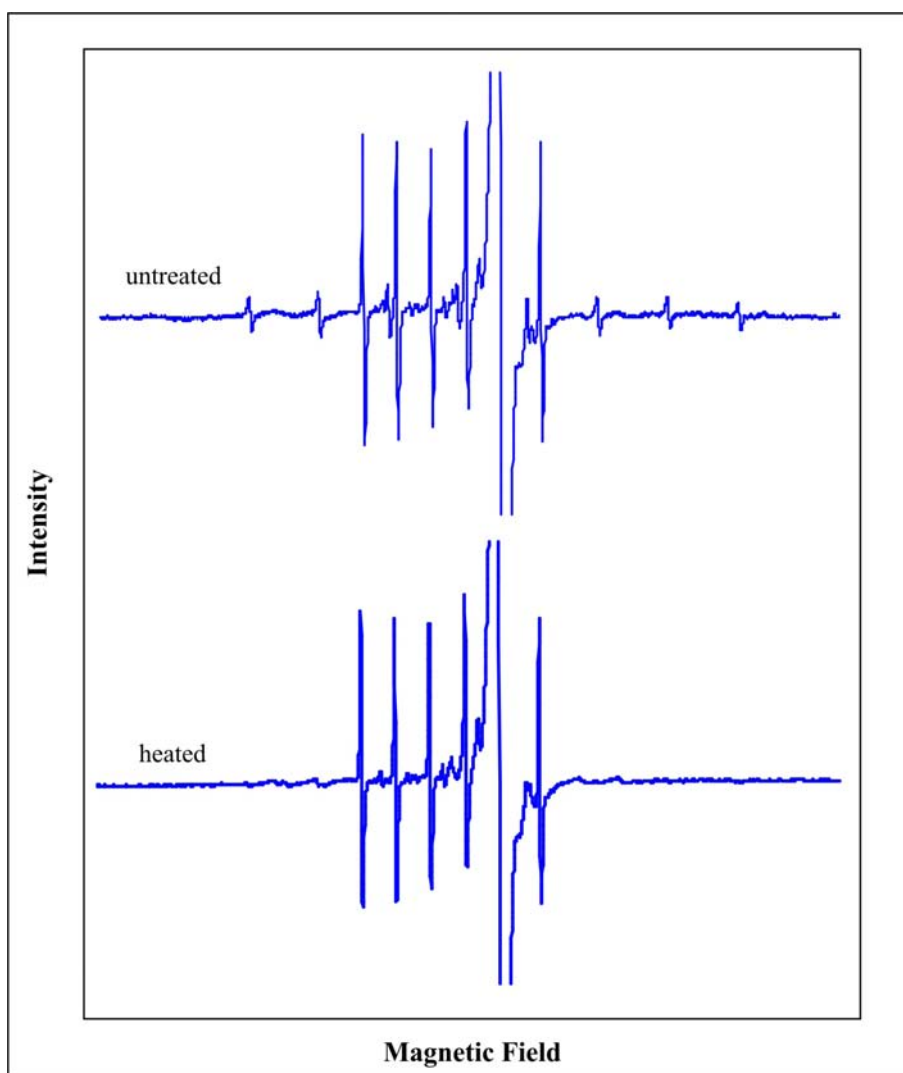


Figure 13.6. The EPR spectrum of untreated and treated green zoisite (sample G89).

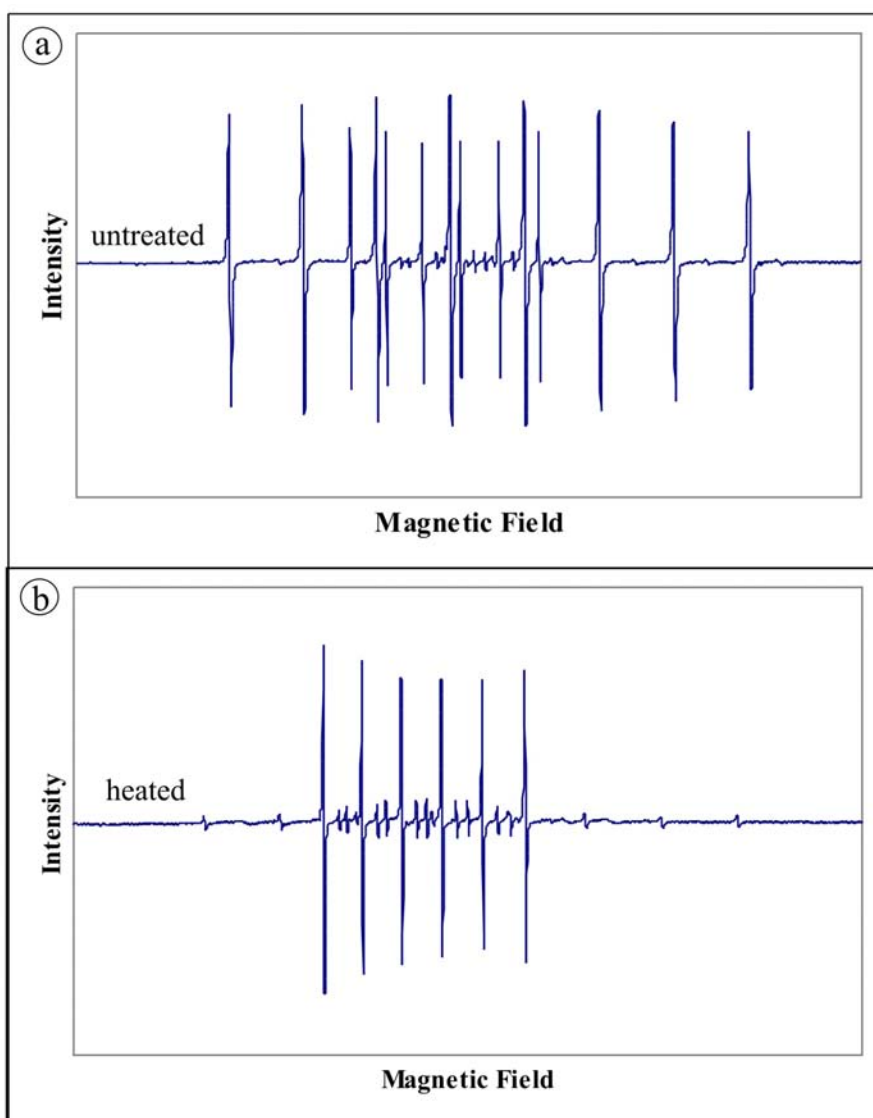


Figure 13.7. The EPR spectrum of untreated and treated yellow zoisite (sample 3).

The samples were again studied optically and photographed. Sample TA2 split in two along a well-developed fracture during the sealing process of the gold-capsule. No annealing of the tanzanite crystals was observed. The crystals did however change colour, from light brown to light blue. The blue colouration is lighter than that normally achieved by heating tanzanite to 620 °C under atmospheric pressure conditions.

### *Atmospheric heating experiments*

#### Method 1:

Tanzanite samples were placed in a 50/50 Al<sub>2</sub>O<sub>3</sub>/talc mixture within a platinum crucible. The crucible was placed in an electrical muffle furnace and heated at various increments. The first colour change of the tanzanite crystals occurs at 360 °C. The yellow / green component changes to a light violet-red colour. With increase in temperature, the colour change becomes more pronounced and at about 500 °C an optimum blue/violet-red dichroism is achieved. Further heating, to around 700 °C, results in a fading of the colour intensity to a lighter blue and lighter violet dichroism. At a temperature of 920 °C the tanzanite dehydrates and changes to a brittle bluish-greenish white substance.

#### Method 2:

Tanzanite samples were heated on a heating stage, covered with a silicon glass. The first noticeable colouration change began at 390 °C and gradually continued to 480 °C. The colouration subsequently become more pronounced and between 520 and 530 °C a large increase in the blue component is observed. A large portion of the colouration however only occurs upon cooling of the sample. At a cooling temperature of about 350 °C, all colouration changes seem to be completed. When heated samples are immersed into water, the colour change upon cooling is easily identified. The sudden cooling of the crystals however frequently leads to formation of cracks.



## 13.2. Radiation treatment

The selected coloured zoisite samples were subjected to both electron and gamma radiation. The samples subjected to electron radiation were irradiated with 1.35 MeV electrons from a van de Graaff electron accelerator at a dose of up to 1500 MGy at a dose rate of 20 MGy/h. The gamma ( $\gamma$ ) radiated zoisite samples were subjected to a dose rate of 2.28 Gy/min over 2960 min period, resulting in a total dosage of ca. 9 KGy.

### 13.2.1. UV/Vis/NIR and EPR Spectroscopy of radiated zoisites

Representative coloured zoisite samples were analysed by means of UV/Vis/NIR and EPR spectroscopy prior to irradiation exposure. The samples were subsequently subjected to either  $\gamma$  or  $e^-$  radiation and re-analysed.

In general, neither UV/Vis/NIR nor EPR spectroscopy could detect any significant change in the coloured zoisites as a result of irradiation. Figure 13.8, indicates the UV/Vis/NIR spectroscopy of blue zoisite, along the three crystallographic axes, before and after exposure to  $\gamma$ -radiation. A slight increase in absorption in the UV region was however observed in two of the  $\gamma$ -radiated samples. This is probably caused by the Si-O bondings that release an electron as a result of radiation treatment.

Blue zoisites were also subjected to both  $\gamma$  and  $e^-$  radiation after heating in order to investigate whether or not the change in colour brought about by heating can be reversed through radiation. None of the heated samples showed any substantial change in its UV/Vis/NIR spectrum after radiation.

The lack of any significant change in the UV/Vis/NIR and EPR spectra of the coloured zoisites as a result of either  $\gamma$  or  $e^-$  radiation indicates that the colour is not due to colour centres and also cannot be enhanced by radiation. Nassau (1983) described the presence of various types of colour centres within minerals and their activation through irradiation. He indicated that  $\gamma$  radiation is usually the best radiation source for producing colour centres. The colouration produced in a mineral due to colour centres are not nearly as stable as colour caused by transition metals in a ligand field. The colour produced by heating of the zoisites is therefore only caused by electron redistribution between transition elements to a more stable energy field configuration.

The colour change as a result of heating of the Merelani zoisites, including tanzanite, therefore appears completely stable and irreversible by means of irradiation.

### 13.3. Conclusions

Through a combination of UV/Vis/NIR and EPR spectroscopy, both before and after heat treatment, a far better understanding of the transitions in the ligand field of the coloured zoisites is achieved. UV/Vis/NIR spectroscopy indicated that  $\text{Ti}^{3+}$  is the only chromophore undergoing a significant change in valence state as a result of heating.  $\text{Ti}^{3+}$  is oxidised to  $\text{Ti}^{4+}$  through heating. Since  $\text{Ti}^{3+}$  is a chromophore and  $\text{Ti}^{4+}$  is colourless, this valence change results in the subtraction of the red, yellow or green colour component of tanzanite, thereby increasing the blue and violet component. This valence change is not observed within the green zoisite, which already has  $\text{Ti}^{4+}$  in its structure. The main chromophore ( $\text{V}^{3+}$ ) within the coloured zoisites does not undergo any valence change as a result of heat treatment. EPR studies indicated that the small quantity of  $\text{V}^{4+}$  present within the coloured zoisites, changes to either  $\text{V}^{5+}$  or  $\text{V}^{3+}$  as a result of heat treatment. It is however more likely that  $\text{V}^{4+}$  converts to  $\text{V}^{3+}$  through a coupled reaction with the  $\text{Ti}^{3+}$  to  $\text{Ti}^{4+}$  transition upon heating. The additional  $\text{V}^{3+}$  ions caused by this reaction can explain the slightly stronger  $\text{V}^{3+}$  signal observed in the coloured zoisites after heat treatment. The stability of the reaction is confirmed by the lack of electron excitation as a result of irradiation of the coloured zoisites.

The general colour change observed in tanzanite upon heating is caused by the disappearance of the red / yellow / green colour caused by the 450 to 460 nm  $\text{Ti}^{3+}$  peak, resulting in a violet colour for the axes. Thus, after heating both  $E//\alpha$  and  $E//\gamma$  exhibit a violet colour while  $E//\beta$  has a blue colour, resulting in a dichroic mineral opposed to the trichroic mineral before heating. Faye and Nickel (1971) proposed that the differences in thermal formation conditions caused the occurrence of natural blue versus brownish trichroic tanzanite. This is however not necessarily true, since blue and brown tanzanite are found in close proximity to each other within the same boudin. It is therefore suggested that oxidation conditions as well as the ratio and amount of V, Ti and possibly Fe capable of being readily reduced could influence the colouration of tanzanite.

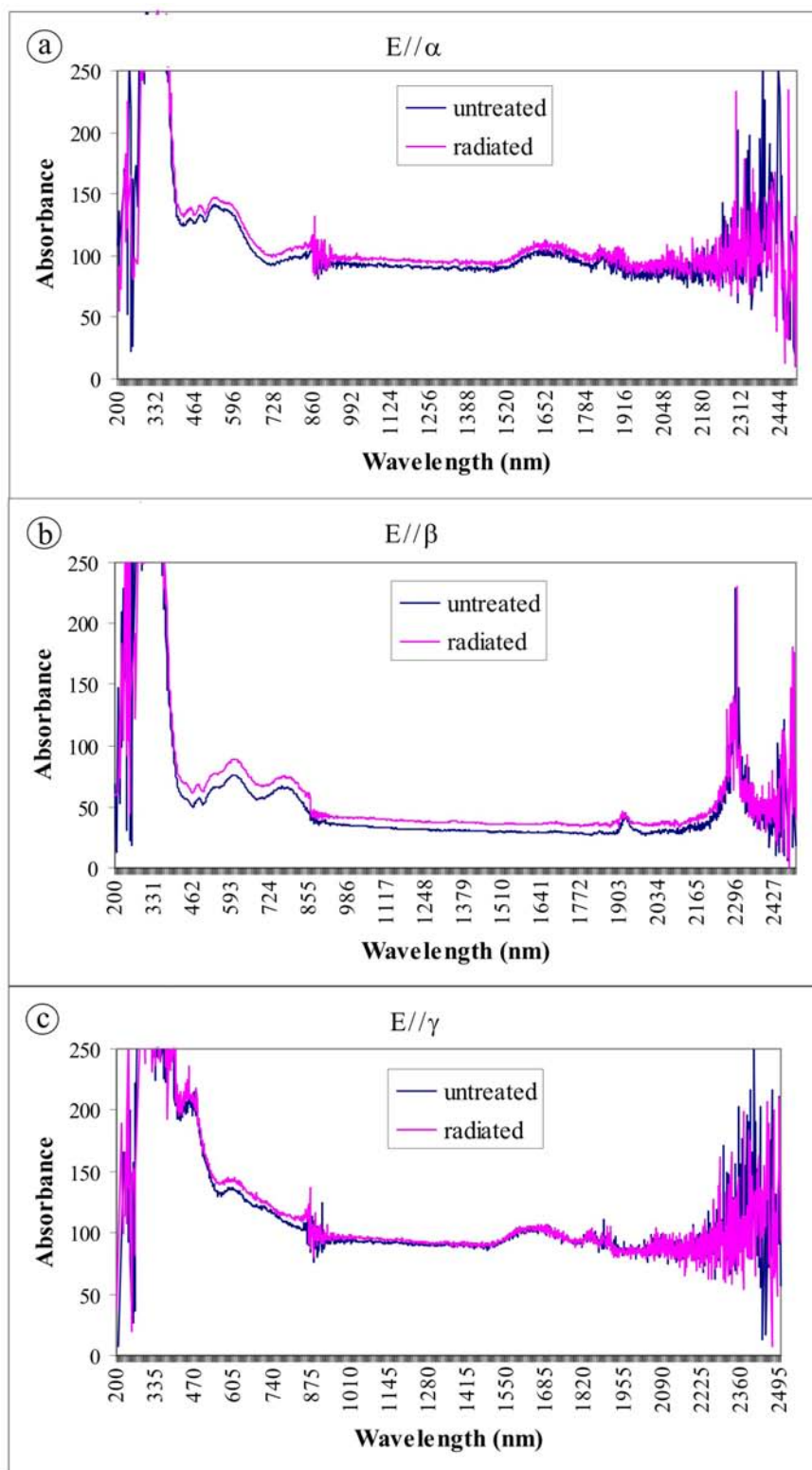
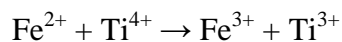


Figure 13.8. UV/Vis/NIR spectroscopy of blue zoisite (sample Rb9) before and after  $\gamma$ -irradiation treatment.

The reaction is expected to be similar to the photochemical oxidation-reduction process described by Nassau (1983) for blue sapphire. He ascribed the blue colour of blue sapphire to the net transfer reaction:



Microprobe analysis of zoisite and tanzanite (Table 12.2) indicates that neither Ti nor Fe is abundant enough to balance the redox reaction alone. It is therefore suggested that a combination of the two, and possibly small amounts of Sr, Mn and Cr partake in the redox reaction.

The lack of colour change within the green zoisite samples is probably caused by the presence of the intervalence charge transfer between  $\text{Ti}^{4+}$  and  $\text{Ti}^{3+}$ , as well as the possible variation in the site occupancies of especially V and Ti within the zoisite structure.

## **Chapter 14**

### **Mining Implications and Conclusions**

#### **14.1. Introduction**

The world-wide wholesale market for polished tanzanite is estimated at between US\$150 million and US\$200 million per annum. The retail sales values of tanzanite set in jewellery were calculated at US\$500 million in 2003 in the USA alone. Despite the large economic value of tanzanite, commercial mining of the deposit was only started in 1999. TanzaniteOne Ltd. is currently still the only large-scale commercial company mining the deposit. It was only since the start of the commercial mining of tanzanite by TanzaniteOne Ltd. (previously AFGEM Ltd.) in Block C, that a detailed geological investigation, as represented in this study, of the deposit was done. A proper understanding of the geology of the deposit is of utmost importance to the mine since selective mining is used. The dimensions and grade of the deposit cannot be determined through core-drilling due to the “nugget” effect of tanzanite mineralisation within boudin structures. All underground development is therefore controlled by the geology of the deposit. The geological and structural model developed and described in this study was used to develop the mine plan, resource calculations and is also currently being used on a day-to-day basis in governing the underground mining activities.

#### **14.2. Mining**

The mine development of TanzaniteOne Ltd. over the last couple of years has been guided by the geological knowledge of the deposit as defined by this study. The planned mine development is constantly being updated with the progressive understanding of the complex mineralised zone and surrounding units.

Decline shafts (Delta, Investor, Askari, Main, TC, CT and Bravo Shaft) are sunk along the apparent to true dip (35 – 45° NW) of the JW-zone (Figure 14.1). This is done in order to intersect the generally NE-plunging fold hinges (ore shoots) situated within the individual fold stacks along the shortest mineable distance. Once a fold stack is intersected within the decline development, the individual F2c boudin角度d fold hinges

(ore shoots) are identified. The individual ore shoots are subsequently mined by means of lateral drives along the plunge of the fold hinges (Figures 14.1 and 14.2). From the main lateral drives, winzes and raises are developed to investigate the “pressure shadow boudin” structures associated with the F2c fold hinges as described in Chapter 5.

The decline shafts are equipped with winder systems that transport ore by means of a skip and track system. Ore is transported within the ore-shoot drives to the decline shafts by means of either monorope or vacuumation systems. These two ore transport methods are the only ones suitable for undulating nature of the drives, since the dimensions, angle and direction of the drives are determined by the localised deviation in degree of boudinage and plunge of the F2c fold hinges (Figure 14.2).

### **14.3. Resource estimation**

A unique method of resource calculation had to be developed for the mine, since the grade of the deposit cannot be surveyed from drill holes along the standard procedures. Resource estimation was subsequently developed from the geological knowledge of the deposit as defined through this study. The model was verified by Ddraig Mineral Developments Limited and incorporated into the CPR used for the listing of TanzaniteOne Ltd. on the London AIM stock exchange.

The geological data was combined with the recorded data from the mine in order to derive acceptable ore resource estimates:

- During the period 2001 to the end of 2003, systematic mining by AFGEM Ltd. resulted in 48 000 t of mined and processed mineralised material at an overall tanzanite recovery of 66 ct/t.
- The volume and tonnage of the ore zone (JW-zone) in Block C can be estimated by considering the length of strike, an average thickness and an estimated dip extent as indicated from the diamond drilling. On the basis of a 2 km strike, a 400 m down dip extent, an average thickness of 3.0 m and a specific gravity of 2.65 an estimated 6.36 million tonnes of ore zone is present in the Block C area to a depth of 400 m.

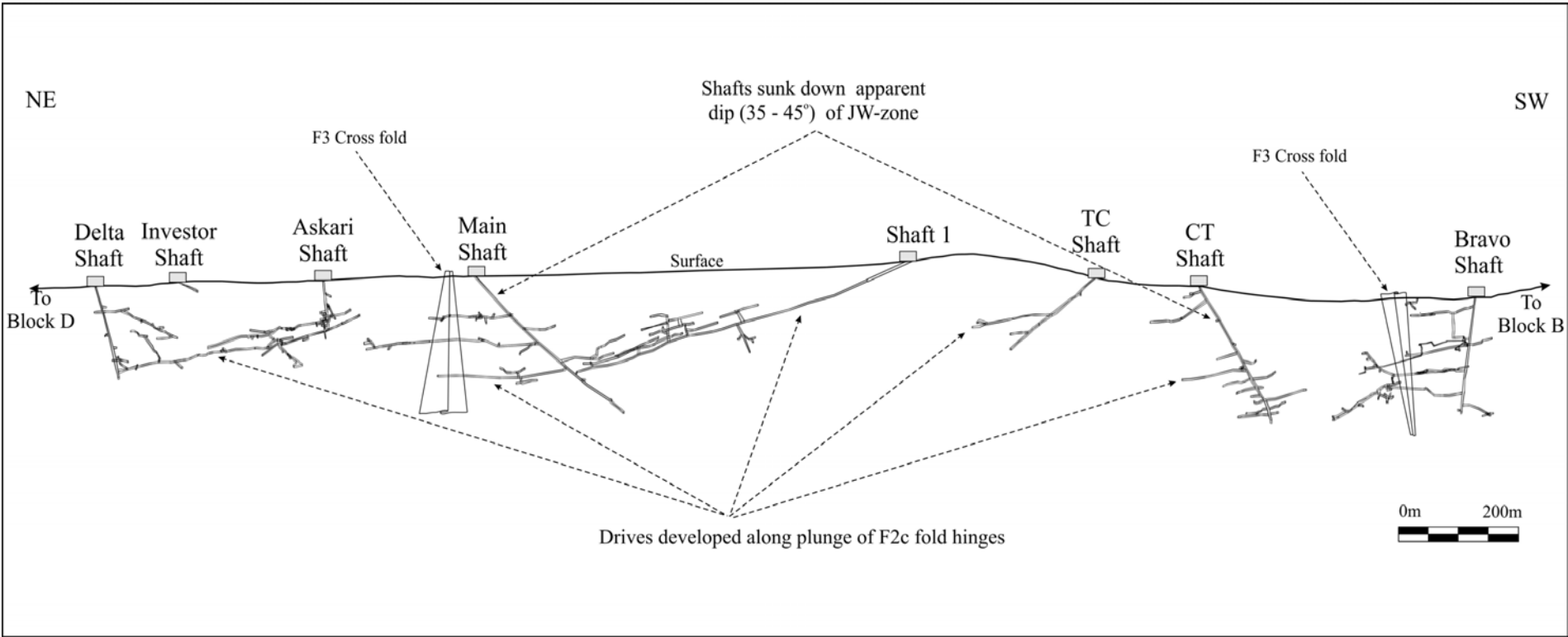


Figure 14.1. Longitudinal section of the Block C mining area. The decline shafts are sunk on apparent dip in the JW-zone, while the lateral drives follow the F2c fold hinges.

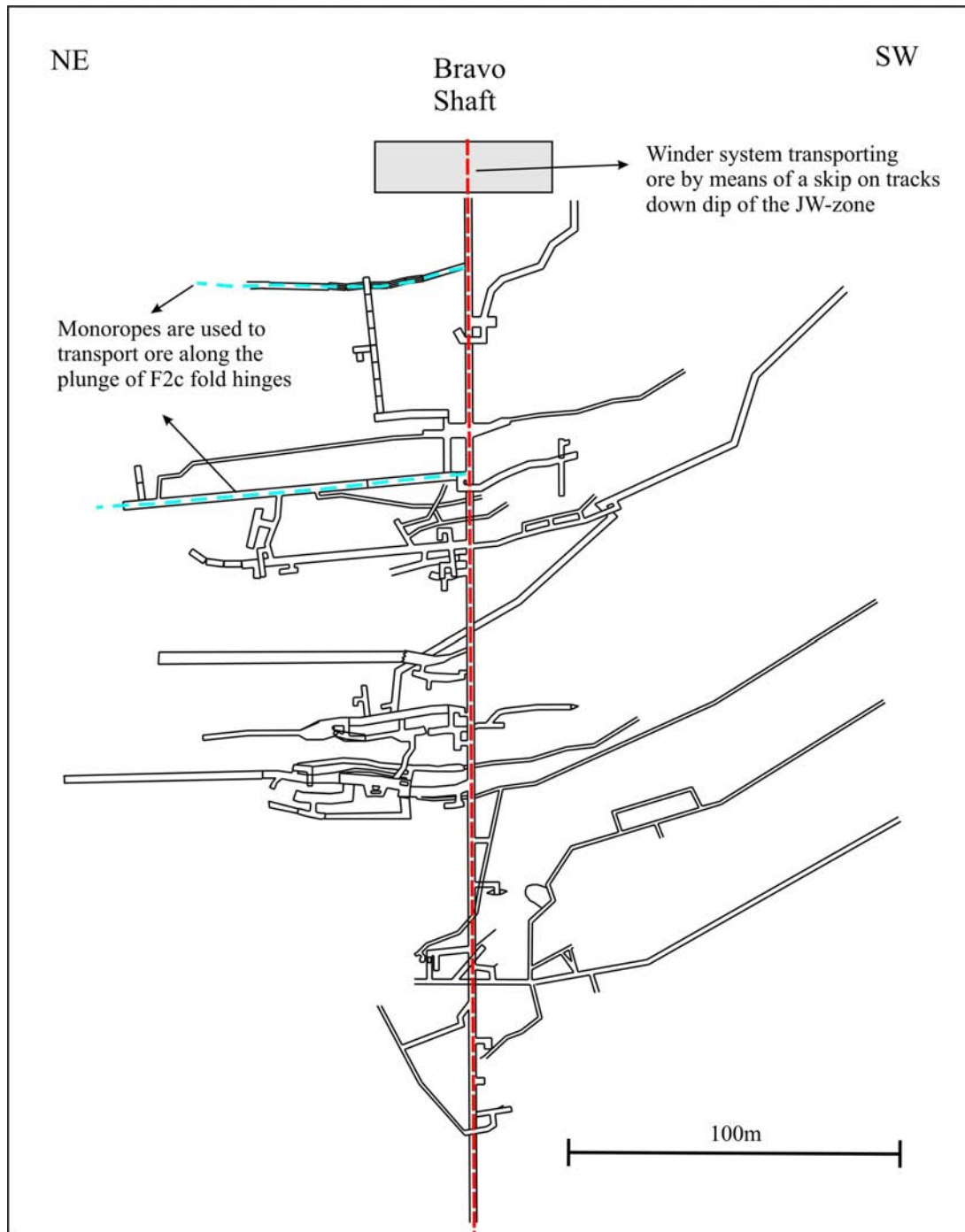


Figure 14.2. Bravo Shaft decline with lateral drives along the F2c fold hinges. The figure indicates the need for a monorope system in the fold hinge drives due to the flexibility allowed by this mining method. The plunge of the fold hinge-line can vary from  $35^{\circ}$  NE to  $5^{\circ}$  SW and the direction from  $0^{\circ}$  to  $40^{\circ}$  NE. The fold noses are also undulating and non-parallel, therefore illustrating the need for a flexible ore extraction method.



From the geological model various different methods were used to estimate the ore resources of the Block C area:

**Method 1**

Mine recovery factors indicate that between 15 and 20% of the JW-zone is highly mineralised. This results in a resource of 0.95 million tonnes for 63 million cts to 1.26 million tonnes for 83 million cts.

**Method 2**

- Recorded grams per fold stack:
  - Shaft 1: 525 115.00 g (2 625 575 ct)
  - Bravo Shaft Level 17 system: 268 347.00 g (1 341 735 ct)
  - The average of the combined fold stacks: 396 731.00 g (1 983 655 ct)
- The down-dip extent of the JW-zone has been proven by core drilling to a vertical depth of 283 m. This equates to a down-dip extent of ca. 400 m at the average dip of 45°.
- The fold stacks occur at ca. 80 – 100 m intervals, resulting in four fold stacks within the 400 m down-dip extent.
- Six fold stacks have been identified within the area along the strike extent. A total of 4 x 6 fold stacks are therefore present within the mining area.
- The total predicted ore resource of the JW-zone is thus  $396\,731 \times 24 = 9\,521\,544.00$  g (47 607 720 ct).
- At the established mine grade of 66 cpt (13.2 gpt) the reserve tonnage of  $9\,521\,544.00$  g / 13.2 gpt = 721 329 t.

**Method 3**

- The average dimensions of the boudinaged isoclinal fold hinges (ore shoots) are 120 m by 2.5 m by 3.5 m.
- The boudinaged ore shoots contain abundant amounts of heavy minerals (see Chapter 4), resulting in an S.G. of 2.80.
- Boudinage isoclinal fold hinge (ore shoot) =  $120 \times 2.5 \times 3.5 \times 2.8 = 2940$  t.
- There are, on average, seven F2c isoclinal fold hinges (ore shoots) per fold stack, resulting in  $2940 \times 7 = 20\,580$  t per fold stack.

- Since there are 24 fold stacks in the mine area it results  $20\,580 \times 24 = 493\,920$  t
- All the above estimates and interpretations are for the definition of a resource for the mine (TanzaniteOne Ltd. prospectus, 2004).

#### **14.4. Alluvial tanzanite potential**

For the preliminary investigation of the eluvial and alluvial tanzanite potential of the soil cover, six soil samples of ca. 25 kg were taken from the Block C area. The samples were divided down to approximately 5 kg and washed with a 100  $\mu\text{m}$  sieve. The samples were subsequently dried and divided by screening into 9 fractions as indicated in Table 14.1. The weight percentage of each fraction was calculated, since the fraction interval was not the same. All the fractions were subsequently inspected for tanzanite, resulting in recovery of two tanzanite crystals from the 2800 – 3350  $\mu\text{m}$  sieve interval of sample S1. A 50 tonne bulk sample was subsequently taken from the same area and processed through the TanzaniteOne Ltd. HMS plant. Although small tanzanite crystals were recovered for the bulk sample, the grade was below the economical cut-off point established for underground mining.

In general, fractions smaller than 2000  $\mu\text{m}$  have no economical value, since this is also the screening size on the HMS plant. From the fraction distribution of the soils (Table 14.1), it is evident that on average, only 39.6 % of the washed soil samples analysed has the potential of containing tanzanite of an economical grade. Before washing, the potential economical percentage of the soils samples drop to ca. 20 %. Even though this figure is very low, the costs involved in alluvial mining are significantly lower than underground mining. The costs per tonne for the mining and processing the alluvial material should therefore be calculated in order to establish an economical cut-off grade for the alluvial deposit. The processing costs of the alluvial material can be lowered by screening out the < 2000  $\mu\text{m}$  fraction before processing.

The alluvial soils of the Merelani deposit do contain tanzanite, but in order to evaluate its economic viability, the costs involved in mining and processing of the material should be determined.

Table 14.1. Weight (g) fractions and fraction percentages of six soil samples from Block C.

<b>Sieve interval</b>	<b>S1 (g)</b>	<b>S2 (g)</b>	<b>S3 (g)</b>	<b>S4 (g)</b>	<b>S5 (g)</b>	<b>S6 (g)</b>
<b>100 - 300</b>	144.04	348.03	455.2	379.59	323.16	292.28
<b>300 - 850</b>	430.40	807.19	681.59	607.5	599.99	392.41
<b>850 - 1000</b>	120.29	152.36	140.81	124.86	113.06	79.57
<b>1000 - 2800</b>	1281.25	1146.98	1041.65	993.8	786.38	655.55
<b>2800 - 3350</b>	174.09	158.3	143.5	132.74	96.79	95.25
<b>3350 - 4000</b>	135.95	115.2	150.72	122.25	75.15	82.32
<b>4000 - 5600</b>	220.96	167.99	240.48	160.23	104.93	132.37
<b>5600 - 8000</b>	137.15	78.14	125.67	80.73	44.00	88.97
<b>&gt;8000</b>	77.92	26.02	61.95	59.45	22.84	59.9
<b>Total (g)</b>	<b>2722.05</b>	<b>3000.21</b>	<b>3041.57</b>	<b>2661.15</b>	<b>2166.3</b>	<b>1878.62</b>
<b>Sieve interval</b>	<b>S1 (%)</b>	<b>S2 (%)</b>	<b>S3 (%)</b>	<b>S4 (%)</b>	<b>S5 (%)</b>	<b>S6 (%)</b>
<b>100 - 300</b>	5.3	11.6	15.0	14.3	14.9	15.6
<b>300 - 850</b>	15.8	26.9	22.4	22.8	27.7	20.9
<b>850 - 1000</b>	4.4	5.1	4.6	4.7	5.2	4.2
<b>1000 - 2800</b>	47.1	38.2	34.2	37.3	36.3	34.9
<b>2800 - 3350</b>	6.4	5.3	4.7	5.0	4.5	5.1
<b>3350 - 4000</b>	5.0	3.8	5.0	4.6	3.5	4.4
<b>4000 - 5600</b>	8.1	5.6	7.9	6.0	4.8	7.0
<b>5600 - 8000</b>	5.0	2.6	4.1	3.0	2.0	4.7
<b>&gt;8000</b>	2.9	0.9	2.0	2.2	1.1	3.2
<b>Total (%)</b>	<b>100.0</b>	<b>100.0</b>	<b>100.0</b>	<b>100.0</b>	<b>100.0</b>	<b>100.0</b>

## **14.5. Other potential economic minerals within the mining area**

### **14.5.1. Graphite**

The Lelatema Mountains are one of the richest flake graphite deposits in the world. The presence of graphite mineralisation in the Merelani area has been known since the 1930's and was commercially mined from 1993 to 1998 by SAMAX Ltd. The graphite was predominantly mined from two rock-types, the kyanite gneisses and the so-called "massive alteration zones". The former produced an average of 6 wt% carbon graphite (Cg) at an exceptionally high quality of over 99% carbon, while the latter contains an average of 11 wt% Cg, but of a slightly lower quality (ca. 96% Cg). Graphite concentrations of over 25 wt% Cg were recorded in certain areas of Merelani tanzanite deposit. The graphite quality is further enhanced by the extraordinary coarse flake size of ca. 300 microns. The Block C graphite deposit was estimated to have a life expectancy of 40 to 50 years at production rate of 15 000 tonnes per year (Davies and Chase, 1994; McRobbie et al., 1995).

Graphite exploration was done by SAMAX Ltd. in the 1990's in other areas within the Lelatema Mountains, such as in the Kimoingan area approx. 5 km ENE of the tanzanite mining area. Initial results from these exploration programs pointed towards a similar grade and quality graphite to that mined in the Merelani tanzanite deposit. The graphite mining potential of the Lelatema Mountains is therefore extremely favourable, especially since it can easily be incorporated into the mining and extraction processes of other minerals within the same graphite-bearing gneisses, such as tanzanite and tsavorite.

### **14.5.2. Gold (Au)**

The protolith investigations of the rocks (Chapter 11) indicate deposition within a back- or fore-arc basin with a volcanic component resembling that of a VMS depositional environment. These types of deposits often contain gold as an accessory mineral and valuable by-product of the base metal mining operations.

Gold assays were done by CSM Associates Ltd., UK, on pyrite samples from the Block C mining area. Three pyrite crystals were analysed by means of Atomic Absorption Spectrophotometry for its gold content. Values of 0.33 ppm (0.33 gram/

tonne), 0.7 ppm (0.7 g/t) and 1.5 ppm (1.5 g/t) were obtained. This initial result, together with the favourable geological setting, definitely warrants further exploration into the gold possibilities of the area.

### **14.5.3. Zinc and other base metals**

As indicated in Chapters 7 and 11, the deposit appears to have a VMS-like component. VMS deposits are one of the largest producers of copper, lead, zinc globally and sometimes contain associated gold and silver. Geochemical analysis of the various lithological units within the tanzanite deposit has yielded whole rock Zn values of over 4500 ppm.

Optical and petrographical investigation of selected units within the Lelatema Mountains revealed localised abundance of Sphalerite (ZnS), especially associated with calc-silicate units situated within the graphitic gneisses. Sphalerite is the main zinc-bearing mineral mined worldwide. VMS deposits show both vertical and lateral zoning, with the lateral zoning often on a regional scale. Since Zn is one of the more soluble metals within a Cu-Pb-Zn ± Au ± Ag deposit, the high values obtained from the graphitic gneisses could indicate the proximity of a mineable size VMS-type deposit. The possibility of a base metal deposit situated within the Lelatema Mountains is further supported by high Ba values of over 4800 ppm obtained from whole rock geochemical analysis.

In general, the high Zn and Ba values as well as the protolith classification suggests the possibility of a VMS type Cu-Pb-Zn ± Au ± Ag deposit located within the Lelatema Mountains. These indicators therefore warrant further exploration for a base metal deposit located within the area.

## **14.6. General implications of this study on tanzanite mining and exploration.**

- This study identified, named and described the mine lithologies (Chapter 3).
- Through a combination of core drilling, trenching, artisanal shafts, underground development and historical data, a surface geology map was produced indicating

the thickness and behaviour of the various lithological units within the mine area (Addendum B).

- The behaviour of the different lithologies at depth was investigated by logging and sampling core obtained from the drill holes (Addendum A).
- The different lithologies were further described in detail by means of petrographical and mineral chemical investigations (Chapters 4 and 6). This served to establish the type and nature of the tanzanite mineralisation (before this study, the deposit was speculated to be related to pegmatite intrusions).
- This study identified and described the complex structural deformational history as well as the structural features (boudins, folds, faults, lineation, foliation) of the deposit (Chapter 5).
- It identified and described the correlation between tanzanite mineralisation and various structural features, including shearing, boudinage and folding. This resulted in the development of a mine model targeting isoclinal fold hinges (ore shoots) within various fold stacks (Chapter 5).
- The behaviour of the ore shoots and associated boudin structures and their relationship and interaction with other structural deformational events was established (Chapter 5).
- The geochemical composition of the various lithological units was determined. This serves in understanding the deposit, as well as establishing a geochemical signature of the rock. The geochemical database and signature of the rocks are of utmost importance in the exploration for other tanzanite deposits (Chapter 7).
- The origin of the graphite and metamorphic fluids as well as the protolith and P-T conditions of the rocks are crucial in determining the depositional setting and characteristics of the deposit (Chapters 8, 9 and 11). This data is essential in the exploration for tanzanite.
- Fluid inclusion studies on tanzanite and associated minerals not only characterised the fluids involved in tanzanite mineralisation but also identified the use of fluid inclusions as an exploration tool for tanzanite (Chapter 10).
- The mineralogy of tanzanite and other coloured zoisites were investigated. This revealed that the colour of tanzanite is predominantly the result of the presence of  $V^{3+}$  and  $Ti^{4+}$  (Chapter 12). The vanadium originates from the abundant

organic graphite situated within the gneisses (Chapter 7). Vanadium is therefore also a key element for the exploration of a tanzanite deposit.

### 14.7. Overview of conclusions

The Merelani tanzanite deposit formed through a unique juxtaposition of various factors, with the most important being the original sedimentary characteristics, metamorphism, complex structural deformation history, geochemical composition of the various lithological units and the influence of skarn reactions driven by hydrothermal fluids. The geological history of the deposit can be summarised as follows:

- Deposition of a sequence of shallow shelf sediments consisting primarily out of various organic carbon ( $\delta^{13}\text{C}$  between  $-22.85\text{ ‰}$  and  $-26.74\text{ ‰}$ ) -rich mudstone horizons and limestone beds associated with a back- or fore-arc spreading basin.
- The sediments also have a volcanic component resulting in enrichment of Ba, Zn, Ni and V. The V combined with the organic complexes and became absorbed in the shales.
- Prograde metamorphism transformed the impure limestone beds into diopside-rich layers that eventually formed the pyroxene relict layers situated within the calc-silicate skarn boudins.
- Progressive increase in the metamorphic P-T conditions, probably due to deep burial and tectonic loading, led to the onset of high-grade ductile deformation. The first phase of structural deformation is either associated with the prograde metamorphic path towards granulite facies peak metamorphic conditions (M1) or with the M1 event itself. This led to the development of the first folding event (F1). The F1 intrafolial fold foliated the schists and gneisses. Peak metamorphism (M1 at ca. 1000 Ma) reached granulite facies conditions of 9 – 12 kbar and 800 °C to 900 °C.
- Shortly after peak metamorphic conditions a second multiphase deformation event (D2) developed as a result of crustal uplift. The D2 event probably occurred between 750 and 600 Ma at P-T conditions estimated at between 8 to 6 kbar and 700 to 600 °C. The D2 event caused the formation of the F2a, b and c folds as well as the development of chocolate-tablet boudinage.
- Skarn-related metamorphism and metasomatic diffusion occurred between the calc-silicates boudins and enveloping graphitic gneisses, resulting in a mass

balance exchange between the gneisses and the calc-silicates. Typical calc-silicate skarn metasomatic and metamorphic reactions resulted in the formation of the graphite-plagioclase gneisses, calc-silicate skarn boudins and skarnoid reaction zones.

- Tanzanite mineralisation occurred at the latter stages of the D2 event. Fission-track dating of tanzanite indicates an age of  $585 \pm 28$  Ma. The P-T conditions for tanzanite formation are estimated at ca. 6 to 5 kbar and  $650 \pm 50$  °C. The influx of hydrothermal fluids as well as a drop in P-T conditions led to tanzanite crystallisation within low-pressure sites situated within the calc-silicate boudin structures. Fluid inclusion studies indicate that the fluids were primarily H<sub>2</sub>S but probably also contained H<sub>2</sub>O and CO<sub>2</sub>. Tanzanite also formed from the hydrothermal fluid driven alteration of green grossular garnet (tsavorite), which already crystallised in the low-pressure site during an earlier stage of the D2 event.
- The association between tanzanite and boudins as well as the stacking and multiple duplication of the boudinaged ore-zone through isoclinal folding resulted in multiple “ore-shoots”. These ore-shoots therefore follow the plunge of the F2c fold closures. Fold-stacks consist of multiple F2c folds and present the most important feature in the mining of tanzanite.
- A third stage of deformation (D3) resulted in the formation of cross folds (F3), which overprinted all the F2c isoclinal folds and boudins resulting in rotation of the “ore-shoots”. The D3 event occurred during the later stages of the Pan-African (550 – 500 Ma) event probably during amphibolite/greenschist facies conditions (M3; ca. 5 kbar and 600 to 520 °C). Large pegmatic veins formed along the fold closures of the intrafolial folds and resulted in the destruction of any pre-existing structure and minerals, including tanzanite.
- Late stage brittle deformation (D4) resulted in the development of predominantly NW – SE striking fractures and faults.

Although the geological history and its components, such as the geochemical composition and structural deformation of the deposit are quite complex, the deposit is probably not unique in occurrence. A distinct possibility exists for all the various factors contributing in the mineralisation of tanzanite to also occur elsewhere. The



most logical place for exploration of such an area would be within the Lelatema Antiform itself. Second order drag folds (F2b) on the western limb of the antiform could result in duplication by Z –type folding of the deposit. It is also possible that similar type tanzanite deposits could be located elsewhere within the Mozambique Belt, within similar boudinaged calc-silicates enveloped by graphitic gneisses, although the chance of this is more rare.

The mineralogical investigations of tanzanite and the other coloured zoisite found within the deposit resulted in the following conclusions:

- Vanadium is the main chromophore in tanzanite and tsavorite from the Merelani area. The vanadium originates from the high amounts of graphite present within the gneiss.
- The colour of the zoisite is also dependant on the valance state of both V and Ti within the crystal lattice. The colour and colour intensity of tanzanite prior to heating is influenced by the presence of  $V^{3+}$  and  $Ti^{3+}$ .
- The green colour zoisites, with the same major and trace element composition as tanzanite, can probably be contributed to the presence of an intervalence charge-transfer reaction between  $Ti^{4+}$  and  $Ti^{3+}$ , not observed in tanzanite.
- The main chromophore ( $V^{3+}$ ) within the coloured zoisites does not undergo any valence change as a result of heat treatment.
- $Ti^{3+}$  is oxidised to  $Ti^{4+}$  through heating. Since  $Ti^{3+}$  is a chromophore and  $Ti^{4+}$  is colourless, this valence change results in the subtraction of the red/yellow/green colour component of tanzanite, thereby increasing the blue and violet component.

In conclusion, the tanzanite deposit can be classified as a stratabound calc-silicate skarn deposit. The term “tanzanite skarn” is suggested as an economical descriptive term for the Merelani tanzanite deposit, as well as for other future tanzanite deposits of a similar nature.

---

## References

- Aitken, B.G., 1983.** T – X<sub>CO<sub>2</sub></sub> stability relations and phase equilibria of a calcic carbonate scapolite. *Geochimica et Cosmochimica Acta*, **47**, 351-362.
- Altshuler, S.A. and Kozyrev, B.M., 1964.** *Electron Paramagnetic Resonance*. New York: Academic Press.
- Andersen, O.K., Mazin, I.I., Liechtenstein, A.I., Jepsen O., Antropov, V.P., Rashkeev, S. N., Anisimov, V. I., Zaanen, J., Rodriguez R.O. and Methfessel, M., 1993.** Density Functional Theory for Photons, Electrons and their Interaction in YBa<sub>2</sub>Cu<sub>3</sub>O<sub>7</sub>. In: *High-Temperature Superconductivity (Conference proceedings BHTSC 1992)*, Editors: Z. Z. Gan, S. S. Xie, Z. X. Zhao. Singapore: World Scientific, 785-794.
- Andersen, O.K., Methfessel, M., Rodriguez, C.O., Blöchl, P. and Polatoglou, H.M., 1989.** Total Energy and Force Calculations with the LMTO Method. In: *Atomistic Simulation of Materials*, Editors: V. Vitek and D. J. Srolovitz. New York: Plenum, 1-13.
- Andriessen, P.A.M., Coolen, J.J.M.M.M. and Hebeda, E.H., 1985.** K-Ar hornblende dating of late Pan-African metamorphism in the Furuu granulite complex of southern Tanzania. *Precambrian Research*, **30**, 351-360.
- Appel, P., Möller, A. and Schenk, V., 1998.** High-pressure granulite facies metamorphism in the Pan-African belt of eastern Tanzania: P-T-t evidence against granulite formation by continent collision. *Journal of Metamorphic Geology*, **16**, 491-509.
- Bagnall, P.S., 1963.** The geology of the North Pare mountains. *Records of the Geological Survey of Tanganyika*, **10**, 7-16.

- Bakker, R.J., 2003.** Package FLUIDS 1. New computer programs for the analysis of fluid inclusion data and for modelling bulk fluid properties. *Chemical Geology*, **194**, 3-23.
- Barker, A.J., 1998.** Introduction to Metamorphic Textures and Microstructures, Second Edition. Standley Thornes Ltd., 161pp.
- Barot, N.R. and Boehm, E., 1992.** Gem quality green zoisite. *Gems & Gemology*, **28**, 1, 4 – 15.
- Bell, K. and Dodson, M.H., 1981.** The geochronology of the Tanzanian shield. *Journal of Geology*, **89**, 109-128.
- Bellanca, A., Masetti, B. and Neri, R., 1997.** Rare earth elements in limestone/marlstone couplets from the Albian – Cenomanian Cismon section (Venetian region, northern Italy): assessing REE sensitivity to environmental changes. *Chemical Geology*, **141**, 141-152.
- Bhatia, M.R. and Taylor, S.R., 1981.** Trace element geochemistry and sedimentary provinces: a study from the Tasman geosynclines, Australia. *Chemical Geology*, **33**, 115-125.
- Bhattacharya, A., Mohanty, L., Maji, A., Sen, S.K. and Raith, M., 1992.** Non-ideal mixing in the phlogopite-annite binary: constraints from experimental data on Mg-Fe partitioning and a reformulation of the biotite-garnet geothermometer. *Contributions to Mineralogy and Petrology*, **111**, 87 – 93.
- Boettcher, A.L., 1970.** The system CaO-Al<sub>2</sub>O<sub>3</sub>-SiO<sub>2</sub>-H<sub>2</sub>O at high pressures and temperatures. *Journal of Petrology*, **11**, 337-379.
- Borthwick, J. and Harmon, R.S., 1982.** A note regarding ClF<sub>3</sub> as an alternative to BrF<sub>5</sub> for oxygen isotope analysis. *Geochimica et Cosmochimica Acta*, **46**, 1665-1668.
- Bowen, R., 1988.** Isotopes in the earth sciences. Elsevier Applied Sciences Publishers LTD, London, 647pp.

- Brady, J.B., 1977.** Metasomatic zones in metamorphic rocks. *Geochimica et Cosmochimica Acta*, **41**, 13-125.
- Brinkmann, D., Staehli, J.L. and Ghose, S., 1969.** Nuclear magnetic resonance of  $^{27}\text{Al}$  and  $^1\text{H}$  in zoisite,  $\text{Ca}_2\text{Al}_3\text{Si}_3\text{O}_{12}(\text{OH})$ . *Journal of Chemical Physics*, **51**, 5128 - 5133.
- Buick, I.S., 1998.** Stable isotopes as tracers of geological processes. E.G.R.U. short course no. 2. La Trobe University, Melbourne, 128pp.
- Buick, I.S., Harley, S.L. and Cartwright, I.C., 1993.** Granulite facies metasomatism: zoned calc-silicate boudins from the Rauer Group, East Antarctica. *Contributions to Mineralogy and Petrology*, **113**, 557-571.
- Burke, K., Dewey, J.F. and Kidd, W.S.F., 1977.** World distribution of structures – the sites of former oceans. *Tectonophysics*, **40**, 69-99.
- Burns, R.G., 1970.** *Mineralogical Applications of Crystal Field Theory*. Cambridge University Press.
- Burns, R.G., 1981.** Intervalence transitions in mixed-valence minerals of iron and titanium. *Annual Review of Earth and Planetary Sciences*, **9**, 345-383.
- Burton, J.C., Taylor, L.A. and Chou, I-M., 1982.** The  $f_{\text{O}_2} - T$  and  $f_{\text{S}_2} - T$  stability relations of Hedenbergite and of Hedenbergite – Johannsenite solid solutions. *Economic Geology*, **77**, 4, 764 – 783.
- Cahen, L., Snelling, N.J., Delhal, J. and Vail, J., 1984.** *The geochronology and evolution of Africa*. Clarendon Press, Oxford, 512pp.
- Calas, G., 1988.** Electron Paramagnetic Resonance. In: *Spectroscopic methods in Mineralogy and Geology*, Editor: F.C.Hawthorne. Mineralogical Society of America, *Reviews in Mineralogy*, **18**, 513–571.
- Carmichael, D.M., 1978.** Metamorphic bathzones and bathograds: a measure of the depth of post-metamorphic uplift and erosion on a regional scale. *American Journal of Science*, **278**, 769-797.

- Cartwright, I. and Valley, J.W., 1992.** Oxygen-isotope geochemistry of the Scourian complex, NW Scotland. *Journal of the Geological Society London*, **149**, 115-126.
- Cartwright, I., Vry, J. and Sandiford, M., 1995.** Changes in stable isotope ratios of metapelites and marbles during regional metamorphism, Mount Lofty Ranges, South Australia: implications for crustal scale fluid flow. *Contributions to Mineralogy and Petrology*, **120**, 292-310.
- Castner, Th., Newell, G.S., Holton, W.C. and Slichter, C.P., 1960.** Note on paramagnetic resonance of iron in glass. *Journal of Chemical Physics*, **32**, 668-673.
- Chamberlain, C.P., Ferry, J.M. and Rumble, D., III, 1990.** The effect of net-transfer reactions on the isotopic composition of minerals. *Contributions to Mineralogy and Petrology*, **105**, 3, 322-336.
- Chou, I.M., Pasteris, J.D. and Seitz, J.C., 1990.** High density volatiles in the system C-O-H-N for the calibration of a laser Raman microprobe. *Geochimica et Cosmochimica Acta*, **54**, 535-543.
- Cilek, V., 1980.** The geology of the Merelani tanzanite deposit. *Sbornik Geologicktch Ved, Loziskova Geologie Mineralogie*, **21**, 183-185.
- Clayton, R.N. and Mayeda, T.K., 1963.** The use of bromine pentafluoride in the extraction of oxygen from oxides and silicates for isotopic analysis. *Geochimica et Cosmochimica Acta*, **27**, 43-52.
- Cohen, A.J. and Makar, L.N., 1984.** Differing effects on ionising radiation in massive and single crystal rose quartz. *Neues Jahrbuch für Mineralogie Mh*, **11**, 513-521.
- Cohen, A.J. and Makar, L.N., 1985.** Dynamic biaxial absorption spectra of  $Ti^{3+}$  and  $Fe^{2+}$  in a natural rose quartz crystal. *Mineralogical Magazine*, **49**, 709-715.
- Coolen, J.J.M.M.M., 1980.** Chemical petrology of the Furua granulite complex, southern Tanzania. *GUA papers in Geology, Series 1, no.13*.

- Coolen, J.J.M.M.M., Priem, H.N.A., Verdurmen, E.A.Th. and Verschure, R.H., 1982.** Possible zircon U-Pb evidence for Pan-African granulite-facies metamorphism in the Mozambique Belt of southern Tanzania. *Precambrian Research*, **17**, 31-40.
- Condie, K.C. and Wronkiewicz, D.J., 1990.** The Cr/Th ratio in Precambrian pelites from the Kaapvaal Craton as an index of craton evolution. *Earth and Planetary Science Letters*, **97**, 256 - 257.
- Coplen, T.B., 1993.** Normalisation of oxygen and hydrogen isotope data. *Chemical Geology*, **72**, 293-297.
- Coplen, T.B., Kendall, C. and Hopple, J., 1983.** Comparison of stable isotope reference samples. *Nature*, **302**, 236-238.
- Cornell, D.H., Thomas, R.J., Bowring, S.A., Armstrong, R.A. and Grantham, G.H., 1996.** Protolith interpretation in metamorphic terranes: a back-arc environment with Besshi-type base metal potential for the Quha Formation, Natal Province, South Africa. *Precambrian Research*, **77**, 243 – 271.
- Craig, J.R. and Vokes, F.M., 1993.** The metamorphism of pyrite and pyritic ores: an overview. *Mineralogical Magazine*, **57**, 3-18.
- Cunningham, A., 2001.** Investigation of small scale mining activities within the Lelatema Mountains. Honours project, University of Stellenbosch, 38pp.
- Cutten, H.N.C., 2002.** The Mozambique belt, Eastern Africa – tectonic evolution of the Mozambique Ocean and Gondwana amalgamation. *Precambrian Geology*. Denver Annual Meeting, Session No. 122.
- Darimont, A., Burke, E.A.J. and Touret, J., 1988.** Nitrogen-rich metamorphic fluids in devonian metasediments from Bastogne. *Belgium Bulletin Minéralogie*, **111**, 321-330.

- Dasgupta, S., Sengupta, P., Guha, D. and Fukuoka, M., 1991.** A refined garnet-biotite Fe-Mg exchange geothermometer and its application in amphibolites and granulites. *Contributions to Mineralogy and Petrology*, **109**, 130 – 137.
- Davies, C., and Chase, R.J., 1994.** The Merelani graphite-tanzanite deposit, Tanzania: An exploration case history. *Exploration and Mining Geology*, **3**, 4, 371-382.
- Dawson, J.B., 1992.** Neogene tectonic sand volcanicity in the North Tanzania sector of the Gregory Rift Valley: contrast with the Kenya sector. *Tectonophysics*, **204**, 81-92.
- Dawson, J.B., 1997.** Neogene-Recent rifting and volcanism in northern Tanzania: relevance for comparisons between the Gardar province and the East African Rift valley. *Mineralogical Magazine*, **61**, 543-548.
- Dawson, J.B., 2002.** Metasomatism and Partial Melting in Upper-Mantle Peridotite Xenoliths from the Lashaine Volcano, Northern Tanzania. *Journal of Petrology*, **43**, 1749-1777.
- de Baar, H.J.W., Bacon, M.P., Brewer, P.G. and Bruland, K.W., 1985.** Rare earth elements in the Pacific and Atlantic oceans. *Geochimica et Cosmochimica Acta*, **49**, 2561-2571.
- de Baar, H.J.W., German, C.G., Elderfield, H. and van Gaans, P., 1988.** Rare earth element distributions in anoxic waters of the Cariaco Trench. *Geochimica et Cosmochimica Acta*, **52**, 1203-1219.
- de Biasi R. S. and Fernandes A. A. R., 1984.** Measurement of Small Concentrations of Cr and Mn in MgO Using Electron Spin Resonance. *Communications of the American Ceramic Society*, September 1984, C-173 – C-175.
- de Bruin, D., 2001.** The analytical conditions used by Council for Geoscience for mantle indicator mineral analysis by electron probe. *Geological Survey Bulletin*, **114**, 172.

- 
- Deer, W.A., Howie, R.A. and Zussman, J., 1986.** Rock-Forming Minerals – Disilicates and Ring Silicates, Vol. 1B, Second Edition. The Geological Society, London, Longman Scientific and Technical, 629pp.
- Deer, W.A., Howie, R.A. and Zussman, J., 1992.** An introduction to the Rock-Forming Minerals, Second Edition. Longman Scientific and Technical, Essex, England, 696pp.
- Dirlam, D.M., Misiorowski, E.B., Tozer, R., Stark, K.B. and Bassett, A.M., 1992.** Gem Wealth of Tanzania, *Gems & Gemology*, **28**, 2, 80-102.
- Dolenc, M., 1976.** Das Tansanitvorkommen Merelani in Tanzanien. *Z. Dtsch. Gemmol. Ges.*, **25**, 86-95
- Dollase, W.A., 1968.** Refinement and comparison of the structures of zoisite and clinozoisite. *American Mineralogist*, **53**, 1882-1898.
- Dubessy, J., Boiron, M.C., Moissette, A., Monnin, C. and Sretenskaya, N., 1992.** Determination of water, hydrates and Ph in fluid inclusions by micro-Raman spectrometry. *European Journal of Mineralogy*, **4**, 885-894.
- Dunkley, D.J., Clarke, G.L. and Harley, S.L., 1999.** Diffusion metasomatism in silica-undersaturated sapphirine-bearing granulite from Rumdoodle Peak, Frammes Mountains, east Antarctica. *Contributions to Mineralogy and Petrology*, **134**, 264-276.
- Dunn, P.J., 1975.** Notes on inclusions in tanzanite and tourmalinated quartz. *Journal of Gemmology*, **14**, 7, 335-338.
- Fairhead, J.D., 1976.** Structure of the lithosphere beneath the Eastern rift, East Africa, deduced from gravity studies. *Tectonophysics*, **30**, 269-298.
- Fairhead, J.D., 1980.** The Structure of the cross-cutting volcanic chain of northern Tanzania and its relation to the East African Rift system. *Tectonophysics*, **65**, 193-208.



- Faye, G.H. and Harris, D.C., 1969.** On the origin of colour and pleochroism in andalusite from Brazil. *Canadian Mineralogist*, **10**, 47-56.
- Faye, G.H. and Nickel, E.H., 1971.** On the pleochroism of vanadium-bearing zoisite from Tanzania. *Canadian Mineralogist*, **10**, 812-821.
- Feng, R. and Kerrich, R., 1990.** Geochemistry of fine-grained clastic sediments in the Archean Abitibi greenstone belt, Canada: Implications for provenance and tectonic setting. *Geochimica et Cosmochimica Acta*, **45**, 633-1652.
- Ferry, J.M., 1992.** Regional metamorphism of the Waits River Formation, eastern Vermont: Delineation of a new type of giant metamorphic hydrothermal system. *Journal of Petrology*, **33**, 45-94.
- Ferry, J.M. and Spear, F.S., 1978.** Experimental calibration of the partitioning of Fe and Mg between biotite and garnet. *Contributions to Mineralogy and Petrology*, **66**, 113-117.
- Fesenko, E.G., Rumanova, I.M. and Belov, N.V., 1955.** The crystal structure of zoisite. *Doklady Akademii Nauk*, **102**, 275-278.
- Floyd, P.A., Winchester, J.A. and Park, R.G., 1989.** Geochemistry and tectonic setting of Lewisian clastic metasediments from the Early Proterozoic Loch Maree Group of Gairloch, NW Scotland. *Precambrian Research*, **45**, 203-214.
- Friedman, I. and O'Neil, J.R., 1977.** Compilation of stable isotope fractionation factors of geochemical interest: U.S. Geological Survey Professional Paper 440-KK.
- Frost, B.R. and Chacko, T., 1989.** The granulite uncertainty principle: limitations on thermometry in granulites. *Journal of Geology*, **97**, 435-450.
- Gabert, G., 1984.** Structural-lithological units of Proterozoic rock in East Africa, their base, cover and mineralisation. In: *Geologie Africaine – African Geology*, Editors: J. Kerkx and J. Michot. Musee Royale de L'Afrique Centrale. Tervuren, Belgium, 11-22.

- Gamble, R. P. 1982.** An experimental study of sulfidation reactions involving Andradite and Hedenbergite. *Economic Geology*, **77**, 4, 784 – 797.
- Gessner, R., 2004.** A study of the local and surface trench geology related to the occurrence of tanzanite, of TanzaniteOne's Merelani Mining Ltd. (MML) Block C Mine. Honours project, University of Stellenbosch, 41pp.
- Ghent, E.D, 1976.** Plagioclase-garnet- $\text{Al}_2\text{SiO}_5$ -quartz: a potential geobarometer – geothermometer. *American Mineralogist*, **61**, 71-714.
- Ghosh, S.K., 1988.** Theory of chocolate-tablet boudinage. *Journal of Structural Geology*, **10**, 6, 541–553.
- Ghosh, S.K., 1993.** *Structural Geology: Fundamentals and Modern Developments*. Pergamon Press, London.
- Ghosh, S.K. and Sengupta, S., 1999.** Boudinage and composite boudinage in superposed deformations and syntectonic migmatization. *Journal of Structural Geology*, **21**, 97-110.
- Goodwin, A.M., 1991.** *Precambrian Geology: The dynamic evolution of the continental crust*. Academic press, Toronto, 666pp.
- Goodwin, A.M., 1996.** *The Principles of Precambrian Geology*. Academic press, Toronto, 327pp.
- Grant, J.A. and Weiblen, P.W., 1971.** Retrograde zoning in garnet near the second sillimanite isograd. *American Journal of Science*, **270**, 281-296.
- Grégoire, M., Lorand, J.P., O'Reilly, S.Y. and Cottin, J.Y., 2000.** Armalcolite - bearing, Ti-rich metasomatic assemblages in harzburgitic xenoliths from the Kerguelen Islands: Implications for the oceanic mantle budget of high-field strength elements. *Geochimica et Cosmochimica Acta*, **64**, 4, 673-694.
- Gresse, P.G., 2002.** Structural setting of the Merelani tanzanite deposit, Tanzania. Internal Report for TanzaniteOne Ltd., 13pp.

- Gresse, P.G., 2003.** Structural setting of the Merelani tanzanite deposit, Tanzania – Revisited. Internal Report for TanzaniteOne Ltd., 11pp.
- Grunow, A., Hanson, R. and Wilson, T., 1996.** Were aspects of Pan-African deformation linked to lapetus opening? *Geology*, **24**, 1063-1066.
- Gübelin, E.J. and Weibel, M., 1975.** Green vanadium grossular garnet from Lualenyi, near Voi, Kenya. *Lapidiary Journal*, **29**, 2, 402-426.
- Harker, A., 1889.** On the local thickening of dykes and beds of folding. *Geological Magazine, New Ser.*, **6**, 59 – 70.
- Harlov, D.E., Hansen, E.C. and Bigler, C., 1998.** Petrologic evidence for K-feldspar metasomatism in granulite facies rocks. *Chemical Geology*, **151**, 373-386.
- Harpum, J.R., 1970.** Summary of the Geology of Tanzania. Geological Survey of Tanzania, Memoir, 1.
- Harris, J.F., 1981.** Summary of the geology of Tanganyika, Part iv: Economic Geology. Government Printer, Dar es Salaam, 143pp.
- Haskin, L.A., Haskin, M.A., Frey, F.A. and Wildeman, T.R., 1968.** Relative and absolute terrestrial abundances of the rare earths. In: *Origin and Distribution of the Elements*, Editor: L.H. Ahrens. Pergamon, Oxford, **1**, 889 – 911.
- Hassan, S., Ishiga, H., Roser, B.P., Dozen, K. and Naka, K., 1999.** Geochemistry of Permian – Triassic shales in the Salt Range, Pakistan: implications for provenance and tectonism at the Gondwana margin. *Chemical Geology*, **158**, 293-314.
- Haule, H.I., Shevchenko, B. and Mwaya, G.T., 1978.** Project report on Merelani tanzanite project. STAMICO, P.O. Box 981, Dodoma.
- Helgeson, H.C., Delany, J.M., Nesbitt, H.W. and Bird, D.K., 1978.** Summary and critique of the thermodynamic properties of rock-forming minerals. *American Journal of Science*, **278A**, 1-299.

- Hepworth, J.V., 1972.** The Mozambique orogenic belt and its foreland in northeast Tanzania: a photogeologically-based study. *Quarterly Journal of the Geological Society of London*, **128**, 461-500.
- Hodges, K.V. and Spear F.S., 1982.** Geothermometry, geobarometry and the  $\text{Al}_2\text{SiO}_5$  triple point at Mt. Moosilauke, New Hampshire. *American Mineralogist*, **67**, 1118-1134.
- Hoefs, J., 1997.** *Stable Isotope Geochemistry*. Springer –Verlag, Berlin, 201pp.
- Hoffman, P.J., 1991.** Did the breakdown of Laurentia turn Gondwanaland inside-out? *Science*, **252**, 1409-1412.
- Holland, T.J.B. and Powell, R., 1998.** An internally consistent thermodynamic dataset for phases of petrological interest. *Journal of Metamorphic Geology*, **16**, 309-343.
- Holmes, A., 1951.** The sequence of Precambrian orogenic belts in South and Central Africa. *Proc. 18<sup>th</sup> Int. Geological Congress, London*, 254-269.
- Hormann, P.K., Raith, M. and Raase, P., 1980.** The granulite complex of Finnish Lapland: petrology and metamorphic conditions in the Ivalojoiki-Inarijarvi area. *Geological Survey of Finland, Bulletin*, **308**, 1-95.
- Hurlbutt, C.S., 1969.** Gem zoisite from Tanzania. *American Mineralogist*, **54**, 702-709.
- Ihinger, P.D. and Stolper, E.M., 1986.** The color of meteoritic hibonite: an indicator of oxygen fugacity. *Earth and Planetary Science Letters*, **78**, 67- 79.
- Indares, A. and Martignole, J., 1985.** Biotite-garnet Geothermometry in the granulite facies: the influence of Ti and Al in biotite. *American Mineralogist*, **70**, 272 – 278.
- Ito, T., Morimoto, N. and Sadanaga, R., 1954.** On the structure of epidote. *Acta Crystallographica*, **7**, 53-59.
- Jacobs, J., Fanning, M., Henjes-Kunst, F., Olesch, M. and Paech, H., 1998.** Continuation of the Mozambique Belt into East Antarctica: Grenville-age

- metamorphism and polyphase Pan-African high-grade events in the Central Dronning Maud Land. *The Journal of Geology*, **106**, 385-406.
- Jamieson, R. and Strong, D., 1981.** A metasomatic mylonite zone within the ophiolite aureole, St. Anthony Complex, Newfoundland. *American Journal of Science*, **281**, 264-281.
- Kato, Y., 1991.** Textural and compositional changes of clinopyroxene replaced by garnet in the Mozumi deposit, Kamioka Mine, Japan. In: *Skarns – their genesis and metallogeny*, Editors: A.M. Aksyuk, L.G. Collins, M. Dobrovolskaya, H. Lun-Chi, G.R. Lowell, G. van Marcke de Lummen, H. Shimazaki, W. Liren, V.A. Zarikov, S.S. Augustithis. 648pp.
- Kepezhinskas, K. B. and Khlestov, V.V., 1971.** Statistical analysis of the epidote group minerals and their paragenetic types. Nauka Publishing House, Moscow, 310pp.
- Kerrick, D.M., 1974.** Review of metamorphic mixed volatile (H<sub>2</sub>O-CO<sub>2</sub>) equilibria. *American Mineralogist*, **59**, 729-762.
- Kisters, F.M., Scheepers, R. and Olivier, B., 2000.** The role of boudinage in localising gemstone-quality tanzanite at the Merelani type-locality, NE-Tanzania, Unpublished manuscript.
- Knowles, C.R., 1987.** A basic program to recast garnet end members. *Computers and Geoscience*, **13**, 655-658.
- Kretz, R., 1983.** Symbols of rock-forming minerals. *American Mineralogist*, **68**, 277-279.
- Lamb, W.M., Valley, J.W and Brown, P.E., 1987.** Post-metamorphic CO<sub>2</sub>-rich fluid inclusions in granulites. *Contributions to Mineralogy and Petrology*, **96**, 485-495.
- Langer, K. and Lattard, D., 1980.** Identification of a low-energy OH-valence vibration in zoisite. *American Mineralogist*, **65**, 779-783.

- 
- Larsen, R.W., Nunez, D.J., Morgan, W.T., Muhoberac, B.B. and Ondrias, M.R., 1992.** Resonance Raman investigation of the effects of copper binding to iron-mesoporphyrin histidine-rich glycoprotein complexes. *Biophysical Journal*, **61**, 1007-1017.
- le Roux, A.P., Späth, A. and Zartman, R.E., 2001.** Lithospheric thickness beneath the southern Kenya Rift: implications from basalt geochemistry. *Contributions to Mineralogy and Petrology*, **142**, 89-106.
- Lehmann, G., 1969.** Zur farbe von rosenquarz. *Neues Jahrbuch für Mineralogie Mon*, **1969**, 222-225.
- Lemmon, E.W., Mclinden, M.O. and Friend, D.G., 2001.** Thermophysical Properties of Fluid Systems. In NIST Chemistry WebBook, NIST Standard Reference Database Number 69, Vol. 20899. Editors: P.J. Linstrom and W.G. Mallard. National Institute of Standards and Technology, Gaithersburg MD, USA.
- Liu, Y.G., Miah, M.R.U. and Schmitt, R.A., 1988.** Cerium: a chemical tracer for paleo-oceanic redox conditions. *Geochimica et Cosmochimica Acta*, **52**, 1361-1371.
- Maboko, M.A.H., Boelrijk, N.A.I.M., Priem, H.N.A. and Verdurmen, Z.W.O., 1985.** Zircon U-Pb and biotite Rb-Sr Dating of the Wami River granulites, eastern granulites, Tanzania: evidence for approximately 715 Ma old granulite-facies metamorphism and final Pan-African cooling approximately 475 Ma ago. *Precambrian Research*, **30**, 361-378.
- Maboko, M.A.H. and Nakamura, E., 1995.** Sm-Nd garnet ages from the Uluguru granulite complex of Eastern Tanzania: further evidence for post-metamorphic slow cooling in the Mozambique belt. *Precambrian Research*, **74**, 195-202.
- Maboko, M.A.H. and Nakamura, E., 1996.** Nd and Sr isotopic mapping of the Archaean-Proterozoic boundary in southeastern Tanzania using granites as probes for crustal growth. *Precambrian Research*, **77**, 105-115.

- MacFarlane, A., 1975.** Brief explanation of the geology of Q.D.S. 72, Arusha Chini, Geological Map, 1:125 000. Geological Survey, Tanzania. Mineral Resource Division, Dodoma.
- MacFarlane, R.M., 1964.** Optical and magnetic properties of trivalent vanadium complexes. *Journal of Chemical Physics*, **40**, 373 –377.
- Malisa, E., 1987.** Geology of the tanzanite gemstone deposits in the Lelatema area, NE Tanzania. *Annales Academy of Science Fennicae III, Geologica-Geographica*, **146**, 160pp.
- Malisa, E., Kinnunen, K. and Koljonen, T., 1986.** Notes on fluid inclusions in vanadiferous zoisite (tanzanite) of the Merelani area, Tanzania. *Bulletin of the Geological Society of Finland*, **58**, 53-58.
- Malisa, E. and Muhongo, S., 1990.** Tectonic setting of gemstone mineralization in the Proterozoic metamorphic terrane of the Mozambique Belt in Tanzania. *Precambrian Research*, **46**, 167-176.
- Manning, P.G., 1969.** An Optical absorption study of the origin of colour and pleochroism in pink and brown tourmaline. *Canadian Mineralogist*, **9**, 678-690.
- Martineau, M.P. and Davies, C., 1996.** Merelani tanzanite – a unique occurrence. *Minerals Industry International*, March, 15-22.
- McClure, D.S., 1962.** Optical spectra of transition metal ions in corundum. *Journal of Chemical Physics*, **36**, 2757 –2779.
- McCrea, J.M., 1950.** On the isotopic chemistry of carbonates and a palaeotemperature scale. *Journal of Chemical Physics*, **18**, 849-857.
- McRobbie, S.J, Davies, C. and Chase, R.J., 1995.** Graphite and tanzanite – a unique combination. *African Mining*, **1**, 363-378.
- Meen, V.B., 1968.** Zoisite - a newly found gem from Tanzania. *Lapidary Journal*, **22**, 636- 637.

- Mendelssohn, M.J. and Milledge, H.J., 1995.** Geologically significant information from routine analysis of the mid-infrared spectra of diamonds. *International Geology Review*, **37**, 95–110.
- Minpet for Windows, version 2.02.** Minpet Geological Software, 146 Du Château, Masson-Angers, Québec, Canada. J8M1J3.
- Möller, A., Mezger, K. and Schenk, V., 1998.** Crustal age domains and the evolution of the continental crust in the Mozambique Belt of Tanzania: Combined Sm-Nd, Rb-Sr and Pb-Pb isotopic evidence. *Journal of Petrology*, **39**, 749-783.
- Möller, A., Mezger, K. and Schenk, V., 2000.** U-Pb dating of metamorphic minerals: Pan-African metamorphism and prolonged slow cooling of high pressure granulites in Tanzania, East Africa. *Precambrian Research*, **104**, 123-146.
- Muhongo, S., 1990.** Evolution of the Proterozoic Granulite Complexes in Eastern Tanzania and implications for the geo-dynamic evolution of the Mozambique Belt of East Africa. Ph.D. Technical University of Berlin. 228pp.
- Muhongo, S. and Lenoir, J.C., 1994.** Pan-African granulite facies metamorphism in the Mozambique belt of Tanzania: U-Pb zircon geochronology. *Journal of the Geological Society of London*, **151**, 343-347.
- Muhongo, S. and Tuisku, P., 1996.** Pan-African high pressure isobaric cooling: evidence from the mineralogy and thermobarometry of the granulite-facies rocks from the Uluguru Mountains, eastern Tanzania. *Journal of African Earth Sciences*, **23**, 443-463.
- Muhongo, S., Tuisku, P. and Mtoni, Y., 1999.** Pan-African pressure-temperature evolution of the Merelani area in the Mozambique belt in NE Tanzania. *Journal of African Earth Sciences*, **29**, 73-85.
- Myer, G.H., 1966.** New data on zoisite and epidote. *American Journal of Science*, **264**, 364-385.



- Naesser, C.W. and Saul, J.M., 1974.** Fission track dating of Tanzanite. *American Mineralogist*, **59**, 613-614.
- Naha, K. and Halyburton, R.V., 1977.** Structural patterns and strain history of superimposed fold system in the Precambrian of Central Rajasthan, India. Parts I & II. *Precambrian Research*, **4**, 39-111.
- Nassau, K., 1983.** *The Physics and Chemistry of Color, the Fifteen Causes of Color.* John Wiley & Sons, New York, 454pp.
- Nesse, W.D., 1991.** *Introduction to Optical Mineralogy, Second Edition.* New York, Oxford University Press, 335pp.
- Newberry, R., 1991.** Scheelite-bearing skarns in the Sierra Nevada region, California: contrasts in zoning and mineral compositions. In: *Skarns – their genesis and metallogeny*, Editors: A.M. Aksyuk, L.G. Collins, M. Dobrovolskaya, H. Lunci, G.R. Lowell, G. van Marcke de Lummen, H. Shimazaki, W. Liren, V.A. Zarikov, S.S. Augustithis. 648pp.
- Newton, R.C., 1965.** The thermal stability of zoisite. *Journal of Geology*, **73**, 431-441.
- Newton, R.C., 1986.** Metamorphic temperatures and pressures of group B and C eclogites. *Geological Society of America*, **164**, 17-30
- Newton, R.C. and Goldsmith, J.R., 1976.** Stability of the end-member scapolites:  $3\text{NaAlSi}_3\text{O}_8\cdot\text{NaCl}$ ,  $3\text{CaAl}_2\text{Si}_2\text{O}_8\cdot\text{CaO}_3$ ,  $3\text{CaAl}_2\text{Si}_2\text{O}_8\cdot\text{CaSO}_4$ . *Zeitschrift für Kristallographie*, **143**, 333-353.
- Newton, R.C. and Haselton, H.T., 1981.** Thermodynamics of the garnet-plagioclase- $\text{Al}_2\text{SiO}_5$ -quartz geobarometer. In: *Thermodynamics of minerals and melts*, Editors: R.C. Newton, A. Navrotsky, and B.J. Wood. Springer-Verlag, New York, 320pp.
- Pake, G.E. and Estle, T.L., 1973.** *The Physical Principles of Electron Paramagnetic Research.* W.A. Benjamin, Advanced Book Program.

- 
- Pallister, J.W., 1971.** The tectonics of East Africa. *Tectonics of Africa*, U.N.E.S.C.O., Paris, **6**, 511-543.
- Park, R.G., 1997.** *Foundations of structural geology*, Third Edition, Graphman and Hall, London, 202pp.
- Passchier, T., 1996.** *Microtectonics*. Springer-Verlag, Berlin, Heidelberg, pp153-196.
- Pinna, P., 1995.** On the dual nature of the Mozambique Belt, Mozambique to Kenya. *Journal of African Earth Sciences*, **21**, 3, 477-480.
- Priem, H.N.A., Boelrijk, N.A.I.M., Hebeda, E.H., Verdurmen, E.A.Th., Verschure, R.H., Oen, I.S. and Westra, L., 1979.** Isotopic age determinations on granitic and gneissic rocks from the Ubendian-USangaran System in southern Tanzania. *Precambrian Research*, **9**, 227-239.
- Quennell, A.M., McKinlay, A.M. and Aitken, A.G., 1959.** Summary of the geology of Tanganyika, part I, Introduction and Stratigraphy. *Geological Survey of Tanganyika, Memoir*, **1**, 264pp.
- Ramberg, H., 1955.** Natural and experimental boudinage and pinch-and-swell structures. *Journal of Geology*, **63**, 512 – 526.
- Ramsay, A.C., 1866.** *The Geology of North Wales*. *Memoirs, Geological Survey of London.*, cvii, 1-22.
- Ramsay, J.G., 1967.** *Folding and Fracturing of Rocks*. McGraw-Hill Incorporated, New York. 568pp.
- Reinhardt, E.W., 1968.** Phase relations in cordierite-bearing gneisses from the Gananoque area. *Canadian Journal of Earth Science*, **5**, 455 – 482.
- Roedder, E., 1963.** Studies of fluid inclusions II: Freezing data and their interpretation. *Economic Geology*, **58**, 167 –211.
- Rosasco, G.J. and Roedder, E., 1979.** Application of a new Raman microprobe spectrometer to nondestructive analysis of sulfate and other ions in individual

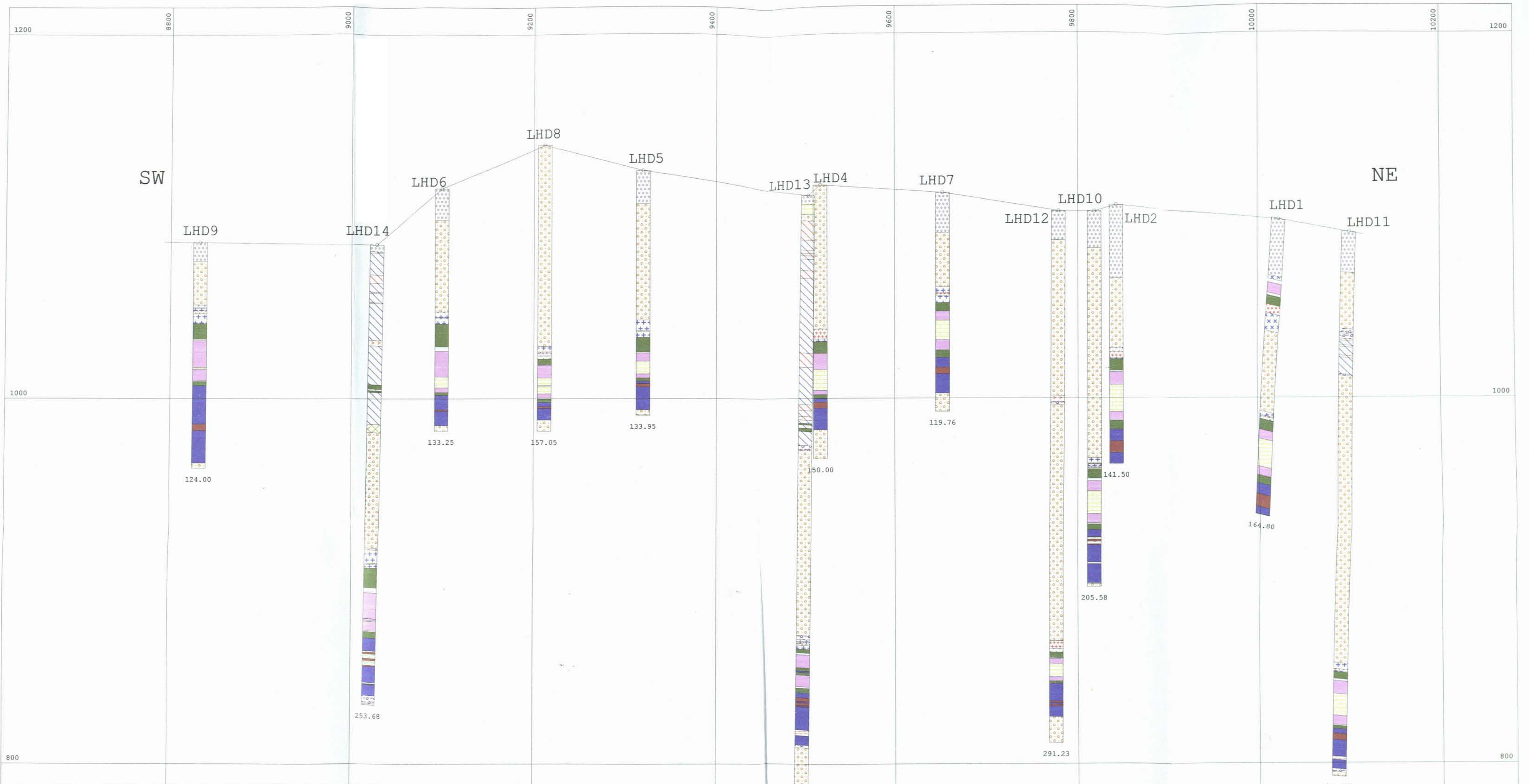
- phases in fluid inclusions in minerals. *Geochimica et Cosmochimica Acta*, **43**, 1907-1915.
- Rossman, G.R., 1974.** Optical spectroscopy of green vanadium apophyllite from Poona, India. *American Mineralogist*, **59**, 621-622.
- Rossman, G.R., 1988.** Optical Spectroscopy. In: *Spectroscopic methods in Mineralogy and Geology*, Editor: F.C. Hawthorne. Mineralogical Society of America, *Reviews in Mineralogy*, **18**, 207-253.
- Rutahindurwa, F.F., Kimogege, S.J. and Sebugwao, D.J., 1997.** The Merelani graphite and gemstone deposit from resource to production. Unpublished internal report for Graphtan Ltd., 19pp.
- Sanderson, D.J., 1974.** Patterns of boudinage and apparent stretching lineation development in folded rocks. *Journal of Geology*, **82**, 651-661.
- Saria, J.L., 1973.** The geology of the Merelani zoisite (tanzanite) bearing area. Unpubl. Rep. Geol. Surv. of Tanzania, Minerals Resource Division, Dodoma, Rep. No. JLS/7.
- Schijf, J., de Baar, H.J.W. and Millero, F.J., 1995.** Vertical distribution and speciation of dissolved rare earth elements in the anoxic brines of Bannock Basin, eastern Mediterranean Sea. *Geochimica et Cosmochimica Acta*, **59**, 3285-3299.
- Schmetzer, K., 1982.** Absorption spectroscopy and color of vanadium(3+)-bearing natural oxides and silicates – a contribution to the crystal chemistry of vanadium. *Neues Jahrbuch für Mineralogie Abhandlungen*, **144**, 73-106.
- Schmetzer, K., 1987.** Zur Deutung der Farbursache blauer Saphire - eine Diskussion. *Neues Jahrbuch für Mineralogie Mh*, **1987**:337-343.
- Schmetzer, K. and Berdesinski, W., 1978.** Das Absorptionsspektrum von Cr<sup>3+</sup> in Zoisit. *Neues Jahrbuch für Mineralogie Mh*, **1978**, 197-202.

- Schmetzer, K. and Bank, H., 1979.** East African tourmalines and their nomenclature. *Journal of Gemmology*, **16**, 5, 310-311.
- Schmetzer, K. and Ottemann, J., 1979.** Kristallchemie und farbe vanadium-haltiger granate. *Neues Jahrbuch für Mineralogie Abhandlungen*, **136**, 146-168.
- Schmetzer, K., Ottemann, J., Bank, H. and Krupp, H., 1979.** Transparent bluish-green kornerupine from East Africa (Kenya and Tanzania). *Gems and Gemology*, **16**, 118.
- Schreurs, J., 1985.** Prograde metamorphism of metapelites, garnet-biotite thermometry and prograde changes of biotite chemistry in high-grade rocks of West Uusimaa, southwest Finland. *Lithos*, **18**, 69-80.
- Shackleton, R.M. 1986.** Precambrian collision tectonics in Africa. In: *Collision tectonics*, Editors: M.R. Coward, A.C. Ries. Geological Society London, Special Publications, **19**, 324-349.
- Shackleton, R.M., 1993a.** Tectonics of the Mozambique Belt in East Africa, Magmatic processes and plate tectonics. In: *Magmatic Processes and Plate Tectonics*, Editors: H.M. Prichard, T.N.M. Alabaster, N.B.W. Harris and C.R. Neary. Geological Society of London Special Publication, **76**, 345-362.
- Shackleton, R.M., 1993b.** Tectonics of the lower crust: a view from the Usambara Mountains, NE Tanzania. *Journal of Structural Geology*, **5**, 663-671.
- Shackleton, R.M., 1996.** The final collision zone between East and West Gondwana: where is it? *Journal of African Earth Sciences*, **23**, 271-287.
- Spear, F.S., 1993.** *Metamorphic phase equilibria and pressure-temperature-time paths.* Mineralogical Society of America, Washington, DC, 799pp.
- Spear, F.S. and Parrish, R.R., 1996.** Petrology and cooling rates of the Valhalla Complex, British Columbia. *Canadian Journal of Petrology*, **37**, 733-765.
- Spear, F.S. and Peacock, S.M., 1989.** *Metamorphic pressure-temperature-time paths.* Short course in geology, **7**, 102.

- Stern, L.A., Chamberlain, C.P., Barnett, D.E. and Ferry, J.M., 1992.** Stable isotope evidence for regional-scale fluid migration in a Barrovian metamorphic terrain, Vermont, USA. *Contributions to Mineralogy and Petrology*, **112**, 475-489.
- Stern, R.J., 1994.** Arc assembly and continental collision in the Neoproterozoic East African Orogen: Implications for the assembly of Gondwanaland. *Annual Reviews in Earth and Planetary Science*, **22**, 319-351.
- Storre, B. and Nitsch, K.H., 1972.** Die Reaktion  $2 \text{Zoisit} + 1 \text{CO}_2 \rightleftharpoons 3 \text{Anorthit} + 1 \text{Calcit} + 1 \text{H}_2\text{O}$ . *Contributions to Mineralogy and Petrology*, **35**, 1-10.
- Stowell, H.H., Menard, T. and Ridgway, C.K., 1996.** Ca-metasomatism and chemical zonation of garnet in contact-metamorphic aureoles, Juneau gold belt, southeastern Alaska. *The Canadian Mineralogist*, **34**, 1195-1209.
- Strömgård, K.E., 1973.** Stress distribution during formation of boudinage and pressure shadows. *Tectonophysics*, **16**, 215-228.
- Tarney, J., 1977.** Petrology, mineralogy and geochemistry of Falkland Plateau basement rocks. Site 330, Deep Sea Drilling Project. In: London, Inst. Rep. Deep sea Drilling Project 36, Editor: P.F. Baker. 893-921.
- Taylor, S.R. and McLennan, S.M., 1985.** *The Continental Crust: Its composition and Evolution*. Oxford, Blackwell Scientific, 312 pp.
- Todd, C.S. and Evans, B.W., 1993.** Limited fluid-rock interactions at marble-gneiss contacts during Cretaceous granulite-facies metamorphism, Seward Peninsula, Alaska. *Contributions to Mineralogy and Petrology*, **114**, 1, 27-41.
- Tsang, T. and Ghose, S., 1971.** Electron paramagnetic resonance of  $\text{V}^{2+}$ ,  $\text{Mn}^{2+}$ ,  $\text{Fe}^{3+}$ , and optical spectra of  $\text{V}^{3+}$  in blue zoisite,  $\text{Ca}_2\text{Al}_3\text{Si}_3\text{O}_{12}(\text{OH})$ . *Journal of Chemical Physics*, **54**, 3, 856-862.
- Tuisku, P. and Muhongo, S., 1999.** P-T evolution of the Neoproterozoic granulites in eastern Tanzania and implications for the crustal evolution of the Mozambique

- Belt of eastern Africa. *Journal of African Earth Sciences*, Special Abstracts Issue GSA 11: Earth Resources for Africa, **28**, 82.
- Valley, J.W., 1986.** Stable Isotope Geochemistry of Metamorphic Rocks. In: *Stable Isotope in High Temperature Geological Processes*, Editors: J.W. Valley, J.R.
- Valley, J.W., Bohlen, S.R., Essene, E.J. and Lamb, W., 1990.** Metamorphism in the Adirondacks. II: The role of fluids. *Journal of Petrology*, **31**, 555-596.
- van den Kerkhof, A.M., 1987.** The fluid evolution of the Harmsarvet ore deposit, central Sweden. *Geologiska Föreningens i Stockholm Förhandlingar*, **109**, 1-12.
- van den Kerkhof, A.M., 1988.** The system CO<sub>2</sub>-CH<sub>4</sub>-N<sub>2</sub> in fluid inclusions: theoretical modelling and geological applications. Ph.D., Free University Amsterdam, 209 pp.
- Vidale, R., 1968.** Calc-silicate bands and metasomatism in a chemical gradient, Unpublished Ph.D., 79pp.
- Vidale, R., 1969.** Metasomatism in a chemical gradient and the formation of calc-silicate bands. *American Journal of Science*, **267**, 857-874.
- Vry J., Brown, P.E., Valley, J.W. and Morrison, J., 1988.** Constraints on granulite genesis from carbon isotope compositions of cordierite and graphite. *Nature*, **322**, 66-68.
- Walraven, F., Pape, J. and Borg, G., 1994.** Implications of Pb-isotopic composition at Geita gold deposit, Sukumaland Greenstone Belt, Tanzania. *Journal of African Earth Sciences*, **18**, 2, 111-121.
- Watson, E.B. and Brenan, J., 1987.** Fluids in the lithosphere. Experimentally determined wetting characteristics of CO<sub>2</sub> - H<sub>2</sub>O fluids and their implications for fluid transport, horst-rock physical characteristics, and fluid inclusion formation. *Earth and Planetary Science Letters*, **85**, 497-515.

- 
- Weaver, B.L., 1980.** Rare-earth element geochemistry of Madras granulites. *Contributions to Mineralogy and Petrology*, **71**, 271-279.
- Webster, R. and Anderson, B.W., 1983.** *Gems: Their Source, Descriptions and Identification*, Fourth Edition. Butterworths Heinemann, London. 1006pp.
- Wedepohl, K.H., Editor, 1974.** *Hand-book of geochemistry*. Vol II-23. Springer-Verlag, Berlin, Heidelberg, New York, pp23-A.
- Wegmann, C.E., 1932.** Note sur le boudinage. *Bulletin de la Societe Geologique Francaise*, 5 Ser. II, 477 – 489.
- Weiss, L.E., 1959.** Geometry of superposed folding. *Bulletin of the Geological Society of America*, **70**, 91-108.
- Wendt, I., Besang, C., Harre,W., Kreuzer, H., Lenz, H. and Muller, P., 1972.** Age determinations of granitic intrusions and metamorphic events in the early Precambrian of Tanzania. *Proceedings of the 24th International Geological Congress, Montreal*, **1**, 295 –314.
- White, E.W. and White, W.B., 1967.** Electron probe and optical study of kyanite. *Science*, **158**, 915.
- Whitney, D.L. and Dilek, Y., 1998.** Characterization and interpretation of P-T paths with multiple thermal peaks. In: *What Drives Metamorphism and Metamorphic Reactions?* Editors: P.J. Treloar and P. O'Brien. *Geological Society of London Special Publications*, **138**, 47-54.
- Wright, J.M., Schrader, H. and Holster, W.T., 1987.** Palaeoredox variations in ancient oceans recorded by rare earth elements in fossil apatite. *Geochimica et Cosmochimica Acta*, **51**, 631-644.
- Yardley, B.W.D., 1989.** *An introduction to Metamorphic Petrology*. Longman Earth Science Series, Pearson Education Ltd., 248pp.
- Zancellor, V., 2004.** *Tanzanite – The True Story*. *Naturalis Historia*. 115pp.



- LEGEND**
- Banded calc-silicate hornfels (BCF)
  - Biotite gneiss (BG)
  - C-zone
  - Calcrete
  - D-zone
  - Dolomitic marble (DM)
  - Graphite calc-silicate schist (GCS)
  - Garnet biotite sillimanite gneiss (GNG)
  - Main ore-zone (JWZ)
  - Kyanite graphite schist (KGS)
  - Kyanite gneiss (HW/FW)
  - Pegmatite
  - GCS/BCF transition zone
  - GNG/UK transition zone
  - GNG/DM transition zone
  - Upper Horizon Ore-zone (UH-Alt)
  - Upper Horizon Kyanite gneiss (UK)
  - Kyanite gneiss units 4 and 3
  - Kyanite gneiss units 6 and 5
  - Calc-silicate skarn boudin
  - FW-alt

HOLE	EAST	NORTH	ELEVATION	EOH	AZIMUTH	DIP
LHD1	281225.58	9607147	1028.74	164.8	136	-80
LHD2	281136.91	9606967.9	1105.48	141.5	0	-90
LHD4	280876.91	9606647.8	1047.12	150	0	-90
LHD5	280701.15	9606451.4	1124.8	133.95	0	-90
LHD6	280408.61	9606235.4	1046.04	133.25	0	-90
LHD7	281030.38	9606779.8	1112.46	119.76	0	-90
LHD8	280550.88	9606345.2	1139.13	157.05	0	-90
LHD9	280089.39	9605977.3	1016.23	124	0	-90
LHD10	281040.52	9606951.6	1035.44	205.58	0	-90
LHD11	281147.35	9607224	1024.98	304.68	103.8	-78
LHD12	280878.4	9606919.8	1033.79	291.23	104.9	-87.3
LHD13	280502.64	9606641.1	1044	394.68	106	-84.1
LHD14	280010.5	9606175.9	1006.11	253.68	105.6	-84.1

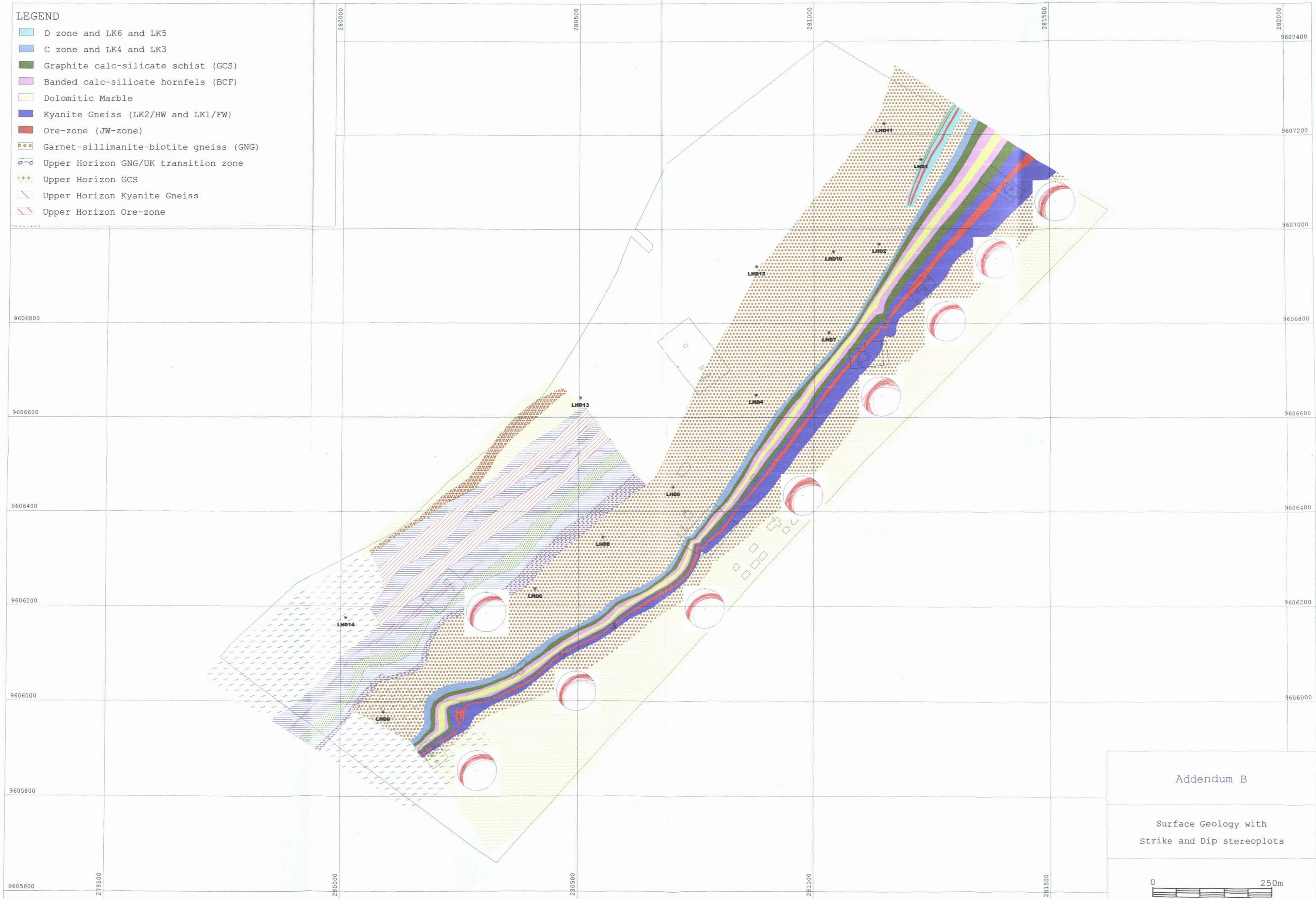
Addendum A

NE-SW Section of the  
drill holes, showing  
the drill logs and  
technical specifications



**LEGEND**

- D zone and LK6 and LK5
- C zone and LK4 and LK3
- Graphite calc-silicate schist (GCS)
- Banded calc-silicate hornfels (BCF)
- Dolomitic Marble
- Kyanite Gneiss (LK2/HW and LK1/FW)
- Ore-zone (JW-zone)
- Garnet-sillimanite-biotite gneiss (GNG)
- Upper Horizon GNG/UK transition zone
- Upper Horizon GCS
- Upper Horizon Kyanite Gneiss
- Upper Horizon Ore-zone



Addendum B

Surface Geology with  
Strike and Dip stereoplots

0 
0
250m



280200

280220

280240

280260

280300

N

### Addendum C: Bravo trench of F3 fold outcrop

#### LEGEND

-  Dolomitic marble (DM)
-  Banded calc-silicate hornfels (BCF)
-  Graphite calc-silicate schist (GCS)
-  Kyanite graphite gneiss (HW)
-  Ore-zone (JW-zone)
-  Calc-silicate boudin
-  Kyanite Graphite Gneiss (FW)
-  Pegmatite
-  Garnet sillimanite biotite gneiss

9606040

9606020

9606000

9605980

No.	Strata	Qup
1	135	14
2	136	15
3	137	16
4	138	17
5	139	18
6	140	19
7	141	20
8	142	21
9	143	22
10	144	23
11	145	24
12	146	25
13	147	26
14	148	27





## Addendum D

Table 1.	Microprobe analyses of garnet from the GNG
Table 2.	Microprobe analyses of biotite from the GNG
Table 3.	Microprobe analyses of plagioclase from the GNG
Table 4.	Microprobe analyses of K-feldspar from the GNG
Table 5.	Microprobe analyses of scapolite from the BCF
Table 6.	Microprobe analyses of feldspar from the BCF
Table 7.	Microprobe analyses of pyroxene from the BCF
Table 8.	Microprobe analyses of biotite from the BCF
Table 9.	Microprobe analyses of garnet from the GCS
Table 10.	Microprobe analyses of pyroxene from the GCS
Table 11.	Microprobe analyses of plagioclase from the GCS
Table 12.	Microprobe analyses of titanite from the GCS
Table 13.	Microprobe analyses of plagioclase from the kyanite-graphite gneiss
Table 14.	Microprobe analyses of mica from the kyanite-graphite gneiss
Table 15.	Microprobe analyses of plagioclase from the JW-zone
Table 16.	Microprobe analyses of biotite from the JW-zone
Table 17.	Microprobe analyses of titanite from the JW-zone
Table 18.	Microprobe analyses of pyroxene from the pyroxene relicts
Table 19.	Microprobe analyses of garnet from boudins
Table 20.	Microprobe analyses of zoisite from boudins
Table 21.	Microprobe analyses of plagioclase from the pyroxene relicts
Table 22.	Microprobe analyses of tsavorite not associated with tanzanite
Table 23.	Microprobe analyses of tsavorite associated with tanzanite

Table 1. Garnet analyses from the GNG.

Sample	SiO <sub>2</sub>	TiO <sub>2</sub>	Al <sub>2</sub> O <sub>3</sub>	Cr <sub>2</sub> O <sub>3</sub>	FeO	MnO	MgO	CaO	Na <sub>2</sub> O	Total	FeO <sub>calc</sub>	Fe <sub>2</sub> O <sub>3calc</sub>	Total <sub>calc</sub>	TSi	TAI	Sum_T
083:Z-1	38.03	0.00	21.70	0.00	32.01	0.23	6.23	1.60	0.00	99.80	32.08	1.88	101.74	2.99	0.01	3.00
083:Z-2	38.03	0.05	21.45	0.01	30.95	0.22	7.16	1.54	0.00	99.41	30.91	1.81	101.17	2.99	0.01	3.00
083:Z-4	37.96	0.05	21.54	0.01	30.88	0.21	7.64	1.56	0.00	99.84	30.82	1.80	101.59	2.97	0.03	3.00
083:Z-5	37.91	0.03	21.50	0.02	30.80	0.23	7.73	1.49	0.00	99.70	30.78	1.80	101.49	2.96	0.04	3.00
083:Z-7	37.75	0.03	21.37	0.02	30.32	0.23	7.62	1.57	0.00	98.90	30.25	1.77	100.60	2.98	0.02	3.00
083:Z-8	37.79	0.00	21.46	0.00	30.30	0.23	7.77	1.53	0.00	99.08	30.27	1.77	100.82	2.97	0.03	3.00
083:Z-12	38.50	0.01	21.95	0.01	30.03	0.20	7.83	1.68	0.00	100.20	30.02	1.76	101.95	2.99	0.01	3.00
083:Z-13	38.38	0.02	22.08	0.00	29.57	0.25	8.05	1.69	0.00	100.04	29.57	1.73	101.77	2.98	0.02	3.00
083:Z-14	38.25	0.04	22.28	0.00	29.84	0.18	7.97	1.77	0.00	100.33	29.86	1.75	102.10	2.96	0.04	3.00
083:Z-15	38.48	0.04	22.06	0.02	30.23	0.24	7.73	1.79	0.00	100.57	30.28	1.77	102.39	2.98	0.03	3.00
083:Z-16	38.32	0.00	21.85	0.01	29.81	0.20	8.03	1.81	0.00	100.03	29.86	1.75	101.82	2.97	0.03	3.00
083:Z-17	38.24	0.00	21.95	0.00	29.69	0.22	8.08	1.90	0.00	100.07	29.70	1.74	101.82	2.96	0.04	3.00
083:Z-18	38.09	0.01	21.63	0.01	29.67	0.20	8.04	1.84	0.00	99.50	29.68	1.74	101.24	2.97	0.03	3.00
083:Z-21	37.85	0.01	21.58	0.00	29.15	0.19	8.07	1.82	0.00	98.68	29.24	1.71	100.48	2.97	0.03	3.00
083:Z-22	38.15	0.00	21.42	0.03	29.40	0.21	8.07	1.95	0.00	99.24	29.39	1.72	100.95	2.98	0.02	3.00
083:Z-23	38.45	0.00	21.79	0.02	29.27	0.20	8.05	1.97	0.00	99.76	29.28	1.71	101.48	2.99	0.01	3.00
083:Z-24	38.30	0.03	21.76	0.03	29.37	0.24	8.01	2.01	0.00	99.75	29.37	1.72	101.46	2.98	0.02	3.00
083:Z-25	38.32	0.03	21.64	0.01	29.61	0.17	8.06	1.95	0.00	99.78	29.60	1.73	101.50	2.98	0.02	3.00
083:Z-26	37.95	0.00	21.72	0.02	29.47	0.21	8.07	2.01	0.00	99.45	29.47	1.72	101.18	2.96	0.04	3.00
083:Z-27	38.42	0.03	21.62	0.03	29.51	0.24	8.13	1.98	0.00	99.96	29.51	1.73	101.69	2.98	0.02	3.00
083:Z-28	38.16	0.00	21.78	0.03	29.56	0.20	8.05	1.98	0.00	99.75	29.56	1.73	101.48	2.97	0.03	3.00
083:Z-29	38.21	0.01	21.45	0.03	29.73	0.27	8.04	1.92	0.00	99.66	29.72	1.74	101.39	2.98	0.02	3.00
083:Z-30	38.12	0.02	21.56	0.00	29.43	0.24	8.00	1.91	0.00	99.27	29.52	1.73	101.08	2.98	0.02	3.00
083:Z-31	38.22	0.03	21.84	0.00	29.65	0.19	8.01	1.88	0.00	99.82	29.64	1.73	101.54	2.97	0.03	3.00
083:Z-33	38.14	0.00	21.48	0.00	29.31	0.24	7.85	1.77	0.00	98.79	29.32	1.71	100.52	3.00	0.00	3.00
083:Z-34	37.99	0.03	21.57	0.00	29.48	0.25	7.86	1.81	0.00	99.00	29.47	1.72	100.72	2.98	0.02	3.00
083:Z-35	38.07	0.00	21.44	0.02	29.73	0.19	7.96	1.74	0.00	99.16	29.72	1.74	100.88	2.98	0.02	3.00
083:Z-36	38.02	0.00	21.24	0.00	29.66	0.17	7.81	1.71	0.00	98.61	29.66	1.73	100.35	3.00	0.00	3.00
083:Z-38	38.23	0.02	21.69	0.00	29.97	0.18	7.83	1.61	0.00	99.55	29.97	1.75	101.30	2.99	0.01	3.00
083:Z-39	38.32	0.01	21.59	0.00	29.76	0.22	7.79	1.61	0.00	99.29	29.77	1.74	101.04	3.00	0.00	3.00
083:Z-41	37.92	0.02	21.33	0.01	29.64	0.20	7.85	1.57	0.00	98.53	29.67	1.74	100.30	2.99	0.01	3.00
083:Z-43	38.39	0.04	21.38	0.01	29.70	0.14	7.80	1.50	0.00	98.96	29.69	1.74	100.69	3.02	0.00	3.02
083:Z-44	37.96	0.00	21.43	0.01	29.70	0.17	7.71	1.59	0.00	98.56	29.70	1.74	100.30	3.00	0.01	3.00
083:Z-47	37.98	0.01	21.19	0.00	30.18	0.24	7.49	1.62	0.00	98.71	30.15	1.76	100.45	3.00	0.00	3.00
083:Z-48	38.04	0.03	21.23	0.00	30.45	0.23	7.43	1.57	0.00	98.97	30.43	1.78	100.73	3.00	0.00	3.00
083:Z-50	38.17	0.00	21.65	0.03	30.98	0.20	7.20	1.51	0.00	99.73	30.97	1.81	101.53	2.99	0.01	3.00
083:Z-51	37.99	0.01	21.79	0.02	31.33	0.18	7.12	1.53	0.00	99.96	31.31	1.83	101.77	2.97	0.03	3.00
083:Z-52	37.98	0.02	21.55	0.03	30.15	0.24	7.34	1.60	0.00	98.90	30.21	1.77	100.73	2.99	0.01	3.00
083:Z-53	38.00	0.02	21.66	0.01	30.47	0.26	7.54	1.50	0.00	99.48	30.46	1.78	101.24	2.98	0.02	3.00
083:Z-54	38.35	0.00	21.65	0.00	29.93	0.19	7.59	1.57	0.00	99.28	29.96	1.75	101.05	3.01	0.00	3.01
083:Z-55	38.50	0.00	21.96	0.00	29.95	0.21	7.97	1.65	0.00	100.24	29.95	1.75	101.99	2.98	0.02	3.00
083:Z-56	38.25	0.03	21.76	0.00	29.71	0.23	7.95	1.63	0.00	99.56	29.72	1.74	101.31	2.98	0.02	3.00
083:Z-57	38.11	0.02	21.60	0.00	29.23	0.21	7.94	1.79	0.00	98.90	29.25	1.71	100.63	2.99	0.01	3.00
083:Z-58	38.36	0.00	21.84	0.00	29.65	0.22	7.89	1.81	0.00	99.78	29.63	1.73	101.49	2.99	0.01	3.00
083:Z-59	38.61	0.00	21.83	0.03	29.57	0.25	7.89	1.87	0.00	100.03	29.57	1.73	101.76	3.00	0.00	3.00
083:Z-60	38.30	0.00	21.69	0.01	29.25	0.13	8.10	1.82	0.00	99.29	29.26	1.71	101.02	2.99	0.01	3.00
083:Z-61	38.08	0.02	21.91	0.02	29.19	0.14	8.01	1.83	0.00	99.22	29.20	1.71	100.92	2.98	0.02	3.00
083:Z-62	38.58	0.00	21.83	0.00	29.74	0.24	8.07	1.93	0.00	100.39	29.71	1.74	102.10	2.98	0.02	3.00
083:Z-63	38.33	0.01	21.86	0.03	29.35	0.19	7.98	2.03	0.00	99.78	29.37	1.72	101.51	2.98	0.02	3.00
083:Z-64	37.83	0.00	22.13	0.01	29.02	0.17	7.94	2.09	0.00	99.19	29.04	1.70	100.90	2.96	0.04	3.00
083:Z-65	38.39	0.00	21.59	0.02	28.92	0.16	7.95	2.16	0.00	99.19	28.92	1.69	100.89	3.00	0.00	3.00

Table 1. Continue 1.

Sample	SiO <sub>2</sub>	TiO <sub>2</sub>	Al <sub>2</sub> O <sub>3</sub>	Cr <sub>2</sub> O <sub>3</sub>	FeO	MnO	MgO	CaO	Na <sub>2</sub> O	Total	FeO <sub>calc</sub>	Fe <sub>2</sub> O <sub>3calc</sub>	Total <sub>calc</sub>	TSi	TAI	Sum_T
083:Z-66	38.51	0.00	21.96	0.03	29.34	0.25	7.97	2.28	0.00	100.34	29.32	1.72	102.03	2.98	0.02	3.00
083:Z-67	38.27	0.03	21.71	0.01	29.59	0.26	8.03	2.24	0.00	100.14	29.57	1.73	101.86	2.97	0.03	3.00
083:Z-68	39.18	0.01	22.33	0.01	29.04	0.15	7.67	2.22	0.00	100.61	29.06	1.70	102.34	3.02	0.00	3.02
083:Z-70	38.59	0.00	21.88	0.01	29.02	0.23	7.92	2.20	0.00	99.86	29.08	1.70	101.62	3.00	0.00	3.00
083:Z-72	38.07	0.00	21.60	0.00	29.26	0.20	7.87	2.26	0.00	99.26	29.25	1.71	100.96	2.98	0.02	3.00
083:Z-73	38.11	0.00	21.43	0.00	28.87	0.22	7.78	2.25	0.00	98.66	28.89	1.69	100.36	3.00	0.00	3.00
083:Z-74	38.50	0.01	21.56	0.03	29.32	0.15	7.91	2.07	0.00	99.55	29.30	1.71	101.24	3.00	0.00	3.00
083:Z-75	38.31	0.00	21.48	0.02	29.82	0.21	7.93	2.00	0.00	99.76	29.79	1.74	101.48	2.99	0.02	3.00
083:Z-78	38.04	0.02	21.50	0.00	29.67	0.21	7.78	1.73	0.00	98.94	29.67	1.74	100.68	2.99	0.01	3.00
083:Z-79	38.10	0.00	21.39	0.00	29.65	0.22	7.87	1.70	0.00	98.93	29.65	1.73	100.66	2.99	0.01	3.00
083:Z-80	37.73	0.01	21.28	0.03	30.00	0.20	7.75	1.64	0.00	98.64	30.01	1.76	100.41	2.98	0.02	3.00
083:Z-82	37.56	0.02	21.56	0.02	30.22	0.24	7.70	1.53	0.00	98.85	30.23	1.77	100.62	2.96	0.04	3.00
083:Z-83	37.93	0.03	21.58	0.02	30.40	0.23	7.23	1.61	0.00	99.03	30.40	1.78	100.80	2.99	0.01	3.00
083:Z-84	37.53	0.00	21.48	0.00	31.46	0.24	7.07	1.53	0.00	99.33	31.41	1.84	101.11	2.96	0.04	3.00
083:Z-86	38.07	0.04	22.03	0.03	31.18	0.20	7.48	1.60	0.00	100.63	31.19	1.82	102.46	2.95	0.05	3.00
083:Z-87	38.12	0.00	22.02	0.04	30.64	0.16	7.68	1.79	0.00	100.46	30.67	1.79	102.28	2.95	0.05	3.00
083:Z-88	37.92	0.02	21.93	0.04	30.13	0.22	7.50	1.87	0.00	99.62	30.16	1.76	101.41	2.96	0.04	3.00
083:Z-90	38.50	0.01	21.76	0.00	29.22	0.24	7.83	2.08	0.00	99.64	29.28	1.71	101.42	3.00	0.00	3.00
083:Z-91	38.50	0.00	21.74	0.05	29.91	0.20	7.97	2.20	0.00	100.57	29.88	1.75	102.29	2.98	0.03	3.00
083:Z-92	38.41	0.01	22.07	0.01	29.77	0.17	8.02	2.44	0.00	100.90	29.77	1.74	102.65	2.95	0.05	3.00
083:Z-93	38.62	0.01	21.70	0.00	29.19	0.18	7.83	2.44	0.00	99.97	29.22	1.71	101.71	3.00	0.00	3.00
083:Z-94	38.68	0.05	21.81	0.00	29.25	0.20	7.91	2.51	0.00	100.40	29.25	1.71	102.11	2.99	0.01	3.00
083:Z-95	38.62	0.00	21.68	0.02	29.35	0.18	8.01	2.53	0.00	100.38	29.34	1.72	102.09	2.99	0.02	3.00
083:Z-96	38.67	0.01	21.72	0.04	29.08	0.26	7.38	2.51	0.00	99.66	29.09	1.70	101.37	3.02	0.00	3.02
083:Z-97	38.36	0.01	21.45	0.01	29.04	0.17	7.92	2.27	0.00	99.23	29.04	1.70	100.93	3.00	0.00	3.00
083:Z-99	38.50	0.00	21.62	0.03	29.38	0.16	7.89	2.04	0.00	99.62	29.37	1.72	101.32	3.00	0.00	3.00
083:Z-100	38.60	0.05	21.82	0.03	29.76	0.17	8.05	1.99	0.00	100.47	29.88	1.75	102.33	2.98	0.02	3.00
083:Z-101	38.26	0.00	21.66	0.04	29.50	0.17	7.98	1.94	0.00	99.55	29.52	1.73	101.30	2.98	0.02	3.00
083:Z-102	38.27	0.03	21.85	0.00	29.37	0.17	7.94	1.85	0.00	99.49	29.38	1.72	101.21	2.99	0.02	3.00
083:Z-103	38.45	0.05	21.64	0.03	29.67	0.21	7.91	1.79	0.00	99.75	29.66	1.73	101.47	3.00	0.00	3.00
083:Z-104	38.28	0.00	21.66	0.02	29.29	0.19	7.83	1.75	0.00	99.03	29.31	1.71	100.76	3.00	0.00	3.00
083:Z-105	38.31	0.04	21.77	0.03	29.98	0.21	7.79	1.66	0.00	99.80	29.94	1.75	101.52	2.99	0.01	3.00
083:Z-106	38.38	0.01	21.70	0.00	30.01	0.20	7.82	1.64	0.00	99.76	30.00	1.75	101.51	2.99	0.01	3.00
083:Z-107	38.53	0.02	21.71	0.03	29.80	0.21	7.65	1.55	0.00	99.51	29.81	1.74	101.26	3.01	0.00	3.01
083:Z-108	38.41	0.02	21.46	0.02	30.18	0.13	7.59	1.51	0.00	99.33	30.16	1.76	101.07	3.01	0.00	3.01
083:Z-109	38.14	0.02	21.65	0.04	30.47	0.21	7.56	1.40	0.00	99.49	30.45	1.78	101.26	2.99	0.01	3.00
083:Z-110	37.44	0.02	21.78	0.00	30.44	0.21	7.27	1.48	0.00	98.65	30.44	1.78	100.43	2.96	0.04	3.00
083:Z-112	38.20	0.00	21.79	0.00	31.99	0.21	6.69	1.54	0.00	100.42	30.49	1.78	100.69	3.02	0.00	3.02
083:Z-113	38.54	0.01	21.91	0.00	30.91	0.28	7.15	1.51	0.00	100.32	30.89	1.81	102.10	3.00	0.00	3.00
083:Z-114	38.63	0.02	21.73	0.02	30.88	0.27	7.42	1.56	0.00	100.53	30.88	1.81	102.34	3.00	0.00	3.00
083:Z-115	38.33	0.02	21.83	0.00	31.11	0.16	7.42	1.53	0.00	100.40	31.10	1.82	102.21	2.98	0.02	3.00
083:Z-116	38.38	0.00	21.93	0.01	30.41	0.21	7.55	1.44	0.00	99.93	30.45	1.78	101.74	2.99	0.01	3.00
083:Z-117	38.39	0.03	21.97	0.02	30.63	0.18	7.74	1.56	0.00	100.51	30.62	1.79	102.29	2.97	0.03	3.00
083:Z-118	38.37	0.02	21.88	0.01	29.79	0.21	7.93	1.66	0.00	99.87	29.84	1.75	101.65	2.98	0.02	3.00
083:Z-120	38.80	0.00	22.22	0.00	29.72	0.14	7.93	1.69	0.00	100.51	29.74	1.74	102.27	3.00	0.00	3.00
083:Z-122	38.58	0.00	22.01	0.02	29.42	0.17	7.91	1.74	0.00	99.85	29.44	1.72	101.59	3.00	0.00	3.00
083:Z-123	38.77	0.03	22.10	0.04	29.19	0.17	7.64	1.82	0.00	99.75	29.20	1.71	101.47	3.02	0.00	3.02
083:Z-125	38.05	0.00	21.76	0.03	29.06	0.23	8.21	1.90	0.00	99.24	29.04	1.70	100.92	2.97	0.03	3.00
083:Z-126	38.38	0.01	21.65	0.01	29.29	0.19	7.90	1.86	0.00	99.29	29.27	1.71	100.99	3.00	0.00	3.00
083:Z-127	38.82	0.01	22.16	0.01	29.43	0.23	7.81	1.88	0.00	100.35	29.42	1.72	102.06	3.00	0.00	3.00
083:Z-128	38.76	0.00	22.01	0.00	29.10	0.20	7.98	1.91	0.00	99.97	29.12	1.70	101.69	3.01	0.00	3.01

Table 1. Continue 2.

Sample	SiO <sub>2</sub>	TiO <sub>2</sub>	Al <sub>2</sub> O <sub>3</sub>	Cr <sub>2</sub> O <sub>3</sub>	FeO	MnO	MgO	CaO	Na <sub>2</sub> O	Total	FeO <sub>calc</sub>	Fe <sub>2</sub> O <sub>3calc</sub>	Total <sub>calc</sub>	TSi	TAl	Sum_T
083:Z-129	38.68	0.04	22.10	0.02	29.59	0.23	7.94	1.87	0.00	100.46	29.57	1.73	102.17	2.99	0.01	3.00
083:Z-130	38.36	0.00	21.97	0.00	29.16	0.19	7.91	1.79	0.00	99.37	29.18	1.71	101.09	2.99	0.01	3.00
083:Z-131	38.67	0.01	22.17	0.00	29.78	0.23	7.84	1.79	0.00	100.49	29.75	1.74	102.20	2.99	0.01	3.00
083:Z-132	38.74	0.01	21.97	0.02	29.78	0.21	7.58	1.66	0.00	99.97	29.78	1.74	101.71	3.02	0.00	3.02
083:Z-133	38.80	0.02	22.09	0.00	30.27	0.22	7.39	1.53	0.00	100.33	30.24	1.77	102.07	3.01	0.00	3.01
083:Z-134	38.84	0.04	22.10	0.01	30.18	0.21	7.26	1.50	0.00	100.13	30.18	1.77	101.90	3.02	0.00	3.02
083:Z-135	38.64	0.00	21.97	0.01	31.32	0.24	7.01	1.54	0.00	100.72	31.26	1.83	102.49	3.00	0.00	3.00
083:Z-136	38.31	0.03	22.24	0.01	30.65	0.22	7.48	1.55	0.00	100.50	30.68	1.79	102.32	2.97	0.03	3.00
083:Z-137	38.53	0.02	22.20	0.02	30.28	0.17	7.35	1.56	0.00	100.13	30.30	1.77	101.92	3.00	0.00	3.00
083:Z-138	38.45	0.00	22.24	0.00	30.20	0.27	7.51	1.51	0.00	100.18	30.21	1.77	101.95	2.99	0.01	3.00
083:Z-140	38.39	0.02	22.46	0.01	30.18	0.23	7.55	1.53	0.00	100.36	30.16	1.76	102.11	2.98	0.02	3.00
083:Z-141	38.12	0.00	21.94	0.00	30.94	0.18	7.06	1.49	0.00	99.73	30.90	1.81	101.50	2.99	0.01	3.00
083:Z-142	38.24	0.00	22.28	0.02	31.25	0.19	7.03	1.51	0.00	100.52	31.23	1.83	102.33	2.97	0.03	3.00
083:Z-143	38.35	0.02	22.26	0.02	31.14	0.22	6.92	1.43	0.00	100.36	31.14	1.82	102.19	2.99	0.01	3.00
083:Z-144	38.49	0.00	21.96	0.02	30.75	0.19	7.12	1.38	0.00	99.92	30.77	1.80	101.73	3.01	0.00	3.01
083:Z-145	37.59	0.05	21.73	0.00	30.29	0.29	7.18	1.36	0.00	98.50	30.32	1.77	100.29	2.98	0.02	3.00
083:Z-146	38.68	0.01	22.30	0.01	30.76	0.22	7.20	1.31	0.00	100.50	30.74	1.80	102.27	3.01	0.00	3.01
083:Z-147	38.23	0.01	21.90	0.01	31.85	0.17	6.26	1.34	0.00	99.77	31.80	1.86	101.57	3.01	0.00	3.01
083:Z-148	38.39	0.00	21.56	0.00	31.43	0.20	6.67	1.36	0.00	99.62	31.45	1.84	101.47	3.02	0.00	3.02
083:Z-149	38.56	0.04	21.77	0.00	31.17	0.25	6.56	1.30	0.00	99.64	31.18	1.82	101.47	3.03	0.00	3.03
083:Z-150	37.99	0.04	21.70	0.00	31.31	0.25	6.48	1.35	0.00	99.12	31.26	1.83	100.90	3.01	0.00	3.01
083:Z-151	38.25	0.00	21.58	0.02	31.70	0.31	6.25	1.34	0.00	99.44	31.68	1.85	101.27	3.02	0.00	3.02
083:Z-153	38.02	0.01	21.95	0.00	31.43	0.22	7.07	1.43	0.00	100.12	31.43	1.84	101.97	2.97	0.03	3.00
083:Z-154	37.86	0.03	21.78	0.00	31.45	0.23	6.97	1.45	0.00	99.77	31.45	1.84	101.61	2.97	0.03	3.00
083:Z-156	37.56	0.06	21.42	0.00	34.48	0.27	5.01	1.40	0.00	100.20	34.32	2.01	102.05	2.98	0.02	3.00
083:Z-157	37.94	0.00	21.63	0.00	31.83	0.28	6.46	1.34	0.00	99.49	31.96	1.87	101.48	2.99	0.01	3.00
083:Z-158	37.16	0.04	21.46	0.02	31.47	0.25	6.90	1.42	0.00	98.73	31.49	1.84	100.59	2.95	0.05	3.00
083:Z-159	37.29	0.00	21.77	0.00	30.73	0.30	7.17	1.46	0.00	98.73	30.77	1.80	100.57	2.95	0.05	3.00
082:G1-4	37.86	0.01	21.36	0.04	30.69	0.44	7.22	1.85	0.01	99.47	30.67	1.79	101.20	2.97	0.03	3.00
082:G1-6	38.14	0.00	21.24	0.04	32.54	0.46	6.32	1.59	0.00	100.33	32.44	1.90	102.13	3.00	0.00	3.00
082:G2-1	37.83	0.00	22.19	0.03	29.59	0.31	7.81	2.23	0.02	100.01	29.73	1.74	101.90	2.93	0.07	3.00
082:G2-2	38.73	0.00	20.80	0.00	29.65	0.33	7.50	2.26	0.01	99.27	29.65	1.73	101.00	3.04	0.00	3.04
082:G2-3	38.43	0.01	20.95	0.03	29.31	0.37	7.36	2.33	0.04	98.84	29.33	1.72	100.57	3.03	0.00	3.03
082:G2-4	38.17	0.02	21.87	0.00	29.44	0.38	7.40	2.31	0.03	99.63	29.43	1.72	101.34	2.98	0.02	3.00
082:G2-8	38.05	0.03	20.69	0.01	33.56	0.43	5.42	1.77	0.01	99.96	33.35	1.95	101.70	3.02	0.00	3.02
108:g1-i	37.80	0.02	22.32	0.04	29.53	0.34	8.22	1.35	0.00	99.64	28.06	1.64	99.80	2.98	0.02	3.00
108:g1-i2	37.37	0.01	22.77	0.03	29.39	0.40	8.06	1.42	0.02	99.47	29.32	1.72	101.12	2.91	0.09	3.00
108:g1-r2	38.40	0.02	22.36	0.02	30.61	0.36	7.70	1.42	0.00	100.90	30.56	1.79	102.64	2.96	0.04	3.00
108:g1m	37.53	0.01	22.47	0.02	29.08	0.30	8.33	1.40	0.00	99.13	29.16	1.71	100.91	2.93	0.07	3.00
108:g1m1	38.28	0.01	22.82	0.01	29.52	0.33	8.55	1.44	0.01	100.97	29.50	1.73	102.68	2.93	0.07	3.00
108:g2-r1	37.76	0.00	22.31	0.04	31.85	0.33	7.07	1.40	0.00	100.75	31.80	1.86	102.56	2.93	0.07	3.00
Minimum	37.16	0.00	20.69	0.00	28.87	0.13	5.01	1.30	0.00	98.50	28.06	1.64	99.80	2.91	0.00	3.00
Maximum	39.18	0.06	22.82	0.05	34.48	0.46	8.55	2.53	0.04	100.97	34.32	2.01	102.68	3.04	0.09	3.04
Mean	38.24	0.01	21.77	0.01	30.10	0.23	7.60	1.75	0.00	99.70	30.07	1.76	101.44	2.99	0.02	3.00
St dev	0.34	0.01	0.33	0.01	0.92	0.06	0.54	0.29	0.00	0.60	0.91	0.05	0.62	0.02	0.02	0.01

Table 1. Continue 3.

Sample	Al VI	Ti	Cr	Sum_A	Fe <sup>2+</sup>	Mg	Mn	Ca	Na	Sum_B	Alm	Gross	Pyrope	Spess	Uvaro	X <sub>Ca</sub>	X <sub>Fe</sub>	X <sub>Mg</sub>
083:Z-1	2.01	0.00	0.00	2.01	2.11	0.73	0.02	0.14	0.00	2.99	70.55	4.50	24.45	0.51	0.00	0.05	0.71	0.24
083:Z-2	1.98	0.00	0.00	1.98	2.03	0.84	0.02	0.13	0.00	3.02	67.36	4.29	27.84	0.50	0.02	0.04	0.67	0.28
083:Z-4	1.95	0.00	0.00	1.95	2.01	0.89	0.01	0.13	0.00	3.05	66.07	4.24	29.20	0.45	0.03	0.04	0.66	0.29
083:Z-5	1.94	0.00	0.00	1.95	2.01	0.90	0.02	0.13	0.00	3.05	65.90	4.04	29.51	0.51	0.05	0.04	0.66	0.30
083:Z-7	1.96	0.00	0.00	1.96	1.99	0.90	0.02	0.13	0.00	3.04	65.67	4.30	29.47	0.50	0.06	0.04	0.66	0.30
083:Z-8	1.96	0.00	0.00	1.96	1.99	0.91	0.02	0.13	0.00	3.04	65.36	4.24	29.89	0.51	0.00	0.04	0.65	0.30
083:Z-12	1.99	0.00	0.00	1.99	1.95	0.91	0.01	0.14	0.00	3.01	64.79	4.61	30.13	0.44	0.02	0.05	0.65	0.30
083:Z-13	1.99	0.00	0.00	1.99	1.92	0.93	0.02	0.14	0.00	3.01	63.81	4.68	30.96	0.54	0.00	0.05	0.64	0.31
083:Z-14	1.99	0.00	0.00	1.99	1.93	0.92	0.01	0.15	0.00	3.01	64.20	4.86	30.54	0.39	0.01	0.05	0.64	0.31
083:Z-15	1.98	0.00	0.00	1.99	1.96	0.89	0.02	0.15	0.00	3.01	64.99	4.88	29.56	0.52	0.05	0.05	0.65	0.30
083:Z-16	1.97	0.00	0.00	1.97	1.94	0.93	0.01	0.15	0.00	3.03	63.95	4.93	30.65	0.44	0.04	0.05	0.64	0.31
083:Z-17	1.97	0.00	0.00	1.97	1.93	0.93	0.01	0.16	0.00	3.03	63.52	5.20	30.80	0.47	0.00	0.05	0.64	0.31
083:Z-18	1.96	0.00	0.00	1.96	1.94	0.94	0.01	0.15	0.00	3.04	63.72	5.01	30.78	0.45	0.04	0.05	0.64	0.31
083:Z-21	1.97	0.00	0.00	1.97	1.92	0.95	0.01	0.15	0.00	3.03	63.35	5.05	31.18	0.42	0.00	0.05	0.63	0.31
083:Z-22	1.96	0.00	0.00	1.96	1.92	0.94	0.01	0.16	0.00	3.04	63.22	5.26	30.95	0.46	0.10	0.05	0.63	0.31
083:Z-23	1.98	0.00	0.00	1.99	1.90	0.93	0.01	0.16	0.00	3.01	63.15	5.37	30.97	0.45	0.07	0.05	0.63	0.31
083:Z-24	1.97	0.00	0.00	1.98	1.91	0.93	0.02	0.17	0.00	3.02	63.20	5.43	30.75	0.52	0.10	0.06	0.63	0.31
083:Z-25	1.96	0.00	0.00	1.97	1.93	0.94	0.01	0.16	0.00	3.03	63.47	5.32	30.81	0.37	0.03	0.05	0.64	0.31
083:Z-26	1.96	0.00	0.00	1.96	1.92	0.94	0.01	0.17	0.00	3.04	63.19	5.45	30.84	0.45	0.06	0.06	0.63	0.31
083:Z-27	1.96	0.00	0.00	1.96	1.92	0.94	0.02	0.17	0.00	3.04	63.06	5.34	30.99	0.52	0.09	0.05	0.63	0.31
083:Z-28	1.96	0.00	0.00	1.97	1.92	0.93	0.01	0.17	0.00	3.03	63.37	5.36	30.75	0.43	0.09	0.05	0.63	0.31
083:Z-29	1.95	0.00	0.00	1.95	1.94	0.93	0.02	0.16	0.00	3.05	63.52	5.16	30.63	0.58	0.11	0.05	0.64	0.31
083:Z-30	1.96	0.00	0.00	1.96	1.93	0.93	0.02	0.16	0.00	3.04	63.53	5.26	30.69	0.52	0.00	0.05	0.64	0.31
083:Z-31	1.97	0.00	0.00	1.97	1.93	0.93	0.01	0.16	0.00	3.03	63.71	5.18	30.69	0.41	0.00	0.05	0.64	0.31
083:Z-33	1.99	0.00	0.00	1.99	1.93	0.92	0.02	0.15	0.00	3.01	63.97	4.96	30.54	0.54	0.00	0.05	0.64	0.31
083:Z-34	1.98	0.00	0.00	1.98	1.93	0.92	0.02	0.15	0.00	3.02	63.99	5.02	30.43	0.56	0.00	0.05	0.64	0.30
083:Z-35	1.96	0.00	0.00	1.96	1.95	0.93	0.01	0.15	0.00	3.04	64.15	4.73	30.62	0.42	0.08	0.05	0.64	0.31
083:Z-36	1.97	0.00	0.00	1.97	1.96	0.92	0.01	0.15	0.00	3.03	64.56	4.77	30.30	0.37	0.00	0.05	0.65	0.30
083:Z-38	1.98	0.00	0.00	1.98	1.96	0.91	0.01	0.14	0.00	3.02	64.89	4.48	30.23	0.41	0.00	0.05	0.65	0.30
083:Z-39	1.99	0.00	0.00	1.99	1.95	0.91	0.02	0.14	0.00	3.01	64.80	4.49	30.22	0.48	0.00	0.05	0.65	0.30
083:Z-41	1.97	0.00	0.00	1.97	1.96	0.92	0.01	0.13	0.00	3.03	64.67	4.38	30.49	0.45	0.02	0.04	0.65	0.31
083:Z-43	1.98	0.00	0.00	1.98	1.95	0.91	0.01	0.13	0.00	3.00	65.04	4.16	30.45	0.32	0.04	0.04	0.65	0.30
083:Z-44	1.99	0.00	0.00	1.99	1.96	0.91	0.01	0.13	0.00	3.01	65.05	4.42	30.12	0.38	0.03	0.04	0.65	0.30
083:Z-47	1.97	0.00	0.00	1.97	1.99	0.88	0.02	0.14	0.00	3.03	65.79	4.54	29.15	0.52	0.00	0.05	0.66	0.29
083:Z-48	1.97	0.00	0.00	1.97	2.01	0.87	0.02	0.13	0.00	3.03	66.25	4.38	28.85	0.51	0.00	0.04	0.66	0.29
083:Z-50	1.99	0.00	0.00	1.99	2.03	0.84	0.01	0.13	0.00	3.01	67.43	4.12	27.93	0.43	0.09	0.04	0.67	0.28
083:Z-51	1.98	0.00	0.00	1.98	2.05	0.83	0.01	0.13	0.00	3.02	67.87	4.17	27.50	0.39	0.07	0.04	0.68	0.28
083:Z-52	1.99	0.00	0.00	2.00	1.99	0.86	0.02	0.14	0.00	3.00	66.28	4.40	28.69	0.53	0.10	0.05	0.66	0.29
083:Z-53	1.98	0.00	0.00	1.98	2.00	0.88	0.02	0.13	0.00	3.02	66.09	4.14	29.17	0.58	0.03	0.04	0.66	0.29
083:Z-54	2.00	0.00	0.00	2.00	1.96	0.89	0.01	0.13	0.00	3.00	65.56	4.40	29.62	0.42	0.00	0.04	0.66	0.30
083:Z-55	1.99	0.00	0.00	1.99	1.94	0.92	0.01	0.14	0.00	3.01	64.42	4.55	30.58	0.46	0.00	0.05	0.64	0.31
083:Z-56	1.98	0.00	0.00	1.99	1.94	0.93	0.02	0.14	0.00	3.02	64.31	4.51	30.68	0.50	0.00	0.05	0.64	0.31
083:Z-57	1.99	0.00	0.00	1.99	1.92	0.93	0.01	0.15	0.00	3.01	63.71	4.98	30.85	0.46	0.01	0.05	0.64	0.31
083:Z-58	1.99	0.00	0.00	1.99	1.93	0.92	0.02	0.15	0.00	3.01	64.06	5.02	30.43	0.48	0.01	0.05	0.64	0.30
083:Z-59	1.99	0.00	0.00	2.00	1.92	0.91	0.02	0.16	0.00	3.01	63.90	5.09	30.40	0.54	0.08	0.05	0.64	0.30
083:Z-60	1.99	0.00	0.00	1.99	1.91	0.94	0.01	0.15	0.00	3.01	63.39	5.03	31.28	0.28	0.02	0.05	0.63	0.31
083:Z-61	1.99	0.00	0.00	2.00	1.91	0.93	0.01	0.15	0.00	3.01	63.52	5.03	31.06	0.32	0.07	0.05	0.64	0.31
083:Z-62	1.97	0.00	0.00	1.97	1.92	0.93	0.02	0.16	0.00	3.03	63.48	5.27	30.73	0.52	0.00	0.05	0.64	0.31
083:Z-63	1.98	0.00	0.00	1.98	1.91	0.93	0.01	0.17	0.00	3.02	63.31	5.52	30.67	0.41	0.09	0.06	0.63	0.31
083:Z-64	1.99	0.00	0.00	1.99	1.90	0.92	0.01	0.18	0.00	3.01	63.08	5.79	30.73	0.37	0.04	0.06	0.63	0.31
083:Z-65	1.99	0.00	0.00	1.99	1.89	0.93	0.01	0.18	0.00	3.01	62.85	5.93	30.80	0.35	0.07	0.06	0.63	0.31
083:Z-66	1.98	0.00	0.00	1.98	1.90	0.92	0.02	0.19	0.00	3.02	62.78	6.17	30.44	0.54	0.08	0.06	0.63	0.30
083:Z-67	1.95	0.00	0.00	1.95	1.92	0.93	0.02	0.19	0.00	3.05	62.90	6.06	30.44	0.56	0.04	0.06	0.63	0.30

Table 1. Continue 4.

Sample	Al VI	Ti	Cr	Sum_A	Fe <sup>2+</sup>	Mg	Mn	Ca	Na	Sum_B	Alm	Gross	Pyrope	Spess	Uvaro	X <sub>Ca</sub>	X <sub>Fe</sub>	X <sub>Mg</sub>
083:Z-68	2.03	0.00	0.00	2.03	1.87	0.88	0.01	0.18	0.00	2.95	63.56	6.17	29.90	0.32	0.04	0.06	0.64	0.30
083:Z-70	2.00	0.00	0.00	2.00	1.89	0.92	0.02	0.18	0.00	3.00	62.87	6.05	30.54	0.51	0.04	0.06	0.63	0.31
083:Z-72	1.97	0.00	0.00	1.97	1.91	0.92	0.01	0.19	0.00	3.03	63.07	6.25	30.25	0.43	0.00	0.06	0.63	0.30
083:Z-73	1.98	0.00	0.00	1.98	1.90	0.91	0.02	0.19	0.00	3.02	63.00	6.27	30.23	0.50	0.01	0.06	0.63	0.30
083:Z-74	1.98	0.00	0.00	1.98	1.91	0.92	0.01	0.17	0.00	3.01	63.41	5.66	30.52	0.32	0.09	0.06	0.63	0.31
083:Z-75	1.96	0.00	0.00	1.96	1.94	0.92	0.01	0.17	0.00	3.04	63.80	5.41	30.27	0.45	0.07	0.06	0.64	0.30
083:Z-78	1.98	0.00	0.00	1.98	1.95	0.91	0.01	0.15	0.00	3.02	64.56	4.82	30.17	0.46	0.00	0.05	0.65	0.30
083:Z-79	1.97	0.00	0.00	1.97	1.95	0.92	0.02	0.14	0.00	3.03	64.35	4.72	30.44	0.49	0.00	0.05	0.64	0.30
083:Z-80	1.95	0.00	0.00	1.96	1.98	0.91	0.01	0.14	0.00	3.04	65.04	4.48	29.95	0.45	0.08	0.05	0.65	0.30
083:Z-82	1.96	0.00	0.00	1.96	1.99	0.90	0.02	0.13	0.00	3.04	65.50	4.18	29.74	0.52	0.06	0.04	0.66	0.30
083:Z-83	1.99	0.00	0.00	2.00	2.00	0.85	0.02	0.14	0.00	3.00	66.70	4.44	28.27	0.51	0.08	0.05	0.67	0.28
083:Z-84	1.95	0.00	0.00	1.95	2.07	0.83	0.02	0.13	0.00	3.05	67.96	4.23	27.28	0.53	0.00	0.04	0.68	0.27
083:Z-86	1.96	0.00	0.00	1.97	2.02	0.87	0.01	0.13	0.00	3.03	66.67	4.30	28.52	0.43	0.09	0.04	0.67	0.29
083:Z-87	1.96	0.00	0.00	1.97	1.99	0.89	0.01	0.15	0.00	3.04	65.50	4.78	29.25	0.36	0.12	0.05	0.66	0.29
083:Z-88	1.98	0.00	0.00	1.98	1.97	0.87	0.02	0.16	0.00	3.02	65.35	5.08	28.97	0.49	0.11	0.05	0.65	0.29
083:Z-90	1.99	0.00	0.00	1.99	1.91	0.91	0.02	0.17	0.00	3.01	63.45	5.78	30.24	0.54	0.00	0.06	0.63	0.30
083:Z-91	1.95	0.00	0.00	1.96	1.93	0.92	0.01	0.18	0.00	3.04	63.43	5.82	30.16	0.44	0.16	0.06	0.63	0.30
083:Z-92	1.95	0.00	0.00	1.95	1.92	0.92	0.01	0.20	0.00	3.05	62.86	6.55	30.18	0.37	0.04	0.07	0.63	0.30
083:Z-93	1.98	0.00	0.00	1.98	1.90	0.91	0.01	0.20	0.00	3.02	62.84	6.72	30.04	0.40	0.00	0.07	0.63	0.30
083:Z-94	1.97	0.00	0.00	1.98	1.89	0.91	0.01	0.21	0.00	3.02	62.54	6.89	30.13	0.44	0.00	0.07	0.63	0.30
083:Z-95	1.96	0.00	0.00	1.96	1.90	0.92	0.01	0.21	0.00	3.04	62.37	6.85	30.33	0.40	0.05	0.07	0.62	0.30
083:Z-96	2.00	0.00	0.00	2.00	1.90	0.86	0.02	0.21	0.00	2.98	63.64	6.90	28.76	0.57	0.13	0.07	0.64	0.29
083:Z-97	1.98	0.00	0.00	1.98	1.90	0.92	0.01	0.19	0.00	3.02	62.81	6.24	30.54	0.37	0.04	0.06	0.63	0.31
083:Z-99	1.99	0.00	0.00	1.99	1.91	0.92	0.01	0.17	0.00	3.01	63.56	5.55	30.44	0.36	0.10	0.06	0.64	0.30
083:Z-100	1.96	0.00	0.00	1.97	1.93	0.93	0.01	0.17	0.00	3.03	63.64	5.33	30.55	0.37	0.10	0.05	0.64	0.31
083:Z-101	1.97	0.00	0.00	1.97	1.92	0.93	0.01	0.16	0.00	3.03	63.60	5.22	30.67	0.37	0.14	0.05	0.64	0.31
083:Z-102	1.99	0.00	0.00	2.00	1.92	0.92	0.01	0.16	0.00	3.01	63.77	5.14	30.71	0.37	0.01	0.05	0.64	0.31
083:Z-103	1.98	0.00	0.00	1.99	1.93	0.92	0.01	0.15	0.00	3.01	64.11	4.87	30.49	0.46	0.08	0.05	0.64	0.31
083:Z-104	2.00	0.00	0.00	2.00	1.92	0.92	0.01	0.15	0.00	3.00	64.14	4.84	30.53	0.42	0.07	0.05	0.64	0.31
083:Z-105	1.99	0.00	0.00	1.99	1.95	0.91	0.01	0.14	0.00	3.01	64.85	4.50	30.07	0.47	0.11	0.05	0.65	0.30
083:Z-106	1.98	0.00	0.00	1.99	1.96	0.91	0.01	0.14	0.00	3.02	64.88	4.54	30.14	0.44	0.00	0.05	0.65	0.30
083:Z-107	2.00	0.00	0.00	2.00	1.95	0.89	0.01	0.13	0.00	2.99	65.29	4.26	29.88	0.46	0.10	0.04	0.65	0.30
083:Z-108	1.98	0.00	0.00	1.99	1.98	0.89	0.01	0.13	0.00	3.00	65.90	4.19	29.57	0.30	0.05	0.04	0.66	0.30
083:Z-109	1.99	0.00	0.00	1.99	2.00	0.88	0.01	0.12	0.00	3.01	66.28	3.79	29.34	0.47	0.11	0.04	0.66	0.29
083:Z-110	1.99	0.00	0.00	1.99	2.01	0.86	0.01	0.13	0.00	3.01	66.87	4.17	28.48	0.48	0.00	0.04	0.67	0.29
083:Z-112	2.03	0.00	0.00	2.03	2.02	0.79	0.01	0.13	0.00	2.95	68.36	4.44	26.73	0.47	0.00	0.04	0.68	0.27
083:Z-113	2.01	0.00	0.00	2.01	2.01	0.83	0.02	0.13	0.00	2.99	67.36	4.23	27.79	0.61	0.00	0.04	0.67	0.28
083:Z-114	1.99	0.00	0.00	1.99	2.01	0.86	0.02	0.13	0.00	3.01	66.58	4.23	28.53	0.59	0.07	0.04	0.67	0.29
083:Z-115	1.98	0.00	0.00	1.98	2.02	0.86	0.01	0.13	0.00	3.02	66.94	4.22	28.48	0.36	0.00	0.04	0.67	0.29
083:Z-116	2.00	0.00	0.00	2.00	1.99	0.88	0.01	0.12	0.00	3.00	66.25	3.99	29.27	0.47	0.02	0.04	0.66	0.29
083:Z-117	1.98	0.00	0.00	1.98	1.98	0.89	0.01	0.13	0.00	3.02	65.72	4.23	29.61	0.38	0.06	0.04	0.66	0.30
083:Z-118	1.99	0.00	0.00	1.99	1.94	0.92	0.01	0.14	0.00	3.01	64.42	4.58	30.53	0.45	0.02	0.05	0.64	0.31
083:Z-120	2.02	0.00	0.00	2.02	1.92	0.91	0.01	0.14	0.00	2.98	64.37	4.69	30.62	0.31	0.01	0.05	0.64	0.31
083:Z-122	2.01	0.00	0.00	2.01	1.91	0.92	0.01	0.15	0.00	2.99	64.08	4.78	30.70	0.38	0.06	0.05	0.64	0.31
083:Z-123	2.03	0.00	0.00	2.03	1.90	0.89	0.01	0.15	0.00	2.95	64.44	5.03	30.03	0.38	0.12	0.05	0.65	0.30
083:Z-125	1.97	0.00	0.00	1.97	1.90	0.96	0.02	0.16	0.00	3.03	62.66	5.13	31.59	0.51	0.11	0.05	0.63	0.32
083:Z-126	1.99	0.00	0.00	2.00	1.91	0.92	0.01	0.16	0.00	3.00	63.72	5.15	30.67	0.43	0.04	0.05	0.64	0.31
083:Z-127	2.02	0.00	0.00	2.02	1.90	0.90	0.02	0.16	0.00	2.98	63.98	5.20	30.29	0.50	0.04	0.05	0.64	0.30
083:Z-128	2.01	0.00	0.00	2.01	1.89	0.92	0.01	0.16	0.00	2.98	63.30	5.32	30.93	0.44	0.00	0.05	0.63	0.31
083:Z-129	2.00	0.00	0.00	2.00	1.91	0.92	0.02	0.16	0.00	3.00	63.78	5.12	30.55	0.51	0.05	0.05	0.64	0.31
083:Z-130	2.01	0.00	0.00	2.01	1.91	0.92	0.01	0.15	0.00	2.99	63.78	5.01	30.80	0.41	0.00	0.05	0.64	0.31
083:Z-131	2.01	0.00	0.00	2.01	1.92	0.90	0.02	0.15	0.00	2.99	64.33	4.94	30.23	0.50	0.01	0.05	0.64	0.30



Table 1. Continue 5.

Sample	Al VI	Ti	Cr	Sum_A	Fe <sup>2+</sup>	Mg	Mn	Ca	Na	Sum_B	Alm	Gross	Pyrope	Spess	Uvaro	X <sub>Ca</sub>	X <sub>Fe</sub>	X <sub>Mg</sub>
083:Z-132	2.01	0.00	0.00	2.02	1.94	0.88	0.01	0.14	0.00	2.97	65.26	4.60	29.62	0.46	0.07	0.05	0.65	0.30
083:Z-133	2.02	0.00	0.00	2.02	1.97	0.86	0.02	0.13	0.00	2.96	66.30	4.30	28.90	0.50	0.00	0.04	0.66	0.29
083:Z-134	2.03	0.00	0.00	2.03	1.97	0.84	0.01	0.13	0.00	2.95	66.67	4.24	28.60	0.48	0.02	0.04	0.67	0.29
083:Z-135	2.01	0.00	0.00	2.01	2.03	0.81	0.02	0.13	0.00	2.99	67.99	4.27	27.18	0.53	0.03	0.04	0.68	0.27
083:Z-136	2.00	0.00	0.00	2.00	1.99	0.86	0.02	0.13	0.00	3.00	66.37	4.28	28.83	0.49	0.03	0.04	0.66	0.29
083:Z-137	2.03	0.00	0.00	2.03	1.97	0.85	0.01	0.13	0.00	2.97	66.48	4.33	28.75	0.38	0.06	0.04	0.67	0.29
083:Z-138	2.02	0.00	0.00	2.02	1.96	0.87	0.02	0.13	0.00	2.98	65.96	4.22	29.23	0.59	0.00	0.04	0.66	0.29
083:Z-140	2.03	0.00	0.00	2.03	1.96	0.87	0.02	0.13	0.00	2.97	65.84	4.24	29.38	0.50	0.04	0.04	0.66	0.29
083:Z-141	2.01	0.00	0.00	2.01	2.03	0.83	0.01	0.13	0.00	2.99	67.80	4.20	27.61	0.39	0.00	0.04	0.68	0.28
083:Z-142	2.01	0.00	0.00	2.02	2.03	0.82	0.01	0.13	0.00	2.98	68.06	4.14	27.30	0.42	0.08	0.04	0.68	0.27
083:Z-143	2.03	0.00	0.00	2.03	2.03	0.80	0.02	0.12	0.00	2.97	68.37	3.96	27.10	0.50	0.07	0.04	0.68	0.27
083:Z-144	2.02	0.00	0.00	2.02	2.01	0.83	0.01	0.12	0.00	2.97	67.73	3.82	27.94	0.42	0.08	0.04	0.68	0.28
083:Z-145	2.01	0.00	0.00	2.01	2.01	0.85	0.02	0.12	0.00	2.99	67.14	3.87	28.35	0.64	0.00	0.04	0.67	0.28
083:Z-146	2.04	0.00	0.00	2.04	2.00	0.83	0.02	0.11	0.00	2.95	67.59	3.68	28.22	0.49	0.02	0.04	0.68	0.28
083:Z-147	2.03	0.00	0.00	2.03	2.10	0.74	0.01	0.11	0.00	2.96	70.90	3.78	24.90	0.37	0.05	0.04	0.71	0.25
083:Z-148	2.00	0.00	0.00	2.00	2.07	0.78	0.01	0.12	0.00	2.98	69.45	3.85	26.25	0.45	0.00	0.04	0.70	0.26
083:Z-149	2.02	0.00	0.00	2.02	2.05	0.77	0.02	0.11	0.00	2.95	69.62	3.73	26.10	0.56	0.00	0.04	0.70	0.26
083:Z-150	2.02	0.00	0.00	2.03	2.07	0.77	0.02	0.12	0.00	2.97	69.78	3.87	25.78	0.57	0.00	0.04	0.70	0.26
083:Z-151	2.01	0.00	0.00	2.01	2.10	0.74	0.02	0.11	0.00	2.97	70.65	3.75	24.84	0.70	0.07	0.04	0.71	0.25
083:Z-153	1.99	0.00	0.00	1.99	2.05	0.82	0.01	0.12	0.00	3.01	68.21	3.99	27.33	0.47	0.00	0.04	0.68	0.27
083:Z-154	1.98	0.00	0.00	1.98	2.06	0.82	0.02	0.12	0.00	3.02	68.40	4.05	27.03	0.51	0.00	0.04	0.68	0.27
083:Z-156	1.99	0.00	0.00	1.99	2.28	0.59	0.02	0.12	0.00	3.01	75.73	3.96	19.69	0.61	0.00	0.04	0.76	0.20
083:Z-157	2.00	0.00	0.00	2.00	2.11	0.76	0.02	0.11	0.00	3.00	70.27	3.76	25.33	0.63	0.01	0.04	0.70	0.25
083:Z-158	1.95	0.00	0.00	1.96	2.09	0.82	0.02	0.12	0.00	3.04	68.65	3.92	26.83	0.55	0.05	0.04	0.69	0.27
083:Z-159	1.98	0.00	0.00	1.98	2.03	0.85	0.02	0.12	0.00	3.02	67.28	4.08	27.97	0.67	0.01	0.04	0.67	0.28
082:G1-4	1.95	0.00	0.00	1.95	2.02	0.85	0.03	0.16	0.00	3.05	66.13	4.99	27.77	0.95	0.12	0.05	0.66	0.28
082:G1-6	1.96	0.00	0.00	1.96	2.13	0.74	0.03	0.13	0.00	3.04	70.20	4.27	24.38	1.02	0.13	0.04	0.70	0.24
082:G2-1	1.96	0.00	0.00	1.96	1.93	0.90	0.02	0.19	0.00	3.04	63.41	6.01	29.70	0.67	0.10	0.06	0.64	0.30
082:G2-2	1.92	0.00	0.00	1.92	1.95	0.88	0.02	0.19	0.00	3.04	64.08	6.27	28.89	0.71	0.00	0.06	0.64	0.29
082:G2-3	1.94	0.00	0.00	1.95	1.93	0.87	0.03	0.20	0.01	3.03	63.88	6.41	28.58	0.83	0.10	0.07	0.64	0.29
082:G2-4	1.99	0.00	0.00	1.99	1.92	0.86	0.03	0.19	0.00	3.01	63.92	6.42	28.66	0.84	0.01	0.06	0.64	0.29
082:G2-8	1.94	0.00	0.00	1.94	2.22	0.64	0.03	0.15	0.00	3.04	72.94	4.92	21.13	0.95	0.04	0.05	0.73	0.21
108:g1-i	2.05	0.00	0.00	2.05	1.85	0.97	0.02	0.11	0.00	2.95	62.64	3.73	32.72	0.77	0.13	0.04	0.63	0.33
108:g1-i2	2.00	0.00	0.00	2.00	1.91	0.94	0.03	0.12	0.00	3.00	63.78	3.87	31.26	0.89	0.10	0.04	0.64	0.31
108:g1-r2	2.00	0.00	0.00	2.00	1.97	0.89	0.02	0.12	0.00	3.00	65.76	3.83	29.53	0.79	0.08	0.04	0.66	0.30
108:g1m	1.99	0.00	0.00	1.99	1.90	0.97	0.02	0.12	0.00	3.01	63.25	3.83	32.21	0.65	0.05	0.04	0.63	0.32
108:g1m1	1.99	0.00	0.00	1.99	1.89	0.98	0.02	0.12	0.00	3.01	62.84	3.91	32.46	0.71	0.03	0.04	0.63	0.33
108:g2-r1	1.98	0.00	0.00	1.98	2.07	0.82	0.02	0.12	0.00	3.02	68.35	3.73	27.07	0.72	0.11	0.04	0.68	0.27

Table 2. Biotite analyses from the GNG.

Sample	Desc	SiO <sub>2</sub>	TiO <sub>2</sub>	Al <sub>2</sub> O <sub>3</sub>	Cr <sub>2</sub> O <sub>3</sub>	FeO	MnO	MgO	CaO	Na <sub>2</sub> O	K <sub>2</sub> O	Total	Si	Al IV	Sum_T
<b>B-1</b>	082/M1/1	37.39	4.19	18.67	0.00	12.45	0.04	15.39	0.11	0.20	9.13	97.57	5.11	2.89	8.00
<b>B-2</b>	082/M1/2	38.43	4.56	19.13	0.00	12.85	0.01	15.34	0.07	0.18	9.15	99.72	5.13	2.87	8.00
<b>B-3</b>	082/M1/4	38.27	4.56	18.60	0.00	12.86	0.01	15.82	0.06	0.18	9.44	99.80	5.12	2.88	8.00
<b>B-4</b>	082/M1/5	38.37	4.54	19.04	0.00	12.99	0.01	15.09	0.07	0.20	9.17	99.48	5.14	2.86	8.00
<b>A-1</b>	082/M2/1	37.22	4.62	18.37	0.00	13.76	0.02	13.67	0.08	0.25	8.89	96.87	5.15	2.85	8.00
<b>A-2</b>	082/M2/1a	37.74	4.63	18.97	0.00	13.48	0.05	14.04	0.03	0.22	9.38	98.55	5.13	2.87	8.00
<b>A-3</b>	082/M2/2	35.98	4.53	18.12	0.00	13.28	0.04	13.59	0.13	0.28	8.74	94.69	5.10	2.90	8.00
<b>A-4</b>	082/M2/2a	37.52	4.73	19.03	0.00	13.49	0.02	14.09	0.05	0.19	9.38	98.51	5.11	2.90	8.00
<b>A-5</b>	082/M2/3	37.52	4.81	19.41	0.00	13.77	0.03	14.90	0.11	0.27	9.02	99.84	5.04	2.97	8.00
<b>A-6</b>	082/M2/5	36.63	4.75	18.54	0.00	13.67	0.00	13.92	0.07	0.24	9.30	97.11	5.07	2.93	8.00
<b>A-7</b>	083:m1-1	36.83	4.29	17.73	0.06	12.82	0.00	13.82	0.00	0.14	9.70	95.39	5.18	2.82	8.00
<b>A-8</b>	083:m1-2	36.62	4.13	17.72	0.09	13.03	0.00	13.55	0.00	0.14	10.01	95.29	5.18	2.82	8.00
<b>A-9</b>	083:m1-3	36.47	4.34	17.29	0.04	12.83	0.00	14.14	0.00	0.17	9.64	94.92	5.17	2.83	8.00
<b>A-10</b>	083:m1-4	36.82	4.51	17.21	0.02	12.55	0.06	13.92	0.00	0.21	9.53	94.83	5.21	2.79	8.00
<b>A-11</b>	083:m2-1	37.72	4.38	18.14	0.10	13.21	0.00	14.13	0.00	0.20	9.83	97.71	5.18	2.82	8.00
<b>A-12</b>	083:m2-2	37.46	4.08	17.97	0.11	13.28	0.01	13.93	0.00	0.15	9.84	96.83	5.20	2.80	8.00
<b>A-13</b>	083:m2-3	37.77	4.59	18.14	0.09	13.82	0.04	14.15	0.00	0.19	9.82	98.61	5.16	2.84	8.00
<b>A-14</b>	083:m2-4	36.96	4.58	17.42	0.03	13.64	0.00	13.37	0.00	0.19	9.67	95.86	5.20	2.80	8.00
<b>B-5</b>	096:m1-2	35.45	4.91	17.26	0.08	11.96	0.00	14.38	0.11	0.25	9.14	93.54	5.08	2.91	7.99
<b>B-6</b>	096:m1-3	36.82	4.30	17.53	0.09	11.71	0.00	14.29	0.00	0.17	9.55	94.46	5.21	2.80	8.00
<b>B-7</b>	096:m1-4	35.96	4.42	17.41	0.09	11.65	0.05	14.58	0.07	0.17	9.16	93.56	5.14	2.87	8.00
<b>B-8</b>	096:m1-5	36.40	4.31	17.91	0.10	12.62	0.00	14.83	0.12	0.21	9.09	95.59	5.10	2.90	8.00
<b>A-15</b>	096:m2-1	37.43	4.63	18.62	0.05	12.33	0.02	14.03	0.11	0.34	9.12	96.68	5.16	2.84	8.00
<b>A-16</b>	096:m2-2	37.44	4.79	18.49	0.01	12.27	0.03	14.45	0.04	0.22	9.73	97.47	5.14	2.86	8.00
<b>A-17</b>	096:m2-3	37.12	4.51	18.67	0.10	12.17	0.06	14.52	0.09	0.22	9.61	97.07	5.11	2.89	8.00
<b>A-18</b>	096:m2-4	37.34	4.60	18.17	0.06	11.37	0.00	14.50	0.03	0.15	9.88	96.10	5.18	2.82	8.00
<b>B-15</b>	096:m3-1	37.31	4.46	18.32	0.06	11.77	0.00	14.72	0.00	0.16	9.76	96.56	5.16	2.84	8.00
<b>B-16</b>	096:m3-2	37.04	4.34	17.94	0.07	11.87	0.00	14.89	0.00	0.18	9.93	96.26	5.15	2.85	8.00
<b>B-17</b>	096:m3-3	37.03	4.24	18.53	0.09	11.10	0.00	15.08	0.00	0.16	9.72	95.95	5.14	2.87	8.00
<b>B-18</b>	096:m3-4	36.73	4.34	18.21	0.01	10.73	0.00	15.01	0.00	0.14	9.61	94.78	5.15	2.85	8.00
<b>B-19</b>	108/g1-1a	38.98	4.43	18.97	0.00	11.80	0.00	16.06	0.01	0.18	9.19	99.63	5.18	2.82	8.00
<b>B-20</b>	108/g1-2a	37.57	4.36	17.87	0.00	11.50	0.01	15.85	0.31	0.34	9.16	96.97	5.15	2.85	8.00
<b>B-21</b>	108/g2-1a	38.54	4.38	18.24	0.00	11.61	0.01	15.46	0.00	0.15	9.37	97.76	5.23	2.77	8.00
<b>Minimum</b>		35.45	4.08	17.21	0.00	10.73	0.00	13.37	0.00	0.14	8.74	93.54	5.04	2.77	7.99
<b>Maximum</b>		38.98	4.91	19.41	0.11	13.82	0.06	16.06	0.31	0.34	10.01	99.84	5.23	2.97	8.00
<b>Mean</b>		37.24	4.48	18.23	0.04	12.55	0.02	14.53	0.05	0.20	9.44	96.79	5.15	2.85	8.00
<b>St. dev</b>		0.59	0.16	0.48	0.04	0.73	0.02	0.58	0.05	0.04	0.29	1.46	0.03	0.03	0.00

Table 2. Continue 1.

Sample	Desc	Al VI	Ti	Fe <sup>2+</sup>	Cr	Mn	Mg	Ca	Na	K	Cations	Fe/(FeMg)	Mg/(FeMg)
<b>B-1</b>	082/M1/1	0.12	0.43	1.42	0.00	0.00	3.14	0.02	0.05	1.59	6.77	0.31	0.69
<b>B-2</b>	082/M1/2	0.14	0.46	1.44	0.00	0.00	3.05	0.01	0.05	1.56	6.71	0.32	0.68
<b>B-3</b>	082/M1/4	0.05	0.46	1.44	0.00	0.00	3.16	0.01	0.05	1.61	6.78	0.31	0.69
<b>B-4</b>	082/M1/5	0.15	0.46	1.46	0.00	0.00	3.01	0.01	0.05	1.57	6.70	0.33	0.67
<b>A-1</b>	082/M2/1	0.14	0.48	1.59	0.00	0.00	2.82	0.01	0.07	1.57	6.69	0.36	0.64
<b>A-2</b>	082/M2/1a	0.17	0.47	1.53	0.00	0.01	2.85	0.01	0.06	1.63	6.71	0.35	0.65
<b>A-3</b>	082/M2/2	0.12	0.48	1.57	0.00	0.00	2.87	0.02	0.08	1.58	6.73	0.35	0.65
<b>A-4</b>	082/M2/2a	0.16	0.48	1.54	0.00	0.00	2.86	0.01	0.05	1.63	6.72	0.35	0.65
<b>A-5</b>	082/M2/3	0.10	0.49	1.55	0.00	0.00	2.98	0.02	0.07	1.54	6.75	0.34	0.66
<b>A-6</b>	082/M2/5	0.10	0.50	1.58	0.00	0.00	2.87	0.01	0.06	1.64	6.77	0.36	0.64
<b>A-7</b>	083:m1-1	0.12	0.45	1.51	0.01	0.00	2.90	0.00	0.04	1.74	6.77	0.34	0.66
<b>A-8</b>	083:m1-2	0.13	0.44	1.54	0.01	0.00	2.86	0.00	0.04	1.81	6.82	0.35	0.65
<b>A-9</b>	083:m1-3	0.05	0.46	1.52	0.00	0.00	2.99	0.00	0.05	1.74	6.82	0.34	0.66
<b>A-10</b>	083:m1-4	0.08	0.48	1.49	0.00	0.01	2.94	0.00	0.06	1.72	6.76	0.34	0.66
<b>A-11</b>	083:m2-1	0.12	0.45	1.52	0.01	0.00	2.90	0.00	0.05	1.72	6.77	0.34	0.66
<b>A-12</b>	083:m2-2	0.14	0.43	1.54	0.01	0.00	2.88	0.00	0.04	1.74	6.79	0.35	0.65
<b>A-13</b>	083:m2-3	0.08	0.47	1.58	0.01	0.01	2.88	0.00	0.05	1.71	6.78	0.35	0.65
<b>A-14</b>	083:m2-4	0.08	0.48	1.60	0.00	0.00	2.80	0.00	0.05	1.74	6.76	0.36	0.64
<b>B-5</b>	096:m1-2	0.00	0.53	1.43	0.01	0.00	3.07	0.02	0.07	1.67	6.80	0.32	0.68
<b>B-6</b>	096:m1-3	0.12	0.46	1.38	0.01	0.00	3.01	0.00	0.05	1.72	6.75	0.31	0.69
<b>B-7</b>	096:m1-4	0.06	0.48	1.39	0.01	0.01	3.10	0.01	0.05	1.67	6.78	0.31	0.69
<b>B-8</b>	096:m1-5	0.06	0.45	1.48	0.01	0.00	3.10	0.02	0.06	1.63	6.80	0.32	0.68
<b>A-15</b>	096:m2-1	0.18	0.48	1.42	0.01	0.00	2.88	0.02	0.09	1.60	6.69	0.33	0.67
<b>A-16</b>	096:m2-2	0.12	0.49	1.41	0.00	0.00	2.96	0.01	0.06	1.70	6.75	0.32	0.68
<b>A-17</b>	096:m2-3	0.14	0.47	1.40	0.01	0.01	2.98	0.01	0.06	1.69	6.77	0.32	0.68
<b>A-18</b>	096:m2-4	0.15	0.48	1.32	0.01	0.00	3.00	0.00	0.04	1.75	6.74	0.31	0.69
<b>B-15</b>	096:m3-1	0.14	0.46	1.36	0.01	0.00	3.03	0.00	0.04	1.72	6.76	0.31	0.69
<b>B-16</b>	096:m3-2	0.09	0.45	1.38	0.01	0.00	3.09	0.00	0.05	1.76	6.83	0.31	0.69
<b>B-17</b>	096:m3-3	0.16	0.44	1.29	0.01	0.00	3.12	0.00	0.04	1.72	6.78	0.29	0.71
<b>B-18</b>	096:m3-4	0.15	0.46	1.26	0.00	0.00	3.14	0.00	0.04	1.72	6.76	0.29	0.71
<b>B-19</b>	108/g1-1a	0.15	0.44	1.31	0.00	0.00	3.18	0.00	0.05	1.56	6.69	0.29	0.71
<b>B-20</b>	108/g1-2a	0.04	0.45	1.32	0.00	0.00	3.24	0.05	0.09	1.60	6.80	0.29	0.71
<b>B-21</b>	108/g2-1a	0.14	0.45	1.32	0.00	0.00	3.13	0.00	0.04	1.62	6.69	0.30	0.70
<b>Minimum</b>		0.00	0.43	1.26	0.00	0.00	2.80	0.00	0.04	1.54	6.69	0.29	0.64
<b>Maximum</b>		0.18	0.53	1.60	0.01	0.01	3.24	0.05	0.09	1.81	6.83	0.36	0.71
<b>Mean</b>		0.11	0.47	1.45	0.00	0.00	2.99	0.01	0.05	1.67	6.76	0.33	0.67
<b>St dev</b>		0.03	0.02	0.08	0.00	0.00	0.10	0.01	0.01	0.06	0.03	0.02	0.02

Table 3. Plagioclase analyses from the GNG.

Sample	SiO <sub>2</sub>	Al <sub>2</sub> O <sub>3</sub>	FeO	MgO	CaO	Na <sub>2</sub> O	K <sub>2</sub> O	Total	Si	Al
082-F-1	60.81	23.81	0.09	0.00	4.79	9.34	0.19	99.03	10.93	5.04
083:F1-1	61.76	23.37	0.00	0.01	4.27	8.84	0.27	98.52	11.09	4.94
083:F1-2	62.57	23.35	0.01	0.03	4.26	8.94	0.31	99.47	11.13	4.89
083:F1-3	62.91	23.56	0.00	0.01	4.28	8.79	0.29	99.83	11.14	4.91
083:F2-2	62.71	23.09	0.00	0.00	4.13	8.73	0.35	99.00	11.19	4.85
083:F2-3	62.66	23.26	0.00	0.00	4.27	8.77	0.34	99.29	11.16	4.88
083:F2-4	62.52	23.08	0.00	0.01	4.21	8.80	0.37	98.98	11.17	4.86
083:F2-5	62.90	23.01	0.00	0.00	4.28	8.82	0.33	99.34	11.19	4.82
083:F2-6	63.04	22.82	0.00	0.01	4.28	8.78	0.37	99.30	11.22	4.78
083:F3-1	63.12	23.76	0.09	0.01	4.18	9.19	0.22	100.56	11.11	4.92
083:F3-2	62.47	23.24	0.00	0.02	4.41	8.90	0.37	99.41	11.13	4.88
083:F3-3	63.15	22.98	0.00	0.00	4.19	9.05	0.36	99.72	11.20	4.80
083:F3-4	62.64	22.88	0.03	0.00	4.30	8.92	0.35	99.11	11.18	4.81
083:F3-5	62.37	23.08	0.05	0.00	4.17	8.93	0.37	98.98	11.15	4.86
083:F3-6	62.52	22.86	0.04	0.00	4.11	8.88	0.34	98.76	11.19	4.82
083:F4B-2	63.79	22.39	0.03	0.00	3.87	8.97	0.07	99.12	11.34	4.69
083:F4B-3	63.70	22.83	0.01	0.00	3.71	8.81	0.03	99.09	11.31	4.77
083:F6-3	62.67	22.69	0.01	0.00	3.98	9.03	0.19	98.57	11.23	4.79
083:F6-5	62.90	22.53	0.10	0.00	4.16	8.78	0.36	98.83	11.25	4.75
083:F7-3	63.52	23.03	0.01	0.00	4.27	8.54	0.22	99.58	11.25	4.80
083:F7-4	64.22	23.00	0.00	0.00	3.82	8.69	0.15	99.88	11.31	4.77
083:F7-5	62.92	23.10	0.03	0.01	3.84	8.98	0.23	99.11	11.21	4.84
083:F7-6	62.26	23.55	0.00	0.00	4.46	8.37	0.33	98.97	11.11	4.95
Minimum	60.81	22.39	0.00	0.00	3.71	8.37	0.03	98.52	10.93	4.69
Maximum	64.22	23.81	0.10	0.03	4.79	9.34	0.37	100.56	11.34	5.04
Mean	62.79	23.10	0.02	0.01	4.18	8.86	0.28	99.24	11.18	4.84
St dev	0.69	0.36	0.03	0.01	0.23	0.20	0.10	0.46	0.09	0.08

Sample	Fe <sup>2+</sup>	Mg	Ca	Na	K	X*	Z*	Ab	An	Or
082-F-1	0.01	0.00	0.92	3.25	0.04	15.96	4.23	77.10	21.90	1.00
083:F1-1	0.00	0.00	0.82	3.08	0.06	16.03	3.97	77.70	20.70	1.60
083:F1-2	0.00	0.01	0.81	3.08	0.07	16.02	3.98	77.80	20.40	1.80
083:F1-3	0.00	0.00	0.81	3.02	0.07	16.05	3.90	77.50	20.80	1.70
083:F2-2	0.00	0.00	0.79	3.02	0.08	16.04	3.89	77.70	20.30	2.00
083:F2-3	0.00	0.00	0.81	3.03	0.08	16.03	3.92	77.30	20.80	2.00
083:F2-4	0.00	0.00	0.81	3.05	0.08	16.02	3.94	77.40	20.50	2.10
083:F2-5	0.00	0.00	0.82	3.04	0.08	16.01	3.93	77.40	20.70	1.90
083:F2-6	0.00	0.00	0.82	3.03	0.08	16.01	3.93	77.10	20.80	2.10
083:F3-1	0.01	0.00	0.79	3.14	0.05	16.03	3.99	78.90	19.80	1.30
083:F3-2	0.00	0.00	0.84	3.07	0.08	16.00	4.00	76.80	21.10	2.10
083:F3-3	0.00	0.00	0.80	3.11	0.08	16.00	3.99	78.00	19.90	2.10
083:F3-4	0.00	0.00	0.82	3.09	0.08	15.99	3.99	77.40	20.60	2.00
083:F3-5	0.01	0.00	0.80	3.10	0.08	16.01	3.99	77.80	20.10	2.10
083:F3-6	0.01	0.00	0.79	3.08	0.08	16.01	3.96	78.00	20.00	2.00
083:F4B-2	0.01	0.00	0.74	3.09	0.02	16.02	3.85	80.50	19.20	0.40
083:F4B-3	0.00	0.00	0.71	3.03	0.01	16.08	3.75	80.90	18.90	0.20
083:F6-3	0.00	0.00	0.76	3.14	0.04	16.02	3.94	79.50	19.40	1.10
083:F6-5	0.02	0.00	0.80	3.05	0.08	16.00	3.94	77.60	20.30	2.10
083:F7-3	0.00	0.00	0.81	2.93	0.05	16.05	3.79	77.40	21.40	1.30
083:F7-4	0.00	0.00	0.72	2.97	0.03	16.08	3.72	79.70	19.40	0.90
083:F7-5	0.00	0.00	0.73	3.10	0.05	16.05	3.89	79.80	18.80	1.40
083:F7-6	0.00	0.00	0.85	2.90	0.07	16.06	3.83	75.70	22.30	1.90
Minimum	0.00	0.00	0.71	2.90	0.01	15.96	3.72	75.70	18.80	0.20
Maximum	0.02	0.01	0.92	3.25	0.08	16.08	4.23	80.90	22.30	2.10
Mean	0.00	0.00	0.80	3.06	0.06	16.03	3.93	78.04	20.35	1.61
St dev	0.00	0.00	0.05	0.07	0.02	0.03	0.10	1.26	0.88	0.57

\*Z = Si + Al + Fe<sup>3+</sup> + Ti

\*X = Mg + Na + Ca + K

Table 4. *K-feldspar analyses from the GNG*

Sample	SiO <sub>2</sub>	Al <sub>2</sub> O <sub>3</sub>	FeO	MgO	CaO	Na <sub>2</sub> O	K <sub>2</sub> O	Total	Si	Al
083:F4-1	63.94	18.52	0.00	0.00	0.09	1.97	14.03	98.54	11.93	4.07
083:F4-2	64.15	18.47	0.00	0.00	0.09	2.04	13.84	98.59	11.95	4.05
083:F4-4	64.40	18.36	0.00	0.00	0.07	1.57	14.64	99.04	11.97	4.02
083:F4B-1	64.55	18.92	0.04	0.01	0.10	1.77	14.22	99.60	11.91	4.11
083:F4B-4	65.04	18.63	0.03	0.01	0.10	1.78	14.23	99.82	11.96	4.04
083:F5-2	63.73	18.35	0.08	0.02	0.09	1.75	14.58	98.59	11.92	4.04
083:F6-7	63.56	18.45	0.08	0.01	0.08	2.61	13.49	98.28	11.89	4.07
083:F7-1	64.21	18.97	0.00	0.01	0.05	1.93	14.02	99.19	11.89	4.14
083:F7-2	65.17	18.78	0.02	0.00	0.15	2.17	13.48	99.76	11.96	4.06
Minimum	63.56	18.35	0.00	0.00	0.05	1.57	13.48	98.28	11.89	4.02
Maximum	65.17	18.97	0.08	0.02	0.15	2.61	14.64	99.82	11.97	4.14
Mean	64.30	18.61	0.03	0.01	0.09	1.95	14.06	99.04	11.93	4.06
St dev	0.55	0.23	0.03	0.01	0.03	0.30	0.41	0.58	0.03	0.04

Sample	Fe <sup>2+</sup>	Mg	Ca	Na	K	X	Z	Ab	An	Or
083:F4-1	0.00	0.00	0.02	0.71	3.34	15.99	4.07	17.50	0.40	82.00
083:F4-2	0.00	0.00	0.02	0.74	3.29	16.00	4.04	18.20	0.40	81.30
083:F4-4	0.00	0.00	0.01	0.57	3.47	15.99	4.05	14.00	0.30	85.70
083:F4B-1	0.01	0.00	0.02	0.63	3.35	16.02	4.01	15.80	0.50	83.70
083:F4B-4	0.01	0.00	0.02	0.64	3.34	16.00	4.00	15.90	0.50	83.60
083:F5-2	0.01	0.01	0.02	0.63	3.48	15.96	4.15	15.40	0.40	84.20
083:F6-7	0.01	0.00	0.02	0.95	3.22	15.96	4.20	22.60	0.40	77.00
083:F7-1	0.00	0.00	0.01	0.69	3.31	16.02	4.02	17.20	0.20	82.50
083:F7-2	0.00	0.00	0.03	0.77	3.16	16.01	3.96	19.50	0.70	79.80
Minimum	0.00	0.00	0.01	0.57	3.16	15.96	3.96	14.00	0.20	77.00
Maximum	0.01	0.01	0.03	0.95	3.48	16.02	4.20	22.60	0.70	85.70
Mean	0.00	0.00	0.02	0.70	3.33	15.99	4.05	17.34	0.42	82.20
St dev	0.01	0.00	0.01	0.11	0.10	0.02	0.08	2.56	0.14	2.60

Table 5. Scapolite analyses from the BCF.

Sample	SiO <sub>2</sub>	TiO <sub>2</sub>	Al <sub>2</sub> O <sub>3</sub>	Cr <sub>2</sub> O <sub>3</sub>	FeO	MnO	MgO	CaO	Na <sub>2</sub> O	Total
089-p1	46.76	0.00	30.30	0.00	0.01	0.00	0.01	16.72	2.10	95.90
089-p1	46.50	0.00	30.77	0.00	0.02	0.00	0.02	17.01	1.97	96.28
089-p1	46.82	0.01	30.44	0.05	0.00	0.00	0.02	16.70	2.10	96.13
089-p1	46.90	0.01	30.26	0.00	0.00	0.00	0.01	16.56	2.12	95.85
089-p2	46.80	0.02	30.67	0.01	0.00	0.00	0.01	16.95	1.84	96.29
089-p2	46.96	0.00	30.58	0.00	0.03	0.00	0.00	17.00	1.96	96.53
089-p2	46.62	0.00	30.31	0.01	0.00	0.00	0.00	16.98	1.97	95.89
089-p2	46.91	0.00	30.78	0.00	0.00	0.00	0.02	16.66	1.97	96.35
<b>Min</b>	46.50	0.00	30.26	0.00	0.00	0.00	0.00	16.56	1.84	95.85
<b>Max</b>	46.96	0.02	30.78	0.05	0.03	0.00	0.02	17.01	2.12	96.53
<b>Mean</b>	46.78	0.01	30.51	0.01	0.01	0.00	0.01	16.82	2.00	96.15

Sample	Si	Ti	Al	Cr	Fe	Mn	Mg	Ca	Na	Me*
089-p1	6.72	0.00	5.13	0.00	0.00	0.00	0.00	2.57	0.58	81.54
089-p1	6.66	0.00	5.20	0.00	0.00	0.00	0.00	2.61	0.55	82.71
089-p1	6.71	0.00	5.14	0.01	0.00	0.00	0.00	2.56	0.58	81.51
089-p1	6.73	0.00	5.12	0.00	0.00	0.00	0.00	2.55	0.59	81.17
089-p2	6.69	0.00	5.17	0.00	0.00	0.00	0.00	2.60	0.51	83.64
089-p2	6.70	0.00	5.15	0.00	0.00	0.00	0.00	2.60	0.54	82.74
089-p2	6.70	0.00	5.14	0.00	0.00	0.00	0.00	2.62	0.55	82.63
089-p2	6.70	0.00	5.18	0.00	0.00	0.00	0.00	2.55	0.55	82.41
<b>Min</b>	6.66	0.00	5.12	0.00	0.00	0.00	0.00	2.55	0.51	81.17
<b>Max</b>	6.73	0.00	5.20	0.01	0.00	0.00	0.00	2.62	0.59	83.64
<b>Mean</b>	6.70	0.00	5.15	0.00	0.00	0.00	0.00	2.58	0.56	82.29

\* Me = Meionite

Table 6. Plagioclase and K-feldspar analyses from the BCF.

Sample	Desc	SiO <sub>2</sub>	Al <sub>2</sub> O <sub>3</sub>	FeO	MgO	CaO	Na <sub>2</sub> O	K <sub>2</sub> O	Total
Plag-1	089:F3-1	46.32	33.93	0.03	0.03	17.54	1.52	0.05	99.41
Plag-2	089:F3-2	46.33	33.97	0.03	0.01	17.11	1.61	0.07	99.13
Plag-3	089:F3-3	46.61	34.11	0.03	0.01	17.37	1.64	0.08	99.83
Plag-4	089:F3-4	47.97	33.74	0.01	0.01	16.89	2.05	0.09	100.75
Plag-5	089:F9-1	46.66	33.75	0.04	0.01	17.25	1.84	0.02	99.57
Plag-6	089:F9-2	46.86	34.15	0.00	0.00	17.19	1.69	0.02	99.91
Plag-7	089:F9-3	46.96	33.04	0.00	0.02	16.88	1.74	0.03	98.66
Min		46.32	33.04	0.00	0.00	16.88	1.52	0.02	98.66
Max		47.97	34.15	0.04	0.03	17.54	2.05	0.09	100.75
Mean		46.82	33.81	0.02	0.01	17.17	1.73	0.05	99.61

Sample	Si	Al	Fe <sup>2+</sup>	Mg	Ca	Na	K	X	Z	Ab	An	Or
Plag-1	8.57	7.39	0.00	0.01	3.48	0.55	0.01	15.96	4.05	13.60	86.10	0.30
Plag-2	8.59	7.41	0.01	0.00	3.40	0.58	0.02	16.00	4.00	14.50	85.10	0.40
Plag-3	8.58	7.40	0.00	0.00	3.43	0.58	0.02	15.98	4.03	14.50	85.10	0.40
Plag-4	8.73	7.23	0.00	0.00	3.30	0.72	0.02	15.97	4.04	17.90	81.60	0.50
Plag-5	8.62	7.34	0.01	0.00	3.41	0.66	0.00	15.95	4.08	16.20	83.80	0.10
Plag-6	8.61	7.39	0.00	0.00	3.38	0.60	0.01	16.00	3.99	15.00	84.80	0.20
Plag-7	8.73	7.23	0.00	0.01	3.36	0.63	0.01	15.96	4.00	15.70	84.20	0.20
Min	8.57	7.23	0.00	0.00	3.30	0.55	0.00	15.95	3.99	13.60	81.60	0.10
Max	8.73	7.41	0.01	0.01	3.48	0.72	0.02	16.00	4.08	17.90	86.10	0.50
Mean	8.63	7.34	0.00	0.00	3.39	0.62	0.01	15.97	4.03	15.34	84.39	0.30

Sample	Desc	SiO <sub>2</sub>	Al <sub>2</sub> O <sub>3</sub>	FeO	MgO	CaO	Na <sub>2</sub> O	K <sub>2</sub> O	Total
K-feld-1	089:F2-2	64.78	18.64	0.02	0.01	0.07	0.93	15.43	99.89
K-feld-2	089:F2-3	64.39	18.53	0.05	0.00	0.04	1.12	15.18	99.30
K-feld-3	089:F2-4	63.80	18.27	0.06	0.01	0.05	1.11	15.52	98.81
Min		63.80	18.27	0.02	0.00	0.04	0.93	15.18	98.81
Max		64.78	18.64	0.06	0.01	0.07	1.12	15.52	99.89
Mean		64.33	18.48	0.04	0.01	0.05	1.06	15.37	99.33

Sample	Si	Al	Fe <sup>2+</sup>	Mg	Ca	Na	K	X	Z	Ab	An	Or
K-feld-1	11.96	4.05	0.00	0.00	0.01	0.33	3.63	16.01	3.99	8.40	0.30	91.30
K-feld-2	11.95	4.05	0.01	0.00	0.01	0.40	3.59	16.00	4.01	10.10	0.20	89.70
K-feld-3	11.94	4.03	0.01	0.00	0.01	0.40	3.71	15.97	4.13	9.80	0.20	90.00
Min	11.94	4.03	0.00	0.00	0.01	0.33	3.59	15.97	3.99	8.40	0.20	89.70
Max	11.96	4.05	0.01	0.00	0.01	0.40	3.71	16.01	4.13	10.10	0.30	91.30
Mean	11.95	4.04	0.01	0.00	0.01	0.38	3.64	15.99	4.04	9.43	0.23	90.33

Table 7. Pyroxene analyses from the BCF.

Sample	Desc	SiO <sub>2</sub>	TiO <sub>2</sub>	Al <sub>2</sub> O <sub>3</sub>	Cr <sub>2</sub> O <sub>3</sub>	FeO	MnO	MgO	CaO	Na <sub>2</sub> O	K <sub>2</sub> O	Total	TSi	TAI	M1Al	M1Ti
<b>BCF-1</b>	103:p1-1	51.97	0.08	1.61	0.02	10.06	0.17	12.32	23.78	0.19	0.00	100.20	1.95	0.05	0.02	0.00
<b>BCF-2</b>	103:p1-3	52.10	0.09	1.74	0.03	10.19	0.16	12.26	23.93	0.17	0.00	100.67	1.95	0.06	0.02	0.00
<b>BCF-3</b>	103:p1-4	51.56	0.08	2.07	0.04	10.07	0.20	12.32	23.85	0.22	0.00	100.41	1.93	0.07	0.02	0.00
<b>BCF-4</b>	103:p2-1	52.86	0.04	1.11	0.04	10.12	0.19	12.63	23.81	0.19	0.00	100.99	1.97	0.03	0.02	0.00
<b>BCF-5</b>	103:p2-2	52.71	0.05	1.16	0.04	10.02	0.22	12.70	23.59	0.18	0.00	100.67	1.97	0.03	0.02	0.00
<b>BCF-6</b>	103:p2-3	51.78	0.08	1.33	0.04	9.95	0.19	12.31	23.51	0.18	0.00	99.37	1.96	0.04	0.02	0.00
<b>BCF-7</b>	103:p2-4	52.31	0.06	1.09	0.02	10.01	0.21	12.46	23.37	0.14	0.00	99.67	1.97	0.03	0.02	0.00
<b>BCF-8</b>	103:p3-2	52.11	0.11	1.48	0.02	9.99	0.19	12.29	23.99	0.19	0.00	100.37	1.95	0.05	0.02	0.00
<b>BCF-9</b>	103:p3-3	51.82	0.04	1.46	0.01	9.79	0.20	12.36	24.31	0.15	0.00	100.14	1.94	0.06	0.01	0.00
<b>BCF-10</b>	103:p3-4	52.47	0.09	1.30	0.03	9.89	0.16	12.46	24.44	0.16	0.00	101.00	1.95	0.05	0.01	0.00
<b>BCF-11</b>	103:p4-1	52.81	0.09	1.46	0.02	9.69	0.18	12.65	23.88	0.17	0.00	100.95	1.96	0.04	0.03	0.00
<b>BCF-12</b>	103:p4-2	51.74	0.10	1.50	0.02	9.72	0.18	12.47	23.72	0.18	0.00	99.63	1.95	0.05	0.02	0.00
<b>BCF-13</b>	103:p4-4	51.72	0.09	1.29	0.06	9.77	0.19	12.61	23.91	0.18	0.00	99.82	1.94	0.06	0.00	0.00
<b>Min</b>		51.56	0.04	1.09	0.01	9.69	0.16	12.26	23.37	0.14	0.00	99.37	1.93	0.03	0.00	0.00
<b>Max</b>		52.86	0.11	2.07	0.06	10.19	0.22	12.70	24.44	0.22	0.00	101.00	1.97	0.07	0.03	0.00
<b>Mean</b>		52.15	0.08	1.43	0.03	9.94	0.19	12.45	23.85	0.18	0.00	100.30	1.95	0.05	0.02	0.00

Sample	M1Fe <sup>3+</sup>	M1Fe <sup>2+</sup>	M1Cr	M1Mg	M2Mg	M2Fe <sup>2+</sup>	M2Mn	M2Ca	M2Na	Ca	Mg	Fe <sup>2+</sup>	Wo	En	Fs
<b>BCF-1</b>	0.04	0.25	0.00	0.69	0.00	0.03	0.01	0.96	0.01	49.67	35.80	14.53	48.62	35.05	16.33
<b>BCF-2</b>	0.04	0.25	0.00	0.68	0.00	0.03	0.01	0.96	0.01	49.77	35.48	14.75	48.77	34.76	16.47
<b>BCF-3</b>	0.07	0.23	0.00	0.69	0.00	0.02	0.01	0.96	0.02	50.33	36.17	13.50	48.66	34.98	16.36
<b>BCF-4</b>	0.03	0.25	0.00	0.70	0.00	0.03	0.01	0.95	0.01	48.91	36.10	14.99	48.17	35.55	16.28
<b>BCF-5</b>	0.03	0.25	0.00	0.71	0.00	0.04	0.01	0.94	0.01	48.56	36.37	15.07	47.89	35.88	16.23
<b>BCF-6</b>	0.03	0.25	0.00	0.69	0.00	0.03	0.01	0.95	0.01	49.25	35.88	14.87	48.42	35.28	16.31
<b>BCF-7</b>	0.01	0.26	0.00	0.70	0.00	0.04	0.01	0.94	0.01	48.32	35.85	15.83	48.00	35.61	16.39
<b>BCF-8</b>	0.04	0.25	0.00	0.69	0.00	0.02	0.01	0.96	0.01	49.95	35.60	14.45	48.92	34.87	16.21
<b>BCF-9</b>	0.06	0.24	0.00	0.69	0.00	0.01	0.01	0.98	0.01	50.80	35.94	13.27	49.30	34.88	15.82
<b>BCF-10</b>	0.05	0.25	0.00	0.69	0.00	0.01	0.01	0.97	0.01	50.43	35.78	13.79	49.25	34.94	15.81
<b>BCF-11</b>	0.02	0.25	0.00	0.70	0.00	0.03	0.01	0.95	0.01	48.99	36.11	14.90	48.55	35.78	15.67
<b>BCF-12</b>	0.04	0.24	0.00	0.70	0.00	0.02	0.01	0.96	0.01	49.71	36.36	13.92	48.61	35.56	15.84
<b>BCF-13</b>	0.06	0.23	0.00	0.71	0.00	0.02	0.01	0.96	0.01	50.14	36.79	13.07	48.57	35.64	15.80
<b>Min</b>	0.01	0.23	0.00	0.68	0.00	0.01	0.01	0.94	0.01	48.32	35.48	13.07	47.89	34.76	15.67
<b>Max</b>	0.07	0.26	0.00	0.71	0.00	0.04	0.01	0.98	0.02	50.80	36.79	15.83	49.30	35.88	16.47
<b>Mean</b>	0.04	0.25	0.00	0.69	0.00	0.02	0.01	0.96	0.01	49.60	36.02	14.38	48.59	35.29	16.12



Table 8. Biotite analyses from the BCF.

Sample	SiO <sub>2</sub>	TiO <sub>2</sub>	Al <sub>2</sub> O <sub>3</sub>	Cr <sub>2</sub> O <sub>3</sub>	FeO	MnO	MgO	CaO	Na <sub>2</sub> O	K <sub>2</sub> O	Total	Si
<b>089:m1-1</b>	46.10	1.57	33.87	0.12	0.15	0.00	2.10	0.01	0.26	10.64	94.82	5.87
<b>089:m1-2</b>	45.74	1.82	33.25	0.03	0.16	0.00	2.03	0.03	0.33	10.80	94.19	5.88
<b>089:m1-3</b>	47.23	1.40	34.45	0.10	0.12	0.00	2.13	0.03	0.26	10.46	96.18	5.91
<b>089:m1-4</b>	47.14	1.37	33.92	0.08	0.12	0.03	1.96	0.00	0.30	10.86	95.78	5.94
<b>089:m1-5</b>	46.72	1.82	33.23	0.04	0.09	0.00	2.18	0.00	0.29	10.48	94.85	5.94
<b>Min</b>	45.74	1.37	33.23	0.03	0.09	0.00	1.96	0.00	0.26	10.46	94.19	5.87
<b>Max</b>	47.23	1.82	34.45	0.12	0.16	0.03	2.18	0.03	0.33	10.86	96.18	5.94
<b>Mean</b>	46.59	1.60	33.74	0.07	0.13	0.01	2.08	0.01	0.29	10.65	95.16	5.91

Sample	Al IV	Sum_T	Al VI	Ti	Fe <sup>2+</sup>	Cr	Mn	Mg	Ca	Na	K	Cations	Fe/(Fe+Mg)
<b>089:m1-1</b>	2.13	8.00	2.95	0.15	0.02	0.01	0.00	0.40	0.00	0.06	1.73	5.32	0.04
<b>089:m1-2</b>	2.12	8.00	2.91	0.18	0.02	0.00	0.00	0.39	0.00	0.08	1.77	5.35	0.04
<b>089:m1-3</b>	2.09	8.00	2.99	0.13	0.01	0.01	0.00	0.40	0.00	0.06	1.67	5.28	0.03
<b>089:m1-4</b>	2.06	8.00	2.97	0.13	0.01	0.01	0.00	0.37	0.00	0.07	1.75	5.31	0.03
<b>089:m1-5</b>	2.06	8.00	2.91	0.17	0.01	0.00	0.00	0.41	0.00	0.07	1.70	5.28	0.02
<b>Min</b>	2.06	8.00	2.91	0.13	0.01	0.00	0.00	0.37	0.00	0.06	1.67	5.28	0.02
<b>Max</b>	2.13	8.00	2.99	0.18	0.02	0.01	0.00	0.41	0.00	0.08	1.77	5.35	0.04
<b>Mean</b>	2.09	8.00	2.95	0.15	0.01	0.01	0.00	0.39	0.00	0.07	1.72	5.31	0.03

Table 9. Garnet analyses from the GCS.

Sample	Desc	SiO <sub>2</sub>	TiO <sub>2</sub>	Al <sub>2</sub> O <sub>3</sub>	Cr <sub>2</sub> O <sub>3</sub>	FeO	MnO	MgO	CaO	Na <sub>2</sub> O	Total	FeO <sub>calc</sub>	Fe <sub>2</sub> O <sub>3calc</sub>	Total <sub>calc</sub>	TSi	TAl	Sum_T
GCS-G-1	112:G1-1	39.38	0.38	19.35	0.57	0.08	0.52	0.55	37.87	0.00	98.69	0.87	0.97	100.46	2.99	0.01	3.00
GCS-G-2	112:G1-10	37.00	0.31	18.34	0.54	0.05	0.43	0.54	36.91	0.00	94.12	0.46	0.52	95.05	2.95	0.05	3.00
GCS-G-3	112:G1-2	38.38	0.34	18.86	0.56	0.08	0.64	0.55	37.01	0.00	96.42	0.27	0.30	96.91	3.00	0.01	3.00
GCS-G-4	112:G1-3	38.48	0.33	18.99	0.55	0.03	0.54	0.49	37.11	0.00	96.53	0.15	0.17	96.82	3.00	0.00	3.00
GCS-G-5	112:G1-4	38.48	0.34	18.87	0.51	0.04	0.58	0.56	36.80	0.00	96.18	0.10	0.11	96.34	3.01	0.00	3.01
GCS-G-6	112:G1-5	37.85	0.36	18.84	0.50	0.05	0.46	0.53	36.75	0.00	95.34	0.07	0.08	95.45	2.99	0.01	3.00
GCS-G-7	112:G1-6	37.98	0.35	18.71	0.55	0.08	0.55	0.55	37.00	0.00	95.75	0.07	0.08	95.83	2.99	0.01	3.00
GCS-G-8	112:G1-7	38.07	0.33	18.93	0.48	0.00	0.47	0.53	37.04	0.00	95.85	0.04	0.04	95.93	2.99	0.01	3.00
GCS-G-9	112:G1-9	37.41	0.34	18.78	0.46	0.04	0.35	0.53	36.90	0.00	94.80	0.04	0.05	94.84	2.97	0.03	3.00
GCS-G-10	112:G2-1	38.01	0.44	17.05	0.99	0.01	0.77	0.49	36.58	0.00	94.34	0.02	0.03	94.39	3.05	0.00	3.05
GCS-G-11	112:G2-10	37.58	0.39	16.49	1.11	0.10	0.77	0.47	36.24	0.00	93.15	0.06	0.07	93.18	3.06	0.00	3.06
GCS-G-12	112:G2-2	38.13	0.44	17.00	1.01	0.00	0.71	0.49	36.53	0.00	94.31	0.03	0.04	94.37	3.06	0.00	3.06
GCS-G-13	112:G2-3	38.04	0.42	16.96	0.95	0.04	0.77	0.45	36.24	0.00	93.88	0.04	0.04	93.92	3.07	0.00	3.07
GCS-G-14	112:G2-4	37.92	0.40	16.74	1.07	0.03	0.81	0.49	36.30	0.00	93.74	0.03	0.04	93.78	3.06	0.00	3.06
GCS-G-15	112:G2-5	38.09	0.35	16.35	1.14	0.04	0.68	0.46	36.46	0.00	93.58	0.04	0.04	93.61	3.08	0.00	3.08
GCS-G-16	112:G2-6	37.75	0.41	16.62	1.01	0.03	0.87	0.47	36.07	0.00	93.22	0.03	0.04	93.26	3.07	0.00	3.07
GCS-G-17	112:G2-8	37.76	0.41	16.67	1.01	0.02	0.87	0.47	36.11	0.00	93.32	0.03	0.03	93.36	3.06	0.00	3.06
GCS-G-18	112:G2-9	37.50	0.38	16.50	1.13	0.05	0.77	0.46	35.94	0.00	92.74	0.04	0.04	92.77	3.06	0.00	3.06
GCS-G-19	112:G3-1	38.42	0.27	18.63	0.71	0.07	0.15	0.57	37.24	0.00	96.05	0.05	0.06	96.10	3.01	0.00	3.01
GCS-G-20	112:G3-10	38.99	0.33	19.63	0.56	0.03	0.42	0.54	37.20	0.00	97.69	0.04	0.04	97.75	3.00	0.00	3.00
GCS-G-21	112:G3-2	38.86	0.28	18.80	0.79	0.07	0.17	0.54	37.65	0.00	97.17	0.06	0.06	97.21	3.01	0.00	3.01
GCS-G-22	112:G3-3	38.83	0.24	19.23	0.71	0.07	0.32	0.52	37.45	0.00	97.36	0.06	0.07	97.43	3.00	0.00	3.00
GCS-G-23	112:G3-4	38.84	0.31	19.04	0.60	0.06	0.37	0.55	37.36	0.00	97.13	0.06	0.07	97.20	3.01	0.00	3.01
GCS-G-24	112:G3-5	38.76	0.27	19.00	0.65	0.05	0.48	0.52	37.28	0.00	97.00	0.05	0.06	97.06	3.01	0.00	3.01
GCS-G-25	112:G3-6	38.40	0.36	18.91	0.66	0.07	0.53	0.57	37.13	0.00	96.64	0.06	0.07	96.70	2.99	0.01	3.00
GCS-G-26	112:G3-7	39.08	0.32	18.80	0.66	0.06	0.54	0.53	37.09	0.00	97.08	0.06	0.07	97.15	3.04	0.00	3.04
GCS-G-27	112:G3-8	38.52	0.37	18.77	0.72	0.01	0.38	0.53	37.19	0.00	96.49	0.04	0.04	96.56	3.01	0.00	3.01
GCS-G-28	112:G3-9	38.53	0.31	18.96	0.65	0.07	0.24	0.53	37.51	0.00	96.80	0.06	0.06	96.84	3.00	0.00	3.00
Min		37.00	0.24	16.35	0.46	0.00	0.15	0.45	35.94	0.00	92.74	0.02	0.03	92.77	2.95	0.00	3.00
Max		39.38	0.44	19.63	1.14	0.10	0.87	0.57	37.87	0.00	98.69	0.87	0.97	100.46	3.08	0.05	3.08
Mean		38.25	0.35	18.21	0.74	0.05	0.54	0.52	36.89	0.00	95.55	0.11	0.12	95.72	3.02	0.01	3.02

Table 9. Continue 1.

Sample	Al VI	Ti	Cr	Sum_A	Fe <sup>2+</sup>	Mg	Mn	Ca	Na	Sum_B	Alm	And	Gross	Pyrope	Spess	Uvaro
GCS-G-1	1.72	0.02	0.03	1.77	0.06	0.06	0.03	3.08	0.00	3.23	1.72	0.00	93.40	1.91	1.03	1.94
GCS-G-2	1.67	0.02	0.03	1.72	0.03	0.06	0.03	3.15	0.00	3.28	0.94	0.00	94.25	1.97	0.88	1.96
GCS-G-3	1.73	0.02	0.04	1.78	0.02	0.06	0.04	3.09	0.00	3.22	0.56	0.00	94.21	1.98	1.32	1.94
GCS-G-4	1.74	0.02	0.03	1.80	0.01	0.06	0.04	3.10	0.00	3.20	0.31	0.00	94.90	1.79	1.11	1.90
GCS-G-5	1.74	0.02	0.03	1.79	0.01	0.07	0.04	3.09	0.00	3.20	0.20	0.00	94.80	2.06	1.20	1.75
GCS-G-6	1.74	0.02	0.03	1.79	0.01	0.06	0.03	3.11	0.00	3.21	0.15	0.00	95.21	1.94	0.96	1.75
GCS-G-7	1.72	0.02	0.03	1.78	0.01	0.06	0.04	3.12	0.00	3.22	0.15	0.00	94.81	1.99	1.13	1.92
GCS-G-8	1.74	0.02	0.03	1.79	0.00	0.06	0.03	3.12	0.00	3.21	0.08	0.00	95.36	1.92	0.97	1.67
GCS-G-9	1.72	0.02	0.03	1.77	0.00	0.06	0.02	3.14	0.00	3.23	0.08	0.00	95.65	1.93	0.72	1.62
GCS-G-10	1.61	0.03	0.06	1.70	0.00	0.06	0.05	3.14	0.00	3.25	0.05	0.00	92.89	1.79	1.60	3.67
GCS-G-11	1.58	0.02	0.07	1.67	0.00	0.06	0.05	3.16	0.00	3.27	0.13	0.00	92.24	1.75	1.63	4.27
GCS-G-12	1.61	0.03	0.06	1.70	0.00	0.06	0.05	3.14	0.00	3.25	0.07	0.00	92.86	1.81	1.48	3.78
GCS-G-13	1.61	0.03	0.06	1.70	0.00	0.05	0.05	3.13	0.00	3.24	0.08	0.00	93.03	1.68	1.62	3.58
GCS-G-14	1.59	0.02	0.07	1.68	0.00	0.06	0.06	3.14	0.00	3.26	0.07	0.00	92.39	1.80	1.69	4.05
GCS-G-15	1.56	0.02	0.07	1.65	0.00	0.06	0.05	3.16	0.00	3.27	0.08	0.00	92.38	1.70	1.43	4.41
GCS-G-16	1.59	0.03	0.07	1.68	0.00	0.06	0.06	3.14	0.00	3.26	0.07	0.00	92.52	1.73	1.84	3.84
GCS-G-17	1.59	0.03	0.07	1.68	0.00	0.06	0.06	3.14	0.00	3.26	0.06	0.00	92.51	1.74	1.84	3.85
GCS-G-18	1.59	0.02	0.07	1.68	0.00	0.06	0.05	3.14	0.00	3.26	0.08	0.00	92.24	1.72	1.63	4.33
GCS-G-19	1.72	0.02	0.04	1.78	0.00	0.07	0.01	3.13	0.00	3.21	0.11	0.00	95.07	2.06	0.31	2.46
GCS-G-20	1.78	0.02	0.03	1.83	0.00	0.06	0.03	3.07	0.00	3.16	0.08	0.00	95.24	1.96	0.87	1.86
GCS-G-21	1.72	0.02	0.05	1.78	0.00	0.06	0.01	3.13	0.00	3.21	0.11	0.00	94.89	1.94	0.36	2.70
GCS-G-22	1.75	0.01	0.04	1.81	0.00	0.06	0.02	3.10	0.00	3.19	0.13	0.00	94.93	1.87	0.66	2.40
GCS-G-23	1.74	0.02	0.04	1.79	0.00	0.06	0.02	3.10	0.00	3.20	0.12	0.00	95.09	1.98	0.76	2.05
GCS-G-24	1.74	0.02	0.04	1.79	0.00	0.06	0.03	3.10	0.00	3.20	0.11	0.00	94.81	1.88	0.99	2.22
GCS-G-25	1.73	0.02	0.04	1.79	0.00	0.07	0.04	3.10	0.00	3.21	0.13	0.00	94.43	2.07	1.10	2.28
GCS-G-26	1.72	0.02	0.04	1.78	0.00	0.06	0.04	3.09	0.00	3.19	0.12	0.00	94.57	1.91	1.12	2.28
GCS-G-27	1.73	0.02	0.04	1.79	0.00	0.06	0.03	3.11	0.00	3.20	0.08	0.00	94.72	1.94	0.79	2.48
GCS-G-28	1.73	0.02	0.04	1.79	0.00	0.06	0.02	3.13	0.00	3.21	0.11	0.00	95.23	1.93	0.49	2.24
Min	1.56	0.01	0.03	1.65	0.00	0.05	0.01	3.07	0.00	3.16	0.05	0.00	92.24	1.68	0.31	1.62
Max	1.78	0.03	0.07	1.83	0.06	0.07	0.06	3.16	0.00	3.28	1.72	0.00	95.65	2.07	1.84	4.41
Mean	1.69	0.02	0.05	1.75	0.01	0.06	0.04	3.12	0.00	3.22	0.21	0.00	94.09	1.88	1.13	2.69

Table 9.b Garnet analyses from the GCS.

Sample	Desc	SiO <sub>2</sub>	TiO <sub>2</sub>	Al <sub>2</sub> O <sub>3</sub>	Cr <sub>2</sub> O <sub>3</sub>	FeO	MnO	MgO	CaO	Na <sub>2</sub> O	Total	FeO <sub>calc</sub>	Fe <sub>2</sub> O <sub>3calc</sub>	Total <sub>calc</sub>	TSi	TAl	Sum_T
GCS-G-29	088:G1-1	37.27	0.37	12.68	1.35	0.05	0.55	0.36	36.47	0.00	89.10	0.80	0.88	90.74	3.16	0.00	3.16
GCS-G-30	088:G1-2	37.62	0.32	12.96	1.33	0.08	0.56	0.35	36.71	0.00	89.93	0.05	0.05	89.95	3.18	0.00	3.18
GCS-G-31	088:G1-3	37.50	0.40	13.15	1.21	0.04	0.56	0.36	36.78	0.00	90.00	0.04	0.05	90.06	3.17	0.00	3.17
GCS-G-32	088:G1-4	37.73	0.30	12.37	1.56	0.10	0.55	0.35	36.27	0.00	89.24	0.07	0.08	89.29	3.22	0.00	3.22
GCS-G-33	088:G1-5	37.71	0.30	12.64	1.33	0.06	0.54	0.33	36.48	0.00	89.39	0.07	0.08	89.47	3.21	0.00	3.21
GCS-G-34	088:G1-6	37.81	0.36	12.75	1.46	0.02	0.64	0.32	36.58	0.00	89.95	0.05	0.05	90.02	3.20	0.00	3.20
GCS-G-35	088:G1-7	37.38	0.39	12.64	1.20	0.04	0.64	0.36	36.76	0.00	89.41	0.04	0.05	89.46	3.18	0.00	3.18
GCS-G-36	088:G1-8	37.44	0.37	12.57	1.29	0.00	0.50	0.33	36.44	0.00	88.94	0.02	0.02	88.98	3.20	0.00	3.20
GCS-G-37	088:G1-9	37.73	0.33	12.51	1.65	0.06	0.77	0.31	36.27	0.00	89.62	0.04	0.04	89.65	3.21	0.00	3.21
GCS-G-38	088:G1-10	37.98	0.35	12.76	1.47	0.04	0.55	0.33	36.78	0.00	90.26	0.42	0.46	91.11	3.19	0.00	3.19
GCS-G-39	088:G1-11	37.65	0.36	12.58	1.52	0.05	0.62	0.34	36.44	0.00	89.56	0.23	0.26	90.00	3.20	0.00	3.20
GCS-G-40	088:G1-12	37.34	0.36	12.44	1.55	0.02	0.67	0.33	36.45	0.00	89.16	0.13	0.14	89.41	3.19	0.00	3.19
GCS-G-41	088:G1-13	37.42	0.37	12.45	1.55	0.04	0.49	0.35	36.63	0.00	89.31	0.08	0.09	89.45	3.19	0.00	3.19
GCS-G-42	088:G1-14	37.47	0.33	12.55	1.60	0.04	0.55	0.37	36.41	0.00	89.32	0.06	0.07	89.41	3.19	0.00	3.19
GCS-G-43	088:G1-15	37.06	0.38	12.33	1.66	0.05	0.54	0.35	36.34	0.00	88.72	0.06	0.06	88.79	3.18	0.00	3.18
GCS-G-44	088:G1-16	37.20	0.36	12.26	1.62	0.03	0.58	0.38	36.61	0.00	89.04	0.04	0.05	89.10	3.18	0.00	3.18
GCS-G-45	088:G1-17	37.44	0.37	12.21	1.83	0.03	0.64	0.35	36.54	0.00	89.41	0.03	0.04	89.45	3.19	0.00	3.19
GCS-G-46	088:G1-18	37.38	0.42	12.41	1.95	0.01	0.70	0.31	36.43	0.00	89.61	0.02	0.03	89.64	3.18	0.00	3.18
GCS-G-47	088:G1-19	37.25	0.37	12.91	1.44	0.00	0.51	0.40	36.58	0.00	89.45	0.01	0.01	89.48	3.17	0.00	3.17
GCS-G-48	088:G1-20	37.82	0.38	13.51	1.44	0.05	0.49	0.46	36.87	0.00	91.03	0.05	0.06	91.08	3.16	0.00	3.16
Min		37.06	0.33	12.21	1.44	0.00	0.49	0.31	36.34	0.00	88.72	0.01	0.01	88.79	3.16	0.00	3.16
Max		37.98	0.42	13.51	1.95	0.05	0.70	0.46	36.87	0.00	91.03	0.42	0.46	91.11	3.20	0.00	3.20
Mean		37.46	0.37	12.58	1.60	0.03	0.58	0.36	36.55	0.00	89.53	0.10	0.12	89.72	3.18	0.00	3.18

Table 9.b Continued.

Sample	Al VI	Ti	Cr	Sum A	Fe <sup>2+</sup>	Mg	Mn	Ca	Na	Sum B	Alm	And	Gross	Pyrope	Spess	Uvaro
GCS-G-29	1.27	0.02	0.09	1.38	0.06	0.05	0.04	3.32	0.00	3.46	1.63	0.00	89.36	1.31	1.15	6.55
GCS-G-30	1.29	0.02	0.09	1.40	0.00	0.04	0.04	3.33	0.00	3.42	0.10	0.00	91.11	1.29	1.17	6.33
GCS-G-31	1.31	0.03	0.08	1.42	0.00	0.05	0.04	3.33	0.00	3.42	0.09	0.00	91.67	1.33	1.18	5.73
GCS-G-32	1.24	0.02	0.11	1.37	0.01	0.05	0.04	3.32	0.00	3.41	0.15	0.00	89.67	1.32	1.17	7.69
GCS-G-33	1.27	0.02	0.09	1.38	0.01	0.04	0.04	3.33	0.00	3.41	0.14	0.00	90.98	1.24	1.14	6.50
GCS-G-34	1.27	0.02	0.10	1.39	0.00	0.04	0.05	3.32	0.00	3.41	0.10	0.00	90.34	1.19	1.34	7.03
GCS-G-35	1.27	0.03	0.08	1.37	0.00	0.05	0.05	3.35	0.00	3.45	0.09	0.00	91.38	1.32	1.33	5.89
GCS-G-36	1.27	0.02	0.09	1.38	0.00	0.04	0.04	3.34	0.00	3.42	0.04	0.00	91.33	1.23	1.05	6.34
GCS-G-37	1.25	0.02	0.11	1.39	0.00	0.04	0.06	3.31	0.00	3.40	0.08	0.00	89.15	1.14	1.62	8.00
GCS-G-38	1.26	0.02	0.10	1.38	0.03	0.04	0.04	3.31	0.00	3.42	0.86	0.00	89.75	1.19	1.15	7.05
GCS-G-39	1.26	0.02	0.10	1.38	0.02	0.04	0.05	3.32	0.00	3.42	0.49	0.00	89.56	1.26	1.31	7.39
GCS-G-40	1.25	0.02	0.11	1.38	0.01	0.04	0.05	3.33	0.00	3.43	0.27	0.00	89.51	1.21	1.42	7.59
GCS-G-41	1.25	0.02	0.10	1.38	0.01	0.05	0.04	3.35	0.00	3.43	0.17	0.00	89.93	1.31	1.04	7.55
GCS-G-42	1.26	0.02	0.11	1.39	0.01	0.05	0.04	3.33	0.00	3.42	0.13	0.00	89.57	1.37	1.17	7.77
GCS-G-43	1.25	0.03	0.11	1.39	0.00	0.05	0.04	3.34	0.00	3.43	0.12	0.00	89.30	1.31	1.15	8.12
GCS-G-44	1.24	0.02	0.11	1.37	0.00	0.05	0.04	3.36	0.00	3.45	0.09	0.00	89.29	1.39	1.23	8.01
GCS-G-45	1.23	0.02	0.12	1.37	0.00	0.04	0.05	3.34	0.00	3.43	0.07	0.00	88.33	1.29	1.34	8.97
GCS-G-46	1.25	0.03	0.13	1.40	0.00	0.04	0.05	3.32	0.00	3.42	0.05	0.00	88.00	1.14	1.48	9.33
GCS-G-47	1.29	0.02	0.10	1.41	0.00	0.05	0.04	3.33	0.00	3.42	0.03	0.00	90.59	1.47	1.07	6.85
GCS-G-48	1.33	0.02	0.10	1.45	0.00	0.06	0.04	3.30	0.00	3.40	0.10	0.00	90.60	1.70	1.03	6.57
<b>Min</b>	1.23	0.02	0.10	1.37	0.00	0.04	0.04	3.30	0.00	3.40	0.03	0.00	88.00	1.14	1.03	6.57
<b>Max</b>	1.33	0.03	0.13	1.45	0.03	0.06	0.05	3.36	0.00	3.45	0.86	0.00	90.60	1.70	1.48	9.33
<b>Mean</b>	1.26	0.02	0.11	1.39	0.01	0.05	0.04	3.33	0.00	3.42	0.21	0.00	89.49	1.33	1.22	7.74

Table 9.c. Garnet analyses from the GCS.

Sample	Desc	SiO <sub>2</sub>	TiO <sub>2</sub>	Al <sub>2</sub> O <sub>3</sub>	Cr <sub>2</sub> O <sub>3</sub>	V <sub>2</sub> O <sub>3</sub>	NiO	FeO	MnO	MgO	CaO	Na <sub>2</sub> O	K <sub>2</sub> O	Total	FeO <sub>calc</sub>	Fe <sub>2</sub> O <sub>3calc</sub>	Total <sub>calc</sub>	TSi
GCS-G-50	404-2-GT-1	38.85	0.27	21.05	0.08	2.10	0.00	0.04	0.17	0.51	35.86	0.03	0.00	98.96	0.02	0.02	98.96	3.01
GCS-G-51	404-2-GT-3	38.91	0.34	18.39	0.44	5.40	0.00	0.03	0.37	0.46	35.93	0.00	0.01	100.28	0.03	0.03	100.30	3.09
GCS-G-52	404-2-GT-4	39.24	0.30	20.40	0.30	2.66	0.04	0.02	0.17	0.45	36.25	0.00	0.02	99.85	0.02	0.03	99.88	3.04
GCS-G-53	404-4-GT-1	38.32	0.25	18.08	0.41	5.50	0.00	0.05	0.22	0.41	35.64	0.00	0.00	98.88	0.04	0.04	98.91	3.09
GCS-G-54	404-4-GT-2	38.83	0.17	19.97	0.26	3.47	0.00	0.08	0.22	0.49	36.19	0.04	0.00	99.72	0.06	0.07	99.76	3.03
GCS-G-55	404-4-GT-3	37.90	0.20	17.90	0.45	5.66	0.00	0.03	0.27	0.41	35.86	0.01	0.00	98.69	0.04	0.05	98.75	3.07
Min		37.90	0.17	17.90	0.08	2.10	0.00	0.02	0.17	0.41	35.64	0.00	0.00	98.69	0.02	0.02	98.75	3.01
Max		39.24	0.34	21.05	0.45	5.66	0.04	0.08	0.37	0.51	36.25	0.04	0.02	100.28	0.06	0.07	100.30	3.09
Mean		38.68	0.26	19.30	0.32	4.13	0.01	0.04	0.24	0.46	35.96	0.01	0.01	99.40	0.03	0.04	99.43	3.05

Sample	Al VI	Ti	Cr	V	Sum_A	Fe <sup>2+</sup>	Ni	Mg	Mn	Ca	Na	Sum_B	Alm	And	Gross	Pyrope	Spess	Uvaro
GCS-G-50	1.92	0.02	0.01	0.13	2.07	0.00	0.00	0.06	0.01	2.98	0.01	3.05	0.04	0.00	97.26	1.93	0.37	0.25
GCS-G-51	1.72	0.02	0.03	0.33	2.10	0.00	0.00	0.05	0.03	3.06	0.00	3.14	0.05	0.00	95.86	1.74	0.79	1.56
GCS-G-52	1.86	0.02	0.02	0.16	2.05	0.00	0.00	0.05	0.01	3.01	0.00	3.07	0.05	0.00	96.93	1.69	0.36	0.97
GCS-G-53	1.72	0.02	0.03	0.34	2.10	0.00	0.00	0.05	0.02	3.08	0.00	3.15	0.08	0.00	96.39	1.57	0.48	1.49
GCS-G-54	1.84	0.01	0.02	0.21	2.07	0.00	0.00	0.06	0.02	3.03	0.01	3.11	0.12	0.00	96.52	1.84	0.47	0.86
GCS-G-55	1.71	0.01	0.03	0.35	2.10	0.00	0.00	0.05	0.02	3.11	0.00	3.18	0.09	0.00	96.07	1.56	0.58	1.65
Min	1.71	0.01	0.01	0.13	2.05	0.00	0.00	0.05	0.01	2.98	0.00	3.05	0.04	0.00	95.86	1.56	0.36	0.25
Max	1.92	0.02	0.03	0.35	2.10	0.00	0.00	0.06	0.03	3.11	0.01	3.18	0.12	0.00	97.26	1.93	0.79	1.65
Mean	1.79	0.02	0.02	0.25	2.08	0.00	0.00	0.05	0.02	3.04	0.00	3.12	0.07	0.00	96.51	1.72	0.51	1.13

Table 10. Pyroxene analyses from the GCS.

Sample	Desc	SiO <sub>2</sub>	TiO <sub>2</sub>	Al <sub>2</sub> O <sub>3</sub>	Cr <sub>2</sub> O <sub>3</sub>	FeO	MnO	MgO	CaO	Na <sub>2</sub> O	K <sub>2</sub> O	Total	TSi	TAI	MIAI	MITi
GSC-1	112:P1-1	53.47	0.05	1.18	0.01	0.08	0.18	18.00	25.45	0.11	0.00	98.53	1.95	0.05	0.01	0.00
GSC-2	112:P1-2	54.13	0.03	1.29	0.01	0.13	0.15	18.12	25.78	0.11	0.00	99.75	1.96	0.05	0.01	0.00
GSC-3	112:P1-3	54.41	0.04	1.14	0.04	0.16	0.11	17.95	25.40	0.13	0.00	99.38	1.97	0.03	0.02	0.00
GSC-4	112:P1-4	54.52	0.02	0.89	0.04	0.13	0.12	18.12	25.63	0.09	0.00	99.56	1.97	0.03	0.01	0.00
GSC-5	112:P1-5	54.65	0.00	1.35	0.00	0.12	0.11	18.06	25.57	0.13	0.00	99.99	1.97	0.03	0.03	0.00
GSC-6	112:P1-6	54.07	0.02	1.18	0.03	0.12	0.15	18.22	25.73	0.14	0.00	99.66	1.95	0.05	0.00	0.00
GSC-7	112:P1-7	54.84	0.03	1.11	0.02	0.07	0.11	18.13	25.49	0.09	0.00	99.89	1.98	0.02	0.03	0.00
GSC-8	112:P1-8	54.66	0.03	1.29	0.02	0.09	0.11	18.12	25.55	0.14	0.00	100.01	1.97	0.03	0.02	0.00
GCS-9	404-1-1	54.49	0.09	1.79	0.64	0.11	0.01	17.30	25.61	0.22	0.01	100.27	1.97	0.04	0.04	0.00
GCS-10	404-1-2	54.90	0.01	1.21	0.15	0.08	0.06	17.71	25.93	0.15	0.03	100.23	1.98	0.02	0.03	0.00
GCS-11	404-1-3	53.92	0.01	1.89	0.65	0.09	0.12	17.04	25.15	0.22	0.02	99.11	1.97	0.03	0.05	0.00
GCS-12	88B:P1-2	55.04	0.01	0.91	0.06	0.11	0.20	17.89	26.05	0.10	0.02	100.39	1.98	0.02	0.02	0.00
GCS-13	88B:P1-3	54.49	0.02	0.95	0.02	0.09	0.22	17.76	25.82	0.12	0.02	99.51	1.98	0.02	0.02	0.00
GCS-14	88B:P1-4	54.78	0.04	1.04	0.04	0.09	0.19	17.83	25.84	0.11	0.02	99.98	1.98	0.02	0.02	0.00
GCS-15	88B:P2-1	54.88	0.04	1.50	0.03	0.11	0.24	17.93	25.35	0.13	0.02	100.23	1.98	0.03	0.04	0.00
GCS-16	88B:P2-2	54.11	0.04	1.50	0.03	0.10	0.21	17.75	25.54	0.16	0.02	99.46	1.96	0.04	0.03	0.00
GCS-17	88B:P2-3	54.12	0.04	1.31	0.01	0.11	0.25	17.81	25.38	0.13	0.02	99.18	1.97	0.03	0.02	0.00
GCS-18	88B:P2-4	54.35	0.05	1.19	0.03	0.12	0.42	17.88	25.33	0.15	0.02	99.54	1.97	0.03	0.02	0.00
GCS-19	88B:P3-1	53.89	0.02	1.70	0.02	0.08	0.21	17.69	25.36	0.17	0.02	99.16	1.96	0.04	0.03	0.00
GCS-20	88B:P3-2	53.73	0.02	1.71	0.04	0.12	0.28	17.67	25.38	0.19	0.02	99.16	1.95	0.05	0.03	0.00
GCS-21	88B:P3-3	54.36	0.02	1.67	0.03	0.09	0.22	17.76	25.65	0.19	0.02	100.01	1.96	0.04	0.03	0.00
GCS-22	88B:P3-4	54.23	0.03	1.49	0.05	0.09	0.24	17.65	25.65	0.15	0.02	99.60	1.97	0.04	0.03	0.00
<b>Min</b>		53.47	0.00	0.89	0.00	0.07	0.01	17.04	25.15	0.09	0.00	98.53	1.95	0.02	0.00	0.00
<b>Max</b>		55.04	0.09	1.89	0.65	0.16	0.42	18.22	26.05	0.22	0.03	100.39	1.98	0.05	0.05	0.00
<b>Mean</b>		54.37	0.03	1.33	0.09	0.10	0.18	17.84	25.57	0.14	0.01	99.66	1.97	0.03	0.02	0.00

Table 10. Continue 1.

Sample	M1Fe <sup>3+</sup>	M1Fe <sup>2+</sup>	M1Cr	M1Mg	M2Mg	M2Fe <sup>2+</sup>	M2Mn	M2Ca	M2Na	Ca	Mg	Fe <sup>2+</sup>	Wo	En	Fs
GSC-1	0.00	0.00	0.00	0.98	0.00	0.00	0.01	1.00	0.01	50.20	49.40	0.40	50.20	49.40	0.40
GSC-2	0.00	0.00	0.00	0.98	0.00	0.00	0.01	1.00	0.01	50.34	49.23	0.43	50.34	49.23	0.43
GSC-3	0.00	0.01	0.00	0.97	0.00	0.00	0.00	0.99	0.01	50.21	49.37	0.42	50.21	49.37	0.42
GSC-4	0.00	0.00	0.00	0.98	0.00	0.00	0.00	0.99	0.01	50.22	49.40	0.39	50.22	49.40	0.39
GSC-5	0.00	0.00	0.00	0.97	0.00	0.00	0.00	0.99	0.01	50.26	49.39	0.36	50.26	49.39	0.36
GSC-6	0.00	0.00	0.00	0.98	0.00	0.00	0.01	1.00	0.01	50.16	49.42	0.41	50.16	49.42	0.41
GSC-7	0.00	0.00	0.00	0.97	0.00	0.00	0.00	0.99	0.01	50.12	49.60	0.28	50.12	49.60	0.28
GSC-8	0.00	0.00	0.00	0.97	0.00	0.00	0.00	0.99	0.01	50.18	49.51	0.31	50.18	49.51	0.31
GCS-9	0.00	0.00	0.02	0.93	0.00	0.00	0.00	0.99	0.02	51.45	48.36	0.19	51.45	48.36	0.19
GCS-10	0.00	0.00	0.00	0.95	0.00	0.00	0.00	1.00	0.01	51.22	48.67	0.12	51.16	48.62	0.22
GCS-11	0.00	0.00	0.02	0.93	0.00	0.00	0.00	0.98	0.02	51.30	48.36	0.34	51.30	48.36	0.34
GCS-12	0.00	0.00	0.00	0.96	0.00	0.00	0.01	1.00	0.01	50.89	48.63	0.48	50.89	48.63	0.48
GCS-13	0.00	0.00	0.00	0.96	0.00	0.00	0.01	1.00	0.01	50.85	48.67	0.48	50.85	48.67	0.48
GCS-14	0.00	0.00	0.00	0.96	0.00	0.00	0.01	1.00	0.01	50.80	48.77	0.43	50.80	48.77	0.43
GCS-15	0.00	0.00	0.00	0.96	0.00	0.00	0.01	0.98	0.01	50.13	49.33	0.55	50.13	49.33	0.55
GCS-16	0.00	0.00	0.00	0.96	0.00	0.00	0.01	0.99	0.01	50.59	48.92	0.48	50.59	48.92	0.48
GCS-17	0.00	0.00	0.00	0.97	0.00	0.00	0.01	0.99	0.01	50.31	49.13	0.56	50.31	49.13	0.56
GCS-18	0.00	0.00	0.00	0.97	0.00	0.00	0.01	0.98	0.01	50.03	49.13	0.84	50.03	49.13	0.84
GCS-19	0.00	0.00	0.00	0.96	0.00	0.00	0.01	0.99	0.01	50.52	49.03	0.46	50.52	49.03	0.46
GCS-20	0.00	0.00	0.00	0.96	0.00	0.00	0.01	0.99	0.01	50.48	48.90	0.63	50.48	48.90	0.63
GCS-21	0.00	0.00	0.00	0.95	0.00	0.00	0.01	0.99	0.01	50.69	48.83	0.48	50.69	48.83	0.48
GCS-22	0.00	0.00	0.00	0.95	0.00	0.00	0.01	1.00	0.01	50.82	48.66	0.52	50.82	48.66	0.52
<b>Min</b>	0.00	0.00	0.00	0.93	0.00	0.00	0.00	0.98	0.01	50.03	48.36	0.12	50.03	48.36	0.19
<b>Max</b>	0.00	0.01	0.02	0.98	0.00	0.00	0.01	1.00	0.02	51.45	49.60	0.84	51.45	49.60	0.84
<b>Mean</b>	0.00	0.00	0.00	0.96	0.00	0.00	0.01	0.99	0.01	50.53	49.03	0.43	50.53	49.03	0.44



Table 11. Plagioclase analyses from the GCS.

Sample	Desc	SiO <sub>2</sub>	Al <sub>2</sub> O <sub>3</sub>	FeO	MgO	CaO	Na <sub>2</sub> O	K <sub>2</sub> O	Total
<b>Plag-1</b>	088B:F1-1	44.07	36.37	0.01	0.00	19.85	0.37	0.02	100.69
<b>Plag-2</b>	088B:F1-2	43.74	35.55	0.00	0.00	19.08	0.40	0.00	98.76
<b>Plag-3</b>	088B:F1-3	43.51	35.70	0.02	0.00	19.26	0.50	0.02	99.01
<b>Plag-4</b>	088B:F1-4	43.45	35.58	0.00	0.00	19.43	0.43	0.04	98.92
<b>Plag-5</b>	92-pl-1	42.23	36.01	0.04	0.01	20.86	0.48	0.01	99.64
<b>Plag-6</b>	92-pl-2	43.12	36.23	0.00	0.00	20.86	0.49	0.02	100.72
<b>Plag-7</b>	92-pl-5	42.06	35.44	0.00	0.01	20.74	0.56	0.02	98.83
<b>Plag-8</b>	92-pl-6	42.08	36.80	0.00	0.01	20.94	0.51	0.01	100.35
<b>Min</b>		42.06	35.44	0.00	0.00	19.08	0.37	0.00	98.76
<b>Max</b>		44.07	36.80	0.04	0.01	20.94	0.56	0.04	100.72
<b>Mean</b>		43.03	35.96	0.01	0.00	20.13	0.47	0.02	99.61

Sample	Si	Al	Fe <sup>2+</sup>	Mg	Ca	Na	K	X	Z	Ab	An	Or
<b>Plag-1</b>	8.10	7.87	0.00	0.00	3.91	0.13	0.01	15.97	4.05	3.20	96.60	0.10
<b>Plag-2</b>	8.18	7.83	0.00	0.00	3.82	0.15	0.00	16.00	3.97	3.70	96.30	0.00
<b>Plag-3</b>	8.13	7.85	0.00	0.00	3.86	0.18	0.00	15.98	4.05	4.50	95.40	0.10
<b>Plag-4</b>	8.13	7.84	0.00	0.00	3.90	0.16	0.01	15.97	4.06	3.90	95.90	0.20
<b>Plag-5</b>	7.90	7.94	0.01	0.00	4.18	0.17	0.00	15.84	4.37	4.00	96.00	0.00
<b>Plag-6</b>	7.97	7.89	0.00	0.00	4.13	0.18	0.00	15.86	4.31	4.10	95.80	0.10
<b>Plag-7</b>	7.94	7.88	0.00	0.00	4.19	0.20	0.01	15.81	4.40	4.60	95.30	0.10
<b>Plag-8</b>	7.82	8.05	0.00	0.00	4.17	0.18	0.00	15.87	4.36	4.20	95.80	0.10
<b>Min</b>	7.82	7.83	0.00	0.00	3.82	0.13	0.00	15.81	3.97	3.20	95.30	0.00
<b>Max</b>	8.18	8.05	0.01	0.00	4.19	0.20	0.01	16.00	4.40	4.60	96.60	0.20
<b>Mean</b>	8.02	7.89	0.00	0.00	4.02	0.17	0.00	15.91	4.19	4.03	95.89	0.09

Table 12. Titanite analyses from the GCS.

Sample	Desc	SiO <sub>2</sub>	Na <sub>2</sub> O	MgO	Al <sub>2</sub> O <sub>3</sub>	NiO	FeO	MnO	Cr <sub>2</sub> O <sub>3</sub>	V <sub>2</sub> O <sub>3</sub>	K <sub>2</sub> O	CaO	TiO <sub>2</sub>	Total
GCS-T-1	88B:T1	30.16	0.02	0.73	5.11	0.00	0.02	0.08	0.00	0.14	0.00	27.49	31.66	95.42
GCS-T-2	88B:T2	30.34	0.01	0.02	5.21	0.00	0.01	0.03	0.00	0.05	0.00	28.37	31.58	95.61
GCS-T-3	88B:T3	30.36	0.00	0.02	5.22	0.00	0.01	0.05	0.00	0.09	0.00	28.54	31.70	95.98
GCS-T-4	404-3-TiT-1	29.81	0.00	0.02	5.27	0.00	0.00	0.00	0.00	1.10	0.02	28.08	30.73	95.03
GCS-T-5	404-3-TiT-2	30.27	0.00	0.02	5.25	0.00	0.05	0.03	0.03	1.26	0.01	28.26	30.46	95.63
GCS-T-6	404-3-TiT-3	30.27	0.00	0.01	5.27	0.04	0.00	0.00	0.04	1.41	0.04	27.95	31.16	96.19
GCS-T-7	404-3-TiT-4	30.38	0.00	0.03	5.42	0.00	0.00	0.05	0.00	0.92	0.01	28.60	30.85	96.27
GCS-T-8	404-5-TiT-1	29.93	0.02	0.03	4.81	0.01	0.09	0.03	0.00	0.60	0.00	27.62	31.92	95.07
GCS-T-9	404-5-TiT-2	29.96	0.00	0.00	4.88	0.00	0.03	0.02	0.03	0.76	0.01	27.91	31.78	95.38
GCS-T-10	404-5-TiT-3	29.90	0.00	0.02	4.92	0.00	0.00	0.00	0.04	0.75	0.03	27.88	31.21	94.74
GCS-T-11	404-5-TiT-4	30.16	0.00	0.03	5.23	0.00	0.03	0.00	0.07	1.21	0.03	27.77	30.58	95.11
GCS-T-12	404-6-TiT-1	30.42	0.00	0.02	5.09	0.00	0.00	0.00	0.00	1.29	0.04	28.29	30.74	95.87
GCS-T-13	404-6-TiT-2	29.77	0.00	0.02	4.92	0.04	0.03	0.00	0.00	0.49	0.03	27.72	32.07	95.10
GCS-T-14	404-6-TiT-3	29.92	0.05	0.00	5.25	0.00	0.00	0.03	0.05	1.34	0.00	28.24	30.88	95.76
GCS-T-15	404-6-TiT-4	29.91	0.00	0.00	5.11	0.00	0.00	0.04	0.03	0.62	0.00	28.05	31.69	95.46
Min		29.77	0.00	0.00	4.81	0.00	0.00	0.00	0.00	0.05	0.00	27.49	30.46	94.74
Max		30.42	0.05	0.73	5.42	0.04	0.09	0.08	0.07	1.41	0.04	28.60	32.07	96.27
Mean		30.10	0.01	0.06	5.13	0.01	0.02	0.02	0.02	0.80	0.01	28.05	31.27	95.51

Sample	Si	Na	Mg	Al	Ni	Fe <sup>2+</sup>	Mn	Cr	V	K	Ca	Ti	SumA	SumB
GCS-T-1	4.05	0.00	0.00	0.84	0.00	0.00	0.00	0.00	0.10	0.00	4.09	3.14	3.99	4.20
GCS-T-2	4.09	0.00	0.00	0.84	0.00	0.01	0.00	0.00	0.11	0.00	4.09	3.09	3.93	4.22
GCS-T-3	4.06	0.00	0.00	0.83	0.00	0.00	0.00	0.00	0.13	0.01	4.02	3.14	3.98	4.16
GCS-T-4	4.08	0.00	0.01	0.86	0.00	0.00	0.01	0.00	0.08	0.00	4.11	3.11	3.97	4.21
GCS-T-5	4.07	0.00	0.01	0.77	0.00	0.01	0.00	0.00	0.05	0.00	4.02	3.26	4.03	4.10
GCS-T-6	4.06	0.00	0.00	0.78	0.00	0.00	0.00	0.00	0.07	0.00	4.05	3.24	4.02	4.13
GCS-T-7	4.08	0.00	0.00	0.79	0.00	0.00	0.00	0.00	0.07	0.00	4.07	3.20	3.99	4.16
GCS-T-8	4.09	0.00	0.01	0.84	0.00	0.00	0.00	0.01	0.11	0.01	4.03	3.12	3.96	4.17
GCS-T-9	4.10	0.00	0.00	0.81	0.00	0.00	0.00	0.00	0.11	0.01	4.08	3.11	3.92	4.20
GCS-T-10	4.05	0.00	0.00	0.79	0.00	0.00	0.00	0.00	0.04	0.01	4.04	3.28	4.07	4.09
GCS-T-11	4.04	0.01	0.00	0.83	0.00	0.00	0.00	0.01	0.12	0.00	4.08	3.14	3.97	4.23
GCS-T-12	4.05	0.00	0.00	0.82	0.00	0.00	0.01	0.00	0.06	0.00	4.07	3.23	4.04	4.14
GCS-T-13	4.08	0.01	0.15	0.81	0.00	0.00	0.01	0.00	0.01	0.00	3.98	3.22	4.04	4.16
GCS-T-14	4.10	0.00	0.00	0.83	0.00	0.00	0.00	0.00	0.00	0.00	4.11	3.21	4.04	4.12
GCS-T-15	4.09	0.00	0.00	0.83	0.00	0.00	0.01	0.00	0.01	0.00	4.12	3.21	4.04	4.14
Min	4.04	0.00	0.00	0.77	0.00	0.00	0.00	0.00	0.00	0.00	3.98	3.09	3.92	4.09
Max	4.10	0.01	0.15	0.86	0.00	0.01	0.01	0.01	0.13	0.01	4.12	3.28	4.07	4.23
Mean	4.07	0.00	0.01	0.82	0.00	0.00	0.00	0.00	0.07	0.00	4.06	3.18	4.00	4.16

Table 13. Plagioclase analyses from the kyanite-graphite gneiss.

Sample	Desc	SiO <sub>2</sub>	Al <sub>2</sub> O <sub>3</sub>	FeO	MgO	CaO	Na <sub>2</sub> O	K <sub>2</sub> O	Total
<b>K-P-1</b>	161:F1-1	61.30	24.77	0.00	0.00	5.79	7.94	0.22	100.02
<b>K-P-2</b>	161:F1-3	62.07	24.29	0.00	0.01	5.74	7.81	0.22	100.15
<b>K-P-3</b>	161:F2-1	62.49	24.00	0.00	0.00	5.86	7.94	0.23	100.52
<b>K-P-4</b>	161:F2-2	62.54	24.19	0.00	0.02	5.53	8.09	0.25	100.62
<b>K-P-5</b>	161:F2-4	61.80	23.14	0.02	0.01	5.83	7.96	0.21	98.96
<b>Min</b>		61.30	23.14	0.00	0.00	5.53	7.81	0.21	98.96
<b>Max</b>		62.54	24.77	0.02	0.02	5.86	8.09	0.25	100.62
<b>Mean</b>		62.04	24.08	0.00	0.01	5.75	7.95	0.23	100.05

Sample	Si	Al	Fe <sup>2+</sup>	Mg	Ca	Na	K	Ab	An	Or
<b>K-P-1</b>	10.87	5.17	0.00	0.00	1.10	2.73	0.05	70.40	28.40	1.30
<b>K-P-2</b>	10.98	5.06	0.00	0.00	1.09	2.68	0.05	70.20	28.50	1.30
<b>K-P-3</b>	11.02	4.98	0.00	0.00	1.11	2.71	0.05	70.10	28.60	1.30
<b>K-P-4</b>	11.01	5.02	0.00	0.00	1.04	2.76	0.06	71.50	27.10	1.40
<b>K-P-5</b>	11.07	4.88	0.00	0.00	1.12	2.76	0.05	70.30	28.40	1.20
<b>Min</b>	10.87	4.88	0.00	0.00	1.04	2.68	0.05	70.10	27.10	1.20
<b>Max</b>	11.07	5.17	0.00	0.00	1.12	2.76	0.06	71.50	28.60	1.40
<b>Mean</b>	10.99	5.02	0.00	0.00	1.09	2.73	0.05	70.50	28.20	1.30

Table 14. Mica analyses from the kyanite-graphite gneiss.

Sample	Desc.	SiO <sub>2</sub>	TiO <sub>2</sub>	Al <sub>2</sub> O <sub>3</sub>	Cr <sub>2</sub> O <sub>3</sub>	FeO	MnO	MgO	CaO	Na <sub>2</sub> O	K <sub>2</sub> O	Total
K-M-1	m1-1	45.94	0.15	37.30	0.57	0.00	0.00	1.30	0.07	0.40	10.26	95.99
K-M-2	m1-2	44.44	0.08	34.46	0.07	0.05	0.00	1.56	0.00	0.34	10.58	91.58
K-M-3	m1-3	47.08	0.01	36.96	0.07	0.00	0.00	1.35	0.06	0.38	10.31	96.22
K-M-4	m1-4	46.14	0.05	35.75	0.48	0.03	0.01	1.21	0.01	0.39	10.65	94.72
K-M-5	m2-1	43.50	0.04	36.09	0.35	0.05	0.00	0.85	0.10	0.41	10.51	91.90
K-M-6	m2-2	45.72	0.05	36.22	0.32	0.00	0.02	1.00	0.05	0.49	10.65	94.52
K-M-7	m2-3	45.75	0.10	34.90	0.07	0.50	0.01	1.54	0.19	0.31	9.96	93.33
K-M-8	m2-4	43.15	0.05	35.95	0.38	0.06	0.00	0.89	0.09	0.43	10.24	91.24
Min		43.15	0.01	34.46	0.07	0.00	0.00	0.85	0.00	0.31	9.96	91.24
Max		47.08	0.15	37.30	0.57	0.50	0.02	1.56	0.19	0.49	10.65	96.22
Mean		45.22	0.07	35.95	0.29	0.09	0.01	1.21	0.07	0.39	10.40	93.69

Sample	Si	Al IV	Sum_T	Al VI	Ti	Fe <sup>2+</sup>	Cr	Mn	Mg	Ca	Na	K
K-M-1	5.48	2.52	8.00	2.72	0.01	0.00	0.05	0.00	0.23	0.01	0.09	1.56
K-M-2	5.57	2.43	8.00	2.66	0.01	0.01	0.01	0.00	0.29	0.00	0.08	1.69
K-M-3	5.58	2.42	8.00	2.75	0.00	0.00	0.01	0.00	0.24	0.01	0.09	1.56
K-M-4	5.59	2.41	8.00	2.69	0.01	0.00	0.05	0.00	0.22	0.00	0.09	1.65
K-M-5	5.44	2.56	8.00	2.76	0.00	0.01	0.04	0.00	0.16	0.01	0.10	1.68
K-M-6	5.55	2.45	8.00	2.73	0.01	0.00	0.03	0.00	0.18	0.01	0.12	1.65
K-M-7	5.61	2.39	8.00	2.66	0.01	0.05	0.01	0.00	0.28	0.03	0.07	1.56
K-M-8	5.43	2.57	8.00	2.77	0.01	0.01	0.04	0.00	0.17	0.01	0.11	1.65
Min	5.43	2.39	8.00	2.66	0.00	0.00	0.01	0.00	0.16	0.00	0.07	1.56
Max	5.61	2.57	8.00	2.77	0.01	0.05	0.05	0.00	0.29	0.03	0.12	1.69
Mean	5.53	2.47	8.00	2.72	0.01	0.01	0.03	0.00	0.22	0.01	0.09	1.62

Sample	Desc.	SiO <sub>2</sub>	TiO <sub>2</sub>	Al <sub>2</sub> O <sub>3</sub>	Cr <sub>2</sub> O <sub>3</sub>	FeO	MnO	MgO	CaO	Na <sub>2</sub> O	K <sub>2</sub> O	Total
K-B-1	m1-1	41.67	1.73	19.52	0.34	0.22	0.22	21.70	0.01	0.17	9.67	95.25
K-B-2	m1-2	41.01	1.63	18.93	0.42	0.19	0.18	22.34	0.04	0.20	10.03	94.97
K-B-3	m1-3	40.32	1.57	19.50	0.31	0.25	0.16	21.95	0.03	0.16	9.87	94.12
K-B-4	m1-4	40.74	1.63	19.16	0.46	0.20	0.15	22.04	0.03	0.16	10.06	94.63
K-B-5	m2-2	38.32	1.77	18.59	0.29	0.16	0.14	23.17	0.03	0.21	10.19	92.87
K-B-6	m2-3	40.05	1.77	19.15	0.21	0.14	0.12	22.35	0.02	0.16	10.17	94.14
K-B-7	m2-4	40.11	1.83	18.84	0.31	0.16	0.07	21.77	0.01	0.17	9.84	93.11
K-B-8	m3-1	39.81	1.76	18.95	0.31	0.20	0.14	22.02	0.14	0.18	9.73	93.24
K-B-9	m3-2	39.62	1.77	19.06	0.21	0.21	0.10	21.22	0.10	0.24	9.57	92.10
K-B-10	m3-3	40.71	1.76	19.22	0.22	0.20	0.14	21.53	0.04	0.27	9.94	94.03
K-B-11	m3-4	40.50	1.82	18.72	0.26	0.23	0.12	22.16	0.05	0.20	9.77	93.83
K-B-12	m4-1	40.35	1.98	18.08	0.12	0.21	0.09	22.83	0.01	0.18	10.08	93.93
K-B-13	m4-2	37.48	1.79	18.69	0.07	0.26	0.13	22.54	0.00	0.19	10.07	91.22
K-B-14	m4-3	40.60	1.99	18.58	0.12	0.18	0.11	22.59	0.00	0.16	10.04	94.37
K-B-15	m4-4	40.40	2.08	18.51	0.08	0.24	0.15	22.67	0.04	0.14	10.03	94.34
K-B-16	m5-1	41.08	2.10	19.34	0.14	0.17	0.16	22.32	0.05	0.21	10.07	95.64
K-B-17	m5-2	40.64	2.02	18.86	0.09	0.19	0.11	22.58	0.01	0.20	10.14	94.84
K-B-18	m5-3	41.23	1.82	19.54	0.12	0.17	0.12	22.38	0.03	0.19	10.08	95.68
K-B-19	m5-4	40.83	1.80	18.92	0.16	0.25	0.10	21.80	0.01	0.22	9.96	94.05
Min		37.48	1.57	18.08	0.07	0.14	0.07	21.22	0.00	0.14	9.57	91.22
Max		41.67	2.10	19.54	0.46	0.26	0.22	23.17	0.14	0.27	10.19	95.68
Mean		40.29	1.82	18.96	0.22	0.20	0.13	22.21	0.03	0.19	9.96	94.02

Sample	Si	Al IV	Sum_T	Al VI	Ti	Fe <sup>2+</sup>	Cr	Mn	Mg	Ca	Na	K
K-B-1	5.47	2.53	8.00	0.49	0.17	0.02	0.04	0.02	4.25	0.00	0.04	1.62
K-B-2	5.43	2.57	8.00	0.38	0.16	0.02	0.04	0.02	4.41	0.01	0.05	1.69
K-B-3	5.38	2.62	8.00	0.44	0.16	0.03	0.03	0.02	4.37	0.00	0.04	1.68
K-B-4	5.41	2.59	8.00	0.41	0.16	0.02	0.05	0.02	4.36	0.00	0.04	1.71
K-B-5	5.22	2.78	8.00	0.21	0.18	0.02	0.03	0.02	4.71	0.00	0.06	1.77
K-B-6	5.35	2.65	8.00	0.37	0.18	0.02	0.02	0.01	4.46	0.00	0.04	1.74
K-B-7	5.41	2.59	8.00	0.40	0.19	0.02	0.03	0.01	4.38	0.00	0.04	1.69
K-B-8	5.37	2.63	8.00	0.37	0.18	0.02	0.03	0.02	4.43	0.02	0.05	1.67
K-B-9	5.40	2.60	8.00	0.45	0.18	0.02	0.02	0.01	4.31	0.02	0.06	1.66
K-B-10	5.43	2.57	8.00	0.45	0.18	0.02	0.02	0.02	4.28	0.01	0.07	1.69
K-B-11	5.42	2.58	8.00	0.37	0.18	0.03	0.03	0.01	4.42	0.01	0.05	1.67
K-B-12	5.41	2.59	8.00	0.26	0.20	0.02	0.01	0.01	4.56	0.00	0.05	1.72
K-B-13	5.20	2.80	8.00	0.26	0.19	0.03	0.01	0.02	4.66	0.00	0.05	1.78
K-B-14	5.41	2.59	8.00	0.32	0.20	0.02	0.01	0.01	4.49	0.00	0.04	1.71
K-B-15	5.39	2.61	8.00	0.30	0.21	0.03	0.01	0.02	4.51	0.01	0.04	1.71
K-B-16	5.40	2.61	8.00	0.39	0.21	0.02	0.02	0.02	4.37	0.01	0.05	1.69
K-B-17	5.39	2.61	8.00	0.33	0.20	0.02	0.01	0.01	4.46	0.00	0.05	1.72
K-B-18	5.41	2.59	8.00	0.43	0.18	0.02	0.01	0.01	4.38	0.00	0.05	1.69
K-B-19	5.45	2.55	8.00	0.42	0.18	0.03	0.02	0.01	4.34	0.00	0.06	1.70
Min	5.20	2.53	8.00	0.21	0.16	0.02	0.01	0.01	4.25	0.00	0.04	1.62
Max	5.47	2.80	8.00	0.49	0.21	0.03	0.05	0.02	4.71	0.02	0.07	1.78
Mean	5.39	2.61	8.00	0.37	0.18	0.02	0.02	0.01	4.43	0.00	0.05	1.70

Table 15. Plagioclase analyses from the JW-zone.

Sample	Desc	SiO <sub>2</sub>	Al <sub>2</sub> O <sub>3</sub>	FeO	MgO	CaO	Na <sub>2</sub> O	K <sub>2</sub> O	Total
J-P-1	149:F1-1	58.61	26.39	0.01	0.00	7.82	6.65	0.38	99.85
J-P-2	149:F1-2	58.69	26.15	0.00	0.00	7.73	6.66	0.34	99.56
J-P-3	149:F1-3	58.53	25.88	0.02	0.00	8.02	6.46	0.34	99.26
J-P-4	149:F1-4	58.86	25.60	0.01	0.00	7.70	6.56	0.33	99.06
J-P-5	149:F2-2	59.37	25.70	0.00	0.00	7.27	6.94	0.32	99.60
J-P-6	149:F2-3	59.38	25.42	0.00	0.00	7.40	6.66	0.19	99.06
J-P-7	149:F2-4	59.26	25.33	0.00	0.00	7.11	6.84	0.26	98.79
J-P-8	149:F3-3	58.65	25.47	0.04	0.01	7.54	6.87	0.30	98.87
J-P-9	396-2-F1	57.26	26.95	0.00	0.00	8.16	6.70	0.32	99.40
J-P-10	396-2-F2	57.93	26.57	0.00	0.00	8.19	7.03	0.29	100.00
J-P-11	396-2-F3	57.75	26.37	0.02	0.03	8.11	6.63	0.35	99.26
J-P-12	396-3-F1	57.66	26.52	0.00	0.00	8.17	6.96	0.29	99.61
J-P-13	396-3-F2	57.75	26.65	0.00	0.00	8.13	6.71	0.30	99.54
J-P-14	396-3-F3	58.17	26.46	0.00	0.00	8.00	6.82	0.32	99.77
J-P-15	396-5-F1	57.65	27.14	0.01	0.00	7.98	6.79	0.34	99.91
J-P-16	396-5-F2	58.00	27.32	0.04	0.00	8.22	6.79	0.33	100.69
J-P-17	396-5-F3	57.96	26.75	0.02	0.00	8.00	6.67	0.35	99.74
J-P-18	416-2-F1	57.61	27.30	0.01	0.00	7.73	6.92	0.28	99.85
J-P-19	416-3-F1	58.20	26.20	0.02	0.01	7.86	7.14	0.21	99.65
J-P-20	416-3-F2	57.65	26.29	0.00	0.01	8.00	6.95	0.14	99.04
Min		57.26	25.33	0.00	0.00	7.11	6.46	0.14	98.79
Max		59.38	27.32	0.04	0.03	8.22	7.14	0.38	100.69
Mean		58.25	26.32	0.01	0.00	7.86	6.79	0.30	99.52

Sample	Si	Al	Fe <sup>2+</sup>	Mg	Ca	Na	K	Ab	An	Or
J-P-1	10.48	5.56	0.00	0.00	1.50	2.31	0.09	59.30	38.50	2.20
J-P-2	10.52	5.52	0.00	0.00	1.48	2.31	0.08	59.70	38.30	2.00
J-P-3	10.53	5.48	0.00	0.00	1.55	2.25	0.08	58.10	39.90	2.00
J-P-4	10.59	5.43	0.00	0.00	1.48	2.29	0.08	59.50	38.60	2.00
J-P-5	10.62	5.41	0.00	0.00	1.39	2.41	0.07	62.10	36.00	1.90
J-P-6	10.66	5.38	0.00	0.00	1.42	2.32	0.04	61.30	37.60	1.20
J-P-7	10.67	5.37	0.00	0.00	1.37	2.39	0.06	62.50	35.90	1.60
J-P-8	10.59	5.41	0.01	0.00	1.46	2.40	0.07	61.20	37.10	1.80
J-P-9	10.32	5.72	0.00	0.00	1.58	2.34	0.07	58.70	39.50	1.80
J-P-10	10.38	5.61	0.00	0.00	1.57	2.44	0.07	59.80	38.50	1.60
J-P-11	10.41	5.60	0.00	0.01	1.57	2.32	0.08	58.50	39.50	2.00
J-P-12	10.37	5.62	0.00	0.00	1.58	2.43	0.07	59.70	38.70	1.60
J-P-13	10.38	5.64	0.00	0.00	1.57	2.34	0.07	58.80	39.40	1.70
J-P-14	10.43	5.59	0.00	0.00	1.54	2.37	0.07	59.60	38.60	1.90
J-P-15	10.33	5.73	0.00	0.00	1.53	2.36	0.08	59.40	38.60	2.00
J-P-16	10.31	5.72	0.01	0.00	1.57	2.34	0.07	58.80	39.30	1.90
J-P-17	10.39	5.65	0.00	0.00	1.54	2.32	0.08	58.90	39.10	2.10
J-P-18	10.32	5.76	0.00	0.00	1.48	2.40	0.06	60.80	37.60	1.60
J-P-19	10.45	5.54	0.00	0.00	1.51	2.49	0.05	61.40	37.40	1.20
J-P-20	10.41	5.59	0.00	0.00	1.55	2.44	0.03	60.60	38.60	0.80
Min	10.31	5.37	0.00	0.00	1.37	2.25	0.03	58.10	35.90	0.80
Max	10.67	5.76	0.01	0.01	1.58	2.49	0.09	62.50	39.90	2.20
Mean	10.46	5.57	0.00	0.00	1.51	2.36	0.07	59.94	38.34	1.75

Table 15. Continue 1.

Sample	Desc	SiO <sub>2</sub>	Al <sub>2</sub> O <sub>3</sub>	FeO	MgO	CaO	Na <sub>2</sub> O	K <sub>2</sub> O	Total
J-P-21	397-4-F2	49.26	32.09	0.06	0.00	14.69	3.08	0.07	99.25
J-P-22	397-4-F1	47.95	33.03	0.00	0.01	15.72	2.71	0.08	99.50
J-P-23	397-1-F1	48.05	32.88	0.00	0.00	15.62	2.57	0.10	99.22
J-P-24	397-1-F2	48.23	32.76	0.01	0.01	15.23	2.74	0.05	99.03
J-P-25	397-1-F3	47.47	33.61	0.00	0.00	16.17	2.26	0.06	99.56
J-P-26	397-3-F2	47.34	33.44	0.00	0.02	15.94	2.28	0.08	99.09
J-P-27	397-5-F2	46.52	34.43	0.03	0.00	16.56	2.15	0.05	99.74
J-P-28	397-5-F3	47.00	34.31	0.00	0.00	16.14	2.24	0.04	99.73
J-P-29	128-F1-1	48.01	32.95	0.03	0.00	15.98	2.25	0.03	99.25
J-P-30	128-F1-2	47.94	33.11	0.00	0.00	16.40	1.99	0.05	99.49
J-P-31	128-F1-3	47.64	33.28	0.00	0.01	16.74	1.92	0.02	99.61
J-P-32	128-F2-1	47.59	33.33	0.00	0.00	16.75	1.85	0.05	99.57
J-P-33	128-F2-2	47.90	33.36	0.00	0.00	16.80	1.82	0.05	99.94
J-P-34	128-F2-3	48.09	33.62	0.00	0.00	17.01	1.77	0.06	100.56
J-P-35	397-2-F3	46.13	33.99	0.05	0.01	16.71	1.91	0.06	98.86
J-P-36	397-2-F1	46.28	33.86	0.01	0.00	16.93	1.80	0.04	98.92
J-P-37	397-2-F2	45.79	34.43	0.03	0.00	17.41	1.72	0.04	99.41
Min		45.79	32.09	0.00	0.00	14.69	1.72	0.02	98.86
Max		49.26	34.43	0.06	0.02	17.41	3.08	0.10	100.56
Mean		47.48	33.44	0.01	0.00	16.28	2.18	0.05	99.45

Sample	Si	Al	Fe <sup>2+</sup>	Mg	Ca	Na	K	Ab	An	Or
J-P-21	9.06	6.95	0.01	0.00	2.89	1.10	0.02	27.40	72.20	0.40
J-P-22	8.83	7.16	0.00	0.00	3.10	0.97	0.02	23.70	75.90	0.50
J-P-23	8.86	7.14	0.00	0.00	3.09	0.92	0.02	22.80	76.60	0.60
J-P-24	8.90	7.12	0.00	0.00	3.01	0.98	0.01	24.50	75.20	0.30
J-P-25	8.73	7.28	0.00	0.00	3.19	0.81	0.01	20.10	79.50	0.30
J-P-26	8.75	7.28	0.00	0.00	3.16	0.82	0.02	20.50	79.10	0.50
J-P-27	8.56	7.47	0.00	0.00	3.27	0.77	0.01	19.00	80.70	0.30
J-P-28	8.64	7.42	0.00	0.00	3.18	0.80	0.01	20.00	79.70	0.20
J-P-29	8.85	7.15	0.01	0.00	3.16	0.80	0.01	20.30	79.50	0.20
J-P-30	8.82	7.17	0.00	0.00	3.23	0.71	0.01	18.00	81.80	0.30
J-P-31	8.76	7.21	0.00	0.00	3.30	0.68	0.01	17.20	82.70	0.10
J-P-32	8.76	7.22	0.00	0.00	3.30	0.66	0.01	16.60	83.10	0.30
J-P-33	8.78	7.20	0.00	0.00	3.30	0.65	0.01	16.40	83.40	0.30
J-P-34	8.76	7.21	0.00	0.00	3.32	0.63	0.01	15.80	83.80	0.40
J-P-35	8.57	7.44	0.01	0.00	3.33	0.69	0.02	17.10	82.50	0.40
J-P-36	8.59	7.40	0.00	0.00	3.37	0.65	0.01	16.10	83.70	0.20
J-P-37	8.48	7.51	0.01	0.00	3.45	0.62	0.01	15.10	84.70	0.20
Min	8.48	6.95	0.00	0.00	2.89	0.62	0.01	15.10	72.20	0.10
Max	9.06	7.51	0.01	0.00	3.45	1.10	0.02	27.40	84.70	0.60
Mean	8.75	7.26	0.00	0.00	3.21	0.78	0.01	19.45	80.24	0.32

Table 16. Biotite analyses from the JW-zone.

Sample	Desc.	SiO <sub>2</sub>	TiO <sub>2</sub>	Al <sub>2</sub> O <sub>3</sub>	Cr <sub>2</sub> O <sub>3</sub>	FeO	MnO	MgO	CaO	Na <sub>2</sub> O	K <sub>2</sub> O	Total
JW-B-1	m1-2	39.46	1.81	17.07	0.09	0.12	0.10	23.40	0.02	0.05	10.00	92.12
JW-B-2	m1-3	40.96	1.86	17.90	0.02	0.20	0.09	23.66	0.02	0.06	10.02	94.79
JW-B-3	m1-4	39.41	1.79	17.32	0.04	0.12	0.07	23.83	0.02	0.09	10.13	92.82
JW-B-4	m1-5	40.47	1.77	17.68	0.06	0.13	0.13	23.69	0.02	0.10	10.06	94.11
JW-B-5	m1-6	40.45	1.76	17.39	0.05	0.19	0.15	23.15	0.05	0.07	9.94	93.20
JW-B-6	m1-7	39.93	1.76	17.21	0.05	0.12	0.13	22.97	0.01	0.13	9.89	92.20
JW-B-7	m1-a	39.54	1.71	17.22	0.02	0.17	0.09	23.68	0.00	0.09	9.99	92.51
JW-B-8	m1-b	39.86	1.74	17.69	0.04	0.16	0.03	23.35	0.04	0.12	9.67	92.70
JW-B-9	m2-3	41.49	1.52	18.94	0.08	0.10	0.11	23.36	0.03	0.10	10.06	95.79
JW-B-10	m2-4	40.44	1.50	18.26	0.12	0.09	0.07	23.15	0.06	0.11	10.00	93.80
JW-B-11	m2-6	40.92	1.67	18.58	0.10	0.10	0.08	22.68	0.03	0.13	10.00	94.29
JW-B-12	m2-7	41.65	1.75	18.31	0.09	0.05	0.06	23.06	0.00	0.10	9.91	94.98
JW-B-13	m2-8	41.31	1.76	18.34	0.12	0.13	0.04	22.96	0.01	0.08	10.00	94.75
JW-B-14	396:1-a	40.75	2.18	16.29	0.08	0.08	0.09	23.00	0.01	0.03	10.28	92.79
JW-B-15	396:1-b	40.66	2.05	16.28	0.06	0.10	0.04	22.69	0.00	0.07	10.15	92.10
JW-B-16	396:1-c	39.95	2.09	16.20	0.04	0.16	0.10	22.61	0.04	0.05	10.18	91.42
JW-B-17	396:4-a	39.21	2.03	17.03	0.10	0.12	0.01	21.99	0.06	0.06	9.79	90.40
JW-B-18	396:4-b	40.50	2.09	16.76	0.14	0.05	0.07	22.22	0.01	0.03	10.12	91.99
JW-B-19	396:4-c	39.38	2.10	16.90	0.11	0.09	0.04	21.71	0.03	0.04	9.84	90.24
JW-B-20	451:m1-1	41.31	1.33	17.00	0.04	0.08	0.14	23.83	0.03	0.05	9.84	93.65
JW-B-21	451:m1-10	40.55	1.42	16.04	0.04	0.13	0.12	24.69	0.03	0.04	10.01	93.07
JW-B-22	451:m1-2	40.84	1.42	16.07	0.04	0.12	0.10	24.32	0.03	0.06	9.90	92.90
JW-B-23	451:m1-3	41.55	1.47	17.16	0.07	0.12	0.06	23.34	0.04	0.04	9.71	93.56
JW-B-24	451:m1-4	41.62	1.50	16.13	0.06	0.17	0.09	23.91	0.05	0.05	10.08	93.66
JW-B-25	451:m1-5	41.09	1.42	15.78	0.07	0.11	0.16	24.25	0.08	0.06	10.10	93.12
JW-B-26	451:m1-6	41.38	1.58	15.95	0.03	0.11	0.12	23.89	0.05	0.07	10.08	93.26
JW-B-27	451:m1-7	40.30	1.62	15.95	0.07	0.14	0.12	24.41	0.01	0.05	9.59	92.26
JW-B-28	451:m1-8	40.04	1.53	16.26	0.08	0.10	0.07	24.27	0.03	0.02	9.80	92.20
JW-B-29	451:m1-9	40.76	1.43	16.24	0.04	0.19	0.15	24.44	0.06	0.06	9.74	93.11
JW-B-30	451:m2-1	40.86	1.61	15.89	0.08	0.21	0.13	24.82	0.03	0.09	10.14	93.86
JW-B-31	451:m2-2	40.75	1.64	15.64	0.08	0.12	0.16	25.31	0.07	0.06	9.90	93.73
JW-B-32	451:m2-6	40.65	1.52	16.01	0.05	0.23	0.15	24.38	0.02	0.03	9.86	92.90
JW-B-33	451:m2-7	40.70	1.51	16.06	0.02	0.13	0.13	24.70	0.02	0.04	10.02	93.33
JW-B-34	451:m2-8	41.32	1.53	16.39	0.07	0.18	0.14	24.71	0.02	0.01	10.10	94.47
JW-B-35	451:m3-1	41.31	1.62	16.04	0.10	0.12	0.08	24.64	0.01	0.06	10.11	94.09
JW-B-36	451:m3-10	40.73	1.53	16.06	0.06	0.08	0.01	24.48	0.01	0.06	10.09	93.11
JW-B-37	451:m3-2	40.68	1.51	15.52	0.06	0.11	0.12	24.15	0.03	0.04	9.94	92.16
JW-B-38	451:m3-3	41.14	1.47	15.80	0.06	0.10	0.09	24.11	0.00	0.05	9.90	92.72
JW-B-39	451:m3-5	41.23	1.49	15.78	0.07	0.16	0.12	24.04	0.00	0.03	10.09	93.01
JW-B-40	451:m3-6	41.34	1.47	16.05	0.10	0.07	0.09	24.74	0.08	0.02	10.25	94.21
JW-B-41	451:m3-7	40.47	1.45	15.62	0.07	0.17	0.07	24.87	0.03	0.05	9.84	92.64
JW-B-42	451:m3-9	41.69	1.67	16.50	0.01	0.15	0.09	24.68	0.00	0.06	9.78	94.63
JW-B-43	452:m1-1	40.34	1.33	16.43	0.26	0.01	0.02	22.96	0.00	0.09	9.68	91.12
JW-B-44	452:m1-2	40.05	1.21	16.33	0.29	0.05	0.00	23.21	0.00	0.07	9.59	90.80
JW-B-45	452:m1-3	39.25	1.45	15.67	0.33	0.00	0.03	22.81	0.00	0.11	9.49	89.14
JW-B-46	452:m1-4	40.29	1.58	16.36	0.28	0.01	0.00	22.70	0.00	0.09	9.44	90.75
JW-B-47	452:m1-5	40.20	1.52	16.95	0.26	0.08	0.04	22.91	0.09	0.13	9.56	91.74
JW-B-48	452:m1-6	39.80	1.47	16.48	0.29	0.00	0.00	23.63	0.07	0.13	9.61	91.48
JW-B-49	452:m1-7	36.45	1.34	14.78	0.30	0.09	0.06	24.01	0.05	0.08	9.64	86.80
JW-B-50	452:m1-8	40.23	1.49	16.48	0.20	0.02	0.03	23.25	0.02	0.09	9.74	91.55
JW-B-51	459:m2-1	40.19	1.53	16.35	0.18	0.04	0.04	23.41	0.03	0.06	9.57	91.40
JW-B-52	459:m2-2	39.86	1.64	16.18	0.16	0.07	0.03	23.44	0.02	0.07	9.82	91.29
JW-B-53	459:m2-3	40.86	1.56	16.11	0.17	0.00	0.00	23.37	0.02	0.07	9.80	91.96
JW-B-54	459:m2-4	39.84	1.71	16.23	0.16	0.02	0.03	23.17	0.01	0.10	9.74	91.01
JW-B-55	459:m2-5	40.65	1.46	16.08	0.16	0.00	0.00	23.51	0.00	0.09	9.87	91.82
JW-B-56	459:m2-6	39.62	1.57	16.20	0.14	0.03	0.02	22.88	0.06	0.11	9.70	90.33
JW-B-57	459:m2-7	39.89	1.43	15.64	0.13	0.02	0.03	23.88	0.06	0.07	9.59	90.74
JW-B-58	459:m2-8	38.41	1.47	17.54	0.17	0.00	0.08	23.70	0.07	0.23	9.48	91.15
Min		36.45	1.21	14.78	0.01	0.00	0.00	21.71	0.00	0.01	9.44	86.80
Max		41.69	2.18	18.94	0.33	0.23	0.16	25.31	0.09	0.23	10.28	95.79
Mean		40.42	1.61	16.57	0.11	0.10	0.08	23.64	0.03	0.07	9.88	92.51

Table 16. Continue 1.

Sample	Si	Al IV	Sum_T	Al VI	Ti	Fe <sup>2+</sup>	Cr	Mn	Mg	Ca	Na	K
JW-B-1	5.40	2.60	8.00	0.15	0.19	0.01	0.01	0.01	4.77	0.00	0.01	1.75
JW-B-2	5.43	2.57	8.00	0.23	0.19	0.02	0.00	0.01	4.68	0.00	0.02	1.70
JW-B-3	5.36	2.64	8.00	0.13	0.18	0.01	0.00	0.01	4.83	0.00	0.02	1.76
JW-B-4	5.41	2.59	8.00	0.20	0.18	0.02	0.01	0.02	4.72	0.00	0.03	1.72
JW-B-5	5.46	2.54	8.00	0.22	0.18	0.02	0.01	0.02	4.66	0.01	0.02	1.71
JW-B-6	5.45	2.55	8.00	0.22	0.18	0.01	0.01	0.02	4.67	0.00	0.03	1.72
JW-B-7	5.39	2.61	8.00	0.15	0.18	0.02	0.00	0.01	4.81	0.00	0.02	1.74
JW-B-8	5.40	2.60	8.00	0.23	0.18	0.02	0.00	0.00	4.72	0.01	0.03	1.67
JW-B-9	5.43	2.57	8.00	0.35	0.15	0.01	0.01	0.01	4.56	0.00	0.03	1.68
JW-B-10	5.42	2.58	8.00	0.30	0.15	0.01	0.01	0.01	4.62	0.01	0.03	1.71
JW-B-11	5.45	2.56	8.00	0.36	0.17	0.01	0.01	0.01	4.50	0.00	0.03	1.70
JW-B-12	5.49	2.51	8.00	0.33	0.17	0.01	0.01	0.01	4.53	0.00	0.03	1.67
JW-B-13	5.47	2.53	8.00	0.33	0.18	0.01	0.01	0.00	4.53	0.00	0.02	1.69
JW-B-14	5.53	2.47	8.00	0.14	0.22	0.01	0.01	0.01	4.65	0.00	0.01	1.78
JW-B-15	5.55	2.45	8.00	0.17	0.21	0.01	0.01	0.01	4.62	0.00	0.02	1.77
JW-B-16	5.51	2.49	8.00	0.14	0.22	0.02	0.00	0.01	4.65	0.01	0.01	1.79
JW-B-17	5.45	2.55	8.00	0.24	0.21	0.01	0.01	0.00	4.56	0.01	0.02	1.74
JW-B-18	5.54	2.47	8.00	0.23	0.22	0.01	0.02	0.01	4.53	0.00	0.01	1.76
JW-B-19	5.49	2.51	8.00	0.26	0.22	0.01	0.01	0.01	4.51	0.00	0.01	1.75
JW-B-20	5.53	2.47	8.00	0.21	0.13	0.01	0.00	0.02	4.76	0.00	0.01	1.68
JW-B-21	5.49	2.51	8.00	0.05	0.15	0.02	0.00	0.01	4.98	0.00	0.01	1.73
JW-B-22	5.53	2.47	8.00	0.09	0.15	0.01	0.00	0.01	4.91	0.00	0.02	1.71
JW-B-23	5.56	2.44	8.00	0.26	0.15	0.01	0.01	0.01	4.66	0.01	0.01	1.66
JW-B-24	5.59	2.42	8.00	0.13	0.15	0.02	0.01	0.01	4.78	0.01	0.01	1.73
JW-B-25	5.56	2.44	8.00	0.07	0.14	0.01	0.01	0.02	4.89	0.01	0.02	1.74
JW-B-26	5.58	2.42	8.00	0.11	0.16	0.01	0.00	0.01	4.80	0.01	0.02	1.73
JW-B-27	5.49	2.51	8.00	0.05	0.17	0.02	0.01	0.01	4.96	0.00	0.01	1.67
JW-B-28	5.47	2.54	8.00	0.08	0.16	0.01	0.01	0.01	4.94	0.00	0.01	1.71
JW-B-29	5.51	2.50	8.00	0.09	0.15	0.02	0.00	0.02	4.92	0.01	0.02	1.68
JW-B-30	5.49	2.51	8.00	0.01	0.16	0.02	0.01	0.02	4.97	0.00	0.02	1.74
JW-B-31	5.48	2.48	7.96	0.00	0.17	0.01	0.01	0.02	5.08	0.01	0.02	1.70
JW-B-32	5.51	2.49	8.00	0.06	0.16	0.03	0.01	0.02	4.93	0.00	0.01	1.71
JW-B-33	5.49	2.51	8.00	0.05	0.15	0.02	0.00	0.02	4.97	0.00	0.01	1.73
JW-B-34	5.51	2.49	8.00	0.08	0.15	0.02	0.01	0.02	4.91	0.00	0.00	1.72
JW-B-35	5.53	2.47	8.00	0.05	0.16	0.01	0.01	0.01	4.92	0.00	0.02	1.73
JW-B-36	5.51	2.49	8.00	0.06	0.16	0.01	0.01	0.00	4.94	0.00	0.02	1.74
JW-B-37	5.56	2.44	8.00	0.05	0.16	0.01	0.01	0.01	4.92	0.00	0.01	1.73
JW-B-38	5.58	2.43	8.00	0.10	0.15	0.01	0.01	0.01	4.87	0.00	0.01	1.71
JW-B-39	5.58	2.42	8.00	0.09	0.15	0.02	0.01	0.01	4.85	0.00	0.01	1.74
JW-B-40	5.53	2.47	8.00	0.06	0.15	0.01	0.01	0.01	4.93	0.01	0.01	1.75
JW-B-41	5.50	2.50	8.00	0.00	0.15	0.02	0.01	0.01	5.04	0.00	0.01	1.71
JW-B-42	5.53	2.47	8.00	0.11	0.17	0.02	0.00	0.01	4.88	0.00	0.02	1.65
JW-B-43	5.55	2.45	8.00	0.22	0.14	0.00	0.03	0.00	4.71	0.00	0.02	1.70
JW-B-44	5.53	2.47	8.00	0.19	0.13	0.01	0.03	0.00	4.78	0.00	0.02	1.69
JW-B-45	5.53	2.47	8.00	0.13	0.15	0.00	0.04	0.00	4.79	0.00	0.03	1.71
JW-B-46	5.56	2.44	8.00	0.22	0.16	0.00	0.03	0.00	4.67	0.00	0.02	1.66
JW-B-47	5.50	2.50	8.00	0.23	0.16	0.01	0.03	0.01	4.67	0.01	0.03	1.67
JW-B-48	5.47	2.53	8.00	0.13	0.15	0.00	0.03	0.00	4.84	0.01	0.04	1.68
JW-B-49	5.33	2.55	7.88	0.00	0.15	0.01	0.04	0.01	5.23	0.01	0.02	1.80
JW-B-50	5.52	2.48	8.00	0.18	0.15	0.00	0.02	0.00	4.75	0.00	0.02	1.70
JW-B-51	5.52	2.48	8.00	0.16	0.16	0.01	0.02	0.01	4.79	0.00	0.02	1.68
JW-B-52	5.49	2.51	8.00	0.12	0.17	0.01	0.02	0.00	4.82	0.00	0.02	1.73
JW-B-53	5.57	2.43	8.00	0.16	0.16	0.00	0.02	0.00	4.75	0.00	0.02	1.71
JW-B-54	5.50	2.50	8.00	0.14	0.18	0.00	0.02	0.00	4.77	0.00	0.03	1.72
JW-B-55	5.56	2.44	8.00	0.15	0.15	0.00	0.02	0.00	4.79	0.00	0.02	1.72
JW-B-56	5.51	2.49	8.00	0.17	0.16	0.00	0.02	0.00	4.75	0.01	0.03	1.72
JW-B-57	5.52	2.48	8.00	0.08	0.15	0.00	0.01	0.00	4.93	0.01	0.02	1.69
JW-B-58	5.31	2.69	8.00	0.16	0.15	0.00	0.02	0.01	4.88	0.01	0.06	1.67
Min	5.31	2.42	7.88	0.00	0.13	0.00	0.00	0.00	4.50	0.00	0.00	1.65
Max	5.59	2.69	8.00	0.36	0.22	0.03	0.04	0.02	5.23	0.01	0.06	1.80
Mean	5.49	2.50	8.00	0.15	0.16	0.01	0.01	0.01	4.79	0.00	0.02	1.71



Table 17. Titanite analyses from the JW-zone.

Sample	Desc	SiO <sub>2</sub>	Na <sub>2</sub> O	MgO	Al <sub>2</sub> O <sub>3</sub>	NiO	FeO	MnO	Cr <sub>2</sub> O <sub>3</sub>	V <sub>2</sub> O <sub>3</sub>	K <sub>2</sub> O	CaO	TiO <sub>2</sub>	Total
JW-T-1	397-8-Tit-1	29.66	0.00	0.03	3.47	0.00	0.01	0.05	0.02	0.49	0.03	27.22	33.73	94.70
JW-T-2	397-8-Tit-2	29.65	0.02	0.02	2.92	0.00	0.00	0.06	0.01	0.16	0.00	27.28	35.32	95.44
JW-T-3	397-8-Tit-3	29.36	0.02	0.03	3.19	0.00	0.05	0.04	0.03	0.63	0.02	27.39	34.15	94.89
JW-T-4	397-8-Tit-4	29.70	0.00	0.00	2.80	0.00	0.05	0.05	0.06	0.16	0.02	27.07	35.21	95.10
JW-T-5	397-8-Tit-5	29.70	0.00	0.00	3.53	0.00	0.00	0.10	0.03	0.64	0.04	26.96	33.77	94.78
Min		29.36	0.00	0.00	2.80	0.00	0.00	0.04	0.01	0.16	0.00	26.96	33.73	94.70
Max		29.70	0.02	0.03	3.53	0.00	0.05	0.10	0.06	0.64	0.04	27.39	35.32	95.44
Mean		29.61	0.01	0.02	3.18	0.00	0.02	0.06	0.03	0.42	0.02	27.18	34.44	94.98

Sample	Si	Na	Mg	Al	Ni	Fe <sup>2+</sup>	Mn	Cr	V	K	Ca	Ti	SumA	SumB
JW-T-1	4.06	0.00	0.01	0.56	0.00	0.00	0.01	0.00	0.04	0.00	3.99	3.47	4.03	4.05
JW-T-2	4.03	0.00	0.00	0.47	0.00	0.00	0.01	0.00	0.01	0.00	3.97	3.61	4.08	4.00
JW-T-3	4.01	0.00	0.01	0.51	0.00	0.01	0.01	0.00	0.06	0.00	4.01	3.51	4.02	4.10
JW-T-4	4.05	0.00	0.00	0.45	0.00	0.01	0.01	0.01	0.01	0.00	3.95	3.61	4.06	3.99
JW-T-5	4.05	0.00	0.00	0.57	0.00	0.00	0.01	0.00	0.06	0.01	3.94	3.47	4.04	4.02
Min	4.01	0.00	0.00	0.45	0.00	0.00	0.01	0.00	0.01	0.00	3.94	3.47	4.02	3.99
Max	4.06	0.00	0.01	0.57	0.00	0.01	0.01	0.01	0.06	0.01	4.01	3.61	4.08	4.10
Mean	4.04	0.00	0.00	0.51	0.00	0.00	0.01	0.00	0.04	0.00	3.97	3.53	4.04	4.03

Table 18. Pyroxene analyses from the pyroxene relict units.

Sample	Desc	SiO <sub>2</sub>	TiO <sub>2</sub>	Al <sub>2</sub> O <sub>3</sub>	Cr <sub>2</sub> O <sub>3</sub>	FeO	MnO	MgO	CaO	Na <sub>2</sub> O	K <sub>2</sub> O	Total	TSi	TAI	MAl	MTi
<b>Boudin-1</b>	397-1-1	53.42	0.23	2.65	0.89	0.04	0.18	16.82	24.89	0.55	0.00	99.67	1.94	0.07	0.05	0.01
<b>Boudin-2</b>	397-1-2	53.74	0.15	2.85	0.77	0.08	0.17	16.68	24.65	0.56	0.02	99.67	1.95	0.05	0.07	0.00
<b>Boudin-3</b>	397-1-3	53.98	0.12	2.50	0.84	0.07	0.21	16.82	24.79	0.56	0.03	99.92	1.95	0.05	0.06	0.00
<b>Boudin-4</b>	397-3-1	53.74	0.06	2.86	0.64	0.04	0.17	16.75	24.66	0.52	0.01	99.45	1.95	0.05	0.07	0.00
<b>Boudin-5</b>	397-3-2	54.25	0.07	2.83	0.63	0.07	0.19	16.95	24.65	0.55	0.02	100.21	1.95	0.05	0.07	0.00
<b>Boudin-6</b>	397-3-3	54.46	0.00	2.45	0.60	0.03	0.19	17.09	24.69	0.56	0.00	100.07	1.96	0.04	0.07	0.00
<b>Boudin-7</b>	397-5-1	53.39	0.14	3.26	1.00	0.12	0.16	16.57	24.48	0.62	0.00	99.74	1.93	0.07	0.07	0.00
<b>Boudin-8</b>	397-5-2	53.67	0.15	3.13	0.83	0.02	0.17	16.60	24.92	0.62	0.00	100.11	1.94	0.07	0.07	0.00
<b>Boudin-9</b>	397-6-1	54.39	0.08	1.87	0.16	0.05	0.15	17.32	24.95	0.34	0.02	99.33	1.98	0.03	0.05	0.00
<b>Boudin-10</b>	397-6-2	54.48	0.12	1.96	0.23	0.09	0.11	17.42	24.80	0.37	0.03	99.61	1.97	0.03	0.06	0.00
<b>Boudin-11</b>	397-7-1	53.27	0.02	3.01	0.76	0.01	0.23	16.58	24.87	0.50	0.01	99.26	1.94	0.06	0.07	0.00
<b>Boudin-12</b>	397-7-2	53.20	0.21	3.26	0.79	0.04	0.22	16.36	24.66	0.58	0.00	99.32	1.94	0.07	0.08	0.01
<b>Boudin-13</b>	397-7-3	53.12	0.00	3.13	0.81	0.03	0.15	16.52	24.55	0.45	0.01	98.77	1.94	0.06	0.08	0.00
<b>Boudin-14</b>	408-3-1	54.37	0.06	1.16	0.11	0.07	0.10	17.35	25.56	0.24	0.01	99.03	1.98	0.02	0.03	0.00
<b>Boudin-15</b>	408-4-2	54.37	0.06	0.96	0.10	0.16	0.18	17.44	25.41	0.18	0.00	98.86	1.99	0.01	0.03	0.00
<b>Boudin-16</b>	408-4-3	54.87	0.00	0.92	0.07	0.20	0.22	17.54	25.64	0.19	0.00	99.65	1.99	0.01	0.03	0.00
<b>Boudin-17</b>	445:P1-1	53.85	0.01	0.92	0.01	0.13	0.34	17.96	25.55	0.15	0.00	98.92	1.96	0.04	0.00	0.00
<b>Boudin-18</b>	445:P1-2	54.77	0.00	0.92	0.00	0.10	0.42	17.95	25.74	0.15	0.00	100.05	1.98	0.03	0.01	0.00
<b>Boudin-19</b>	445:P1-3	54.53	0.00	0.89	0.02	0.18	0.37	18.05	25.66	0.15	0.00	99.85	1.97	0.03	0.01	0.00
<b>Boudin-20</b>	445:P1-4	54.27	0.01	0.91	0.02	0.16	0.39	17.96	25.70	0.16	0.00	99.58	1.97	0.04	0.00	0.00
<b>Boudin-21</b>	445:P1-5	54.38	0.01	0.91	0.01	0.13	0.32	18.09	25.49	0.15	0.00	99.49	1.97	0.03	0.01	0.00
<b>Boudin-22</b>	445:P2-1	54.61	0.00	0.90	0.01	0.10	0.40	17.95	25.59	0.17	0.00	99.73	1.98	0.03	0.01	0.00
<b>Boudin-23</b>	445:P2-2	54.82	0.01	0.66	0.01	0.09	0.29	18.04	25.67	0.12	0.00	99.71	1.98	0.02	0.01	0.00
<b>Boudin-24</b>	445:P2-3	54.50	0.00	0.78	0.00	0.12	0.37	18.19	26.04	0.11	0.00	100.11	1.96	0.03	0.00	0.00
<b>Boudin-25</b>	445:P2-4	54.56	0.00	0.86	0.03	0.14	0.33	17.91	25.84	0.13	0.00	99.80	1.97	0.03	0.01	0.00
<b>Boudin-26</b>	445:P2-5	55.02	0.00	0.77	0.03	0.09	0.36	18.14	25.86	0.15	0.00	100.42	1.98	0.02	0.01	0.00
<b>Boudin-27</b>	446:P1-1	53.70	0.04	0.90	0.01	0.10	0.40	18.01	25.84	0.16	0.00	99.16	1.95	0.04	0.00	0.00
<b>Boudin-28</b>	446:P1-2	53.96	0.01	0.82	0.02	0.15	0.39	17.92	25.72	0.17	0.00	99.16	1.96	0.04	0.00	0.00
<b>Boudin-29</b>	446:P1-3	53.72	0.04	0.73	0.00	0.16	0.45	17.85	26.16	0.18	0.00	99.29	1.95	0.03	0.00	0.00
<b>Boudin-30</b>	446:P1-4	53.82	0.01	0.75	0.01	0.14	0.44	18.00	25.52	0.20	0.00	98.89	1.96	0.03	0.00	0.00
<b>Boudin-31</b>	446:P1-5	54.03	0.00	0.85	0.02	0.11	0.40	17.96	25.72	0.19	0.00	99.28	1.96	0.04	0.00	0.00
<b>Boudin-32</b>	446:P1-6	54.90	0.00	0.79	0.02	0.10	0.47	18.23	25.76	0.18	0.00	100.45	1.97	0.03	0.00	0.00
<b>Boudin-33</b>	446:P2-1	54.15	0.03	0.82	0.01	0.11	0.42	17.76	26.18	0.12	0.00	99.60	1.96	0.04	0.00	0.00
<b>Boudin-34</b>	446:P2-2	54.23	0.00	1.01	0.00	0.15	0.41	17.74	25.75	0.15	0.00	99.44	1.97	0.03	0.01	0.00
<b>Boudin-35</b>	446:P2-3	53.74	0.00	1.03	0.00	0.11	0.43	17.81	25.69	0.16	0.00	98.97	1.96	0.04	0.00	0.00
<b>Boudin-36</b>	446:P2-4	53.83	0.00	0.92	0.00	0.09	0.43	17.90	25.98	0.17	0.00	99.32	1.95	0.04	0.00	0.00
<b>Boudin-37</b>	446:P2-5	54.54	0.00	0.75	0.01	0.11	0.38	18.14	26.20	0.14	0.00	100.27	1.96	0.03	0.00	0.00
<b>Boudin-38</b>	446:P2-6	54.10	0.02	0.80	0.01	0.06	0.35	18.11	25.92	0.17	0.00	99.54	1.96	0.03	0.00	0.00
<b>Boudin-39</b>	446:P2-7	54.11	0.00	0.84	0.03	0.10	0.36	18.03	25.85	0.15	0.00	99.47	1.96	0.04	0.00	0.00

Table 18. Continue 1.

Sample	Desc	SiO <sub>2</sub>	TiO <sub>2</sub>	Al <sub>2</sub> O <sub>3</sub>	Cr <sub>2</sub> O <sub>3</sub>	FeO	MnO	MgO	CaO	Na <sub>2</sub> O	K <sub>2</sub> O	Total	TSi	TAl	MAl	MTi
<b>Boudin-40</b>	446:P2-8	53.96	0.00	0.98	0.00	0.15	0.45	17.92	25.84	0.17	0.00	99.47	1.96	0.04	0.00	0.00
<b>Boudin-41</b>	446:P3-1	54.09	0.00	1.00	0.02	0.13	0.38	17.91	25.91	0.20	0.00	99.64	1.96	0.04	0.00	0.00
<b>Boudin-42</b>	446:P3-2	54.30	0.00	0.90	0.03	0.16	0.50	17.77	25.53	0.17	0.00	99.36	1.97	0.03	0.01	0.00
<b>Boudin-43</b>	446:P3-3	53.93	0.00	0.86	0.01	0.07	0.51	17.76	25.41	0.18	0.00	98.73	1.97	0.03	0.01	0.00
<b>Boudin-44</b>	446:P3-4	54.17	0.01	0.89	0.01	0.12	0.39	17.93	25.60	0.17	0.00	99.29	1.97	0.03	0.01	0.00
<b>Boudin-45</b>	446:P3-5	54.00	0.01	0.92	0.00	0.14	0.41	17.85	25.73	0.19	0.00	99.25	1.96	0.04	0.00	0.00
<b>Boudin-46</b>	446:P3-6	53.82	0.05	0.93	0.00	0.12	0.42	17.80	25.59	0.16	0.00	98.89	1.96	0.04	0.00	0.00
<b>Boudin-47</b>	446:P3-7	54.27	0.03	0.88	0.00	0.12	0.41	17.89	25.50	0.17	0.00	99.27	1.97	0.03	0.01	0.00
<b>Boudin-48</b>	446:P3-8	53.89	0.01	0.91	0.00	0.08	0.38	17.87	25.73	0.16	0.00	99.03	1.96	0.04	0.00	0.00
<b>Boudin-49</b>	446:P3-9	54.07	0.04	1.05	0.05	0.14	0.46	17.84	25.51	0.19	0.00	99.35	1.96	0.04	0.01	0.00
<b>Boudin-50</b>	446:P4-1	54.92	0.03	1.16	0.00	0.12	0.40	18.03	25.84	0.14	0.00	100.64	1.97	0.03	0.02	0.00
<b>Boudin-51</b>	446:P4-2	54.79	0.02	1.08	0.00	0.08	0.41	17.87	25.65	0.20	0.00	100.10	1.97	0.03	0.02	0.00
<b>Boudin-52</b>	456:P1-1	54.94	0.01	0.86	0.01	0.11	0.37	17.88	25.33	0.14	0.00	99.65	1.99	0.01	0.03	0.00
<b>Boudin-53</b>	456:P1-11	54.19	0.04	0.84	0.00	0.14	0.35	17.94	25.50	0.17	0.00	99.17	1.97	0.03	0.01	0.00
<b>Boudin-54</b>	456:P1-2	54.66	0.01	0.82	0.01	0.13	0.33	17.94	25.32	0.12	0.00	99.34	1.99	0.02	0.02	0.00
<b>Boudin-55</b>	456:P1-3	54.10	0.03	0.90	0.00	0.16	0.33	17.85	25.41	0.17	0.00	98.95	1.97	0.03	0.01	0.00
<b>Boudin-56</b>	456:P1-4	55.00	0.00	0.87	0.00	0.11	0.38	17.97	25.63	0.15	0.00	100.11	1.98	0.02	0.02	0.00
<b>Boudin-57</b>	456:P1-5	54.42	0.04	0.87	0.00	0.11	0.37	17.79	25.27	0.14	0.00	99.01	1.98	0.02	0.02	0.00
<b>Boudin-58</b>	456:P1-6	54.57	0.02	0.78	0.03	0.12	0.30	17.75	25.19	0.14	0.00	98.90	1.99	0.01	0.03	0.00
<b>Boudin-59</b>	456:P1-7	54.43	0.01	0.78	0.00	0.13	0.32	18.09	25.64	0.16	0.00	99.56	1.97	0.03	0.00	0.00
<b>Boudin-60</b>	456:P1-8	54.81	0.00	0.84	0.02	0.14	0.40	17.61	25.44	0.14	0.00	99.40	1.99	0.01	0.03	0.00
<b>Boudin-61</b>	456:P1-9	54.50	0.02	0.82	0.00	0.13	0.42	17.50	25.59	0.15	0.00	99.13	1.99	0.01	0.02	0.00
<b>Boudin-62</b>	456:P2-1	54.08	0.02	0.87	0.00	0.14	0.46	17.93	25.30	0.15	0.00	98.95	1.97	0.03	0.01	0.00
<b>Boudin-63</b>	456:P2-2	54.99	0.04	0.85	0.01	0.09	0.42	17.91	25.15	0.12	0.00	99.58	1.99	0.01	0.03	0.00
<b>Boudin-64</b>	456:P2-3	54.53	0.04	0.87	0.01	0.14	0.31	17.80	25.39	0.13	0.00	99.22	1.98	0.02	0.02	0.00
<b>Boudin-65</b>	456:P2-4	54.70	0.00	0.75	0.00	0.12	0.29	17.99	25.50	0.11	0.00	99.46	1.98	0.02	0.02	0.00
<b>Boudin-66</b>	456:P3-1	54.90	0.00	0.90	0.01	0.12	0.40	18.00	26.04	0.19	0.00	100.56	1.97	0.03	0.01	0.00
<b>Boudin-67</b>	456:P3-2	54.32	0.03	0.89	0.05	0.09	0.38	17.67	25.34	0.16	0.00	98.93	1.98	0.02	0.02	0.00
<b>Boudin-68</b>	456:P3-3	54.32	0.02	0.83	0.00	0.13	0.34	17.63	25.68	0.17	0.00	99.12	1.98	0.02	0.01	0.00
<b>Boudin-69</b>	456:P3-4	54.29	0.01	0.85	0.00	0.13	0.30	17.58	25.52	0.16	0.00	98.84	1.98	0.02	0.02	0.00
<b>Boudin-70</b>	456:P4-1	55.10	0.02	0.84	0.01	0.10	0.31	18.08	25.48	0.16	0.00	100.10	1.99	0.02	0.02	0.00
<b>Boudin-71</b>	456:P4-2	54.41	0.01	0.89	0.00	0.08	0.39	17.83	25.17	0.15	0.00	98.93	1.98	0.02	0.02	0.00
<b>Boudin-72</b>	456:P4-3	54.45	0.00	0.87	0.01	0.08	0.38	17.90	25.33	0.19	0.00	99.21	1.98	0.02	0.02	0.00
<b>Boudin-73</b>	456:P4-4	54.82	0.02	0.84	0.00	0.13	0.37	17.85	25.55	0.15	0.00	99.73	1.98	0.02	0.02	0.00
<b>Boudin-74</b>	456:P5-1	54.74	0.00	0.93	0.02	0.06	0.36	17.91	25.40	0.17	0.00	99.59	1.98	0.02	0.02	0.00
<b>Boudin-75</b>	456:P5-2	54.06	0.00	1.55	0.01	1.17	0.28	17.19	24.36	0.20	0.00	98.82	1.98	0.02	0.05	0.00
<b>Boudin-76</b>	456:P5-3	54.65	0.00	0.94	0.00	0.12	0.36	17.94	25.60	0.13	0.00	99.74	1.98	0.02	0.02	0.00
<b>Boudin-77</b>	456:P5-4	54.68	0.00	0.88	0.01	0.09	0.31	17.97	25.71	0.15	0.00	99.80	1.98	0.02	0.01	0.00
<b>Boudin-78</b>	457:p1-2	55.09	0.02	1.07	0.00	0.12	0.21	18.12	25.46	0.18	0.00	100.27	1.98	0.02	0.03	0.00
<b>Boudin-79</b>	457:p1-3	55.18	0.00	1.02	0.00	0.15	0.22	18.09	25.51	0.20	0.00	100.37	1.98	0.02	0.03	0.00

Table 18. Continue 2.

Sample	Desc	SiO <sub>2</sub>	TiO <sub>2</sub>	Al <sub>2</sub> O <sub>3</sub>	Cr <sub>2</sub> O <sub>3</sub>	FeO	MnO	MgO	CaO	Na <sub>2</sub> O	K <sub>2</sub> O	Total	TSi	TAl	MAl	MTi
<b>Boudin-80</b>	457:p1-4	54.94	0.00	1.10	0.03	0.17	0.19	18.20	25.63	0.17	0.00	100.43	1.97	0.03	0.02	0.00
<b>Boudin-81</b>	457:p3-1	54.29	0.02	1.13	0.00	0.09	0.10	18.20	25.70	0.17	0.00	99.70	1.96	0.04	0.01	0.00
<b>Boudin-82</b>	457:p3-2	54.27	0.03	1.08	0.00	0.15	0.17	18.46	25.82	0.19	0.00	100.17	1.95	0.05	0.00	0.00
<b>Boudin-83</b>	457:p3-3	54.55	0.03	1.05	0.00	0.13	0.17	18.23	25.79	0.19	0.00	100.14	1.96	0.04	0.01	0.00
<b>Boudin-84</b>	457:p3-4	54.35	0.01	1.17	0.00	0.16	0.11	18.24	25.69	0.21	0.00	99.94	1.96	0.04	0.01	0.00
<b>Boudin-85</b>	460:P1-1	54.44	0.02	0.79	0.01	0.14	0.23	17.77	25.77	0.15	0.00	99.32	1.98	0.02	0.01	0.00
<b>Boudin-86</b>	460:P1-2	54.38	0.01	0.81	0.00	0.06	0.31	17.80	25.85	0.12	0.00	99.34	1.98	0.03	0.01	0.00
<b>Boudin-87</b>	460:P2-1	54.87	0.00	0.91	0.03	0.12	0.32	17.84	25.66	0.15	0.00	99.90	1.98	0.02	0.02	0.00
<b>Boudin-88</b>	460:P2-2	54.30	0.05	0.92	0.00	0.10	0.35	17.90	25.27	0.13	0.00	99.02	1.98	0.02	0.02	0.00
<b>Boudin-89</b>	460:P2-3	54.16	0.06	0.86	0.02	0.11	0.35	18.00	25.48	0.14	0.00	99.18	1.97	0.03	0.01	0.00
<b>Boudin-90</b>	460:P2-4	54.51	0.04	0.95	0.03	0.09	0.32	17.92	25.68	0.15	0.00	99.69	1.97	0.03	0.01	0.00
<b>Boudin-91</b>	460:P3-1	54.75	0.00	0.89	0.00	0.09	0.40	17.83	26.11	0.14	0.00	100.21	1.97	0.03	0.01	0.00
<b>Boudin-92</b>	460:P3-2	54.61	0.01	0.84	0.00	0.09	0.38	17.42	25.51	0.12	0.00	98.98	1.99	0.01	0.03	0.00
<b>Boudin-93</b>	460:P3-3	54.63	0.03	0.76	0.01	0.14	0.37	17.53	25.71	0.12	0.00	99.30	1.99	0.01	0.02	0.00
<b>Boudin-94</b>	460:P3-4	54.62	0.03	0.75	0.03	0.09	0.41	17.52	25.84	0.13	0.00	99.42	1.99	0.01	0.02	0.00
<b>Boudin-95</b>	460:P3-5	54.59	0.00	0.79	0.00	0.10	0.40	17.58	25.71	0.14	0.00	99.31	1.99	0.01	0.02	0.00
<b>Boudin-96</b>	460:P3-6	54.19	0.01	0.84	0.02	0.17	0.35	17.68	25.57	0.10	0.00	98.93	1.98	0.02	0.01	0.00
<b>Boudin-97</b>	6\2f	52.94	0.04	2.26	0.00	0.15	0.40	16.39	26.90	0.18	0.08	99.34	1.93	0.07	0.03	0.00
<b>Boudin-98</b>	7\1e	56.88	0.04	1.23	0.02	0.11	0.25	16.10	25.00	0.13	0.03	99.79	2.07	0.00	0.05	0.00
<b>Min</b>		52.94	0.00	0.66	0.00	0.01	0.10	16.10	24.36	0.10	0.00	98.73	1.93	0.00	0.00	0.00
<b>Max</b>		56.88	0.23	3.26	1.00	1.17	0.51	18.46	26.90	0.62	0.08	100.64	2.07	0.07	0.08	0.01
<b>Average</b>		54.35	0.03	1.16	0.10	0.12	0.33	17.71	25.51	0.21	0.00	99.52	1.97	0.03	0.02	0.00

Table 18. Continue 3.

Sample	M1Fe <sup>3+</sup>	M1Fe <sup>2+</sup>	M1Cr	M1Mg	M2Mg	M2Fe <sup>2+</sup>	M2Mn	M2Ca	M2Na	Ca (Wo)	Mg (En)	Fe <sup>2+</sup> + Mn (Fs)
Boudin-1	0.00	0.00	0.03	0.91	0.00	0.00	0.01	0.97	0.04	51.36	48.29	0.36
Boudin-2	0.00	0.00	0.02	0.90	0.00	0.00	0.01	0.96	0.04	51.30	48.30	0.41
Boudin-3	0.00	0.00	0.02	0.91	0.00	0.00	0.01	0.96	0.04	51.24	48.38	0.38
Boudin-4	0.00	0.00	0.02	0.91	0.00	0.00	0.01	0.96	0.04	51.24	48.42	0.34
Boudin-5	0.00	0.00	0.02	0.91	0.00	0.00	0.01	0.95	0.04	50.89	48.69	0.42
Boudin-6	0.00	0.00	0.02	0.92	0.00	0.00	0.01	0.95	0.04	50.76	48.89	0.36
Boudin-7	0.00	0.00	0.03	0.89	0.00	0.00	0.01	0.95	0.04	51.32	48.34	0.34
Boudin-8	0.00	0.00	0.02	0.89	0.00	0.00	0.01	0.96	0.04	51.74	47.95	0.31
Boudin-9	0.00	0.00	0.01	0.94	0.00	0.00	0.01	0.97	0.02	50.71	48.98	0.32
Boudin-10	0.00	0.00	0.01	0.94	0.01	0.00	0.00	0.96	0.03	50.41	49.27	0.32
Boudin-11	0.00	0.00	0.02	0.90	0.00	0.00	0.01	0.97	0.04	51.67	47.93	0.39
Boudin-12	0.00	0.00	0.02	0.89	0.00	0.00	0.01	0.96	0.04	51.78	47.79	0.43
Boudin-13	0.00	0.00	0.02	0.90	0.00	0.00	0.01	0.96	0.03	51.49	48.21	0.30
Boudin-14	0.00	0.00	0.00	0.94	0.00	0.00	0.00	1.00	0.02	51.29	48.44	0.27
Boudin-15	0.00	0.01	0.00	0.95	0.00	0.00	0.01	1.00	0.01	50.88	48.59	0.54
Boudin-16	0.00	0.01	0.00	0.95	0.00	0.00	0.01	1.00	0.01	50.90	48.45	0.66
Boudin-17	0.00	0.00	0.00	0.98	0.00	0.00	0.01	1.00	0.01	50.19	49.09	0.73
Boudin-18	0.00	0.00	0.00	0.97	0.00	0.00	0.01	1.00	0.01	50.35	48.85	0.80
Boudin-19	0.00	0.01	0.00	0.97	0.00	0.00	0.01	0.99	0.01	50.11	49.05	0.85
Boudin-20	0.00	0.01	0.00	0.97	0.00	0.00	0.01	1.00	0.01	50.27	48.88	0.85
Boudin-21	0.00	0.00	0.00	0.98	0.00	0.00	0.01	0.99	0.01	49.97	49.34	0.70
Boudin-22	0.00	0.00	0.00	0.97	0.00	0.00	0.01	0.99	0.01	50.22	49.01	0.77
Boudin-23	0.00	0.00	0.00	0.97	0.00	0.00	0.01	1.00	0.01	50.26	49.15	0.59
Boudin-24	0.00	0.00	0.00	0.98	0.00	0.00	0.01	1.01	0.01	50.33	48.92	0.75
Boudin-25	0.00	0.00	0.00	0.97	0.00	0.00	0.01	1.00	0.01	50.54	48.74	0.72
Boudin-26	0.00	0.00	0.00	0.97	0.00	0.00	0.01	1.00	0.01	50.26	49.05	0.69
Boudin-27	0.00	0.00	0.00	0.98	0.00	0.00	0.01	1.01	0.01	50.38	48.85	0.77
Boudin-28	0.00	0.01	0.00	0.97	0.00	0.00	0.01	1.00	0.01	50.35	48.81	0.83
Boudin-29	0.00	0.01	0.00	0.97	0.00	0.00	0.01	1.02	0.01	50.82	48.25	0.93
Boudin-30	0.00	0.00	0.00	0.98	0.00	0.00	0.01	1.00	0.01	50.02	49.09	0.90
Boudin-31	0.00	0.00	0.00	0.97	0.00	0.00	0.01	1.00	0.01	50.32	48.89	0.79
Boudin-32	0.00	0.00	0.00	0.98	0.00	0.00	0.01	0.99	0.01	49.95	49.18	0.87
Boudin-33	0.00	0.00	0.00	0.96	0.00	0.00	0.01	1.02	0.01	51.02	48.16	0.81
Boudin-34	0.00	0.01	0.00	0.96	0.00	0.00	0.01	1.00	0.01	50.62	48.52	0.87
Boudin-35	0.00	0.00	0.00	0.97	0.00	0.00	0.01	1.00	0.01	50.48	48.69	0.84
Boudin-36	0.00	0.00	0.00	0.97	0.00	0.00	0.01	1.01	0.01	50.65	48.55	0.80
Boudin-37	0.00	0.00	0.00	0.97	0.00	0.00	0.01	1.01	0.01	50.55	48.70	0.75
Boudin-38	0.00	0.00	0.00	0.98	0.00	0.00	0.01	1.01	0.01	50.39	48.98	0.63
Boudin-39	0.00	0.00	0.00	0.97	0.00	0.00	0.01	1.00	0.01	50.39	48.90	0.71

Table 18. Continue 4.

Sample	M1Fe <sup>3+</sup>	M1Fe <sup>2+</sup>	M1Cr	M1Mg	M2Mg	M2Fe <sup>2+</sup>	M2Mn	M2Ca	M2Na	Ca (Wo)	Mg (En)	Fe <sup>2+</sup> + Mn (Fs)
Boudin-40	0.00	0.01	0.00	0.97	0.00	0.00	0.01	1.00	0.01	50.42	48.65	0.92
Boudin-41	0.00	0.00	0.00	0.97	0.00	0.00	0.01	1.00	0.01	50.57	48.64	0.78
Boudin-42	0.00	0.01	0.00	0.96	0.00	0.00	0.02	0.99	0.01	50.28	48.70	1.02
Boudin-43	0.00	0.00	0.00	0.97	0.00	0.00	0.02	1.00	0.01	50.24	48.86	0.91
Boudin-44	0.00	0.00	0.00	0.97	0.00	0.00	0.01	1.00	0.01	50.25	48.97	0.79
Boudin-45	0.00	0.00	0.00	0.97	0.00	0.00	0.01	1.00	0.01	50.45	48.70	0.85
Boudin-46	0.00	0.00	0.00	0.97	0.00	0.00	0.01	1.00	0.01	50.39	48.77	0.84
Boudin-47	0.00	0.00	0.00	0.97	0.00	0.00	0.01	0.99	0.01	50.19	48.99	0.82
Boudin-48	0.00	0.00	0.00	0.97	0.00	0.00	0.01	1.00	0.01	50.49	48.79	0.71
Boudin-49	0.00	0.00	0.00	0.97	0.00	0.00	0.01	0.99	0.01	50.21	48.86	0.93
Boudin-50	0.00	0.00	0.00	0.96	0.00	0.00	0.01	0.99	0.01	50.33	48.87	0.80
Boudin-51	0.00	0.00	0.00	0.96	0.00	0.00	0.01	0.99	0.01	50.39	48.85	0.76
Boudin-52	0.00	0.00	0.00	0.97	0.00	0.00	0.01	0.98	0.01	50.07	49.18	0.75
Boudin-53	0.00	0.00	0.00	0.97	0.00	0.00	0.01	0.99	0.01	50.15	49.09	0.76
Boudin-54	0.00	0.00	0.00	0.97	0.00	0.00	0.01	0.99	0.01	50.05	49.34	0.61
Boudin-55	0.00	0.01	0.00	0.97	0.00	0.00	0.01	0.99	0.01	50.19	49.05	0.76
Boudin-56	0.00	0.00	0.00	0.97	0.00	0.00	0.01	0.99	0.01	50.24	49.01	0.76
Boudin-57	0.00	0.00	0.00	0.97	0.00	0.00	0.01	0.99	0.01	50.22	49.19	0.58
Boudin-58	0.00	0.00	0.00	0.97	0.00	0.00	0.01	0.99	0.01	50.16	49.18	0.66
Boudin-59	0.00	0.00	0.00	0.98	0.00	0.00	0.01	1.00	0.01	50.11	49.20	0.69
Boudin-60	0.00	0.00	0.00	0.95	0.00	0.00	0.01	0.99	0.01	50.51	48.65	0.85
Boudin-61	0.00	0.00	0.00	0.95	0.00	0.00	0.01	1.00	0.01	50.83	48.37	0.80
Boudin-62	0.00	0.00	0.00	0.97	0.00	0.00	0.01	0.99	0.01	49.88	49.19	0.93
Boudin-63	0.00	0.00	0.00	0.97	0.00	0.00	0.01	0.98	0.01	49.83	49.37	0.80
Boudin-64	0.00	0.00	0.00	0.97	0.00	0.00	0.01	0.99	0.01	50.32	49.09	0.59
Boudin-65	0.00	0.00	0.00	0.97	0.00	0.00	0.01	0.99	0.01	50.14	49.22	0.64
Boudin-66	0.00	0.00	0.00	0.96	0.00	0.00	0.01	1.00	0.01	50.57	48.64	0.80
Boudin-67	0.00	0.00	0.00	0.96	0.00	0.00	0.01	0.99	0.01	50.38	48.88	0.74
Boudin-68	0.00	0.00	0.00	0.96	0.00	0.00	0.01	1.00	0.01	50.77	48.50	0.73
Boudin-69	0.00	0.00	0.00	0.96	0.00	0.00	0.01	1.00	0.01	50.72	48.61	0.67
Boudin-70	0.00	0.00	0.00	0.97	0.00	0.00	0.01	0.98	0.01	50.00	49.37	0.63
Boudin-71	0.00	0.00	0.00	0.97	0.00	0.00	0.01	0.98	0.01	49.99	49.27	0.74
Boudin-72	0.00	0.00	0.00	0.97	0.00	0.00	0.01	0.99	0.01	50.06	49.22	0.72
Boudin-73	0.00	0.00	0.00	0.96	0.00	0.00	0.01	0.99	0.01	50.32	48.91	0.78
Boudin-74	0.00	0.00	0.00	0.97	0.00	0.00	0.01	0.99	0.01	50.15	49.20	0.65
Boudin-75	0.00	0.02	0.00	0.94	0.00	0.02	0.01	0.96	0.01	49.30	48.41	2.30
Boudin-76	0.00	0.00	0.00	0.97	0.00	0.00	0.01	0.99	0.01	50.26	49.00	0.74
Boudin-77	0.00	0.00	0.00	0.97	0.00	0.00	0.01	1.00	0.01	50.38	49.00	0.62
Boudin-78	0.00	0.00	0.00	0.97	0.00	0.00	0.01	0.98	0.01	49.99	49.50	0.51
Boudin-79	0.00	0.01	0.00	0.97	0.00	0.00	0.01	0.98	0.01	50.05	49.38	0.57

Table 18. Continue 5.

Sample	M1Fe <sup>3+</sup>	M1Fe <sup>2+</sup>	M1Cr	M1Mg	M2Mg	M2Fe <sup>2+</sup>	M2Mn	M2Ca	M2Na	Ca (Wo)	Mg (En)	Fe <sup>2+</sup> + Mn (Fs)
<b>Boudin-80</b>	0.00	0.01	0.00	0.97	0.00	0.00	0.01	0.99	0.01	50.02	49.43	0.55
<b>Boudin-81</b>	0.00	0.00	0.00	0.98	0.00	0.00	0.00	0.99	0.01	50.22	49.49	0.29
<b>Boudin-82</b>	0.00	0.01	0.00	0.99	0.00	0.00	0.01	0.99	0.01	49.89	49.63	0.49
<b>Boudin-83</b>	0.00	0.00	0.00	0.98	0.00	0.00	0.01	0.99	0.01	50.18	49.36	0.46
<b>Boudin-84</b>	0.00	0.01	0.00	0.98	0.00	0.00	0.00	0.99	0.02	50.10	49.49	0.41
<b>Boudin-85</b>	0.00	0.00	0.00	0.96	0.00	0.00	0.01	1.00	0.01	50.74	48.69	0.57
<b>Boudin-86</b>	0.00	0.00	0.00	0.96	0.00	0.00	0.01	1.01	0.01	50.78	48.65	0.57
<b>Boudin-87</b>	0.00	0.00	0.00	0.96	0.00	0.00	0.01	0.99	0.01	50.48	48.84	0.68
<b>Boudin-88</b>	0.00	0.00	0.00	0.97	0.00	0.00	0.01	0.99	0.01	50.01	49.29	0.70
<b>Boudin-89</b>	0.00	0.00	0.00	0.98	0.00	0.00	0.01	0.99	0.01	50.07	49.22	0.71
<b>Boudin-90</b>	0.00	0.00	0.00	0.97	0.00	0.00	0.01	1.00	0.01	50.42	48.95	0.64
<b>Boudin-91</b>	0.00	0.00	0.00	0.96	0.00	0.00	0.01	1.01	0.01	50.89	48.36	0.75
<b>Boudin-92</b>	0.00	0.00	0.00	0.95	0.00	0.00	0.01	1.00	0.01	50.90	48.36	0.74
<b>Boudin-93</b>	0.00	0.00	0.00	0.95	0.00	0.00	0.01	1.00	0.01	50.91	48.30	0.80
<b>Boudin-94</b>	0.00	0.00	0.00	0.95	0.00	0.00	0.01	1.01	0.01	51.06	48.17	0.78
<b>Boudin-95</b>	0.00	0.00	0.00	0.95	0.00	0.00	0.01	1.00	0.01	50.85	48.38	0.78
<b>Boudin-96</b>	0.00	0.01	0.00	0.96	0.00	0.00	0.01	1.00	0.01	50.55	48.64	0.81
<b>Boudin-97</b>	0.00	0.01	0.00	0.89	0.00	0.00	0.01	1.05	0.01	53.65	45.48	0.86
<b>Boudin-98</b>	0.00	0.00	0.00	0.88	0.00	0.00	0.01	0.98	0.01	52.43	46.98	0.60

Table 19. Garnet analyses from the calc-silicate skarn boudins.

Sample	SiO <sub>2</sub>	TiO <sub>2</sub>	Al <sub>2</sub> O <sub>3</sub>	Cr <sub>2</sub> O <sub>3</sub>	FeO	MnO	MgO	CaO	Na <sub>2</sub> O	Total	FeO <sub>calc</sub>	Fe <sub>2</sub> O <sub>3calc</sub>	Total <sub>calc</sub>	TSi	TAI	Sum_T
446-1	37.61	0.31	21.48	0.09	0.08	1.24	0.49	35.66	0.04	96.99	0.06	0.07	97.05	2.91	0.09	3.00
446-2	39.10	0.30	21.92	0.06	0.04	1.01	0.61	36.16	0.00	99.20	0.05	0.06	99.27	2.96	0.04	3.00
446-2ra	38.35	0.74	21.46	0.01	0.08	0.88	0.65	35.99	0.01	98.18	0.07	0.07	98.24	2.94	0.07	3.00
446-2rb	38.97	0.28	22.01	0.05	0.05	0.58	0.39	36.89	0.00	99.23	0.06	0.07	99.30	2.95	0.05	3.00
446-3a	39.00	0.69	21.72	0.00	0.13	0.92	0.56	36.74	0.04	99.78	0.09	0.10	99.85	2.94	0.06	3.00
446-4	38.35	0.23	21.83	0.12	0.06	0.96	0.46	36.28	0.01	98.31	0.08	0.09	98.41	2.93	0.07	3.00
446-5	39.35	0.70	22.19	0.04	0.07	0.92	0.52	36.40	0.01	100.20	0.07	0.08	100.29	2.95	0.05	3.00
446-5a	38.78	0.30	21.98	0.01	0.06	0.93	0.51	36.10	0.01	98.68	0.07	0.08	98.76	2.95	0.05	3.00
446-5b	38.91	0.44	21.99	0.04	0.00	0.56	0.39	36.69	0.02	99.05	0.03	0.04	99.12	2.95	0.05	3.00
446-6	38.84	0.46	21.90	0.01	0.05	0.75	0.44	36.28	0.01	98.74	0.04	0.05	98.78	2.95	0.05	3.00
446:G1-1	38.83	0.24	21.03	0.09	0.05	0.63	0.46	35.84	0.00	97.16	0.05	0.05	97.21	3.00	0.00	3.00
446:G1-2	39.49	0.24	21.82	0.05	0.01	0.76	0.45	35.71	0.00	98.53	0.03	0.03	98.57	3.01	0.00	3.01
446:G1-3	39.01	0.26	21.63	0.00	0.02	0.42	0.41	36.27	0.00	98.01	0.02	0.02	98.04	2.99	0.02	3.00
446:G1-4	39.01	0.59	21.55	0.00	0.03	0.58	0.63	36.11	0.00	98.50	0.03	0.03	98.53	2.97	0.03	3.00
446:G2-1	39.25	0.22	22.10	0.02	0.02	0.44	0.42	36.66	0.00	99.14	0.03	0.03	99.17	2.97	0.03	3.00
446:G2-2	38.64	0.26	21.50	0.02	0.06	0.61	0.47	36.39	0.00	97.96	0.05	0.05	97.99	2.96	0.04	3.00
446:G2-3	39.53	0.24	21.98	0.01	0.02	0.45	0.38	36.72	0.00	99.32	0.03	0.04	99.37	2.99	0.01	3.00
446:G3-1	38.94	0.28	21.24	0.09	0.10	0.81	0.56	36.32	0.00	98.34	0.07	0.07	98.38	2.97	0.03	3.00
446:G3-2	38.82	0.58	21.33	0.00	0.08	0.23	0.64	36.97	0.00	98.65	0.07	0.08	98.73	2.95	0.05	3.00
446:G3-3	39.35	0.18	21.90	0.01	0.06	0.58	0.50	36.54	0.00	99.13	0.07	0.08	99.21	2.98	0.02	3.00
446:G3-4	39.38	0.14	21.90	0.00	0.03	0.50	0.53	37.03	0.00	99.53	0.05	0.06	99.61	2.97	0.03	3.00
446:G3-5	39.16	0.16	21.99	0.03	0.04	0.43	0.48	37.07	0.00	99.37	0.05	0.05	99.42	2.95	0.05	3.00
447-G-1	38.07	0.30	22.01	0.02	0.05	0.42	0.45	34.06	0.03	95.40	0.05	0.05	95.45	2.99	0.01	3.00
447-G-2	38.13	0.30	21.55	0.02	0.09	1.19	0.51	34.19	0.02	96.00	0.07	0.07	96.06	2.98	0.02	3.00
447-G-3	38.97	0.28	22.01	0.06	0.07	1.07	0.52	34.11	0.01	97.10	0.07	0.08	97.18	3.01	0.00	3.01
447-G-4	38.79	0.26	21.61	0.02	0.12	1.02	0.56	33.26	0.02	95.65	0.09	0.11	95.73	3.05	0.00	3.05
447-G-5	38.82	0.28	21.36	0.08	0.12	1.26	0.48	32.91	0.01	95.32	0.11	0.12	95.42	3.06	0.00	3.06
3-G-1d	39.55	0.35	22.27	0.07	0.13	0.39	0.47	35.36	0.02	98.61	0.12	0.13	98.72	3.01	0.00	3.01
460:G1-2	39.08	0.33	21.71	0.01	0.04	0.50	0.52	36.66	0.00	98.85	0.07	0.08	98.96	2.97	0.04	3.00
460:G1-3	39.26	0.32	22.00	0.02	0.06	0.60	0.56	36.74	0.00	99.56	0.07	0.08	99.64	2.96	0.04	3.00
460:G1-6	39.01	0.32	22.15	0.00	0.08	0.58	0.54	36.73	0.00	99.42	0.07	0.08	99.50	2.94	0.06	3.00
460:G1-7	38.59	0.32	21.67	0.02	0.10	0.64	0.60	36.55	0.00	98.49	0.09	0.10	98.57	2.94	0.06	3.00
460:G2-1	39.35	0.22	21.50	0.01	0.01	0.42	0.40	36.92	0.00	98.84	0.05	0.05	98.93	2.99	0.01	3.00
460:G2-2	39.03	0.28	21.24	0.05	0.07	1.04	0.53	36.36	0.00	98.62	0.06	0.07	98.67	2.97	0.03	3.00
460:G2-3	39.05	0.26	21.45	0.03	0.07	0.86	0.55	36.47	0.00	98.74	0.07	0.07	98.80	2.97	0.03	3.00
460:G2-4	39.18	0.25	21.17	0.06	0.07	1.05	0.50	36.10	0.00	98.38	0.07	0.08	98.45	2.99	0.01	3.00
460:G2-5	39.32	0.24	21.58	0.03	0.07	0.41	0.44	37.13	0.00	99.22	0.07	0.08	99.29	2.97	0.03	3.00
460:G3-1	39.00	0.28	22.13	0.01	0.05	0.86	0.54	35.88	0.00	98.74	0.06	0.06	98.81	2.96	0.04	3.00
460:G3-2	39.05	0.32	22.02	0.01	0.09	0.92	0.54	35.91	0.00	98.86	0.07	0.08	98.92	2.97	0.04	3.00
460:G3-3	39.38	0.31	21.99	0.02	0.08	0.87	0.57	36.07	0.00	99.30	0.08	0.08	99.38	2.98	0.02	3.00
460:G3-4	39.32	0.27	22.00	0.00	0.01	0.67	0.53	36.16	0.00	98.95	0.04	0.05	99.03	2.98	0.02	3.00
Min	37.61	0.14	21.03	0.00	0.00	0.23	0.38	32.91	0.00	95.32	0.02	0.02	95.42	2.91	0.00	3.00
Max	39.55	0.74	22.27	0.12	0.13	1.26	0.65	37.13	0.04	100.20	0.12	0.13	100.29	3.06	0.09	3.06
Mean	38.97	0.33	21.75	0.03	0.06	0.73	0.51	36.06	0.01	98.44	0.06	0.07	98.51	2.97	0.03	3.00



Table 19. Continued.

Sample	Al VI	Ti	Cr	Sum_A	Fe <sup>2+</sup>	Mg	Mn	Ca	Na	Sum_B	Alm	And	Gross	Pyrope	Spess	Uvaro
446-1	1.87	0.02	0.01	1.89	0.00	0.06	0.08	2.96	0.01	3.11	0.13	0.00	94.95	1.82	2.63	0.29
446-2	1.91	0.02	0.00	1.93	0.00	0.07	0.07	2.93	0.00	3.07	0.11	0.00	95.35	2.25	2.11	0.18
446-2ra	1.87	0.04	0.00	1.91	0.00	0.07	0.06	2.95	0.00	3.09	0.14	0.00	95.51	2.41	1.85	0.04
446-2rb	1.91	0.02	0.00	1.93	0.00	0.04	0.04	2.99	0.00	3.07	0.12	0.00	97.08	1.45	1.21	0.15
446-3a	1.86	0.04	0.00	1.90	0.01	0.06	0.06	2.97	0.01	3.10	0.19	0.00	95.71	2.04	1.90	0.00
446-4	1.89	0.01	0.01	1.91	0.01	0.05	0.06	2.97	0.00	3.09	0.16	0.00	95.71	1.69	2.02	0.37
446-5	1.91	0.04	0.00	1.95	0.01	0.06	0.06	2.93	0.00	3.05	0.15	0.00	95.87	1.92	1.92	0.12
446-5a	1.92	0.02	0.00	1.93	0.00	0.06	0.06	2.94	0.00	3.07	0.14	0.00	95.91	1.90	1.95	0.03
446-5b	1.91	0.03	0.00	1.94	0.00	0.05	0.04	2.98	0.00	3.06	0.07	0.00	97.08	1.46	1.18	0.12
446-6	1.92	0.03	0.00	1.94	0.00	0.05	0.05	2.96	0.00	3.06	0.09	0.00	96.64	1.64	1.58	0.02
446-G1-1	1.92	0.01	0.01	1.93	0.00	0.05	0.04	2.97	0.00	3.07	0.10	0.00	96.54	1.73	1.34	0.30
446-G1-2	1.96	0.01	0.00	1.98	0.00	0.05	0.05	2.92	0.00	3.02	0.05	0.00	96.47	1.71	1.62	0.15
446-G1-3	1.94	0.02	0.00	1.95	0.00	0.05	0.03	2.98	0.00	3.05	0.04	0.00	97.53	1.53	0.89	0.00
446-G1-4	1.91	0.03	0.00	1.94	0.00	0.07	0.04	2.95	0.00	3.06	0.06	0.00	96.38	2.34	1.22	0.00
446-G2-1	1.94	0.01	0.00	1.95	0.00	0.05	0.03	2.97	0.00	3.05	0.05	0.00	97.41	1.54	0.93	0.07
446-G2-2	1.90	0.02	0.00	1.92	0.00	0.05	0.04	2.99	0.00	3.08	0.09	0.00	96.81	1.75	1.28	0.08
446-G2-3	1.94	0.01	0.00	1.96	0.00	0.04	0.03	2.97	0.00	3.05	0.07	0.00	97.59	1.39	0.94	0.02
446-G3-1	1.89	0.02	0.01	1.91	0.00	0.06	0.05	2.97	0.00	3.09	0.14	0.00	95.82	2.08	1.70	0.27
446-G3-2	1.86	0.03	0.00	1.90	0.01	0.07	0.02	3.01	0.00	3.10	0.15	0.00	97.04	2.34	0.47	0.00
446-G3-3	1.93	0.01	0.00	1.94	0.00	0.06	0.04	2.96	0.00	3.06	0.14	0.00	96.76	1.86	1.22	0.02
446-G3-4	1.91	0.01	0.00	1.92	0.00	0.06	0.03	2.99	0.00	3.08	0.10	0.00	96.92	1.94	1.04	0.00
446-G3-5	1.91	0.01	0.00	1.92	0.00	0.05	0.03	3.00	0.00	3.08	0.10	0.00	97.16	1.77	0.90	0.09
447-G-1	2.03	0.02	0.00	2.05	0.00	0.05	0.03	2.87	0.00	2.95	0.11	0.00	96.96	1.79	0.94	0.08
447-G-2	1.97	0.02	0.00	1.99	0.00	0.06	0.08	2.87	0.00	3.01	0.15	0.00	95.09	1.97	2.62	0.06
447-G-3	2.00	0.02	0.00	2.03	0.00	0.06	0.07	2.83	0.00	2.96	0.15	0.00	95.23	2.01	2.37	0.18
447-G-4	2.00	0.02	0.00	2.02	0.01	0.07	0.07	2.80	0.00	2.94	0.21	0.00	95.09	2.23	2.31	0.08
447-G-5	1.99	0.02	0.01	2.01	0.01	0.06	0.08	2.78	0.00	2.93	0.24	0.00	94.68	1.94	2.86	0.24
3-G-1d	2.00	0.02	0.00	2.02	0.01	0.05	0.03	2.88	0.00	2.97	0.25	0.00	96.83	1.79	0.84	0.20
460-G1-2	1.91	0.02	0.00	1.93	0.01	0.06	0.03	2.98	0.00	3.08	0.15	0.00	96.86	1.92	1.04	0.04
460-G1-3	1.91	0.02	0.00	1.93	0.00	0.06	0.04	2.97	0.00	3.07	0.14	0.00	96.51	2.04	1.25	0.06
460-G1-6	1.91	0.02	0.00	1.93	0.01	0.06	0.04	2.97	0.00	3.07	0.15	0.00	96.65	1.98	1.21	0.01
460-G1-7	1.88	0.02	0.00	1.90	0.01	0.07	0.04	2.98	0.00	3.10	0.18	0.00	96.23	2.20	1.33	0.07
460-G2-1	1.91	0.01	0.00	1.92	0.00	0.05	0.03	3.00	0.00	3.08	0.10	0.00	97.53	1.46	0.87	0.04
460-G2-2	1.88	0.02	0.00	1.90	0.00	0.06	0.07	2.97	0.00	3.10	0.12	0.00	95.62	1.93	2.18	0.16
460-G2-3	1.89	0.02	0.00	1.91	0.00	0.06	0.06	2.97	0.00	3.09	0.14	0.00	95.99	2.01	1.78	0.08
460-G2-4	1.90	0.02	0.00	1.92	0.00	0.06	0.07	2.96	0.00	3.08	0.14	0.00	95.63	1.83	2.20	0.20
460-G2-5	1.90	0.01	0.00	1.91	0.00	0.05	0.03	3.01	0.00	3.09	0.14	0.00	97.32	1.61	0.84	0.10
460-G3-1	1.94	0.02	0.00	1.96	0.00	0.06	0.06	2.92	0.00	3.04	0.12	0.00	96.04	2.00	1.82	0.02
460-G3-2	1.94	0.02	0.00	1.95	0.01	0.06	0.06	2.92	0.00	3.05	0.15	0.00	95.86	2.01	1.94	0.04
460-G3-3	1.94	0.02	0.00	1.95	0.01	0.07	0.06	2.92	0.00	3.05	0.16	0.00	95.82	2.13	1.84	0.06
460-G3-4	1.94	0.02	0.00	1.96	0.00	0.06	0.04	2.94	0.00	3.04	0.09	0.00	96.55	1.96	1.40	0.00
Min	1.86	0.01	0.00	1.89	0.00	0.04	0.02	2.78	0.00	2.93	0.04	0.00	94.68	1.39	0.47	0.00
Max	2.03	0.04	0.01	2.05	0.01	0.07	0.08	3.01	0.01	3.11	0.25	0.00	97.59	2.41	2.86	0.37
Mean	1.92	0.02	0.00	1.94	0.00	0.06	0.05	2.95	0.00	3.05	0.13	0.00	96.31	1.89	1.55	0.10

Table 20. Zoisite analyses from the calc-silicate skarn boudins.

Sample	Desc	SiO <sub>2</sub>	TiO <sub>2</sub>	Al <sub>2</sub> O <sub>3</sub>	Cr <sub>2</sub> O <sub>3</sub>	Fe <sub>2</sub> O <sub>3</sub>	MnO	MgO	CaO	Na <sub>2</sub> O	Total
Z-1	18-2:Z1-1	39.75	0.05	32.59	0.02	0.02	0.00	0.06	24.51	0.00	96.99
Z-2	18-2:Z1-2	39.75	0.00	32.36	0.02	0.00	0.06	0.03	24.39	0.00	96.61
Z-3	18-2:Z1-3	39.14	0.01	32.03	0.05	0.01	0.04	0.03	24.41	0.00	95.73
Z-4	18-2:Z1-4	39.55	0.00	32.11	0.04	0.00	0.00	0.05	24.22	0.01	95.98
Z-5	18-2:Z1-5	39.35	0.02	32.11	0.02	0.00	0.02	0.06	24.18	0.01	95.76
Z-6	18-2:Z1-6	39.41	0.03	31.91	0.00	0.02	0.00	0.04	24.02	0.01	95.45
Z-7	18-2:Z1-7	39.52	0.01	32.03	0.00	0.02	0.04	0.04	24.46	0.02	96.12
Z-8	18-2:Z1-8	39.39	0.06	31.84	0.07	0.01	0.02	0.03	24.53	0.00	95.95
Z-9	18-7:Z2-1	39.81	0.01	33.11	0.00	0.02	0.00	0.03	23.94	0.00	96.91
Z-10	18-7:Z2-12	38.84	0.01	31.34	0.00	0.00	0.01	0.08	24.37	0.00	94.65
Z-11	18-7:Z2-13	39.23	0.03	32.31	0.00	0.01	0.00	0.05	24.62	0.00	96.25
Z-12	18-7:Z2-17	39.44	0.03	32.18	0.00	0.07	0.01	0.05	24.42	0.01	96.20
Z-13	18-7:Z2-18	39.21	0.04	31.78	0.02	0.00	0.00	0.04	24.45	0.00	95.54
Z-14	18-7:Z2-2	39.71	0.04	32.35	0.02	0.00	0.00	0.01	24.60	0.02	96.75
Z-15	18-7:Z2-3	39.41	0.02	32.10	0.00	0.03	0.01	0.02	24.52	0.01	96.13
Z-16	18-7:Z2-4	40.26	0.01	35.00	0.02	0.02	0.01	0.04	23.27	0.04	98.67
Z-17	18-7:Z2-6	39.25	0.02	31.68	0.00	0.01	0.00	0.05	24.41	0.01	95.44
Z-18	18-7:Z2-7	39.05	0.00	31.62	0.00	0.00	0.02	0.05	24.54	0.01	95.30
Z-19	18-7:Z2-8	39.30	0.02	31.67	0.01	0.02	0.00	0.03	24.39	0.00	95.43
Z-20	18-7:Z3-1	38.53	0.04	31.64	0.02	0.01	0.02	0.26	24.20	0.30	95.03
Z-21	18-7:Z3-2	38.85	0.03	31.50	0.04	0.05	0.00	0.01	24.37	0.03	94.87
Z-22	18-7:Z3-3	39.67	0.04	32.28	0.00	0.03	0.02	0.02	24.47	0.02	96.55
Z-23	18-7:Z3-5	39.25	0.06	31.77	0.00	0.02	0.02	0.02	24.46	0.02	95.63
Z-24	18-7:Z3-6	39.30	0.03	31.60	0.04	0.03	0.01	0.15	24.15	0.02	95.32
Z-25	18-7:Z3-7	38.89	0.04	30.86	0.00	0.02	0.04	0.22	23.99	0.02	94.09
Z-26	2:Z2-10	40.03	0.05	31.53	0.05	0.02	0.01	0.07	23.75	0.12	95.63
Z-27	2:Z2-14	39.00	0.07	31.82	0.00	0.02	0.00	0.03	23.69	0.04	94.68
Z-28	2:Z2-2	39.85	0.07	31.36	0.05	0.03	0.03	0.07	23.69	0.16	95.31
Z-29	2:Z2-7	38.83	0.04	31.16	0.01	0.05	0.01	0.12	23.91	0.19	94.31
Z-30	2:Z3-5	39.77	0.04	30.77	0.04	0.03	0.02	0.08	23.81	0.15	94.71
Z-31	2:Z3-8	39.93	0.05	31.62	0.01	0.01	0.01	0.06	24.04	0.10	95.84
Z-32	408-1-Z-1	38.77	0.01	34.16	0.04	0.04	0.06	0.02	24.43	0.00	97.53
Z-33	408-1-Z-2	38.52	0.00	33.77	0.00	0.00	0.10	0.04	24.30	0.00	96.73
Z-34	408-1-Z-3	38.91	0.00	33.77	0.02	0.03	0.00	0.04	24.07	0.02	96.86
Z-35	408-2-Z-1	37.63	0.00	33.34	0.00	0.00	0.01	0.02	24.06	0.01	95.07

Table 20. Continue 1.

Sample	Desc	SiO <sub>2</sub>	TiO <sub>2</sub>	Al <sub>2</sub> O <sub>3</sub>	Cr <sub>2</sub> O <sub>3</sub>	Fe <sub>2</sub> O <sub>3</sub>	MnO	MgO	CaO	Na <sub>2</sub> O	Total
Z-36	408-2-Z-2	38.44	0.02	33.43	0.01	0.08	0.07	0.05	24.12	0.01	96.23
Z-37	408-2-Z-3	38.50	0.09	33.78	0.05	0.08	0.05	0.04	23.88	0.01	96.48
Z-38	447:P1-1	39.29	0.00	31.51	0.00	0.04	0.02	0.07	24.42	0.01	95.35
Z-39	447:P1-2	39.09	0.01	31.25	0.00	0.00	0.00	0.06	24.34	0.01	94.76
Z-40	447:P1-3	39.01	0.05	31.48	0.00	0.00	0.00	0.08	24.28	0.01	94.90
Z-41	447:P1-5	39.10	0.05	32.14	0.00	0.02	0.00	0.05	24.50	0.00	95.86
Z-42	447:P1-6	39.04	0.03	32.50	0.02	0.01	0.01	0.05	24.67	0.00	96.32
Z-43	447:P1-7	38.78	0.02	32.95	0.04	0.01	0.00	0.05	24.37	0.02	96.24
Z-44	447:P1-8	38.51	0.02	32.79	0.02	0.00	0.03	0.04	24.68	0.03	96.11
Z-45	447:Z1-1	39.82	0.07	32.56	0.03	0.05	0.01	0.07	24.44	0.02	97.07
Z-46	447:Z2-1	39.72	0.07	32.58	0.00	0.01	0.00	0.08	24.28	0.01	96.76
Z-47	447:Z2-2	39.98	0.04	32.78	0.00	0.03	0.00	0.06	24.29	0.01	97.20
Z-48	447:Z2-3	40.11	0.07	32.75	0.00	0.03	0.04	0.06	24.37	0.02	97.44
Z-49	447:Z2-4	40.32	0.02	32.71	0.01	0.06	0.05	0.08	24.21	0.02	97.49
Z-50	447:Z2-5	39.97	0.05	32.63	0.03	0.06	0.01	0.05	24.49	0.01	97.29
Z-51	447:Z2-6	40.09	0.03	32.88	0.00	0.03	0.03	0.06	24.41	0.00	97.53
Z-52	447:Z2-8	40.11	0.04	32.38	0.00	0.01	0.01	0.06	24.06	0.01	96.68
Z-53	447:Z2B	38.93	0.04	31.54	0.00	0.00	0.02	0.06	23.76	0.00	94.36
Z-54	447:Z3-1	38.66	0.02	31.98	0.02	0.01	0.00	0.05	24.04	0.06	94.82
Z-55	447:Z3-2	39.35	0.06	31.44	0.00	0.06	0.02	0.05	24.44	0.01	95.43
Z-56	447:Z3-3	39.03	0.03	31.54	0.01	0.07	0.00	0.05	24.42	0.01	95.15
Z-57	447:Z3-4	38.95	0.04	31.25	0.01	0.00	0.00	0.06	24.14	0.00	94.45
Z-58	447:Z3-5	38.82	0.06	30.86	0.05	0.03	0.00	0.06	23.98	0.02	93.87
Z-59	447:Z3-6	38.90	0.01	32.22	0.00	0.02	0.03	0.04	24.41	0.02	95.63
Z-60	447:Z3-7	39.01	0.05	32.26	0.00	0.02	0.00	0.05	24.38	0.00	95.77
Z-61	447:Z3-8	38.88	0.06	32.34	0.00	0.03	0.00	0.05	24.43	0.00	95.79
Z-62	447:Z4-2	39.40	0.04	32.02	0.00	0.02	0.00	0.04	24.38	0.02	95.93
Z-63	447:Z4-3	39.65	0.04	31.98	0.01	0.01	0.01	0.05	24.39	0.02	96.15
Z-64	447:Z4-4	39.55	0.03	31.91	0.03	0.02	0.04	0.04	23.93	0.00	95.55
Z-65	447:Z4-5	39.48	0.05	31.80	0.00	0.03	0.00	0.04	24.26	0.00	95.66
Z-66	447:Z4-6	39.54	0.03	32.14	0.00	0.05	0.00	0.05	24.45	0.03	96.28
Z-67	447:Z4-7	39.67	0.04	32.16	0.03	0.01	0.01	0.03	24.31	0.00	96.26
Min		37.63	0.00	30.77	0.00	0.00	0.00	0.01	23.27	0.00	93.87
Max		40.32	0.09	35.00	0.07	0.08	0.10	0.26	24.68	0.30	98.67
Mean		39.30	0.03	32.17	0.01	0.02	0.02	0.06	24.26	0.03	95.89

Table 20. Continue 2.

Sample	Sample	Si	Al IV	Sum_T	Al VI	Ti	Cr	Fe <sup>3+</sup>	Mg	Mn	Na	Ca	Sum_cat
Z-1	18-2:Z1-1	3.04	0.00	3.04	2.93	0.00	0.00	0.00	0.01	0.00	0.00	2.01	4.95
Z-2	18-2:Z1-2	3.05	0.00	3.05	2.92	0.00	0.00	0.00	0.00	0.00	0.00	2.00	4.94
Z-3	18-2:Z1-3	3.03	0.00	3.03	2.92	0.00	0.00	0.00	0.00	0.00	0.00	2.03	4.96
Z-4	18-2:Z1-4	3.05	0.00	3.05	2.92	0.00	0.00	0.00	0.01	0.00	0.00	2.00	4.93
Z-5	18-2:Z1-5	3.05	0.00	3.05	2.93	0.00	0.00	0.00	0.01	0.00	0.00	2.00	4.94
Z-6	18-2:Z1-6	3.06	0.00	3.06	2.92	0.00	0.00	0.00	0.01	0.00	0.00	2.00	4.92
Z-7	18-2:Z1-7	3.05	0.00	3.05	2.91	0.00	0.00	0.00	0.00	0.00	0.00	2.02	4.94
Z-8	18-2:Z1-8	3.05	0.00	3.05	2.90	0.00	0.00	0.00	0.00	0.00	0.00	2.03	4.94
Z-9	18-7:Z2-1	3.04	0.00	3.04	2.97	0.00	0.00	0.00	0.00	0.00	0.00	1.96	4.93
Z-10	18-7:Z2-12	3.05	0.00	3.05	2.90	0.00	0.00	0.00	0.01	0.00	0.00	2.05	4.96
Z-11	18-7:Z2-13	3.03	0.00	3.03	2.93	0.00	0.00	0.00	0.01	0.00	0.00	2.03	4.98
Z-12	18-7:Z2-17	3.04	0.00	3.04	2.92	0.00	0.00	0.00	0.01	0.00	0.00	2.02	4.95
Z-13	18-7:Z2-18	3.05	0.00	3.05	2.91	0.00	0.00	0.00	0.00	0.00	0.00	2.03	4.95
Z-14	18-7:Z2-2	3.04	0.00	3.04	2.92	0.00	0.00	0.00	0.00	0.00	0.00	2.02	4.95
Z-15	18-7:Z2-3	3.04	0.00	3.04	2.92	0.00	0.00	0.00	0.00	0.00	0.00	2.03	4.95
Z-16	18-7:Z2-4	3.00	0.00	3.00	3.08	0.00	0.00	0.00	0.01	0.00	0.01	1.86	4.95
Z-17	18-7:Z2-6	3.05	0.00	3.05	2.90	0.00	0.00	0.00	0.01	0.00	0.00	2.03	4.94
Z-18	18-7:Z2-7	3.04	0.00	3.04	2.90	0.00	0.00	0.00	0.01	0.00	0.00	2.05	4.96
Z-19	18-7:Z2-8	3.05	0.00	3.05	2.90	0.00	0.00	0.00	0.00	0.00	0.00	2.03	4.94
Z-20	18-7:Z3-1	3.02	0.00	3.02	2.92	0.00	0.00	0.00	0.03	0.00	0.05	2.03	5.03
Z-21	18-7:Z3-2	3.04	0.00	3.04	2.90	0.00	0.00	0.00	0.00	0.00	0.00	2.04	4.96
Z-22	18-7:Z3-3	3.05	0.00	3.05	2.92	0.00	0.00	0.00	0.00	0.00	0.00	2.01	4.94
Z-23	18-7:Z3-5	3.05	0.00	3.05	2.90	0.00	0.00	0.00	0.00	0.00	0.00	2.03	4.95
Z-24	18-7:Z3-6	3.06	0.00	3.06	2.89	0.00	0.00	0.00	0.02	0.00	0.00	2.01	4.93
Z-25	18-7:Z3-7	3.07	0.00	3.07	2.87	0.00	0.00	0.00	0.03	0.00	0.00	2.03	4.93
Z-26	2:Z2-10	3.10	0.00	3.10	2.87	0.00	0.00	0.00	0.01	0.00	0.02	1.97	4.87
Z-27	2:Z2-14	3.05	0.00	3.05	2.93	0.00	0.00	0.00	0.00	0.00	0.01	1.99	4.93
Z-28	2:Z2-2	3.09	0.00	3.09	2.87	0.00	0.00	0.00	0.01	0.00	0.02	1.97	4.88
Z-29	2:Z2-7	3.06	0.00	3.06	2.89	0.00	0.00	0.00	0.01	0.00	0.03	2.02	4.95
Z-30	2:Z3-5	3.11	0.00	3.11	2.83	0.00	0.00	0.00	0.01	0.00	0.02	2.00	4.87
Z-31	2:Z3-8	3.08	0.00	3.08	2.88	0.00	0.00	0.00	0.01	0.00	0.02	1.99	4.89
Z-32	408-1-Z-1	2.95	0.05	3.00	3.01	0.00	0.00	0.00	0.00	0.00	0.00	1.99	5.01
Z-33	408-1-Z-2	2.96	0.05	3.00	3.01	0.00	0.00	0.00	0.01	0.01	0.00	2.00	5.01
Z-34	408-1-Z-3	2.98	0.03	3.00	3.02	0.00	0.00	0.00	0.01	0.00	0.00	1.97	5.00
Z-35	408-2-Z-1	2.94	0.06	3.00	3.01	0.00	0.00	0.00	0.00	0.00	0.00	2.01	5.02

Table 20. Continue 3.

Sample	Sample	Si	Al IV	Sum_T	Al VI	Ti	Cr	Fe <sup>3+</sup>	Mg	Mn	Na	Ca	Sum_cat
Z-36	408-2-Z-2	2.96	0.04	3.00	3.00	0.00	0.00	0.01	0.01	0.01	0.00	1.99	5.01
Z-37	408-2-Z-3	2.96	0.04	3.00	3.01	0.01	0.00	0.01	0.01	0.00	0.00	1.97	5.00
Z-38	447:P1-1	3.06	0.00	3.06	2.89	0.00	0.00	0.00	0.01	0.00	0.00	2.04	4.94
Z-39	447:P1-2	3.06	0.00	3.06	2.88	0.00	0.00	0.00	0.01	0.00	0.00	2.04	4.93
Z-40	447:P1-3	3.05	0.00	3.05	2.90	0.00	0.00	0.00	0.01	0.00	0.00	2.03	4.94
Z-41	447:P1-5	3.03	0.00	3.03	2.93	0.00	0.00	0.00	0.01	0.00	0.00	2.03	4.97
Z-42	447:P1-6	3.01	0.00	3.01	2.95	0.00	0.00	0.00	0.01	0.00	0.00	2.04	5.00
Z-43	447:P1-7	2.99	0.01	3.00	2.98	0.00	0.00	0.00	0.01	0.00	0.00	2.01	5.01
Z-44	447:P1-8	2.98	0.02	3.00	2.97	0.00	0.00	0.00	0.01	0.00	0.00	2.05	5.02
Z-45	447:Z1-1	3.04	0.00	3.04	2.93	0.00	0.00	0.00	0.01	0.00	0.00	2.00	4.95
Z-46	447:Z2-1	3.04	0.00	3.04	2.94	0.00	0.00	0.00	0.01	0.00	0.00	1.99	4.94
Z-47	447:Z2-2	3.04	0.00	3.04	2.94	0.00	0.00	0.00	0.01	0.00	0.00	1.98	4.94
Z-48	447:Z2-3	3.05	0.00	3.05	2.93	0.00	0.00	0.00	0.01	0.00	0.00	1.98	4.93
Z-49	447:Z2-4	3.06	0.00	3.06	2.92	0.00	0.00	0.00	0.01	0.00	0.00	1.97	4.91
Z-50	447:Z2-5	3.04	0.00	3.04	2.93	0.00	0.00	0.00	0.01	0.00	0.00	2.00	4.94
Z-51	447:Z2-6	3.04	0.00	3.04	2.94	0.00	0.00	0.00	0.01	0.00	0.00	1.99	4.94
Z-52	447:Z2-8	3.07	0.00	3.07	2.92	0.00	0.00	0.00	0.01	0.00	0.00	1.97	4.90
Z-53	447:Z2B	3.06	0.00	3.06	2.92	0.00	0.00	0.00	0.01	0.00	0.00	2.00	4.92
Z-54	447:Z3-1	3.02	0.00	3.02	2.95	0.00	0.00	0.00	0.01	0.00	0.01	2.02	4.98
Z-55	447:Z3-2	3.06	0.00	3.06	2.88	0.00	0.00	0.00	0.01	0.00	0.00	2.04	4.93
Z-56	447:Z3-3	3.05	0.00	3.05	2.90	0.00	0.00	0.00	0.01	0.00	0.00	2.04	4.95
Z-57	447:Z3-4	3.06	0.00	3.06	2.89	0.00	0.00	0.00	0.01	0.00	0.00	2.03	4.93
Z-58	447:Z3-5	3.07	0.00	3.07	2.87	0.00	0.00	0.00	0.01	0.00	0.00	2.03	4.92
Z-59	447:Z3-6	3.02	0.00	3.02	2.95	0.00	0.00	0.00	0.00	0.00	0.00	2.03	4.99
Z-60	447:Z3-7	3.02	0.00	3.02	2.94	0.00	0.00	0.00	0.01	0.00	0.00	2.02	4.98
Z-61	447:Z3-8	3.01	0.00	3.01	2.95	0.00	0.00	0.00	0.01	0.00	0.00	2.03	4.99
Z-62	447:Z4-2	3.05	0.00	3.05	2.92	0.00	0.00	0.00	0.00	0.00	0.00	2.02	4.95
Z-63	447:Z4-3	3.06	0.00	3.06	2.90	0.00	0.00	0.00	0.01	0.00	0.00	2.01	4.93
Z-64	447:Z4-4	3.06	0.00	3.06	2.91	0.00	0.00	0.00	0.01	0.00	0.00	1.99	4.91
Z-65	447:Z4-5	3.06	0.00	3.06	2.90	0.00	0.00	0.00	0.01	0.00	0.00	2.01	4.93
Z-66	447:Z4-6	3.05	0.00	3.05	2.92	0.00	0.00	0.00	0.01	0.00	0.00	2.02	4.95
Z-67	447:Z4-7	3.05	0.00	3.05	2.92	0.00	0.00	0.00	0.00	0.00	0.00	2.01	4.93
<b>Min</b>		2.94	0.00	3.00	2.83	0.00	0.00	0.00	0.00	0.00	0.00	1.86	4.87
<b>Max</b>		3.11	0.06	3.11	3.08	0.01	0.00	0.01	0.03	0.01	0.05	2.05	5.03
<b>Mean</b>		3.04	0.00	3.04	2.92	0.00	0.00	0.00	0.01	0.00	0.00	2.01	4.95

Table 21. Plagioclase analyses from the pyroxene relict units.

Sample	Desc	SiO <sub>2</sub>	Al <sub>2</sub> O <sub>3</sub>	FeO	MgO	CaO	Na <sub>2</sub> O	K <sub>2</sub> O	Total
<b>Plag-1</b>	137:F2-1	44.79	35.35	0.03	0.00	17.99	0.95	0.00	99.10
<b>Plag-2</b>	137:F2-2	45.52	35.41	0.03	0.00	18.11	0.94	0.02	100.02
<b>Plag-3</b>	137:F2-3	46.19	34.89	0.05	0.01	17.38	1.32	0.01	99.85
<b>Plag-4</b>	137:F2-4	44.96	34.85	0.05	0.00	18.26	0.94	0.00	99.07
<b>Plag-5</b>	137:F3-1	45.05	34.64	0.00	0.01	18.39	0.90	0.00	99.00
<b>Plag-6</b>	137:F3-2	44.38	35.19	0.00	0.01	18.76	0.67	0.00	98.99
<b>Plag-7</b>	137:F3-3	44.68	34.57	0.00	0.02	18.34	0.76	0.00	98.37
<b>Plag-8</b>	137:F3-4	44.74	34.33	0.03	0.01	18.76	0.72	0.01	98.60
<b>Min</b>		44.38	34.33	0.00	0.00	17.38	0.67	0.00	98.37
<b>Max</b>		46.19	35.41	0.05	0.02	18.76	1.32	0.02	100.02
<b>Mean</b>		45.04	34.90	0.02	0.01	18.25	0.90	0.01	99.12

Sample	Si	Al	Fe <sup>2+</sup>	Mg	Ca	Na	K	Ab	An	Or
<b>Plag-1</b>	8.32	7.73	0.01	0.00	3.58	0.34	0.00	8.70	91.30	0.00
<b>Plag-2</b>	8.37	7.67	0.01	0.00	3.57	0.33	0.00	8.60	91.30	0.10
<b>Plag-3</b>	8.49	7.56	0.01	0.00	3.42	0.47	0.00	12.10	87.90	0.10
<b>Plag-4</b>	8.36	7.63	0.01	0.00	3.64	0.34	0.00	8.50	91.50	0.00
<b>Plag-5</b>	8.38	7.59	0.00	0.00	3.67	0.33	0.00	8.20	91.80	0.00
<b>Plag-6</b>	8.27	7.72	0.00	0.00	3.74	0.24	0.00	6.00	94.00	0.00
<b>Plag-7</b>	8.37	7.62	0.00	0.01	3.68	0.28	0.00	7.00	93.00	0.00
<b>Plag-8</b>	8.37	7.56	0.00	0.00	3.76	0.26	0.00	6.50	93.40	0.10
<b>Min</b>	8.27	7.56	0.00	0.00	3.42	0.24	0.00	6.00	87.90	0.00
<b>Max</b>	8.49	7.73	0.01	0.01	3.76	0.47	0.00	12.10	94.00	0.10
<b>Mean</b>	8.37	7.64	0.00	0.00	3.63	0.32	0.00	8.20	91.78	0.04

Table 22. Tsvavorite analyses of tsvavorite not associated with tanzanite mineralisation.

Sample	Desc	SiO <sub>2</sub>	Al <sub>2</sub> O <sub>3</sub>	MgO	Na <sub>2</sub> O	FeO	MnO	Cr <sub>2</sub> O <sub>3</sub>	CaO	TiO <sub>2</sub>	K <sub>2</sub> O	V <sub>2</sub> O <sub>3</sub>	Total	FeO <sub>calc</sub>	TSi	TAI	Sum_T
<b>Tsavo-1</b>	167-Ts1-2	38.52	21.94	0.55	0.00	0.03	0.31	0.00	37.43	0.36	0.01	0.00	99.15	0.03	2.91	0.09	3.00
<b>Tsavo-2</b>	167-Ts1-3	38.46	21.60	0.46	0.03	0.04	0.33	0.00	37.42	0.24	0.00	0.00	98.59	0.04	2.92	0.08	3.00
<b>Tsavo-3</b>	167-Ts1-4	38.45	21.62	0.48	0.00	0.04	0.29	0.07	37.58	0.15	0.02	0.00	98.70	0.04	2.92	0.08	3.00
<b>Tsavo-4</b>	167-Ts1-5	38.45	21.59	0.53	0.00	0.03	0.33	0.00	37.33	0.38	0.00	0.00	98.64	0.03	2.92	0.08	3.00
<b>Tsavo-5</b>	168-Ts1-1	39.16	22.53	0.58	0.00	0.06	0.33	0.04	38.02	0.22	0.00	0.30	101.24	0.06	2.91	0.09	3.00
<b>Tsavo-6</b>	168-Ts1-2	39.05	22.00	0.49	0.00	0.09	0.17	0.01	37.79	0.32	0.00	0.07	99.99	0.09	2.93	0.07	3.00
<b>Tsavo-7</b>	168-Ts1-3	38.55	21.62	0.54	0.01	0.05	0.34	0.06	37.26	0.12	0.00	0.35	98.89	0.05	2.93	0.07	3.00
<b>Tsavo-8</b>	168-Ts1-4	38.65	21.69	0.56	0.04	0.07	0.30	0.06	37.31	0.26	0.00	0.23	99.16	0.07	2.93	0.07	3.00
<b>Tsavo-9</b>	168-Ts1-5	38.61	22.05	0.57	0.02	0.01	0.37	0.08	37.45	0.15	0.00	0.38	99.70	0.01	2.91	0.09	3.00
<b>Tsavo-10</b>	168-Ts2-1	38.99	21.33	0.55	0.00	0.10	0.50	0.06	36.81	0.35	0.00	0.73	99.43	0.10	2.97	0.04	3.00
<b>Tsavo-11</b>	168-Ts2-2	38.96	21.96	0.50	0.00	0.05	0.47	0.01	37.38	0.24	0.02	0.00	99.58	0.05	2.93	0.07	3.00
<b>Tsavo-12</b>	168-Ts2-3	38.50	20.99	0.59	0.00	0.07	0.51	0.05	36.91	0.17	0.03	0.69	98.51	0.07	2.95	0.05	3.00
<b>Tsavo-13</b>	168-Ts2-4	38.73	21.81	0.52	0.00	0.05	0.36	0.00	37.16	0.25	0.00	0.00	98.88	0.05	2.94	0.06	3.00
<b>Tsavo-14</b>	168-Ts3-1	39.14	22.36	0.53	0.00	0.05	0.37	0.03	37.02	0.28	0.00	0.31	100.08	0.05	2.94	0.06	3.00
<b>Tsavo-15</b>	168-Ts3-2	39.06	22.19	0.50	0.00	0.06	0.33	0.04	37.23	0.12	0.02	0.24	99.79	0.06	2.94	0.06	3.00
<b>Tsavo-16</b>	168-Ts3-3	39.56	22.25	0.56	0.01	0.03	0.39	0.07	36.98	0.23	0.00	0.42	100.51	0.03	2.96	0.04	3.00
<b>Tsavo-17</b>	168-Ts4-1	38.59	21.91	0.50	0.00	0.06	0.51	0.06	37.00	0.23	0.00	0.00	98.87	0.06	2.93	0.07	3.00
<b>Tsavo-18</b>	168-Ts4-2	39.45	22.14	0.51	0.00	0.07	0.28	0.02	37.05	0.29	0.01	0.00	99.82	0.07	2.96	0.04	3.00
<b>Tsavo-19</b>	168-Ts4-3	38.91	22.30	0.54	0.00	0.07	0.33	0.00	37.27	0.31	0.01	0.00	99.74	0.07	2.92	0.08	3.00
<b>Tsavo-20</b>	182-Ts1-1	38.00	21.99	0.45	0.00	0.03	0.35	0.06	37.57	0.24	0.00	0.18	98.86	0.03	2.89	0.12	3.00
<b>Tsavo-21</b>	182-Ts1-3	38.55	22.31	0.48	0.00	0.06	0.38	0.00	37.59	0.17	0.00	0.15	99.70	0.06	2.90	0.10	3.00
<b>Tsavo-22</b>	182-Ts1-4	37.88	21.86	0.49	0.03	0.10	0.41	0.01	37.34	0.30	0.00	0.12	98.53	0.10	2.89	0.12	3.00
<b>Tsavo-23</b>	182-Ts1-5	38.76	22.33	0.53	0.00	0.06	0.38	0.01	37.16	0.22	0.00	0.09	99.52	0.06	2.92	0.08	3.00
<b>Tsavo-24</b>	182-Ts2-1	38.00	21.93	0.33	0.00	0.05	0.63	0.09	37.08	0.13	0.00	0.30	98.52	0.05	2.90	0.10	3.00
<b>Tsavo-25</b>	182-Ts2-2	38.32	21.98	0.41	0.02	0.05	0.66	0.07	36.96	0.17	0.01	0.27	98.90	0.05	2.91	0.09	3.00
<b>Tsavo-26</b>	183-Ts1-2	39.81	22.45	0.50	0.00	0.03	0.48	0.02	36.76	0.22	0.00	0.29	100.55	0.03	2.98	0.02	3.00
<b>Tsavo-27</b>	183-Ts1-3	40.75	23.30	0.54	0.00	0.06	0.53	0.00	35.83	0.22	0.00	0.02	101.25	0.06	3.02	0.00	3.02
<b>Tsavo-28</b>	183-Ts1-4	38.93	22.07	0.51	0.00	0.06	0.59	0.01	36.75	0.21	0.00	0.07	99.21	0.06	2.94	0.06	3.00
<b>Tsavo-29</b>	183-Ts2-1	39.61	21.96	0.54	0.00	0.01	0.57	0.00	36.73	0.21	0.01	0.35	99.98	0.01	2.98	0.02	3.00
<b>Tsavo-30</b>	183-Ts2-2	40.09	23.05	0.55	0.02	0.02	0.47	0.01	36.56	0.26	0.00	0.33	101.36	0.02	2.97	0.03	3.00

Table 22. Continue 1.

Sample	Desc	SiO <sub>2</sub>	Al <sub>2</sub> O <sub>3</sub>	MgO	Na <sub>2</sub> O	FeO	MnO	Cr <sub>2</sub> O <sub>3</sub>	CaO	TiO <sub>2</sub>	K <sub>2</sub> O	V <sub>2</sub> O <sub>3</sub>	Total	FeO <sub>calc</sub>	TSi	TAI	Sum_T
<b>Tsavo-31</b>	183-Ts2-3	39.96	22.08	0.55	0.00	0.04	0.53	0.03	36.55	0.26	0.00	0.35	100.35	0.04	3.00	0.00	3.00
<b>Tsavo-32</b>	183-Ts2-4	40.11	22.24	0.53	0.00	0.05	0.50	0.02	36.45	0.17	0.00	0.28	100.36	0.05	3.01	0.00	3.01
<b>Tsavo-33</b>	187-Ts1-1	39.48	21.63	0.58	0.01	0.05	0.48	0.08	36.90	0.28	0.00	0.85	100.35	0.05	2.98	0.02	3.00
<b>Tsavo-34</b>	187-Ts1-2	39.14	22.09	0.52	0.00	0.07	0.56	0.02	36.66	0.25	0.00	0.99	100.30	0.07	2.96	0.05	3.00
<b>Tsavo-35</b>	187-Ts1-3	39.59	22.00	0.57	0.02	0.06	0.31	0.03	37.41	0.25	0.00	0.04	100.26	0.06	2.96	0.04	3.00
<b>Tsavo-36</b>	187-Ts1-4	39.19	20.93	0.60	0.00	0.08	0.56	0.06	36.74	0.23	0.00	0.84	99.23	0.08	2.99	0.01	3.00
<b>Tsavo-37</b>	187-Ts1-5	39.75	21.74	0.62	0.00	0.09	0.51	0.13	36.78	0.22	0.01	0.83	100.67	0.09	2.99	0.01	3.00
<b>Tsavo-38</b>	187-Ts2-1	39.51	22.10	0.60	0.00	0.05	0.36	0.00	37.38	0.17	0.02	0.12	100.29	0.05	2.96	0.04	3.00
<b>Tsavo-39</b>	187-Ts2-2	39.89	22.84	0.54	0.00	0.05	0.42	0.02	37.12	0.27	0.01	0.21	101.36	0.05	2.96	0.04	3.00
<b>Tsavo-40</b>	187-Ts2-3	39.82	22.60	0.54	0.00	0.08	0.37	0.00	36.81	0.13	0.00	0.34	100.68	0.08	2.97	0.03	3.00
<b>Tsavo-41</b>	187-Ts2-4	39.52	22.15	0.59	0.00	0.07	0.41	0.02	37.10	0.21	0.00	0.31	100.38	0.07	2.96	0.04	3.00
<b>Tsavo-42</b>	187-Ts2-5	39.65	22.48	0.58	0.01	0.07	0.34	0.07	37.06	0.19	0.00	0.16	100.61	0.07	2.96	0.04	3.00
<b>Tsavo-43</b>	187-Ts3-1	40.53	23.00	0.51	0.02	0.02	0.24	0.00	37.28	0.20	0.00	0.16	101.96	0.02	2.98	0.02	3.00
<b>Tsavo-44</b>	187-Ts3-2	39.65	22.19	0.57	0.00	0.06	0.70	0.05	36.68	0.20	0.01	0.31	100.41	0.06	2.97	0.03	3.00
<b>Tsavo-45</b>	187-Ts3-3	40.28	22.61	0.56	0.00	0.08	0.41	0.06	36.85	0.19	0.00	0.22	101.27	0.08	2.99	0.01	3.00
<b>Tsavo-46</b>	187-Ts3-4	39.66	22.45	0.60	0.00	0.00	0.59	0.01	36.98	0.28	0.00	0.20	100.79	0.00	2.96	0.04	3.00
<b>Tsavo-47</b>	187-Ts3-5	39.75	22.28	0.57	0.00	0.08	0.66	0.03	36.63	0.13	0.00	0.27	100.40	0.08	2.98	0.02	3.00
<b>Tsavo-48</b>	188-Ts1-2	38.65	22.08	0.45	0.00	0.03	0.38	0.00	36.93	0.31	0.02	0.00	98.84	0.03	2.93	0.07	3.00
<b>Tsavo-49</b>	198-Ts1-1	40.37	23.07	0.55	0.00	0.04	0.59	0.02	36.38	0.25	0.01	0.09	101.37	0.04	2.99	0.01	3.00
<b>Tsavo-50</b>	198-Ts1-2	40.05	23.17	0.55	0.03	0.03	0.55	0.04	36.36	0.15	0.00	0.07	100.99	0.03	2.97	0.03	3.00
<b>Tsavo-51</b>	198-Ts1-3	39.82	22.90	0.51	0.00	0.11	0.56	0.00	36.56	0.18	0.00	0.03	100.67	0.11	2.97	0.04	3.00
<b>Tsavo-52</b>	198-Ts2-1	39.63	21.98	0.55	0.00	0.04	0.40	0.00	36.55	0.44	0.02	0.00	99.60	0.04	2.99	0.01	3.00
<b>Tsavo-53</b>	198-Ts2-2	40.18	22.65	0.55	0.00	0.04	0.37	0.01	36.41	0.36	0.00	0.02	100.59	0.04	3.00	0.00	3.00
<b>Tsavo-54</b>	198-Ts2-3	40.19	22.66	0.60	0.01	0.04	0.44	0.00	36.29	0.39	0.00	0.03	100.65	0.04	2.99	0.01	3.00
<b>Tsavo-55</b>	85-Ts-5-1	39.23	21.21	0.57	0.00	0.04	0.36	0.05	36.92	0.26	0.00	0.10	98.73	0.04	2.98	0.02	3.00
<b>Tsavo-56</b>	85-Ts-5-2	39.46	21.45	0.59	0.00	0.06	0.28	0.03	36.90	0.33	0.02	0.00	99.10	0.06	2.99	0.01	3.00
<b>Tsavo-57</b>	85-Ts-5-3	39.19	21.21	0.56	0.00	0.05	0.26	0.05	37.06	0.34	0.00	0.12	98.83	0.05	2.98	0.02	3.00
<b>Tsavo-58</b>	85-Ts1-1	39.42	21.31	0.48	0.00	0.06	0.50	0.06	37.22	0.23	0.00	0.06	99.32	0.06	2.98	0.02	3.00
<b>Tsavo-59</b>	85-Ts1-4	39.40	21.17	0.58	0.02	0.07	0.38	0.00	36.87	0.30	0.00	0.19	98.97	0.07	2.99	0.01	3.00
<b>Tsavo-60</b>	85-Ts1-5	39.31	21.55	0.50	0.02	0.03	0.45	0.00	37.07	0.27	0.00	0.09	99.30	0.03	2.97	0.03	3.00



Table 22. Continue 2.

Sample	Desc	SiO <sub>2</sub>	Al <sub>2</sub> O <sub>3</sub>	MgO	Na <sub>2</sub> O	FeO	MnO	Cr <sub>2</sub> O <sub>3</sub>	CaO	TiO <sub>2</sub>	K <sub>2</sub> O	V <sub>2</sub> O <sub>3</sub>	Total	FeO <sub>calc</sub>	TSi	TAI	Sum_T
<b>Tsavo-61</b>	85-Ts2-1	39.98	21.79	0.51	0.00	0.07	0.32	0.00	37.57	0.35	0.00	0.00	100.58	0.07	2.98	0.02	3.00
<b>Tsavo-62</b>	85-Ts4-1	39.06	21.24	0.52	0.02	0.11	0.27	0.00	37.21	0.31	0.02	0.00	98.75	0.11	2.97	0.03	3.00
<b>Tsavo-63</b>	85-Ts4-3	39.25	21.82	0.50	0.02	0.14	0.29	0.00	36.88	0.26	0.00	0.00	99.16	0.14	2.97	0.03	3.00
<b>Tsavo-64</b>	86-Ts1-2	39.91	22.68	0.52	0.00	0.06	0.30	0.03	36.91	0.21	0.00	0.15	100.77	0.06	2.97	0.03	3.00
<b>Tsavo-65</b>	86-Ts1-3	39.67	22.66	0.54	0.04	0.01	0.32	0.00	36.73	0.21	0.00	0.20	100.37	0.01	2.97	0.03	3.00
<b>Tsavo-66</b>	86-Ts2-3b	39.95	22.74	0.36	0.00	0.05	0.65	0.03	36.27	0.29	0.01	0.06	100.41	0.05	2.99	0.01	3.00
<b>Tsavo-67</b>	86-Ts2-4	40.15	22.95	0.35	0.00	0.03	0.65	0.00	36.78	0.15	0.00	0.10	101.15	0.03	2.98	0.02	3.00
<b>Tsavo-68</b>	86-Ts2-5	39.67	22.86	0.39	0.00	0.07	0.64	0.04	36.37	0.24	0.00	0.22	100.49	0.07	2.97	0.03	3.00
<b>Tsavo-69</b>	90-Ts2-1	38.70	21.92	0.60	0.00	0.01	0.60	0.06	36.52	0.20	0.00	0.07	98.68	0.01	2.94	0.06	3.00
<b>Tsavo-70</b>	90-Ts4-1	39.12	22.09	0.54	0.00	0.10	0.25	0.00	36.85	0.32	0.00	0.00	99.27	0.10	2.95	0.05	3.00
<b>Tsavo-71</b>	92-Ts1-1	39.22	22.79	0.52	0.02	0.06	0.34	0.01	36.85	0.33	0.00	0.01	100.16	0.06	2.93	0.07	3.00
<b>Tsavo-72</b>	92-Ts1-2	39.63	22.29	0.54	0.00	0.04	0.38	0.03	37.02	0.37	0.00	0.04	100.34	0.04	2.96	0.04	3.00
<b>Tsavo-73</b>	92-Ts1-3	39.72	22.33	0.45	0.00	0.04	0.15	0.01	37.36	0.21	0.02	0.00	100.27	0.04	2.97	0.03	3.00
<b>Tsavo-74</b>	92-Ts1-4	39.39	22.39	0.54	0.01	0.08	0.31	0.00	36.61	0.27	0.00	0.11	99.70	0.08	2.96	0.04	3.00
<b>Tsavo-75</b>	92-Ts1-5	39.30	22.25	0.53	0.00	0.03	0.35	0.08	37.13	0.29	0.01	0.05	100.00	0.03	2.95	0.05	3.00
<b>Tsavo-76</b>	92-Ts2-1	39.51	22.05	0.41	0.00	0.04	0.55	0.07	36.87	0.21	0.00	0.37	100.07	0.04	2.97	0.03	3.00
<b>Tsavo-77</b>	92-Ts2-2	39.31	22.46	0.53	0.00	0.09	0.47	0.07	36.19	0.26	0.00	0.11	99.49	0.09	2.97	0.03	3.00
<b>Tsavo-78</b>	92-Ts2-3	39.42	22.13	0.47	0.00	0.05	0.54	0.04	36.69	0.22	0.00	0.17	99.75	0.05	2.97	0.03	3.00
<b>Tsavo-79</b>	92-Ts2-4	39.71	22.38	0.55	0.00	0.07	0.49	0.07	36.43	0.29	0.00	0.39	100.36	0.07	2.98	0.02	3.00
<b>Tsavo-80</b>	92-Ts2-5	39.41	22.06	0.53	0.00	0.06	0.55	0.01	36.65	0.18	0.00	0.21	99.67	0.06	2.97	0.03	3.00
<b>Tsavo-81</b>	92-Ts3-1	39.66	22.40	0.53	0.01	0.09	0.69	0.03	36.70	0.19	0.00	0.23	100.54	0.09	2.97	0.04	3.00
<b>Tsavo-82</b>	92-Ts3-2	39.31	22.37	0.54	0.01	0.02	0.76	0.04	36.42	0.21	0.00	0.28	99.95	0.02	2.96	0.04	3.00
<b>Tsavo-83</b>	92-Ts3-3	39.49	22.23	0.49	0.00	0.07	0.73	0.03	36.34	0.14	0.00	0.23	99.74	0.07	2.98	0.02	3.00
<b>Tsavo-84</b>	92-Ts3-4	39.48	22.20	0.53	0.00	0.01	0.68	0.04	36.38	0.15	0.01	0.22	99.70	0.01	2.98	0.02	3.00
<b>Tsavo-85</b>	92-Ts3-5	39.53	22.29	0.50	0.02	0.06	0.76	0.00	36.38	0.19	0.00	0.35	100.10	0.06	2.97	0.03	3.00
<b>Tsavo-86</b>	92-Ts4-1	39.85	22.59	0.51	0.00	0.09	0.31	0.00	36.95	0.18	0.00	0.09	100.57	0.09	2.97	0.03	3.00
<b>Tsavo-87</b>	92-Ts4-2	39.50	22.33	0.45	0.00	0.09	0.35	0.00	36.92	0.19	0.00	0.05	99.88	0.09	2.97	0.03	3.00
<b>Tsavo-88</b>	92-Ts4-3	39.66	22.51	0.46	0.00	0.06	0.35	0.11	36.61	0.20	0.00	0.07	100.03	0.06	2.97	0.03	3.00
<b>Tsavo-89</b>	92-Ts4-4	39.85	22.59	0.50	0.00	0.02	0.33	0.00	36.36	0.22	0.04	0.11	100.01	0.02	2.99	0.01	3.00
<b>Tsavo-90</b>	92-Ts4-5	39.28	22.30	0.53	0.04	0.07	0.28	0.03	36.75	0.16	0.01	0.00	99.46	0.07	2.96	0.04	3.00
<b>Min</b>		37.88	20.93	0.33	0.00	0.00	0.15	0.00	35.83	0.12	0.00	0.00	98.51	0.00	2.89	0.00	3.00
<b>Max</b>		40.75	23.30	0.62	0.04	0.14	0.76	0.13	38.02	0.44	0.04	0.99	101.96	0.14	3.02	0.12	3.02
<b>Average</b>		39.36	22.16	0.52	0.01	0.05	0.44	0.03	36.90	0.24	0.00	0.19	99.91	0.05	2.96	0.04	3.00

Table 22. Continue 3.

Sample	Al VI	K	V	Ti	Cr	Fe <sup>2+</sup>	Mg	Mn	Ca	Na	Cations	Alm	And	Gross	Pyrope	Spess	Uvaro	X <sub>Ca</sub>	X <sub>Fe</sub>	X <sub>Mg</sub>
Tsavo-1	1.86	0.00	0.00	0.02	0.00	0.00	0.06	0.02	3.03	0.00	5.00	0.06	0.00	97.30	2.00	0.64	0.00	0.97	0.00	0.02
Tsavo-2	1.86	0.00	0.00	0.01	0.00	0.00	0.05	0.02	3.05	0.01	5.00	0.08	0.00	97.42	1.68	0.67	0.00	0.98	0.00	0.02
Tsavo-3	1.85	0.00	0.00	0.01	0.00	0.00	0.06	0.02	3.06	0.00	5.00	0.07	0.00	97.36	1.75	0.59	0.24	0.98	0.00	0.02
Tsavo-4	1.86	0.00	0.00	0.02	0.00	0.00	0.06	0.02	3.04	0.00	5.00	0.06	0.00	97.34	1.93	0.67	0.01	0.97	0.00	0.02
Tsavo-5	1.87	0.00	0.02	0.01	0.00	0.00	0.06	0.02	3.02	0.00	5.02	0.13	0.00	97.03	2.06	0.66	0.12	0.97	0.00	0.02
Tsavo-6	1.87	0.00	0.00	0.02	0.00	0.01	0.06	0.01	3.04	0.00	5.00	0.18	0.00	97.68	1.76	0.34	0.04	0.98	0.00	0.02
Tsavo-7	1.87	0.00	0.02	0.01	0.00	0.00	0.06	0.02	3.04	0.00	5.02	0.10	0.00	97.02	1.96	0.71	0.19	0.97	0.00	0.02
Tsavo-8	1.86	0.00	0.01	0.02	0.00	0.00	0.06	0.02	3.03	0.01	5.01	0.14	0.00	96.85	2.03	0.62	0.18	0.97	0.00	0.02
Tsavo-9	1.87	0.00	0.02	0.01	0.01	0.00	0.06	0.02	3.03	0.00	5.02	0.03	0.00	96.85	2.04	0.75	0.26	0.97	0.00	0.02
Tsavo-10	1.88	0.00	0.04	0.02	0.00	0.01	0.06	0.03	3.00	0.00	5.04	0.20	0.00	96.55	1.99	1.05	0.20	0.97	0.00	0.02
Tsavo-11	1.88	0.00	0.00	0.01	0.00	0.00	0.06	0.03	3.02	0.00	5.00	0.11	0.00	97.10	1.81	0.96	0.02	0.97	0.00	0.02
Tsavo-12	1.85	0.00	0.04	0.01	0.00	0.00	0.07	0.03	3.03	0.00	5.05	0.14	0.00	96.49	2.15	1.05	0.16	0.97	0.00	0.02
Tsavo-13	1.88	0.00	0.00	0.01	0.00	0.00	0.06	0.02	3.02	0.00	5.00	0.11	0.00	97.25	1.90	0.74	0.00	0.97	0.00	0.02
Tsavo-14	1.92	0.00	0.02	0.02	0.00	0.00	0.06	0.02	2.98	0.00	5.02	0.09	0.00	97.10	1.94	0.76	0.10	0.97	0.00	0.02
Tsavo-15	1.91	0.00	0.01	0.01	0.00	0.00	0.06	0.02	3.00	0.00	5.02	0.12	0.00	97.25	1.82	0.68	0.13	0.97	0.00	0.02
Tsavo-16	1.93	0.00	0.03	0.01	0.00	0.00	0.06	0.03	2.97	0.00	5.03	0.05	0.00	96.82	2.06	0.81	0.21	0.97	0.00	0.02
Tsavo-17	1.88	0.00	0.00	0.01	0.00	0.00	0.06	0.03	3.01	0.00	5.00	0.11	0.00	96.82	1.84	1.06	0.18	0.97	0.00	0.02
Tsavo-18	1.92	0.00	0.00	0.02	0.00	0.01	0.06	0.02	2.98	0.00	5.00	0.15	0.00	97.36	1.85	0.59	0.06	0.97	0.00	0.02
Tsavo-19	1.90	0.00	0.00	0.02	0.00	0.01	0.06	0.02	3.00	0.00	5.00	0.15	0.00	97.20	1.96	0.69	0.00	0.97	0.00	0.02
Tsavo-20	1.85	0.00	0.01	0.01	0.00	0.00	0.05	0.02	3.06	0.00	5.01	0.05	0.00	97.41	1.63	0.73	0.19	0.98	0.00	0.02
Tsavo-21	1.88	0.00	0.01	0.01	0.00	0.00	0.05	0.02	3.03	0.00	5.01	0.12	0.00	97.38	1.73	0.77	0.00	0.97	0.00	0.02
Tsavo-22	1.85	0.00	0.01	0.02	0.00	0.01	0.06	0.03	3.05	0.00	5.01	0.20	0.00	97.04	1.77	0.84	0.04	0.97	0.00	0.02
Tsavo-23	1.90	0.00	0.01	0.01	0.00	0.00	0.06	0.02	3.00	0.00	5.01	0.12	0.00	97.15	1.93	0.78	0.03	0.97	0.00	0.02
Tsavo-24	1.87	0.00	0.02	0.01	0.01	0.00	0.04	0.04	3.03	0.00	5.02	0.09	0.00	97.10	1.21	1.30	0.30	0.97	0.00	0.01
Tsavo-25	1.88	0.00	0.02	0.01	0.00	0.00	0.05	0.04	3.01	0.00	5.02	0.10	0.00	96.76	1.48	1.38	0.22	0.97	0.00	0.02
Tsavo-26	1.95	0.00	0.02	0.01	0.00	0.00	0.06	0.03	2.95	0.00	5.02	0.06	0.00	97.03	1.85	1.00	0.06	0.97	0.00	0.02
Tsavo-27	2.03	0.00	0.00	0.01	0.00	0.00	0.06	0.03	2.84	0.00	4.98	0.13	0.00	96.70	2.04	1.14	0.00	0.97	0.00	0.02
Tsavo-28	1.91	0.00	0.00	0.01	0.00	0.00	0.06	0.04	2.98	0.00	5.00	0.13	0.00	96.72	1.87	1.23	0.04	0.97	0.00	0.02
Tsavo-29	1.93	0.00	0.02	0.01	0.00	0.00	0.06	0.04	2.96	0.00	5.02	0.03	0.00	96.82	1.96	1.20	0.00	0.97	0.00	0.02
Tsavo-30	1.99	0.00	0.02	0.02	0.00	0.00	0.06	0.03	2.91	0.00	5.02	0.04	0.00	96.82	2.03	0.98	0.03	0.97	0.00	0.02

Table 22. Continue 4.

Sample	Al VI	K	V	Ti	Cr	Fe <sup>2+</sup>	Mg	Mn	Ca	Na	Cations	Alm	And	Gross	Pyrope	Spess	Uvaro	X <sub>Ca</sub>	X <sub>Fe</sub>	X <sub>Mg</sub>
Tsavo-31	1.95	0.00	0.02	0.02	0.00	0.00	0.06	0.03	2.94	0.00	5.02	0.08	0.00	96.71	2.01	1.11	0.09	0.97	0.00	0.02
Tsavo-32	1.96	0.00	0.02	0.01	0.00	0.00	0.06	0.03	2.93	0.00	5.01	0.10	0.00	96.84	1.95	1.05	0.07	0.97	0.00	0.02
Tsavo-33	1.90	0.00	0.05	0.02	0.01	0.00	0.07	0.03	2.98	0.00	5.05	0.11	0.00	96.48	2.11	0.99	0.26	0.97	0.00	0.02
Tsavo-34	1.92	0.00	0.06	0.01	0.00	0.00	0.06	0.04	2.97	0.00	5.06	0.14	0.00	96.72	1.91	1.17	0.07	0.97	0.00	0.02
Tsavo-35	1.90	0.00	0.00	0.01	0.00	0.00	0.06	0.02	3.00	0.00	5.00	0.11	0.00	97.06	2.04	0.63	0.08	0.97	0.00	0.02
Tsavo-36	1.87	0.00	0.05	0.01	0.00	0.01	0.07	0.04	3.00	0.00	5.05	0.16	0.00	96.28	2.19	1.17	0.20	0.97	0.00	0.02
Tsavo-37	1.91	0.00	0.05	0.01	0.01	0.01	0.07	0.03	2.96	0.00	5.05	0.17	0.00	96.12	2.27	1.06	0.38	0.97	0.00	0.02
Tsavo-38	1.90	0.00	0.01	0.01	0.00	0.00	0.07	0.02	3.00	0.00	5.01	0.10	0.00	97.01	2.16	0.73	0.00	0.97	0.00	0.02
Tsavo-39	1.95	0.00	0.01	0.02	0.00	0.00	0.06	0.03	2.95	0.00	5.01	0.09	0.00	97.01	1.97	0.87	0.07	0.97	0.00	0.02
Tsavo-40	1.96	0.00	0.02	0.01	0.00	0.01	0.06	0.02	2.95	0.00	5.02	0.15	0.00	97.09	1.99	0.77	0.00	0.97	0.00	0.02
Tsavo-41	1.91	0.00	0.02	0.01	0.00	0.01	0.07	0.03	2.98	0.00	5.02	0.15	0.00	96.80	2.15	0.84	0.06	0.97	0.00	0.02
Tsavo-42	1.93	0.00	0.01	0.01	0.00	0.01	0.06	0.02	2.96	0.00	5.01	0.15	0.00	96.81	2.11	0.70	0.21	0.97	0.00	0.02
Tsavo-43	1.98	0.00	0.01	0.01	0.00	0.00	0.06	0.02	2.94	0.00	5.01	0.04	0.00	97.51	1.87	0.50	0.00	0.98	0.00	0.02
Tsavo-44	1.93	0.00	0.02	0.01	0.00	0.00	0.06	0.04	2.95	0.00	5.02	0.12	0.00	96.20	2.08	1.45	0.15	0.96	0.00	0.02
Tsavo-45	1.96	0.00	0.01	0.01	0.00	0.01	0.06	0.03	2.93	0.00	5.01	0.16	0.00	96.78	2.03	0.85	0.18	0.97	0.00	0.02
Tsavo-46	1.93	0.00	0.01	0.02	0.00	0.00	0.07	0.04	2.95	0.00	5.01	0.00	0.00	96.56	2.19	1.22	0.03	0.97	0.00	0.02
Tsavo-47	1.94	0.00	0.02	0.01	0.00	0.01	0.06	0.04	2.94	0.00	5.02	0.15	0.00	96.31	2.09	1.37	0.08	0.96	0.00	0.02
Tsavo-48	1.90	0.00	0.00	0.02	0.00	0.00	0.05	0.02	3.00	0.00	5.00	0.05	0.00	97.49	1.66	0.79	0.00	0.98	0.00	0.02
Tsavo-49	2.00	0.00	0.01	0.01	0.00	0.00	0.06	0.04	2.89	0.00	5.01	0.09	0.00	96.59	2.03	1.24	0.05	0.97	0.00	0.02
Tsavo-50	2.00	0.00	0.00	0.01	0.00	0.00	0.06	0.04	2.89	0.00	5.00	0.05	0.00	96.51	2.03	1.15	0.11	0.97	0.00	0.02
Tsavo-51	1.97	0.00	0.00	0.01	0.00	0.01	0.06	0.04	2.92	0.00	5.00	0.22	0.00	96.72	1.89	1.18	0.00	0.97	0.00	0.02
Tsavo-52	1.94	0.00	0.00	0.03	0.00	0.00	0.06	0.03	2.95	0.00	5.00	0.09	0.00	97.06	2.02	0.83	0.00	0.97	0.00	0.02
Tsavo-53	1.98	0.00	0.00	0.02	0.00	0.00	0.06	0.02	2.91	0.00	5.00	0.08	0.00	97.09	2.04	0.77	0.02	0.97	0.00	0.02
Tsavo-54	1.98	0.00	0.00	0.02	0.00	0.00	0.07	0.03	2.90	0.00	5.00	0.08	0.00	96.71	2.23	0.93	0.00	0.97	0.00	0.02
Tsavo-55	1.88	0.00	0.00	0.02	0.00	0.00	0.06	0.02	3.01	0.00	5.00	0.07	0.00	96.96	2.07	0.75	0.15	0.97	0.00	0.02
Tsavo-56	1.90	0.00	0.01	0.02	0.00	0.00	0.07	0.02	2.99	0.00	5.01	0.12	0.00	97.05	2.15	0.57	0.10	0.97	0.00	0.02
Tsavo-57	1.88	0.00	0.01	0.02	0.00	0.00	0.06	0.02	3.02	0.00	5.00	0.11	0.00	97.16	2.04	0.53	0.17	0.97	0.00	0.02
Tsavo-58	1.88	0.00	0.00	0.01	0.00	0.00	0.05	0.03	3.02	0.00	5.00	0.11	0.00	96.96	1.73	1.03	0.18	0.97	0.00	0.02
Tsavo-59	1.89	0.00	0.00	0.02	0.00	0.01	0.07	0.03	3.00	0.00	5.00	0.15	0.00	96.85	2.12	0.79	0.00	0.97	0.00	0.02
Tsavo-60	1.89	0.00	0.00	0.02	0.00	0.00	0.06	0.03	3.00	0.00	5.00	0.06	0.00	97.08	1.83	0.92	0.01	0.97	0.00	0.02

Table 22. Continue 5.

Sample	Al VI	K	V	Ti	Cr	Fe <sup>2+</sup>	Mg	Mn	Ca	Na	Cations	Alm	And	Gross	Pyrope	Spess	Uvaro	X <sub>Ca</sub>	X <sub>Fe</sub>	X <sub>Mg</sub>
Tsavo-61	1.90	0.00	0.01	0.02	0.00	0.00	0.06	0.02	3.00	0.00	5.01	0.14	0.00	97.36	1.83	0.65	0.01	0.97	0.00	0.02
Tsavo-62	1.87	0.00	0.00	0.02	0.00	0.01	0.06	0.02	3.03	0.00	5.00	0.22	0.00	97.26	1.89	0.56	0.00	0.97	0.00	0.02
Tsavo-63	1.91	0.00	0.01	0.02	0.00	0.01	0.06	0.02	2.99	0.00	5.01	0.28	0.00	97.16	1.85	0.60	0.00	0.97	0.00	0.02
Tsavo-64	1.96	0.00	0.01	0.01	0.00	0.00	0.06	0.02	2.95	0.00	5.01	0.12	0.00	97.26	1.90	0.63	0.08	0.97	0.00	0.02
Tsavo-65	1.96	0.00	0.01	0.01	0.00	0.00	0.06	0.02	2.94	0.01	5.01	0.01	0.00	97.15	1.99	0.67	0.00	0.97	0.00	0.02
Tsavo-66	1.99	0.00	0.00	0.02	0.00	0.00	0.04	0.04	2.91	0.00	5.01	0.09	0.00	97.09	1.35	1.38	0.09	0.97	0.00	0.01
Tsavo-67	1.99	0.00	0.01	0.01	0.00	0.00	0.04	0.04	2.93	0.00	5.01	0.07	0.00	97.29	1.29	1.35	0.00	0.97	0.00	0.01
Tsavo-68	1.98	0.00	0.01	0.01	0.00	0.00	0.04	0.04	2.92	0.00	5.01	0.15	0.00	96.95	1.44	1.34	0.12	0.97	0.00	0.01
Tsavo-69	1.90	0.00	0.00	0.01	0.00	0.00	0.07	0.04	2.97	0.00	5.01	0.02	0.00	96.35	2.19	1.26	0.19	0.97	0.00	0.02
Tsavo-70	1.92	0.00	0.00	0.02	0.00	0.01	0.06	0.02	2.98	0.00	5.00	0.20	0.00	97.28	1.99	0.53	0.00	0.97	0.00	0.02
Tsavo-71	1.94	0.00	0.00	0.02	0.00	0.00	0.06	0.02	2.95	0.00	5.00	0.12	0.00	97.12	1.92	0.72	0.03	0.97	0.00	0.02
Tsavo-72	1.93	0.00	0.00	0.02	0.00	0.00	0.06	0.02	2.97	0.00	5.00	0.08	0.00	97.09	1.96	0.79	0.08	0.97	0.00	0.02
Tsavo-73	1.94	0.00	0.00	0.01	0.00	0.00	0.05	0.01	2.99	0.00	5.00	0.08	0.00	97.97	1.63	0.31	0.02	0.98	0.00	0.02
Tsavo-74	1.95	0.00	0.01	0.02	0.00	0.01	0.06	0.02	2.95	0.00	5.01	0.17	0.00	97.14	2.00	0.65	0.00	0.97	0.00	0.02
Tsavo-75	1.91	0.00	0.00	0.02	0.01	0.00	0.06	0.02	2.98	0.00	5.01	0.05	0.00	97.06	1.93	0.72	0.24	0.97	0.00	0.02
Tsavo-76	1.93	0.00	0.02	0.01	0.00	0.00	0.05	0.04	2.97	0.00	5.02	0.08	0.00	97.07	1.49	1.14	0.22	0.97	0.00	0.02
Tsavo-77	1.96	0.00	0.01	0.02	0.00	0.01	0.06	0.03	2.93	0.00	5.01	0.19	0.00	96.64	1.99	0.99	0.20	0.97	0.00	0.02
Tsavo-78	1.93	0.00	0.01	0.01	0.00	0.00	0.05	0.04	2.96	0.00	5.01	0.11	0.00	96.90	1.74	1.14	0.12	0.97	0.00	0.02
Tsavo-79	1.96	0.00	0.02	0.02	0.00	0.00	0.06	0.03	2.93	0.00	5.02	0.14	0.00	96.60	2.03	1.03	0.20	0.97	0.00	0.02
Tsavo-80	1.93	0.00	0.01	0.01	0.00	0.00	0.06	0.04	2.96	0.00	5.01	0.12	0.00	96.74	1.95	1.15	0.04	0.97	0.00	0.02
Tsavo-81	1.94	0.00	0.01	0.01	0.00	0.01	0.06	0.04	2.94	0.00	5.02	0.19	0.00	96.28	1.94	1.44	0.09	0.96	0.00	0.02
Tsavo-82	1.94	0.00	0.02	0.01	0.00	0.00	0.06	0.05	2.94	0.00	5.02	0.04	0.00	96.24	1.99	1.59	0.13	0.96	0.00	0.02
Tsavo-83	1.95	0.00	0.01	0.01	0.00	0.00	0.06	0.05	2.94	0.00	5.01	0.15	0.00	96.42	1.81	1.52	0.10	0.97	0.00	0.02
Tsavo-84	1.95	0.00	0.01	0.01	0.00	0.00	0.06	0.04	2.94	0.00	5.01	0.01	0.00	96.49	1.96	1.42	0.12	0.97	0.00	0.02
Tsavo-85	1.95	0.00	0.02	0.01	0.00	0.00	0.06	0.05	2.93	0.00	5.02	0.13	0.00	96.30	1.85	1.60	0.01	0.96	0.00	0.02
Tsavo-86	1.96	0.00	0.01	0.01	0.00	0.01	0.06	0.02	2.95	0.00	5.01	0.19	0.00	97.30	1.87	0.64	0.00	0.97	0.00	0.02
Tsavo-87	1.94	0.00	0.00	0.01	0.00	0.01	0.05	0.02	2.97	0.00	5.00	0.18	0.00	97.43	1.65	0.73	0.01	0.98	0.00	0.02
Tsavo-88	1.96	0.00	0.00	0.01	0.01	0.00	0.05	0.02	2.94	0.00	5.00	0.12	0.00	97.11	1.69	0.74	0.34	0.97	0.00	0.02
Tsavo-89	1.99	0.00	0.01	0.01	0.00	0.00	0.06	0.02	2.92	0.00	5.01	0.05	0.00	97.40	1.86	0.70	0.00	0.97	0.00	0.02
Tsavo-90	1.94	0.00	0.00	0.01	0.00	0.01	0.06	0.02	2.97	0.01	5.00	0.15	0.00	97.06	1.94	0.59	0.10	0.97	0.00	0.02
Min	1.85	0.00	0.00	0.01	0.00	0.00	0.04	0.01	2.84	0.00	4.98	0.00	0.00	96.12	1.21	0.31	0.00	0.96	0.00	0.01
Max	2.03	0.00	0.06	0.03	0.01	0.01	0.07	0.05	3.06	0.01	5.06	0.28	0.00	97.97	2.27	1.60	0.38	0.98	0.00	0.02
Average	1.92	0.00	0.01	0.01	0.00	0.00	0.06	0.03	2.97	0.00	5.01	0.11	0.00	96.95	1.91	0.91	0.09	0.97	0.00	0.02

Table 23. Tsavorite analyses from tsavorite associated with tanzanite mineralisation.

Sample	Desc	SiO <sub>2</sub>	Al <sub>2</sub> O <sub>3</sub>	MgO	Na <sub>2</sub> O	FeO	MnO	Cr <sub>2</sub> O <sub>3</sub>	CaO	TiO <sub>2</sub>	K <sub>2</sub> O	V <sub>2</sub> O <sub>3</sub>	Total	FeO <sub>calc</sub>	Fe <sub>2</sub> O <sub>3calc</sub>	TSi	TAl	Sum_T
<b>Tsavo-91</b>	40-Ts2-1	39.01	20.84	0.48	0.03	0.05	0.50	0.11	36.96	0.24	0.00	0.53	98.73	0.05	0.06	2.98	0.02	3.00
<b>Tsavo-92</b>	40-Ts2-3	39.93	21.01	0.56	0.00	0.02	0.51	0.13	36.60	0.23	0.02	0.54	99.56	0.04	0.04	3.03	0.00	3.03
<b>Tsavo-93</b>	40-Ts3-3	39.51	21.50	0.51	0.00	0.08	0.34	0.01	37.23	0.35	0.00	0.03	99.55	0.07	0.08	2.98	0.02	3.00
<b>Tsavo-94</b>	76-Ts1-1	38.76	22.10	0.51	0.00	0.03	0.61	0.07	36.72	0.14	0.00	0.27	99.23	0.05	0.06	2.94	0.06	3.00
<b>Tsavo-95</b>	76-Ts1-4	38.84	21.98	0.54	0.00	0.06	0.43	0.07	37.00	0.29	0.00	0.35	99.54	0.05	0.06	2.94	0.06	3.00
<b>Tsavo-96</b>	76-Ts1-5	38.23	22.13	0.48	0.00	0.05	0.31	0.02	37.48	0.25	0.02	0.14	99.10	0.05	0.05	2.89	0.11	3.00
<b>Tsavo-97</b>	76-Ts2-2	38.38	22.33	0.47	0.00	0.07	0.38	0.03	37.24	0.10	0.00	0.00	99.00	0.07	0.08	2.90	0.10	3.00
<b>Tsavo-98</b>	76-Ts2-3	38.62	22.34	0.51	0.01	0.06	0.42	0.02	37.04	0.24	0.00	0.12	99.35	0.06	0.07	2.92	0.09	3.00
<b>Tsavo-99</b>	76-Ts3-2	38.84	22.12	0.49	0.02	0.07	0.47	0.01	37.06	0.30	0.02	0.03	99.41	0.07	0.08	2.93	0.07	3.00
<b>Tsavo-100</b>	76-Ts4-1	38.82	22.35	0.49	0.01	0.09	0.37	0.01	36.90	0.27	0.02	0.00	99.32	0.07	0.08	2.93	0.07	3.00
<b>Tsavo-101</b>	76-Ts4-2	38.35	22.05	0.48	0.00	0.04	0.35	0.00	37.39	0.29	0.00	0.12	99.06	0.06	0.06	2.90	0.10	3.00
<b>Tsavo-102</b>	76-Ts4-3	38.86	22.29	0.48	0.00	0.07	0.35	0.00	37.03	0.30	0.04	0.00	99.42	0.06	0.07	2.93	0.07	3.00
<b>Tsavo-103</b>	148-Ts2-1	39.06	21.50	0.58	0.00	0.03	0.39	0.05	36.69	0.24	0.00	0.27	98.80	0.02	0.02	2.97	0.03	3.00
<b>Tsavo-104</b>	148-Ts3-2	38.53	21.61	0.48	0.00	0.03	0.26	0.04	37.22	0.22	0.03	0.13	98.53	0.03	0.03	2.94	0.07	3.00
<b>Tsavo-105</b>	148-Ts4-3	38.58	21.60	0.55	0.00	0.09	0.44	0.01	36.95	0.29	0.01	0.22	98.75	0.06	0.07	2.94	0.06	3.00
<b>Tsavo-106</b>	150-Ts2-1	38.59	22.08	0.53	0.00	0.01	0.25	0.00	37.28	0.27	0.00	0.06	99.05	0.04	0.04	2.92	0.08	3.00
<b>Tsavo-107</b>	150-Ts2-2	38.78	21.99	0.44	0.00	0.03	0.24	0.02	37.22	0.26	0.00	0.04	99.02	0.03	0.04	2.94	0.06	3.00
<b>Tsavo-108</b>	150-Ts3-1	38.51	21.85	0.51	0.00	0.02	0.54	0.00	36.97	0.24	0.00	0.08	98.72	0.03	0.04	2.93	0.07	3.00
<b>Tsavo-109</b>	150-Ts3-2	38.75	21.87	0.50	0.02	0.05	0.53	0.06	36.86	0.26	0.00	0.00	98.90	0.04	0.05	2.94	0.06	3.00
<b>Tsavo-110</b>	150-Ts3-3	38.77	22.23	0.53	0.00	0.04	0.42	0.03	36.87	0.22	0.00	0.05	99.16	0.04	0.04	2.93	0.07	3.00
<b>Tsavo-111</b>	151-Ts1-1	38.13	22.24	0.60	0.01	0.08	0.61	0.06	36.36	0.19	0.00	0.59	98.88	0.06	0.07	2.91	0.09	3.00
<b>Tsavo-112</b>	151-Ts1-2	38.54	21.96	0.54	0.00	0.02	0.53	0.05	36.61	0.24	0.00	0.45	98.93	0.04	0.04	2.93	0.07	3.00
<b>Tsavo-113</b>	151-Ts1-3	38.99	22.52	0.51	0.00	0.03	0.37	0.01	36.68	0.36	0.02	0.08	99.58	0.04	0.04	2.94	0.06	3.00
<b>Tsavo-114</b>	155-Ts1-1	39.81	22.23	0.55	0.00	0.05	0.26	0.04	36.93	0.28	0.00	0.33	100.48	0.06	0.07	2.98	0.02	3.00
<b>Tsavo-115</b>	155-Ts1-2	39.72	22.66	0.54	0.00	0.05	0.28	0.00	36.66	0.22	0.01	0.32	100.45	0.05	0.06	2.97	0.03	3.00
<b>Tsavo-116</b>	155-Ts1-3	39.72	22.39	0.52	0.01	0.06	0.25	0.00	36.79	0.21	0.00	0.34	100.29	0.06	0.06	2.98	0.02	3.00
<b>Tsavo-117</b>	155-Ts2-1	39.40	22.56	0.56	0.00	0.03	0.46	0.04	36.63	0.27	0.00	0.24	100.18	0.04	0.05	2.95	0.05	3.00
<b>Tsavo-118</b>	155-Ts2-2	39.61	22.30	0.55	0.00	0.07	0.44	0.01	36.64	0.15	0.03	0.03	99.82	0.06	0.06	2.98	0.02	3.00
<b>Tsavo-119</b>	155-Ts2-3	39.32	22.36	0.55	0.00	0.04	0.52	0.03	36.59	0.21	0.00	0.04	99.65	0.05	0.05	2.96	0.04	3.00
<b>Tsavo-120</b>	155-Ts3-1	39.81	22.64	0.59	0.00	0.06	0.31	0.05	36.53	0.24	0.00	0.30	100.54	0.06	0.06	2.98	0.02	3.00
<b>Tsavo-121</b>	155-Ts3-2	40.04	22.65	0.55	0.00	0.04	0.18	0.02	36.93	0.25	0.00	0.00	100.66	0.05	0.05	2.98	0.02	3.00
<b>Tsavo-122</b>	155-Ts3-3	39.38	22.54	0.53	0.00	0.09	0.32	0.07	36.67	0.23	0.00	0.31	100.14	0.07	0.08	2.96	0.04	3.00
<b>Tsavo-123</b>	155-Ts4-1	39.85	21.98	0.55	0.03	0.07	0.50	0.06	36.53	0.15	0.00	0.61	100.32	0.07	0.08	3.00	0.00	3.00
<b>Tsavo-124</b>	155-Ts4-2	39.85	22.81	0.49	0.00	0.08	0.27	0.01	37.03	0.29	0.00	0.00	100.82	0.07	0.08	2.96	0.04	3.00
<b>Min</b>		38.13	20.84	0.44	0.00	0.01	0.18	0.00	36.36	0.10	0.00	0.00	98.53	0.02	0.02	2.89	0.00	3.00
<b>Max</b>		40.04	22.81	0.60	0.03	0.09	0.61	0.13	37.48	0.36	0.04	0.61	100.82	0.07	0.08	3.03	0.11	3.03
<b>Mean</b>		39.05	22.11	0.52	0.00	0.05	0.39	0.03	36.89	0.24	0.01	0.19	99.50	0.05	0.06	2.95	0.05	3.00

Table 23. Continue 1.

Sample	Al VI	K	V	Ti	Cr	Fe <sup>2+</sup>	Mg	Mn	Ca	Na	Cations	Alm	Gross	Pyrope	Spess	Uvaro	X <sub>Ca</sub>	X <sub>Fe</sub>	X <sub>Mg</sub>
Tsavo-91	1.86	0.00	0.03	0.014	0.01	0.00	0.06	0.03	3.03	0.00	5.03	0.11	96.62	1.76	1.04	0.36	0.97	0.00	0.02
Tsavo-92	1.88	0.00	0.03	0.013	0.01	0.00	0.06	0.03	2.98	0.00	5.01	0.07	96.39	2.06	1.07	0.41	0.97	0.00	0.02
Tsavo-93	1.89	0.00	0.00	0.02	0.00	0.00	0.06	0.02	3.01	0.00	5.00	0.15	97.27	1.84	0.70	0.03	0.97	0.00	0.02
Tsavo-94	1.91	0.00	0.02	0.008	0.00	0.00	0.06	0.04	2.98	0.00	5.02	0.10	96.51	1.88	1.28	0.22	0.97	0.00	0.02
Tsavo-95	1.89	0.00	0.02	0.016	0.00	0.00	0.06	0.03	3.00	0.00	5.02	0.11	96.82	1.97	0.88	0.23	0.97	0.00	0.02
Tsavo-96	1.87	0.00	0.01	0.014	0.00	0.00	0.05	0.02	3.04	0.00	5.01	0.10	97.46	1.75	0.63	0.07	0.98	0.00	0.02
Tsavo-97	1.89	0.00	0.00	0.006	0.00	0.00	0.05	0.02	3.02	0.00	5.00	0.14	97.27	1.71	0.79	0.09	0.97	0.00	0.02
Tsavo-98	1.90	0.00	0.01	0.013	0.00	0.00	0.06	0.03	3.00	0.00	5.01	0.13	97.05	1.86	0.86	0.06	0.97	0.00	0.02
Tsavo-99	1.90	0.00	0.00	0.017	0.00	0.00	0.06	0.03	3.00	0.00	5.00	0.14	97.00	1.79	0.97	0.02	0.97	0.00	0.02
Tsavo-100	1.92	0.00	0.00	0.016	0.00	0.00	0.06	0.02	2.98	0.00	5.00	0.15	97.20	1.81	0.77	0.03	0.97	0.00	0.02
Tsavo-101	1.87	0.00	0.01	0.016	0.00	0.00	0.05	0.02	3.03	0.00	5.01	0.12	97.43	1.74	0.72	0.00	0.97	0.00	0.02
Tsavo-102	1.91	0.00	0.00	0.017	0.00	0.00	0.05	0.02	2.99	0.00	5.00	0.13	97.38	1.76	0.73	0.00	0.97	0.00	0.02
Tsavo-103	1.90	0.00	0.02	0.014	0.00	0.00	0.07	0.03	2.99	0.00	5.02	0.04	96.89	2.12	0.81	0.15	0.97	0.00	0.02
Tsavo-104	1.87	0.00	0.01	0.013	0.00	0.00	0.05	0.02	3.04	0.00	5.01	0.06	97.54	1.74	0.53	0.12	0.98	0.00	0.02
Tsavo-105	1.87	0.00	0.01	0.017	0.00	0.00	0.06	0.03	3.01	0.00	5.02	0.13	96.90	2.02	0.92	0.03	0.97	0.00	0.02
Tsavo-106	1.89	0.00	0.00	0.015	0.00	0.00	0.06	0.02	3.02	0.00	5.00	0.07	97.50	1.93	0.51	0.00	0.98	0.00	0.02
Tsavo-107	1.90	0.00	0.00	0.015	0.00	0.00	0.05	0.02	3.02	0.00	5.00	0.07	97.75	1.62	0.49	0.06	0.98	0.00	0.02
Tsavo-108	1.88	0.00	0.01	0.013	0.00	0.00	0.06	0.04	3.01	0.00	5.01	0.07	96.95	1.85	1.12	0.00	0.97	0.00	0.02
Tsavo-109	1.89	0.00	0.00	0.015	0.00	0.00	0.06	0.03	3.00	0.00	5.00	0.08	96.73	1.84	1.10	0.18	0.97	0.00	0.02
Tsavo-110	1.91	0.00	0.00	0.013	0.00	0.00	0.06	0.03	2.99	0.00	5.00	0.08	97.03	1.93	0.88	0.08	0.97	0.00	0.02
Tsavo-111	1.90	0.00	0.04	0.011	0.00	0.00	0.07	0.04	2.97	0.00	5.04	0.13	96.16	2.22	1.27	0.18	0.96	0.00	0.02
Tsavo-112	1.90	0.00	0.03	0.014	0.00	0.00	0.06	0.03	2.99	0.00	5.03	0.08	96.67	1.99	1.11	0.15	0.97	0.00	0.02
Tsavo-113	1.94	0.00	0.00	0.021	0.00	0.00	0.06	0.02	2.96	0.00	5.01	0.07	97.25	1.87	0.78	0.03	0.97	0.00	0.02
Tsavo-114	1.94	0.00	0.02	0.016	0.00	0.00	0.06	0.02	2.96	0.00	5.02	0.13	97.22	2.00	0.55	0.11	0.97	0.00	0.02
Tsavo-115	1.97	0.00	0.02	0.012	0.00	0.00	0.06	0.02	2.94	0.00	5.02	0.11	97.29	2.00	0.59	0.01	0.97	0.00	0.02
Tsavo-116	1.95	0.00	0.02	0.012	0.00	0.00	0.06	0.02	2.96	0.00	5.02	0.12	97.41	1.91	0.53	0.00	0.97	0.00	0.02
Tsavo-117	1.95	0.00	0.01	0.015	0.00	0.00	0.06	0.03	2.94	0.00	5.02	0.09	96.77	2.07	0.96	0.12	0.97	0.00	0.02
Tsavo-118	1.95	0.00	0.00	0.009	0.00	0.00	0.06	0.03	2.95	0.00	5.00	0.12	96.90	2.01	0.93	0.04	0.97	0.00	0.02
Tsavo-119	1.94	0.00	0.00	0.012	0.00	0.00	0.06	0.03	2.95	0.00	5.00	0.10	96.71	2.01	1.09	0.09	0.97	0.00	0.02
Tsavo-120	1.97	0.00	0.02	0.014	0.00	0.00	0.07	0.02	2.93	0.00	5.02	0.12	96.90	2.16	0.66	0.16	0.97	0.00	0.02
Tsavo-121	1.97	0.00	0.00	0.014	0.00	0.00	0.06	0.01	2.95	0.00	5.00	0.10	97.45	2.03	0.37	0.05	0.98	0.00	0.02
Tsavo-122	1.95	0.00	0.02	0.013	0.00	0.00	0.06	0.02	2.95	0.00	5.02	0.15	97.01	1.97	0.66	0.21	0.97	0.00	0.02
Tsavo-123	1.94	0.00	0.04	0.009	0.00	0.00	0.06	0.03	2.94	0.01	5.04	0.14	96.49	2.01	1.04	0.17	0.97	0.00	0.02
Tsavo-124	1.96	0.00	0.00	0.016	0.00	0.01	0.05	0.02	2.95	0.00	5.00	0.15	97.48	1.78	0.56	0.03	0.98	0.00	0.02
Min	1.86	0.00	0.00	0.01	0.00	0.00	0.05	0.01	2.93	0.00	5.00	0.04	96.16	1.62	0.37	0.00	0.96	0.00	0.02
Max	1.97	0.00	0.04	0.02	0.01	0.01	0.07	0.04	3.04	0.01	5.04	0.15	97.75	2.22	1.28	0.41	0.98	0.00	0.02
Mean	1.91	0.00	0.01	0.01	0.00	0.00	0.06	0.03	2.98	0.00	5.01	0.11	97.04	1.91	0.82	0.10	0.97	0.00	0.02

Addendum E. Norm-calculations of the kyanite –graphite gneiss and JW-zone.

Sample	BO-018	BO-019	BO-020	BO-021	BO-022	BO-023	BO-024	BO-025	BO-026	BO-062	BO-063	BO-064	BO-078	BO-079	BO-133
<b>Quartz</b>	51.63	39.32	56.79	51.90	44.14	51.81	52.36	49.81	53.07	51.59	50.25	58.46	48.27	38.69	59.98
<b>Orthoclase</b>	13.62	16.86	11.83	14.60	10.97	14.10	17.19	16.08	14.72	17.04	11.97	13.76	10.53	31.34	15.07
<b>Albite</b>	10.54	12.14	10.79	9.81	11.04	9.17	9.10	6.51	11.51	7.47	4.52	8.12	13.84	12.11	6.31
<b>Anorthite</b>	4.24	21.66	4.64	3.73	24.18	9.01	4.37	14.14	5.85	6.80	19.99	4.83	17.74	3.28	2.41
<b>Nepheline</b>	0.00	0.00	0.00	0.00	0.00	0.00	0.00	0.00	0.00	0.00	0.00	0.00	0.00	0.00	0.00
<b>Corundum</b>	8.33	0.00	6.72	8.48	0.00	4.76	7.05	3.75	5.24	6.97	2.89	6.33	1.86	3.89	7.71
<b>Actinolite</b>	0.00	0.00	0.00	0.00	0.00	0.00	0.00	0.00	0.00	0.00	0.00	0.00	0.00	0.00	0.00
<b>Di Wo</b>	0.00	0.11	0.00	0.00	0.96	0.00	0.00	0.00	0.00	0.00	0.00	0.00	0.00	0.00	0.00
<b>Di En</b>	0.00	0.10	0.00	0.00	0.82	0.00	0.00	0.00	0.00	0.00	0.00	0.00	0.00	0.00	0.00
<b>Di Fs</b>	0.00	0.00	0.00	0.00	0.00	0.00	0.00	0.00	0.00	0.00	0.00	0.00	0.00	0.00	0.00
<b>En</b>	3.46	2.41	2.66	3.36	1.91	4.99	2.84	2.35	3.18	3.13	2.67	2.92	2.38	2.56	2.55
<b>Fs</b>	0.00	0.00	1.31	0.00	0.00	0.48	0.00	0.00	0.00	0.00	0.00	0.41	0.00	0.17	0.00
<b>Forsterite</b>	0.00	0.00	0.00	0.00	0.00	0.00	0.00	0.00	0.00	0.00	0.00	0.00	0.00	0.00	0.00
<b>Fayalite</b>	0.00	0.00	0.00	0.00	0.00	0.00	0.00	0.00	0.00	0.00	0.00	0.00	0.00	0.00	0.00
<b>Magnetite</b>	5.01	1.70	3.79	4.87	1.50	4.13	4.06	4.55	3.36	0.36	1.34	3.70	2.98	5.66	3.03
<b>Haematite</b>	0.61	3.79	0.00	0.71	2.77	0.00	0.44	1.08	1.40	4.10	4.45	0.00	0.68	0.00	0.73
<b>Ilmenite</b>	1.92	1.53	1.19	1.88	1.38	1.31	1.91	1.40	1.36	1.90	1.40	1.22	1.60	1.87	1.64
<b>Apatite</b>	0.64	0.38	0.28	0.67	0.34	0.26	0.68	0.35	0.32	0.65	0.52	0.24	0.12	0.43	0.57
<b>Total</b>	<b>100.00</b>	<b>100.00</b>	<b>100.00</b>	<b>100.00</b>	<b>100.00</b>	<b>100.00</b>	<b>100.00</b>	<b>100.00</b>	<b>100.00</b>	<b>100.00</b>	<b>100.00</b>	<b>100.00</b>	<b>100.00</b>	<b>100.00</b>	<b>100.00</b>

Addendum E. Continued.

<b>Sample</b>	<b>BO-134</b>	<b>BO-135</b>	<b>BO-160</b>	<b>BO-161</b>	<b>BO-162</b>	<b>BO-163</b>	<b>BO-172</b>	<b>BO-173</b>	<b>BO-174</b>	<b>BO-175</b>	<b>BO-176</b>	<b>BO-177</b>	<b>BO-178</b>	<b>BO-180</b>
<b>Quartz</b>	48.28	48.27	66.05	60.34	56.95	46.95	34.68	51.71	65.61	46.57	35.99	34.84	63.29	51.99
<b>Orthoclase</b>	0.14	6.02	10.98	11.14	2.21	3.25	27.30	17.16	12.55	29.73	27.77	14.99	13.18	12.04
<b>Albite</b>	5.67	22.40	3.73	6.46	9.47	20.52	16.63	12.64	10.17	9.35	12.38	25.65	6.31	10.38
<b>Anorthite</b>	31.03	13.15	2.58	3.59	20.54	19.24	8.66	3.81	3.24	7.53	13.58	14.51	3.04	5.64
<b>Nepheline</b>	0.00	0.00	0.00	0.00	0.00	0.00	0.00	0.00	0.00	0.00	0.00	0.00	0.00	0.00
<b>Corundum</b>	0.00	0.99	7.47	9.39	2.09	1.15	1.55	6.50	2.28	0.67	0.66	1.36	6.33	9.42
<b>Actinolite</b>	0.00	0.00	0.00	0.00	0.00	0.00	0.00	0.00	0.00	0.00	0.00	0.00	0.00	0.00
<b>Di Wo</b>	3.63	0.00	0.00	0.00	0.00	0.00	0.00	0.00	0.00	0.00	0.00	0.00	0.00	0.00
<b>Di En</b>	2.97	0.00	0.00	0.00	0.00	0.00	0.00	0.00	0.00	0.00	0.00	0.00	0.00	0.00
<b>Di Fs</b>	0.20	0.00	0.00	0.00	0.00	0.00	0.00	0.00	0.00	0.00	0.00	0.00	0.00	0.00
<b>En</b>	0.00	3.18	1.89	3.16	2.07	2.28	2.00	3.09	1.56	1.59	2.43	2.83	1.56	2.57
<b>Fs</b>	0.00	0.05	0.56	0.00	2.09	0.00	0.49	0.39	0.00	0.00	1.93	0.00	0.67	1.65
<b>Forsterite</b>	0.00	0.00	0.00	0.00	0.00	0.00	0.00	0.00	0.00	0.00	0.00	0.00	0.00	0.00
<b>Fayalite</b>	0.00	0.00	0.00	0.00	0.00	0.00	0.00	0.00	0.00	0.00	0.00	0.00	0.00	0.00
<b>Magnetite</b>	5.53	4.72	4.59	1.87	3.10	4.96	6.46	3.04	1.00	3.30	3.31	3.18	4.27	4.44
<b>Haematite</b>	0.00	0.00	0.00	2.08	0.00	0.08	0.00	0.00	1.75	0.14	0.00	0.65	0.00	0.00
<b>Ilmenite</b>	1.14	1.09	1.57	1.73	1.25	1.27	1.45	1.49	1.77	0.94	1.51	1.57	1.19	1.70
<b>Apatite</b>	0.21	0.14	0.58	0.24	0.22	0.29	0.77	0.17	0.07	0.19	0.44	0.43	0.17	0.17
<b>Total</b>	<b>98.80</b>	<b>100.00</b>	<b>100.00</b>	<b>100.00</b>	<b>100.00</b>	<b>100.00</b>	<b>100.00</b>	<b>100.00</b>	<b>100.00</b>	<b>100.00</b>	<b>100.00</b>	<b>100.00</b>	<b>100.00</b>	<b>100.00</b>



## **Addendum F**

Table 1.	Whole-rock XRF analyses
Table 2.	Average, minimum, maximum, standard deviation and standard error of the whole-rock compositions of the GNG units.
Table 3.	Average, minimum, maximum, standard deviation and standard error of the whole-rock compositions of the BCF units.
Table 4.	Average, minimum, maximum, standard deviation and standard error of the whole-rock compositions of the GCS units.
Table 5.	Average, minimum, maximum, standard deviation and standard error of the whole-rock compositions of the Kyanite-graphite gneisses
Table 6.	Average, minimum, maximum, standard deviation and standard error of the whole-rock compositions of the graphite-plagioclase gneisses.
Table 7.	Average, minimum, maximum, standard deviation and standard error of the whole-rock compositions of the pyroxene relict units.
Table 8.	Average, minimum, maximum, standard deviation and standard error of the whole-rock compositions of the hydrothermal boudins.

Table 1. Whole-rock XRF analyses.

Sample	SiO <sub>2</sub>	TiO <sub>2</sub>	Al <sub>2</sub> O <sub>3</sub>	Fe <sub>2</sub> O <sub>3</sub> T	FeO	Fe <sub>2</sub> O <sub>3</sub>	MnO	MgO	CaO	Na <sub>2</sub> O	K <sub>2</sub> O	P <sub>2</sub> O <sub>5</sub>	Cr <sub>2</sub> O <sub>3</sub>	LOI	NiO	TOTAL	H <sub>2</sub> O-
LHD/14-8	67.34	0.63	11.89	4.75	*	*	0.05	1.05	2.00	0.81	2.30	0.21	0.03	7.47	0.04	98.60	0.00
LHD/11-4	67.65	0.89	12.31	3.73	*	*	0.01	1.12	0.82	0.62	2.43	0.09	0.04	8.75	0.06	98.90	0.33
LHD/11-6	69.16	0.63	12.21	3.58	*	*	0.01	1.04	1.02	0.76	2.58	0.14	0.03	6.99	0.03	98.40	0.21
LHD/11-8	64.86	0.74	11.65	5.06	*	*	0.04	1.28	2.09	0.80	2.43	0.18	0.04	9.49	0.05	98.80	0.13
LHD/14-1	65.48	0.66	12.41	3.86	*	*	0.02	1.57	1.79	0.66	2.65	0.08	0.02	8.79	0.02	98.70	0.67
LHD/14-3	69.45	0.51	11.46	3.96	*	*	0.01	1.09	1.32	0.73	2.04	0.07	0.02	8.06	0.02	99.00	0.31
LHD/14-5	67.65	0.59	11.98	4.01	*	*	0.02	1.21	1.83	1.02	2.50	0.18	0.02	7.15	0.03	98.30	0.15
LHD/14-6	70.06	0.44	10.18	4.05	*	*	0.05	0.83	2.35	1.13	1.72	0.14	0.02	7.68	0.02	98.70	0.07
LHD/14-10	71.45	0.36	7.59	6.05	*	*	0.02	0.31	0.71	0.00	2.76	0.10	0.04	9.64	0.04	99.10	0.01
LHD/14-12	69.61	0.50	11.90	5.14	*	*	0.03	0.84	1.49	0.92	2.27	0.47	0.02	5.44	0.02	98.70	0.01
LHD/13-3	69.37	0.40	10.25	4.00	*	*	0.01	0.92	0.92	0.54	1.95	0.11	0.01	8.61	0.00	98.50	1.39
LHD/13-4	71.31	0.45	10.48	2.24	*	*	0.00	0.53	1.38	1.05	1.98	0.13	0.01	9.25	0.01	99.70	0.92
LHD/13-7	67.29	0.56	9.78	3.27	*	*	0.01	1.77	1.08	0.72	2.30	0.12	0.02	11.44	0.02	99.80	1.40
LHD/13-9	67.47	0.76	11.17	4.25	*	*	0.01	1.18	0.57	0.69	2.49	0.13	0.04	10.35	0.04	99.40	0.29
LHD/13-10	68.80	0.72	11.44	4.66	*	*	0.04	1.18	0.88	0.71	2.36	0.13	0.03	8.18	0.04	99.50	0.34
LHD/13-13	69.11	0.60	12.01	5.46	*	*	0.04	1.21	1.51	1.34	2.46	0.18	0.03	6.14	0.03	100.20	0.05
LHD/13-15	67.01	0.66	12.43	5.03	*	*	0.04	0.85	0.85	0.94	2.59	0.13	0.03	8.84	0.05	99.50	0.01
LHD/13-17	66.43	0.65	12.33	4.76	*	*	0.04	0.98	0.69	0.83	2.95	0.11	0.03	9.11	0.06	99.00	0.01
LHD/13-19	64.43	0.78	13.04	4.93	*	*	0.03	0.90	0.87	1.20	2.99	0.20	0.04	9.64	0.06	99.20	0.08
LHD/13-21	69.97	0.46	11.31	4.85	*	*	0.02	0.95	2.21	2.13	1.56	0.25	0.02	5.34	0.02	99.10	0.02
LHD/11-3	68.08	0.50	10.43	3.39	*	*	0.01	0.60	1.74	1.64	1.68	0.09	0.02	10.36	0.02	99.20	0.64
LHD/11-5	64.62	0.62	12.62	4.39	*	*	0.01	0.73	2.25	0.85	1.43	0.16	0.03	9.37	0.03	98.30	1.22
LHD/14-11	64.75	0.57	11.58	4.70	*	*	0.06	0.67	5.09	0.71	1.32	0.15	0.03	9.42	0.05	99.10	0.04
LHD/13-5	66.51	0.41	10.48	4.78	*	*	0.02	0.86	1.97	1.12	2.51	0.16	0.01	9.71	0.01	99.60	1.10
LHD/13-8	69.48	0.48	10.92	3.24	*	*	0.00	1.08	1.14	0.57	1.92	0.08	0.02	9.65	0.02	99.30	0.71
LHD/13-12	69.80	0.50	10.35	4.88	*	*	0.04	0.88	2.61	1.38	1.63	0.11	0.02	7.88	0.02	100.20	0.08
LHD/13-14	63.60	0.57	11.64	4.59	*	*	0.07	0.69	5.71	0.97	1.40	0.17	0.03	9.69	0.05	99.30	0.10
LHD/13-16	57.99	0.51	10.67	4.64	*	*	0.11	3.06	10.48	1.16	0.88	0.12	0.02	9.31	0.04	99.00	0.07
LHD/14-2	66.14	0.54	10.74	4.18	*	*	0.02	1.04	0.44	0.34	1.57	0.08	0.02	11.34	0.02	98.90	2.44
LHD/14-4	65.41	0.46	10.28	5.64	*	*	0.03	0.88	1.70	0.08	1.28	0.10	0.02	10.44	0.03	98.60	2.31
LHD/13-11	60.44	0.47	10.16	4.65	*	*	0.14	6.19	7.71	1.47	1.04	0.15	0.03	7.39	0.03	99.90	0.04
LHD/13-41	68.17	0.49	10.64	5.69	*	*	0.05	1.39	3.35	1.45	1.03	0.10	0.01	7.10	0.02	99.50	0.00
LHD/13-6	46.45	0.30	17.74	15.05	*	*	0.02	0.63	0.50	0.09	0.11	0.19	0.02	15.91	0.09	99.90	2.87
LHD/11-2	57.10	0.76	14.81	10.25	*	*	0.11	2.10	4.56	0.42	1.34	0.12	0.03	6.57	0.05	99.00	0.81
LHD/13-2	56.06	0.67	12.54	10.60	*	*	0.02	1.25	0.94	0.62	0.58	0.16	0.02	10.91	0.02	100.30	5.92
LHD/11-7	63.00	0.55	12.10	6.06	*	*	0.01	0.76	2.37	0.85	1.19	0.15	0.02	10.79	0.05	99.30	1.38
LHD/13-6	46.45	0.30	17.74	15.05	*	*	0.02	0.63	0.50	0.09	0.11	0.19	0.02	15.91	0.09	99.90	2.87
LHD/14-24	58.45	0.57	11.28	5.41	*	*	0.04	0.69	9.77	0.01	0.94	0.11	0.02	10.77	0.04	98.10	0.00

Table 1. Continue 1.

Sample	As	Ba	Ce	Co	Cr	Cu	Ga	Hf	Mo	Nb	Ni	Pb	Rb	Nd	Sc	Sr	Th	U	V	Y	Zn	Zr	La
LHD/14-8	*	1790	47	*	532	85	14	*	59	14	293	10	51	33	*	216	11	13	667	41	578	233	25
LHD/11-4	*	2507	32	*	858	125	12	*	64	18	412	9	51	26	*	188	10	16	920	45	24	277	17
LHD/11-6	*	1701	24	*	667	69	14	*	46	12	196	15	53	16	*	177	8	10	759	31	104	218	15
LHD/11-8	*	2013	0	*	761	90	15	*	53	15	272	7	52	20	*	209	7	9	949	38	437	222	16
LHD/14-1	*	2027	33	*	466	63	16	*	83	12	149	16	58	30	*	374	7	11	860	36	431	277	25
LHD/14-3	*	1523	0	*	268	71	12	*	42	9	131	10	44	18	*	158	9	9	395	20	85	176	16
LHD/14-5	*	1718	21	*	400	69	14	*	73	12	211	18	58	25	*	187	9	14	660	36	744	190	16
LHD/14-6	*	1170	32	*	260	54	12	*	47	9	128	10	37	23	*	206	7	11	464	30	263	141	18
LHD/14-10	*	1892	22	*	691	61	4	*	14	7	247	7	60	24	*	107	7	8	158	46	200	83	25
LHD/14-12	*	1317	34	*	301	65	15	*	39	9	147	8	46	23	*	154	7	6	446	40	269	187	18
LHD/13-3	*	1645	0	*	232	30	12	*	33	8	24	9	43	17	*	203	7	7	461	21	68	149	0
LHD/13-4	*	1518	29	*	235	62	14	*	40	8	47	10	38	24	*	176	9	16	391	27	45	159	13
LHD/13-7	*	1661	0	*	372	76	12	*	45	9	127	12	40	17	*	120	8	9	643	20	53	166	15
LHD/13-9	*	1854	32	*	748	121	12	*	126	10	271	14	53	21	*	128	7	10	1029	24	733	178	14
LHD/13-10	*	1774	0	*	696	96	13	*	82	12	239	9	50	16	*	124	4	6	826	31	1039	195	17
LHD/13-13	*	1694	0	*	524	69	17	*	74	11	148	15	55	17	*	175	10	12	754	28	835	191	9
LHD/13-15	*	1809	24	*	605	70	15	*	53	15	261	11	56	26	*	175	9	10	748	41	281	229	15
LHD/13-17	*	1671	0	*	573	68	17	*	64	14	367	12	67	18	*	139	9	9	1011	33	558	200	14
LHD/13-19	*	1819	54	*	701	86	18	*	45	17	432	11	58	36	*	172	14	10	596	39	454	261	35
LHD/13-21	*	927	21	*	234	46	17	*	40	9	117	10	37	19	*	172	8	10	427	34	205	157	19
LHD/11-3	*	1580	0	*	375	122	14	*	90	9	133	14	32	15	*	158	8	17	604	21	66	175	0
LHD/11-5	*	1403	70	*	543	70	18	*	67	14	238	9	35	39	*	191	11	28	1044	65	181	244	46
LHD/14-11	*	1220	47	*	483	62	17	*	64	15	379	7	30	25	*	261	11	21	924	55	563	214	29
LHD/13-5	*	1837	44	*	232	47	14	*	34	8	70	17	54	24	*	225	8	15	425	23	91	143	28
LHD/13-8	*	1580	0	*	374	71	12	*	58	9	122	14	46	15	*	165	8	15	746	29	55	171	15
LHD/13-12	*	1350	0	*	328	66	15	*	58	8	118	13	38	15	*	188	5	9	613	33	389	150	0
LHD/13-14	*	1319	51	*	437	58	17	*	63	15	351	7	34	31	*	270	14	23	833	57	957	225	40
LHD/13-16	*	886	28	*	372	44	22	*	46	15	197	8	22	22	*	487	9	17	718	56	483	233	26
LHD/14-2	*	1191	0	*	531	65	13	*	106	10	133	17	36	17	*	234	10	15	1058	27	413	164	17
LHD/14-4	*	1259	0	*	364	68	14	*	68	8	226	10	31	14	*	162	7	17	616	23	581	141	11
LHD/13-11	*	747	25	*	545	88	22	*	91	11	188	11	34	24	*	232	9	10	823	36	1631	151	0
LHD/13-41	*	467	32	*	201	64	14	*	32	12	100	13	32	26	*	171	8	7	394	34	181	181	14
LHD/13-6	*	52	0	*	247	84	16	*	*	6	818	0	6	26	*	18	4	95	576	54	1329	84	*
LHD/11-2	*	461	38	*	564	74	16	*	*	10	472	8	62	24	*	122	8	5	291	40	1464	167	*
LHD/13-2	*	214	27	*	324	56	18	*	*	14	152	11	14	22	*	185	10	13	410	26	462	174	*
LHD/11-7	*	1103	44	*	509	71	14	*	*	13	344	9	31	31	*	213	12	22	913	32	261	248	*
LHD/13-6	*	52	0	*	247	84	16	*	29	6	818	0	6	26	*	18	4	95	576	54	1329	84	14
LHD/14-24	*	2030	52	*	300	9	23	*	52	17	290	0	20	37	*	721	13	21	631	67	492	237	35

Table 1. Continue 2.

Sample	SiO <sub>2</sub>	TiO <sub>2</sub>	Al <sub>2</sub> O <sub>3</sub>	Fe <sub>2</sub> O <sub>3</sub> T	FeO	Fe <sub>2</sub> O <sub>3</sub>	MnO	MgO	CaO	Na <sub>2</sub> O	K <sub>2</sub> O	P <sub>2</sub> O <sub>5</sub>	Cr <sub>2</sub> O <sub>3</sub>	LOI	NiO	TOTAL	H <sub>2</sub> O-
LHD/10-11	62.00	0.58	10.81	4.96	*	*	0.07	0.57	5.74	0.13	1.08	0.18	0.03	11.86	0.05	98.40	0.39
LHD/11-2	57.10	0.76	14.81	10.25	*	*	0.11	2.10	4.56	0.42	1.34	0.12	0.03	6.57	0.05	99.00	0.81
LHD/13-2	56.06	0.67	12.54	10.60	*	*	0.02	1.25	0.94	0.62	0.58	0.16	0.02	10.91	0.02	100.30	5.92
LHD/10-12	64.04	0.59	12.94	4.21	*	*	0.04	0.72	4.23	0.82	1.98	0.13	0.02	8.68	0.04	98.70	0.21
LHD/11-7	63.00	0.55	12.10	6.06	*	*	0.01	0.76	2.37	0.85	1.19	0.15	0.02	10.79	0.05	99.30	1.38
LHD/13-20	61.66	0.61	11.73	4.57	*	*	0.08	1.05	7.04	1.63	1.42	0.21	0.03	9.28	0.05	99.40	0.08
LHD/13-18	55.76	0.45	8.59	3.49	*	*	0.07	0.86	9.11	0.83	0.14	0.20	0.04	18.76	0.07	98.60	0.23
LHD/14-9	52.69	0.37	7.15	4.31	*	*	0.06	0.57	10.39	0.00	0.02	0.28	0.04	20.78	0.08	96.90	0.18
BO-004	50.56	0.35	6.78	3.79	0.45	3.29	0.06	1.52	10.20	0.64	0.72	0.20	0.07	24.31	*	99.23	2.96
BO-005	58.45	0.51	5.75	4.89	0.32	4.54	0.02	0.06	3.14	0.23	0.37	0.19	0.04	25.47	*	99.10	3.97
BO-006	64.77	0.71	11.90	5.23	0.77	4.38	0.02	1.13	1.45	1.35	2.04	0.16	0.06	10.28	*	99.08	0.65
BO-001	58.57	0.61	8.98	2.91	0.59	2.26	0.02	0.55	7.26	0.54	1.53	0.13	0.08	18.61	*	99.76	1.26
BO-002	48.31	0.42	7.02	3.08	0.72	2.28	0.09	2.77	22.12	0.26	2.25	0.09	0.02	12.61	*	99.04	0.43
LHD/11-1	58.27	1.49	20.92	10.71	*	*	0.06	2.91	0.76	0.41	1.72	0.07	0.04	2.35	0.01	100.10	0.35
LHD/13-1	59.12	1.36	17.98	6.65	*	*	0.03	2.59	1.39	1.00	2.33	0.25	0.03	5.44	0.01	99.00	0.84
LHD/10-1	61.55	1.40	18.36	10.78	*	*	0.09	3.32	0.81	0.03	1.77	0.18	0.04	1.38	0.01	100.00	0.27
BO-008	55.30	1.56	20.77	13.97	11.48	1.21	0.10	3.64	0.84	0.74	1.90	0.13	0.06	0.47	*	99.49	0.22
BO-038	59.55	1.37	20.12	11.44	7.79	2.79	0.06	3.21	0.72	0.34	1.80	0.10	0.03	1.34	*	100.08	0.23
BO-053	58.55	1.35	20.15	12.37	9.04	2.33	0.08	3.35	0.89	0.52	1.91	0.16	0.03	0.69	*	100.05	0.09
BO-048	58.73	1.36	20.27	11.69	8.78	1.93	0.07	3.38	0.78	0.61	1.82	0.09	0.03	1.08	*	99.92	0.22
BO-069	58.37	1.35	20.10	10.12	7.46	1.83	0.05	2.52	0.51	0.19	2.14	0.04	0.03	4.29	*	99.70	0.52
BO-007	60.13	1.29	19.72	11.71	10.40	0.16	0.11	3.33	1.02	0.86	1.32	0.12	0.05	0.01	*	99.67	0.26
LHD/13-40	55.99	1.70	20.95	13.90	*	*	0.11	3.85	0.98	0.84	1.73	0.17	0.03	0.72	0.02	101.00	0.04
BO-047	59.15	1.61	18.78	12.82	9.37	2.41	0.12	3.63	0.90	0.38	1.66	0.15	0.03	0.70	*	99.92	0.21
BO-075	52.14	1.57	22.79	13.22	8.91	3.32	0.09	3.63	0.43	0.22	1.77	0.03	0.03	3.81	*	99.76	0.31
LHD/14-13	67.01	0.72	12.09	6.22	*	*	0.04	1.58	2.25	1.58	1.51	0.13	0.02	6.07	0.02	99.30	0.01
LHD/11-9	66.64	0.59	11.21	5.11	*	*	0.05	1.49	2.92	1.02	1.80	0.13	0.01	7.76	0.02	98.90	0.12
LHD/13-23	69.93	0.42	9.80	4.96	*	*	0.04	0.75	2.77	1.84	1.74	0.11	0.02	7.55	0.02	99.90	0.02
BO-009	65.80	0.52	9.52	8.36	4.14	3.76	0.06	1.15	2.61	1.28	1.51	0.16	0.03	8.28	*	99.28	0.17
BO-054	68.97	0.51	10.44	4.70	1.31	3.25	0.05	1.02	2.19	1.28	2.35	0.14	0.03	7.84	*	99.51	0.09
BO-049	62.98	1.01	14.14	5.89	2.88	2.69	0.06	2.41	2.78	2.07	1.90	0.28	0.02	6.12	*	99.63	0.20
BO-140	66.95	0.82	6.04	2.16	0.90	1.16	0.02	2.31	3.36	0.68	1.47	0.19	0.02	15.78	*	99.77	0.46
LHD/10-2	68.92	0.57	10.40	3.11	*	*	0.02	1.12	1.94	0.83	1.81	0.06	0.02	9.03	0.02	98.60	0.74
BO-141	65.20	0.66	11.15	4.15	1.74	2.22	0.02	0.24	1.24	0.82	2.55	0.16	0.02	13.11	*	99.32	0.54
BO-153	63.65	0.57	13.41	6.14	2.58	3.27	0.06	2.63	3.74	1.95	1.95	0.30	0.02	5.40	*	99.82	0.37
BO-166	64.67	0.84	7.43	5.99	2.52	3.20	0.05	1.63	1.01	0.75	2.51	0.14	0.04	14.60	*	99.66	0.33
BO-033	61.46	0.57	10.38	10.95	1.17	9.65	0.04	1.27	1.26	0.49	1.53	0.18	0.02	11.80	*	99.92	2.19
BO-039	67.96	0.56	9.49	5.58	2.23	3.10	0.02	1.08	1.96	0.92	1.60	0.13	0.03	10.24	*	99.55	0.52
BO-055	69.53	0.55	10.45	4.33	1.73	2.40	0.05	1.27	3.01	1.06	1.24	0.15	0.03	7.85	*	99.52	0.11

Table 1. Continue 3.

Sample	As	Ba	Ce	Co	Cr	Cu	Ga	Hf	Mo	Nb	Ni	Pb	Rb	Nd	Sc	Sr	Th	U	V	Y	Zn	Zr	La
LHD/10-11	*	770	45	*	445	58	24	*	67	15	351	4	29	35	*	199	14	25	919	63	612	254	35
LHD/11-2	*	461	38	*	564	74	16	*	28	10	472	8	62	24	*	122	8	5	291	40	1464	167	24
LHD/13-2	*	214	27	*	324	56	18	*	26	14	152	11	14	22	*	185	10	13	410	26	462	174	20
LHD/10-12	*	1538	70	*	426	76	14	*	53	15	289	5	49	44	*	215	14	19	819	53	572	226	48
LHD/11-7	*	1103	44	*	509	71	14	*	63	13	344	9	31	31	*	213	12	22	913	32	261	248	30
LHD/13-20	*	1440	42	*	463	60	18	*	58	17	341	9	36	36	*	267	14	25	870	63	550	245	32
LHD/13-18	*	1062	49	*	677	52	14	*	96	10	597	5	3	36	*	355	15	31	1558	66	1271	185	41
LHD/14-9	*	521	0	*	668	55	18	*	132	7	661	7	0	24	*	296	7	45	1670	65	1235	104	26
BO-004	10.00	1014	26	5	406	49	11	5	42	6	664	12	21	*	12	279	5	32	2244	83	1388	129	*
BO-005	10.00	1002	61	6	249	7	25	5	78	8	224	10	8	*	11	193	8	35	1654	18	537	152	*
BO-006	10.00	1766	39	5	391	87	18	7	49	11	231	10	59	*	14	203	6	14	773	39	99	224	*
BO-001	10.00	1816	39	5	428	33	10	6	61	9	210	11	39	*	17	215	5	12	1656	41	472	160	*
BO-002	10.00	598	18	5	106	25	11	5	8	7	22	15	89	*	14	414	6	3	47	24	110	77	*
LHD/11-1	*	350	23	*	672	53	29	*	5	14	60	10	58	20	*	122	9	0	273	42	147	231	16
LHD/13-1	*	813	26	*	575	62	26	*	13	16	33	11	93	21	*	513	7	6	415	24	126	193	0
LHD/10-1	*	383	36	*	764	46	23	*	3	13	94	7	63	28	*	92	13	0	274	45	144	231	*
BO-008	10.00	558	75	39	440	89	25	6	15	13	93	8	74	*	24	101	6	3	269	44	154	236	*
BO-038	10.00	352	67	39	195	76	27	7	4	16	83	9	65	*	27	110	7	3	243	41	154	215	*
BO-053	10.00	414	64	21	208	56	24	6	3	13	78	10	67	*	29	100	6	4	245	45	145	210	*
BO-048	10.00	364	59	25	208	67	24	7	5	12	97	10	71	*	27	100	5	3	250	42	154	206	*
BO-069	10.00	430	57	7	172	42	27	7	3	15	18	11	90	*	29	119	5	3	213	45	114	213	*
BO-007	10.00	355	58	16	390	31	22	6	15	9	68	5	45	*	24	128	5	3	218	44	114	201	*
LHD/13-40	*	422	53	*	642	84	27	*	3	18	94	4	57	36	*	119	8	0	253	54	181	248	26
BO-047	10.00	401	58	21	239	67	23	7	3	32	94	9	62	*	28	85	5	3	232	43	172	227	*
BO-075	10.00	635	105	12	198	53	27	7	3	14	47	7	74	*	32	128	9	4	278	49	171	229	*
LHD/14-13	*	793	26	*	277	57	20	*	32	13	101	12	45	24	*	137	5	7	375	27	205	188	19
LHD/11-9	*	1155	39	*	231	80	15	*	37	13	95	16	47	28	*	145	10	11	413	35	249	197	19
LHD/13-23	*	1482	0	*	239	63	12	*	41	8	136	12	39	23	*	154	7	11	407	25	239	146	20
BO-009	11.04	1480	9	5	218	85	17	5	43	6	118	14	47	*	13	159	5	4	611	22	236	149	*
BO-054	10.00	1647	20	5	48	76	17	5	26	8	88	19	57	*	11	163	5	8	466	31	255	142	*
BO-049	10.00	755	68	17	134	70	21	7	21	28	89	14	79	*	20	301	12	10	506	33	196	207	*
BO-140	10.00	730	10	44	40	139	13	9	41	19	92	22	34	*	12	77	5	5	372	14	17	278	*
LHD/10-2	*	1353	0	*	419	92	14	*	45	8	136	12	43	16	*	128	7	14	524	25	92	148	17
BO-141	10.00	2073	21	23	81	102	18	6	27	11	101	17	49	*	14	283	5	3	1064	14	16	169	*
BO-153	10.00	777	20	5	155	77	22	5	10	5	102	23	67	*	13	202	5	8	356	26	93	88	*
BO-166	10.00	1455	8	17	80	174	13	9	44	14	205	29	63	*	8	165	5	3	734	6	28	267	*
BO-033	10.00	1303	44	5	107	111	16	6	81	9	487	9	46	*	14	136	5	55	882	34	504	170	*
BO-039	10.00	1309	29	7	61	94	15	6	33	10	126	12	45	*	11	129	5	6	561	27	96	153	*
BO-055	10.00	831	13	5	52	78	17	6	32	18	70	15	41	*	11	144	5	7	540	25	158	184	*

Table 1. Continue 4.

Sample	SiO <sub>2</sub>	TiO <sub>2</sub>	Al <sub>2</sub> O <sub>3</sub>	Fe <sub>2</sub> O <sub>3</sub> T	FeO	Fe <sub>2</sub> O <sub>3</sub>	MnO	MgO	CaO	Na <sub>2</sub> O	K <sub>2</sub> O	P <sub>2</sub> O <sub>5</sub>	Cr <sub>2</sub> O <sub>3</sub>	LOI	NiO	TOTAL	H <sub>2</sub> O-
BO-050	63.95	0.65	11.77	5.46	3.42	1.66	0.08	0.97	6.01	0.31	0.40	0.14	0.05	10.01	*	99.80	0.23
BO-142	71.76	0.75	7.25	3.31	1.32	1.84	0.04	0.58	1.10	0.51	2.51	0.09	0.03	11.24	*	99.17	0.77
BO-143	54.63	1.72	14.49	8.28	3.31	4.60	0.03	3.95	1.59	0.29	1.54	0.54	0.05	12.83	*	99.95	4.55
BO-157	69.17	0.44	9.81	4.61	1.84	2.56	0.02	0.76	2.90	1.30	1.02	0.10	0.03	9.45	*	99.63	0.25
BO-168	69.78	0.49	10.13	4.08	1.63	2.27	0.03	1.30	0.28	0.14	0.75	0.20	0.03	12.92	*	100.00	1.63
LHD/14-14A	68.02	0.44	10.59	5.28	*	*	0.06	0.89	3.39	0.93	1.70	0.11	0.01	7.45	0.03	99.00	0.07
LHD/14-14B	66.49	0.44	10.30	5.20	*	*	0.07	0.91	4.53	0.42	1.03	0.16	0.02	8.79	0.03	98.40	0.06
LHD/13-24	56.15	0.43	9.10	17.59	*	*	0.04	0.99	3.29	1.29	0.95	0.11	0.02	10.41	0.05	100.40	0.00
LHD/10-3	69.89	0.39	8.82	3.52	*	*	0.01	0.79	2.17	0.61	1.12	0.05	0.02	10.85	0.02	98.70	0.45
LHD/11-10	69.08	0.44	9.30	5.31	*	*	0.04	0.91	3.00	0.65	1.21	0.14	0.02	8.65	0.03	98.80	0.06
1-C-ZONE	61.69	0.71	11.55	7.38	4.68	2.18	0.08	0.99	6.39	0.70	0.63	0.33	0.04	9.02	*	99.51	0.48
LHD/12-2	67.99	0.49	9.98	5.42	*	*	0.05	1.14	2.92	1.52	1.48	0.14	0.02	8.37	0.02	99.50	0.00
LHD/12-1	66.16	0.54	10.30	5.87	*	*	0.06	1.56	3.98	1.68	0.89	0.16	0.02	8.93	0.02	100.30	0.12
BO-155	46.15	1.18	15.75	0.93	0.37	0.51	0.12	11.16	16.29	0.72	0.72	1.23	0.02	4.97	*	99.22	0.51
BO-156	48.12	2.39	8.67	2.13	0.85	1.19	0.20	16.68	13.19	0.34	0.69	0.58	0.04	6.47	*	99.50	0.40
LHD/10-4	68.06	0.55	9.98	5.24	*	*	0.02	1.05	2.20	0.76	1.70	0.09	0.02	9.35	0.02	99.30	0.24
LHD/11-11	56.66	0.60	12.95	4.02	*	*	0.06	1.12	4.47	0.33	3.24	0.31	0.05	14.64	0.06	98.60	0.10
LHD/12-3	65.03	0.72	11.44	4.88	*	*	0.04	1.00	1.66	0.95	2.39	0.42	0.04	10.96	0.05	99.50	0.00
LHD/13-25	64.11	0.66	11.76	6.73	*	*	0.02	1.13	1.80	0.57	2.12	0.18	0.04	9.31	0.02	98.40	0.01
BO-011	55.69	0.60	10.63	6.84	3.83	2.59	0.03	0.78	0.82	0.56	2.35	0.21	0.06	20.90	*	99.47	0.20
BO-040	63.28	0.73	12.32	6.34	2.21	3.89	0.02	1.06	1.48	0.83	2.91	0.17	0.02	10.67	*	99.81	0.82
BO-056	67.96	0.53	10.56	4.98	0.90	3.98	0.04	1.07	1.94	0.90	2.17	0.14	0.05	9.40	*	99.72	0.12
BO-051	64.31	0.75	11.17	4.43	1.35	2.93	0.04	0.85	1.01	0.60	2.80	0.22	0.04	13.28	*	99.50	0.14
BO-145	68.76	0.99	10.46	3.57	1.24	2.19	0.02	0.15	0.09	0.45	2.73	0.18	0.03	12.26	*	99.69	0.61
BO-158	64.05	0.65	10.42	6.13	2.13	3.76	0.05	1.44	1.55	0.83	3.50	0.14	0.02	10.69	*	99.45	0.20
BO-159	65.24	0.54	10.42	6.67	2.32	4.09	0.05	1.47	1.69	0.91	2.94	0.12	0.05	9.34	*	99.45	0.21
LHD/14-15	61.34	0.64	11.61	5.28	*	*	0.02	0.93	1.82	0.92	2.81	0.20	0.04	13.53	0.09	99.20	0.02
BO-170	66.63	0.52	10.33	6.36	2.21	3.90	0.02	1.05	1.34	0.61	2.37	0.06	0.02	10.46	*	99.77	0.26
LHD/12-4	50.56	0.40	7.50	3.33	*	*	0.05	0.64	9.43	0.47	0.54	0.21	0.04	23.74	0.08	98.30	1.27
LHD/13-30	55.71	0.37	7.38	3.30	*	*	0.05	1.03	8.30	0.00	0.61	0.31	0.05	20.51	0.07	97.90	0.16
LHD/14-16	52.79	0.41	7.94	3.88	*	*	0.05	0.42	10.34	0.00	0.40	0.24	0.04	20.78	0.07	97.50	0.12
LHD/10-5	55.29	0.40	7.90	3.77	*	*	0.07	0.44	5.03	0.22	0.45	0.25	0.04	22.29	0.08	98.70	2.53
LHD/11-12	53.02	0.36	7.00	3.34	*	*	0.06	0.69	10.81	0.00	0.51	0.70	0.05	21.24	0.08	98.00	0.11
LHD/13-26	51.75	0.41	7.76	6.53	*	*	0.06	0.72	9.81	0.00	0.35	0.22	0.04	19.14	0.07	97.10	0.23
BO-012	53.99	0.55	9.14	4.19	1.40	2.64	0.06	1.65	9.81	0.51	1.11	0.23	0.05	18.06	*	99.35	0.52
BO-031	55.11	0.49	7.93	4.24	1.22	2.89	0.06	1.44	8.93	0.21	1.09	0.40	0.03	20.16	*	100.09	1.47
BO-041	52.12	0.34	6.40	3.06	0.90	2.06	0.06	0.91	9.67	0.15	0.30	0.23	0.03	26.55	*	99.82	1.53
BO-057	55.56	0.43	7.67	3.81	1.26	2.41	0.06	0.76	9.82	0.18	0.74	0.25	0.03	20.19	*	99.51	0.38
BO-052	52.00	0.36	6.73	3.72	1.58	1.97	0.05	1.07	10.30	0.12	0.30	0.30	0.03	24.72	*	99.70	0.38
BO-070	51.01	0.28	4.93	2.94	1.05	1.77	0.05	0.40	9.11	0.06	0.00	0.28	0.05	30.24	*	99.35	1.54

Table 1. Continue 5.

Sample	As	Ba	Ce	Co	Cr	Cu	Ga	Hf	Mo	Nb	Ni	Pb	Rb	Nd	Sc	Sr	Th	U	V	Y	Zn	Zr	La
BO-050	10.00	1516	61	7	83	90	24	9	47	16	255	11	15	*	12	313	10	26	988	57	475	251	*
BO-142	10.00	2371	25	28	58	105	13	8	39	13	98	17	57	*	13	174	5	3	341	11	12	228	*
BO-143	12.25	1536	92	302	347	159	37	6	7	33	1152	15	89	*	25	20	5	27	921	45	306	199	*
BO-157	10.00	1498	36	7	66	76	16	6	34	7	155	8	28	*	11	233	5	11	550	30	140	151	*
BO-168	10.00	1125	45	26	38	65	21	5	18	6	215	13	35	*	12	118	5	13	712	29	108	152	*
LHD/14-14A	*	1631	27	*	206	74	10	*	35	9	166	8	40	21	*	160	8	10	381	35	252	151	26
LHD/14-14B	*	1177	27	*	249	78	14	*	37	9	170	7	29	24	*	167	8	13	438	37	311	149	22
LHD/13-24	*	1009	0	*	310	300	14	*	76	9	325	13	29	18	*	161	10	14	636	35	235	127	14
LHD/10-3	*	1158	23	*	414	104	12	*	52	7	145	6	27	24	*	172	8	15	603	27	107	129	13
LHD/11-10	*	1110	0	*	274	104	11	*	44	8	171	10	33	17	*	179	9	9	493	29	161	133	18
1-C-ZONE	10.00	1137	60	5	236	90	26	8	55	15	252	12	20	*	13	301	9	24	1021	66	539	246	*
LHD/12-2	*	1049	24	*	261	78	14	*	42	10	105	14	36	23	*	175	8	8	442	36	181	156	15
LHD/12-1	*	942	24	*	398	80	16	*	38	9	114	10	29	23	*	228	8	8	448	37	243	138	17
BO-155	10.00	664	81	5	44	5	48	5	5	14	31	8	39	*	43	541	6	24	559	78	103	52	*
BO-156	10.00	257	88	5	106	5	33	5	14	41	48	7	19	*	50	205	11	40	1094	70	225	89	*
LHD/10-4	*	1359	19	*	301	73	12	*	43	10	100	7	42	19	*	169	7	9	488	27	62	152	21
LHD/11-11	*	2012	37	*	748	79	17	*	91	12	457	15	72	27	*	430	10	22	1352	58	846	156	23
LHD/12-3	*	2180	20	*	757	100	11	*	48	14	330	9	60	26	*	200	9	9	821	47	497	217	25
LHD/13-25	*	1724	30	*	664	72	13	*	81	13	106	9	55	24	*	206	10	12	1017	42	555	219	19
BO-011	10.00	2315	23	5	441	97	10	5	81	10	225	15	81	*	23	199	6	9	1919	40	547	185	*
BO-040	12.21	2414	56	6	145	74	17	9	43	17	258	12	83	*	12	222	9	10	689	36	299	255	*
BO-056	10.00	1738	25	7	82	82	12	5	42	18	207	9	60	*	11	166	5	8	750	24	471	149	*
BO-051	10.00	2833	46	5	229	188	13	7	69	14	655	17	86	*	14	285	8	21	2013	56	1059	192	*
BO-145	10.00	2969	71	25	177	66	11	12	57	22	118	17	68	*	14	235	11	14	575	55	26	348	*
BO-158	10.00	2265	62	5	98	111	15	6	76	12	201	14	82	*	14	171	5	3	853	20	1103	190	*
BO-159	10.00	1728	36	5	96	85	15	5	58	8	173	13	73	*	13	132	5	4	820	19	522	153	*
LHD/14-15	*	1964	20	*	773	119	9	*	94	12	644	19	80	24	*	201	11	25	1614	52	1109	149	28
BO-170	10.00	1708	18	16	85	68	14	6	48	8	87	13	61	*	16	142	5	15	839	21	75	146	*
LHD/12-4	*	835	32	*	618	72	10	*	124	8	571	8	14	23	*	301	10	34	1520	63	1247	113	28
LHD/13-30	*	1821	0	*	887	101	11	*	82	8	591	7	16	21	*	377	8	39	1222	64	1134	117	23
LHD/14-16	*	788	28	*	498	25	17	*	105	8	516	6	8	26	*	354	8	40	1280	65	1079	110	25
LHD/10-5	*	1254	39	*	604	63	12	*	105	9	679	8	9	40	*	333	10	32	1472	65	1277	149	30
LHD/11-12	*	1467	0	*	650	72	10	*	103	9	569	7	13	21	*	396	9	39	1501	67	1334	125	17
LHD/13-26	*	1112	0	*	544	78	13	*	111	8	514	8	9	24	*	276	11	35	1347	61	1597	119	15
BO-012	10.00	1958	36	5	268	45	13	5	83	8	429	11	33	*	9	338	5	34	1859	59	1081	143	*
BO-031	10.00	2720	63	5	112	63	14	6	70	7	432	12	31	*	11	414	7	38	1665	65	802	138	*
BO-041	10.00	1325	38	5	118	68	13	5	80	11	526	9	7	*	8	300	5	34	1752	65	1064	125	*
BO-057	10.00	1475	42	5	113	69	13	5	82	10	517	8	21	*	10	333	5	35	1656	66	1456	147	*
BO-052	10.00	546	36	5	118	121	16	5	105	6	595	15	8	*	10	330	5	41	1893	66	1059	93	*
BO-070	10.00	134	12	5	138	91	13	5	180	3	795	15	5	*	9	40	5	35	2333	72	1568	60	*

Table 1. Continue 6.

Sample	SiO <sub>2</sub>	TiO <sub>2</sub>	Al <sub>2</sub> O <sub>3</sub>	Fe <sub>2</sub> O <sub>3</sub> T	FeO	Fe <sub>2</sub> O <sub>3</sub>	MnO	MgO	CaO	Na <sub>2</sub> O	K <sub>2</sub> O	P <sub>2</sub> O <sub>5</sub>	Cr <sub>2</sub> O <sub>3</sub>	LOI	NiO	TOTAL	H <sub>2</sub> O-
LHD/12-9	54.61	0.39	7.81	3.58	*	*	0.05	0.63	9.61	0.00	0.19	0.22	0.04	20.03	0.07	97.70	0.48
LHD/13-32	51.46	0.37	6.91	3.34	*	*	0.07	0.40	9.24	0.00	0.01	0.27	0.04	25.72	0.08	98.10	0.24
LHD/14-21	54.16	0.43	7.85	3.96	*	*	0.07	1.12	11.66	0.00	0.38	0.23	0.04	17.47	0.07	97.60	0.13
LHD/10-8	54.25	0.41	7.86	4.58	*	*	0.05	0.87	7.84	0.00	0.23	0.29	0.04	21.38	0.07	99.20	1.36
LHD/11-15	54.54	0.42	8.54	3.78	*	*	0.06	0.84	10.11	0.00	0.07	0.22	0.04	19.70	0.07	98.60	0.20
BO-017	55.18	0.49	8.83	4.12	1.17	2.82	0.06	0.96	10.27	0.36	0.53	0.22	0.05	17.88	*	98.96	0.22
BO-032	59.13	0.49	8.98	4.05	1.94	1.90	0.04	0.80	6.33	0.38	1.69	0.17	0.03	18.22	*	100.32	0.42
BO-045	57.43	0.46	8.29	4.66	1.53	2.96	0.07	1.04	6.88	0.15	1.10	0.26	0.04	18.91	*	99.28	1.41
BO-061	52.85	0.41	7.30	3.89	0.90	2.89	0.13	0.98	11.06	0.35	0.49	0.37	0.03	21.49	*	99.34	1.67
BO-074	44.91	0.41	7.92	3.74	0.72	2.94	0.11	4.36	18.80	0.36	0.02	0.17	0.04	19.15	*	99.99	0.10
BCF1	64.87	0.41	8.44	3.96	*	*	0.06	2.07	9.28	0.33	2.12	0.08	0.01	5.58	0.01	97.40	0.21
BCF3	52.38	0.39	8.10	4.38	*	*	0.08	2.60	18.33	0.00	2.30	0.05	0.01	5.02	0.01	93.70	0.04
BCF5	57.64	0.45	8.88	5.41	*	*	0.09	2.84	13.28	0.00	2.10	0.07	0.01	2.10	0.01	92.90	0.06
BCF7	64.34	0.49	9.50	5.37	*	*	0.08	1.72	8.86	0.00	2.51	0.09	0.01	3.29	0.01	96.30	0.03
BCF10	57.75	0.49	8.74	4.17	*	*	0.07	2.29	12.46	0.00	2.57	0.09	0.02	9.70	0.01	98.70	0.37
BCF11	59.64	0.49	8.93	5.18	*	*	0.06	1.49	11.44	0.68	2.69	0.10	0.01	8.41	0.01	99.30	0.14
BO-013	68.02	0.58	10.28	4.97	2.41	2.30	0.08	1.57	5.47	0.46	3.12	0.11	0.04	4.37	*	99.07	0.31
BO-035	60.86	0.57	10.91	5.26	3.11	1.81	0.07	2.50	11.53	0.42	3.21	0.11	0.02	3.89	*	99.34	0.18
BO-042	61.94	0.53	9.77	4.39	1.40	2.84	0.09	2.58	11.33	0.30	2.74	0.11	0.02	5.73	*	99.51	0.39
BO-058	63.61	0.48	8.84	4.88	2.70	1.88	0.06	2.41	11.12	0.25	2.43	0.12	0.01	5.28	*	99.50	0.12
BO-071	49.41	0.41	7.42	5.01	3.92	0.66	0.10	5.56	21.83	0.17	1.87	0.07	0.00	7.56	*	99.41	0.08
BCF4	63.11	0.51	9.23	4.71	*	*	0.07	1.93	10.54	0.00	2.62	0.11	0.01	1.78	0.01	94.70	0.02
BCF2	60.63	0.46	10.06	5.43	*	*	0.07	2.16	9.62	0.79	3.05	0.08	0.01	3.09	0.01	95.50	0.06
BCF6	63.69	0.48	10.07	4.74	*	*	0.04	1.66	9.34	0.26	2.56	0.08	0.02	2.43	0.01	95.40	0.05
BO-016	62.56	0.57	9.78	5.61	3.13	2.13	0.19	2.69	9.64	0.68	3.17	0.10	0.02	3.57	*	98.58	0.17
BO-037	63.53	0.50	9.48	4.48	2.46	1.74	0.08	1.76	11.92	0.13	2.46	0.11	0.02	4.52	*	98.96	0.13
BO-044	58.31	0.55	10.61	5.04	2.77	1.96	0.06	2.36	12.52	0.15	3.07	0.12	0.02	6.39	*	99.18	0.79
BO-060	63.20	0.53	9.56	5.55	3.05	2.16	0.09	2.33	10.33	0.42	2.91	0.11	0.01	4.28	*	99.32	0.06
BO-073	60.59	0.49	9.62	4.52	2.49	1.76	0.11	2.09	13.56	0.18	2.60	0.08	0.02	4.95	*	98.83	0.02
BCF8	59.72	0.52	10.02	4.35	*	*	0.06	2.07	11.06	0.00	2.86	0.09	0.02	7.54	0.01	98.70	0.38
BCF9	63.09	0.52	10.00	5.19	*	*	0.05	1.68	8.78	0.00	2.95	0.07	0.02	6.21	0.01	98.70	0.14
BO-059	3.23	0.07	1.12	0.83	0.62	0.14	0.02	15.59	36.68	0.03	0.18	0.03	0.00	42.02	*	99.79	0.16
LHD/12-8	17.73	0.33	7.25	3.21	*	*	0.01	10.46	27.67	0.37	1.35	0.05	0.02	26.24	0.01	94.70	0.02
LHD/12-7	2.70	0.01	0.64	0.46	*	*	0.01	5.14	45.47	0.00	0.15	0.00	0.01	40.74	0.00	95.40	0.05
BO-072	15.29	0.18	3.43	1.97	1.13	0.72	0.03	1.41	45.14	0.07	0.81	0.04	0.00	30.39	*	98.77	0.03
BO-014	1.40	0.03	0.31	0.15	0.11	0.02	0.02	14.93	39.27	0.02	0.04	0.02	0.02	43.92	*	100.07	0.21
BO-036	1.64	0.04	0.43	0.38	0.23	0.13	0.02	18.05	34.39	0.02	0.09	0.03	0.02	44.43	*	99.47	0.12
BO-043	2.09	0.05	0.54	0.48	0.36	0.08	0.02	12.51	40.59	0.02	0.17	0.03	0.02	42.93	*	99.40	0.18
BO-015	9.99	0.24	4.42	1.76	1.22	0.40	0.03	17.66	29.34	0.14	0.59	0.06	0.02	35.11	*	99.34	0.17
LHD/12-11	67.97	0.65	11.97	4.35	*	*	0.04	1.02	1.10	1.16	2.39	0.14	0.03	7.88	0.04	98.60	0.00



Table 1. Continue 7.

Sample	As	Ba	Ce	Co	Cr	Cu	Ga	Hf	Mo	Nb	Ni	Pb	Rb	Nd	Sc	Sr	Th	U	V	Y	Zn	Zr	La
LHD/12-9	*	953	25	*	520	35	14	*	103	10	518	6	5	27	*	401	9	38	1211	68	855	135	27
LHD/13-32	*	103	35	*	638	42	20	*	122	8	654	5	0	29	*	281	7	38	1394	65	1084	116	24
LHD/14-21	*	1591	26	*	559	54	11	*	105	9	559	8	8	30	*	416	9	44	1451	65	1319	120	25
LHD/10-8	*	569	35	*	640	34	18	*	116	9	509	4	4	30	*	380	8	38	1338	64	1129	131	26
LHD/11-15	*	661	30	*	623	20	20	*	103	10	553	6	2	31	*	355	8	43	1538	69	1219	143	25
BO-017	10.00	1364	38	5	257	73	16	5	86	9	436	15	15	*	7	261	7	33	1504	69	1306	156	*
BO-032	10.00	1692	64	5	133	104	17	5	83	10	598	15	59	*	11	324	6	32	1914	67	1180	144	*
BO-045	10.00	1728	46	5	166	58	16	6	65	8	452	10	36	*	11	269	5	28	1539	65	997	141	*
BO-061	10.00	1645	40	5	137	48	16	5	49	8	500	11	15	*	8	269	3	26	1369	58	950	121	*
BO-074	10.00	316	35	5	65	10	25	5	48	9	240	8	5	*	12	311	7	27	1287	62	809	135	*
BCF1	*	642	31	*	188	60	13	*	8	13	26	11	73	21	*	312	11	7	72	41	95	120	13
BCF3	*	762	-23	*	113	47	11	*	3	14	20	14	90	16	*	367	11	0	43	35	128	98	13
BCF5	*	776	-22	*	154	85	12	*	3	15	34	16	75	18	*	311	12	0	55	44	179	115	20
BCF7	*	910	35	*	151	88	11	*	2	16	61	12	87	27	*	267	14	4	58	44	139	131	25
BCF10	*	660	26	*	187	65	12	*	3	13	49	12	83	21	*	284	12	0	60	39	154	106	27
BCF11	*	757	27	*	177	73	12	*	2	14	40	11	86	29	*	241	12	0	58	38	115	109	19
BO-013	10.00	943	34	5	260	72	15	5	14	16	41	15	114	*	14	257	8	3	91	39	181	134	*
BO-035	10.00	899	32	8	58	70	17	5	3	16	37	18	118	*	16	239	12	3	77	34	134	130	*
BO-042	10.63	763	32	12	49	73	17	5	3	11	44	17	105	*	16	271	11	4	66	35	138	110	*
BO-058	10.00	654	40	14	43	79	14	6	3	13	40	14	89	*	15	305	7	3	66	41	120	120	*
BO-071	10.00	739	16	5	21	48	11	5	3	8	18	16	76	*	16	254	8	3	38	26	122	73	*
BCF4	*	810	29	*	170	64	13	*	2	16	26	12	94	20	*	268	11	0	57	46	110	125	16
BCF2	*	1126	24	*	219	59	13	*	2	14	24	13	99	21	*	251	13	0	68	37	117	125	20
BCF6	*	840	38	*	200	71	15	*	2	14	37	12	85	22	*	206	11	0	62	37	135	116	22
BO-016	10.00	1024	27	5	145	66	15	5	7	14	32	15	123	*	16	250	7	3	68	35	128	129	*
BO-037	10.00	1042	45	12	43	58	14	5	3	18	32	16	100	*	13	308	9	3	61	39	130	126	*
BO-044	10.00	1007	42	9	59	62	15	5	3	36	46	18	116	*	18	215	9	5	77	34	143	119	*
BO-060	10.00	896	36	5	50	75	16	5	3	15	37	16	114	*	17	263	8	4	62	37	127	120	*
BO-073	10.00	790	27	14	30	66	16	6	3	11	34	12	116	*	14	447	8	3	49	26	105	107	*
BCF8	*	936	30	*	199	62	15	*	3	16	60	14	92	27	*	261	13	0	66	38	150	121	21
BCF9	*	1068	0	*	183	78	13	*	3	14	44	11	92	22	*	195	13	0	63	36	127	123	17
BO-059	10.00	355	5	5	5	5	5	5	3	3	7	5	8	*	8	55	5	3	27	4	37	16	*
LHD/12-8	*	3116	0	*	179	6	7	*	-2	8	14	6	56	20	*	107	6	0	60	29	90	69	15
LHD/12-7	*	61	0	*	0	0	0	*	3	3	0	0	8	12	*	93	0	0	5	10	21	11	0
BO-072	10.00	652	32	5	5	5	6	5	3	3	5	11	28	*	7	215	5	3	22	28	88	30	*
BO-014	10.00	10	5	5	5	5	5	5	3	3	5	5	5	*	5	50	5	3	12	3	11	9	*
BO-036	10.00	112	5	5	5	5	5	5	3	3	5	5	5	*	7	49	5	3	16	3	17	10	*
BO-043	10.00	135	5	6	5	5	5	5	3	3	13	7	9	*	4	56	5	4	29	4	53	13	*
BO-015	10.00	186	10	5	34	5	7	5	3	3	8	8	27	*	11	100	5	3	36	9	36	39	*
LHD/12-11	*	1887	41	*	677	101	11	*	62	15	286	7	47	31	*	177	8	8	837	39	524	209	28

Table 1. Continue 8.

Sample	SiO <sub>2</sub>	TiO <sub>2</sub>	Al <sub>2</sub> O <sub>3</sub>	Fe <sub>2</sub> O <sub>3</sub> T	FeO	Fe <sub>2</sub> O <sub>3</sub>	MnO	MgO	CaO	Na <sub>2</sub> O	K <sub>2</sub> O	P <sub>2</sub> O <sub>5</sub>	Cr <sub>2</sub> O <sub>3</sub>	LOI	NiO	TOTAL	H <sub>2</sub> O-
LHD/13-33	64.78	0.73	12.02	5.06	*	*	0.03	0.93	1.07	0.70	2.41	0.19	0.04	10.67	0.07	98.70	0.00
LHD/14-22	63.26	0.77	12.93	6.06	*	*	0.04	1.11	1.02	0.97	2.51	0.18	0.04	9.05	0.07	98.00	0.00
LHD/11-16	62.59	0.73	12.40	4.79	*	*	0.04	1.01	1.06	1.65	2.48	0.23	0.04	11.82	0.07	99.00	0.09
LHD/10-9	61.73	0.87	13.25	4.76	*	*	0.03	1.20	1.43	0.65	2.69	0.51	0.04	11.41	0.07	98.80	0.17
BO-018	63.13	0.89	12.73	5.93	2.12	3.58	0.05	1.22	1.06	1.10	2.03	0.26	0.07	10.67	*	99.16	0.14
BO-021	63.04	0.87	12.69	5.87	2.07	3.57	0.04	1.18	0.98	1.02	2.17	0.27	0.07	11.10	*	99.29	0.24
BO-024	63.35	0.87	11.73	4.85	1.85	2.80	0.02	0.98	1.08	0.93	2.51	0.27	0.07	12.40	*	99.04	0.40
BO-062	63.21	0.87	12.23	4.74	0.86	3.79	0.02	1.09	1.50	0.77	2.51	0.26	0.04	12.25	*	99.47	0.33
BO-133	64.68	0.73	10.62	3.97	1.43	2.38	0.02	0.86	0.67	0.63	2.15	0.22	0.04	14.88	*	99.45	0.29
BO-134	58.95	0.51	10.63	5.41	1.95	3.24	0.06	1.01	7.91	0.57	0.02	0.08	0.02	14.92	*	100.07	0.21
BO-079	53.50	0.75	10.04	5.26	2.06	2.97	0.02	0.78	0.68	1.09	4.03	0.15	0.05	22.83	*	99.16	0.68
BO-160	67.40	0.71	9.61	5.07	2.11	2.73	0.02	0.65	0.72	0.38	1.60	0.23	0.04	12.77	*	99.20	0.16
BO-161	68.07	0.82	12.64	4.41	1.23	3.04	0.03	1.14	0.77	0.69	1.70	0.10	0.04	9.03	*	99.45	0.17
BO-172	56.77	0.63	10.68	6.34	2.41	3.67	0.03	0.66	1.78	1.62	3.80	0.29	0.05	16.51	*	99.18	0.29
BO-173	66.33	0.69	11.92	3.64	1.61	1.85	0.03	1.09	0.76	1.32	2.56	0.07	0.05	11.20	*	99.65	0.21
BO-174	73.19	0.82	6.83	3.25	0.99	2.15	0.02	0.55	0.61	1.06	1.87	0.03	0.05	11.20	*	99.50	0.17
BO-019	63.87	0.74	12.32	5.76	1.08	4.56	0.07	0.92	4.25	1.32	2.62	0.16	0.04	7.06	*	99.14	0.12
BO-022	63.93	0.65	11.67	4.45	0.95	3.40	0.05	0.98	4.94	1.17	1.66	0.14	0.04	9.35	*	99.05	0.27
BO-025	63.75	0.65	11.61	5.62	1.71	3.72	0.12	0.83	2.68	0.68	2.40	0.14	0.05	10.80	*	99.35	1.70
BO-063	62.75	0.65	11.70	5.73	0.90	4.73	0.05	0.94	3.79	0.47	1.78	0.21	0.02	11.30	*	99.38	1.38
BO-135	70.90	0.54	10.64	5.09	1.82	3.07	0.07	1.20	2.57	2.50	0.96	0.06	0.04	4.59	*	99.17	0.11
BO-148	64.82	0.64	10.71	4.90	1.99	2.70	0.02	0.84	2.41	1.71	2.17	0.08	0.03	11.29	*	99.60	0.32
BO-078	66.61	0.76	11.75	4.11	1.47	2.47	0.05	0.86	3.29	1.48	1.61	0.05	0.02	9.11	*	99.68	0.51
BO-162	67.07	0.58	10.49	4.50	2.34	1.89	0.04	0.73	3.76	0.99	0.33	0.09	0.02	11.16	*	99.77	0.44
BO-163	66.28	0.61	11.65	5.30	1.90	3.19	0.05	0.83	3.67	2.21	0.50	0.12	0.05	8.55	*	99.81	0.14
BO-175	69.81	0.45	9.78	3.67	1.31	2.21	0.03	0.58	1.48	1.01	4.59	0.08	0.05	7.88	*	99.40	0.20
BO-176	63.22	0.71	11.76	4.75	2.44	2.04	0.06	0.87	2.66	1.31	4.20	0.18	0.03	9.74	*	99.48	0.24
BO-177	64.47	0.76	13.26	4.34	1.55	2.61	0.04	1.04	2.90	2.79	2.33	0.18	0.03	7.55	*	99.68	0.17
LHD/10-10	64.27	0.60	11.94	3.73	*	*	0.04	0.78	3.02	1.38	2.52	0.18	0.03	9.71	0.06	98.40	0.17
LHD/11-17	65.40	0.57	11.64	4.15	*	*	0.06	0.64	4.08	1.62	2.13	0.14	0.03	8.75	0.05	99.40	0.10
LHD/12-12	64.28	0.55	12.81	4.39	*	*	0.07	1.37	4.51	1.45	1.33	0.12	0.02	7.89	0.03	98.80	0.00
LHD/14-23	65.54	0.60	11.88	3.95	*	*	0.05	0.72	3.80	1.19	2.95	0.17	0.03	7.95	0.06	98.80	0.00
LHD/13-34	61.58	0.63	11.59	4.84	*	*	0.06	1.46	6.09	0.58	1.34	0.15	0.03	10.32	0.05	98.80	0.08
LHD/13-36	64.91	0.61	12.56	4.56	*	*	0.07	1.01	4.73	0.89	1.62	0.20	0.02	6.94	0.03	98.10	0.00
W2J1	66.16	0.66	9.26	3.20	1.04	2.05	0.01	0.86	1.05	0.79	3.38	0.05	*	12.09	*	97.65	0.17
W5J1	64.04	0.61	10.64	4.08	1.40	2.52	0.00	0.81	2.82	1.12	1.01	0.07	*	11.76	*	97.20	0.21
R10J2	69.57	0.68	10.61	1.95	0.45	1.45	0.00	0.46	1.22	1.01	3.90	0.06	*	7.94	*	97.60	0.20
R10J1	68.47	0.53	10.39	2.17	0.50	1.62	0.00	0.50	1.16	0.92	3.82	0.06	*	9.25	*	97.50	0.18
W10J1	63.51	0.69	10.38	4.67	1.04	3.51	0.01	0.91	1.44	0.98	2.79	0.07	*	12.07	*	97.90	0.36

Table 1. Continue 9.

Sample	As	Ba	Ce	Co	Cr	Cu	Ga	Hf	Mo	Nb	Ni	Pb	Rb	Nd	Sc	Sr	Th	U	V	Y	Zn	Zr	La
LHD/13-33	*	2576	34	*	782	155	11	*	72	16	527	7	58	27	*	278	12	13	1113	47	582	210	32
LHD/14-22	*	2203	41	*	820	110	12	*	49	18	461	6	59	33	*	201	12	15	753	50	440	251	29
LHD/11-16	*	2691	39	*	849	128	11	*	66	16	487	6	59	30	*	302	10	11	1078	51	665	206	26
LHD/10-9	*	2680	55	*	912	131	11	*	63	18	500	9	65	45	*	277	11	12	1097	64	527	231	32
BO-018	10.00	2033	34	11	461	107	14	7	57	15	496	13	63	*	20	237	5	10	1072	43	500	232	*
BO-021	10.00	2354	26	5	455	113	12	7	51	14	361	11	68	*	21	248	8	9	1187	44	435	240	*
BO-024	10.00	2206	30	5	478	142	11	8	73	15	683	11	71	*	19	259	7	12	1606	48	656	234	*
BO-062	10.00	2486	64	5	208	152	13	8	55	18	334	12	70	*	16	280	8	14	1363	51	340	231	*
BO-133	10.00	3299	44	5	249	178	10	7	85	17	552	14	62	*	14	292	8	11	1755	43	514	199	*
BO-134	10.00	150	46	5	72	14	41	9	65	12	235	8	5	*	13	380	10	23	881	64	699	228	*
BO-079	10.00	4757	41	19	302	509	10	8	126	15	860	19	110	*	12	458	5	13	3098	19	92	196	*
BO-160	10.00	2105	40	5	199	167	10	5	103	13	549	12	46	*	10	241	6	13	1978	44	1064	172	*
BO-161	10.00	1998	66	6	232	67	11	11	32	18	340	9	52	*	13	181	12	13	608	47	164	328	*
BO-172	10.00	1363	50	5	241	396	12	5	116	12	887	13	112	*	13	264	6	19	3248	48	2133	144	*
BO-173	10.00	2168	59	5	246	166	19	6	72	13	493	12	67	*	13	157	10	17	1101	31	369	174	*
BO-174	10.00	1839	5	12	278	76	9	8	19	15	387	7	44	*	10	146	6	7	522	17	26	248	*
BO-019	10.00	1801	64	5	273	88	13	7	49	15	313	9	76	*	18	224	9	22	1156	56	707	249	*
BO-022	10.00	1666	43	14	301	60	18	8	63	12	324	8	48	*	10	334	6	18	1135	53	475	246	*
BO-025	10.00	1575	91	5	349	64	15	7	57	12	463	10	63	*	13	147	8	19	947	41	803	229	*
BO-063	10.00	1309	71	5	85	64	20	8	42	17	296	8	53	*	10	173	7	23	941	57	493	246	*
BO-135	10.00	1151	36	5	70	78	10	11	26	18	119	12	30	*	12	325	5	4	419	37	101	301	*
BO-148	10.00	1727	73	14	134	132	10	9	64	14	419	7	57	*	14	177	5	22	1524	90	393	278	*
BO-078	10.00	1081	37	9	122	76	13	10	30	16	262	11	48	*	10	172	6	29	862	27	271	323	*
BO-162	10.00	340	49	5	99	70	18	7	58	13	383	10	20	*	10	145	10	24	1181	51	585	233	*
BO-163	10.00	704	39	11	82	107	15	8	39	13	263	11	23	*	14	162	5	16	896	32	460	246	*
BO-175	10.00	1704	50	5	89	69	9	5	78	9	366	10	115	*	9	216	6	24	941	50	1687	199	*
BO-176	10.00	1696	54	5	171	86	11	8	45	15	398	10	114	*	12	193	6	15	1051	41	561	259	*
BO-177	10.00	2463	44	5	60	75	13	9	35	16	210	8	65	*	16	296	3	10	634	41	641	283	*
LHD/10-10	*	1532	57	*	593	97	12	*	77	17	426	6	58	36	*	212	10	18	1027	53	823	250	44
LHD/11-17	*	1446	39	*	447	82	12	*	67	15	282	7	57	26	*	202	11	19	836	52	481	233	32
LHD/12-12	*	1262	54	*	364	84	16	*	41	15	228	8	34	31	*	288	11	14	655	44	343	256	40
LHD/14-23	*	1728	31	*	512	84	12	*	68	15	409	9	72	27	*	226	13	28	939	61	750	237	35
LHD/13-34	*	1323	34	*	533	62	18	*	55	15	335	5	35	30	*	453	10	23	780	54	477	220	42
LHD/13-36	*	1438	53	*	336	54	15	*	41	16	227	6	36	35	*	311	9	14	584	49	330	249	40
W2J1	*	1811	48	*	536	6	11	*	71	0	144	10	90	19	18	240	7	12	2029	16	159	190	26
W5J1	*	3206	51	*	435	7	11	*	60	0	180	13	43	22	12	331	10	18	1610	5	228	179	26
R10J2	*	2118	67	*	393	17	10	*	40	0	78	5	101	26	12	236	6	11	1329	29	88	245	41
R10J1	*	1783	63	*	419	14	10	*	37	0	58	3	100	29	12	175	5	11	1409	36	102	217	32
W10J1	*	1915	51	*	474	12	11	*	70	0	148	9	77	25	18	260	8	15	2095	5	137	186	32

Table 1. Continue 10.

Sample	SiO <sub>2</sub>	TiO <sub>2</sub>	Al <sub>2</sub> O <sub>3</sub>	Fe <sub>2</sub> O <sub>3</sub> T	FeO	Fe <sub>2</sub> O <sub>3</sub>	MnO	MgO	CaO	Na <sub>2</sub> O	K <sub>2</sub> O	P <sub>2</sub> O <sub>5</sub>	Cr <sub>2</sub> O <sub>3</sub>	LOI	NiO	TOTAL	H <sub>2</sub> O-
W10G1	62.57	0.59	11.35	5.80	0.63	5.10	0.01	0.35	0.28	0.19	0.19	0.07	*	13.50	*	98.50	3.60
W10G2	58.91	0.56	11.64	5.37	0.99	4.27	0.09	0.26	8.92	0.10	0.00	0.07	*	10.65	*	98.60	2.03
188.000	63.53	0.68	10.53	3.97	0.59	3.32	0.01	1.05	0.88	0.46	3.56	0.05	*	12.59	*	97.85	0.55
R7G1	61.05	0.74	16.52	7.99	*	*	0.18	0.46	11.87	0.01	0.05	0.12	*	15.03	*	98.99	*
R7G2	72.89	0.72	15.74	7.32	*	*	0.03	0.37	1.95	0.03	0.08	0.11	*	18.48	*	99.25	*
W5G1	75.33	0.68	15.35	5.98	*	*	0.01	0.60	0.47	0.03	0.16	0.13	*	19.97	*	98.75	*
W5G2	67.42	0.65	13.41	6.70	*	*	0.12	0.56	10.19	0.13	0.03	0.08	*	13.74	*	99.29	*
W5G3	75.30	0.63	15.35	4.42	*	*	0.02	1.22	0.79	0.22	1.21	0.19	*	16.49	*	99.32	*
IV-2	65.02	0.59	9.32	5.00	*	*	0.08	1.28	10.14	0.97	0.10	0.09	0.01	9.09	0.05	101.74	*
BF/KIA-2	63.59	0.69	11.07	6.54	*	*	0.08	1.70	5.75	0.92	2.61	0.05	0.01	8.15	0.03	101.18	*
KIA-4JWZ	63.52	0.58	12.69	5.06	*	*	0.09	1.43	3.26	2.24	3.47	0.09	0.01	7.49	0.08	100.03	*
LHD/10-12	64.04	0.59	12.94	4.21	*	*	0.04	0.72	4.23	0.82	1.98	0.13	0.02	8.68	0.04	98.70	0.21
LHD/10-11	62.00	0.58	10.81	4.96	*	*	0.07	0.57	5.74	0.13	1.08	0.18	0.03	11.86	0.05	98.40	0.39
LHD/14-24	58.45	0.57	11.28	5.41	*	*	0.04	0.69	9.77	0.01	0.94	0.11	0.02	10.77	0.04	98.10	0.03
R2BR	60.28	0.33	9.13	15.22	1.08	14.02	0.20	2.19	10.83	0.11	0.14	0.15	*	19.92	*	98.57	*
KIA1/L15	57.20	0.48	15.71	5.87	*	*	0.11	1.39	14.29	0.80	0.07	0.10	0.01	3.88	0.04	99.95	*
181.000	57.63	0.47	12.81	6.49	0.41	6.03	0.01	0.42	0.19	0.11	0.21	0.04	*	14.20	*	98.10	5.49
182.000	63.00	0.59	8.33	3.78	0.54	3.18	0.01	0.85	4.37	0.70	1.60	0.04	*	13.32	*	97.25	0.70
183.000	58.22	0.58	12.53	5.24	0.50	4.69	0.10	*	5.70	0.13	*	0.08	*	13.84	*	98.60	2.20
184.000	55.36	0.47	11.67	4.76	0.63	4.06	0.17	*	10.45	0.06	*	0.08	*	14.32	*	98.70	1.33
186.000	49.17	0.39	16.99	8.75	0.59	8.10	0.02	0.16	2.75	0.05	*	0.24	*	16.34	*	99.10	4.24
187.000	61.71	0.50	12.72	4.97	0.77	4.11	0.02	*	2.85	0.05	*	0.11	*	13.31	*	98.40	2.17
R5B2	48.92	0.20	5.65	8.38	1.40	6.82	0.29	6.90	17.32	0.19	*	0.03	*	8.28	*	98.35	2.17
185.000	47.04	0.77	17.46	6.63	*	*	0.34	2.08	23.91	0.02	0.04	0.61	*	17.02	*	98.90	*
W10B	57.86	0.15	3.81	1.70	*	*	0.35	12.57	22.36	0.12	*	0.02	*	6.32	*	98.96	*
R7B1	52.54	0.21	4.55	2.27	0.45	1.77	0.37	13.53	24.04	0.10	0.02	0.09	*	8.14	*	97.71	*
BF/KIA-4	35.26	0.84	13.31	4.58	*	*	0.43	4.10	27.27	0.45	0.07	0.17	0.01	13.32	0.04	99.84	*
W2B	50.57	0.16	3.63	1.65	0.32	1.29	0.33	12.51	22.91	0.12	*	0.05	*	6.58	*	98.55	0.06
KIA2 RELICT	45.95	0.29	5.17	1.42	*	*	0.36	17.18	25.59	0.51	0.05	0.14	0.01	3.77	0.01	100.43	*
KIA3 RELICT	45.47	0.73	13.01	3.28	*	*	0.38	2.47	26.44	0.73	0.06	0.14	0.01	7.44	0.02	100.19	*
KIA RELICT	39.54	0.74	13.36	5.19	*	*	0.35	6.42	26.19	0.63	0.06	0.13	0.01	6.86	0.03	99.52	*
IV-2 RELICT	43.25	0.20	6.04	1.38	*	*	0.37	15.47	26.09	0.74	0.08	0.07	0.01	6.88	0.01	100.58	*
BO-137	47.91	0.24	7.22	3.55	1.27	2.14	0.44	12.67	21.59	0.42	0.02	0.11	0.02	5.54	*	99.70	0.32
BO-150	55.87	0.20	12.46	3.59	1.29	2.16	0.41	6.30	16.39	0.20	0.02	0.04	0.02	4.26	*	99.75	0.31
BO-076	50.09	0.23	5.22	3.15	1.85	1.09	0.37	14.57	22.53	0.03	0.02	0.05	0.00	3.26	*	99.53	0.25
BO-137	47.91	0.24	7.22	3.55	1.27	2.14	0.44	12.67	21.59	0.42	0.02	0.11	0.02	5.54	*	99.70	0.32
BO-150	55.87	0.20	12.46	3.59	1.29	2.16	0.41	6.30	16.39	0.20	0.02	0.04	0.02	4.26	*	99.75	0.31
BO-076	50.09	0.23	5.22	3.15	1.85	1.09	0.37	14.57	22.53	0.03	0.02	0.05	0.00	3.26	*	99.53	0.25
LHD/12-13	67.64	0.60	11.05	5.42	*	*	0.04	1.14	1.95	1.26	2.13	0.15	0.03	7.58	0.03	98.90	0.00
LHD/13-37	69.95	0.58	12.17	4.23	*	*	0.05	0.91	0.91	0.66	2.20	0.10	0.03	6.72	0.03	98.50	0.00

Table 1. Continue 11.

Sample	As	Ba	Ce	Co	Cr	Cu	Ga	Hf	Mo	Nb	Ni	Pb	Rb	Nd	Sc	Sr	Th	U	V	Y	Zn	Zr	La
W10G1	*	2105	89	*	318	257	17	*	38	1	428	6	18	41	14	188	10	27	1560	18	689	234	43
W10G2	*	36	75	*	525	20	33	*	39	2	869	0	3	44	8	439	12	21	682	71	2897	252	46
188.000	*	1907	86	*	459	52	13	*	57	0	156	5	99	44	12	203	6	13	1780	17	120	226	47
R7G1	0.00	385	169	4	492	48	34	*	64	19	475	3	*	*	17	405	11	31	1066	176	885	306	*
R7G2	0.00	422	89	13	305	169	32	*	62	18	570	1	*	*	22	149	14	28	1185	44	1024	287	*
W5G1	52.00	319	206	8	297	142	16	*	54	17	562	1	*	*	24	217	15	25	2871	100	1090	240	*
W5G2	0.00	40	101	7	325	85	27	*	66	13	405	7	*	*	13	411	10	36	1047	101	1373	262	*
W5G3	0.00	1228	109	13	286	67	14	*	63	15	279	*	*	*	18	143	12	43	1733	42	250	237	*
IV-2	*	23	43	*	133	11	36	*	*	15	264	0	1	27	*	710	17	22	760	60	48	216	*
BF/KIA-2	*	3577	261	*	137	12	12	*	*	21	209	6	68	28	*	313	18	21	789	55	490	263	*
KIA-4JWZ	*	2823	228	*	171	10	13	*	*	21	491	12	105	35	*	269	18	37	1257	55	1330	225	*
LHD/10-12	*	1538	70	*	426	76	14	*	*	15	289	5	49	44	*	215	14	19	819	53	572	226	*
LHD/10-11	*	770	45	*	445	58	24	*	*	15	351	4	29	35	*	199	14	25	919	63	612	254	*
LHD/14-24	*	2030	52	*	300	9	23	*	*	17	290	0	20	37	*	721	13	21	631	67	492	237	*
R2BR	0.40	3	68	0	283	163	23	*	49	6	2298	*	*	*	7	75	6	16	908	84	4508	153	*
KIA1/L15	*	67	97	*	70	14	74	*	*	12	177	3	2	49	*	1009	22	21	364	56	293	192	*
181.000	*	2360	86	*	233	92	24	*	36	0	971	4	14	41	15	145	11	14	746	26	2131	192	39
182.000	*	1599	50	*	403	1	13	*	33	0	236	11	55	19	15	364	10	11	1746	13	229	202	31
183.000	*	43	92	*	377	159	36	*	43	0	347	5	4	48	12	264	10	43	852	69	991	252	61
184.000	*	22	100	*	564	9	46	*	57	0	463	0	2	55	7	182	10	21	641	23	604	280	64
186.000	*	13	67	*	340	2	89	*	29	2	562	5	5	29	10	468	13	24	1395	7	1244	171	55
187.000	*	40	79	*	372	0	30	*	43	0	410	1	2	46	11	215	12	65	1379	96	1150	229	51
R5B2	*	8	13	*	456	12	22	*	25	1	2179	2	7	10	8	77	1	10	1230	35	3643	146	13
185.000	0.00	*	62	7	422	2	62	*	92	20	404	*	*	*	16	108	14	20	870	97	622	506	*
W10B	0.00	16	2	1	189	7	15	*	27	5	83	*	*	*	1	83	5	4	333	33	474	77	*
R7B1	0.10	38	76	2	201	13	16	*	20	6	119	3	*	*	0	118	7	11	425	119	356	119	*
BF/KIA-4	*	9	155	*	140	17	60	*	*	29	234	6	5	71	*	117	29	20	860	78	62	356	*
W2B	*	8	41	*	220	2	15	*	16	0	60	1	2	25	5	106	0	15	621	45	391	106	26
KIA2 RELICT	*	53	14	*	83	13	23	*	*	14	69	3	5	16	*	131	7	19	306	33	59	187	*
KIA3 RELICT	*	23	94	*	95	19	60	*	*	24	217	8	3	50	*	771	21	20	761	81	208	390	*
KIA RELICT	*	4	140	*	139	17	60	*	*	28	90	7	2	89	*	41	33	31	689	64	54	265	*
IV-2 RELICT	*	13	3	*	69	14	25	*	*	9	63	7	3	11	*	115	9	10	354	34	299	151	*
BO-137	*	88	21	*	29	28	21	*	*	8	49	9	5	*	*	162	5	3	298	19	242	48	*
BO-150	*	75	5	*	15	18	43	*	*	4	55	8	5	*	*	210	5	9	305	31	231	75	*
BO-076	*	81	54	*	21	20	14	*	*	10	18	9	5	*	*	119	8	4	332	14	112	51	*
BO-137	10.00	88	21	5	29	28	21	5	18	8	49	9	5	*	11	162	5	3	298	19	242	48	*
BO-150	13.14	75	5	5	15	18	43	5	16	4	55	8	5	*	8	210	5	9	305	31	231	75	*
BO-076	11.43	81	54	5	21	20	14	5	3	10	18	9	5	*	15	119	8	4	332	14	112	51	*
LHD/12-13	*	1609	33	*	432	83	12	*	64	12	207	14	48	30	*	145	10	10	663	34	664	187	16
LHD/13-37	*	1768	35	*	516	70	10	*	50	13	223	9	44	26	*	168	11	10	635	36	285	226	21

Table 1. Continue 12.

Sample	SiO <sub>2</sub>	TiO <sub>2</sub>	Al <sub>2</sub> O <sub>3</sub>	Fe <sub>2</sub> O <sub>3</sub> T	FeO	Fe <sub>2</sub> O <sub>3</sub>	MnO	MgO	CaO	Na <sub>2</sub> O	K <sub>2</sub> O	P <sub>2</sub> O <sub>5</sub>	Cr <sub>2</sub> O <sub>3</sub>	LOI	NiO	TOTAL	H <sub>2</sub> O-
LHD/13-39	67.05	0.65	11.71	5.32	*	*	0.05	1.22	1.38	0.86	2.07	0.14	0.03	7.79	0.03	98.30	0.00
LHD/10-13	67.63	0.62	11.34	4.08	*	*	0.03	1.10	1.51	0.98	2.08	0.12	0.03	9.37	0.04	99.00	0.12
LHD/11-18	68.38	0.61	12.20	5.10	*	*	0.05	1.06	1.14	2.27	2.39	0.11	0.04	6.25	0.04	99.70	0.08
LHD/11-20	70.75	0.49	11.00	4.38	*	*	0.05	0.94	1.64	1.94	2.01	0.23	0.02	6.07	0.02	99.60	0.06
LHD/14-25	72.68	0.79	15.23	5.22	*	*	0.05	1.07	1.23	0.85	2.35	0.14	0.03	6.53	0.03	106.20	0.00
BO-020	71.50	0.59	11.93	4.96	2.25	2.46	0.06	1.00	1.02	1.20	1.88	0.12	0.05	5.02	*	99.34	0.13
BO-023	69.23	0.64	11.58	4.80	1.94	2.65	0.07	1.86	1.82	1.01	2.22	0.11	0.05	5.75	*	99.14	0.18
BO-026	67.16	0.64	11.05	4.96	1.47	3.33	0.04	1.14	1.21	1.22	2.23	0.13	0.05	9.40	*	99.22	0.45
BO-064	70.49	0.59	11.18	4.30	1.76	2.34	0.03	1.07	1.01	0.88	2.13	0.10	0.02	7.67	*	99.49	0.14
BO-138	77.68	0.46	9.61	2.35	0.77	1.50	0.05	0.69	0.95	0.94	1.50	0.03	0.02	4.87	*	99.16	0.13
BO-139	48.26	1.11	24.56	9.20	4.73	3.95	0.13	2.06	2.65	3.76	2.82	0.05	0.04	4.77	*	99.41	0.13
BO-152	70.21	0.59	10.90	4.26	1.04	3.11	0.02	0.98	0.91	0.93	1.82	0.07	0.04	9.31	*	100.02	0.35
BO-080	74.01	0.26	12.28	2.43	1.00	1.32	0.02	0.23	0.96	0.97	2.11	0.06	0.04	5.77	*	99.12	0.20
BO-165	50.27	0.80	10.39	7.11	2.53	4.30	0.14	0.20	14.77	0.31	0.25	12.11	0.03	4.09	*	100.16	0.17
BO-081	67.21	0.66	14.08	4.28	1.76	2.33	0.03	1.19	1.16	1.48	2.16	0.12	0.02	7.29	*	99.70	0.23
BO-178	71.69	0.57	10.10	4.92	2.02	2.68	0.03	0.57	0.64	0.68	2.03	0.07	0.02	7.86	*	99.16	0.12
BO-180	64.77	0.81	14.21	5.82	2.74	2.77	0.05	0.93	1.11	1.11	1.84	0.07	0.03	8.95	*	99.72	0.20
BO-077	65.42	0.59	11.70	5.42	2.22	2.95	0.02	0.81	1.27	0.57	2.71	0.72	0.03	10.21	*	99.44	0.68
BO-179	58.56	0.45	10.17	4.82	1.98	2.62	0.16	8.30	9.48	1.16	1.08	0.19	0.04	5.10	*	99.51	0.32
BO-154	42.32	1.33	11.22	11.94	5.01	6.36	0.29	11.01	9.35	0.38	1.81	0.74	0.06	9.61	*	100.06	1.74
LHD/11-19	65.50	0.55	11.15	3.55	*	*	0.06	0.68	4.45	1.07	1.80	0.09	0.04	9.99	0.05	99.10	0.08
LHD/14-26	66.86	0.64	12.42	4.50	*	*	0.06	0.73	3.52	2.18	1.88	0.26	0.02	5.89	0.03	98.90	0.00
LHD/13-38	65.58	0.62	11.89	4.28	*	*	0.06	0.75	4.03	1.39	1.87	0.14	0.03	8.21	0.05	98.90	0.05
BO-003	63.36	0.44	7.83	4.55	0.50	4.00	0.14	1.85	8.18	0.62	2.05	0.10	0.06	10.53	*	99.71	2.42
BO-034	60.23	1.50	20.20	6.32	1.71	4.42	0.06	3.40	0.88	0.72	1.91	0.11	0.03	4.41	*	99.77	0.48
LHD/12-5	70.12	0.36	7.15	3.32	*	*	0.01	0.31	0.95	0.14	2.55	0.21	0.06	14.32	0.04	99.50	0.00
LHD/14-17	68.85	0.38	6.50	3.94	*	*	0.01	0.31	0.65	0.00	2.32	0.21	0.06	15.74	0.05	99.00	0.01
LHD/14-20	69.63	0.34	6.29	3.32	*	*	0.01	0.27	0.99	0.00	2.47	0.16	0.05	14.31	0.05	98.00	0.14
LHD/13-27	71.65	0.43	7.00	4.94	*	*	0.01	0.34	0.40	0.00	2.69	0.12	0.05	11.54	0.03	99.20	0.00
LHD/13-42	66.77	0.58	11.80	5.35	*	*	0.05	1.51	2.54	1.81	1.85	0.13	0.02	7.11	0.02	99.50	0.01
LHD/13-22	69.42	0.46	11.54	5.20	*	*	0.03	0.95	2.22	3.46	1.56	0.25	0.01	5.43	0.02	100.50	0.01
LHD/14-7	56.45	1.73	15.77	6.83	*	*	0.11	2.81	6.28	0.86	3.77	1.08	0.01	2.02	0.01	97.80	0.05
KIA-3/4	66.86	0.75	11.63	4.83	*	*	0.06	1.75	1.37	2.25	3.22	0.12	0.01	7.25	0.06	100.17	*
KIA-4JWZ	63.56	0.54	11.96	5.69	*	*	0.10	1.53	6.06	1.42	1.16	0.11	0.01	7.05	0.05	99.23	*
BF10/HW	65.35	0.76	11.16	5.54	*	*	0.08	1.56	8.09	0.70	0.08	0.10	0.01	7.95	0.04	101.42	*
BF10/KGG	59.28	0.46	18.37	2.66	*	*	0.08	2.80	1.71	3.33	3.39	0.04	0.01	8.10	0.01	100.23	*
KIA1-SZ	72.42	0.40	8.78	2.79	*	*	0.06	0.88	5.12	0.61	1.03	0.10	0.01	8.26	0.03	100.50	*
BO-046	37.58	0.29	5.65	4.06	1.40	2.51	0.04	0.29	0.56	0.02	0.03	0.08	0.03	51.20	*	99.81	1.72
BO-136	93.43	0.18	0.89	0.89	0.32	0.54	0.04	0.82	1.65	0.10	0.02	0.05	0.02	0.74	*	98.79	0.13
LHD/13-35	71.84	0.64	11.80	3.61	*	*	0.02	1.06	0.78	0.42	2.56	0.18	0.03	6.01	0.03	99.00	0.05
R9K	72.93	0.72	12.21	4.76	*	*	0.01	1.03	3.37	1.96	1.39	0.10	*	12.09	*	98.49	*

Table 1. Continue 13.

Sample	As	Ba	Ce	Co	Cr	Cu	Ga	Hf	Mo	Nb	Ni	Pb	Rb	Nd	Sc	Sr	Th	U	V	Y	Zn	Zr	La	
LHD/13-39	*	1690	45	*	527	88	10	*	71	13	225	10	43	31	*	149	9	7	696	35	768	210	22	
LHD/10-13	*	1632	32	*	582	*	*	*	*	*	*	*	*	25	*	*	*	*	821	*	*	*	27	
LHD/11-18	*	1876	34	*	641	100	11	*	66	14	260	8	48	31	*	173	12	11	735	42	685	210	26	
LHD/11-20	*	1560	22	*	355	63	12	*	34	12	106	9	42	16	*	184	7	7	443	39	181	209	19	
LHD/14-25	*	1871	48	*	587	89	12	*	58	16	252	10	46	30	*	182	12	9	691	41	547	236	31	
BO-020	10.00	1425	22	5	336	60	12	8	35	11	131	8	44	*	14	213	5	4	437	32	174	251	*	
BO-023	10.00	1531	19	5	338	68	13	6	60	9	143	13	55	*	15	189	5	9	728	27	486	196	*	
BO-026	10.00	1562	17	5	310	88	14	5	67	9	317	13	55	*	13	142	5	9	928	25	751	186	*	
BO-064	10.00	1678	30	5	130	88	12	6	59	12	205	13	51	*	10	143	5	8	775	28	745	195	*	
BO-138	10.00	1140	17	5	99	48	12	7	25	11	119	10	36	*	6	187	5	4	422	16	215	228	*	
BO-139	10.00	2011	73	5	68	127	24	10	7	28	103	21	77	*	26	838	6	3	902	68	248	199	*	
BO-152	10.00	1395	30	5	229	92	14	6	43	10	366	10	46	*	12	118	6	8	943	27	573	197	*	
BO-080	10.00	2146	5	5	81	47	16	5	56	3	168	10	40	*	6	132	5	13	681	29	708	72	*	
BO-165	10.00	95	591	36	120	86	11	15	21	16	190	11	9	*	9	123	5	14	463	529	69	506	*	
BO-081	10.00	1330	29	5	136	80	20	5	70	9	139	14	60	*	7	144	5	5	768	15	859	176	*	
BO-178	10.00	1699	20	12	131	77	12	6	62	9	227	13	44	*	12	124	5	5	933	24	425	177	*	
BO-180	10.00	1483	58	5	152	126	17	6	48	16	209	11	44	*	12	117	6	10	1187	35	219	169	*	
BO-077	10.00	2062	39	22	157	104	14	6	46	11	312	16	58	*	14	107	6	6	910	85	141	179	*	
BO-179	10.00	529	15	5	101	67	20	5	79	9	165	10	56	*	17	124	7	11	767	32	2155	170	*	
BO-154	11.45	1127	121	5	462	122	31	5	8	23	162	13	105	*	31	185	5	8	430	29	458	146	*	
LHD/11-19	*	1346	30	*	405	52	13	*	61	13	241	6	48	18	*	229	9	20	707	49	359	229	25	
LHD/14-26	*	1784	55	*	292	66	14	*	40	15	192	7	36	35	*	385	9	9	560	42	391	229	34	
LHD/13-38	*	1465	43	*	431	77	12	*	53	14	339	9	46	30	*	232	10	20	705	51	473	234	28	
BO-003	10.00	626	35	12	363	86	11	5	27	10	327	17	72	*	13	286	7	6	187	36	329	113	*	
BO-034	10.00	496	38	11	187	64	30	7	8	22	111	12	79	*	35	86	5	7	277	44	249	237	*	
LHD/12-5	*	2458	38	*	1020	72	6	*	15	9	306	7	73	41	*	189	11	21	208	69	113	97	32	
LHD/14-17	*	2312	28	*	1185	84	5	*	26	11	378	19	68	32	*	206	10	18	320	67	236	91	20	
LHD/14-20	*	3111	-18	*	1008	70	4	*	30	9	386	5	63	20	*	169	7	16	421	56	207	82	24	
LHD/13-27	*	1773	25	*	1023	69	4	*	7	11	198	39	72	25	*	148	9	9	130	63	99	100	20	
LHD/13-42	*	1196	46	*	283	73	14	*	50	14	152	12	47	33	*	189	11	12	485	44	342	219	25	
LHD/13-22	*	1124	-20	*	244	60	16	*	40	9	138	8	37	20	*	152	9	9	410	38	203	156	13	
LHD/14-7	*	4804	204	*	149	22	18	*	24	19	57	16	40	103	*	3775	5	0	309	33	330	224	118	
KIA-3/4	*	4608	328	*	145	9	16	*	*	20	385	17	91	36	*	329	15	25	1135	52	776	235	*	
KIA-4JWZ	*	1559	150	*	132	10	17	*	*	18	254	8	36	31	*	301	23	27	853	56	468	246	*	
BF10/HW	*	121	35	*	118	10	32	*	*	13	184	4	3	21	*	952	13	31	851	43	920	213	*	
BF10/KGG	*	3409	251	*	60	6	26	*	*	15	64	6	116	30	*	493	19	14	530	28	792	170	*	
KIA1-SZ	*	*	*	*	*	*	*	*	*	*	*	*	*	*	*	*	*	*	*	*	*	*	*	*
BO-046	10.00	125	29	5	38	39	13	5	31	5	328	7	5	*	8	33	5	11	460	20	338	109	*	
BO-136	10.00	88	5	8	5	6	9	5	10	4	5	5	5	*	3	38	5	4	49	10	6	18	*	
LHD/13-35	*	1899	39	*	453	56	8	*	35	13	204	7	50	24	*	173	7	6	509	32	279	242	18	
R9K	3.80	3640	37	6	387	7	9	*	96	10	171	2	*	*	17	330	15	19	2046	27	240	200	*	

Table 2. Average, minimum, maximum, standard deviation and standard error of the whole-rock compositions of the GNG units.

	Valid N	Mean	Minimum	Maximum	Std. Dev.	Std. Error
<b>SiO<sub>2</sub></b>	12	58.07	52.14	61.55	2.50	0.72
<b>TiO<sub>2</sub></b>	12	1.45	1.29	1.70	0.13	0.04
<b>Al<sub>2</sub>O<sub>3</sub></b>	12	20.08	17.98	22.79	1.30	0.37
<b>Fe<sub>2</sub>O<sub>3T</sub></b>	12	11.61	6.65	13.97	1.99	0.58
<b>FeO</b>	8	9.15	7.46	11.48	1.31	0.46
<b>Fe<sub>2</sub>O<sub>3</sub></b>	8	2.00	0.16	3.32	0.98	0.35
<b>MnO</b>	12	0.08	0.03	0.12	0.03	0.01
<b>MgO</b>	12	3.28	2.52	3.85	0.42	0.12
<b>CaO</b>	12	0.84	0.43	1.39	0.24	0.07
<b>Na<sub>2</sub>O</b>	12	0.51	0.03	1.00	0.30	0.09
<b>K<sub>2</sub>O</b>	12	1.82	1.32	2.33	0.25	0.07
<b>P<sub>2</sub>O<sub>5</sub></b>	12	0.12	0.03	0.25	0.06	0.02
<b>Cr<sub>2</sub>O<sub>3</sub></b>	12	0.04	0.03	0.06	0.01	0.00
<b>LOI</b>	12	1.86	0.01	5.44	1.74	0.50
<b>NiO</b>	4	0.01	0.01	0.02	0.00	0.00
<b>TOTAL</b>	12	99.89	99.00	101.00	0.47	0.13
<b>H<sub>2</sub>O-</b>	12	0.30	0.04	0.84	0.21	0.06
<b>As</b>	8	10.00	10.00	10.00	0.00	0.00
<b>Ba</b>	12	456.52	350.36	813.31	142.31	41.08
<b>Ce</b>	12	56.77	23.26	105.24	22.05	6.37
<b>Co</b>	8	22.48	6.77	39.48	11.75	4.15
<b>Cr</b>	12	391.91	172.11	763.94	219.69	63.42
<b>Cu</b>	12	60.49	30.93	88.56	17.18	4.96
<b>Ga</b>	12	25.35	22.21	28.55	2.05	0.59
<b>Hf</b>	8	6.63	5.78	7.18	0.50	0.18
<b>Mo</b>	12	6.25	2.79	14.86	4.81	1.39
<b>Nb</b>	12	15.44	9.41	32.37	5.73	1.65
<b>Ni</b>	12	71.54	17.94	97.45	26.89	7.76
<b>Pb</b>	12	8.56	4.49	11.25	2.19	0.63
<b>Rb</b>	12	68.07	45.49	92.63	13.43	3.88
<b>Nd</b>	4	26.36	19.67	36.00	7.48	3.74
<b>Sc</b>	8	27.48	23.51	31.75	2.66	0.94
<b>Sr</b>	12	143.25	85.21	513.36	117.40	33.89
<b>Ta</b>	8	5.61	5.00	8.51	1.22	0.43
<b>Th</b>	12	6.98	5.00	13.01	2.41	0.70
<b>U</b>	12	1.58	-4.28	6.04	3.51	1.01
<b>V</b>	12	263.74	212.58	414.85	52.26	15.08
<b>W</b>	8	3.90	3.00	6.05	1.28	0.45
<b>Y</b>	12	43.12	24.04	53.62	6.94	2.00
<b>Zn</b>	12	147.91	113.78	180.67	21.58	6.23
<b>Zr</b>	12	220.06	192.97	248.33	16.23	4.68
<b>La</b>	4	12.29	-9.63	26.07	15.32	7.66



Table 3. Average, minimum, maximum, standard deviation and standard error of the whole-rock compositions of the BCF.

	Valid N	Mean	Minimum	Maximum	Std. Dev.	Std. Error
<b>SiO<sub>2</sub></b>	21	60.90	49.41	68.02	4.21	0.92
<b>TiO<sub>2</sub></b>	21	0.50	0.39	0.58	0.05	0.01
<b>Al<sub>2</sub>O<sub>3</sub></b>	21	9.44	7.42	10.91	0.85	0.18
<b>Fe<sub>2</sub>O<sub>3T</sub></b>	21	4.89	3.96	5.61	0.48	0.11
<b>FeO</b>	10	2.74	1.40	3.92	0.65	0.21
<b>Fe<sub>2</sub>O<sub>3</sub></b>	10	1.93	0.66	2.84	0.55	0.17
<b>MnO</b>	21	0.08	0.04	0.19	0.03	0.01
<b>MgO</b>	21	2.30	1.49	5.56	0.84	0.18
<b>CaO</b>	21	11.54	5.47	21.83	3.41	0.74
<b>Na<sub>2</sub>O</b>	21	0.25	0.00	0.79	0.25	0.05
<b>K<sub>2</sub>O</b>	21	2.66	1.87	3.21	0.37	0.08
<b>P<sub>2</sub>O<sub>5</sub></b>	21	0.09	0.05	0.12	0.02	0.00
<b>Cr<sub>2</sub>O<sub>3</sub></b>	21	0.02	0.00	0.04	0.01	0.00
<b>LOI</b>	21	5.03	1.78	9.70	2.09	0.46
<b>NiO</b>	11	0.01	0.01	0.01	0.00	0.00
<b>TOTAL</b>	21	97.76	92.90	99.51	2.10	0.46
<b>H<sub>2</sub>O-</b>	21	0.18	0.02	0.79	0.19	0.04
<b>As</b>	10	10.06	10.00	10.63	0.20	0.06
<b>Ba</b>	21	859.19	641.74	1125.70	141.87	30.96
<b>Ce</b>	21	24.00	-23.10	45.06	20.46	4.46
<b>Co</b>	10	9.00	5.00	14.44	3.99	1.26
<b>Cr</b>	21	128.45	20.74	260.14	73.99	16.15
<b>Cu</b>	21	67.81	47.24	87.92	10.52	2.30
<b>Ga</b>	21	13.83	10.84	17.37	1.98	0.43
<b>Hf</b>	10	5.21	4.63	5.84	0.37	0.12
<b>Mo</b>	21	3.69	1.83	14.08	2.78	0.61
<b>Nb</b>	21	15.14	8.41	35.68	5.16	1.13
<b>Ni</b>	21	37.10	17.52	61.25	11.33	2.47
<b>Pb</b>	21	13.98	10.68	17.88	2.26	0.49
<b>Rb</b>	21	96.45	73.01	122.98	15.35	3.35
<b>Nd</b>	11	22.14	15.61	28.51	3.84	1.16
<b>Sc</b>	10	15.47	13.33	18.02	1.57	0.50
<b>Sr</b>	21	274.84	195.34	446.55	55.84	12.19
<b>Ta</b>	10	5.67	5.00	11.72	2.13	0.67
<b>Th</b>	21	10.45	6.70	13.79	2.26	0.49
<b>U</b>	21	0.44	-4.09	6.64	3.89	0.85
<b>V</b>	21	62.73	38.45	91.06	11.58	2.53
<b>W</b>	10	5.02	3.00	12.68	3.10	0.98
<b>Y</b>	21	37.29	25.86	46.30	5.13	1.12
<b>Zn</b>	21	132.30	94.63	181.36	21.42	4.67
<b>Zr</b>	21	116.96	72.78	134.49	13.70	2.99
<b>La</b>	11	19.45	13.19	26.92	4.37	1.32

Table 4. Average, minimum, maximum, standard deviation and standard error of the whole-rock compositions of the GCS.

	Valid N	Mean	Minimum	Maximum	Std. Dev.	Std. Error
<b>SiO<sub>2</sub></b>	22	53.52	44.91	59.13	2.84	0.61
<b>TiO<sub>2</sub></b>	22	0.41	0.28	0.55	0.06	0.01
<b>Al<sub>2</sub>O<sub>3</sub></b>	22	7.66	4.93	9.14	0.92	0.20
<b>Fe<sub>2</sub>O<sub>3T</sub></b>	22	3.90	2.94	6.53	0.74	0.16
<b>FeO</b>	11	1.24	0.72	1.94	0.35	0.11
<b>Fe<sub>2</sub>O<sub>3</sub></b>	11	2.48	1.77	2.96	0.47	0.14
<b>MnO</b>	22	0.06	0.04	0.13	0.02	0.00
<b>MgO</b>	22	1.01	0.40	4.36	0.81	0.17
<b>CaO</b>	22	9.69	5.03	18.80	2.57	0.55
<b>Na<sub>2</sub>O</b>	22	0.16	0.00	0.51	0.17	0.04
<b>K<sub>2</sub>O</b>	22	0.50	0.00	1.69	0.42	0.09
<b>P<sub>2</sub>O<sub>5</sub></b>	22	0.28	0.17	0.70	0.11	0.02
<b>Cr<sub>2</sub>O<sub>3</sub></b>	22	0.04	0.03	0.05	0.01	0.00
<b>LOI</b>	22	21.25	17.47	30.24	3.20	0.68
<b>NiO</b>	11	0.07	0.07	0.08	0.00	0.00
<b>TOTAL</b>	22	98.84	97.10	100.32	0.94	0.20
<b>H<sub>2</sub>O-</b>	22	0.75	0.10	2.53	0.71	0.15
<b>As</b>	11	10.00	10.00	10.00	0.00	0.00
<b>Ba</b>	22	1184.34	102.82	2719.54	652.38	139.09
<b>Ce</b>	22	29.15	-20.53	64.30	22.81	4.86
<b>Co</b>	11	5.00	5.00	5.00	0.00	0.00
<b>Cr</b>	22	382.09	64.57	887.44	253.90	54.13
<b>Cu</b>	22	61.08	9.67	121.13	28.21	6.01
<b>Ga</b>	22	14.95	10.18	25.27	3.74	0.80
<b>Hf</b>	11	5.26	5.00	6.24	0.37	0.11
<b>Mo</b>	22	95.93	47.63	180.24	28.35	6.04
<b>Nb</b>	22	8.40	3.00	10.62	1.60	0.34
<b>Ni</b>	22	534.22	240.23	795.37	108.14	23.06
<b>Pb</b>	22	9.10	4.28	15.16	3.33	0.71
<b>Rb</b>	22	14.57	-1.30	58.68	13.98	2.98
<b>Nd</b>	11	27.52	21.04	40.25	5.50	1.66
<b>Sc</b>	11	9.57	6.63	11.65	1.50	0.45
<b>Sr</b>	22	320.72	39.96	415.72	79.22	16.89
<b>Ta</b>	11	5.00	5.00	5.00	0.00	0.00
<b>Th</b>	22	7.20	2.74	10.62	2.13	0.45
<b>U</b>	22	35.65	26.46	43.58	4.77	1.02
<b>V</b>	22	1547.51	1211.16	2332.77	271.94	57.98
<b>W</b>	11	3.00	3.00	3.00	0.00	0.00
<b>Y</b>	22	64.97	58.09	71.55	3.15	0.67
<b>Zn</b>	22	1161.19	801.84	1597.06	218.41	46.57
<b>Zr</b>	22	126.37	59.54	155.79	21.34	4.55
<b>La</b>	11	24.09	15.05	30.10	4.50	1.36

Table 5. Average, minimum, maximum, standard deviation and standard error of the whole-rock compositions of the kyanite-graphite gneisses.

	Valid N	Mean	Minimum	Maximum	Std. Dev.	Std. Error
<b>SiO<sub>2</sub></b>	66	66.44	55.69	72.68	3.38	0.42
<b>TiO<sub>2</sub></b>	66	0.65	0.36	1.01	0.14	0.02
<b>Al<sub>2</sub>O<sub>3</sub></b>	66	11.38	6.04	15.23	1.44	0.18
<b>Fe<sub>2</sub>O<sub>3T</sub></b>	66	4.92	2.16	8.36	1.07	0.13
<b>FeO</b>	25	2.00	0.86	4.14	0.80	0.16
<b>Fe<sub>2</sub>O<sub>3</sub></b>	25	3.08	1.16	4.09	0.72	0.14
<b>MnO</b>	66	0.03	0.00	0.07	0.02	0.00
<b>MgO</b>	66	1.13	0.15	2.63	0.41	0.05
<b>CaO</b>	66	1.65	0.09	7.91	1.10	0.14
<b>Na<sub>2</sub>O</b>	66	0.97	0.00	2.27	0.44	0.05
<b>K<sub>2</sub>O</b>	66	2.27	0.02	3.50	0.50	0.06
<b>P<sub>2</sub>O<sub>5</sub></b>	66	0.17	0.06	0.51	0.09	0.01
<b>Cr<sub>2</sub>O<sub>3</sub></b>	66	0.03	0.01	0.07	0.01	0.00
<b>LOI</b>	66	9.51	5.02	20.90	2.99	0.37
<b>NiO</b>	41	0.04	0.00	0.09	0.02	0.00
<b>TOTAL</b>	66	99.30	98.00	106.20	0.99	0.12
<b>H<sub>2</sub>O-</b>	66	0.23	-0.11	1.40	0.30	0.04
<b>As</b>	25	10.13	10.00	12.21	0.48	0.10
<b>Ba</b>	66	1783.41	150.39	3298.53	555.00	68.32
<b>Ce</b>	66	25.91	-19.69	70.84	22.44	2.76
<b>Co</b>	25	9.82	5.00	44.28	9.40	1.88
<b>Cr</b>	66	414.48	39.53	912.34	248.13	30.54
<b>Cu</b>	65	89.79	14.03	187.57	33.47	4.15
<b>Ga</b>	65	13.87	4.33	41.22	4.52	0.56
<b>Hf</b>	25	6.87	5.00	12.40	1.76	0.35
<b>Mo</b>	65	55.13	10.26	126.45	20.21	2.51
<b>Nb</b>	65	12.66	5.00	27.53	4.04	0.50
<b>Ni</b>	65	246.65	23.99	682.76	158.10	19.61
<b>Pb</b>	65	12.20	5.92	29.44	4.34	0.54
<b>Rb</b>	65	55.15	5.00	85.71	14.13	1.75
<b>Nd</b>	41	24.77	15.69	45.27	6.42	1.00
<b>Sc</b>	25	14.61	8.15	23.49	3.66	0.73
<b>Sr</b>	65	197.66	77.08	430.31	66.66	8.27
<b>Ta</b>	25	5.32	5.00	11.09	1.26	0.25
<b>Th</b>	65	8.03	4.48	13.53	2.38	0.30
<b>U</b>	65	10.35	3.00	25.33	4.48	0.56
<b>V</b>	66	803.55	158.10	2012.83	379.59	46.72
<b>W</b>	25	3.47	3.00	11.18	1.69	0.34
<b>Y</b>	65	35.40	6.03	63.84	12.23	1.52
<b>Zn</b>	65	421.13	16.34	1109.36	294.03	36.47
<b>Zr</b>	65	199.33	82.67	348.15	45.99	5.70
<b>La</b>	41	20.39	-8.72	35.37	7.56	1.18

Table 6. Average, minimum, maximum, standard deviation and standard error of the whole-rock compositions of the graphite-plagioclase gneisses.

	Valid N	Mean	Minimum	Maximum	Std. Dev.	Std. Error
<b>SiO<sub>2</sub></b>	54	65.01	48.31	71.76	4.38	0.60
<b>TiO<sub>2</sub></b>	54	0.59	0.39	1.72	0.18	0.03
<b>Al<sub>2</sub>O<sub>3</sub></b>	54	10.71	5.75	14.49	1.50	0.20
<b>Fe<sub>2</sub>O<sub>3T</sub></b>	54	4.97	1.95	17.59	2.24	0.30
<b>FeO</b>	29	1.61	0.32	4.68	0.97	0.18
<b>Fe<sub>2</sub>O<sub>3</sub></b>	29	3.03	1.45	9.65	1.60	0.30
<b>MnO</b>	54	0.05	0.00	0.14	0.03	0.00
<b>MgO</b>	54	1.13	0.06	6.19	0.93	0.13
<b>CaO</b>	54	3.64	0.28	22.12	3.22	0.44
<b>Na<sub>2</sub>O</b>	54	1.03	0.08	2.79	0.57	0.08
<b>K<sub>2</sub>O</b>	54	1.72	0.33	4.59	0.95	0.13
<b>P<sub>2</sub>O<sub>5</sub></b>	54	0.14	0.05	0.54	0.08	0.01
<b>Cr<sub>2</sub>O<sub>3</sub></b>	50	0.03	0.01	0.08	0.01	0.00
<b>LOI</b>	54	9.97	4.59	25.47	2.99	0.41
<b>NiO</b>	25	0.03	0.01	0.06	0.01	0.00
<b>TOTAL</b>	54	99.18	97.20	100.40	0.69	0.09
<b>H<sub>2</sub>O-</b>	54	0.61	-0.03	4.55	0.95	0.13
<b>As</b>	25	10.09	10.00	12.25	0.45	0.09
<b>Ba</b>	54	1399.80	340.13	3206.17	494.05	67.23
<b>Ce</b>	54	37.02	-22.88	91.62	27.61	3.76
<b>Co</b>	25	20.11	5.00	301.81	59.02	11.80
<b>Cr</b>	54	287.49	38.11	593.08	163.73	22.28
<b>Cu</b>	54	76.65	6.07	300.11	43.32	5.90
<b>Ga</b>	54	15.23	8.71	37.11	5.02	0.68
<b>Hf</b>	25	7.16	5.06	10.97	1.67	0.33
<b>Mo</b>	54	51.62	7.14	105.55	20.29	2.76
<b>Nb</b>	54	11.52	0.42	32.55	5.35	0.73
<b>Ni</b>	54	243.17	22.35	1151.82	170.13	23.15
<b>Pb</b>	54	10.20	3.36	16.82	3.24	0.44
<b>Rb</b>	54	47.40	8.18	115.30	24.96	3.40
<b>Nd</b>	29	24.12	13.78	39.40	6.57	1.22
<b>Sc</b>	29	13.14	9.06	24.90	3.24	0.60
<b>Sr</b>	54	218.82	20.21	487.48	83.30	11.34
<b>Ta</b>	25	5.00	5.00	5.00	0.00	0.00
<b>Th</b>	54	7.70	2.53	13.60	2.42	0.33
<b>U</b>	54	16.67	3.00	54.75	8.88	1.21
<b>V</b>	54	847.56	46.82	2029.09	385.57	52.47
<b>W</b>	25	3.35	3.00	7.86	1.10	0.22
<b>Y</b>	54	39.21	5.50	89.73	15.61	2.12
<b>Zn</b>	54	399.80	11.60	1686.55	337.41	45.92
<b>Zr</b>	54	201.65	76.63	323.42	52.04	7.08
<b>La</b>	29	23.61	-9.47	46.07	15.35	2.85

Table 7. Average, minimum, maximum, standard deviation and standard error of the whole-rock compositions of the pyroxene relict units.

	Valid N	Mean	Minimum	Maximum	Std. Dev.	Std. Error
<b>SiO<sub>2</sub></b>	11	46.54	35.26	55.87	5.67	1.71
<b>TiO<sub>2</sub></b>	11	0.37	0.16	0.84	0.26	0.08
<b>Al<sub>2</sub>O<sub>3</sub></b>	11	8.35	3.63	13.36	3.85	1.16
<b>Fe<sub>2</sub>O<sub>3T</sub></b>	11	3.14	1.38	5.19	1.23	0.37
<b>FeO</b>	6	1.31	0.32	1.85	0.56	0.23
<b>Fe<sub>2</sub>O<sub>3</sub></b>	6	1.65	1.09	2.16	0.55	0.22
<b>MnO</b>	11	0.39	0.33	0.44	0.04	0.01
<b>MgO</b>	11	10.81	2.47	17.18	5.05	1.52
<b>CaO</b>	11	23.56	16.39	27.27	3.18	0.96
<b>Na<sub>2</sub>O</b>	11	0.39	0.03	0.74	0.26	0.08
<b>K<sub>2</sub>O</b>	10	0.04	0.02	0.08	0.02	0.01
<b>P<sub>2</sub>O<sub>5</sub></b>	11	0.10	0.04	0.17	0.04	0.01
<b>Cr<sub>2</sub>O<sub>3</sub></b>	10	0.01	0.00	0.02	0.01	0.00
<b>LOI</b>	11	6.06	3.26	13.32	2.84	0.86
<b>NiO</b>	5	0.02	0.01	0.04	0.02	0.01
<b>TOTAL</b>	11	99.76	98.55	100.58	0.54	0.16
<b>H<sub>2</sub>O-</b>	6	0.25	0.06	0.32	0.10	0.04
<b>As</b>	3	11.52	10.00	13.14	1.57	0.91
<b>Ba</b>	11	47.62	4.00	88.42	36.33	10.95
<b>Ce</b>	11	54.72	2.50	155.00	53.07	16.00
<b>Co</b>	3	5.00	5.00	5.00	0.00	0.00
<b>Cr</b>	11	78.18	15.06	220.23	65.82	19.85
<b>Cu</b>	11	17.87	2.24	28.11	7.11	2.14
<b>Ga</b>	11	32.23	13.88	60.00	19.34	5.83
<b>Hf</b>	3	5.00	5.00	5.00	0.00	0.00
<b>Mo</b>	4	13.38	3.00	18.09	6.98	3.49
<b>Nb</b>	11	12.97	0.46	28.50	9.38	2.83
<b>Ni</b>	11	83.65	18.02	233.50	73.04	22.02
<b>Pb</b>	11	6.65	1.48	9.02	2.58	0.78
<b>Rb</b>	11	3.92	1.50	5.00	1.37	0.41
<b>Nd</b>	6	43.50	10.50	88.50	31.69	12.94
<b>Sc</b>	4	9.76	4.54	15.10	4.54	2.27
<b>Sr</b>	11	186.54	40.50	770.50	198.17	59.75
<b>Ta</b>	3	5.00	5.00	5.00	0.00	0.00
<b>Th</b>	11	11.85	0.47	32.50	10.64	3.21
<b>U</b>	11	12.40	3.00	31.00	9.12	2.75
<b>V</b>	11	468.80	298.04	860.00	217.33	65.53
<b>W</b>	3	3.00	3.00	3.00	0.00	0.00
<b>Y</b>	11	39.24	14.32	81.00	24.57	7.41
<b>Zn</b>	11	182.59	53.50	390.78	111.14	33.51
<b>Zr</b>	11	156.92	47.98	390.00	127.15	38.34
<b>La</b>	1	25.86	25.86	25.86		

Table 8. Average, minimum, maximum, standard deviation and standard error of the whole-rock compositions of the calc-silicate skarn boudins.

	Valid N	Mean	Minimum	Maximum	Std. Dev.	Std. Error
<b>SiO<sub>2</sub></b>	15	56.89	47.04	64.04	5.32	1.37
<b>TiO<sub>2</sub></b>	15	0.46	0.15	0.77	0.17	0.04
<b>Al<sub>2</sub>O<sub>3</sub></b>	15	11.09	3.81	17.46	4.18	1.08
<b>Fe<sub>2</sub>O<sub>3T</sub></b>	15	5.91	1.70	15.22	3.21	0.83
<b>FeO</b>	9	0.71	0.41	1.40	0.33	0.11
<b>Fe<sub>2</sub>O<sub>3</sub></b>	9	5.87	1.77	14.02	3.61	1.20
<b>MnO</b>	15	0.14	0.01	0.37	0.14	0.04
<b>MgO</b>	12	3.51	0.16	13.53	4.81	1.39
<b>CaO</b>	15	10.59	0.19	24.04	8.07	2.08
<b>Na<sub>2</sub>O</b>	15	0.23	0.01	0.82	0.29	0.07
<b>K<sub>2</sub>O</b>	9	0.67	0.02	1.98	0.75	0.25
<b>P<sub>2</sub>O<sub>5</sub></b>	15	0.13	0.02	0.61	0.14	0.04
<b>Cr<sub>2</sub>O<sub>3</sub></b>	4	0.02	0.01	0.03	0.01	0.00
<b>LOI</b>	15	12.01	3.88	19.92	4.34	1.12
<b>NiO</b>	4	0.04	0.04	0.05	0.01	0.00
<b>TOTAL</b>	15	98.52	97.25	99.95	0.62	0.16
<b>H<sub>2</sub>O-</b>	10	1.89	0.03	5.49	1.79	0.57
<b>As</b>	4	0.13	0.00	0.40	0.19	0.09
<b>Ba</b>	14	610.43	2.50	2360.34	877.11	234.42
<b>Ce</b>	15	63.97	2.10	99.91	28.28	7.30
<b>Co</b>	4	2.40	0.00	6.70	2.99	1.50
<b>Cr</b>	15	338.67	69.50	563.71	127.18	32.84
<b>Cu</b>	15	41.10	0.45	162.50	56.48	14.58
<b>Ga</b>	15	34.05	13.38	89.35	23.42	6.05
<b>Mo</b>	11	41.17	20.30	92.00	20.19	6.09
<b>Nb</b>	15	6.72	0.07	20.30	7.26	1.87
<b>Ni</b>	15	611.81	82.60	2297.50	693.61	179.09
<b>Pb</b>	12	3.26	-3.82	11.06	3.54	1.02
<b>Rb</b>	11	17.10	1.50	54.50	19.32	5.82
<b>Nd</b>	11	37.50	10.30	54.69	13.48	4.07
<b>Sc</b>	11	9.15	0.20	16.20	5.31	1.60
<b>Sr</b>	15	282.92	75.40	1008.50	265.73	68.61
<b>Ta</b>	4	0.00	0.00	0.00	0.00	0.00
<b>Th</b>	15	10.78	1.43	22.00	4.82	1.24
<b>U</b>	15	21.68	3.90	64.64	14.91	3.85
<b>V</b>	15	883.94	333.40	1745.91	405.58	104.72
<b>W</b>	4	1.58	0.00	2.30	1.06	0.53
<b>Y</b>	15	56.00	6.59	119.40	33.48	8.64
<b>Zn</b>	15	1194.61	228.70	4507.80	1274.99	329.20
<b>Zr</b>	15	215.79	77.40	505.70	97.19	25.10
<b>La</b>	7	44.93	13.08	63.87	18.38	6.95

Table 9. Average, minimum, maximum, standard deviation and standard error of the whole-rock compositions of the skarnoid reaction zones.

	Valid N	Mean	Minimum	Maximum	Std. Dev.	Std. Error
<b>SiO<sub>2</sub></b>	12	66.05	58.91	75.33	5.52	1.59
<b>TiO<sub>2</sub></b>	12	0.65	0.56	0.74	0.06	0.02
<b>Al<sub>2</sub>O<sub>3</sub></b>	12	12.78	9.32	16.52	2.44	0.70
<b>Fe<sub>2</sub>O<sub>3T</sub></b>	12	5.74	3.97	7.99	1.22	0.35
<b>FeO</b>	4	0.81	0.59	1.04	0.24	0.12
<b>Fe<sub>2</sub>O<sub>3</sub></b>	4	4.05	3.32	5.10	0.81	0.41
<b>MnO</b>	12	0.06	0.01	0.18	0.06	0.02
<b>MgO</b>	12	0.85	0.26	1.70	0.48	0.14
<b>CaO</b>	12	4.66	0.28	11.87	4.45	1.28
<b>Na<sub>2</sub>O</b>	12	0.52	0.01	2.24	0.66	0.19
<b>K<sub>2</sub>O</b>	12	1.19	0.00	3.56	1.47	0.43
<b>P<sub>2</sub>O<sub>5</sub></b>	12	0.09	0.05	0.19	0.04	0.01
<b>Cr<sub>2</sub>O<sub>3</sub></b>	3	0.01	0.01	0.01	0.00	0.00
<b>LOI</b>	12	13.10	7.49	19.97	3.95	1.14
<b>NiO</b>	3	0.06	0.03	0.08	0.02	0.01
<b>TOTAL</b>	12	99.28	97.85	101.74	1.19	0.34
<b>H<sub>2</sub>O-</b>	4	1.64	0.36	3.60	1.51	0.75
<b>As</b>	5	10.40	0.00	52.00	23.26	10.40
<b>Ba</b>	12	1231.45	23.00	3576.50	1214.78	350.68
<b>Ce</b>	12	125.40	43.00	261.00	72.11	20.82
<b>Co</b>	5	9.08	3.90	13.20	3.92	1.75
<b>Cr</b>	12	326.82	132.50	525.28	137.23	39.61
<b>Cu</b>	12	73.64	9.50	256.95	78.15	22.56
<b>Ga</b>	12	21.51	11.37	35.50	9.88	2.85
<b>Mo</b>	9	56.96	38.02	69.54	11.36	3.79
<b>Nb</b>	12	11.83	0.45	21.00	8.31	2.40
<b>Ni</b>	12	404.56	147.74	868.73	209.46	60.47
<b>Pb</b>	11	4.11	-2.50	12.00	4.28	1.29
<b>Rb</b>	7	52.98	0.50	105.00	44.96	16.99
<b>Nd</b>	7	34.85	24.87	44.19	8.39	3.17
<b>Sc</b>	9	16.34	8.48	23.70	4.90	1.63
<b>Sr</b>	12	308.76	143.30	709.50	161.99	46.76
<b>Ta</b>	5	5.80	0.00	17.00	8.14	3.64
<b>Th</b>	12	12.39	5.65	18.00	3.98	1.15
<b>U</b>	12	26.46	12.76	42.50	8.88	2.56
<b>V</b>	12	1402.04	682.19	2871.30	641.79	185.27
<b>W</b>	5	2.38	0.00	6.40	2.40	1.07
<b>Y</b>	12	61.92	4.78	175.90	46.81	13.51
<b>Zn</b>	12	861.00	48.00	2896.90	796.69	229.99
<b>Zr</b>	12	244.46	186.04	305.50	32.13	9.28
<b>La</b>	4	41.95	32.06	47.50	6.89	3.44

Table 10. Average, minimum, maximum, standard deviation and standard error of the whole-rock compositions of the dolomitic marbles.

	Valid N	Mean	Minimum	Maximum	Std. Dev.	Std. Error
SiO <sub>2</sub>	8	6.76	1.40	17.73	6.65	2.35
TiO <sub>2</sub>	8	0.12	0.01	0.33	0.12	0.04
Al <sub>2</sub> O <sub>3</sub>	8	2.27	0.31	7.25	2.54	0.90
Fe <sub>2</sub> O <sub>3T</sub>	8	1.15	0.15	3.21	1.06	0.38
FeO	6	0.61	0.11	1.22	0.47	0.19
Fe <sub>2</sub> O <sub>3</sub>	6	0.25	0.02	0.72	0.26	0.11
MnO	8	0.02	0.01	0.03	0.01	0.00
MgO	8	11.97	1.41	18.05	6.00	2.12
CaO	8	37.32	27.67	45.47	6.63	2.35
Na <sub>2</sub> O	8	0.08	0.00	0.37	0.13	0.04
K <sub>2</sub> O	8	0.42	0.04	1.35	0.46	0.16
P <sub>2</sub> O <sub>5</sub>	8	0.03	0.00	0.06	0.02	0.01
Cr <sub>2</sub> O <sub>3</sub>	8	0.01	0.00	0.02	0.01	0.00
LOI	8	38.22	26.24	44.43	6.85	2.42
NiO	2	0.00	0.00	0.01	0.00	0.00
TOTAL	8	98.37	94.70	100.07	2.09	0.74
H <sub>2</sub> O-	8	0.12	0.02	0.21	0.08	0.03
As	6	10.00	10.00	10.00	0.00	0.00
Ba	8	578.24	10.00	3115.66	1045.55	369.66
Ce	8	1.43	-27.26	32.32	18.94	6.70
Co	6	5.11	5.00	5.69	0.28	0.11
Cr	8	27.63	-16.49	178.61	62.50	22.10
Cu	8	4.06	-3.96	6.42	3.28	1.16
Ga	8	4.83	-2.62	7.49	3.20	1.13
Hf	6	5.00	5.00	5.00	0.00	0.00
Mo	8	2.40	-1.81	3.04	1.70	0.60
Nb	8	3.54	2.53	7.79	1.73	0.61
Ni	8	6.67	-3.65	13.89	5.46	1.93
Pb	8	5.35	-4.67	11.20	4.55	1.61
Rb	8	18.25	5.00	56.40	17.97	6.35
Nd	2	15.97	12.29	19.65	5.20	3.68
Sc	6	7.01	4.12	11.10	2.45	1.00
Sr	8	90.56	49.12	214.93	55.64	19.67
Ta	6	5.18	5.00	6.07	0.44	0.18
Th	8	3.95	-4.30	5.91	3.35	1.18
U	8	1.28	-4.49	3.87	3.46	1.22
V	8	25.77	4.81	60.00	16.94	5.99
W	6	3.00	3.00	3.00	0.00	0.00
Y	8	11.39	3.00	29.03	10.88	3.85
Zn	8	44.25	11.30	89.68	30.58	10.81
Zr	8	24.70	9.04	69.22	20.99	7.42
La	2	0.79	-13.63	15.21	20.39	14.42



## **Addendum G**

Table 1. Correlation matrix determined through Statistica v.7, for the GCS.

Table 2. Correlation matrix determined through Statistica v.7, for the kyanite-graphite gneisses.

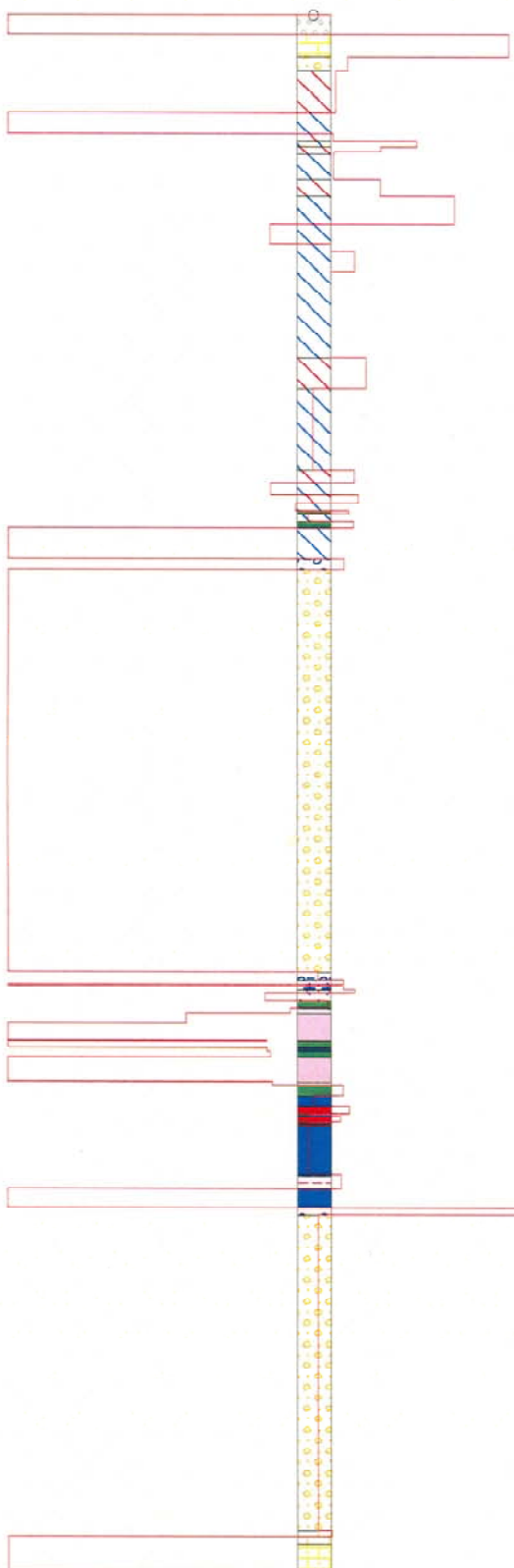
Table 1. Correlation matrix determined through Statistica v.7, for the GCS.

	SiO <sub>2</sub>	TiO <sub>2</sub>	Al <sub>2</sub> O <sub>3</sub>	Fe <sub>2</sub> O <sub>3</sub> T	FeO	Fe <sub>2</sub> O <sub>3</sub>	MnO	MgO	CaO	Na <sub>2</sub> O	K <sub>2</sub> O	LOI	Ba	Cr	Cu	Mo	Nb	Ni	Pb	Rb	Sr	Th	U	V	Y	Zn	Zr
SiO <sub>2</sub>	1.00	0.54	0.47	0.52	0.75	-0.18	-0.45	-0.69	-0.87	-0.12	0.81	-0.39	0.68	0.06	0.49	0.06	0.33	0.18	0.27	0.77	0.21	-0.07	0.19	0.04	-0.05	0.14	0.38
TiO <sub>2</sub>	0.54	1.00	0.96	0.83	0.49	0.34	0.02	0.13	-0.16	0.37	0.72	-0.93	0.73	0.10	-0.20	-0.40	0.53	-0.60	-0.10	0.68	0.62	0.34	-0.08	-0.45	-0.43	-0.37	0.80
Al <sub>2</sub> O <sub>3</sub>	0.47	0.96	1.00	0.82	0.45	0.37	0.08	0.23	-0.06	0.45	0.69	-0.97	0.60	0.12	-0.23	-0.52	0.64	-0.65	-0.13	0.66	0.63	0.37	-0.20	-0.51	-0.38	-0.38	0.87
Fe <sub>2</sub> O <sub>3</sub> T	0.52	0.83	0.82	1.00	0.41	0.58	0.13	0.11	-0.22	0.32	0.69	-0.85	0.65	0.20	-0.20	-0.54	0.30	-0.51	-0.12	0.65	0.55	0.24	-0.19	-0.44	-0.21	-0.41	0.69
FeO	0.75	0.49	0.45	0.41	1.00	-0.50	-0.45	-0.39	-0.59	-0.32	0.62	-0.37	0.32	-0.31	0.63	0.28	0.23	0.05	0.38	0.64	0.22	0.07	0.34	0.00	-0.33	-0.06	0.13
Fe <sub>2</sub> O <sub>3</sub>	-0.18	0.34	0.37	0.58	-0.50	1.00	0.52	0.45	0.32	0.59	0.10	-0.48	0.32	0.47	-0.75	-0.76	0.08	-0.53	-0.45	0.04	0.33	0.17	-0.49	-0.42	0.10	-0.34	0.54
MnO	-0.45	0.02	0.08	0.13	-0.45	0.52	1.00	0.51	0.62	0.24	-0.30	-0.23	-0.04	-0.18	-0.66	-0.54	0.06	-0.51	-0.48	-0.28	0.08	-0.28	-0.70	-0.67	-0.48	-0.52	0.11
MgO	-0.69	0.13	0.23	0.11	-0.39	0.45	0.51	1.00	0.87	0.34	-0.26	-0.32	-0.24	-0.14	-0.71	-0.48	0.12	-0.72	-0.48	-0.22	0.29	0.46	-0.40	-0.45	-0.22	-0.55	0.24
CaO	-0.87	-0.16	-0.06	-0.22	-0.59	0.32	0.62	0.87	1.00	0.19	-0.64	-0.06	-0.48	-0.20	-0.64	-0.30	0.02	-0.56	-0.44	-0.61	0.06	0.26	-0.33	-0.44	-0.22	-0.33	0.00
Na <sub>2</sub> O	-0.12	0.37	0.45	0.32	-0.32	0.59	0.24	0.34	0.19	1.00	0.32	-0.41	0.17	0.73	-0.47	-0.59	0.13	-0.19	-0.02	0.30	0.27	0.00	-0.34	0.04	0.24	-0.02	0.48
K <sub>2</sub> O	0.81	0.72	0.69	0.69	0.62	0.10	-0.30	-0.26	-0.64	0.32	1.00	-0.61	0.76	0.21	0.15	-0.29	0.37	-0.05	0.11	0.98	0.49	0.07	0.03	0.04	-0.02	-0.11	0.58
LOI	-0.39	-0.93	-0.97	-0.85	-0.37	-0.48	-0.23	-0.32	-0.06	-0.41	-0.61	1.00	-0.57	-0.04	0.34	0.59	-0.62	0.73	0.25	-0.59	-0.63	-0.38	0.30	0.63	0.40	0.42	-0.87
Ba	0.68	0.73	0.60	0.65	0.32	0.32	-0.04	-0.24	-0.48	0.17	0.76	-0.57	1.00	0.08	-0.09	-0.41	0.43	-0.30	-0.17	0.65	0.63	0.05	0.07	-0.28	-0.28	-0.38	0.63
Cr	0.06	0.10	0.12	0.20	-0.31	0.47	-0.18	-0.14	-0.20	0.73	0.21	-0.04	0.08	1.00	-0.13	-0.21	-0.18	0.26	0.25	0.15	-0.08	-0.09	-0.03	0.44	0.62	0.40	0.19
Cu	0.49	-0.20	-0.23	-0.20	0.63	-0.75	-0.66	-0.71	-0.64	-0.47	0.15	0.34	-0.09	-0.13	1.00	0.61	-0.19	0.66	0.74	0.16	-0.16	-0.14	0.68	0.49	0.21	0.39	-0.40
Mo	0.06	-0.40	-0.52	-0.54	0.28	-0.76	-0.54	-0.48	-0.30	-0.59	-0.29	0.59	-0.41	-0.21	0.61	1.00	-0.53	0.63	0.57	-0.22	-0.69	-0.05	0.49	0.57	0.11	0.56	-0.72
Nb	0.33	0.53	0.64	0.30	0.23	0.08	0.06	0.12	0.02	0.13	0.37	-0.62	0.43	-0.18	-0.19	-0.53	1.00	-0.57	-0.49	0.32	0.61	0.17	-0.21	-0.58	-0.39	-0.27	0.81
Ni	0.18	-0.60	-0.65	-0.51	0.05	-0.53	-0.51	-0.72	-0.56	-0.19	-0.05	0.73	-0.30	0.26	0.66	0.63	-0.57	1.00	0.62	-0.01	-0.60	-0.47	0.37	0.87	0.60	0.73	-0.67
Pb	0.27	-0.10	-0.13	-0.12	0.38	-0.45	-0.48	-0.48	-0.44	-0.02	0.11	0.25	-0.17	0.25	0.74	0.57	-0.49	0.62	1.00	0.15	-0.36	0.03	0.48	0.57	0.35	0.39	-0.42
Rb	0.77	0.68	0.66	0.65	0.64	0.04	-0.28	-0.22	-0.61	0.30	0.98	-0.59	0.65	0.15	0.16	-0.22	0.32	-0.01	0.15	1.00	0.38	0.08	-0.06	0.06	-0.02	-0.09	0.51
Sr	0.21	0.62	0.63	0.55	0.22	0.33	0.08	0.29	0.06	0.27	0.49	-0.63	0.63	-0.08	-0.16	-0.69	0.61	-0.60	-0.36	0.38	1.00	0.25	0.18	-0.44	-0.31	-0.61	0.69
Th	-0.07	0.34	0.37	0.24	0.07	0.17	-0.28	0.46	0.26	0.00	0.07	-0.38	0.05	-0.09	-0.14	-0.05	0.17	-0.47	0.03	0.08	0.25	1.00	0.16	-0.20	0.12	-0.20	0.36
U	0.19	-0.08	-0.20	-0.19	0.34	-0.49	-0.70	-0.40	-0.33	-0.34	0.03	0.30	0.07	-0.03	0.68	0.49	-0.21	0.37	0.48	-0.06	0.18	0.16	1.00	0.48	0.19	0.22	-0.28
V	0.04	-0.45	-0.51	-0.44	0.00	-0.42	-0.67	-0.45	-0.44	0.04	0.04	0.63	-0.28	0.44	0.49	0.57	-0.58	0.87	0.57	0.06	-0.44	-0.20	0.48	1.00	0.69	0.66	-0.56
Y	-0.05	-0.43	-0.38	-0.21	-0.33	0.10	-0.48	-0.22	-0.22	0.24	-0.02	0.40	-0.28	0.62	0.21	0.11	-0.39	0.60	0.35	-0.02	-0.31	0.12	0.19	0.69	1.00	0.62	-0.18
Zn	0.14	-0.37	-0.38	-0.41	-0.06	-0.34	-0.52	-0.55	-0.33	-0.02	-0.11	0.42	-0.38	0.40	0.39	0.56	-0.27	0.73	0.39	-0.09	-0.61	-0.20	0.22	0.66	0.62	1.00	-0.30
Zr	0.38	0.80	0.87	0.69	0.13	0.54	0.11	0.24	0.00	0.48	0.58	-0.87	0.63	0.19	-0.40	-0.72	0.81	-0.67	-0.42	0.51	0.69	0.36	-0.28	-0.56	-0.18	-0.30	1.00

Table 2. Correlation matrix determined through Statistica v.7, for the kyanite-graphite gneisses.

	SiO <sub>2</sub>	TiO <sub>2</sub>	Al <sub>2</sub> O <sub>3</sub>	Fe <sub>2</sub> O <sub>3</sub> T	MnO	MgO	CaO	Na <sub>2</sub> O	K <sub>2</sub> O	P <sub>2</sub> O <sub>5</sub>	Cr <sub>2</sub> O <sub>3</sub>	LOI	NiO	TOTAL	Ba	Cr	Cu	Mo	Ni	Pb	Rb	Sr	Th	U	V	Zn	Zr
<b>SiO<sub>2</sub></b>	1.00	-0.49	-0.36	-0.19	-0.13	-0.30	-0.34	0.20	-0.55	-0.42	-0.66	-0.76	-0.67	0.36	-0.51	-0.58	-0.49	-0.48	-0.69	-0.16	-0.75	-0.66	-0.37	-0.56	-0.76	-0.48	-0.24
<b>TiO<sub>2</sub></b>	-0.49	1.00	0.72	0.19	0.11	0.43	-0.24	-0.13	0.42	0.21	0.66	0.26	0.62	0.14	0.60	0.73	0.73	0.49	0.62	-0.07	0.44	0.23	0.41	0.15	0.60	0.38	0.75
<b>Al<sub>2</sub>O<sub>3</sub></b>	-0.36	0.72	1.00	0.12	0.36	0.29	-0.05	0.08	0.40	0.29	0.40	-0.02	0.45	0.33	0.36	0.43	0.36	0.38	0.45	0.04	0.34	0.41	0.56	0.18	0.49	0.39	0.75
<b>Fe<sub>2</sub>O<sub>3</sub>T</b>	-0.19	0.19	0.12	1.00	0.39	-0.01	0.04	0.11	0.01	0.16	0.34	-0.12	0.22	0.07	0.00	0.22	0.09	0.00	0.19	-0.22	0.26	-0.11	0.19	-0.16	0.07	0.34	0.07
<b>MnO</b>	-0.13	0.11	0.36	0.39	1.00	0.07	0.37	0.34	0.02	0.16	0.14	-0.23	0.18	0.17	-0.06	0.06	0.04	0.02	0.16	-0.08	0.05	0.16	0.23	-0.05	0.05	0.41	0.21
<b>MgO</b>	-0.30	0.43	0.29	-0.01	0.07	1.00	0.19	0.01	-0.08	-0.06	-0.09	0.02	-0.11	-0.02	-0.05	-0.02	0.12	0.29	-0.09	0.34	-0.03	0.12	-0.10	-0.09	0.21	0.12	0.37
<b>CaO</b>	-0.34	-0.24	-0.05	0.04	0.37	0.19	1.00	0.13	-0.22	0.20	-0.20	0.13	-0.15	-0.09	-0.34	-0.31	-0.24	0.00	-0.14	0.33	0.00	0.42	-0.11	0.36	0.03	0.06	-0.27
<b>Na<sub>2</sub>O</b>	0.20	-0.13	0.08	0.11	0.34	0.01	0.13	1.00	-0.41	0.04	-0.26	-0.47	-0.11	0.13	-0.30	-0.29	-0.10	-0.16	-0.16	-0.05	-0.35	-0.14	0.02	-0.16	-0.21	0.01	0.04
<b>K<sub>2</sub>O</b>	-0.55	0.42	0.40	0.01	0.02	-0.08	-0.22	-0.41	1.00	0.25	0.75	0.54	0.71	-0.03	0.67	0.74	0.39	0.46	0.71	0.17	0.83	0.41	0.45	0.39	0.64	0.50	0.30
<b>P<sub>2</sub>O<sub>5</sub></b>	-0.42	0.21	0.29	0.16	0.16	-0.06	0.20	0.04	0.25	1.00	0.31	0.20	0.36	-0.08	0.27	0.28	0.23	0.05	0.35	-0.13	0.34	0.35	0.19	0.09	0.27	0.23	0.13
<b>Cr<sub>2</sub>O<sub>3</sub></b>	-0.66	0.66	0.40	0.34	0.14	-0.09	-0.20	-0.26	0.75	0.31	1.00	0.57	0.87	-0.09	0.78	0.96	0.70	0.48	0.86	-0.18	0.76	0.36	0.52	0.38	0.70	0.56	0.36
<b>LOI</b>	-0.76	0.26	-0.02	-0.12	-0.23	0.02	0.13	-0.47	0.54	0.20	0.57	1.00	0.58	-0.16	0.57	0.54	0.48	0.39	0.62	0.11	0.65	0.48	0.23	0.57	0.66	0.29	-0.12
<b>NiO</b>	-0.67	0.62	0.45	0.22	0.18	-0.11	-0.15	-0.11	0.71	0.36	0.87	0.58	1.00	-0.09	0.75	0.85	0.76	0.44	0.99	-0.07	0.79	0.38	0.57	0.50	0.76	0.55	0.32
<b>TOTAL</b>	0.36	0.14	0.33	0.07	0.17	-0.02	-0.09	0.13	-0.03	-0.08	-0.09	-0.16	-0.09	1.00	-0.02	-0.04	0.00	-0.02	-0.07	0.00	-0.14	-0.13	0.17	-0.11	-0.08	0.06	0.05
<b>Ba</b>	-0.51	0.60	0.36	0.00	-0.06	-0.05	-0.34	-0.30	0.67	0.27	0.78	0.57	0.75	-0.02	1.00	0.85	0.75	0.41	0.76	-0.24	0.60	0.51	0.47	0.32	0.65	0.36	0.45
<b>Cr</b>	-0.58	0.73	0.43	0.22	0.06	-0.02	-0.31	-0.29	0.74	0.28	0.96	0.54	0.85	-0.04	0.85	1.00	0.77	0.50	0.83	-0.19	0.72	0.34	0.45	0.33	0.74	0.52	0.43
<b>Cu</b>	-0.49	0.73	0.36	0.09	0.04	0.12	-0.24	-0.10	0.39	0.23	0.70	0.48	0.76	0.00	0.75	0.77	1.00	0.51	0.78	-0.17	0.46	0.22	0.46	0.34	0.65	0.44	0.37
<b>Mo</b>	-0.48	0.49	0.38	0.00	0.02	0.29	0.00	-0.16	0.46	0.05	0.48	0.39	0.44	-0.02	0.41	0.50	0.51	1.00	0.44	0.38	0.49	0.36	0.18	0.42	0.79	0.76	0.24
<b>Ni</b>	-0.69	0.62	0.45	0.19	0.16	-0.09	-0.14	-0.16	0.71	0.35	0.86	0.62	0.99	-0.07	0.76	0.83	0.78	0.44	1.00	-0.04	0.79	0.41	0.60	0.54	0.76	0.55	0.31
<b>Pb</b>	-0.16	-0.07	0.04	-0.22	-0.08	0.34	0.33	-0.05	0.17	-0.13	-0.18	0.11	-0.07	0.00	-0.24	-0.19	-0.17	0.38	-0.04	1.00	0.29	0.07	-0.01	0.42	0.21	0.28	-0.12
<b>Rb</b>	-0.75	0.44	0.34	0.26	0.05	-0.03	0.00	-0.35	0.83	0.34	0.76	0.65	0.79	-0.14	0.60	0.72	0.46	0.49	0.79	0.29	1.00	0.46	0.42	0.57	0.76	0.60	0.17
<b>Sr</b>	-0.66	0.23	0.41	-0.11	0.16	0.12	0.42	-0.14	0.41	0.35	0.36	0.48	0.38	-0.13	0.51	0.34	0.22	0.36	0.41	0.07	0.46	1.00	0.25	0.47	0.54	0.26	0.28
<b>Th</b>	-0.37	0.41	0.56	0.19	0.23	-0.10	-0.11	0.02	0.45	0.19	0.52	0.23	0.57	0.17	0.47	0.45	0.46	0.18	0.60	-0.01	0.42	0.25	1.00	0.46	0.37	0.28	0.43
<b>U</b>	-0.56	0.15	0.18	-0.16	-0.05	-0.09	0.36	-0.16	0.39	0.09	0.38	0.57	0.50	-0.11	0.32	0.33	0.34	0.42	0.54	0.42	0.57	0.47	0.46	1.00	0.60	0.32	-0.04
<b>V</b>	-0.76	0.60	0.49	0.07	0.05	0.21	0.03	-0.21	0.64	0.27	0.70	0.66	0.76	-0.08	0.65	0.74	0.65	0.79	0.76	0.21	0.76	0.54	0.37	0.60	1.00	0.68	0.31
<b>Zn</b>	-0.48	0.38	0.39	0.34	0.41	0.12	0.06	0.01	0.50	0.23	0.56	0.29	0.55	0.06	0.36	0.52	0.44	0.76	0.55	0.28	0.60	0.26	0.28	0.32	0.68	1.00	0.14
<b>Zr</b>	-0.24	0.75	0.75	0.07	0.21	0.37	-0.27	0.04	0.30	0.13	0.36	-0.12	0.32	0.05	0.45	0.43	0.37	0.24	0.31	-0.12	0.17	0.28	0.43	-0.04	0.31	0.14	1.00

0  
10  
20  
30  
40  
50  
60  
70  
80  
90  
100  
110  
120  
130  
140  
150  
160  
170  
180  
190  
200  
210  
220  
230  
240  
250  
260  
270  
280  
290  
300  
310  
320  
330  
340  
350  
360  
370  
380  
390

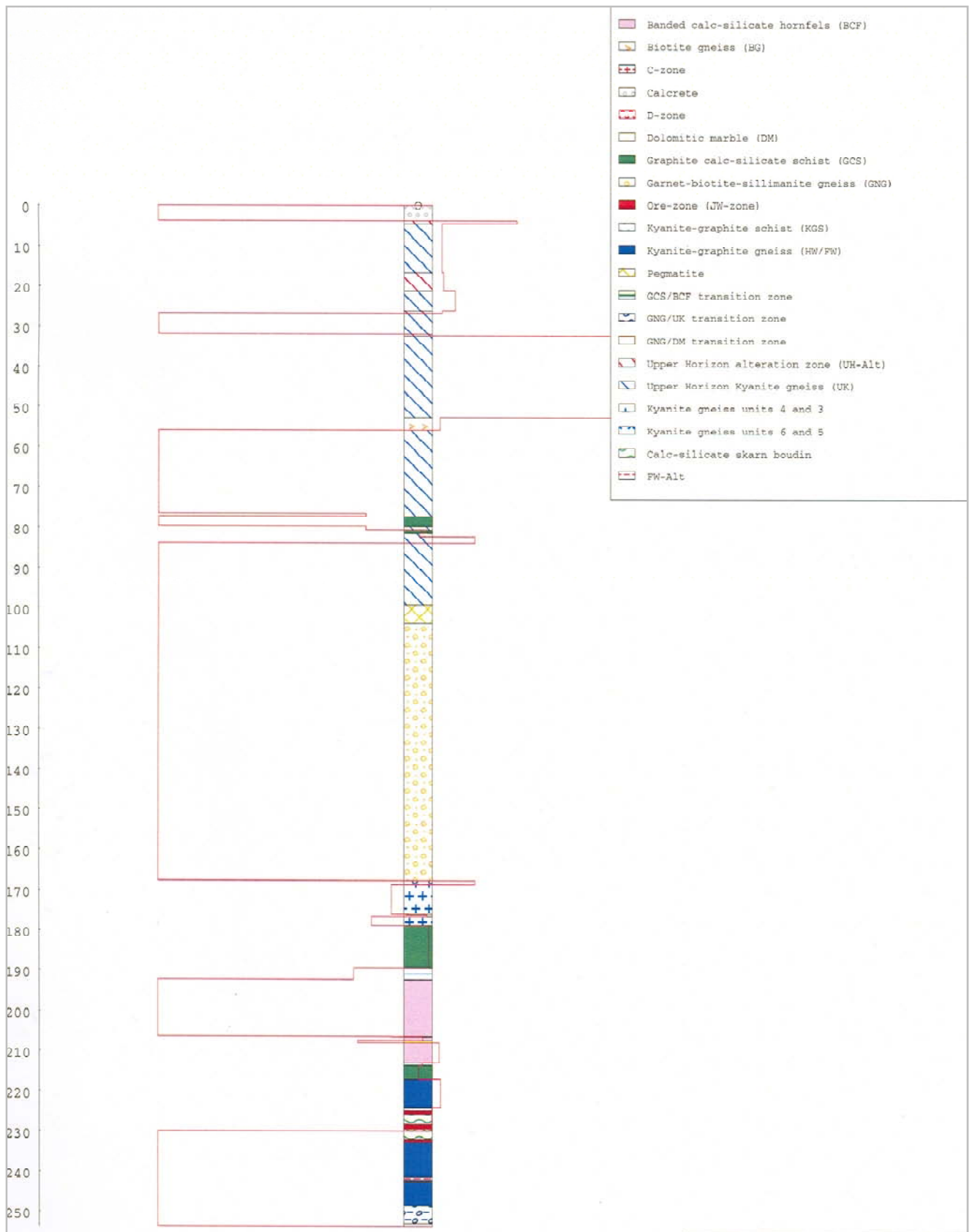


395

- LEGEND**
- Banded calc-silicate hornfels (BCF)
  - Biotite gneiss (BG)
  - C-zone
  - Calccrete
  - D-zone
  - Dolomitic marble (DM)
  - Graphite calc-silicate schist (GCS)
  - Garnet-biotite-sillimanite gneiss (GNG)
  - Ore-zone (JW-zone)
  - Kyanite-graphite schist (KGS)
  - Kyanite-graphite gneiss (HW/FW)
  - Pegmatite
  - GCS/BCF transition zone
  - GNG/UK transition zone
  - GNG/DM transition zone
  - Upper Horizon alteration zone (UH-Alt)
  - Upper Horizon Kyanite gneiss (UK)
  - Kyanite gneiss units 4 and 3
  - Kyanite gneiss units 6 and 5
  - Calc-silicate skarn boudin
  - FW-Alt

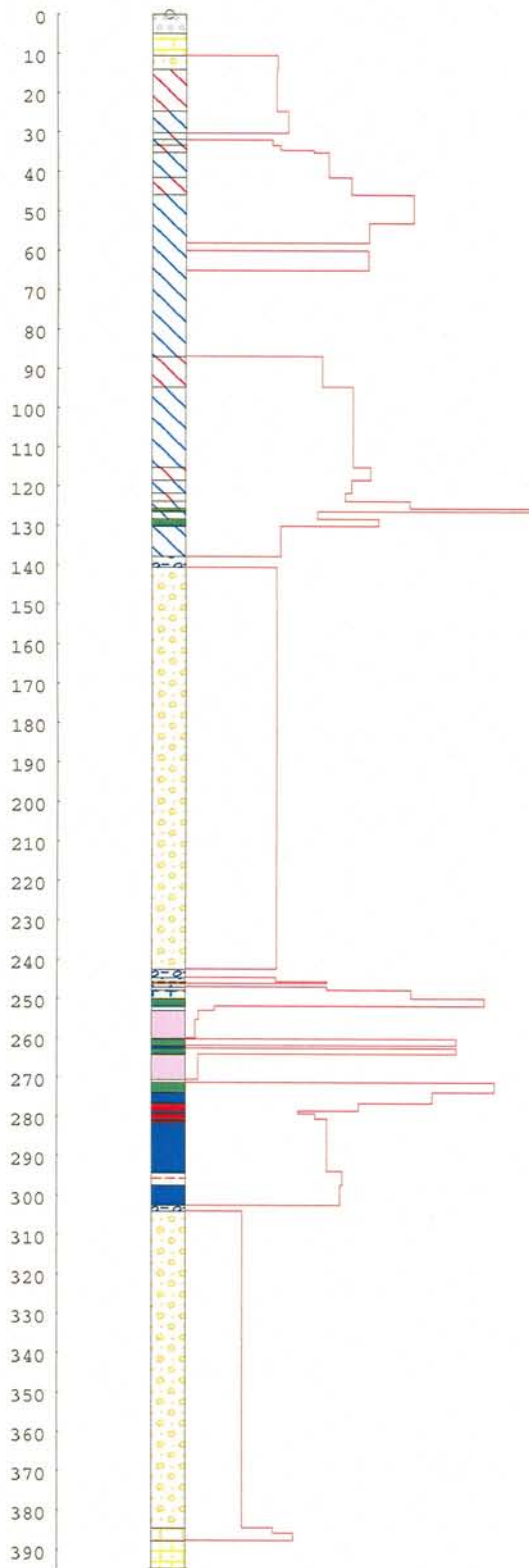
Addendum H

LHD 13  
(Root1/Root2)\*100



Addendum H

LMD 14  
(Root1/Root2)\*100

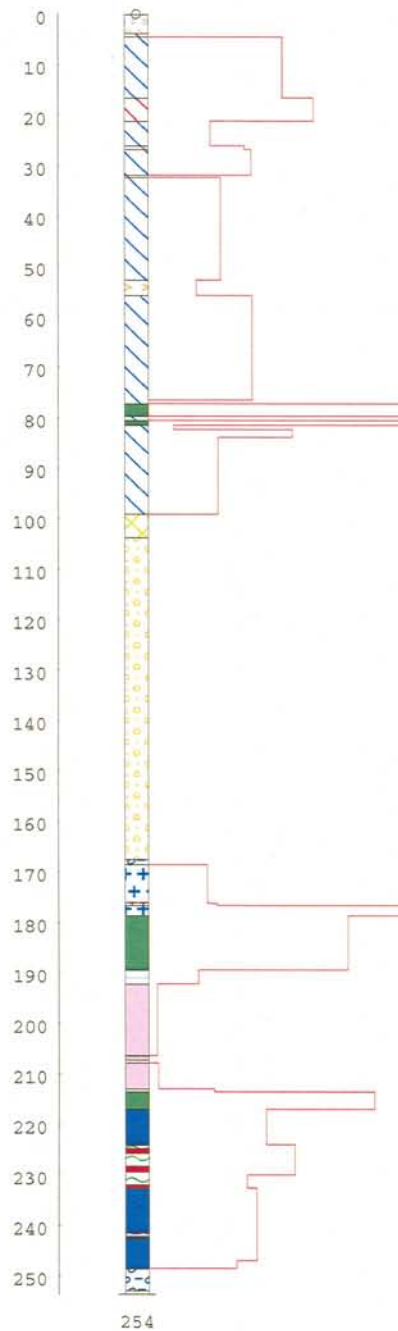


395

- LEGEND**
- Banded calc-silicate hornfels (BCF)
  - Biotite gneiss (BG)
  - C-zone
  - Calccrete
  - D-zone
  - Dolomitic marble (DM)
  - Graphite calc-silicate schist (GCS)
  - Garnet-biotite-sillimanite gneiss (GNG)
  - Ore-zone (JW-zone)
  - Kyanite-graphite schist (KGS)
  - Kyanite-graphite gneiss (HW/FW)
  - Pegmatite
  - GCS/BCF transition zone
  - GNG/UK transition zone
  - GNG/DM transition zone
  - Upper Horizon alteration zone (UH-Alt)
  - Upper Horizon Kyanite gneiss (UK)
  - Kyanite gneiss units 4 and 3
  - Kyanite gneiss units 6 and 5
  - Calc-silicate skarn boudin
  - FW-Alt

Addendum I

LHD 13 Vanadium plot



- LEGEND**
- Banded calc-silicate hornfels (BCF)
  - Biotite gneiss (BG)
  - C-zone
  - Calccrete
  - D-zone
  - Dolomitic marble (DM)
  - Graphite calc-silicate schist (GCS)
  - Garnet-biotite-sillimanite gneiss (GNG)
  - Ore-zone (JW-zone)
  - Kyanite-graphite schist (KGS)
  - Kyanite-graphite gneiss (HW/FW)
  - Pegmatite
  - GCS/BCF transition zone
  - GNG/UK transition zone
  - GNG/DM transition zone
  - Upper Horizon alteration zone (UH-Alt)
  - Upper Horizon Kyanite gneiss (UK)
  - Kyanite gneiss units 4 and 3
  - Kyanite gneiss units 6 and 5
  - Calc-silicate skarn boudin
  - FW-Alt

Addendum I

LHD 14 Vanadium plot

## **Addendum J**

Table 1. Fluid inclusion data from quartz and tanzanite samples.

Table 2. Fluid inclusion data of the tsavorite samples.



Table 1. Fluid inclusion data from quartz and tanzanite samples.

Sample: Quartz A						
Inclusion	Depth (mm)	Tfreez (°C)	Tm (°C)	Te (°C)	Secondary Tm (°C)	Th (°C)
1	0.008	-120	-85.9	95		32.8
2		-120	-86.1			33.6
3		-120	-85.8			33.8
4		-120	-86.2			35.1
5	0.016	>-130	-86.7	96		33.2
6		>-130	-86.1			35
7		>-130	-86			35.4
8	0.027	>-130	-86.4			34.1
9		>-130	-86.1			35.4
10		>-130	-85.8	95		36.3
11		>-130	-88.5			53.9
12	0.033	>-130	-87.4			32.9
13		>-130	-86.5	96		33.8
14		>-130				34.1
15		>-130	-88.1			35
16		>-130	-88.2			34.5
17		>-130				36.1
18		>-130				36.1
19		>-130	-88.3			35.2
20		>-130	-88.1	95		35.7
21		>-130	-88.1			36.3
22		>-130	-87.8			35.4
23		>-130	-88			37.2

Sample: Quartz B						
Inclusion		Tfreez (°C)	Tm (°C)	Te (°C)	Secondary Tm (°C)	Th (°C)
1		-43.2	-4	-4.6		
2		-48.5	3.7			
3		-47.7	-4.3			
4		-48.6	-4.1			147.1
5		-47.5	-3.5	-3.9		155.1
6		-47.4	-4.3			154.7
7			-3	-4		166.6
8			-3.8			161.1
9						157.5
10			-3.6			167.7
11		-48.8	-4.5			
12		-42.6	-2.2			173.3
13		-49.2	-4.4			
14		-49	-4.8			
15		-49.1	-4	-5		
16		-47.8	-3.9	-5		
17		-48.5	-3.9	-5		
18		-48.3	-3.7			
19		-48.7	-3.8			
20		-47.8	-4.3			
21		-48.9	-4.2			
22		-49.1	-3.3			210.7
23		-48.9	-3.8			165.6
24		-48.4	-3.2			176.4
25		-48.6	-4			171.4
26		-49.4	-4.3			162.3

Table 1. Continue 1.

Tanzanite (Tanz A)						
Inclusion	Tfreez (°C)	Tm (°C)	Te (°C)	Secondary Tm (°C)	Th (°C)	
1		-84.7			47	
2		-84.5			42	
3		-85.3			42.9	
4		-83.5	92		43.8	
5		-84.8			40.8	
6	-101.2	-84.3			38.2	
7	-102	-84.2			40.5	
8	-102.2	-84.2	92		38.5	
9	-98	-84.7			41.8	
10	-105	-84.6			39.5	
11		-83.8			40.1	
12	-100	-84.9			29	Small bubble
12	-99.6	-85.3			40.7	Large bubble
13		-83.9			40.3	
14	-99.8	-84.3		-31.2	39	
15		-84.1			42.5	
16					43.3	
17	-112.5	-84.4		-38.8	39.5	
18		-84.7			40.1	
19		-84.6		-3.8	39.1	
20		-85			40.8	
21		-85.2			40.1	
22	-105.4	-85			39	
26	-105.8	-84.6		-10.1	38.4	
31		-84.3			37.1	

Table 2. Fluid inclusion data of the tsavorite samples.

Sample: Tsavorite 1						
Number	Size (mm)	Ts (°C)	Te (°C)	Tm (°C)	Th (°C)	Comments
1	3.795			-12		
2	4.468					
3	3.499	-50	-46	-23		
4	3.174			-21		
5	3.266					
6	2.953		-42.3	1.1		
7	2.784			-16.4		
8	2.917			16		
9	2.162					
10i	2.755	-27		-17.3		Double inclusion
10ii				-11		
11	2.516		-42	5.5		
12	2.958			-16.3		
13	2.849			16		
14	2.787			23.7		
15i	3.142	-66		-40		Double inclusion
15ii		-89		20		
16i	5.348	0	-122	-88		Double inclusion
16ii		-63*		23		
17i	2.839	-9.9	-65	-20		Double inclusion
17ii		-45		-38		
18i	2.48	-59*	-82	-51	-5	Double inclusion
18ii				18		
19i	2.571	-53	-103	-60	-5	Double inclusion
19ii				16		
20i	4.385	-98*	-117	-90	-70	Double inclusion
20ii		19		24.9		
21i	2.824	-40*		-40		Double inclusion
21ii		15		22.9		
22i	2.338	-54	-122	-83.3	-17	Double inclusion
22ii		13.8		21.2		
23i	2.296	-70*	-107	-99	-47.5	Double inclusion
23ii		21		23		
24i	3.156	-61.9*	-115	-89	-18	Double inclusion
24ii		-1.7		4.1		
25	2.207	15.7		17.9		
26i	1.937	-86.9*	-118	-58	-25	Double inclusion
26ii		20		21.4		
27i	2.136	-54.3*	-101	-50	-33.2	Double inclusion
27ii		14		18.5		
28	2.757	19	-110	24.7		
29i	4.34	-57.5*	-106.9	-101.3	-22.3	Double inclusion
29ii				18		
30	2.343			6.9		Double inclusion
31	1.878			26.3		
32i	2.717	14.7	-100.5	20.1		Double inclusion
32ii		-5.8		3.4		
33i	3.502	11.3	-120.2	-88.5	-20.3	Double inclusion
33ii		17.4		23.3		
34	2		-103.1	31.9		
35i	2.095	-62.1*	-106	-38.1	-13	Double inclusion
35ii		20		27.3		
36i	1.958	-46*	-116.2	-88.3	-20.1	Double inclusion
36ii		17		29.7		
37	2.433	23	-104	24.4		
38	2.142		-113	21.2		
39i	2.852	11.6	-104.3	-87	-63	Double inclusion
39ii				27		
40i	1.732	-65.5*/-110	-110.1	-77.7	-22.1	Double inclusion
40ii				5.5		
41	4.341		-119	14.7		
42	4.202		-104	2.1		
43	2.585	-30*	-101.4	-87.3		
44	7.884	-30	-115	21.3		
45	6.103	-37				
46	3.829		-106	3		
47	5.159			23.2		
48	21.303		-110	2		
49i	5.688	-24*	-119	-73.8	7	Triple inclusion
49ii		-45*	-119	-87.7	-15	
49iii			-105	21		

Table 2. Continue 1.

Sample: Tsaveorite 63						
Number	Size (mm)	Ts (°C)	Te (°C)	Tm (°C)	Th (°C)	Comments
1	1.338	-47.4*/ -16.8	-114.9	-84.9	-26.4	
2	3.008	-2.6*/ -40.8	-99.6	-31.7	17.2	
3	1.411	-3.2*	-90.1	-12.5	13.1	
4	1.351	-8.8	-88.2	-5	10.2	
5	0.969		-67.6	-50.8		
6	1.429		-124.5	-55.6	-5.1	
7	1.199	-30.1*	-108.4	-72.4	-5.1	
8i	2.794	-74.4	-102.8	-90.6	-13	Double inclusion
8ii		-1.9		-27.4		
9	2.959					
10i	1.482	-69.1*	-101.4	-93.17		
10ii		-35.7		-19.8		
10iii		-21.8				
11i	2.582	-50.3	-97.2	-86.6		Double inclusion
11ii				-4.1		
12	1.65	-14.4*/2.1	-70.7	-18.6	2.3	
13i	2.868	-35.7*/-104.4	-111.5	-32.5	-12.1	Double inclusion
13ii		-11.7*/-111.5		2.2	12.4	
14	1.674	-31.7	-100.9	-60	-6.5	
15	3.515	-49.8		-1.9		
16	1.292		-98.5	-7.2		
17	1.305		-31.5	-26.1		
18	1.859	-12.4	-75.6	19		
19	2.455	-45.4	-98	-5.6		
20	2.566	-20*/-53	-99.8	-17.4		
21	1.546	-19*/-67.4		-25.1		
22	5.99	-22.9	-71.2	-3.1		
23			-112.8			
24						
25i	19.029		-97.1	16.2		
25ii		-66.7		-53.4	20.4	
25iii		5.8		6.3		
25iv				-87	15.4	
26i	3.142	-12.1*	-129.9	-91.5	8.4	
26ii						
26iii		-48.9		-1.1		
26iv		-105.5		-99.1	-38.8	
27	6.218	-51.5*	-97.9	-89.3	-36.3	no bubble at room temp.
28	2.723	-55.7	-76.6	-11.7		
29	1.661			11.6		
30	2.429	-6.9	-58.6	-4.1		
31	5.919					
32	7.307	-37.5*/-62.5	-118.7	-53.9	15.3	
		10.2*/-22.3		0.4	27.1	
33i				-32.2	12	Double inclusion
33ii				-23.4	23.6	Double inclusion
34i	2.236	-62*	-105.4	-79.1	-22.9	Double inclusion
34ii		-44.3*		21.2		
35	7.379	-97.2		-88.5		
36	5.884	10.1		11.9		
37	5.301	27	-104.7	0		
38	6.163	2.2	-88	19.6		
39	1.678	-23.4	-55	-11.9		
40	1.824	-67.2	-110.7	-20.4		

\* Bubble appearance temperature

Table 2. Continue 2.

Sample: Tsavorite 66						
Number	Size (mm)	Ts (°C)	Te (°C)	Tm (°C)	Th (°C)	Comments
1i	2.303	-48.8*	-77.7	-71.7	-39.6	
1ii		-34.9		22.3		Double inclusion
2i	38.887	-13.8	-98.7	10.3	21.2	
2ii		-22.4		26.7		Double inclusion
3i	5.073	17.5	-64.9	10.4		
3ii		13.2		15.2		
3iii		-54.9		-13.6		
4i	42.01	-45.1	-114	22.9		Double inclusion
4ii		-8.2	-88.4	13.2		
5	14.471		-126.7	-87.9		
6i	3.137	3.4	-113.8	-88.3		Double inclusion
6ii		-53.9				
7	2.277		-96.9	-89.9		
8	12.42	-4.5	-95.9	1.2		
9	5.157	-37.7		31		
10	23.424	4.5	-105.6	9.1		
11	21.608		-124.6	15.9		
12	31.576	10.3	-123.4	8.1		
13	20.358					
14	12.997		-105.1	-6.2		
15	9.452	-6.7	-138.3	-90.5	-45.5	
16i	4.552	19.2	-109.6	3.2		
16ii		-4.9				Double inclusion
17i	8.163	-5.3	-94.9	13.5	18.2	Double inclusion
17ii		-51.9		5.3		Double inclusion
18	7.889		-115.3	24		
19	6.841		-104.1	21		
20i	10.324	-6.7	-116.6	15.8		Double inclusion
20ii		-44.5		-16.6		Double inclusion
21	12.765		-120.1	22.9		
25	5.677	7		16.4		
26	5.252	-54	-95.4	14.9		
27	4.847	-38.3	-96.3	-8.9	0.7	
28	3.891	-29.1	-97.3	10.1		
29	4.757	-31.2*	-96.5	-14.3		
30i	4.528	-38.3	-111.9	5.1		Double inclusion
30ii			-39.3	-30.4	-23.6	
33	8.093	-7.3	-111.1	15.7		
34i	8.263	-29.8	-108.7	-8.5	17.7	Double inclusion
34ii		-43.2	-89.9	8.1		Double inclusion
38	4.618	-51.7	-93.2	11.2		
39	5.836	-49.8	-118			
40i	2.929	-27.3	-116.7	-27.1	-10.7	Double inclusion
40ii		-55	-88.9	12.4		
47ii	5.142	-54.9	-116.5	5.1	18.9	
47ii		-18.8		-25.5	17	
48	21.029	-76.5	-114.9	12.6		
49i	5.348	-45.5	-118.9	14		
49b	8.013	-15.8	-106	9.7		
50	8.386	-11.3	-94.6	5.6		
51i	6.029	-77.6	-107.8	-14.5	19.1	Double inclusion
51ii		-57.6	-83.4	20.2		
52	4.381	-45.3	-77.4	19.8		
55		-1	-121.3	14.4	20	
56i	9.942	-1.2	-116	5.7	21.9	Double inclusion
56ii		-2.6	-80.6	10	23.8	Double inclusion
57i	5.665	-69	-122.1	-22.4	2.1	Double inclusion
57ii				15.5	25.1	Double inclusion
58	4.314	4.2	-108.7	10.3	21.7	
67	4.683	13.2	-72.3	22.3		
72	3.322		-105.2	22.7		
74i	6.204	3.7*/-14.7	-101.5	-6.3	20	Double inclusion
74ii			-115.3	8.8		Double inclusion
76	5.307		-96.6	-20		
77	13.428	4.4*/-64	-116.3	13.1		
		-78.7*	138	-55.7	-42.4	
89i	6.767	-25.2*	109.8	1.2	8.8	Double inclusion
89ii				-6.9	-3.9	Double inclusion
94	3.795	4.3*	-97.7	10.1		
95	6.911		-134.5	-70		
116	4.873	-7.7	-95.8	3.7		
131	5.858	-10.3*/-54.5	-124.6	-52.6	8.1	
137	6.075					
138	9.607					
139	12.272	-94.5	-130.4	-90.3	-31.8	
140i	16.687	-26.5	-97.9	11.3		Double inclusion
140ii		-89.9*/-94.5	-90.5	-44.1	-27	Double inclusion
142	20.557	-26.3	-94.9	11.3	19.7	
		-46.8		20.3		
		-77.5				

Table 1. Electron microprobe analyses of blue zoisite (tanzanite).

Sample	SiO <sub>2</sub>	Al <sub>2</sub> O <sub>3</sub>	MgO	Na <sub>2</sub> O	FeO	MnO	Cr <sub>2</sub> O <sub>3</sub>	CaO	TiO <sub>2</sub>	K <sub>2</sub> O	V <sub>2</sub> O <sub>3</sub>	Total
40-Tz1-1	39.40	33.86	0.04	0.00	0.02	0.00	0.01	24.77	0.00	0.00	0.01	98.11
40-Tz1-10	38.60	33.55	0.00	0.03	0.04	0.06	0.00	24.62	0.02	0.00	0.01	96.94
40-Tz1-2	39.80	33.90	0.04	0.00	0.00	0.00	0.00	25.10	0.00	0.02	0.09	98.95
40-Tz1-3	39.49	33.61	0.00	0.00	0.00	0.04	0.05	24.79	0.00	0.01	0.00	97.98
40-Tz1-4	39.56	33.70	0.03	0.00	0.00	0.01	0.01	24.75	0.00	0.03	0.00	98.09
40-Tz1-5	39.27	33.79	0.04	0.00	0.04	0.05	0.04	24.67	0.00	0.00	0.01	97.91
40-Tz1-6	38.72	33.37	0.02	0.00	0.00	0.04	0.00	24.42	0.00	0.00	0.02	96.59
40-Tz1-7	38.74	33.23	0.01	0.00	0.02	0.00	0.00	24.50	0.00	0.00	0.00	96.50
40-Tz1-8	38.97	33.34	0.02	0.02	0.00	0.00	0.00	24.68	0.00	0.00	0.00	97.03
40-Tz1-9	38.75	33.43	0.06	0.00	0.02	0.03	0.00	24.71	0.00	0.00	0.07	97.07
40-Tz2-1	38.79	32.87	0.04	0.00	0.02	0.07	0.00	24.59	0.00	0.00	0.07	96.44
40-Tz2-2	39.01	33.08	0.06	0.04	0.01	0.05	0.00	24.62	0.00	0.02	0.04	96.94
40-Tz2-3	39.15	33.36	0.00	0.00	0.03	0.02	0.00	24.82	0.00	0.02	0.08	97.47
40-Tz2-4	38.62	33.06	0.01	0.00	0.00	0.00	0.08	24.56	0.03	0.00	0.00	96.35
40-Tz2-5	38.40	33.03	0.04	0.01	0.02	0.00	0.12	24.65	0.00	0.00	0.00	96.28
85-Tz1-1	39.28	32.47	0.01	0.00	0.00	0.03	0.02	24.74	0.00	0.00	0.09	96.62
85-Tz1-2	39.56	33.17	0.04	0.00	0.00	0.00	0.01	24.61	0.00	0.00	0.04	97.43
85-Tz1-3	39.46	33.01	0.01	0.00	0.00	0.04	0.02	24.86	0.00	0.01	0.06	97.48
85-Tz1-4	39.61	32.88	0.05	0.03	0.03	0.04	0.00	24.91	0.00	0.00	0.07	97.63
85-Tz2-1	39.06	32.55	0.01	0.00	0.00	0.00	0.02	24.54	0.00	0.00	0.06	96.23
85-Tz2-2	39.05	32.33	0.02	0.00	0.02	0.02	0.02	24.66	0.00	0.00	0.03	96.14
85-Tz2-3	39.10	32.47	0.00	0.03	0.03	0.00	0.06	24.80	0.00	0.00	0.06	96.54
85-Tz2-4	39.15	32.32	0.00	0.00	0.00	0.03	0.02	24.52	0.00	0.00	0.00	96.04
BO-12-1	38.97	32.53	0.04	0.05	0.00	0.27	0.03	25.03	0.00	0.00	0.05	96.96
BO-12-2	39.44	33.27	0.04	0.00	0.00	0.19	0.05	24.76	0.00	0.00	0.00	97.74
BO-12-3	39.23	32.79	0.00	0.00	0.00	0.32	0.05	25.26	0.00	0.00	0.01	97.65
BO-13-1	38.98	32.71	0.08	0.01	0.05	0.32	0.02	24.64	0.00	0.01	0.00	96.80
BO-13-2	39.29	32.74	0.03	0.05	0.02	0.28	0.02	24.73	0.00	0.02	0.00	97.18
BO-13-3	38.92	32.83	0.03	0.00	0.02	0.44	0.00	24.39	0.03	0.02	0.00	96.66
BO-19-1	38.76	32.99	0.03	0.01	0.00	0.25	0.03	24.84	0.00	0.01	0.00	96.92
BO-19-2	39.08	32.53	0.02	0.01	0.00	0.31	0.04	24.73	0.00	0.00	0.00	96.72
BO-19-3	38.82	33.33	0.00	0.02	0.01	0.26	0.03	24.93	0.00	0.00	0.00	97.39
BO-26-1	39.19	33.07	0.07	0.00	0.00	0.34	0.04	24.91	0.01	0.02	0.18	97.81
BO-26-2	39.38	33.22	0.03	0.03	0.00	0.19	0.05	24.85	0.00	0.03	0.10	97.87
BO-26-3	39.43	32.74	0.08	0.00	0.00	0.32	0.05	24.90	0.00	0.00	0.05	97.58
BO-26-4	39.16	33.23	0.04	0.00	0.03	0.21	0.04	24.75	0.06	0.00	0.06	97.56
BO-26-5	39.32	33.16	0.00	0.00	0.00	0.28	0.07	24.80	0.00	0.00	0.10	97.73
BO-27-1	39.21	33.68	0.01	0.01	0.00	0.33	0.04	25.16	0.00	0.01	0.00	98.44
BO-27-2	39.39	33.29	0.03	0.01	0.07	0.40	0.03	25.00	0.00	0.00	0.08	98.31
BO-27-3	39.46	33.56	0.01	0.01	0.04	0.15	0.00	24.98	0.00	0.00	0.04	98.25
BO-27-4	38.38	33.01	0.05	0.02	0.00	0.28	0.04	24.81	0.00	0.00	0.08	96.67
BO-27-5	39.35	33.12	0.04	0.00	0.00	0.19	0.04	24.99	0.02	0.02	0.12	97.89
BO-32-1	39.48	32.89	0.04	0.00	0.01	0.32	0.01	24.59	0.00	0.00	0.00	97.34
BO-32-2	39.31	32.83	0.04	0.02	0.00	0.10	0.05	24.61	0.00	0.00	0.00	96.95
BO-32-3	39.45	33.09	0.06	0.00	0.00	0.24	0.05	24.86	0.00	0.00	0.00	97.75
BO-59-1	38.99	33.00	0.00	0.02	0.00	0.21	0.03	24.61	0.00	0.00	0.00	96.85
BO-59-10	39.47	32.96	0.00	0.03	0.01	0.31	0.05	24.71	0.00	0.03	0.01	97.56
BO-59-2	38.62	32.21	0.00	0.00	0.00	0.12	0.04	24.45	0.00	0.00	0.11	95.54
BO-59-3	39.24	33.30	0.00	0.00	0.00	0.28	0.05	24.71	0.00	0.00	0.00	97.58
BO-59-4	39.37	32.87	0.00	0.00	0.00	0.22	0.02	24.46	0.04	0.00	0.02	97.00
BO-59-5	38.50	31.63	0.01	0.00	0.00	0.20	0.05	24.65	0.01	0.00	0.00	95.04
BO-59-6	38.72	32.98	0.07	0.01	0.03	0.43	0.06	24.68	0.00	0.00	0.00	96.99
BO-59-7	38.79	32.08	0.03	0.00	0.01	0.22	0.04	24.72	0.00	0.00	0.00	95.89
BO-59-8	38.93	32.14	0.04	0.01	0.02	0.17	0.00	24.90	0.00	0.03	0.00	96.25
BO-59-9	39.02	32.96	0.00	0.00	0.00	0.27	0.06	24.73	0.00	0.00	0.18	97.22
Min	38.38	31.63	0.00	0.00	0.00	0.00	0.00	24.39	0.00	0.00	0.00	95.04
Max	39.80	33.90	0.08	0.05	0.07	0.44	0.12	25.26	0.06	0.03	0.18	98.95
Mean	39.11	33.00	0.03	0.01	0.01	0.16	0.03	24.75	0.00	0.01	0.04	97.14

Table 1. Continued.

Sample	Si	Al IV	Sum_T	Al VI	Ti	Cr	Fe <sup>2+</sup>	Mn	Mg	Ca	Na	K	V	Sum_B
40-Tz1-1	2.98	0.02	3.00	2.99	0.00	0.00	0.00	0.00	0.01	2.01	0.00	0.00	0.00	2.01
40-Tz1-10	2.96	0.04	3.00	2.99	0.00	0.00	0.00	0.00	0.00	2.02	0.00	0.00	0.00	2.03
40-Tz1-2	2.99	0.01	3.00	2.98	0.00	0.00	0.00	0.00	0.01	2.02	0.00	0.00	0.01	2.02
40-Tz1-3	2.99	0.01	3.00	2.99	0.00	0.00	0.00	0.00	0.00	2.01	0.00	0.00	0.00	2.01
40-Tz1-4	2.99	0.01	3.00	2.99	0.00	0.00	0.00	0.00	0.00	2.01	0.00	0.00	0.00	2.01
40-Tz1-5	2.98	0.02	3.00	2.99	0.00	0.00	0.00	0.00	0.01	2.00	0.00	0.00	0.00	2.01
40-Tz1-6	2.98	0.03	3.00	2.99	0.00	0.00	0.00	0.00	0.00	2.01	0.00	0.00	0.00	2.02
40-Tz1-7	2.98	0.02	3.00	2.99	0.00	0.00	0.00	0.00	0.00	2.02	0.00	0.00	0.00	2.02
40-Tz1-8	2.98	0.02	3.00	2.99	0.00	0.00	0.00	0.00	0.00	2.02	0.00	0.00	0.00	2.03
40-Tz1-9	2.97	0.03	3.00	2.98	0.00	0.00	0.00	0.00	0.01	2.03	0.00	0.00	0.00	2.04
40-Tz2-1	2.99	0.01	3.00	2.97	0.00	0.00	0.00	0.00	0.00	2.03	0.00	0.00	0.00	2.04
40-Tz2-2	2.99	0.01	3.00	2.97	0.00	0.00	0.00	0.00	0.01	2.02	0.01	0.00	0.00	2.04
40-Tz2-3	2.98	0.02	3.00	2.98	0.00	0.00	0.00	0.00	0.00	2.03	0.00	0.00	0.00	2.03
40-Tz2-4	2.98	0.02	3.00	2.98	0.00	0.01	0.00	0.00	0.00	2.03	0.00	0.00	0.00	2.03
40-Tz2-5	2.97	0.03	3.00	2.97	0.00	0.01	0.00	0.00	0.01	2.04	0.00	0.00	0.00	2.05
85-Tz1-1	3.02	0.00	3.02	2.94	0.00	0.00	0.00	0.00	0.00	2.04	0.00	0.00	0.01	2.04
85-Tz1-2	3.01	0.00	3.01	2.97	0.00	0.00	0.00	0.00	0.01	2.01	0.00	0.00	0.00	2.01
85-Tz1-3	3.01	0.00	3.01	2.96	0.00	0.00	0.00	0.00	0.00	2.03	0.00	0.00	0.00	2.03
85-Tz1-4	3.01	0.00	3.01	2.95	0.00	0.00	0.00	0.00	0.01	2.03	0.01	0.00	0.00	2.04
85-Tz2-1	3.01	0.00	3.01	2.96	0.00	0.00	0.00	0.00	0.00	2.03	0.00	0.00	0.00	2.03
85-Tz2-2	3.02	0.00	3.02	2.94	0.00	0.00	0.00	0.00	0.00	2.04	0.00	0.00	0.00	2.04
85-Tz2-3	3.01	0.00	3.01	2.94	0.00	0.00	0.00	0.00	0.00	2.05	0.01	0.00	0.00	2.05
85-Tz2-4	3.03	0.00	3.03	2.94	0.00	0.00	0.00	0.00	0.00	2.03	0.00	0.00	0.00	2.03
BO-12-1	2.99	0.01	3.00	2.94	0.00	0.00	0.00	0.02	0.00	2.06	0.01	0.00	0.00	2.09
BO-12-2	3.00	0.00	3.00	2.97	0.00	0.00	0.00	0.01	0.00	2.02	0.00	0.00	0.00	2.03
BO-12-3	2.99	0.01	3.00	2.94	0.00	0.00	0.00	0.02	0.00	2.06	0.00	0.00	0.00	2.09
BO-13-1	3.00	0.01	3.00	2.96	0.00	0.00	0.00	0.02	0.01	2.03	0.00	0.00	0.00	2.06
BO-13-2	3.01	0.00	3.01	2.95	0.00	0.00	0.00	0.02	0.00	2.03	0.01	0.00	0.00	2.06
BO-13-3	2.99	0.01	3.00	2.97	0.00	0.00	0.00	0.03	0.00	2.01	0.00	0.00	0.00	2.04
BO-19-1	2.98	0.02	3.00	2.96	0.00	0.00	0.00	0.02	0.00	2.04	0.00	0.00	0.00	2.07
BO-19-2	3.01	0.00	3.01	2.95	0.00	0.00	0.00	0.02	0.00	2.04	0.00	0.00	0.00	2.06
BO-19-3	2.97	0.03	3.00	2.97	0.00	0.00	0.00	0.02	0.00	2.04	0.00	0.00	0.00	2.06
BO-26-1	2.98	0.02	3.00	2.95	0.00	0.00	0.00	0.02	0.01	2.03	0.00	0.00	0.01	2.06
BO-26-2	2.99	0.01	3.00	2.96	0.00	0.00	0.00	0.01	0.00	2.02	0.00	0.00	0.01	2.04
BO-26-3	3.01	0.00	3.01	2.94	0.00	0.00	0.00	0.02	0.01	2.03	0.00	0.00	0.00	2.06
BO-26-4	2.98	0.02	3.00	2.97	0.00	0.00	0.00	0.01	0.00	2.02	0.00	0.00	0.00	2.04
BO-26-5	2.99	0.01	3.00	2.96	0.00	0.00	0.00	0.02	0.00	2.02	0.00	0.00	0.01	2.04
BO-27-1	2.97	0.04	3.00	2.97	0.00	0.00	0.00	0.02	0.00	2.04	0.00	0.00	0.00	2.06
BO-27-2	2.98	0.02	3.00	2.95	0.00	0.00	0.00	0.03	0.00	2.03	0.00	0.00	0.00	2.06
BO-27-3	2.99	0.02	3.00	2.98	0.00	0.00	0.00	0.01	0.00	2.03	0.00	0.00	0.00	2.04
BO-27-4	2.96	0.04	3.00	2.96	0.00	0.00	0.00	0.02	0.01	2.05	0.00	0.00	0.01	2.07
BO-27-5	2.99	0.01	3.00	2.95	0.00	0.00	0.00	0.01	0.01	2.04	0.00	0.00	0.01	2.05
BO-32-1	3.01	0.00	3.01	2.96	0.00	0.00	0.00	0.02	0.00	2.01	0.00	0.00	0.00	2.04
BO-32-2	3.01	0.00	3.01	2.96	0.00	0.00	0.00	0.01	0.01	2.02	0.00	0.00	0.00	2.03
BO-32-3	3.00	0.00	3.00	2.96	0.00	0.00	0.00	0.02	0.01	2.03	0.00	0.00	0.00	2.05
BO-59-1	2.99	0.01	3.00	2.97	0.00	0.00	0.00	0.01	0.00	2.02	0.00	0.00	0.00	2.04
BO-59-10	3.01	0.00	3.01	2.96	0.00	0.00	0.00	0.02	0.00	2.02	0.00	0.00	0.00	2.04
BO-59-2	3.01	0.00	3.01	2.95	0.00	0.00	0.00	0.01	0.00	2.04	0.00	0.00	0.01	2.05
BO-59-3	2.99	0.01	3.00	2.98	0.00	0.00	0.00	0.02	0.00	2.02	0.00	0.00	0.00	2.03
BO-59-4	3.01	0.00	3.01	2.96	0.00	0.00	0.00	0.01	0.00	2.01	0.00	0.00	0.00	2.02
BO-59-5	3.02	0.00	3.02	2.92	0.00	0.00	0.00	0.01	0.00	2.07	0.00	0.00	0.00	2.08
BO-59-6	2.97	0.03	3.00	2.96	0.00	0.00	0.00	0.03	0.01	2.03	0.00	0.00	0.00	2.07
BO-59-7	3.01	0.00	3.01	2.93	0.00	0.00	0.00	0.01	0.00	2.06	0.00	0.00	0.00	2.07
BO-59-8	3.01	0.00	3.01	2.93	0.00	0.00	0.00	0.01	0.01	2.06	0.00	0.00	0.00	2.08
BO-59-9	2.99	0.01	3.00	2.96	0.00	0.00	0.00	0.02	0.00	2.03	0.00	0.00	0.01	2.05
Min	2.96	0.00	3.00	2.92	0.00	0.00	0.00	0.00	0.00	2.00	0.00	0.00	0.00	2.01
Max	3.03	0.04	3.03	2.99	0.00	0.01	0.00	0.03	0.01	2.07	0.01	0.00	0.01	2.09
Mean	2.99	0.01	3.00	2.96	0.00	0.00	0.00	0.01	0.00	2.03	0.00	0.00	0.00	2.04

Table 2. Electron microprobe analyses of green zoisite.

Sample	SiO <sub>2</sub>	Al <sub>2</sub> O <sub>3</sub>	MgO	Na <sub>2</sub> O	FeO	MnO	Cr <sub>2</sub> O <sub>3</sub>	CaO	TiO <sub>2</sub>	K <sub>2</sub> O	V <sub>2</sub> O <sub>3</sub>	Total
BO-58-1	39.13	32.64	0.00	0.00	0.00	0.19	0.07	24.75	0.06	0.00	0.00	96.84
BO-58-2	39.69	33.16	0.01	0.05	0.02	0.11	0.08	24.89	0.11	0.01	0.00	98.13
BO-58-3	39.36	32.93	0.00	0.02	0.02	0.07	0.06	24.83	0.04	0.00	0.00	97.33
BO-68-1	39.20	32.92	0.00	0.04	0.00	0.02	0.00	24.90	0.09	0.00	0.00	97.17
BO-68-2	39.23	33.14	0.00	0.02	0.01	0.11	0.02	24.85	0.00	0.01	0.03	97.43
BO-68-3	39.55	33.38	0.00	0.00	0.00	0.03	0.05	24.78	0.06	0.01	0.04	97.90
BO-71-1	39.78	33.82	0.00	0.00	0.01	0.28	0.01	25.46	0.11	0.00	0.01	99.48
BO-71-10	39.26	32.84	0.00	0.03	0.00	0.08	0.00	25.16	0.06	0.01	0.03	97.48
BO-71-2	39.58	33.45	0.00	0.02	0.00	0.28	0.03	25.16	0.08	0.00	0.02	98.62
BO-71-3	40.06	33.34	0.00	0.03	0.00	0.28	0.00	25.26	0.06	0.01	0.00	99.05
BO-71-4	40.02	33.53	0.00	0.02	0.00	0.22	0.00	25.08	0.07	0.00	0.00	98.93
BO-71-5	40.20	33.62	0.00	0.03	0.00	0.14	0.01	25.32	0.13	0.00	0.00	99.44
BO-71-6	39.96	33.51	0.01	0.03	0.00	0.11	0.00	25.32	0.08	0.00	0.00	99.01
BO-71-7	39.60	33.10	0.00	0.00	0.00	0.08	0.00	25.16	0.11	0.03	0.00	98.08
BO-71-8	39.86	33.60	0.00	0.00	0.00	0.09	0.00	25.07	0.05	0.00	0.00	98.67
BO-71-9	40.03	33.30	0.00	0.03	0.00	0.04	0.07	25.03	0.02	0.00	0.02	98.54
BO-90-1	38.71	32.48	0.00	0.00	0.00	0.07	0.00	24.89	0.03	0.00	0.00	96.18
BO-90-2	39.27	33.60	0.00	0.02	0.00	0.02	0.00	25.00	0.06	0.00	0.00	97.96
BO-90-3	39.15	33.22	0.00	0.03	0.00	0.06	0.00	25.18	0.03	0.02	0.00	97.68
BO-90-4	39.15	33.22	0.00	0.03	0.00	0.06	0.00	25.18	0.03	0.02	0.00	97.68
BO-90-5	39.36	32.78	0.01	0.00	0.00	0.08	0.04	25.16	0.06	0.00	0.05	97.52
Min	38.71	32.48	0.00	0.00	0.00	0.02	0.00	24.75	0.00	0.00	0.00	96.18
Max	40.20	33.82	0.01	0.05	0.02	0.28	0.08	25.46	0.13	0.03	0.05	99.48
Mean	39.53	33.22	0.00	0.02	0.00	0.11	0.02	25.07	0.06	0.01	0.01	98.05

Sample	Si	Al IV	Sum_T	Al VI	Ti	Cr	Fe <sup>2+</sup>	Mn	Mg	Ca	Na	K	V	Sum_B
BO-58-1	3.00	0.00	3.00	2.95	0.00	0.00	0.00	0.01	0.00	2.04	0.00	0.00	0.00	2.05
BO-58-2	3.01	0.00	3.01	2.96	0.01	0.01	0.00	0.01	0.00	2.02	0.01	0.00	0.00	2.03
BO-58-3	3.00	0.00	3.00	2.96	0.00	0.00	0.00	0.00	0.00	2.03	0.00	0.00	0.00	2.04
BO-68-1	3.00	0.00	3.00	2.96	0.01	0.00	0.00	0.00	0.00	2.04	0.01	0.00	0.00	2.05
BO-68-2	2.99	0.01	3.00	2.97	0.00	0.00	0.00	0.01	0.00	2.03	0.00	0.00	0.00	2.04
BO-68-3	3.00	0.00	3.00	2.98	0.00	0.00	0.00	0.00	0.00	2.01	0.00	0.00	0.00	2.02
BO-71-1	2.98	0.02	3.00	2.96	0.01	0.00	0.00	0.02	0.00	2.04	0.00	0.00	0.00	2.06
BO-71-10	3.00	0.00	3.00	2.95	0.00	0.00	0.00	0.01	0.00	2.06	0.00	0.00	0.00	2.07
BO-71-2	2.99	0.01	3.00	2.96	0.01	0.00	0.00	0.02	0.00	2.03	0.00	0.00	0.00	2.05
BO-71-3	3.01	0.00	3.01	2.95	0.00	0.00	0.00	0.02	0.00	2.03	0.00	0.00	0.00	2.06
BO-71-4	3.01	0.00	3.01	2.96	0.00	0.00	0.00	0.01	0.00	2.02	0.00	0.00	0.00	2.03
BO-71-5	3.00	0.00	3.00	2.96	0.01	0.00	0.00	0.01	0.00	2.03	0.00	0.00	0.00	2.04
BO-71-6	3.00	0.00	3.00	2.96	0.00	0.00	0.00	0.01	0.00	2.04	0.00	0.00	0.00	2.05
BO-71-7	3.00	0.00	3.00	2.96	0.01	0.00	0.00	0.01	0.00	2.04	0.00	0.00	0.00	2.05
BO-71-8	3.00	0.00	3.00	2.98	0.00	0.00	0.00	0.01	0.00	2.02	0.00	0.00	0.00	2.03
BO-71-9	3.02	0.00	3.02	2.95	0.00	0.00	0.00	0.00	0.00	2.02	0.01	0.00	0.00	2.03
BO-90-1	2.99	0.01	3.00	2.95	0.00	0.00	0.00	0.01	0.00	2.06	0.00	0.00	0.00	2.07
BO-90-2	2.98	0.02	3.00	2.98	0.00	0.00	0.00	0.00	0.00	2.03	0.00	0.00	0.00	2.03
BO-90-3	2.98	0.02	3.00	2.96	0.00	0.00	0.00	0.00	0.00	2.05	0.00	0.00	0.00	2.06
BO-90-4	2.98	0.02	3.00	2.96	0.00	0.00	0.00	0.00	0.00	2.05	0.00	0.00	0.00	2.06
BO-90-5	3.00	0.00	3.00	2.94	0.00	0.00	0.00	0.01	0.00	2.06	0.00	0.00	0.00	2.06
Min	2.98	0.00	3.00	2.94	0.00	0.00	0.00	0.00	0.00	2.01	0.00	0.00	0.00	2.02
Max	3.02	0.02	3.02	2.98	0.01	0.01	0.00	0.02	0.00	2.06	0.01	0.00	0.00	2.07
Average	3.00	0.01	3.00	2.96	0.00	0.00	0.00	0.01	0.00	2.04	0.00	0.00	0.00	2.05



Table 3. Electron microprobe analyses of orange zoisite.

Sample	SiO <sub>2</sub>	Al <sub>2</sub> O <sub>3</sub>	MgO	Na <sub>2</sub> O	FeO	MnO	Cr <sub>2</sub> O <sub>3</sub>	CaO	TiO <sub>2</sub>	K <sub>2</sub> O	V <sub>2</sub> O <sub>3</sub>	Total
BO - 82-10	38.14	32.08	0.06	0.00	0.04	0.33	0.00	24.45	0.02	0.02	0.00	95.12
BO - 82-7	39.03	32.98	0.08	0.03	0.00	0.08	0.05	24.87	0.00	0.00	0.00	97.11
BO - 82-8	39.06	33.07	0.05	0.01	0.01	0.22	0.00	24.53	0.00	0.01	0.00	96.97
BO - 82-9	38.65	32.24	0.10	0.03	0.08	0.18	0.02	24.78	0.00	0.01	0.00	96.07
BO-81-1	38.61	32.11	0.18	0.05	0.03	0.40	0.04	24.35	0.00	0.00	0.00	95.77
BO-81-2	39.36	33.11	0.14	0.05	0.03	0.41	0.03	24.31	0.00	0.02	0.00	97.45
BO-81-3	38.89	33.23	0.14	0.05	0.00	0.43	0.00	24.60	0.00	0.00	0.00	97.34
BO-81-4	39.51	33.04	0.16	0.00	0.00	0.45	0.02	24.70	0.00	0.01	0.00	97.88
BO-81-5	39.05	32.54	0.16	0.00	0.00	0.43	0.00	24.32	0.00	0.00	0.00	96.50
BO-81-6	38.78	32.65	0.19	0.00	0.00	0.43	0.00	24.47	0.00	0.00	0.00	96.52
BO-81-7	39.02	32.65	0.13	0.02	0.00	0.29	0.02	24.39	0.02	0.00	0.00	96.53
BO-81-8	39.11	32.74	0.19	0.00	0.03	0.33	0.02	24.40	0.00	0.01	0.00	96.83
BO-82-1	38.82	32.91	0.08	0.00	0.02	0.28	0.02	24.60	0.00	0.00	0.00	96.72
BO-82-2	38.86	32.83	0.09	0.00	0.00	0.33	0.00	24.56	0.02	0.00	0.00	96.69
BO-82-3	38.73	32.37	0.10	0.00	0.00	0.33	0.01	24.41	0.00	0.00	0.00	95.95
BO-82-4	38.51	32.39	0.11	0.00	0.03	0.43	0.03	24.46	0.00	0.02	0.00	95.97
BO-85-1	38.96	32.39	0.06	0.00	0.01	0.39	0.08	24.55	0.00	0.00	0.00	96.43
BO-85-2	39.25	32.97	0.01	0.00	0.02	0.51	0.05	24.75	0.00	0.00	0.00	97.55
BO-85-3	39.11	32.99	0.03	0.00	0.00	0.30	0.02	24.68	0.00	0.01	0.00	97.13
BO-85-4	39.10	32.57	0.06	0.00	0.00	0.31	0.03	24.70	0.00	0.01	0.07	96.78
BO-85-5	39.11	32.73	0.01	0.03	0.00	0.47	0.05	24.51	0.00	0.00	0.00	96.90
BO-85-6	39.26	32.83	0.00	0.00	0.00	0.47	0.03	24.69	0.00	0.01	0.00	97.29
BO-86-1	39.03	32.43	0.00	0.00	0.02	0.43	0.11	24.65	0.00	0.00	0.07	96.66
BO-86-2	39.31	32.61	0.02	0.00	0.02	0.28	0.15	24.61	0.00	0.00	0.00	96.99
BO-86-3	39.28	32.74	0.03	0.02	0.02	0.20	0.00	24.46	0.00	0.00	0.05	96.74
BO-86-4	39.15	32.61	0.04	0.00	0.00	0.25	0.00	24.64	0.00	0.00	0.00	96.68
BO-86-5	39.28	33.17	0.00	0.00	0.00	0.34	0.00	24.63	0.01	0.00	0.06	97.43
Min	38.14	32.08	0.00	0.00	0.00	0.08	0.00	24.31	0.00	0.00	0.00	95.12
Max	39.51	33.23	0.19	0.05	0.08	0.51	0.15	24.87	0.02	0.02	0.07	97.88
Average	39.00	32.70	0.08	0.01	0.01	0.34	0.03	24.56	0.00	0.00	0.01	96.74

Sample	Si	Al IV	Sum_T	Al VI	Ti	Cr	Fe <sup>2+</sup>	Mn	Mg	Ca	Na	K	V	Sum_B
BO - 82-10	2.99	0.01	3.00	2.95	0.00	0.00	0.00	0.02	0.01	2.05	0.00	0.00	0.00	2.08
BO - 82-7	2.99	0.01	3.00	2.96	0.00	0.00	0.00	0.01	0.01	2.04	0.00	0.00	0.00	2.06
BO - 82-8	2.99	0.01	3.00	2.98	0.00	0.00	0.00	0.02	0.01	2.01	0.00	0.00	0.00	2.04
BO - 82-9	3.00	0.00	3.00	2.94	0.00	0.00	0.01	0.01	0.01	2.06	0.00	0.00	0.00	2.09
BO-81-1	3.00	0.00	3.00	2.94	0.00	0.00	0.00	0.03	0.02	2.03	0.01	0.00	0.00	2.08
BO-81-2	3.00	0.00	3.00	2.97	0.00	0.00	0.00	0.03	0.02	1.99	0.01	0.00	0.00	2.04
BO-81-3	2.97	0.03	3.00	2.96	0.00	0.00	0.00	0.03	0.02	2.02	0.01	0.00	0.00	2.07
BO-81-4	3.00	0.00	3.00	2.96	0.00	0.00	0.00	0.03	0.02	2.01	0.00	0.00	0.00	2.06
BO-81-5	3.01	0.00	3.01	2.95	0.00	0.00	0.00	0.03	0.02	2.01	0.00	0.00	0.00	2.05
BO-81-6	2.99	0.01	3.00	2.95	0.00	0.00	0.00	0.03	0.02	2.02	0.00	0.00	0.00	2.07
BO-81-7	3.00	0.00	3.00	2.96	0.00	0.00	0.00	0.02	0.02	2.01	0.00	0.00	0.00	2.05
BO-81-8	3.00	0.00	3.00	2.96	0.00	0.00	0.00	0.02	0.02	2.01	0.00	0.00	0.00	2.05
BO-82-1	2.99	0.02	3.00	2.97	0.00	0.00	0.00	0.02	0.01	2.03	0.00	0.00	0.00	2.05
BO-82-2	2.99	0.01	3.00	2.96	0.00	0.00	0.00	0.02	0.01	2.02	0.00	0.00	0.00	2.06
BO-82-3	3.00	0.00	3.00	2.95	0.00	0.00	0.00	0.02	0.01	2.03	0.00	0.00	0.00	2.06
BO-82-4	2.99	0.01	3.00	2.95	0.00	0.00	0.00	0.03	0.01	2.03	0.00	0.00	0.00	2.08
BO-85-1	3.01	0.00	3.01	2.94	0.00	0.01	0.00	0.03	0.01	2.03	0.00	0.00	0.00	2.06
BO-85-2	3.00	0.01	3.00	2.96	0.00	0.00	0.00	0.03	0.00	2.02	0.00	0.00	0.00	2.06
BO-85-3	2.99	0.01	3.00	2.97	0.00	0.00	0.00	0.02	0.00	2.02	0.00	0.00	0.00	2.05
BO-85-4	3.00	0.00	3.00	2.95	0.00	0.00	0.00	0.02	0.01	2.03	0.00	0.00	0.00	2.06
BO-85-5	3.00	0.00	3.00	2.96	0.00	0.00	0.00	0.03	0.00	2.02	0.01	0.00	0.00	2.05
BO-85-6	3.00	0.00	3.00	2.96	0.00	0.00	0.00	0.03	0.00	2.02	0.00	0.00	0.00	2.05
BO-86-1	3.00	0.00	3.00	2.94	0.00	0.01	0.00	0.03	0.00	2.03	0.00	0.00	0.00	2.06
BO-86-2	3.01	0.00	3.01	2.94	0.00	0.01	0.00	0.02	0.00	2.02	0.00	0.00	0.00	2.04
BO-86-3	3.01	0.00	3.01	2.96	0.00	0.00	0.00	0.01	0.00	2.01	0.00	0.00	0.00	2.03
BO-86-4	3.01	0.00	3.01	2.95	0.00	0.00	0.00	0.02	0.00	2.03	0.00	0.00	0.00	2.05
BO-86-5	2.99	0.01	3.00	2.97	0.00	0.00	0.00	0.02	0.00	2.01	0.00	0.00	0.00	2.03
Min	2.97	0.00	3.00	2.94	0.00	0.00	0.00	0.01	0.00	1.99	0.00	0.00	0.00	2.03
Max	3.01	0.03	3.01	2.98	0.00	0.01	0.01	0.03	0.02	2.06	0.01	0.00	0.00	2.09
Mean	3.00	0.00	3.00	2.96	0.00	0.00	0.00	0.02	0.01	2.02	0.00	0.00	0.00	2.06

Table 4. Electron microprobe analyses of yellow / colourless zoisite.

Sample	SiO <sub>2</sub>	Al <sub>2</sub> O <sub>3</sub>	MgO	Na <sub>2</sub> O	FeO	MnO	Cr <sub>2</sub> O <sub>3</sub>	CaO	TiO <sub>2</sub>	K <sub>2</sub> O	V <sub>2</sub> O <sub>3</sub>	Total
BO-53-1	39.60	33.35	0.00	0.02	0.00	0.02	0.00	24.73	0.00	0.01	0.00	97.72
BO-53-2	39.75	33.32	0.04	0.00	0.00	0.07	0.00	24.62	0.00	0.00	0.09	97.90
BO-53-3	40.35	33.31	0.00	0.00	0.01	0.04	0.00	24.65	0.00	0.01	0.02	98.39
BO-55-1	39.32	32.58	0.05	0.02	0.01	0.03	0.00	24.93	0.00	0.00	0.06	96.99
BO-55-2	39.76	33.07	0.00	0.00	0.00	0.07	0.00	24.84	0.00	0.01	0.00	97.74
BO-55-3	39.54	32.86	0.03	0.00	0.00	0.08	0.05	24.74	0.00	0.00	0.00	97.30
BO-56-1	38.85	32.17	0.02	0.00	0.00	0.03	0.00	24.28	0.00	0.00	0.15	95.51
BO-56-10	39.27	32.87	0.00	0.00	0.00	0.00	0.00	24.72	0.00	0.01	0.09	96.95
BO-56-2	39.56	33.23	0.04	0.00	0.02	0.06	0.01	24.65	0.00	0.01	0.01	97.57
BO-56-3	40.01	33.17	0.00	0.00	0.01	0.08	0.06	24.91	0.03	0.00	0.00	98.27
BO-56-4	39.44	33.20	0.02	0.01	0.01	0.05	0.02	24.93	0.00	0.00	0.05	97.71
BO-56-5	39.35	32.69	0.03	0.00	0.00	0.04	0.00	24.43	0.00	0.00	0.00	96.54
BO-56-6	39.42	33.10	0.02	0.03	0.00	0.04	0.03	24.85	0.00	0.00	0.06	97.54
BO-56-7	39.64	32.79	0.02	0.01	0.00	0.00	0.00	24.99	0.00	0.00	0.08	97.53
BO-56-8	39.81	32.89	0.00	0.04	0.00	0.03	0.01	24.82	0.00	0.00	0.03	97.64
BO-56-9	39.23	32.62	0.03	0.00	0.00	0.04	0.00	24.54	0.00	0.00	0.00	96.46
BO-95-2	40.33	33.33	0.05	0.00	0.00	0.06	0.00	24.71	0.00	0.00	0.00	98.48
BO-95-3	39.55	33.02	0.00	0.02	0.02	0.01	0.00	24.87	0.00	0.00	0.00	97.47
BO-95-4	39.37	32.89	0.01	0.00	0.00	0.05	0.03	24.92	0.00	0.01	0.00	97.28
BO-95-5	39.75	33.45	0.03	0.00	0.00	0.08	0.03	24.77	0.00	0.01	0.01	98.14
BO-95-6	38.94	32.70	0.01	0.00	0.03	0.06	0.01	24.63	0.00	0.00	0.00	96.37
Min	38.85	32.17	0.00	0.00	0.00	0.00	0.00	24.28	0.00	0.00	0.00	95.51
Max	40.35	33.45	0.05	0.04	0.03	0.08	0.06	24.99	0.03	0.01	0.15	98.48
Mean	39.56	32.98	0.03	0.02	0.01	0.05	0.02	24.74	0.03	0.01	0.05	97.50

Sample	Si	Al IV	Sum_T	Al VI	Ti	Cr	Fe <sup>2+</sup>	Mn	Mg	Ca	Na	K	V	Sum_B
BO-53-1	3.01	0.00	3.01	2.98	0.00	0.00	0.00	0.00	0.00	2.01	0.00	0.00	0.00	2.01
BO-53-2	3.01	0.00	3.01	2.97	0.00	0.00	0.00	0.00	0.01	2.00	0.00	0.00	0.01	2.01
BO-53-3	3.04	0.00	3.04	2.95	0.00	0.00	0.00	0.00	0.00	1.99	0.00	0.00	0.00	1.99
BO-55-1	3.01	0.00	3.01	2.94	0.00	0.00	0.00	0.00	0.01	2.05	0.00	0.00	0.00	2.06
BO-55-2	3.02	0.00	3.02	2.96	0.00	0.00	0.00	0.00	0.00	2.02	0.00	0.00	0.00	2.03
BO-55-3	3.02	0.00	3.02	2.95	0.00	0.00	0.00	0.01	0.00	2.02	0.00	0.00	0.00	2.03
BO-56-1	3.02	0.00	3.02	2.94	0.00	0.00	0.00	0.00	0.00	2.02	0.00	0.00	0.01	2.03
BO-56-10	3.01	0.00	3.01	2.96	0.00	0.00	0.00	0.00	0.00	2.03	0.00	0.00	0.01	2.03
BO-56-2	3.01	0.00	3.01	2.98	0.00	0.00	0.00	0.00	0.00	2.01	0.00	0.00	0.00	2.02
BO-56-3	3.02	0.00	3.02	2.95	0.00	0.00	0.00	0.01	0.00	2.02	0.00	0.00	0.00	2.02
BO-56-4	3.00	0.00	3.00	2.97	0.00	0.00	0.00	0.00	0.00	2.03	0.00	0.00	0.00	2.04
BO-56-5	3.02	0.00	3.02	2.96	0.00	0.00	0.00	0.00	0.00	2.01	0.00	0.00	0.00	2.02
BO-56-6	3.00	0.00	3.00	2.97	0.00	0.00	0.00	0.00	0.00	2.03	0.00	0.00	0.00	2.04
BO-56-7	3.02	0.00	3.02	2.94	0.00	0.00	0.00	0.00	0.00	2.04	0.00	0.00	0.00	2.04
BO-56-8	3.03	0.00	3.03	2.94	0.00	0.00	0.00	0.00	0.00	2.02	0.01	0.00	0.00	2.03
BO-56-9	3.02	0.00	3.02	2.96	0.00	0.00	0.00	0.00	0.00	2.02	0.00	0.00	0.00	2.03
BO-95-2	3.03	0.00	3.03	2.95	0.00	0.00	0.00	0.00	0.01	1.99	0.00	0.00	0.00	2.00
BO-95-3	3.01	0.00	3.01	2.96	0.00	0.00	0.00	0.00	0.00	2.03	0.00	0.00	0.00	2.03
BO-95-4	3.01	0.00	3.01	2.96	0.00	0.00	0.00	0.00	0.00	2.04	0.00	0.00	0.00	2.04
BO-95-5	3.01	0.00	3.01	2.98	0.00	0.00	0.00	0.01	0.00	2.01	0.00	0.00	0.00	2.02
BO-95-6	3.00	0.00	3.00	2.97	0.00	0.00	0.00	0.00	0.00	2.03	0.00	0.00	0.00	2.04
Min	3.00	0.00	3.00	2.94	0.00	0.00	0.00	0.00	0.00	1.99	0.00	0.00	0.00	1.99
Max	3.04	0.00	3.04	2.98	0.00	0.00	0.00	0.01	0.01	2.05	0.01	0.00	0.01	2.06
Mean	3.01	0.00	3.01	2.96	0.00	0.00	0.00	0.00	0.00	2.02	0.00	0.00	0.00	2.03

## **Addendum L**

Table 1. Laser ablation ICP-MS analyses of blue zoisite (tanzanite).

Table 2. Laser ablation ICP-MS analyses of green zoisite.

Table 3. Laser ablation ICP-MS analyses of orange zoisite.

Table 4. Laser ablation ICP-MS analyses of colourless zoisite.

Table 5. Laser ablation ICP-MS analyses of “golden” zoisite.

Table 1. Laser ablation ICP-MS analyses of blue zoisite (tanzanite).

Sample	62	63	64	65	66	67		100
Sc	23	24	16	45	11	20	Sc	26
Ti	617	549	577	593	721	543	Ti	653
V	1641	1369	1594	2177	1481	2243	V	1798
Cr	126	103	128	158	133	164	Cr	134
Fe	44	75	75	69	37	15	Fe	-11
Co	0	0	0	0	0	0	Zn	-2
Ni	1	0	0	0	0	0	Ga	135
Cu	0	0	0	0	0	0	Sr	1264
Zn	5	5	3	2	1	1	Y	322
Ga	116	204	122	111	118	116	Zr	37
Rb	0	0	0	0	0	0	La	3
Sr	1843	2593	1911	1350	2528	2737	Ce	13
Y	101	72	87	109	176	170	Pr	3
Zr	25	23	17	31	42	12	Nd	23
Cs	0	0	0	0	0	0	Sm	15
La	87	62	38	61	49	75	Eu	5
Ce	141	114	71	99	93	137	Gd	26
Pr	16	15	9	12	14	18	Tb	6
Nd	67	64	40	49	79	78	Dy	43
Sm	19	16	11	15	29	21	Ho	9
Eu	5	4	2	4	6	5	Er	23
Gd	20	16	13	17	32	24	Tm	3
Dy	18	14	14	18	29	27	Yb	17
Er	8	5	7	9	15	14	Lu	2
Yb	5	3	6	6	12	9	Hf	2
Lu	1	0	1	1	1	1	Ta	0
Hf	1	1	1	1	2	1	Pb	-4
Pb	0	1	0	0	0	0		
TREE	386	314	213	293	361	409		193
n	1	1	2	2	1	2	n	3

Table 1. Continue 1.

Sample	Ti	V	Cr	Mn	Co	Ni	Ga	Rb	Sr	Y	Th	U	colour
31A	331	1440	122	68	0	2	97	0	1536	124	9	14	light blue
31B	330	1431	118	69	0	4	92	0	1538	122	9	14	light blue
32A	323	1046	56	88	0	0	227	0	4037	47	18	23	light blue
32B	314	972	53	88	0	0	233	0	4058	44	21	25	light blue
13A	333	1205	93	66	0	0	122	0	1844	48	8	13	light blue
13B	405	1040	80	67	1	0	116	0	2410	47	5	11	light blue
8A	291	1305	106	92	0	0	136	0	1871	62	5	14	light blue
8B	299	1298	107	95	0	0	138	0	1947	62	5	14	light blue
Average	328	1217	92	79	0	1	145	0	2405	69	10	16	light blue

Sample	Ti	V	Cr	Mn	Co	Ni	Ga	Rb	Sr	Y	Th	U	colour
5A	283	1844	138	80	1	0	107	0	935	67	5	15	blue
5B	298	1804	136	83	1	1	104	0	999	68	5	16	blue
6B	285	2015	158	69	0	1	99	0	792	77	10	15	blue
7A	289	2000	180	75	0	1	90	0	1311	148	3	22	blue
7B	263	1680	161	60	0	0	80	0	1258	115	2	15	blue
10A	307	1791	137	90	0	1	112	0	1102	68	4	16	blue
10B	301	1702	131	93	0	1	109	0	1155	70	4	16	blue
11A	258	1333	115	69	0	-1	108	0	1568	60	6	8	blue
11B	260	1365	117	69	0	1	107	0	1541	59	6	8	blue
12A	235	1863	139	30	0	1	98	0	2229	116	8	18	blue
12B	214	1744	140	30	0	0	105	0	2081	92	5	12	blue
14A	260	1449	129	72	0	0	114	0	1506	63	4	10	blue
14B	261	1367	119	72	0	1	112	0	1505	58	3	9	blue
15A	340	1739	136	54	1	0	95	-1	1010	80	7	11	blue
15B	332	1712	141	57	1	3	92	0	1002	79	7	11	blue
16A	253	1720	137	66	1	2	102	-1	1396	72	5	12	blue
16B	268	1815	155	69	1	1	105	-1	1386	84	6	15	blue
17A	283	1751	121	67	0	0	87	-1	1218	102	5	10	blue
17B	277	1983	122	62	1	0	101	-1	1268	86	3	8	blue
18A	302	2132	157	74	0	3	87	-1	849	92	10	17	blue
18B	295	2239	168	76	1	0	98	-1	874	85	10	19	blue
18C	290	2141	217	82	2	6	91	-1	831	86	10	18	blue
19A	257	2080	168	52	1	0	95	-1	1380	64	33	11	blue
19B	240	2049	156	54	1	0	94	-1	1369	66	35	9	blue
20A	265	1556	126	65	0	0	91	-2	1395	83	15	8	blue
20B	262	1503	128	67	0	1	92	-2	1391	77	14	7	blue
21A	147	1389	84	5	0	1	81	-1	1358	105	10	3	blue
21B	169	1208	86	5	0	-1	80	-2	1557	106	13	3	blue
21C	176	1188	98	6	0	0	75	-1	1598	97	10	4	blue
27A	345	1363	75	65	0	0	106	0	1607	71	7	12	blue
27B	409	1400	77	65	0	0	102	0	1730	82	7	12	blue
28A	284	1655	102	62	0	0	101	0	1322	100	11	21	blue
28B	277	1584	100	71	0	1	103	0	1449	79	6	12	blue
37E	369	1605	161	55	0	1	93	-2	1347	95	8	12	blue
35B	302	1767	136	90	0	1	113	0	1210	72	5	15	blue
35C	377	1343	110	62	0	1	102	0	1407	80	8	11	blue
35D	151	1136	100	12	0	1	97	0	1822	97	13	6	blue
38C	291	2291	301	66	0	0	94	-2	854	95	21	16	blue
38D	264	2139	162	63	0	1	91	0	780	79	18	15	blue
38E	282	2199	164	63	0	0	92	0	810	82	18	16	blue
38F	280	2149	158	65	0	0	88	0	831	81	18	16	blue
38G	271	2205	163	66	1	1	94	0	804	87	19	16	blue
38H	283	2147	168	62	0	0	90	0	810	87	19	16	blue
39E	242	1709	134	31	0	0	67	0	1839	59	32	5	blue
39F	252	1714	132	36	0	1	68	0	1830	70	27	5	blue
39G	241	1673	137	36	0	0	73	0	1835	51	35	4	blue
39H	240	1707	140	40	0	0	80	0	1808	59	25	5	blue
Average	273	1744	139	59	0	1	95	0	1318	82	12	12	blue

Table 1. Continue 2.

Elements	50-1(blue)	50-2(blue)	50-3(clear)	50-4(clear)	50-5(clear)	50-6(clear)	50-7(clear)	50-8(clear)	50-9(clear)	50-10(clear)	50-11(clear)	50-12(clear)	50-13(clear)	50-14(clear)
Sc	4	7	1	0	0	0	0	-1	-1	-1	0	0	0	0
Ti	480	491	529	546	511	505	561	527	531	518	534	535	527	517
V	1167	1875	279	224	237	266	193	240	259	403	300	393	415	525
Cr	84	120	15	12	15	17	12	15	13	19	18	17	18	28
Fe	11	18	5	13	9	-2	4	2	-11	-15	-3	-2	-5	-16
Co	0	0	0	0	0	0	0	0	0	0	0	0	0	0
Ni	1	0	-1	-1	0	0	0	-1	-1	-1	-1	-2	-2	-1
Cu	0	0	0	0	0	0	0	1	0	0	0	1	1	1
Zn	0	1	1	2	0	-1	-1	-1	0	0	-2	2	0	0
Ga	71	85	72	74	80	88	76	82	83	83	86	98	95	101
Rb	0	0	0	0	0	0	0	0	0	0	0	0	0	0
Sr	1639	1804	1765	1796	1831	1530	1742	1874	1853	1831	1924	2366	2118	2047
Y	107	67	42	41	19	28	42	34	41	44	47	35	39	51
Zr	1	1	3	3	1	2	3	2	2	2	2	8	6	5
Cs	0	0	0	0	0	0	0	0	0	0	0	0	0	0
La	38	20	7	6	3	2	5	5	5	5	6	6	8	11
Ce	52	28	11	9	5	3	8	7	8	8	10	10	12	15
Pr	6	3	1	1	1	0	1	1	1	1	1	1	1	2
Nd	23	13	5	4	2	1	4	4	4	4	4	5	5	7
Sm	5	3	1	1	1	1	1	1	1	1	1	1	1	2
Eu	1	1	1	1	0	0	1	1	1	1	1	1	1	1
Gd	7	5	2	2	1	1	2	1	2	2	2	2	2	2
Dy	12	7	4	4	2	2	4	3	4	4	4	3	4	5
Er	10	6	4	4	2	3	4	3	4	4	5	3	4	5
Yb	8	5	4	4	2	4	5	4	5	6	7	4	5	6
Lu	1	1	0	0	0	1	1	1	1	1	1	1	1	1
Hf	0	0	0	0	0	0	0	0	0	0	0	0	0	1
Pb	0	-1	-1	-1	-1	-1	-2	-1	-2	-2	-2	-2	-2	-3
TREE	164	91	40	36	19	18	35	30	36	38	42	38	44	56

Table 1. Continue 3.

Elements	50-15(clear)	50-16(blue)	50-17(blue)	50-18(blue)	50-19(blue)	50-20(blue)	50-21(blue)	50-22(blue)	50-23(blue)	50-24(blue)	50-25(blue)	50-26(blue)	50-27(blue)
<b>Sc</b>	0	5	18	15	22	21	20	22	21	13	18	13	11
<b>Ti</b>	533	522	599	536	615	614	610	608	618	603	627	683	685
<b>V</b>	789	6196	1618	4813	1727	1720	1716	1689	1702	1477	1682	1394	1302
<b>Cr</b>	52	431	148	341	148	150	146	145	148	140	141	127	126
<b>Fe</b>	-17	-1	44	10	60	59	41	53	63	36	43	42	42
<b>Co</b>	0	0	0	0	0	0	0	0	0	0	0	0	0
<b>Ni</b>	-2	-2	-1	-1	-2	-1	0	-1	-1	-1	0	0	-2
<b>Cu</b>	1	1	1	1	1	0	1	1	0	0	0	0	1
<b>Zn</b>	0	-1	0	0	2	1	1	2	3	1	2	1	1
<b>Ga</b>	99	129	140	133	146	149	146	152	152	140	153	137	143
<b>Rb</b>	0	0	0	0	0	0	0	0	0	0	0	0	0
<b>Sr</b>	1978	2290	1759	2054	1847	1821	1827	1828	1837	1708	1869	1764	1724
<b>Y</b>	110	294	118	242	126	124	123	121	122	107	124	149	158
<b>Zr</b>	2	1	21	5	24	24	23	24	24	15	23	30	32
<b>Cs</b>	0	0	0	0	0	0	0	0	0	0	0	0	0
<b>La</b>	40	166	33	365	36	32	32	30	30	23	30	39	39
<b>Ce</b>	56	221	68	505	74	70	67	63	64	49	64	83	84
<b>Pr</b>	6	23	9	53	10	10	10	9	9	7	9	12	12
<b>Nd</b>	23	85	46	195	48	46	45	43	42	33	42	54	56
<b>Sm</b>	5	17	13	35	14	13	13	12	13	11	12	16	18
<b>Eu</b>	2	4	3	5	3	3	3	3	3	3	3	4	4
<b>Gd</b>	6	24	15	33	16	16	15	16	16	13	15	19	22
<b>Dy</b>	10	38	17	34	19	18	18	18	18	16	19	23	24
<b>Er</b>	10	22	10	19	10	10	10	10	10	9	10	13	13
<b>Yb</b>	11	14	7	12	8	8	7	8	7	7	8	10	10
<b>Lu</b>	2	2	1	2	1	1	1	1	1	1	1	1	1
<b>Hf</b>	0	0	1	0	1	1	1	1	1	1	1	1	1
<b>Pb</b>	-2	-1	-1	0	-2	-2	-1	-2	-2	-2	-2	-2	-2
<b>TREE</b>	171	617	224	1256	241	228	222	214	213	174	215	274	286

Table 2. Laser ablation ICP-MS analyses of green zoisite.

Sample	89	89	89	89	89	91	91	91	91	91	91	Sample	90	61	61	61
	Blue-1	Blue-2	Blue-3	Green-1	Green-2	Green-4	Blue-1	Blue-2	Green-1	Green-2	Green-3			Green-1	Blue	Blue-1
Sc	0	-1	0	0	-1	-1	-1	0	1	-1	-1	Sc	-1	23	16	19
Ti	504	503	504	512	620	547	508	516	610	785	545	Ti	538	586	652	658
V	2629	2151	2609	2492	2218	1802	2065	2098	1641	1306	1306	V	2037	1506	1429	1475
Cr	123	117	121	113	101	109	75	98	71	58	41	Cr	53	104	101	100
Fe	18	6	2	13	10	-5	17	-3	-8	-5	-4	Fe	11	67	34	38
Zn	-3	-3	-2	-4	-4	27	-2	-3	-5	-2	-3	Zn	-1	-1	-4	-2
Ga	142	143	143	141	130	126	146	155	146	127	123	Ga	129	203	200	199
Sr	530	467	536	560	688	675	856	584	1094	1420	1034	Sr	604	2580	3040	3047
Y	13	13	18	14	21	15	15	20	29	39	14	Y	8	46	58	54
Zr	3	2	3	3	18	19	5	3	24	48	16	Zr	5	15	20	22
La	2	2	11	9	9	2	16	12	31	19	7	La	2	299	535	574
Ce	5	4	22	18	17	5	28	21	48	29	12	Ce	5	454	792	870
Pr	1	1	3	2	2	1	3	3	5	4	1	Pr	1	48	83	90
Nd	3	2	11	9	9	3	12	10	20	14	6	Nd	4	172	283	301
Sm	1	1	2	2	2	1	2	2	4	3	1	Sm	1	26	41	44
Eu	2	1	2	2	2	1	2	1	2	2	1	Eu	1	6	9	9
Gd	1	1	2	2	2	1	2	2	3	2	1	Gd	1	18	25	25
Tb	0	0	0	0	0	0	0	0	0	0	0	Tb	0	2	3	3
Dy	2	1	3	2	3	2	2	2	3	4	2	Dy	1	10	14	13
Ho	0	0	1	1	1	1	1	1	1	1	1	Ho	0	2	2	2
Er	1	1	2	1	2	2	1	2	3	4	2	Er	1	3	4	4
Tm	0	0	0	0	0	0	0	0	1	1	0	Tm	0	0	0	0
Yb	1	1	1	1	3	3	1	2	3	6	2	Yb	1	2	2	2
Lu	0	0	0	0	0	0	0	0	1	1	0	Lu	0	0	0	0
Hf	0	0	0	0	1	1	0	0	1	2	1	Hf	0	1	1	1
Ta	0	0	0	0	0	0	0	0	0	0	0	Ta	0	0	0	0
Pb	-2	-2	-1	-2	-2	-2	-3	-2	-2	-4	-3	Pb	-2	-3	-3	-3
TREE	20	16	60	50	54	23	72	58	126	92	38	TREE	19	1044	1795	1939
												n	4			



Table 2. Continued.

Sample	69	70	71	58	58	58	58	68	68	68
				green-1	green-2	green-3	blue-1	green-1	blue-1	green-2
Sc	15	24	0	2	0	0	0	0	0	0
Ti	540	571	982	907	967	984	884	960	801	939
V	2078	2586	1366	1227	1690	1673	2089	1551	2271	1154
Cr	168	208	160	158	169	178	213	180	237	149
Fe	11	18	15	26	-6	1	-3	7	6	-7
Co	0	0	0	1	0	0	0	0	0	0
Ni	-1	-1	0	3	-1	0	0	0	0	0
Cu	0	0	0	3	-1	1	1	0	0	0
Zn	1	3	0	4	0	2	3	2	1	2
Ga	218	174	109	102	116	125	138	119	143	86
Rb	0	0	0	0	0	0	0	0	0	0
Sr	2240	1785	3072	2755	2741	3177	2880	3263	2691	2949
Y	130	175	98	113	74	79	108	105	165	116
Zr	11	24	94	92	103	104	86	100	74	73
Cs	0	0	0	0	0	0	0	0	0	0
La	17	23	3	3	4	4	9	6	10	6
Ce	31	45	7	7	7	8	17	11	18	11
Pr	5	7	1	1	1	1	2	1	2	2
Nd	25	32	5	6	5	6	10	8	11	8
Sm	11	12	3	3	2	2	4	3	5	3
Eu	3	3	3	3	3	3	4	3	5	3
Gd	17	18	5	6	4	4	6	5	8	6
Dy	21	26	11	12	9	9	13	11	19	12
Er	11	15	12	13	8	9	12	13	19	13
Yb	9	13	18	20	11	13	17	21	25	18
Lu	1	2	3	3	2	2	2	3	4	3
Hf	1	1	2	2	2	2	2	2	2	2
Pb	-1	-1	-1	-1	-2	-2	-2	-2	-2	-2
<b>TREE</b>	152	197	72	80	57	64	99	87	126	85
n	2	1	3							

Table 3. Laser ablation ICP-MS analyses of orange zoisites.

Sample	80	81	82	83	84	85	86	87	88	Sample	54
<b>Sc</b>	17	33	16	20	14	7	22	7	19	<b>Cu</b>	0
<b>Ti</b>	538	574	623	568	542	619	580	607	578	<b>Ti</b>	595
<b>V</b>	554	903	1272	996	1065	745	1028	819	909	<b>V</b>	1016
<b>Cr</b>	29	55	78	65	58	31	68	32	63	<b>Cr</b>	54
<b>Fe</b>	208	86	15	34	257	99	27	99	43	<b>Fe</b>	241
<b>Zn</b>	22	5	-1	1	18	4	1	4	2	<b>Zn</b>	18
<b>Ga</b>	298	349	254	295	231	257	286	256	322	<b>Ga</b>	255
<b>Sr</b>	3316	3286	3656	3575	4643	3806	3590	3614	3284	<b>Sr</b>	4489
<b>Y</b>	17	39	67	39	15	23	43	19	38	<b>Y</b>	16
<b>Zr</b>	9	19	28	15	13	29	19	24	16	<b>Zr</b>	16
<b>La</b>	5527	2020	678	1413	5368	1466	1496	1869	1422	<b>La</b>	5050
<b>Ce</b>	4208	2945	997	1953	4862	1965	2048	2540	2284	<b>Ce</b>	5010
<b>Pr</b>	868	297	107	195	500	196	200	248	252	<b>Pr</b>	470
<b>Nd</b>	2333	896	372	615	1312	623	622	761	839	<b>Nd</b>	1273
<b>Sm</b>	146	85	50	66	88	66	63	75	90	<b>Sm</b>	86
<b>Eu</b>	14	13	9	11	11	12	11	13	14	<b>Eu</b>	11
<b>Gd</b>	41	33	31	30	26	29	29	29	38	<b>Gd</b>	27
<b>Tb</b>	3	3	4	3	2	2	3	2	3	<b>Dy</b>	5
<b>Dy</b>	6	10	16	10	5	8	11	7	11	<b>Er</b>	1
<b>Ho</b>	1	1	2	1	1	1	2	1	1	<b>Yb</b>	0
<b>Er</b>	1	3	4	3	1	1	3	1	2	<b>Lu</b>	0
<b>Tm</b>	0	0	0	0	0	0	0	0	0	<b>Hf</b>	1
<b>Yb</b>	0	1	2	1	0	0	2	0	1	<b>Cs</b>	0
<b>Lu</b>	0	0	0	0	0	0	0	0	0	<b>Rb</b>	0
<b>Hf</b>	0	1	1	1	1	1	1	1	1	<b>Co</b>	0
<b>Ta</b>	0	0	0	0	0	0	0	0	0	<b>Ni</b>	1
<b>Pb</b>	22	4	-1	-1	8	0	-1	1	2	<b>Pb</b>	8
<b>TREE</b>	13148	6309	2275	4301	12177	4371	4490	5547	4960	<b>TREE</b>	11935
<b>n</b>	5	3	2	2	4	2	2	2	2		4

Table 4. Laser ablation ICP-MS analyses of colourless zoisites.

Sample	92	92	92	92	92	92	99
	Blue-1	Colourless-1	Colourless-2	Colourless-3	Blue-2	Blue-3	Colourless
Sc	4	3	3	1	3	0	5
Ti	501	528	500	520	484	465	524
V	1353	584	507	664	1602	4454	487
Cr	54	23	22	22	36	103	25
Fe	15	2	3	59	-13	2	-2
Zn	0	-2	-2	95	-1	-1	-3
Ga	131	99	98	95	131	115	87
Sr	2434	2664	1939	2427	2320	1737	2950
Y	35	34	74	27	47	79	37
Zr	1	2	1	3	1	0	8
La	13	22	16	18	14	42	36
Ce	20	35	26	25	20	58	48
Pr	2	4	3	3	2	7	5
Nd	9	14	12	10	9	30	16
Sm	2	3	3	2	2	9	3
Eu	1	1	1	1	2	3	1
Gd	3	3	3	2	3	11	3
Tb	0	1	1	0	1	2	0
Dy	4	4	7	3	5	13	4
Ho	1	1	2	1	1	3	1
Er	3	3	7	2	5	6	3
Tm	0	0	1	0	1	1	0
Yb	3	2	10	2	5	3	3
Lu	0	0	2	0	1	0	0
Hf	0	0	0	0	0	0	0
Ta	0	0	0	0	0	0	0
Pb	3	-2	-3	-2	-3	-2	-3
TREE	63	94	93	71	71	187	123
n	1	1	1	1	1	1	2

Sample	Ti	V	Cr	Mn	Co	Ni	Ga	Rb	Sr	Y	Th	U
4A	221	147	44	16	0	3	54	0	1479	42	3	27
4B	242	151	23	17	0	3	58	1	1613	44	6	33
34B	192	945	90	38	0	1	162	0	1193	60	24	24
34C	200	937	85	35	0	1	162	0	1327	56	36	23
35A	172	429	48	12	0	0	75	0	1795	61	14	9
37A	182	194	27	15	0	-1	63	-2	1585	33	2	14
37B	261	158	43	11	1	2	64	-3	1639	37	3	14
37C	188	383	46	14	0	1	76	-2	1803	41	2	22
37D	204	431	72	9	0	0	75	-2	2142	99	2	12
37F	243	173	64	7	3	1	57	-2	2879	59	2	9
37G	246	185	72	6	1	1	59	-2	2884	58	2	9
37H	242	197	92	8	0	-1	62	-2	2962	61	2	10
37I	241	203	86	8	0	0	64	-2	2870	64	2	10
37J	238	204	120	8	0	-1	64	-2	2883	53	2	9
37K	208	272	112	13	0	0	72	-2	2247	38	3	11
37L	252	216	118	8	0	1	64	-2	2979	56	3	8
38A	209	343	146	19	0	-1	77	-2	1869	36	2	14
38B	211	724	199	25	0	0	81	-2	1807	43	7	16
39A	171	412	14	16	0	-1	76	0	1902	19	0	10
39B	218	325	25	10	0	1	72	0	2559	35	1	7
39C	205	350	28	10	0	1	77	0	2402	36	1	6
39D	195	472	37	11	0	0	80	0	2369	50	3	6

Table 4. Continued.

<b>Sample 60</b>	<b>60 Blue-1</b>	<b>60 Colourless-1</b>	<b>60 Blue-2</b>	<b>60 Colourless-2</b>	<b>60 Blue-3</b>
<b>Sc</b>	22	0	25	2	21
<b>Ti</b>	663	501	642	496	649
<b>V</b>	1857	256	1938	424	1840
<b>Cr</b>	140	15	146	16	137
<b>Fe</b>	43	0	40	-12	32
<b>Co</b>	0	0	0	0	0
<b>Ni</b>	0	2	0	0	0
<b>Cu</b>	-1	1	0	0	0
<b>Zn</b>	3	4	2	3	2
<b>Ga</b>	106	82	110	92	108
<b>Rb</b>	0	0	0	0	0
<b>Sr</b>	1456	1704	1434	2005	1418
<b>Y</b>	125	55	122	65	120
<b>Zr</b>	28	2	27	2	27
<b>Cs</b>	0	0	0	0	0
<b>La</b>	106	6	94	8	103
<b>Ce</b>	172	8	158	12	169
<b>Pr</b>	21	1	19	1	21
<b>Nd</b>	88	4	81	6	87
<b>Sm</b>	23	1	20	2	23
<b>Eu</b>	6	1	5	1	5
<b>Gd</b>	24	2	21	2	23
<b>Dy</b>	22	4	21	5	21
<b>Er</b>	10	5	10	6	9
<b>Yb</b>	6	6	6	7	6
<b>Lu</b>	1	1	1	1	1
<b>Hf</b>	1	0	1	0	1
<b>Pb</b>	-2	-3	-2	-4	-2
<b>TREE</b>	480	40	437	50	470

Table 5. Laser ablation ICP-MS analyses of “golden” zoisites.

Sample	Ti	V	Cr	Mn	Co	Ni	Ga	Rb	Sr	Y	Th	U
9A	450	1166	111	61	0	1	106	0	2040	121	8	13
9B	466	1191	115	64	0	1	109	0	2109	120	6	12
22A	122	2083	136	12	2	3	89	0	1478	60	25	7
22B	149	2024	153	10	0	0	86	0	1543	87	21	5
23A	282	1125	63	83	0	0	133	0	2348	54	5	8
23B	298	1074	54	82	0	0	149	0	2203	62	4	12
24A	312	1340	75	97	0	1	157	0	2078	67	5	13
24B	313	1363	80	95	0	0	162	0	2076	69	5	13
25A	354	1165	68	70	0	0	182	0	2921	68	7	18
25B	288	1216	76	94	0	0	169	0	2374	50	3	9
26A	296	1227	92	77	0	1	106	0	1765	83	6	12
26B	299	1242	86	81	0	-1	112	0	1693	87	6	14
29A	313	1352	58	75	0	2	190	0	2371	58	8	20
29B	434	1112	26	62	0	0	174	0	3275	77	13	15
30A	267	1265	104	81	0	1	126	0	1692	59	3	10
30B	269	1279	95	81	0	1	123	0	1706	58	3	10
33A	458	1263	78	56	0	1	107	0	2238	98	20	17
33B	460	1260	63	59	0	1	111	0	2292	91	22	16
34A	212	1410	145	42	0	0	147	0	1109	76	9	23

Sample	53	55	56	Sample	95	96	97	98
Sc	17	22	14	Sc	25	17	27	16
Ti	559	567	627	Ti	592	594	605	567
V	1472	1675	1741	V	1640	1688	1500	1614
Cr	147	188	149	Cr	115	127	101	138
Fe	33	30	30	Fe	44	40	76	94
Co	0	0	0	Zn	2	1	1	1
Ni	0	1	0	Ga	154	125	209	100
Cu	0	0	0	Sr	3185	1949	2864	2330
Zn	3	3	2	Y	93	92	47	96
Ga	216	242	221	Zr	21	21	19	9
Rb	0	0	0	La	67	43	537	97
Sr	2778	2598	2930	Ce	123	91	761	171
Y	148	192	183	Pr	16	12	79	21
Zr	15	14	23	Nd	66	57	279	92
Cs	0	0	0	Sm	15	13	39	21
La	374	243	107	Eu	3	3	8	4
Ce	689	469	217	Gd	16	14	23	22
Pr	89	64	31	Tb	3	2	3	3
Nd	367	283	143	Dy	16	14	11	18
Sm	77	74	41	Ho	3	3	2	3
Eu	14	15	10	Er	7	8	3	7
Gd	64	70	45	Tm	1	1	0	1
Dy	36	44	38	Yb	4	7	2	5
Er	10	13	13	Lu	1	1	0	1
Yb	5	7	7	Hf	1	1	1	0
Lu	1	1	1	Ta	0	0	0	0
Hf	1	1	1	Pb	-1	-2	-1	0
Pb	2	0	-1					
TREE	1726	1283	656	TREE	340	269	1748	468
n	2	2	2	n	2	2	2	2

Table 5. Continued.

Sample	59		59		Sample	59b	
	Golden-1	Blue-1	Golden-2	Blue-2		Golden-1	Blue-1
Sc	14	8	14	9	Sc	17	11
Ti	591	687	579	670	Ti	570	665
V	1548	1863	1516	1820	V	1526	1848
Cr	153	151	152	140	Cr	162	157
Fe	62	-18	7	-8	Fe	20	14
Zn	-2	-4	0	-4	Zn	2	3
Ga	248	196	245	208	Ga	230	196
Sr	2887	3173	2947	3221	Sr	2934	3119
Y	188	227	165	203	Y	174	238
Zr	12	23	11	22	Zr	13	27
La	414	36	508	31	La	517	44
Ce	773	71	946	63	Ce	931	78
Pr	103	11	122	10	Pr	119	11
Nd	434	58	501	55	Nd	490	59
Sm	96	26	101	24	Sm	100	26
Eu	18	6	18	6	Eu	19	6
Gd	81	35	79	33	Gd	83	38
Tb	11	6	10	5	Dy	45	37
Dy	48	37	43	33	Er	11	21
Ho	7	8	6	7	Yb	4	17
Er	12	20	11	18	Lu	1	2
Tm	1	3	1	2	Hf	1	1
Yb	5	16	4	14	Pb	2	-2
Lu	1	2	1	2	Co	0	0
Hf	1	1	1	1	Ni	0	1
Ta	0	0	0	0	Cu	0	1
Pb	0	-4	0	-4	Rb	0	0
TREE	2004	336	2351	305	TREE	2320	339